

How social stigma can  
amplify a pandemic p. 1419

Diet, microbiota, and kidney  
disease pp. 1426 & 1518

Binary companions shape  
stellar winds p. 1497

# Science

\$15  
18 SEPTEMBER 2020  
[sciencemag.org](https://www.sciencemag.org)

AAAS

## PLASTIC POLLUTION

Prospects for managing growing amounts of waste

pp. 1455 & 1515





# CONTENTS

18 SEPTEMBER 2020 • VOLUME 369 • ISSUE 6510

## 1419

Stigma adds to the anguish of an HIV-positive woman.

## NEWS

### IN BRIEF

**1410** News at a glance

### IN DEPTH

#### **1412** Pandemic inspires push to shrink jails, prisons

New research focuses on the health and public safety impacts of “decarceration” *By K. Servick*

PODCAST

#### **1414** Viral heart damage under scrutiny

Researchers are hunting for myocarditis in COVID-19 survivors *By J. Couzin-Frankel*

#### **1415** Trials begin for a new weapon against Parkinson’s: light

Patients report benefits, but how near-infrared protects brain cells is unclear, and some scientists are skeptical *By G. Sinha*

#### **1416** Ancient DNA tracks Vikings across Europe

Massive sequencing effort shows people of diverse genetic backgrounds adopted Viking culture *By A. Curry*

#### **1418** Global efforts to protect biodiversity fall short

New report finds glimmers of progress, but nations are not achieving targets *By E. Stokstad*

### FEATURES

#### **1419** The burden of stigma

Past epidemics reveal how social stigma amplifies the dangers of infectious disease *By V. Chandrasekhar*

## INSIGHTS

### PERSPECTIVES

#### **1424** An unexpected audience

Experiments with magic effects might be informative about cognition in animals *By E. Garcia-Pelegrin et al.*

PODCAST

#### **1426** The gut microbiota in kidney disease

Dietary changes induce posttranslational modifications of microbial proteins to alter metabolite production *By J. L. Pluznick*

REPORT p. 1518

#### **1427** Messengers from the microbiota

Microbiota produce inosine, a metabolite that modulates effector T cells and tumor immunity *By F. Y. Shaikh and C. L. Sears*

REPORT p. 1481

#### **1429** Protecting the sewershed

As cities use sewage as a water source, proactive policies must safeguard public health *By S. Harris-Lovett and D. Sedlak*

#### **1431** Tempus fugit: How time flies during development

Developmental-timing differences between species are linked to protein turnover

*By R. Iwata and P. Vanderhaeghen*

RESEARCH ARTICLES pp. 1449 & 1450

#### **1432** Multiplicative suppression of decoherence

Combining different protocols extends the life of a quantum system

*By P. Hemmer*

REPORT p. 1493

#### **1433** Advance in global ocean acoustics

Earthquakes can be used to define changes in ocean heat content *By C. Wunsch*

REPORT p. 1510

### POLICY FORUM

#### **1435** Global citizen deliberation on genome editing

Global governance can be informed by a deliberative assembly composed of lay citizens *By J. S. Dryzek et al.*

### BOOKS ET AL.

#### **1438** Why the West is WEIRD

Catholicism’s policy forbidding cousins to wed may have led to the distinctive characteristics of Western society *By P. Grosjean*



**1439 A case study of Oliver Sacks**

Interviews and archival footage paint a tender portrait of neurology's greatest storyteller *By L. J. Snyder*

**LETTERS****1440 Portugal's airport plans threaten wetlands**

*By J. A. Alves and M. P. Dias*

**1440 Systemic racism in higher education**

*By P. H. Barber et al.*

**1441 University-pharmacy partnerships for COVID-19**

*By V. J. Venditto et al.*

**RESEARCH****IN BRIEF**

**1443** From *Science* and other journals

**REVIEW****1446 Urban ecology**

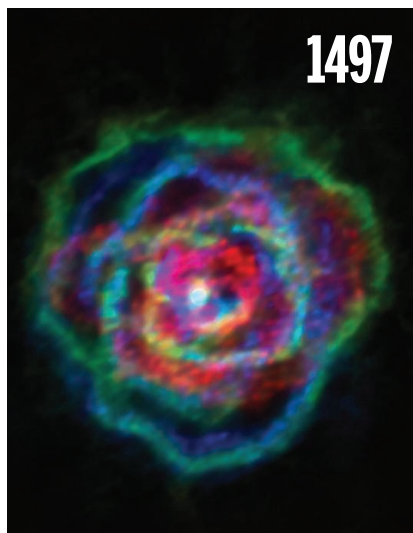
The ecological and evolutionary consequences of systemic racism in urban environments *C. J. Schell et al.*

REVIEW SUMMARY; FOR FULL TEXT:  
DX.DOI.ORG/10.1126/SCIENCE.AAY4497

**1447 Neurodevelopment**

Looking at neurodevelopment through a big data lens *J. Briscoe and O. Marin*

REVIEW SUMMARY; FOR FULL TEXT:  
DX.DOI.ORG/10.1126/SCIENCE.AAZ8627

**RESEARCH ARTICLES****1448 Inflammasomes**

HDAC6 mediates an aggresome-like mechanism for NLRP3 and pyrin inflammasome activation *V. G. Magupalli et al.*

**Developmental biology**

**1449** Species-specific pace of development is associated with differences in protein stability *T. Rayon et al.*

RESEARCH ARTICLE SUMMARY;  
FOR FULL TEXT:  
DX.DOI.ORG/10.1126/SCIENCE.ABA7667

**1450** Species-specific segmentation clock periods are due to differential biochemical reaction speeds *M. Matsuda et al.*

PERSPECTIVE p. 1431

**1455 Plastic pollution**

Evaluating scenarios toward zero plastic pollution *W. W. Y. Lau et al.*

REPORT p. 1515

**1461 Surface chemistry**

Following the microscopic pathway to adsorption through chemisorption and physisorption wells *D. Borodin et al.*

**1465 Coronavirus**

Assessing the impact of coordinated COVID-19 exit strategies across Europe *N. W. Ruktanonchai et al.*

**1470 Structural biology**

90S pre-ribosome transformation into the primordial 40S subunit *J. Cheng et al.*

REPORT p. 1477

**REPORTS****1477 Structural biology**

Cryo-EM structure of 90S small ribosomal subunit precursors in transition states *Y. Du et al.*

RESEARCH ARTICLE p. 1470

**1481 Microbiome**

Microbiome-derived inosine modulates response to checkpoint inhibitor immunotherapy *L. F. Mager et al.*

PERSPECTIVE p. 1427

**1490 Water structure**

Reversible structural transformations in supercooled liquid water from 135 to 245 K *L. Kringle et al.*

**1493 Quantum systems**

Universal coherence protection in a solid-state spin qubit *K. C. Miao et al.*

PERSPECTIVE p. 1432

**1497 Stellar evolution**

(Sub)stellar companions shape the winds of evolved stars *L. Decin et al.*

**1501 Coronavirus**

Structure-based design of prefusion-stabilized SARS-CoV-2 spikes *C.-L. Hsieh et al.*

**1505 Coronavirus**

Structural basis for neutralization of SARS-CoV-2 and SARS-CoV by a potent therapeutic antibody *Z. Lv et al.*

**1510 Ocean warming**

Seismic ocean thermometry *W. Wu et al.*

PERSPECTIVE p. 1433; VIDEO

**1515 Plastic pollution**

Predicted growth in plastic waste exceeds efforts to mitigate plastic pollution *S. B. Borrelle et al.*

RESEARCH ARTICLE p. 1455

**1518 Microbiota**

Diet posttranslationally modifies the mouse gut microbial proteome to modulate renal function *L. Lobel et al.*

PERSPECTIVE p. 1426

**DEPARTMENTS****1409 Editorial**

Trump lied about science *By H. Holden Thorp*

**1534 Working Life**

Delivering a difference *By Dennis Macejak*

**ON THE COVER**

Plastic waste collects at a landfill near Talesh, northern Iran. Plastic production has surged in recent decades, and plastic waste is accumulating rapidly in every area of the environment.



Reducing the amount of plastic pollution in the near future will require concerted global intervention. See pages 1455 and 1515. *Photo: Ashkan Shabani/Redux*

Science Careers ..... 1525



# Trump lied about science

**W**hen President Donald Trump began talking to the public about coronavirus disease 2019 (COVID-19) in February and March, scientists were stunned at his seeming lack of understanding of the threat. We assumed that he either refused to listen to the White House briefings that must have been occurring or that he was being deliberately sheltered from information to create plausible deniability for federal inaction. Now, because famed *Washington Post* journalist Bob Woodward recorded him, we can hear Trump's own voice saying that he understood precisely that severe acute respiratory syndrome coronavirus 2 (SARS-CoV-2) was deadly and spread through the air. As he was playing down the virus to the public, Trump was not confused or inadequately briefed: He flat-out lied, repeatedly, about science to the American people. These lies demoralized the scientific community and cost countless lives in the United States.

Over the years, this page has commented on the scientific foibles of U.S. presidents. Inadequate action on climate change and environmental degradation during both Republican and Democratic administrations have been criticized frequently. Editorials have bemoaned endorsements by presidents on teaching intelligent design, creationism, and other antiscience in public schools. These matters are still important. But now, a U.S. president has deliberately lied about science in a way that was imminently dangerous to human health and directly led to widespread deaths of Americans.

This may be the most shameful moment in the history of U.S. science policy.

In an interview with Woodward on 7 February 2020, Trump said he knew that COVID-19 was more lethal than the flu and that it spread through the air. "This is deadly stuff," he said. But on 9 March, he tweeted that the "common flu" was worse than COVID-19, while economic advisor Larry Kudlow and presidential counselor Kellyanne Conway assured the public that the virus was contained. On 19 March, Trump told Woodward that he did not want to level with the American people about the danger of the virus. "I wanted to always play it down," he said, "I still like playing it down." Playing it down meant lying about the fact that he knew the country was in grave danger.

It also meant silencing health officials who tried to

tell the truth. On 25 February, Nancy Messonnier, director of the National Center for Immunization and Respiratory Diseases (of the Centers for Disease Control and Prevention), said, "It's not so much a question of if this will happen anymore, but rather more a question of exactly when this will happen and how many people in this country will have severe illness." She was right and Trump knew it. But he shut her down. He also tried to control messaging from Anthony Fauci, the nation's foremost leader on infectious diseases. Trump's supporters insisted that Fauci and Messonnier were not being muzzled, but now we have clear evidence in emails that they were.

Trump also knew that the virus could be deadly for young people. "It's not just old, older," he told Woodward on 19 March. "Young people, too, plenty of young people."

Yet, he has insisted that schools and universities reopen and that college football should resume. He recently added to his advisory team Scott Atlas—a neuroradiologist with no expertise in epidemiology—who has advocated for a risky and misguided course: somehow isolating the older and more vulnerable while allowing the virus free rein among young people. The opening of colleges and schools has accelerated the spread of the virus and will mean

untold suffering among both students and the people to whom they are now spreading the virus.

Monuments in Washington, D.C., have chiseled into them words spoken by real leaders during crises. "Confidence," said Franklin Roosevelt, "thrives on honesty, on honor, on the sacredness of obligations, on faithful protection and on unselfish performance."

We can be thankful that science has embraced these words. Researchers are tirelessly developing vaccines and investigating the origins of the virus so that future pandemics may be prevented. Health care workers have braved exposure to treat COVID-19 patients and reduce the death rate; many of these frontline workers have become infected, and some have died in these acts of courage. These individuals embody Roosevelt's call to faithful protection and unselfish performance.

They have seen neither quality exhibited by their president and his coconspirators. Trump was not clueless, and he was not ignoring the briefings. Listen to his own words. Trump lied, plain and simple.

— H. Holden Thorp



**H. Holden Thorp**  
Editor-in-Chief,  
*Science Journals*.  
hthorp@aaas.org;  
@hholdenthorp

**"These lies...  
cost countless  
lives..."**



“It’s also more deadly than even your strenuous flus. This is deadly stuff.”

**U.S. President Donald Trump**, to journalist Bob Woodward in February about the virus that causes COVID-19. Publicly, Trump called the disease no worse than the seasonal flu.

## IN BRIEF

Edited by **Jeffrey Brainard**

Smog and wildfire smoke in San Francisco have caused air-quality warnings daily for the past month.



### POLLUTION

## Western U.S. wildfires spur health research

Scientists last week mounted efforts to study the long-term health consequences of wildfire smoke that has blanketed the U.S. West Coast and made air quality in some areas among the worst on Earth. The fires’ direct effects killed more than 30 people in three states, some trapped in burning homes; California has suffered its worst year of wildfires, with more than 1.2 million hectares burned. Previous research has documented risks from air pollution’s microscopic particulates, which can lodge deep in the lungs, seep into the bloodstream, and cause respiratory

and cardiovascular disease. Now, a Stanford University group is mailing blood testing kits to people in the San Francisco Bay Area to look for markers of inflammation in their blood. Other researchers—at the California Air Resources Board and the University of California campuses in Davis, Los Angeles, and San Francisco—are studying the wildfire smoke to follow up on evidence, collected elsewhere in the United States and in other countries, suggesting air pollution increases transmission of COVID-19 and leads to worse health outcomes in people with the disease.

## Execs ousted over Aboriginal site

**ARCHAEOLOGY** | Outrage over the destruction of a 46,000-year-old archaeological site in Australia has led to the resignations of three top executives of the mining giant Rio Tinto, the company announced last week, amid calls for better protection of Aboriginal cultural locations. In 2013, Western Australia’s state government granted Rio Tinto permission to disturb Juukan Gorge, which contained two rock shelters. One year later, researchers determined that one of the caves had likely been continually occupied since the last ice age and was far richer in artifacts than previously thought. These include wooden tools and an unusual braid of human hair woven from strands from several individuals. But current regulations do not allow for

reconsideration of permits, even in light of new information. In May, Rio Tinto blasted the site, destroying the caves. Aboriginal leaders warn that hundreds of similarly significant sites are facing destruction if existing approvals are not renegotiated.

## NOAA hire draws criticism

**POLITICS** | The U.S. atmospheric research agency has hired a researcher who has a long history of rejecting established climate science for a senior position, NPR first reported last week. David Legates, a geography professor at the University of Delaware, Newark, will oversee observation and prediction at the National Oceanic and Atmospheric Administration. Legates has promoted the work of fringe climate researchers and industry-funded

scientists and suggested burning fossil fuels would create a more habitable planet for humans. Some scientists fear the move signals that the Trump administration will expand its challenges of mainstream climate science and censor the next *National Climate Assessment*; previous versions of the quadrennial report have documented that global warming is increasing wildfires, coastal flooding, and other effects.

## Poor nations need sepsis data

**BIOMEDICINE** | The World Health Organization (WHO) is pressing for more action to combat sepsis, a life-threatening organ dysfunction that can follow an infection. Sepsis kills about 11 million people per year worldwide,



85% of them in low- or middle-income regions, especially sub-Saharan Africa and Southeast Asia. Survivors are often disabled or die within a year. WHO says too little is known about the prevalence of sepsis and who is at high risk. It adds that there's a critical need for quick and cheap diagnostics to detect sepsis early so treatment is more likely to save lives. The organization is urging more research funding and especially surveillance across low- and middle-income countries, where far less is known about the condition than in wealthy countries.

## Dread pig virus hits Germany

**LIVESTOCK HEALTH** | The virus that causes African swine fever, deadly to pigs and wild boar, was discovered last week in Germany, Europe's largest pork producer. It was found in the carcass of a wild boar in Schenkendöbern, 7 kilometers from the border with Poland, where the disease has been spreading since 2014. The decayed state of the carcass suggests the virus entered Germany weeks ago. Authorities put up a 12-kilometer fence to prevent spread and will search for other dead

boar; local pig farms are being inspected. German law requires biosecurity measures, such as disinfecting boots and tools, to protect farmed pigs. Belgium and the Czech Republic have successfully contained small outbreaks of African swine fever in boar. The virus also spreads through contaminated pork products. China, the largest market for German pork outside the European Union, immediately banned imports.

## Navajo Nation cuts COVID-19 cases

**INFECTIOUS DISEASES** | In a welcome bit of news, the Navajo Nation last week reported a day with no new cases of COVID-19, the first since March and part of a steady decline in infections. In May, the Navajo, the largest U.S. tribe, reported more cases per capita than hard-hit New York state at the time. Navajo officials attribute the progress to control measures, including curfews, mandated mask wearing, contact tracing, and effective public health communications. Still, the Navajo Nation faces a continuing risk of severe cases because its people have high rates of diabetes and other preexisting conditions.

## IN OTHER NEWS

**OLD-STYLE VACCINE** The United Kingdom has become the first Western government to invest in an inactivated virus vaccine against COVID-19. It will front an initial \$558 million for 60 million doses of the vaccine, which its manufacturer, Valneva, hopes to start testing in people in December. Vaccines that use chemically killed viruses are a proven, 20th century technology that most major companies developing COVID-19 vaccines have shunned, preferring gene- and protein-based vaccines because of their perceived safety and manufacturing benefits.

**LIFE ON VENUS?** Venus's clouds contain a surprise ingredient: an unstable gas, phosphine, that on Earth is commonly produced by some microbes, a research team reports in *Nature Astronomy*. Known nonliving chemical processes can't explain the phosphine levels on our nearest planetary neighbor, but as-yet-unknown chemical processes may be at work, scientists say.

**CDC CASTIGATED** Political appointees in the Trump administration have sought to review and edit weekly scientific reports by the U.S. Centers for Disease Control and Prevention (CDC) before publication, *Politico* reported. Some appointees have complained that CDC's reports about COVID-19 were biased against President Donald Trump and undermined his predictions that it will end soon. CDC officials have defended the *Morbidity and Mortality Weekly Report* but compromised on some requests for wording changes, *Politico* said.

**CENSUS RULING** A three-judge U.S. federal panel blocked an order by President Donald Trump excluding undocumented immigrants from the 2020 census, saying he "exceeded his authority." Census-derived state population counts are used to apportion seats in Congress.

**CRISPR FIGHT** A U.S. patent appeals board has upheld the Broad Institute's "priority" for its claim of first using the CRISPR genome editor in eukaryotic cells, an invention that could support lucrative applications in human medicine. But the ruling left room for a group led by the University of California to continue to pursue competing claims for related patents. A final priority hearing will be held.

## MARINE CONSERVATION

### First survey tallies deep-sea corals worldwide

**O**cean researchers this week released the first comprehensive survey of deep coral reefs in the high seas—the roughly two-thirds of the ocean outside of national jurisdictions. They hope the study will help persuade policymakers to give these vulnerable, poorly understood ecosystems greater protection in global agreements currently under negotiation. The team identified 116 reefs, most between 200 and 1200 meters beneath the surface of the Atlantic and Pacific oceans, on seamounts, escarpments, and submarine ridges. A handful were found more than 2 kilometers deep, the researchers report in *Frontiers in Marine Science*. Only one-fifth are protected from bottom fishing. The Coral Reefs on the High Seas Coalition, a group of researchers and conservation groups, suspects many more deep-sea reefs exist and is raising money for expeditions to unexplored waters to look for them.

A diverse, dense coral community was found at Debussy Seamount in the Pacific Ocean.

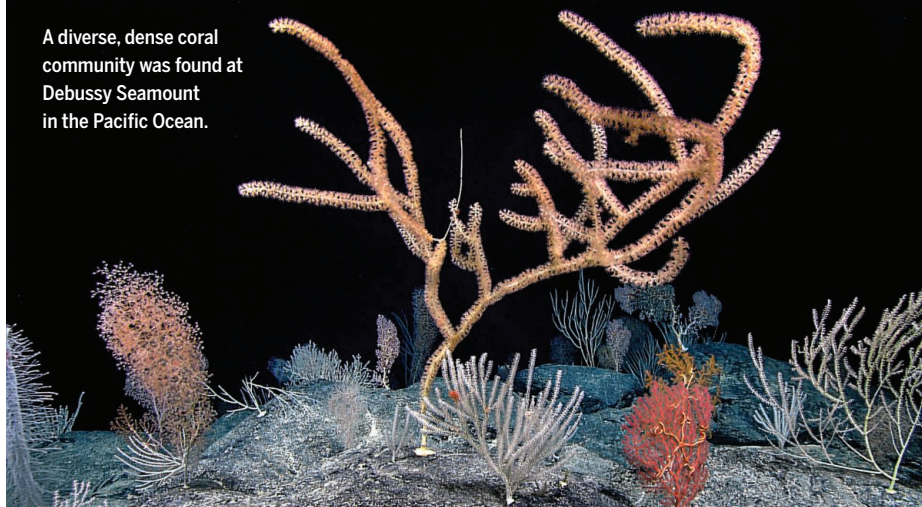


PHOTO: NOAA OFFICE OF OCEAN EXPLORATION AND RESEARCH





## IN DEPTH

Outbreaks of the pandemic coronavirus in correctional facilities have prompted moves to reduce populations.

### COVID-19

# Pandemic inspires push to shrink jails, prisons

New research focuses on the health and public safety impacts of “decarceration”

By **Kelly Servick**

**E**ven before COVID-19 began to sweep through U.S. correctional facilities, Michael Daniels saw the storm coming. As the director of justice policy and programs for Franklin county in Ohio, Daniels knew the county’s two jails, with about 1950 inmates, wouldn’t allow for social distancing to control the coronavirus’ spread. So, back in March, he asked his team: How could they get as many people as possible out of there quickly?

In New York City, Elizabeth Glazer, director of the Mayor’s Office of Criminal Justice, was having similar conversations. The pandemic “distilled to its essence [how] we think about the use of jail,” she says. “Was it worth putting somebody in jail if you thought that they were at risk of getting COVID?”

As they feared, crowded jails and prisons have been deadly. By now 120,000 COVID-19 cases and 1000 deaths have been documented among people incarcerated in U.S. prisons alone. As cases surged, public health experts amplified a long-standing, unfulfilled demand of criminal justice reform advocates: Lock fewer people up. Because of the virus, such decarceration efforts suddenly made speedy progress. “Pol-

icy recommendations that we were unable to get traction on for 2 years—we were able to get them done in 3 weeks,” Daniels says.

Nationwide, jail populations plunged by about 25% between March and June, according to an analysis by the nonprofit Vera Institute of Justice. New York City and Franklin county both managed reductions of 30% in their jails, which primarily hold people charged with crimes but not yet convicted. Populations of prisons, which hold people serving sentences after a conviction, budged much less; an analysis by the Marshall Project and the Associated Press found an 8% decrease nationwide during that period.

The result is a major experiment in public health and criminal justice. Initial studies suggest decarceration has lowered infection rates in some jails. But overcrowding persists, and advocates urge further reductions. A committee convened by the U.S. National Academies of Sciences, Engineering, and Medicine (NASEM) is developing best practices for decarceration as a COVID-19 response, slated for publication in October. And scientists hope to study potential social consequences of population reductions, including changes in crime rates.

“We’ve created ... a society that has relied on incarceration as a solution to our social problems—and recently, that system was downgraded by like 30%,” says Vincent Schiraldi, a justice policy researcher at the Columbia School of Social Work. “Shame on us if we don’t study that in a sophisticated way.”

Prison and jail outbreaks heighten the inequality of COVID-19’s burden. People of color are incarcerated at higher rates than white people and tend to get longer sentences, and people who are incarcerated have higher rates of underlying health conditions that predispose them to severe COVID-19. Meanwhile, the safety of people in prisons is entangled with that of the surrounding community. The virus

can travel back and forth with employees (23,000 infections have been documented among prison staff) and with people held for short jail stays or transferred between facilities. A June study in *Health Affairs* estimated that 15.7% of COVID-19 cases documented in Illinois by mid-April were associated with people moving through Chicago’s Cook County Jail.

“If we care about the community rates [of COVID-19], then we have to care about

Science’s COVID-19 reporting is supported by the Pulitzer Center and the Heising-Simons Foundation.



prisons and jails,” says Emily Wang, a physician at the Yale School of Medicine who heads its Health Justice Lab and co-chairs the NASEM committee on decarceration.

Jurisdictions have taken various tacks to reduce populations. New York City did it primarily by releasing two groups from jails: people being held for parole violations and those serving short sentences. The strategy in Franklin county included waiving some cash bail requirements, expanding the use of electronic monitoring to allow more people to await trial at home, and encouraging citations rather than arrests for certain misdemeanors.

Nationwide, the population drop in jails reflected a drop-off in arrests—likely because fewer crimes were committed during lockdowns and law enforcement officers aimed to avoid unnecessary physical contact, says Michael Jacobson, a sociologist at the City University of New York who has analyzed data on crime and policing in 50 cities.

To reduce prison populations, some states, including California, Oklahoma, Illinois, and Colorado, have halted the transfer of people who would normally move from jail to prison after sentencing. Governors have also commuted the sentences of inmates who were deemed medically vulnerable or were nearing the end of their sentences. And some states are trying to ramp up mental health care, addiction treatment, and other services that ultimately divert people from prisons. “The most successful [approach] is simply to not put people in to begin with,” Annette Chambers-Smith, director of the Ohio Department of Rehabilitation and Correction, told attendees in a 20 August NASEM webcast. “Turn the tap off.”

As populations dropped, some researchers tried to track the effects on disease spread. Wang and her colleagues estimated the reproduction number of the virus—how many people are infected by each newly infected person—over 83 days at a large urban jail, which they did not identify publicly. As the jail reduced its population by 25% and moved about two-thirds of residents into private cells, that number dropped from 8.25 to 1.72, they reported in a June preprint on medRxiv. (It later dipped below one, indicating the outbreak was in check, after the jail set up widespread testing of asymptomatic people.)

In another study, published 21 August in *JAMA*, Harvard University epidemiologist Monik Jiménez and colleagues found that among 13 county jails in Massachusetts, those with greater reductions in population from early April to early July also

had lower rates of COVID-19 infections. Jiménez notes, however, that limited and inconsistent testing data make it hard to sort out exactly how much decarceration helped prevent infections.

Lauren Brinkley-Rubinstein, a community psychologist at the University of North Carolina, Chapel Hill, aims to better predict such health effects. Through the COVID Prison Project, her team pulls daily case counts from state prison reports. She collaborated with researchers at Stanford University and the University of Miami to group 103 Texas prisons based on rates of COVID-19 cases and deaths. Prisons classified as “low outbreak” were at 85% capacity, the team reported in a preprint last week on medRxiv, proposing that number as a “benchmark” for reducing infections.

With Wang’s team and researchers at Stanford, Brinkley-Rubinstein hopes to combine case numbers with publicly available data about the layout of different fa-

and head of the Covid-19 Behind Bars Data Project, which tracks efforts to improve conditions and reduce populations in jails and prisons.

There’s no evidence so far that pandemic-inspired releases have raised crime rates. A July analysis of 29 U.S. locations by the American Civil Liberties Union found no relationship between reductions in jail populations and crime trends between March and May. Both Glazer’s and Daniels’s teams have thus far found very few reoffenses among the people released early from the New York City and Franklin county jails. Criminologist Daniel Nagin and statistician Amelia Haviland at Carnegie Mellon University plan to document the impact of the pandemic on jail populations and explore how population changes in U.S. jails relate to crime rates.

A potential downside of the pandemic’s speedy decarceration, says Matthew Akiyama, a clinician and public health researcher at the Albert Einstein College of Medicine, is that “discharge planning wasn’t as rigorous as it might have been.” People released from prison already struggle to access medical care, addiction treatment, and other supports for re-entry into society, he notes, and the new releases “left people floating in the wind, to a certain extent.”

But the threat of COVID-19 has also inspired new forms of support. On 27 August, California Governor Gavin Newsom announced a joint effort with philanthropic groups to provide \$30 million to organizations that offer transportation, quarantine housing, health care, and other services to people released from prison. California and New York City have set up hotel stays for people leaving jail, allowing them to quarantine and avoid crowded homeless shelters. Such initial stability may help them thrive long term, Glazer says.

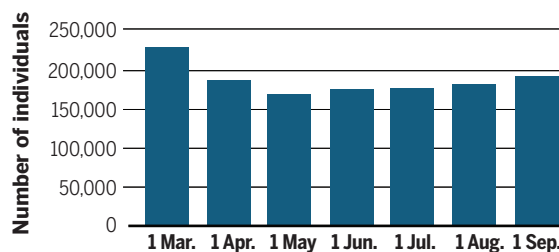
But many jail systems, including Glazer’s in New York City and Daniels’s in Franklin county, have seen upticks in their populations since the rapid plunges earlier in the pandemic—likely at least in part because rates of arrest rebounded.

Local officials are trying to hang on to the recent progress, Daniels says. Franklin county’s municipal court has made the issuance of citations standard for some offenses and downgraded failure to appear in court from a jailable offense. Now that he’s confident the county can quickly shrink its jails without risking public safety, there’s no reason they shouldn’t stay that way, he says. “Not if I can help it.” ■

With reporting by Eli Cahan.

## Getting out of jail

In a sample of about 650 U.S. jails, populations fell steeply as the pandemic took off in the spring, then slowly rose again.



cilities and how inmates are housed. That might help them forecast how changes in a given facility’s population will influence its risk of COVID-19, she says. “I can say all day long, ‘Reduce your population,’ [but] a department of corrections might come back to me and say, ‘OK, but how many? Who should I target? How many should I release?’ That precision is very important.”

Other researchers aim to document the effects of the speedy decarceration on public safety. Decades of criminology research suggest many inmates can be released with minimal risk of recidivism, Jacobson says. But the fear of releasing even one person who might commit a crime helps explain why researchers have had little opportunity to study the effects of rapid, large-scale decarceration before the pandemic. Even now, political calculations explain why jails—most of whose inmates have not been convicted—shrank more than prison populations during the pandemic, says Sharon Dolovich, a law professor at the University of California, Los Angeles,



## COVID-19

# Viral heart damage under scrutiny

Researchers are hunting for myocarditis in COVID-19 survivors

By Jennifer Couzin-Frankel

**T**his fall, cardiologist Sam Mohiddin will embrace a new role—that of research subject. MRI scans of his heart at St. Bartholomew's Hospital in London, where he works, will help answer a pressing question: Do people who suffered a mild or moderate bout of COVID-19 months ago, as he did, need to worry about their heart health?

Fears that COVID-19 can cause the cardiac inflammation called myocarditis have grown, as doctors report seeing previously healthy people whose COVID-19 experience is trailed by myocarditis-induced heart failure. Mohiddin recently treated 42-year-old Abul Kashem, who had typical COVID-19 symptoms in April, including loss of smell and mild shortness of breath. A month later, he fell critically ill from severe myocarditis. “I’m just grateful to be alive,” says Kashem, who spent more than 2 weeks in an intensive care unit. Why did this happen? he wonders.

How the virus might damage heart muscle is just one question researchers are now probing. Other studies are following people during and after acute illness to learn how common heart inflammation is after COVID-19, how long it lingers, and

whether it responds to specific treatments. Researchers also want to know whether patients fare similarly to those with myocarditis from other causes, which can include chemotherapy and other viruses. In more than half of virus-induced cases, the inflammation resolves without incident.

But some cases lead to arrhythmia and impaired heart function, or, rarely, the need for a heart transplant. Because millions are now contracting the coronavirus, even a small proportion who suffer severe myocarditis would amount to a lot of people. “Are we going to have an increase of patients with heart failure secondary to this?” asks Peter Liu, a cardiologist and chief scientific officer of the University of Ottawa Heart Institute.

Whether SARS-CoV-2, the virus that causes COVID-19, induces cardiac injury including myocarditis more often, or with greater severity, than other viruses is still unclear. Because SARS-CoV-2 can trigger an intense immune response throughout the body, survivors may be at heightened risk of cardiac inflammation. Another idea suggests COVID-19 patients might be prone to the condition

because the virus enters cells by binding with the angiotensin-converting enzyme 2 (ACE2) receptor, which sits on heart muscle cells. But researchers caution against outrunning the data. “It’s a good hypothesis, but it’s not a tested one,” says Leslie Cooper, a cardiologist at the Mayo Clinic in Jacksonville, Florida, about ACE2.

One reason it’s hard to say whether COVID-19 poses a special risk of myocarditis is uncertainty about its prevalence after other infections. Echocardiogram studies after some influenza outbreaks suggest up to 10% of flu patients have transient heart abnormalities, Liu says. But such studies are scarce. “We don’t scan patients after they had the flu,” says Valentina Püntmann, a cardiologist at University Hospital Frankfurt.

Püntmann fueled concerns about myocarditis when she did just that with COVID-19 patients. Her team used MRI to scan the hearts of 100 COVID-19 patients an average of 71 days after they had tested positive. The scans showed cardiac abnormalities in 78 people, with 60 appearing to have active inflammation. Most also described lingering symptoms, such as fatigue and mild shortness of breath, leading Püntmann to wonder whether heart inflammation might be responsible.

Although the work by Püntmann and her colleagues, published in July in *JAMA Cardiology*, prompted alarming headlines, many researchers say it needs to be replicated. Cardiologists urge anyone with symptoms like shortness of breath or chest discomfort after COVID-19 to see a doctor, but they worry about a flood of healthy recovered people clamoring for heart assessments. “Here’s the good news: We’re going to find out” how likely cardiac injury is, says Matthew Martinez, director of sports cardiology at Morristown Medical Center.

Because of the physical demands of sports, team doctors need to be on guard for myocarditis. A paper in *JAMA Cardiology* last week reported a study of 26 athletes at Ohio State University after COVID-19; four had developed myocarditis. Professional sports leagues are also scanning the hearts of athletes who were infected with SARS-CoV-2. Those with myocarditis, re-



In Genoa, Italy, a recovered COVID-19 patient undergoes a test of heart function.



ardless of whether they have symptoms, are benched, in part out of fear that myocarditis could lead to sudden death during intense activity. Martinez, who's helping coordinate the research for the National Basketball Association and Major League Soccer, predicts a flow of data on athletes over the coming months. "Those of us in this space are willing to ruin a Saturday or a Sunday to get this done."

He stresses, though, that even if researchers can clarify the average duration of myocarditis and its risks for a young athlete, those may be very different for a 50-year-old with obesity or high blood pressure, especially if they were sick enough with COVID-19 to be hospitalized. "In those individuals, I am going to be more cautious" and screen for heart injury, he says.

Others are pursuing clues to how COVID-19 can damage the heart, which might point to ways to head off the damage. "SARS-CoV-2 does challenge your immune system in unconventional ways," Liu says. Autopsies of heart tissue after COVID-19 have revealed inflammation in the heart's blood vessels instead of its muscle cells, the site of the inflammation caused by other infections. Another autopsy study found scattered death of heart cells, but the authors noted the mechanism of injury was unknown. "There's been a lot of discussion whether this is myocarditis" as typically defined, Liu says. Regardless, he and others hope for clinical trials to test whether preventive strategies, such as taking beta blocker drugs, might head off heart failure in someone flagged as high risk after COVID-19.

While Mohiddin volunteers for a study of survivors, he's also running one: a trial that aims to recruit 140 people while they are hospitalized with COVID-19 or soon after, 20 with severe myocarditis and the rest without. He and colleagues will look for abnormal T cell levels in the blood of people with myocarditis, which could help explain whether and how the immune system is causing cardiac injury. He is also exploring whether immune cell patterns in the blood presage myocarditis later.

Even if COVID-19 rarely causes serious myocarditis, one hypothesis is that mild cases could heighten the risk of heart disease years later. Scar tissue can form as myocarditis heals, and earlier work has shown residual cardiac inflammation portends worse heart health. As cardiologists, "We're in the business of identifying asymptomatic risk factors," such as hypertension, Mohiddin says. "It's not difficult to imagine that in the future, clinical practitioners will ask a new patient, 'Did you have COVID?'" ■



Alan Minson says his Parkinson's symptoms improved after he started to use a "light helmet" in July 2019.

#### NEURODEGENERATIVE DISEASES

## Trials begin for a new weapon against Parkinson's: light

Patients report benefits, but how near-infrared protects brain cells is unclear, and some scientists are skeptical

By **Gunjan Sinha**

**L**ight therapy can help lift moods, heal wounds, and boost the immune system. Can it improve symptoms of Parkinson's disease, too? A first-of-its-kind trial scheduled to launch this fall in France aims to find out. In seven patients, a fiber optic cable implanted in their brain will deliver pulses of near-infrared (NIR) light directly to the substantia nigra, a region deep in the brain that degenerates in Parkinson's disease. The team, led by neurosurgeon Alim-Louis Benabid of the Clinatec Institute—a partnership between several government-funded research institutes and industry—hopes the light will protect cells there from dying.

The study is one of several set to explore how Parkinson's patients might benefit from light. "I am so excited," says neuropsychologist Dawn Bowers of the University of Florida College of Medicine, who is recruiting patients for a trial in which NIR will be beamed into the skull instead of delivered with an implant.

Small tests in people with Parkinson's and animal models of the disease have already suggested benefits, but some mainstream Parkinson's researchers are skeptical. No one has shown exactly how light might protect the key neurons—or why it should have any effect at all on cells buried deep in the brain that never see the light of day. Much or all of the encouraging hints seen so far in people may be the result of the placebo effect, skeptics say. Because there are no biomarkers that correlate well with changes in Parkinson's symptoms, "we are reliant on observing behavior," says neurobiologist David Sulzer of Columbia University Irving Medical Center, an editor of the journal *npj Parkinson's Disease*. "It's not easy to guard against placebo effects."

But proponents point to a Parkinson's therapy named deep brain stimulation (DBS), in which electricity of a specific frequency is applied to affected brain regions. Invented by Benabid more than 30 years ago, DBS has become a standard approach for treating tremors and other severe motor symptoms in Parkinson's patients even though its mode of action isn't entirely clear



either. The well-documented healing effect of low-level laser therapy on other tissues is also encouraging, says Michael Hamblin, a researcher at the Wellman Center for Photomedicine at Massachusetts General Hospital. In some countries, doctors routinely use lasers to treat pain or speed up wound healing.

Ten years ago, John Mitrofanis, a neuroanatomist at the University of Sydney, was inspired to try light in Parkinson's after a colleague told him that light in the NIR range protected retinal cells against toxins. In a 2012 study, he and colleagues showed in a mouse model of Parkinson's that NIR light shined into mice's heads protected dopamine-producing cells in the substantia nigra from a neurotoxin.

Excited, Mitrofanis called Benabid, with whom he once spent a year studying DBS. Benabid, "being the surgeon, said, 'We have to develop a light device that gets close to the area,'" Mitrofanis recalls. The researchers reasoned that light shining from outside the skull would not penetrate deep enough to make a difference in larger animals.

In 2017, together with research fellow Cécile Moro, they injected 20 macaques with a neurotoxin known to cause Parkinson's symptoms. In nine of them, they also delivered NIR to the midbrain area through an implanted device. Mitrofanis recalls how the first NIR-treated monkey behaved after a 3-week recovery period: "He was moving around like there was nothing wrong. We looked at each other and just hugged. ... It was euphoric." Overall, NIR-treated monkeys developed fewer symptoms than the untreated group and retained 20% to 60% more of the brain cells targeted by the neurotoxin.

Mitrofanis also struck up a collaboration with Catherine Hamilton, a retired occupational physician in Tasmania who had treated her own arthritic knee by wrapping it with light-emitting diodes (LEDs). In a study of six Parkinson's patients published last year, Hamilton, Mitrofanis, and others reported that wearing a helmet lined with LEDs improved facial expression, auditory processing, engagement in conversation, sleep quality, and motivation, though it did not have much effect on motor symptoms. "If I miss a day session, there is a gradual change in me," says Alan Minson, a Parkinson's patient living in Longford, Australia, who started to use a helmet in July 2019. "Bad dreams come back, my tolerance level goes way down, and my lethargy goes way up." Ann Liebert of the University of Sydney is planning a study in 120 patients using a more sophisticated helmet. In a similar ef-

fort, Bowers will randomize 24 patients to externally applied NIR or sham light and watch for behavioral and motor benefits.

Bowers will also look for signs that, as some have proposed, light boosts brain cells' energy-producing mitochondria. Test tube experiments have shown that light can trigger the enzyme cytochrome C oxidase, which is present on mitochondrial membranes, to rev up cellular energy production, which in turn might increase blood flow and stimulate cells to churn out several neuroprotective proteins and growth factors. "But I'm not convinced a transcranial device can penetrate deeply enough to show substantial improvements," Bowers says. She's more hopeful about Benabid's trial.

That study will follow 14 early-stage Parkinson's patients for 4 years, seven of whom will be treated periodically with pulses of 670-nanometer light delivered to the brain via a thin laser diode cable. The other seven patients will not be operated on; an ethical review board ruled against subjecting them to surgery without a chance of benefit. The main objective is to prove the implant is safe, Benabid says, but the researchers will also evaluate disease progression. "It has to make a big difference," he says.

"There is no reason [to do] extensive surgery for mild improvement."

The researchers plan to use common imaging methods to quantify the number of dopamine-producing cells in patients. But a protective effect may be hard to detect. "The major problem with all neuroprotection trials in Parkinson's disease is that the diagnosis appears to occur after more than 50% of dopamine-producing cells are gone," Sulzer says. Unless the improvement is huge, "the signal might be too small to detect."

The team will also look for clinical benefits. But because researchers grade Parkinson's symptoms by observing patients performing specific tasks, assessments are largely subjective, and symptoms vary over time; everyone has good days and bad days, Sulzer says. Because the control group will not undergo surgery, it will be especially hard to rule out placebo effects.

Yet Sulzer is giving studies like Benabid's the benefit of the doubt. The absence of a clear mechanism isn't a reason to dismiss the therapy, he says. "There are many things we don't understand," Sulzer says. "I am skeptical and also think it is an intriguing area of pursuit." ■

Gunjan Sinha is a science journalist in Berlin.

## ARCHAEOLOGY

# Ancient DNA tracks Vikings across Europe

Massive sequencing effort shows people of diverse genetic backgrounds adopted Viking culture

By **Andrew Curry**

It was a Viking saga written in genes. In 2008, construction work on an isolated Estonian beach near the town of Salme uncovered the skeletons of more than 40 powerfully built men. They were buried around 750 C.E. in two ships with Viking-style weapons and treasure—apparently the aftermath of a raid gone wrong. DNA from the bones has now added a poignant detail: Four of the men, buried shoulder to shoulder holding their swords, were brothers.

The new data come from a massive effort to sequence the DNA of Vikings across Europe. The results, published today in *Nature*, trace how the Vikings radiated across Europe from their Scandinavian homeland, and how people with roots elsewhere also took up Viking ways. "The big story is in line with what's told by archaeologists and historians," says Erika Hagelberg, an ancient DNA expert at the University of Oslo who was not part of the research team. "It's the small details of particular sites that are really compelling." The Estonian site, for example, offers powerful evidence that the crew was a tight-knit group from the same village or town. "Four brothers buried together is new and unique ... [and] adds a new dimension," says Cat Jarman, an archaeologist working for the Museum of Cultural History in Oslo, who was not part of the research team.

Over the course of almost 10 years, a team led by geneticist Eske Willerslev of the University of Cambridge and the University of Copenhagen assembled samples from across Scandinavia dating to the Viking Age, from about 750 C.E. to 1050 C.E., as well as some earlier and later samples. The team also gathered human remains from burials elsewhere in Europe and beyond that had Viking grave goods or burial styles. "We approached every place where we could see there should exist somehow an association with Vikings," Willerslev says. Ultimately, the team was able





DNA from Viking-era burials around Europe—like this one of a woman in Varnhem, Sweden—revealed individual histories and identities.

to sequence 442 Viking Age genomes from as far afield as Italy, Ukraine, and the doomed Viking settlements of Greenland.

The results tell dramatic stories of individual mobility, such as a pair of cousins buried in Oxford, U.K., and Denmark, separated in death by hundreds of kilometers of open ocean. The genetic details may also rewrite popular perceptions of Vikings, including their looks: Viking Age Scandinavians were more likely to have black hair than people living there today. And comparing DNA and archaeology at individual sites suggests that for some in the Viking bands, “Viking” was a job description, not a matter of heredity.

Viking-style graves excavated on the United Kingdom’s Orkney islands contained individuals with no Scandinavian DNA, whereas some people buried in Scandinavia had Irish and Scottish parents. And several individuals in Norway were buried as Vikings, but their genes identified them as Saami, an Indigenous group genetically closer to East Asians and Siberians than to Europeans. “These identities aren’t genetic or ethnic, they’re social,” Jarman says. “To have backup for that from DNA is powerful.”

The results also settle a centuries-old argument about the geography of raiding. Sagas written down centuries after the first expeditions suggest Vikings from certain regions favored specific destinations, but other scholars suggested the Viking command of the waves made them equal-opportunity raiders and traders.

DNA in hand, researchers for the first time could conclusively trace the origins of people from the far edges of the Viking diaspora back to their roots in Scandinavia. “We can follow the patterns of contact suggested by written sources, but disputed by historians for decades,” says co-author Søren Sindbæk, an archaeologist at Aarhus University.

They found that Vikings from what is now Sweden moved east to the Baltics, Poland, and the rivers of Russia and Ukraine, whereas Danes were more likely to head west to what is today England. Norwegians were most likely to set sail for the North Atlantic Ocean, colonizing Ireland, Iceland, and eventually Greenland (see map, below). “This is

detail one couldn’t do based just on archaeology,” Willerslev says.

To the team’s surprise, there was little evidence of genetic mixture within Scandinavia itself. Although a few coastal settlements and island trading hubs were hot spots of genetic diversity, Scandinavian populations farther inland stayed genetically stable—and separate—for centuries. “We can separate a Norwegian person from a Swedish person from a Danish person,” Sindbæk says.

The DNA has raised new questions, too. Study co-author and National Museum of Denmark archaeologist Jette Arneborg says DNA recovered from burials in Greenland

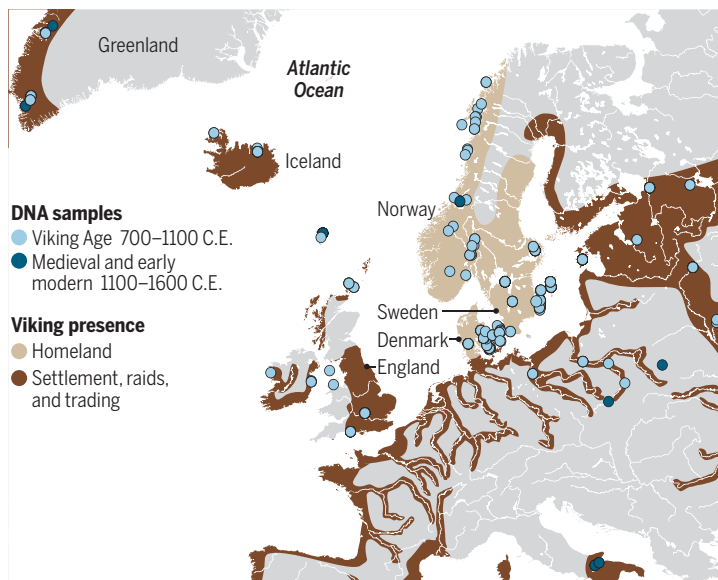
shows a mix of Scandinavian men from what is now Norway and women from the British Isles. Yet the artifacts and burials look completely Scandinavian. The women “have British genes but we can’t see them in the archaeology,” she says. “The DNA is going to make us think more about what’s happening here.”

Other mysteries remain. Viking settlements in the Americas have not yielded bones for sequencing, leaving the identity of the first European settlers in the Americas a mystery. And to the east, more samples may help illuminate the role of Vikings in the origins of the early Russian state, a topic that remains “extremely politically charged,” Sindbæk says. “This data has the potential to resolve some of these debates.” ■

Andrew Curry is a journalist in Berlin.

## Age of exploration

Viking ships sailed forth from Scandinavia, traversing the waterways of Europe and reaching across the Atlantic Ocean. Vikings from different homelands preferred certain destinations; for example, men from Norway settled Greenland, DNA data now show.





## CONSERVATION BIOLOGY

# Global efforts to protect biodiversity fall short

New report finds glimmers of progress, but nations are not achieving targets

By Erik Stokstad

A major report card on the state of biodiversity gives failing grades to the world's nations. The United Nations's *Global Biodiversity Outlook 5*, released this week, concludes that the world has not met ambitious targets set 10 years ago to protect nature. "We are losing biodiversity and that has very real consequences to people's health, prosperity, and well-being," says Jane Lubchenco, a marine ecologist at Oregon State University, Corvallis, who was not involved in the report.

There is still time to halt—and even reverse—the loss of biodiversity, the report

concludes. But that will require rapid and substantial changes in agriculture, industry, and other activities. "More than anything, it's telling us we have quite a lot more to do. Not more of the same, but more of the tougher transformational shifts," says Lina Barrera, head of international policy at Conservation International, an environmental organization. One such change would be including the value of biodiversity in economic decisions, such as infrastructure investment or farm subsidies.

In 2010, the 196 nations that belong to the U.N. Convention on Biological Diversity (CBD) agreed to 20 goals for preserving flora and fauna, known as the Aichi

biodiversity targets. Every few years, CBD has evaluated progress, based on national reports and other sources. This latest *Outlook* also reflected trends revealed by a major scientific review by several hundred researchers (*Science*, 10 May 2019, p. 517).

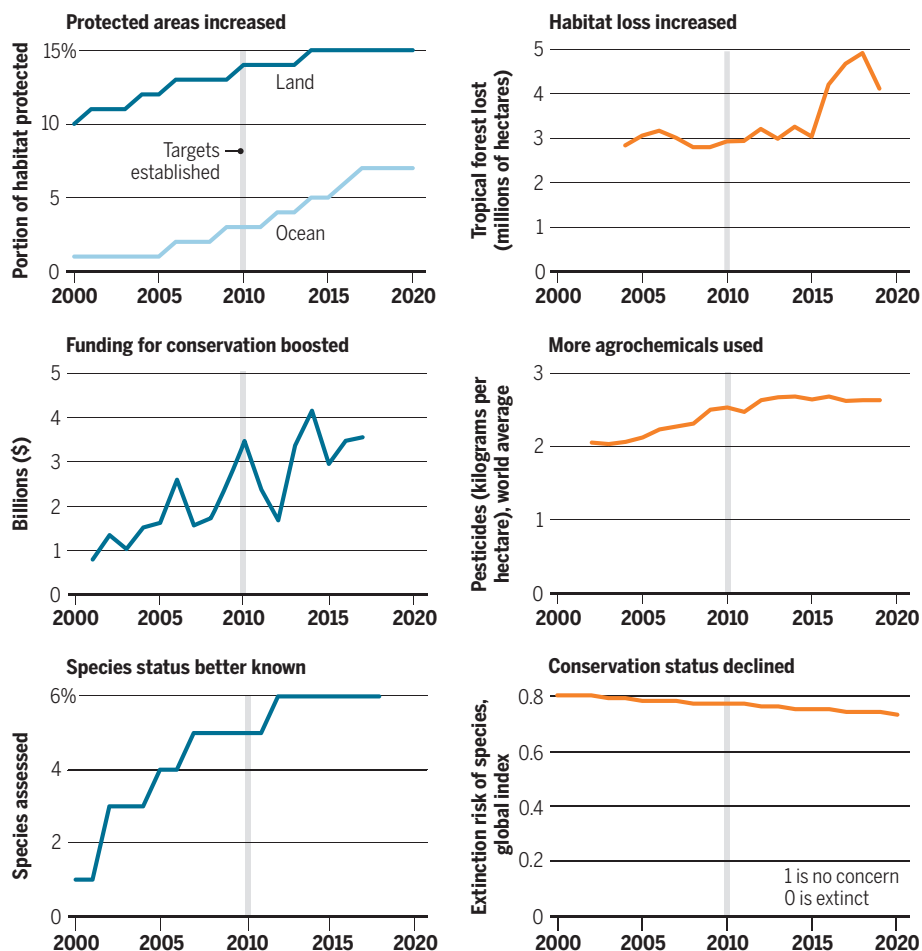
The new assessment finds some bright spots. Fisheries are becoming more sustainable in nations with good management schemes. Invasive species are being eradicated on ever more islands. Perhaps most encouraging, the extent of protected areas has risen substantially to 15% of land and 7% of the ocean (see graphs, left). But those figures are still short of the targets of 17% and 10%, respectively, and Lubchenco notes that only 2.5% of the ocean has been highly protected so far. Overall, nations reported they were on track to meet an average of 34% of their own targets, although many were not as ambitious as the global Aichi targets. They reported progress, for example, on raising awareness about conservation, building research capacity, and creating strategies for protecting species.

It's not enough, the report says. Only six targets have been even partially reached and some indicators are headed the wrong way. For example, while global pesticide use has been relatively flat, many nations have increased their use of chemicals that harm pollinators. In general, progress is being swamped by growing consumption of energy and materials, and the destruction of habitat by new farms, roads, and dams. As a consequence, biodiversity continues to be lost, the report finds. "Things are not going to change much until we deal with the root issues, and this is much more difficult," says ecologist Sandra Díaz of Argentina's National Scientific and Technical Research Council and the National University of Córdoba.

Observers hope the report's sobering conclusions will motivate countries to press for more progress and higher goals when they meet in May 2021 to set new CBD targets for 2030. Draft targets already released are "roughly moving in the right direction," Barrera says. One proposal, for example, calls for protecting a total of 30% of land and marine habitat. "That is ambitious, but it is absolutely necessary," Lubchenco says. Achieving the next round of targets will be "very high stakes for everybody," Díaz says, "not just ecologists and conservationists."

## A lost decade

In 2010, the Convention on Biological Diversity set 20 global targets for safeguarding nature. None has been achieved; a few trends are headed in the right direction (left), but many are discouraging (right).







## FEATURES

Fearing stigma, an HIV-positive girl in Kenya who lost her mother to AIDS recounted her story anonymously to health care workers.

# THE BURDEN OF STIGMA

Past epidemics reveal how social stigma amplifies the dangers of infectious disease

By **Vaishnavi Chandrashekhar**, in Mumbai, India

PHOTO: AP PHOTO/BEN CURTIS

**O**ne day at the end of April, dentist Azmera Shaikh tested positive for the novel coronavirus. That afternoon, feeling feverish and achy, she and her mother, who had also tested positive, descended from their apartment here to board an ambulance to the hospital. They were startled to find a dozen or so neighbors lined up with mobile phones in hand. Pictures and videos of their departure soon circulated on WhatsApp and Facebook. “We were entertainment,” Shaikh says. “We were the joke of the town.”

A volunteer with the nonprofit Doctors for You, Shaikh had seen the fear and distrust brought by the pandemic while working in the slums of eastern Mumbai. Some areas had not allowed her team to set up screening camps for fear that residents would be assumed infected with SARS-CoV-2, the virus that causes COVID-19. But she didn’t expect her educated, middle-class neighbors to behave similarly.

Soon, her entire family was in quarantine. The rules made it difficult for her fa-

ther and brother to put out garbage and get groceries. Yet neighbors did not help. Their attitude, Shaikh says, was “more traumatizing than the illness itself.”

As the coronavirus spread early this year, people around the world responded in similar ways. In Nepal, health care workers were thrown out of rental apartments. In Haiti, hospitals treating COVID-19 patients were attacked. In the United States, many people avoided East Asian-dominated neighborhoods, linking the virus with people from China, where the outbreak began.

Some doctors in Chennai, India, avoided getting tested because of the trouble they

*Science’s COVID-19 reporting is supported by the Pulitzer Center and the Heising-Simons Foundation.*





Even today, some people with leprosy live sequestered, like this patient looking out of her living quarters in a leprosy colony in New Delhi.

might face with neighbors if they turned out to have the virus, notes medical anthropologist Mitchell Weiss, a professor emeritus at the Swiss Tropical and Public Health Institute. As doctors, they should know better because testing is critical to reducing outbreaks, he says. “This is the toxicity of stigma.”

Yet those responses would have been familiar to our ancestors. From ancient times, humans have feared disease and shunned those thought to have it. But today, when we have a larger arsenal of tools to fight disease, including testing, contact tracing, and treatment, those old responses can undermine public health efforts. Stigma not only encourages people to hide illness and avoid treatment, but also intensifies patient stress and reinforces socioeconomic inequality.

The history of epidemics, including those of leprosy, cholera, and HIV, shows how costly stigma can be—both to individual patients and to societies as a whole. Such costs don’t usually show up in conventional epidemiological studies, Weiss says, but are part of what the World Health Organization (WHO) calls “the hidden burden” of disease.

**RELICS OF PAST DISEASES** pepper the Indian port city of Mumbai. A 160-year-old temple to Sitladevi, the goddess of smallpox, is still open to worshipers. Nineteenth cen-

tury crosses to ward off bubonic plague are sprinkled around Catholic neighborhoods. And a sprawling 130-year-old leprosy home still stands in what was once the outskirts of colonial Bombay.

The word “stigma” originally referred to a mark on the body. Later it came to denote a metaphorical mark of disgrace. Sociologists define stigma as the social devaluing of people who possess a trait seen as negative or deviant, such as a physical or mental disability or even an ethnicity. Almost every sense of the term comes together in leprosy.

The association is ancient: The biblical book of Leviticus depicts leprosy as a manifestation of spiritual sin, calling people with the condition “unclean” and directing them to live “outside the camp.” (Biblical leprosy likely referred to other skin conditions, but the diseases were conflated.) In India, where the disease is thought to have originated, ancient Hindu texts proscribed marriage into families that had a member with leprosy. In Europe, people with the disease were cast out of town or sent to leprosariums.

“In infectious disease, stigma is rooted in an exaggerated fear of contamination,” Weiss says. Some psychologists suggest stigma may have developed under evolutionary pressure to protect the social group from infected members. (A similar hypothesis proposes that the emotion of

disgust evolved to prevent humans from ingesting pathogens.) Avoiding people with infectious diseases probably did help ancient societies mitigate epidemics, Weiss notes. “In situations of plague or other highly contagious diseases, these fears may not be unreasonable. But how you act on those concerns may become unreasonable or unwarranted.”

History suggests stigma often sweeps beyond realistic concerns about contagion. In the mid to late 1800s, people in the United Kingdom panicked over leprosy, seeing the disease in racist terms, notes medical historian Shubhada Pandya, who is associated with the Acworth Leprosy Museum in Mumbai. An 1862 article in *The BMJ* said the countries of Asia were “infested” with leprosy “in proportion to the physical and moral degradation of their people.” An 1898 colonial law empowered officials in India to round up and isolate homeless patients in institutions that were often segregated by sex to prevent procreation.

In 1873, Norwegian scientist Gerhard Armauer Hansen isolated the bacterium that causes leprosy. During the mid to late 20th century, researchers developed treatments and the disease became less common. Still, people with leprosy continued to be shunned. Patients themselves internalized the stigma: Just last year, research-





The actions of leaders and celebrities such as the Dalai Lama, shown here touching a man with leprosy in New Delhi, can reduce the stigma of disease.

ers who interviewed residents of a leprosy colony in Ghana reported that even people who were cured preferred to stay in the colony because they were ashamed of their disease and expected to be ostracized at home.

Health-related stigma can sometimes have a “compounding effect” on other kinds of prejudice, exacerbating inequality, says Wim van Brakel, medical director of NLR, an international nongovernmental organization to fight leprosy in Amsterdam. For example, according to a 1996 ethnographic study in Thailand, many older people associated leprosy with begging, probably because in the past, ostracism and disability threw patients with the disease into poverty and eventually begging. A similarly outdated view has shaped perceptions in India. “The image people have is that if I get leprosy, I become like that maimed beggar at the traffic light,” van Brakel says.

The bright spot is that helping people with one aspect of their plight may alleviate others. In a randomized controlled study of leprosy patients in Indonesia from 2011 to 2014, van Brakel found that improving their socioeconomic situation with loans and training helped reduce

their perceptions of social stigma and boost their participation in society.

Yet uprooting old views remains a challenge. Even in 2018, a survey of people in Cameroon indicated that one-quarter of 233 respondents believed leprosy was caused by a spell. Most knew the disease was curable, but more than one-quarter said they

would not marry someone who had had it. In India, laws making the disease grounds for divorce were removed only last year.

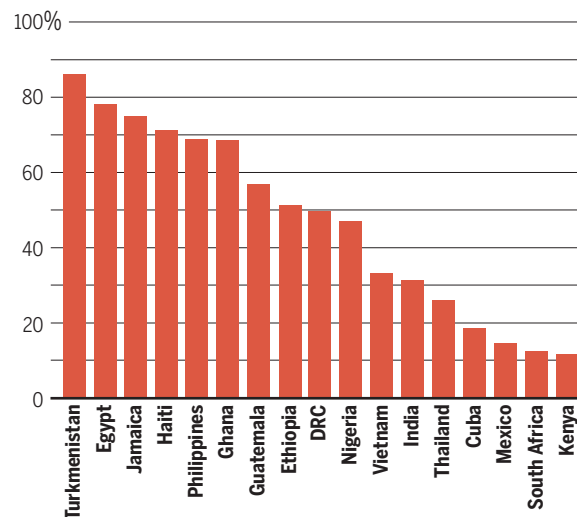
Even the disease’s name has come to mean outcast: We describe those we shun as “lepers.” Scientists tried to change the name to Hansen’s disease, but the old name stuck. Ashim Chowla, former head of the nonprofit Lepira India, says people today still flinch when he tells them he has been treated for leprosy. “The identity never really goes away.”

Chowla, now CEO of the India HIV/AIDS Alliance, admits to some schadenfreude seeing people in his middle-class neighborhood turn on each other today because of COVID-19. Indian elites “who never thought they would get the diseases of the poor,” he says, are getting a taste of “the ostracism that leprosy patients have faced for thousands of years.”

**LEPROSY HAS LONG EPITOMIZED** the stigma associated with disease. But in the 1980s, a virus emerged that quickly became the new “gold standard of stigma,” Weiss says: HIV. At first, AIDS, the disease caused by HIV, was seen as a health threat largely for gay men, injecting drug

## Quantifying fear

In some countries, most people said they wouldn’t buy vegetables from a seller who had HIV. But people in other nations were less fearful.





users, and sex workers. The initial response was marked by moral panic, similar to old views of leprosy. Some religious groups saw the illness as a curse or punishment. People with the disease faced discrimination and government neglect in most countries, says Laura Nyblade, an expert on HIV discrimination with RTI International.

Social scientists like Weiss had used survey and interview methods to measure stigma and discrimination in mental illness and leprosy, creating “stigma scales” to quantify it. With the advance of HIV, researchers began to develop similar scales for that virus. In 2008, the Joint United Nations Programme on HIV/AIDS (UNAIDS) launched the People Living with HIV Stigma Index as a tool to generate evidence for advocacy. By November 2017, more than 100,000 people living with HIV had been interviewed in more than 50 languages by trained interviewers who themselves had HIV. Interviewers asked, for example, whether someone had been insulted for being HIV-positive or been denied access to health care.

Studies showed stigmatization burdened people with HIV psychologically, as Shaikh and her family experienced with the coronavirus. Stigma also caused people to hide their disease, lessened adherence to treatment, and worsened health outcomes. People with HIV who perceived high levels of social stigma were 2.4 times as likely to delay entering care until very ill, according to a meta-analysis of 10 studies published in 2017. One in five people living with HIV avoided going to medical facilities because they feared discrimination, according to data collected from 2011 to 2016 in 19 countries. And University of Washington researchers found in 2019 that Black women living with HIV who scored high on stigma measures also reported more days of missed treatments and higher viral loads.

All those findings suggest stigmatization can spur the spread of disease. In some settings, stigma could be responsible for 35% to 51% of infant infections with HIV because it reduced mothers’ adherence to treatment, according to a 2017 modeling study by Nyblade and colleagues.

People already living at the margins suffer even more. In one study in Russia, 30% of female sex workers said they had been refused medical care because of their work, which puts them at risk of contracting HIV. In a study in Argentina, 40.7% of transgender women, who have higher rates of HIV, said they avoided clinics because of their transgender identity. According to a 2015 survey in New York City, African migrants with undocumented status chose not to disclose HIV status to families and communities, fearing they might lose needed social sup-

port. Like other marginalized groups, they “stayed hidden and disengaged with health care,” the study said.

As with leprosy, social attitudes were intensified by legal discriminations that never fully went away. Some aspects of HIV transmission, such as not disclosing that one is infected, are still criminalized in 72 countries, including the United States, according to UNAIDS. Thirty countries ban people’s entry or residence on the basis of HIV status.

“A critical lesson from HIV is that addressing stigma from the outset of a pandemic can be critical to an effective response,” Nyblade says. “If people fear stigma, they



A 1909 illustration reflects the vilification of Irish cook Mary Mallon, who unwittingly spread typhoid.

will be reluctant to get tested, disclose they have symptoms, and seek care.” More than 30 years after the disease emerged, she says, “stigma continues to be a major barrier to ending the HIV pandemic.”

**STIGMATIZATION OFTEN DEEPENS** existing fault lines based on class, caste, race, or any “outsider” status. Those dynamics can be self-perpetuating: Marginalized groups who live in crowded conditions with less access to health care are often hit harder by disease—and then are blamed for it.

Migrants are especially vulnerable to vilification. Mary Mallon, an Irish immigrant cook in early 1900s New York City, was dubbed “Typhoid Mary” for being an asymptomatic carrier of the typhoid bacte-

ria. After infecting several wealthy households, where some members died, she was forced into quarantine in a hospital on an island near the city, where, she complained in a letter to her lawyer, she was “a peep show” for visitors. In late 2010, Dominicans blamed migrant workers for a cholera outbreak that began when Nepali peacekeepers inadvertently introduced it to neighboring Haiti. Researchers from Emory University found that Dominicans connected the outbreak to character flaws or unhygienic habits among immigrant Haitians, who faced structural problems including lack of access to safe water and sanitation. One year into the epidemic, the government may have worsened the situation by making it more difficult for immigrants to get the legal status needed for health insurance.

COVID-19, too, may become associated with specific groups, says medical anthropologist Alexandra Brewis-Slade of Arizona State University, Tempe. “It is politically expedient and useful to be able to blame and distract,” giving politicians an excuse for public policy failures, she says. Stigmatization “discourages investment [in combating disease] because it devalues the people who would benefit most,” she says. “Stigma is often beneficial to those in power.”

Nyblade agrees that “COVID-19 may provide an excuse to further stigmatize already stigmatized groups.” In India, where a Hindu nationalist party is in power, many people targeted an international Muslim conference held in the country in March with the social media hashtag #Corona-Jihad. The Bombay High Court recently dismissed police charges filed against attendees for spreading the disease.

Indeed, many incidents in the current pandemic echo familiar patterns of animosity, especially in areas where the coronavirus has newly entered. Apartment dwellers on the outskirts of Mumbai, where COVID-19 cases have been growing, recently tried to throw out resident nurses because of fear that the nurses would bring the virus home. In the Indian state of Karnataka, 35 migrant workers who had returned to their village from Mumbai in June were quarantined. When seven tested positive, the group vanished overnight. “They feared reprisals,” says Edward Premdas Pinto, a public health activist at the Centre for Health and Social Justice who works in the region.

In one rural village, Pinto says, an elderly man returned from the hospital to find that his family had fled the house, fearing his return. He hanged himself. And in the United States, an advocacy group has recorded about 2600 hate-related incidents against Asian Americans between





A woman gets a free COVID-19 test from a health care worker who reaches from inside a mobile testing bus in Hyderabad, India. Some health care workers and people with COVID-19 in India face ostracism and animosity.

March and August, including spitting, racial slurs, and even assault. Many abusers specifically referred to the coronavirus.

**MONTHS AFTER** her traumatic experience with her Mumbai neighbors, Shaikh believes attitudes have improved as people have become more familiar with COVID-19. For those working to curb stigma, past pandemics can offer some lessons.

In leprosy and HIV, good information about mode of transmission and available treatments helped improve attitudes. HIV also showed that “sunlight itself can be a cure” for stigma, Weiss says. “Bringing attention to the existence of stigma enables people to [look for] areas where they can make their system function more effectively.” A strong health system is critical, too, say Indian public health activists, because it builds trust in medical authorities.

As seen with leprosy, language matters, which is why WHO in 2015 recommended against using countries, regions, animals, or people when naming viruses. Language remains a flash point with the coronavirus, with U.S. President Donald Trump regularly referring to “the China virus.” In March, some public health experts tried—and failed—to convert the prescription for “social distancing” into “physical distancing” because of the

potential connotations of the original phrase in societies riven by class, caste, and ethnicity. (In psychology, the social distance scale is a measure of racial or ethnic prejudice.)

Brewis-Slade cites New Zealand as a model for its “clear leadership, communicated with empathy and compassion.” The country has seen its share of prejudice during the pandemic; East Asians and historically oppressed Pacific Islanders have faced racist comments. But the government has quickly condemned such incidents while explicitly encouraging testing.

“People who we know have tested positive to COVID-19 are to be commended; they have done their bit” to protect others, Ashley Bloomfield, New Zealand’s director of health services, said in a press conference last month. There is “no shame or blame” in being infected with a virus, he said.

Pinto also stresses the importance of balanced media coverage. Indian TV news channels have stoked fear with a singular focus on the rising number of infections, he says. “Talking about recovery rate and success stories would help.” U.S. basketball player Magic Johnson’s 1991 disclosure of his HIV-positive status, for example, helped change public perceptions of the disease.

Hearing from other people in the community can be even more effective than

listening to experts or celebrities, Nyblade says. In RTI-led research in Ghana and Tanzania, she and colleagues set up training workshops and other activities in five of 10 selected clinics and then compared attitudes among the health care workers toward people with HIV. Learning from trained peers rather than experts had more impact. “Seeing and hearing people who are ‘just like you’ tell their stories can help dispel myths and misconceptions and break down the ‘othering’ process,” Nyblade says.

That kind of contact may be even more important during an outbreak, when isolation and quarantine are necessary but may compound suspicion. In Mumbai, Shaikh found that community outreach—going door to door with local volunteers and spending time with families—helped change attitudes in the slum where she works. Initially, no one would admit to having symptoms or report their contacts. Now, they’re coming forward to be tested and are more amenable to entering a care facility. A similar approach has helped authorities flatten the curve in Dharavi, one of the city’s largest slums.

The challenge, Shaikh says, is to help people understand that “we have to fight COVID-19 and not COVID-19 patients.” ■

Vaishnavi Chandrashekhar is a journalist in Mumbai.



# INSIGHTS

## PERSPECTIVES



Corvid birds, like this Florida scrub jay (*Aphelocoma coerulescens*), exhibit behaviors reminiscent of techniques used in magical effects.

## NEUROSCIENCE

# An unexpected audience

Experiments with magic effects might be informative about cognition in animals

By **Elias Garcia-Pelegrin, Alexandra K. Schnell, Clive Wilkins, Nicola S. Clayton**

In the past decade, the study of magic effects has started to gain attention from the scientific community, particularly psychologists. This interest stems from what magic effects might reveal about the blind spots in our perception and roadblocks in our thinking. The study of magic effects may offer researchers opportunities for new lines of inquiry about perception and attention. Moreover, because magic effects capitalize on our ability to remember what happened and our ability to anticipate what will happen next, using magical frameworks elicits ways to investigate complex cognitive abilities such as mental time travel (i.e., remembering the past and anticipating the future). Moving beyond the intersection between magic and the human mind, the application of magic effects to investigate the animal mind can

prompt the comparison of behavioral reactions among diverse species, in which magic effects might exploit similar perceptible blind spots and cognitive roadblocks.

The internet is filled with videos of magicians performing magic effects to animals (mostly captive primates and domesticated pets), in which the attentive animal spectators appear to react with awe and exultation when objects or food magically vanish. Without further investigation, it cannot be assumed that the animal audiences in the videos are amazed and surprised by the magic effect, akin to a human spectator. However, these encounters prompt investigation about the extent to which animals are susceptible to the same techniques of deception commonly used by magicians.

Over the past several decades, comparative psychologists, perhaps unintentionally, have been using magic effects as a methodological tool to explore a diverse range of cognitive abilities in animals. For instance, when investigating how dogs and great apes mentally represent different kinds of objects, experimenters have used devices inspired by

props commonly used in magic effects, such as boxes with false bottoms (1). Researchers have also investigated causal cognition in New Caledonian crows using invisible string, a see-through thread frequently used for levitation effects, to determine how crows respond to objects moving “without” human interaction (2). Moreover, violation of expectation paradigms, in which a subject is presented with a series of expected and unexpected outcomes, has been extensively used in comparative cognition (the investigation of cognitive mechanisms in diverse species and their origins). Such a premise is directly comparable to magic effects, given that the result of both magic and violation of expectation paradigms aim to elicit the same reaction from the observer, namely being surprised by witnessing the unexpected. Although animal subjects do not typically verbalize their surprise at unexpected events, surprise can be measured by using looking time. For example, if the subject finds an event surprising, they spend significantly longer looking at the event compared with an event that is deemed ordinary.

Department of Psychology, University of Cambridge, Cambridge, UK. Email: eg573@cam.ac.uk

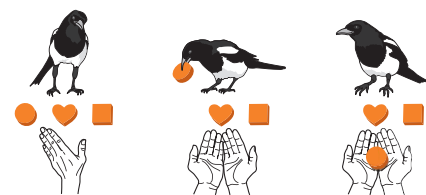
Although magical effects have permeated the field of comparative cognition, the scientific community has yet to study whether animals can be deceived by the same magic methodologies that would deceive a human observer. This is an interesting query because the use of magic effects to deceive animals could only be feasible if both human and animal spectators shared some analogous cognitive processes that capitalize on perceptive blind spots and cognitive roadblocks. Investigating the psychology behind magic effects in humans offers comparative psychologists an accessible pathway to formulate initial hypotheses to test in animal audiences. For example, the vanishing ball—an effect in which the magician seemingly vanishes a ball in thin air—could be used to investigate whether past experiences and current expectations alter the animal's perception. In humans, the illusion's success appears to be reliant on the spectator's expectation of the ball's movement and the social cues elicited by the magician (3). Using a similar design with animals could be insightful, regarding both the animal's expectations (i.e., throwing a ball toward the ceiling will make the ball go upward) and whether human body language offers an animal audience social cues when priming such illusions.

A popular magic technique is misdirection, the manipulation of the spectator by the magician to prevent the discovery of the cause of a magic effect. Controlling the audience's attention is an important skill for magicians, otherwise spectators might discover the mechanics behind the effect. Some species have been observed using behavioral tactics that can be considered analogous to misdirection. For example, chimpanzees sometimes divert their gaze from a desired object to detract a competitor's attention from it (4). Jays (i.e., corvids) will protect their food caches from possible pilferers by moving them several times or discretely hiding the food while performing several bluff caching events, thereby making it difficult for the observer to trace the genuine cache location (5).

The use of analogous methodologies by a diverse range of animal taxa to deceive conspecifics suggests that some misdirection techniques could exploit similar blind spots in attention. It also prompts the question of whether misdirection techniques used by magicians can also effectively fool animal minds. However, when doing so, experimenters must engage the attentional mechanisms of their spectators, because misdirection techniques are contingent on this. This might be challenging with animal subjects who might not pay sufficient attention to humans. Engaging the undivided attention of our closest relative, the chimpanzee, is one of the major challenges

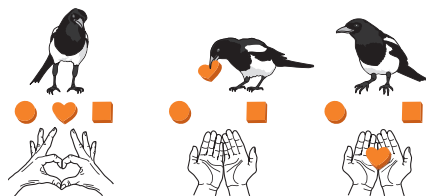
## Hand gestures influence choice

A priming experiment to observe whether a magpie's choice can be influenced by human hand gestures is shown. Magpies are first trained to discriminate between three differently shaped objects and exchange any shaped object for a food reward.



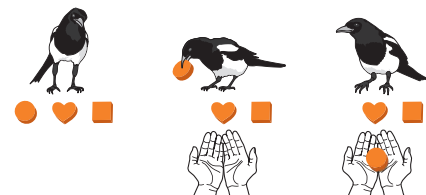
### Condition 1: Random priming

A random priming hand gesture is followed by asking the subject for any object.



### Condition 2: Priming

A heart-shaped hand gesture is made before asking for an object.



### Control condition: No priming

The experimenter does not make any hand gesture before asking for an object.

of implementing experimental designs on apes (6). Offering them long periods of intensive training, during which the ape must pay close attention to human movement, might ameliorate the challenge. By contrast, corvids possess sophisticated attentional mechanisms and are a suitable candidate for this line of research because they follow human gaze around particular objects and monitor human attentional states (7, 8).

In addition to misdirection, magicians often rely on our cognitive abilities to create a magical illusion. One such ability is object permanence—the ability to represent objects in the mind's eye when the object is out of sight. This ability appears to be adaptive for diverse taxa. For example, object permanence is harnessed by corvids during caching to successfully cache and recover because individuals must understand and remember that hidden items continue to exist even when they are out of sight (9). The ability to form a mental representation of an object when it is out of sight and to maintain it in memory is also vital for conjuring magic effects, because most ef-

fects tend to involve the appearance and disappearance of objects. Thus, object permanence paradigms grant a suitable starting point for comparative psychologists to investigate the analogous mechanisms of both human and animal observers of magic.

Interesting insights into object permanence have been made when adopting magic as a framework of study. When using a fake transfer technique (i.e., where the magician pretends to place an object in one hand while keeping it in the initial hand instead), human observers appear to retain the erroneous belief that a coin is placed inside the hand only for a limited period of time. Elongated reveal times seem to decrease the strength of this belief significantly (10), suggesting that inducing a false belief of object permanence might be contingent on not allowing enough time for the spectator to replay the events in their mind. Given the current research on object permanence in diverse taxa, translating the fake transfer technique to a suitable animal and paradigm (e.g., corvid caching) might elucidate the degree of commonality with object permanence abilities in humans and highlight whether perception of object permanence and memory of the hidden location in animal minds can be manipulated in analogous ways.

Although the science of magic has mainly focused on the exploitation of simpler mechanisms such as attention and perception, magic effects also use techniques that affect complex cognitive abilities such as memory and mental time travel. For example, magicians often alter the spectator's recollection of an event and induce fake memories through suggestions. When researchers suggested to human subjects that a “magic” key, which had been previously bent, would continue to bend once the effect finished, the spectators were more likely to report that they had observed the bending process during and after the magic effect (11). Other effects such as the “one ahead principle” exploit the spectator's inability to effectively deconstruct memories to make them think that the magician can read their mind. This is done by the magician forcing the outcome of one of the predictions while altering the order of events that the spectator is experiencing. Given the reconstructive nature of human memory, the spectator will recall the sequences in the order they occurred, instead of dissecting it into the events that were key for the experience (12). Such effects could only be investigated with species that possess mental time travel abilities, given that, evidently, one cannot exploit the faults of a nonexistent mechanism. Current research suggests that corvids exhibit sophisticated mental time travel abilities (13, 14) and



therefore are ideal subjects for experiments with such magic effects.

The application of similar techniques adapted to an animal audience might reveal whether animals that possess complex memory abilities also encounter comparable constraints. The imperative use of language in this kind of research is a strong barrier if one is to transpose it to an animal audience. However, recent research on humans raises the possibility that simple choices can be influenced by using hand gestures (15), thus offering a more relevant way to test for analogous roadblocks in animal memories. Magical frameworks ought to be the subject of in-depth methodological inspection and theorization. A good starting point might be the use of hand gestures depicting simple primes to observe if humans can influence choice in corvids. For example, subjects could be trained to discriminate between three differently shaped objects and asked, by the experimenter, to retrieve any object in exchange for a reward. Experimental conditions could include whether making heart-shape gestures, when asking, primes the subject to retrieve the heart object instead of the circular or rectangular object (see the figure).

The psychology of magic offers the scientific community a powerful methodological tool for testing the perceptive blind spots and cognitive roadblocks in diverse taxa. Studying whether animals can be deceived by the same magic effects that deceive humans can offer a window into the cognitive parallels and variances in attention, perception, and mental time travel, especially those species thought to possess the necessary prerequisites to be deceived by magic effects. Magical frameworks offer alternative and innovative avenues for hypothesis testing and experimental design, and it is hoped that future researchers will incorporate them into their investigations of the animal mind. ■

#### REFERENCES AND NOTES

1. J. Bräuer, J. Call, *J. Comp. Psychol.* **125**, 353 (2011).
2. A. H. Taylor, R. Miller, R. D. Gray, *Proc. Natl. Acad. Sci. U.S.A.* **109**, 16389 (2012).
3. G. Kuhn, M. F. Land, *Curr. Biol.* **16**, 950 (2006).
4. A. Whiten, R. W. Byrne, *Behav. Brain Sci.* **11**, 233 (1988).
5. N. S. Clayton, C. Wilkins, *Curr. Biol.* **29**, R349 (2019).
6. D. A. Leavens, K. A. Bard, W. D. Hopkins, *Anim. Cogn.* **22**, 487 (2019).
7. A. M. P. von Bayern, N. J. Emery, *Curr. Biol.* **19**, 602 (2009).
8. T. Bugnyar, M. Stöwe, B. Heinrich, *Proc. R. Soc. London Ser. B* **271**, 1331 (2004).
9. L. H. Salviczek, N. J. Emery, B. Schlinger, N. S. Clayton, *J. Comp. Psychol.* **123**, 295 (2009).
10. T. Beth, V. Ekroll, *Psychol. Res.* **79**, 513 (2015).
11. R. Wiseman, E. Greening, *Br. J. Psychol.* **96**, 115 (2005).
12. N. Clayton, C. Wilkins, *Interface Focus* **7**, 20160112 (2017).
13. N. S. Clayton, A. Dickinson, *Nature* **395**, 272 (1998).
14. C. R. Raby, D. M. Alexis, A. Dickinson, N. S. Clayton, *Nature* **445**, 919 (2007).
15. A. Pailhès, G. Kuhn, *Proc. Natl. Acad. Sci. U.S.A.* **117**, 17675 (2020).

10.1126/science.abc6805

#### BIOMEDICINE

# The gut microbiota in kidney disease

Dietary changes induce posttranslational modifications of microbial proteins to alter metabolite production

By Jennifer L. Pluznick

**C**hronic kidney disease affects 9% of the global population (1) and can have severe impacts on both the individual and societal levels. Although various conditions, such as diabetes, are well known risk factors for chronic kidney disease, in recent years interest has been growing regarding a potential role for the gut microbiota in modulating outcomes in kidney disease (2). Simultaneously, in the microbiology field, there has been a growing appreciation for the intersection of diet and the gut microbiota as a driver of changes in host health (3). To date, a common model has been that diet acts to alter the relative abundances (or diversity) of gut microbes, which can then lead to changes in gut microbial metabolite production (4). However, on page 1518 of this issue, Lobel *et al.* (5) report that diet can posttranslationally modify the gut microbial proteome, which can alter microbial metabolite production to drive changes in renal function.

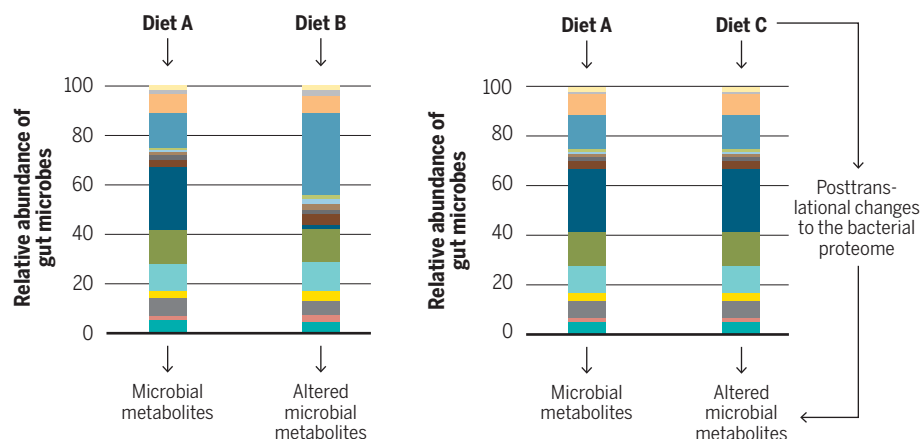
The primary function of the kidney is to maintain homeostasis against the many in-

sults and challenges from the external and internal environment. Functions including acid-base balance, water balance, blood pressure regulation, and glucose homeostasis require exquisite coordination and regulation by the kidney. Thus, it is not surprising that when kidney function falters, chronic kidney disease is associated with symptoms that are emblematic of the wide influence of renal function on health, including uremia (the retention of waste products in the blood that would normally be excreted in the urine), as well as edema, acidosis, anemia, and bone disease.

Risk factors for chronic kidney disease include conditions such as diabetes, hypertension, and heart disease. In addition to these comorbidities, the progression of kidney disease can be strongly influenced by dietary modulations—for example, the DASH (dietary approaches to stop hypertension) diet has shown to be protective (6). The positive influence of the DASH diet on kidney disease progression has been suggested to be due to a lowering of blood pressure, a lowered dietary acid load, and/or a lower likelihood of promoting inflammation and endothelial cell dys-

## Dietary influences on gut microbiota

The diet can modulate the gut microbial taxa (represented by different colors), thereby influencing metabolite production (left side of the figure). By contrast, Lobel *et al.* find that diet does not modulate the bacterial taxa, but rather posttranslationally influences the bacterial proteome, which alters microbial metabolite production (right side of the figure).



GRAPHIC: X. LIU/SCIENCE

function (6). A low-protein diet is another dietary intervention used in chronic kidney disease patients, and a benefit of this approach appears to be a decrease in uremic toxins. Uremic toxins are compounds that are retained in the blood when kidney function is compromised, and increases in uremic toxins promote a variety of pathologies, including endothelial dysfunction.

Because gut microbes produce uremic toxins (including p-cresyl sulfate, indole and indole derivatives, and trimethylamine *N*-oxide), the production or modulation of these substances by gut microbes has also been a focus of research (7). Although the role of the gut microbiota to produce uremic toxins is well-known, Lobel *et al.* introduce an entirely new twist on this paradigm: the idea that dietary changes can trigger posttranslational modifications of microbial proteins that alter uremic toxin formation, and thereby influence chronic kidney disease progression. Specifically, Lobel *et al.* report a dietary intervention that induced a posttranslational modification (S-sulfhydration) of a microbial enzyme, leading to a decrease in uremic toxin production that had a protective effect in a mouse model of kidney disease. This is a notable finding because posttranslational changes drove this outcome, and the gut microbial community composition itself was not found to be altered (see the figure).

In recent years, a number of studies have shown that changes in the gut microbiota (typically, changes in the relative proportion of various bacteria) are associated with a wide diversity of diseases and conditions, including obesity, diabetes, bipolar disorder, and depression. However, many of these studies have been correlative—they have reported shifts in bacterial abundances in affected individuals, but it is often unclear why these shifts occur, or whether they are causal. Are the shifts somehow promoting the associated phenotype? Or are they reacting to it? In at least one case, a change in bacterial abundance in type 2 diabetes was tied to a pharmaceutical intervention common in the affected group, rather than a consequence of the disease itself (8), highlighting the complexity inherent in these studies. To move research forward, it is imperative that studies go beyond reporting associations, and begin to unravel mechanisms underlying these shifts, and to understand the consequences.

The study of Lobel *et al.* goes a step beyond the taxonomic approach by highlighting the idea that a “shift” in bacterial com-

position is not the only explanation for a change in function of the gut microbiota. If posttranslational modifications of the bacterial proteome modulate host physiology or pathophysiology, then simply determining bacterial abundance will not reveal all of the key information. In retrospect, this should not be surprising: In mammalian research, it has been known for decades that the relative abundance of messenger RNA (mRNA) is not informative about everything that is happening at the protein, posttranslational, or functional level. Similarly, it is not surprising that, for some situations, species-level abundances of gut microbes fail to provide the full picture of what is happening in health and disease.

The findings of Lobel *et al.* emphasize the importance of not simply measuring bacterial abundances, but instead truly understanding functional processes that underlie host–microbiota interactions. Although such studies are difficult, Lobel *et al.* provide a blueprint for how they can be accomplished. Furthermore, these studies imply that the progression of chronic kidney disease may be modified by new strategies that alter the gut microbiota and/or the enzymatic activities of the gut microbial proteome.

Looking ahead, these types of approaches can yield dividends for not only chronic kidney disease, but for a large array of other diseases and conditions for which the microbiota have been implicated. By definition, these types of studies require a multidisciplinary approach as one must be cognizant of not only microbial biology and posttranslational modification modalities but must also understand the whole-animal physiology and pathophysiology of disease. Thus, this represents a great opportunity for scientists from diverse fields to come together. By pooling the diverse knowledge and approaches of varied fields, advances in understanding of host–microbiome interactions and disease progression can be made, and perhaps new approaches to disease treatment and prevention can be uncovered. ■

#### REFERENCES AND NOTES

1. G. B. D. C. K. D. Collaboration, *Lancet* **395**, 709 (2020).
2. S. Noel *et al.*, *Nephron Clin. Pract.* **127**, 139 (2014).
3. S. Mills, C. Stanton, J. A. Lane, G. J. Smith, R. P. Ross, *Nutrients* **11**, 923 (2019).
4. J. L. Sonnenburg, F. Bäckhed, *Nature* **535**, 56 (2016).
5. L. Lobel *et al.*, *Science* **369**, 1518 (2020).
6. C. M. Rebholz *et al.*, *Am. J. Kidney Dis.* **68**, 853 (2016).
7. W. L. Lau, J. Savoj, M. B. Nakata, N. D. Vaziri, *Clin. Sci. (London)* **132**, 509 (2018).
8. K. Forslund *et al.*, *Nature* **528**, 262 (2015).

#### ACKNOWLEDGMENTS

This work was supported by NIH DK107726 and NIH HL128512 (to J.L.P.).

Department of Physiology, Johns Hopkins School of Medicine, Baltimore, MD, USA. Email: jpluznick@jhmi.edu

10.1126/science.abd8344

#### IMMUNOTHERAPY

# Messengers from the microbiota

Microbiota produce inosine, a metabolite that modulates effector T cells and tumor immunity

By **Fyza Y. Shaikh<sup>1</sup>** and **Cynthia L. Sears<sup>1,2</sup>**

Immunotherapy sometimes leads to stunning therapeutic success in a wide range of cancers. However—except in melanoma, microsatellite instable (MSI) colorectal cancer, Hodgkin's lymphoma, and Merkel cell carcinoma—only ~15 to 30% of cancer patients respond to treatment. Thus, identification of the determinants of response are under intense investigation, and the gut microbiota is proposed to be a critical determinant for immunotherapy responses. On page 1481 of this issue, Mager *et al.* (1) show that inosine produced by specific gut bacteria, *Bifidobacterium pseudolongum* or *Akkermansia muciniphila*, enhances immune checkpoint inhibitor (ICI; a type of immunotherapy) efficacy in numerous mouse models. They propose that impaired gut barrier function from ICI treatment facilitates inosine systemic translocation, resulting in adenosine 2A receptor ( $A_{2A}R$ )-dependent activation of T helper 1 ( $T_H1$ ) antitumor effector cells that yield tumor shrinkage. These intriguing data provide a potential framework to directly link microbe-induced metabolite synthesis and ICI therapeutic efficacy.

Step-by-step examples of a microbiota, metabolite, immune effector, tumor response (or nonresponse) cascade in humans do not yet exist. However, the complexity presented by the hundreds to thousands of human gut bacteria may be reduced by enhancing the understanding of the biosynthetic metabolite redundancy among bacterial species (2). Accruing experimental and human data linking bacterial metabolites to human physiology and disease are encouraging. For example, studies of the interactions of bacterial me-

<sup>1</sup>Department of Oncology, Johns Hopkins University School of Medicine, Baltimore, MD, USA. <sup>2</sup>Department of Medicine, Johns Hopkins University School of Medicine, Baltimore, MD, USA. Email: csears@jhmi.edu



tabolites and human G protein-coupled receptors (GPCRs), a critical receptor class that mediates drug action, suggest that multiple simple bacterial metabolites, produced by more than one bacterial species, are GPCR agonists and affect immune and neurologic function (3, 4).

Furthermore, molecular approaches to modify bacterial genomes, such as CRISPR-Cas9-based gene deletion, enable characterization of how single molecules produced by specific bacteria affect host function. For example, using this approach, analysis of a *Clostridium sporogenes* mutant deficient in the production of branched short chain fatty acids (SCFAs) revealed a previously unknown capacity for branched SCFAs to regulate the numbers of immunoglobulin A (IgA)-producing plasma cells in the small intestine (5). Fermentation of dietary fiber by the gut microbiota produces SCFAs (acetate, propionate, and butyrate). SCFAs are the most abundant microbial metabolites in the gut that act through gut mucosal GPCRs (GPCRs 41, 43, and 109A) and are known for their critical role in colon homeostasis. SCFAs regulate the phenotype and/or function of macrophages, neutrophils, dendritic cells, and CD4<sup>+</sup> T cells [especially regulatory T cells (T<sub>reg</sub> cells)] and have recently been found to promote CD8<sup>+</sup> T effector function and memory potential (6, 7).

Early translational studies in cancer patients suggest that SCFAs limit anti-CTLA-4 (cytotoxic T lymphocyte-associated antigen 4) ICI responses but promote anti-PD-1 (programmed cell death protein 1) ICI responses (8, 9). ICIs block inhibitory immune cell and tumor molecules to unleash an antitumor immune response. ICIs, particularly anti-CTLA-4, likely alter intestinal barrier function in humans. Altered barrier function is associated with microbiota disruption (dysbiosis) that contributes to acute colitis, inflammatory bowel diseases, as well as colorectal cancer. Thus, better understanding of the effect of ICIs on the gut microbiota, its metabolic capacity, and metabolite-mediated downstream effects on colon mucosal immunity and tumor immune responses is needed. It is clear that untangling which gut microbiota species and metabolites, singly or together, modify human disease and therapeutic outcomes is a difficult challenge.

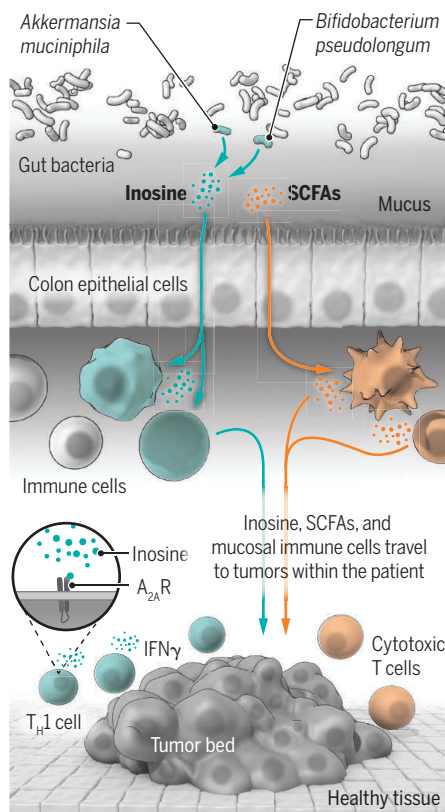
Inosine is another key metabolite produced by the gut bacteria. This endogenous purine nucleoside is formed by deamination of adenosine. Prior data support an immunosuppressive role for inosine, which activates A<sub>2A</sub>R signaling to limit inflammation, block T<sub>H</sub>1 cell differentiation, promote T<sub>reg</sub> cell activity, and thus

## Microbial signaling

Diet and medications yield microbiota that produce metabolites such as inosine or short chain fatty acids (SCFAs), which regulate mucosal and systemic immune cells. Inosine acts in the tumor microenvironment, through activation of adenosine 2A receptor (A<sub>2A</sub>R) signaling in T helper 1 (T<sub>H</sub>1) cells and regulates antitumor immunity in a context-dependent manner.

### Immune checkpoint inhibitor (ICI) therapy

ICIs disrupt the gut barrier, which allows bacterial metabolites, such as inosine, to promote antitumor immunity in an interferon-γ (IFNγ)-dependent manner.



inhibit tumor immunity in vivo. A<sub>2A</sub>R is also a GPCR and a target for drug development. Pharmacologic antagonists of A<sub>2A</sub>R enhance antitumor immunity in multiple mouse models and are currently in oncology clinical trials. Conversely, inosine supplementation was recently reported to enhance the antitumor efficacy of ICI therapy and adoptive T cell transfer in pre-clinical mouse models, but only in models that used tumor cells unable to catabolize inosine to support cell growth (10). These data suggest that, at least in some circumstances, inosine can relieve tumor-imposed metabolic restrictions on T cells.

Mager *et al.* build on this theme by showing with in vitro assays that inosine displays context-dependent actions (see the figure). Inosine boosted or inhibited T<sub>H</sub>1 differentiation of naïve T cells in the pres-

ence or absence, respectively, of exogenous interferon-γ. Prior work similarly identified highly context-dependent, oncogenic T<sub>reg</sub> cell action (11). Collectively, these data highlight that “company matters” in the highly pleomorphic and ever-expanding characterization of immune cell function, especially within the tumor microenvironment. Whether context-dependent inosine action is relevant to human T<sub>H</sub>1 cell differentiation or effector cell biology and/or affects current human cancer therapy trials of A<sub>2A</sub>R antagonists deserves scrutiny. Further analysis of microbial, serum, and immune cell samples from patients undergoing ICI treatment will clarify the impact of the observations by Mager *et al.*

Despite the exciting explosion of microbiota studies over the past 15 years, pinning down which microbial members or mediators are validated biomarkers for human disease prognosis or therapeutic response, has been elusive. Encouragingly, microbiota-based therapeutics are emerging for the treatment of *Clostridioides difficile* infection (12). Although the highly positive causal findings in microbiota studies in mice are thrilling, perhaps implausibly so, these results contrast sharply with diverse and inconsistent findings in microbiota human studies to date. Diet and drug exposure (antibiotics and non-antibiotics) (13), both recent and distant (14, 15), seem to modify microbiota-linked human disease outcomes, yet these factors are rarely included as prospectively collected variables in human study analyses. These gaps in outcomes emphasize that to harness the putative power of the microbiota for therapeutic success, well-designed, well-powered human studies tied to translational laboratory studies are needed to define circumstances that are addressable with microbiota-based treatments. ■

## REFERENCES AND NOTES

1. L. F. Mager *et al.*, *Science* **369**, 1481 (2020).
2. P. C. Dorrestein, S. K. Mazmanian, R. Knight, *Immunity* **40**, 824 (2014).
3. H. Chen *et al.*, *Cell* **177**, 1217 (2019).
4. D. A. Colosimo *et al.*, *Cell Host Microbe* **26**, 273 (2019).
5. C.-J. Guo *et al.*, *Science* **366**, eaav1282 (2019).
6. M. Luu *et al.*, *Sci. Rep.* **8**, 14430 (2018).
7. A. Bachem *et al.*, *Immunity* **51**, 285 (2019).
8. C. Coutzac *et al.*, *Nat. Commun.* **11**, 2168 (2020).
9. M. Nomura *et al.*, *JAMA Netw. Open* **3**, e202895 (2020).
10. T. Wang *et al.*, *Nat. Metab.* **2**, 635 (2020).
11. A. L. Geis *et al.*, *Cancer Discov.* **5**, 1098 (2015).
12. B. H. McGovern *et al.*, *Clin. Infect. Dis.* **ciaa387** 10.1093/cid/ciaa387 (2020).
13. L. Maier *et al.*, *Nature* **555**, 623 (2018).
14. L. Derosa *et al.*, *Ann. Oncol.* **29**, 1437 (2018).
15. J. Zhang *et al.*, *Gut* **68**, 1971 (2019).

## ACKNOWLEDGMENT

The authors thank J. Powell and D. Pardoll for helpful discussions.

10.1126/science.abe0709



## WATER QUALITY

# Protecting the sewershed

As cities use sewage as a water source, proactive policies must safeguard public health

By **Sasha Harris-Lovett<sup>1</sup>** and **David Sedlak<sup>1,2</sup>**

**U**rban population growth and less-reliable precipitation patterns due to climate change are putting pressure on the drinking water supplies of cities worldwide (1). At the same time, water treatment technologies are improving and becoming cheaper. These combined conditions have led urban water supply managers to look favorably on a nontraditional drinking water source: sewage (2). Purifying sewage to meet drinking water quality standards, a process known as potable water reuse, is technically feasible and can be cost-effective for augmenting urban water supplies. For these reasons, potable water reuse systems are becoming popular in the United States, Singapore, and Australia, among other places (3).

These new water supplies require reassessment of the policies and strategies for management of sewage and drinking water. Traditionally, water supply managers and regulators in the United States and much of the world have assumed that cities would

get their drinking water from the most pristine sources available. When contaminants of health concern were detected, regulators imposed additional standards for drinking water treatment, such as maximum contaminant levels for a particular chemical (4).

Using sewage as a water source requires a different approach. In the era of potable water reuse, a proactive regulatory strategy is especially necessary to protect public health, and regulations must adapt to take this practice into account. Sewage is, by definition, highly polluted. Although water treatment technologies can produce recycled water that meets current drinking water standards, the existing approaches of waiting until health impacts are recognized before acting to regulate a particular chemical found in the recycled water (as is current practice in the United States) may not adequately protect public health. In the European Union, the approach of prohibiting potable reuse systems because they are deemed too risky is also not wholly effective because of the prevalence of unplanned water reuse (5).

As planned potable water reuse systems become more common, water management must undergo a paradigm shift. This is not the first time the water industry has faced this type of challenge. In the late 20th cen-

Advanced technologies can convert raw sewage (left container) into drinking water (right container) by removing the vast majority of pollutants (center container) in the process. Proactive policies to identify, prevent, and monitor trace levels of remaining contaminants in drinking water are needed to protect public health.

tury, water managers and regulators in the United States recognized that preventing pollution of water supplies from diffuse sources, such as farm runoff and pastures, was often more effective and cheaper than finding ways to purify contaminated drinking water (6). The push for watershed protection in the 1990s changed the way that water utilities managed drinking water and provides lessons for protecting drinking water in the era of potable water reuse.

Watershed protection regulations such as the 1996 amendment to the Safe Drinking Water Act prevented pollution throughout the hydrologic basin from which cities obtained drinking water (6). In the United States, federal funds were allocated to help water managers meet new watershed protection requirements (6). These policies changed the status quo: Many water utilities restructured their organizations to acquire and manage land, to develop expertise in rangeland conservation and forestry, and to work closely with stakeholders throughout the watershed.

Wastewater was left out of previous watershed protection efforts. Because it is increasingly integral to urban water supplies, it now merits explicit consideration. This nontraditional water source requires an extension of watershed protection programs to include the “sewershed”—the network of sewers and sewage collection infrastructure in cities. Today, a sewershed protection approach is needed alongside existing watershed protection programs to preserve the safety of drinking water supplies.

Sewershed protection is a proactive regulatory approach to address the potential health risks associated with contaminants in sewage. Sewershed protection, paired with water treatment technologies, can safeguard drinking water supplies by curbing discharges of chemicals that have the potential to pass through water treatment systems. The same features of watershed protection should apply to sewershed protection: prioritizing resource allocation, ensuring stakeholder involvement in the development of goals, and finding integrated solutions.

For potable water reuse systems, much of the attention on chemical contamination has focused thus far on characterizing and removing pharmaceuticals, personal care products, and disinfection by-products (2).

<sup>1</sup>Berkeley Water Center, University of California, Berkeley, CA, USA. <sup>2</sup>Department of Civil and Environmental Engineering, University of California, Berkeley, CA, USA. Email: sedlak@berkeley.edu



The presence of these chemical compounds is relatively uniform across sewersheds, and gains made in understanding the sources of these compounds and options for treating them will apply to a range of cities considering or employing potable water reuse.

This is an important step, but it is insufficient to ensure the ongoing safety of potable water reuse systems. Characterization and control of industrial chemicals in sewersheds are also necessary (7). Chemicals intentionally discharged or accidentally released by factories or commercial enterprises to sewersheds are less predictable than chemicals sourced from households. Industrial chemical discharges to sewers vary greatly depending on which industries are present; sewersheds with industrial discharges may have concentrations of chemicals that are several orders of magnitude larger than those without industrial discharges (8).

Although the 1972 Clean Water Act regulates discharges of contaminants into surface waters in the United States to protect aquatic ecosystems, there is no comparable regulation to ensure that what goes into sewers is safe to be used as an eventual drinking water supply. Most existing industrial waste discharge permits and wastewater source control programs are relics of a previous era when the primary concern was the introduction of chemicals that could prevent the microbes at the sewage treatment plant from doing the work of cleaning wastewater. Regulations for sewershed protection must take into account the potential risks that chemicals in the sewershed pose to public health, as well as the cost and effectiveness of existing technologies to purify wastewater to drinking water standards (9). In sewersheds with higher risk of drinking water contamination due to large volumes of industrial chemical discharges to a sewershed relative to the volume of municipal wastewater, sewershed protection regulations might prohibit potable water reuse or require more extensive treatment and monitoring.

Some cities have begun to pursue proactive sewershed protection policies. For example, in Orange County, California, where potable water reuse has been practiced for more than 40 years, the wastewater utility has imposed strict limits on industrial discharges of toxic chemicals that have the potential to pass through its advanced treatment system. Similar practices have been less extensive in other cities that are planning and operating potable water reuse systems (10).

The concept of sewershed protection should not be restricted to places that are planning or operating potable water reuse systems. Treated wastewater is ubiquitous

in surface waters, as evidenced by the presence of organic chemical contaminants derived from treated wastewater in more than 80% of streams in the United States (11). Wastewater effluent dominates the flow of more than 900 streams in the United States and many European rivers at some times of year (5, 12). Many cities already rely upon water that originates in a sewershed; for example, Philadelphia, Berlin, and Houston all draw drinking water from surface waters with substantial contributions of wastewater effluent (2, 5, 13).

The sewershed protection concept also has implications for the quantity of recycled water that is potentially available. Household-scale water reuse and indoor water conservation can be important practices that are strongly supported within communities; however, a sewershed approach that explicitly acknowledges and plans for sewage being part of the water supply is essential to coordinating investments in water conservation and potable water reuse to produce a reliable supply of safe drinking water. Household- and neighborhood-scale water conservation efforts, such as greywater recycling and low-flow appliances, can reduce flows to municipal wastewater treatment plants, thereby concentrating pollutants and reducing the overall quantity of water available for municipal water reuse. Even under circumstances where industrial discharge to sewers is not a major concern, more efficient indoor water use has the potential to concentrate pollutants in sewage (6).

Recognition that sewers are part of the water supply requires important changes to U.S. policy, including the Clean Water Act and the Toxic Substances Control Act, and dictates a need for additional scientific research to protect drinking water supplies and public health. Regulators must implement policies to mandate more extensive monitoring and disclosure of chemicals discharged to sewers by commercial and industrial operations. Wastewater utilities must work with stakeholders to initiate real-time monitoring of chemicals in sewage, and create a mechanism for diverting or providing additional treatment at potable water reuse systems if release of a chemical occurs as the result of a spill.

Scientists and funding agencies must intensify research on the identification, fate, transformation, and health effects of chemicals in wastewater to enable more informed decision-making about potable water reuse. Special attention should be given to sewersheds that have a high contribution of wastewater from industrial, commercial, and medical sources, and these should not be considered for water reuse if

there is not clear evidence of robust water treatment, reliable system operations and maintenance, and rapid disaster response capacity. Chemicals that have the greatest likelihood of passing through advanced water treatment facilities, or that produce toxic by-products during the water treatment process, must be identified, monitored, and controlled. This would enable more reliable water quality and create the possibility of tailoring treatment plants to the local composition of sewage in a particular sewershed.

Finally, support for the development of biodegradable, nontoxic chemical alternatives for compounds that are difficult to remove during water treatment is urgently needed. Policies to support green chemistry would lessen potential health risks associated with using sewage as a water supply. Regulations similar to Europe's REACH legislation, which place the burden of proof of chemical safety on the manufacturer, may be more protective of health than the U.S. Toxic Substances Control Act (14) and are therefore more appropriate in the era of potable water reuse, provided that sewershed safety is considered.

Changes such as these are foundational to a sewershed protection approach. They will help to mitigate the risks posed by using sewage as a source of water supply, identify sewersheds where potable water reuse is a less desirable option, and protect public health in the era of potable water reuse. ■

## REFERENCES AND NOTES

1. C. J. Vörösmarty, P. Green, J. Salisbury, R. B. Lammers, *Science* **289**, 284 (2000).
2. National Research Council, *Water Reuse: Potential for Expanding the Nation's Water Supply Through Reuse of Municipal Wastewater* (2012); <https://bit.ly/3hwFZgB>.
3. A. N. Angelakis, T. Asano, A. Bahri, B. E. Jimenez, G. Tchobanoglous, *Front. Environ. Sci.* **6**, 26 (2018).
4. U.S. Public Health Service, *Public Health Service Drinking Water Standards* (1962), vol. 2.
5. J. E. Drewes *et al.*, *Characterization of Unplanned Water Reuse in the EU—Final Report* (European Commission Directorate-General for Environment, 2017); <https://bit.ly/3jBrQRd>.
6. U.S. Environmental Protection Agency, *Understanding the Safe Drinking Water Act* (2004).
7. C. E. Scruggs *et al.*, *J. Am. Water Works Assoc.* **112**, 10 (2020).
8. P. J. Phillips *et al.*, *Environ. Sci. Technol.* **44**, 4910 (2010).
9. E. L. Marron, W. A. Mitch, U. V. Gunten, D. L. Sedlak, *Acc. Chem. Res.* **52**, 615 (2019).
10. S. R. Harris-Lovett, C. Binz, D. L. Sedlak, M. Kiparsky, B. Truffer, *Environ. Sci. Technol.* **49**, 7552 (2015).
11. D. W. Kolpin *et al.*, *Environ. Sci. Technol.* **36**, 1202 (2002).
12. J. Rice, P. Westerhoff, *Nat. Geosci.* **10**, 587 (2017).
13. U.S. Environmental Protection Agency, *2012 Guidelines for Water Reuse*; <https://bit.ly/32UoF11>.
14. M. R. Schwarzman, M. P. Wilson, *Science* **326**, 1065 (2009).

## ACKNOWLEDGMENTS

We thank S. Matsoyan for research support. Funding for this research was provided by the NSF Engineering Research Center for Reinventing the Nation's Urban Water Infrastructure (ReNUWIt) under grant EEC-1028968.

10.1126/science.abd0700

# Tempus fugit: How time flies during development

Developmental-timing differences between species are linked to protein turnover

By Ryohei Iwata<sup>1,2,3,4,5,6</sup> and  
Pierre Vanderhaeghen<sup>1,2,3,4,5,6</sup>

**F**ugit irreparabile tempus,” wrote Virgil, a reminder that our lives are defined by the irreversible flow of time. As soon as the egg is fertilized, embryonic cells follow a developmental program strictly organized in time. The sequence typically is conserved throughout evolution, but individual events can occur over species-specific time scales. Such differences can have marked effects. For instance, it takes 3 months to generate cerebral cortex neurons in a human but only 1 week in a mouse. This prolonged neurogenesis likely contributes to evolutionary expansion of the human brain (1). But the mechanisms underlying developmental time scales remain largely unknown. On pages 1449 and 1450 of this issue, Rayon *et al.* (2) and Matsuda *et al.* (3), respectively, report an association between species-specific developmental time scales and the speed of biochemical reactions that support protein turnover.

Cell differentiation during mammalian development uses two types of timing mechanisms (biological clocks) based on oscillations or unidirectional processes (hourglass clocks). Modeling development in pluripotent stem cells (PSCs) from various species shows that the pace of differentiation of many cell types in an *in vitro* setting largely recapitulates the species-specific timing observed in embryos (4, 5). Even when human neurons are transplanted as single cells in a mouse brain, they follow their own prolonged developmental timeline (6). This suggests that cell-intrinsic mechanisms, yet to be discovered, dictate the timing of developmental trajectories in a species-specific manner.

Matsuda *et al.* examined a biological rhythm typical of vertebrate embryos: the “somite segmentation clock,” by which the body is built segment (or somite) by segment, thanks to waves of expression of specific genes (oscillations) in presomitic mesodermal (PSM) cells. Using *in vitro* modeling with mouse and human PSCs, the authors exam-

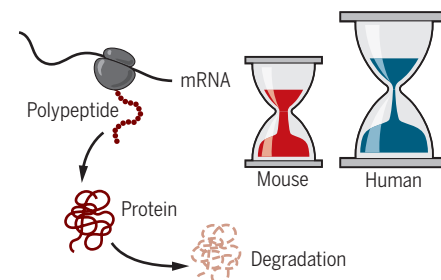
ined waves of expression of *HES7* (hes family bHLH transcription factor 7), a segmental-clock master gene. They found similar waves in PSM cells of both species, but the period of oscillations in human cells was ~5 hours instead of 2 hours (as in mouse cells), consistent with another recent report (7).

What might underlie such cell-intrinsic

differences? Evolutionary divergence in developmental processes usually occurs as a result of changes in the gene regulatory networks (GRNs) that control them (8). The authors examined the GRN of segmental oscillations, and except for the period of oscillation, they found no obvious difference between human and mouse gene expression. They then swapped the mouse and human genome sequences containing the *HES7* locus. The human *HES7* gene transplanted in mouse cells displayed fast oscillations like the mouse gene, whereas the mouse gene transplanted in the human cells displayed slower, human-like oscillations (see the figure). Thus, even DNA cis-regulatory components of the GRN do not appear to dictate the time scale of *HES7* oscillations. However, Matsuda *et al.* found important species-specific differences in a different mechanism: the speed of biochemical reactions leading to protein turnover (production and decay). Human cells displayed slower kinetics of protein expression (including “expression delays” related to RNA transcription, splicing, and translation) and a slower rate of protein decay, mostly related to degradation. Many examined parameters showed a twofold difference in mouse versus human cells, matching the time differences observed for the segmentation clock.

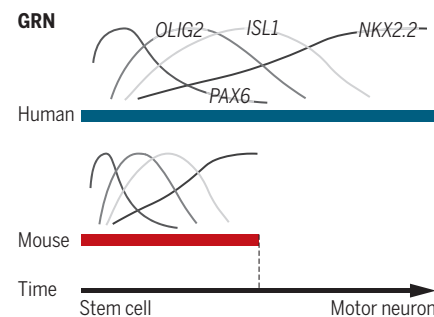
Rather than being dominated by clock-like oscillations, the developmental process is specified mostly by cell-fate transitions, by which embryonic cells gradually and irreversibly become differentiated cells. Could it be that similar mechanisms regulate these hourglass-like timing events as well? Rayon *et al.* explored this notion using a motor neuron (MN) developmental model from mouse and human PSCs. Examination of MN development *in vitro* revealed that the underlying GRN is similar in both species, except that human motoneurogenesis takes 2.5 times longer in the human cell model versus the mouse. The authors then examined the influence of sonic hedgehog, the key morphogen that induces MN fate (by changing timing and intensity of the signal), and the MN-development master gene *OLIG2* (oligodendrocyte transcription factor 2) (by inserting the human gene in mouse cells) but found no effects that explained the species-specific time differences. They then analyzed protein stability during MN development and found that the mean protein half-life was doubled in human cells compared with mouse cells,

## Same events, distinct timing

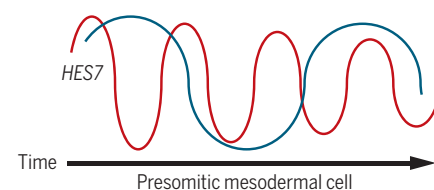


## Kinetics of protein turnover

Species-specific protein turnover speeds (hourglasses) mirror differences in, and might specify, developmental time scales.



## Segmentation clock



## Developmental time scales

The same gene regulatory network (GRN) drives motoneurogenesis over a time scale that is doubled in human versus mouse stem cells. The time period for *HES7* oscillations is also doubled in human (blue) versus mouse (red) presomitic cells.

*HES7*, hes family bHLH transcription factor 7; *ISL1*, insulin gene enhancer protein 1; mRNA, messenger RNA; *NKX2.2*, homeobox protein *Nkx2.2*; *OLIG2*, oligodendrocyte transcription factor 2; *PAX6*, paired box protein *Pax-6*.

<sup>1</sup>Vlaams Instituut voor Biotechnologie—Center for Brain & Disease Research, 3000 Leuven, Belgium. <sup>2</sup>Department of Neurosciences, Katholieke Universiteit (KU) Leuven, 3000 Leuven, Belgium. <sup>3</sup>Leuven Brain Institute, 3000 Leuven, Belgium. <sup>4</sup>Université Libre de Bruxelles (ULB), 1070 Brussels, Belgium. <sup>5</sup>Institut de Recherches en Biologie Humaine et Moléculaire (IRIBHM), 1070 Brussels, Belgium. <sup>6</sup>ULB Neuroscience Institute, 1070 Brussels, Belgium. Email: pierre.vanderhaeghen@kuleuven.vib.be



which is consistent with the findings of Matsuda *et al.* Both studies point to protein turnover as a potential source of variation in developmental time scales. Each group tested this hypothesis further by in silico modeling of their experimental systems, which predicted, in each case, a prominent influence of the delay in protein production and protein decay on developmental time scales.

That protein turnover affects the timing of development is provocative and attractive but must be validated by experimental evidence for causal relationship between the two (by altering the production and decay of proteins and mRNA, and then examining the developmental time scale). Such experiments will also help to determine the respective contributions of expression delay versus protein decay, on which each study puts a somewhat different emphasis. The consistent results from both studies also raise questions about the mechanisms upstream of interspecies differences in protein turnover. Metabolism is an attractive candidate. Protein turnover requires a considerable amount of energy (9), and metabolic rewiring has emerged as a central instructor of cell fate transitions (10), although through epigenetic remodeling rather than changes in proteostasis. Another question is whether the same principles apply to developmental events that display more pronounced time scale differences. For example, GRN divergence might operate through specific genes that modulate the timing of human cortical neurogenesis (11). Furthermore, metabolism and protein turnover might display differences depending on the cell context or the specific protein involved. And known correlations between developmental timing, life span, and aging across species (12) might all be causally linked to differences in metabolism and protein turnover. ■

#### REFERENCES AND NOTES

1. A. M. M. Sousa *et al.*, *Cell* **170**, 226 (2017).
2. T. Rayon *et al.*, *Science* **369**, eaba7667 (2020).
3. M. Matsuda *et al.*, *Science* **369**, 1450 (2020).
4. J. van den Ameelen *et al.*, *Trends Neurosci.* **37**, 334 (2014).
5. M. Ebisuya, J. Briscoe, *Development* **145**, dev164368 (2018).
6. D. Linaro *et al.*, *Neuron* **104**, 972 (2019).
7. M. Diaz-Cuadros *et al.*, *Nature* **580**, 113 (2020).
8. E. H. Davidson, D. H. Erwin, *Science* **311**, 796 (2006).
9. J. Labbadia, R. I. Morimoto, *Annu. Rev. Biochem.* **84**, 435 (2015).
10. N. Shyh-Chang *et al.*, *Development* **140**, 2535 (2013).
11. I. K. Suzuki *et al.*, *Cell* **173**, 1370 (2018).
12. A. A. Fushan *et al.*, *Aging Cell* **14**, 352 (2015).

#### ACKNOWLEDGMENTS

P.V. is funded by the European Research Council, Belgian Fonds Wetenschappelijk Onderzoek, Excellence of Science Research programme, AXA Research Fund, Belgian Queen Elizabeth Foundation, and Fondation Université Libre de Bruxelles. R.I. was supported by the Belgian Fonds de la Recherche Scientifique.

10.1126/science.abe0953

## QUANTUM SYSTEMS

# Multiplicative suppression of decoherence

Combining different protocols extends the life of a quantum system

By Philip Hemmer<sup>1,2</sup>

Optically addressed quantum spin systems have been explored for a number of applications, with quantum information being one of the most exciting. However, noise fields destroy quantum information, especially in solids, through a process called decoherence. This process limits how well quantum information devices perform. The spin decoherence problem has been studied for decades, and many protocols have been devised to suppress it. All of these protocols have limitations, which drives the search for new and better strategies. On page 1493 of this issue, Miao *et al.* (1) show that in some cases, two substantially different protocols can be combined to get a multiplicative improvement of the coherence time.

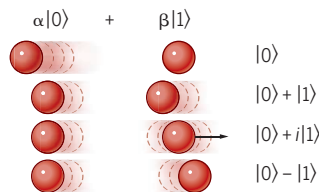
To explain how quantum coherence is protected, first defining it in a simple way is useful. A qubit or quantum bit is often depicted as a superposition of logical “0” and “1” states, written as  $(\alpha|0\rangle + \beta|1\rangle)$ . Hence, at least until readout, a qubit can be viewed as analog, rather than digital. In addition to the relative magnitude of the 0 and 1 components, the relative phase is also important. This is because quantum states are often based on oscillators. Phase is simply a way of specifying where an oscillator is in its cycle at a particular snapshot in time (see the figure). For example, a vibrating ball might be stalled at its maximal displaced position or be at its maximal speed with momentary zero displacement (2). Quantum coherence is then defined as a precise magnitude and phase relationship between two quantum oscillators.

## Creating quantum systems

The magnitude and phase information of a qubit is illustrated with a pair of oscillating balls.

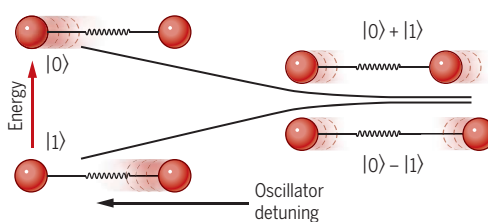
### Setting up the system

The relative magnitude and phase are shown using an idealized stroboscopic picture, where the arrow represents the instantaneous speed of the ball. Each oscillating ball is represented mathematically with a  $|0\rangle$  or  $|1\rangle$ .



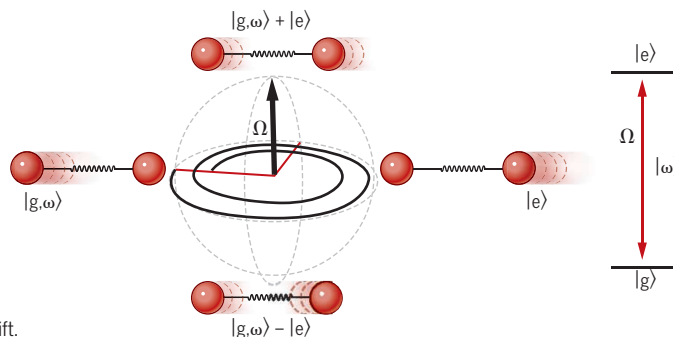
### Coupling oscillators

Interactions between qubit oscillators can be represented by coupling the balls with a spring. The original qubit states do not interact when their oscillation frequencies are far apart. However, near degeneracy the coupling favors special coupled vibration modes that are stable against phase drifts.



### Adding a different force

A different way to stabilize a system is through rotation ( $\Omega$ ) caused by a strong, resonant drive field. In this situation the special coupled vibration states shown at top and bottom are stable against small changes in rotation direction due to phase drift.



Decoherence arises when any noise source alters either the magnitude or phase of one of the qubit's oscillators differently than the other. One popular technique to suppress decoherence is through the use of "decoherence-protected subspaces" (DPSs). Constructing such a subspace from the above two-oscillator system is accomplished by weakly coupling them by adding a spring (see the figure). When the two oscillators are far detuned from each other, the spring has no effect. However, near zero detuning, the spring effectively causes the relative phases to have different energies, and this can act like a barrier to suppress phase decoherence. In fact, certain phases become constants of motion, also called normal modes, of the coupled system. Examples of normal modes are the in- and out-of-phase cases,  $(|0\rangle + |1\rangle) = |+\rangle$  and  $(|0\rangle - |1\rangle) = |-\rangle$ , neglecting normalization. Because these normal modes are so stable, using these as the qubit states makes more sense than the original  $|0\rangle$  and  $|1\rangle$ . So, the qubit now becomes  $(\alpha|+\rangle + \beta|-\rangle)$  in a DPS.

The next question is how to create and use one of these DPSs. Many possible approaches exist, but the examples in Miao *et al.* are useful to consider. The first DPS involves using a spin-1 system in a low-symmetry crystal. The levels of a spin-1 system in a strong magnetic field are, using the notation from Miao *et al.*,  $|+1z\rangle$ ,  $|1z\rangle$ ,  $|0\rangle$ . The  $|0\rangle$  state is not affected by the magnetic field and therefore is already one state of a DPS. To construct the other state, the magnetic field is removed. The  $|+1z\rangle$ ,  $|1z\rangle$  states then naturally become coupled to each other by interactions present in a low-symmetry host, like electric field or strain. This gives  $|+\rangle$  and  $|-\rangle$  states analogous to those mentioned above and completes the DPS.

The challenge is to construct a second DPS that is sufficiently different from the first such that it results in a multiplicative improvement in coherence time. The authors use a strong alternating current field to resonantly drive a transition between two of the above DPS states. Such a driven two-level system is often modeled by a Bloch vector, which is a three-dimensional representation of the relative magnitude and phase (see the figure). The driving field causes rotation about the axis shown at a rate equal to the Rabi frequency,  $\Omega$ . Decoherence corresponds to rotation about an orthogonal axis, and so it is suppressed by a large  $\Omega$ . This process is analogous to a mechanical gyro, where

attempts to tilt its rotation axis appear to be resisted by an invisible force. Special points on the Bloch sphere traced out by the Bloch vector correspond to normal modes called "dressed states"  $(|g, \omega\rangle + |e\rangle)$  and  $(|g, \omega\rangle - |e\rangle)$  that are used to construct the second DPS, denoted as  $|+1\rangle$  and  $|-1\rangle$  by the authors.

Dressed states are not normally used for DPS states because they are sensitive to the strength of the driving field. However, Miao *et al.* developed a clever scheme to overcome this problem by driving a direct transition between the dressed states ( $\beta$ ) to probe and correct the driving field strength. This resulted in a further increase in coherence time of two orders of magnitude.

The authors' key accomplishment is that DPSs can be combined to achieve multiplicative decoherence suppression. These demonstrations stimulate the imagination in a way that can lead to breakthroughs. For example, could decoherence be further suppressed if the dressed states themselves were strongly driven by a second resonant field (i.e., "nested" dressed states), possibly with a different Rabi frequency? Classically, this process is analogous to achieving a higher level of noise suppression by independently modulating a signal at two frequencies and demodulating it at the sum or difference frequency. An analogous sum-frequency heterodyne experiment showed quantum-like classical entanglement (4), so there may be additional information-processing advantages as a side benefit to the decoherence protection.

This leads to the question of whether other schemes might generate a DPS with multiplicative benefit. In Miao *et al.*, the probing transition between dressed states was electric-dipole, whereas the original resonant drive was magnetic dipole. The possibility of using this to achieve further decoherence suppression should be considered. In Miao *et al.*, the authors still have one unused DPS state. By upgrading the experimental geometry to access this state, it could be possible to simultaneously implement yet another DPS. This might, for example, be accomplished using a Raman-like scheme. By demonstrating a multiplicative advantage combining two DPSs, Miao *et al.* open the door to new DPS approaches that may substantially enhance the performance of future quantum information systems. ■

#### REFERENCES AND NOTES

1. K. C. Miao *et al.*, *Science* **369**, 1493 (2020).
2. P. R. Hemmer, M. G. Prentiss, *J. Opt. Soc. Am. B* **5**, 1613 (1988).
3. A. S. M. Windsor, C. Wei, S. A. Holmstrom, J. P. D. Martin, N. B. Manson, *Phys. Rev. Lett.* **80**, 3045 (1998).
4. K. F. Lee, J. E. Thomas, *Phys. Rev. A* **69**, 052311 (2004).

<sup>1</sup>Electrical and Computer Engineering, Texas A&M University, College Station, TX, USA. <sup>2</sup>Zavoisky Physical-Technical Institute, Federal Research Center "Kazan Scientific Center of RAS," Kazan, Russia. Email: prhemmer@ece.tamu.edu

## OCEANOGRAPHY

# Advance in global ocean acoustics

## Earthquakes can be used to define changes in ocean heat content

By Carl Wunsch

In the past 50 years, the major conceptual revolution in physical oceanography is the transformation from considering the ocean as a large-scale, extremely slowly changing fluid to a fundamentally turbulent one. The ocean changes across a wide range of temporal and spatial scales, from millimeters to 30,000 km and from seconds to multi-millennia, with major regional differences. Because ocean exploration relied on a few slow, expensive ships exploring over many decades and depicting only the grossest mappable global properties, observing the variability is a forbidding challenge. The ocean is very noisy, filled with short-spatial scale structures that make obtaining large-scale average properties problematic. The oceanographic community responded by developing altimetric and gravity satellites, the Argo profiling system, and ever more capable models. On page 1510 of this issue, Wu *et al.* (2) demonstrate how an intriguing combination of physical oceanography and classical seismological techniques potentially opens the way for an entirely new and globally capable observation system.

The fluid ocean has been known for hundreds of years as a good transmitter of sound. This property contrasts with the opacity of the ocean to electromagnetic radiation at all useful wavelengths. The use of acoustic depth sounding from ships dates back to the beginning of the 20th century. At about the same time, navies recognized that reliable submarine detection required acoustic detection. Acoustic methods have come to be used recently in a variety of ways, including local signaling from ships to release an anchor from an instrument moored to the seafloor, for the tracking of subsurface drifting instruments

Department of Earth and Planetary Sciences, Harvard University, Cambridge, MA 02138, USA. Email: cwunsch@fas.harvard.edu



(2), and in measuring devices that use acoustic backscatter techniques over meter scales. Biologists have long listened to the sounds of marine organisms of all sizes and shapes. Nonetheless, observational systems designed to study the physics of the fluid ocean relied initially on purely mechanical devices and, more recently, on instruments that electronically recorded data internally.

The use of acoustics was neglected for several reasons. Ocean acoustics were mainly the domain of classified navy work directed at short-range immediate detection of submarines or for hiding submarines from acoustic detection. This situation resulted in acoustics not being part of the normal toolkit for ocean observations. Remarkable and useful as the satellites and Argo systems have proven, these

anomalies inside a patient. Over the next several decades, numerous experiments on spatial scales from hundreds to more than 10,000 km repeatedly demonstrated the fundamental utility of the technique (see the figure) (4, 5). These programs used artificial sound sources because these removed the analogous seismological problem of having to determine source location and timing from the same data as was being used to study the medium, and the sources could be placed anywhere. Acoustic tomography was not, as originally envisioned, exploited on a continuing global basis. A federally funded program to establish a Pacific Ocean-wide prototype [Acoustic Tomography of the Ocean Circulation (ATOC)] triggered an outcry that the experiment was going to deafen and thus destroy the marine mam-

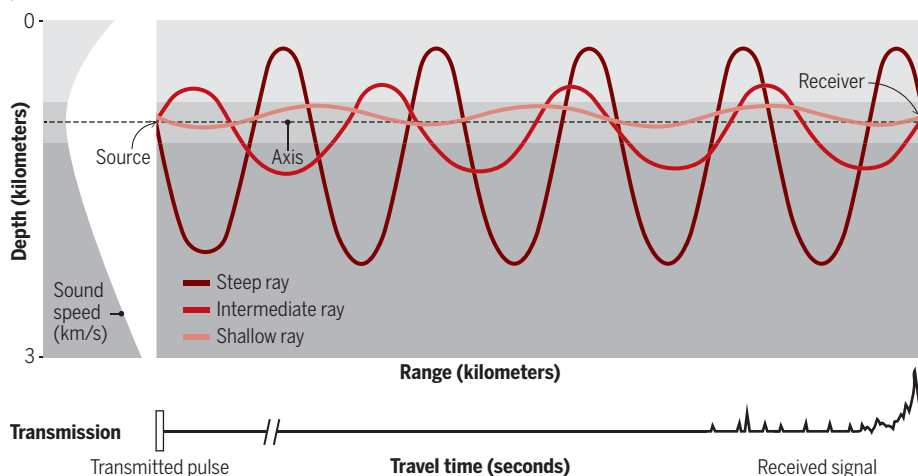
This situation may be about to undergo change. A great variety of natural and artificial sound sources are detectable in the ocean, including earthquakes, shipping noise, breakup of floating ice sheets, oil exploration, rainfall, breaking waves, and large marine mammals, such as blue whales capable of signaling each other over ocean basin distances. From an information extraction point of view, use of natural sources brings back the seismologists' hypocenter problem: finding source timing and three-dimensional space location. Wu *et al.* have now shown that acoustic integrals from the sound signature of ordinary earthquakes can be used, quantitatively, to determine changes in oceanic temperatures and, consequently, changing heat content. The authors evade the hypocenter problem by relying on "repeating" earthquakes, but more general possible solutions now also exist.

Great advantages can accrue from major noise suppression obtained by averaging over months and years. One intriguing possibility is that quantitative deep ocean measurements can be made from purely land-based seismic stations. At the other extreme, Project Mermaid (6) has shown the feasibility of detecting tomographic signals on drifting floats. If some fraction of the Argo floats carried relatively cheap hydrophones, developing a true set of intersecting tomographic integrals is possible. These could also serve as ocean rain gauges (7).

Several quantitative questions will need to be answered to determine how useful the technique may be. The applicability of the technique globally depends on whether repeating earthquake hypocenters are accurate enough globally. If so, historic earthquake records might be used to infer ocean temperatures long before direct measurements became available. Whether noise sources such as ships and ice-sheet breakups, now tracked from space, can be accurately combined with their acoustic signatures is not clear. With enough receivers, the potential exists for blue whales or other marine mammals to be used as tomographic sources. This approach may not only benefit our understanding of the fluid ocean but also help us to understand biological systems in the ocean. ■

## Temperature profiles from sound

The sound speed minimum in the ocean acts as an acoustic waveguide. Many different sources can generate acoustic waves. These include explosions, earthquakes, or perhaps even whale song. Rays emanating from the source at different angles cycle between different depths on their way to the receiver. The varying vertical properties change the travel time for different rays as they move from source to receiver. This different sampling permits tomographic reconstruction of a temperature profile. Intersecting vertical planes permit full three-dimensional results.



techniques have provided only partially adequate coverage of an electromagnetically opaque ocean with a mean depth of 3800 m. Existing methods produce point values with sometimes uncontrollable spatial distributions, leaving them susceptible to distorted sampling in both time and space

In 1979, the idea was developed that exploitation of the oceanic transparency to sound coupled with modern acoustic source technology and inverse methods would permit determination of large-scale averages, with useful top-to-bottom resolution of the ocean temperature (heat content) (3). The methodology was called "ocean acoustic tomography" for its analog with the mathematics of medical tomography, which also involves using measured integrals to find

mals of the ocean. That led in turn to years of often ill-tempered permitting processes with various U.S. agencies and public hearings. (Tomographic signal levels are a small fraction of those in the ocean from shipping, oil exploration, and naval activities.) A different problem involved the technology of acoustic sources, which had to be (i) low power to work from batteries and (ii) large in size to obtain low frequencies and finite bandwidths. The consequence was that the sources were both cumbersome to handle at sea and relatively expensive in both dollars and shiptime. Despite all of these difficulties, active-source acoustic tomography remains useful, particularly in the Arctic Sea, but in the hands of a comparatively small group of experts.

## REFERENCES AND NOTES

1. W. Wu *et al.*, *Science* **369**, 1510 (2020).
2. T. Rossby, D. Webb, *Deep-Sea Res.* **17**, 359 (1970).
3. W. Munk, C. Wunsch, *Deep-Sea Res.* **26A**, 439 (1979).
4. W. Munk, P. Worcester, C. Wunsch, *Ocean Acoustic Tomography* (Cambridge Univ. Press, 1995).
5. B. M. Howe *et al.*, *Front. Mar. Sci.* **6**, 426 (2019).
6. F. J. Simons *et al.*, *J. Acoust. Soc. Am.* **146**, 3067 (2019).
7. J. A. Nystuen, *J. Atmos. Ocean. Technol.* **13**, 74 (1996).

10.1126/science.abe0960

## BIOTECHNOLOGY

# Global citizen deliberation on genome editing

Global governance can be informed by a deliberative assembly composed of lay citizens

By John S. Dryzek, Dianne Nicol, Simon Niemeyer, Sonya Pemberton, Nicole Curato, André Bächtiger, Philip Batterham, Bjørn Bedsted, Simon Burall, Michael Burgess, Gaetan Burgio, Yuriy Castelfranchi, Hervé Chneiweiss, George Church, Merlin Crossley, Jantina de Vries, Mahmud Farooque, Marit Hammond, Baogang He, Ricardo Mendonça, Jennifer Merchant, Anna Middleton, John E. J. Rasko, Ine Van Hoyweghen, Antoine Vergne

Genome editing technologies provide vast possibilities for societal benefit, but also substantial risks and ethical challenges. Governance and regulation of such technologies have not kept pace in a systematic or internationally consistent manner, leaving a complex, uneven, and incomplete web of national and international regulation (1). How countries choose to regulate these emergent technologies matters not just locally, but globally, because the implications of technological developments do not stop at national boundaries. Practices deemed unacceptable in one country may find a more permissive home in another: not necessarily through national policy choice, but owing to a persistent national legal and regulatory void that enables “ethics dumping” (2)—for example, if those wanting to edit genes to “perfect” humans seek countries with little governance capacity. Just as human rights are generally recognized as a matter of global concern, so too should technologies that may impinge on the question of what it means to be human. Here we show how, as the global governance vacuum is filled, deliberation by a global citizens’ assembly should play a role, for legitimate and effective governance.

## INCLUSIVE PARTICIPATION

Calls for inclusive participation are common among those concerned with the technology and its governance (3), when it comes to applications in humans, food, agriculture, and environmental conservation (4). International organizations such as the World Health Organization (WHO), the United Nations Educational, Scientific and Cultural Organization, and the Organization for Economic

Co-operation and Development; science bodies such as the U.S. National Academies of Sciences, Engineering, and Medicine (5) and the UK-based Nuffield Council on Bioethics; and many others have joined the call. The WHO’s Expert Advisory Committee on Developing Global Standards for Governance and Oversight of Human Gene Editing is exploring public engagement at various scales (6), involving a registry of genome editing trials, dissemination of scientific findings translated into many languages, consultation with a broad range of stakeholders from around the world through videoconference seminars or web-based dialogue, and collaboration with other international organizations and nongovernmental organizations (NGOs). This is a call for action, but not a design for how to act in a way that involves citizens, still less at the crucial global level.

In 2018, the international Association for Responsible Research and Innovation in Genome Editing (ARRIGE) was created, aiming to bring civil society into the discussion (7). But civil society is not the same as the citizenry, and to date ARRIGE has only got as far as a website, open meetings, and international expert meetings. Others have called for monitoring and learning that would involve experts, scholars, policy-makers, and organizations (8). However important they may be, such initiatives do not fully address the practicalities and specifics that would enable meaningful participation of citizens from around the world. We propose a crucial, complementary effort, which would involve global public deliberation to explore the science and its implications, beginning with a global citizens’ assembly.

There is already vast experience with citizen deliberation at local and national levels, on complex issues including those involving scientific and technological risk accompa-

nying potential benefits. Relevant models include citizens’ assemblies, citizens’ juries, deliberative polls, and consensus conferences (9). They can be game-changers: Citizens’ assemblies on same-sex marriage, abortion, and climate change in Ireland led to changes not just in law but to the texture of Irish politics—overturning the presupposition that some obstacles to reform were immutable. Currently there is no experience with global citizens’ forums [globally oriented multicountry exercises such as World Wide Views (10) have citizens deliberate only with fellow-nationals]. The challenge to consider complex issues in multiple languages is formidable, but Europe-wide forums such as Europolis have demonstrated the success of simultaneous translation.

## GLOBAL CITIZENS ASSEMBLY

How would a global citizens’ deliberation be constituted? We propose a citizens’ assembly model (rather than any of its smaller alternatives, such as citizens’ juries) that would at a minimum be composed of 100 people. Participants would be recruited throughout the world. Stratified random sampling would yield a broad spread in terms of nationality, cultures, level of education, age, income, religion, and gender. Care would be needed to protect the integrity of sampling from political interference, and in some places, it might be necessary to argue for the legitimacy of stratified random sampling (as opposed to, say, selecting only elders). Increasing the size beyond 100 could promote representativeness, though increase logistical challenges.

Participants could, where possible, be recruited from nationally organized forums (themselves with members recruited through stratified random sampling) on specific aspects of genome editing. This offers the advantage that citizens would join the global process with considerable knowledge and experience. A hundred or more citizens would bring to bear all kinds of relevant local knowledge and different worldviews. They would meet over a week or more, hear presentations from experts and advocates, deliberate among themselves in small groups (each of which would have a facilitator) then in plenary session, and produce a report that summarized key concerns and recommendations. There would be an advisory committee with members from relevant interests and expert communities, ensuring that participants receive balanced information.

What would a global citizens’ assembly do? Like any such body, it would need an initial charge: possibly, “Should there be global principles for the regulation of genome editing technologies?” Assuming

Author affiliations are listed in the supplementary materials.  
Email: john.dryzek@canberra.edu.au



the assembly felt there ought to be such principles (rather than defer to national variety), it would then consider their content. There is generally a place for universal principles in global governance, even if they are implemented nationally. Think of the Sustainable Development Goals, applying universally, implemented nationally. The assembly would not address the local content of applications, such as gene editing research involving human embryos in the United Kingdom. Although we cannot predict what principles the assembly would highlight, one might specify from whom and in what terms co-design of field trials (with participation by those who stand to either gain or lose) is needed in light of the risk that wealthy actors may use developing countries as sites for the field testing of technologies (such as gene drive technology to kill pests). Another might be genome editing justice: How should we think about the allocation of scarce resources given that some applications may benefit a small number of the relatively wealthy (for example, gene drives for Lyme disease) whereas others may benefit large numbers of the poor (for example, gene drives for malaria)?

The citizens' assembly would not legislate; its report would have no standing in international law. However, for good reasons that the assembly would make public, it should help shape what happens next. The idea is to inspire a more effective response in global institutions [notably, the UN Food and Agriculture Organization (FAO) and the WHO], national governments, civil society, and the private sector. The report would be a first draft of informed global public opinion regarding genome editing. Here, public opinion can be defined not in terms of unreflective mass responses to survey questions, but as a provisional and dynamic outcome of inclusive and competent public discourse supported by evidence-based science that connects to public values.

Who should fund and organize the assembly? Funding should come from independent bodies with no material stake in the technology. International organizations such as the WHO and FAO would be appropriate, as would foundations. National (and European Union) research councils could contribute on the grounds of social scientific research questions, including testing the deliberative capacities of the global citizenry. We can be more specific about organizations that have the necessary capacity, neutrality, and experience in running citizen deliberation. A consortium under construction includes Missions Publiques and the Danish Board of Technology (both of which have run large multinational processes), Involve (UK), the ECAST (Expert

and Citizen Assessment of Science and Technology) network of academics and practitioners (U.S.), and institutes such as the Centre for Deliberative Democracy and Global Governance at the University of Canberra, and School of Population and Public Health at the University of British Columbia. This networked expertise puts the consortium in a position to make precise and implement what others have only called for in very general terms.

What kind of influence should the assembly seek? A citizens' assembly that met immediately prior to, say, global negotiations organized by the United Nations would be in a good position to influence those negotiations (think of the public consultations that preceded negotiation of the Sustainable Development Goals in 2015). But deliberative democracy requires larger publics to be active, so equally important is the role of the assembly in stimulating broader informed participation. Its activities and conclusions would be witnessed, publicized, and amplified through documentary film, social media, and the more traditional media. This suggests that appropriate timing would be early in the life of the issue's presence on the global agenda.

### THREE ESSENTIAL REASONS

There are three essential reasons why a global citizens' assembly on genome editing would be a good idea. The first concerns the legitimacy of any collective decisions in global governance. Public confidence in technologies and their application can be secured by public participation in decisions about the regulation of those technologies. At the global level, legitimacy cannot be secured through elected representation, which is unavailable. There is increasing awareness of the benefits of linking citizen deliberations to wider public debate as a way of facilitating conditions for the public to come to terms with the issue and create trust with experts and decision-makers (11). Evidence shows that nonparticipants can more readily trust their deliberating fellow-citizens than politicians. For issues that are not yet on the public radar, citizens' assemblies provide mechanisms for anticipating considered public responses that would only otherwise occur well after implementation of technologies, when public outcry can be costly and disruptive (12).

The second reason concerns the current disconnect between expertise and public values (13). As it stands, public views on genome editing (whether applied to humans, animals, or plants) are generally not well formed, mainly owing to the novelty and highly technical nature of the issues involved. Those who do have well-considered views

are often highly knowledgeable, but knowledge does not imply a warrant to make value judgments for a broader public, or impose framings of issues on a public that might be amenable to competing frames. Sometimes those with considered views are perceived as embedded in specific interests (be it as health care professionals, scientists, corporations, or activists) and accompanying framings that may constrain their ability to reflect on broad public interests. Good deliberation remedies this disconnect through productive integration of scientific knowledge, lay knowledge, and public values, meaning that specialists can learn about broader publics, and publics can learn about expert framings. Two decades of national-level experience on complex risk-related issues shows that citizens' forums are an effective vehicle for this vital integration of science and society. Citizens' forums can also help develop public values on distinctive issues such as genome editing, where opinions and framings have yet to solidify, thus further contributing to anticipatory governance. Without such values, it is not obvious what public need the technology would be serving.

The third reason concerns the generation of a much-needed kind of considered input into governmental decisions, about detailed applications no less than broad questions about whether or not to pursue the technology. Aside from introducing previously marginalized perspectives, evidence shows that a well-designed process involving lay citizens can bring reflective judgment to bear in a way that stakeholders, activists, and politicians may not (because they are too invested in advocacy). In a jury trial, we trust lay jurors to reach a reflective judgment based on what they hear from advocates on both sides of a case. Similarly, citizens' forums can effectively judge the merits of different sides.



ILLUSTRATION: ALICE MOLLON



In Oregon, the Citizens' Initiative Review provides considered assessment of the best arguments for and against referendum measures (such as one on labeling of genetically modified food) which are often not the arguments that advocates for both sides stress. We might expect scientists and ethicists also to be better than stakeholders, activists, and politicians when it comes to reflective judgment. But though we might expect scientists to be good at reflecting on scientific values, their role gives them no special insight on the public interest. Ethicists are professionally capable when it comes to moral principles—but these are not necessarily the same as public values. Citizens' forums also prove good at creatively identifying courses of action that meet the main concerns of different sides.

A global citizens' assembly would not replicate existing international consultations. The pattern of self-appointed representation from global civil society (dominated by NGOs from wealthy countries) is highly incomplete, especially in representing the marginalized and poor. Random selection yields more cognitive diversity than self-appointment. This diversity can be harnessed in deliberative interaction to yield epistemic problem-solving gains. Interacting NGOs and organized interests usually produce compromise; interacting citizens are more likely to produce reasoned outcomes whose typically high level of agreement on content can be open to far-reaching options (see the 2020 French Convention Citoyenne pour le Climat). Deliberating citizens can find ways around impasses bedeviling experts and advocates, as demonstrated for solar geoengineering governance in a process organized by the Consortium for Science, Policy and Outcomes in 2018. Any persistent disagreement will illuminate contextual and cultural differences.

The three reasons will hold to the degree the citizens' assembly is well designed, drawing on evidence about what works and what doesn't. Fortunately there is an extensive body of empirical research to draw upon: on the impact of different facilitation styles on equality of participation; on the best way to generate principles to govern interaction within the assembly; on the optimal number of deliberating citizens in small groups; on the time (normally at least 2 or 3 days) needed for citizens to learn, reflect, clarify disagreements, and crystallize preferences; on the best way to conduct stratified random sampling; on the importance of gravitas in inducing selected citizens to accept invitations to participate; on the importance of citizens' perception of the impact of the forum; and on the most appropriate form of the final report (notably the degree to which it should contain reasons rather than simply conclusions or votes) (14).

Critics of public engagement worry that it can be used subtly to build support for existing policies by not challenging dominant framings. In health policy, citizens' forums have been designed and introduced to address such criticisms, by enabling deeper scrutiny of the implications of scientific findings, by broadening the kind of rationales for action that can be contemplated, by scrutinizing the meaning of the public interest, by being more inclusive of different forms of reasoning, and by avoiding overly narrow framings of issues (15). Citizens' forum conclusions can contravene existing government policy; on genome editing, there is currently something of a policy void, so it is not obvious what a dominant policy framing is to begin with. Still, organizers and facilitators should take care that powerful framings (such as the idea that technical expertise is more important than local knowledge) are

not taken as given, and are open to challenge. Worries about lack of impact can be assuaged by fostering strong connections with relevant governmental bodies in advance of the deliberative process.

## MORE THAN JUST "CHECKING THE BOX"

What are the limitations? A global citizens' assembly would in the first instance offer a snapshot, only dealing with the issues as presented by the state of the science at one time. However, it would be possible to re-convene global assemblies periodically (with different citizen participants) to refine or reconsider principles. A more continuous conversation, which could include how principles identified by the citizens' assembly should apply, or might need to be re-thought in light of subsequent scientific developments, could be supplied elsewhere (8). Our proposal could also be joined to any more authoritative international institutions that develop, as well as to subsequent national deliberative processes.

A global citizens' assembly should do much more than simply check a "public participation" box. It would be the beginning of more effective global public deliberation, not its end, informing wider publics as much as the process of decision-making. If the global community is serious about public participation on genome editing, it is time to move beyond the rhetoric. Robust, legitimate, democratic, and effective action drawing on lessons from existing practice is possible, and it is time to move in this direction. ■

## REFERENCES AND NOTES

1. R. Isasi et al., *Science* **351**, 337 (2016).
2. D. Schroeder et al., Eds, *Ethics Dumping: Studies from North-South Research Collaboration* (Springer, 2018).
3. S. Burall, *Nature* **555**, 438 (2018).
4. N. Kofler et al., *Science* **362**, 527 (2018).
5. National Academies Committee on Human Gene Editing, *Human Genome Editing: Science, Ethics and Governance* (National Academies Press, 2017).
6. M. Hamburg, E. Cameron, *Nature* **575**, 287 (2019).
7. H. Chneiweiss et al., *Transgenic Res.* **26**, 709 (2017).
8. S. Jasanoff, J. B. Hurlbut, *Nature* **555**, 435 (2018).
9. K. Grönlund, A. Bächtiger, M. Setälä, Eds, *Deliberative Mini-Publics: Involving Citizens in the Democratic Process* (ECPR Press, 2014).
10. M. Rask, R. Worthington, *Governing Biodiversity through Democratic Deliberation* (Routledge, 2015).
11. M. E. Warren, J. Gastil, *J. Polit.* **77**, 562 (2015).
12. M. K. MacKenzie, K. O'Doherty, *J. Public Delib.* **7**, 1 (2011).
13. D. Sarewitz, *Nature* **522**, 413 (2015).
14. D. M. Farrell et al., *Deliberative Mini-Publics: Core Design Features*, Centre for Deliberative Democracy and Global Governance Working Paper 2019/5 (2019).
15. K. C. O'Doherty, M. M. Burgess, *Res. Ethics Rev.* **9**, 55 (2013).

## ACKNOWLEDGMENTS

A.M. provides genetic counseling and ethics advice for RareMark, Congenica. G.C. documents financial and advisory interests at <http://arep.med.harvard.edu/gmc/tech.html> (see also SM).

## SUPPLEMENTARY MATERIALS

[science.sciencemag.org/content/369/6510/1435/suppl/DC1](http://science.sciencemag.org/content/369/6510/1435/suppl/DC1)

10.1126/science.abb5931





BOOKS *et al.*

## SOCIAL SCIENCE

# Why the West is WEIRD

Catholicism's policy forbidding cousins to wed may have led to the distinctive characteristics of Western society

By **Pauline Grosjean**

A few years after the end of Tajikistan's half-decade-long civil war, I was on an assignment in the former Soviet republic and announced my intention to purchase vegetables at the market. My local friends scoffed. "It's impossible," they said. "You have no cousins at the market. People will sell you a poison tomato." The poison tomato, I learned, was a wilted tomato made to look fresh by injecting it with water (usually from a nearby sewer). As Joseph Henrich recounts in his new book, *The WEIRDest People in the World*, the Tajik civil war—which pitted clan against clan and, sometimes, neighbor against neighbor—resulted in a collapse of trust that made people more suspicious of nonrelatives.

This trajectory is puzzling, as it contrasts sharply with political development in Western Europe. There, conflict and intergroup competition paved the way for strong and democratic states. So what accounts for the difference between these two groups?

War's impact on cultural and institutional evolution, Henrich argues, depends on preexisting conditions, especially people's psychological dispositions. In Europe, after the collapse of the Carolingian Empire, clans had been destroyed by the

Roman Catholic Church, and people were already infused with a sense of universal morality. War further deepened their commitments to voluntary associations, such as universities, merchant guilds, and monasteries. It also reinforced Christian norms and motivated greater contributions to the public good, igniting the perpetuation of liberal values and strong impersonal states.

Henrich's argument is that Catholicism, by forbidding cousin marriage, enabled Europe to escape the "tyranny of cousins" (1). More importantly, he argues, it explains how—in the process—Western Europeans became "WEIRD" (Western, educated, industrialized, rich, and democratic).

The first part of the book describes WEIRD people in broad strokes, painting them as individualistic, often guilty but never ashamed, patient, hardworking, achievement oriented, and trusting of strangers. Here, Henrich provides a backhanded criticism of the field of psychology, which claims to uncover how humans make choices, while relying mainly on WEIRD subjects. (Ironically, Henrich notes, the desire to uncover universal truths is another trait commonly seen in WEIRD people.)

The second part of the book provides a comparative political account of how societies scale up from families to states. Here, Henrich adds a twist, describing

Forbidding cousin marriage weakened familial bonds, creating a psychologically distinct culture.

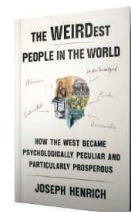
how institutional development feeds back into psychology. Citing data from his own research, he argues that religion not only enhances prosociality, enables the provision of public goods, and can legitimize political institutions but also shapes our cognition by, for example, making us think about moral universals.

The third section of the book focuses on how Catholicism, and later Protestantism, shaped institutions and psychology. Unlike other religions, Catholicism historically forbade cousin marriage and affinal remarriage (for example, marrying an in-law after the death of one's spouse), limited adoption, and encouraged individual ownership. By doing so, the Church managed to break what was, and remains, the biggest threat to states, the largest hurdle to the development of impersonal markets, and the greatest inhibitor of individualism: clannishness.

But how and why did the Church home in on cousin marriage prohibition? And why did some people and not others adopt and convert to Catholicism (and later Protestantism)? Henrich describes how ecological endowments shape people's psychology and can make them more likely to adopt certain norms and institutions, but he never specifically applies this argument to the reasons Western Europeans adopted Catholicism in the first place. He does, however, suggest that the Europeans'

propensity for late marriage was a consequence of the Church's marriage prohibitions. This is inconsistent with the evidence that there has been much variation over time in the age at marriage and also the fact that it dropped sharply when 19th-century Europeans migrated to the colonies of the United States or Australia, where land was much more abundant.

Another point that Henrich does not address is the role that states may have played as competitors and regulators of the Church. In many parts of Africa and the Pacific, where states are weak, Catholic and Protestant churches are as successful as they are nepotistic and corrupt. What accounts for this difference? I will continue to follow Henrich's work and avidly await the answer. ■



**The WEIRDest People in the World**  
Joseph Henrich  
Farrar, Straus and Giroux,  
2020. 704 pp.

## REFERENCES AND NOTES

1. An expression coined by Francis Fukuyama in his book *The Origins of Political Order: From Prehuman Times to the French Revolution* (Farrar, Straus and Giroux, 2011).

10.1126/science.abc6138

The reviewer is at the Department of Economics, University of New South Wales, Sydney, NSW 2052, Australia. Email: p.grosjean@unsw.edu.au

## SCIENCE LIVES

# A case study of Oliver Sacks

Interviews and archival footage paint a tender portrait of neurology's greatest storyteller

By **Laura J. Snyder**

“I’m an inveterate storyteller,” confesses the celebrated neurologist and writer Oliver Sacks at the start of *Oliver Sacks: His Own Life*. “I tell many stories, some comic, some tragic.” Tales of both types abound in this elegiac yet lighthearted film based on director Ric Burns’s interviews with Sacks and his friends, colleagues, family members, and patients in the months before and after the physician’s death in 2015 at the age of 82. The result is a vivid portrait of an ebullient, provocative, brilliant man who transformed the practice of medicine and spearheaded the neurodiversity movement.

Born into an upper-middle-class Jewish family in northwest London in 1933, Sacks was the youngest of four sons. He was an outsider: one of only three Jews at his elite prep school; a gay adolescent at a time when gay sex was illegal; an introverted, dreamy, chemistry-obsessed boy in a family of accomplished physicians. His father was a general practitioner who made house calls, and his mother was one of the first female surgeons in England. His two eldest brothers were already studying medicine when he was in high school.

Sacks dutifully followed his expected career path and was drawn to neurology when

his third brother, Michael, developed schizophrenia. But after completing medical training, Sacks fled the homophobic confines of his nation and family—his mother had called him “an abomination.” Paul Theroux tells Burns that Sacks’s “great luck” was ending up in Los Angeles in 1960, where he found ample “guys, weights, drugs, and hospitals.”

“I liked pushing myself to the maximum,” Sacks shrugs. This meant motorcycling all night at top speed to reach the Grand Canyon, 500 miles away, by sunrise; squat lifting 600 pounds for a California state record; bingeing food; and swallowing fistfuls of amphetamines. Images of a buff Sacks during his bodybuilding years contrast with his admission that he was “playing with death.” By the early 1970s he had given up both drugs and sex, remaining celibate for 35 years before falling deeply in love with writer and photographer Bill Hayes.

As a bench scientist, Sacks was a disaster, losing the myelin he had spent months extracting from earthworms and helplessly watching his lab notes blow off his motorcycle. He found his métier as a clinician. Drawn to patients with severe neurological disorders—outsiders like himself—he saw them as individuals, not merely diseased brains. He spent hours conversing with them, trying to understand what it was like to live with their conditions. Surgeon and writer Atul Gawande describes Sacks’s impact on the medical profession as showing it that there are important “truths to

be found going deeply into human lives.”

In 1966, Sacks was working in the Bronx at the Beth Abraham Hospital, home to 80 survivors of the encephalitis lethargica (“sleepy sickness”) pandemic of the 1910s and 1920s. Listening to nurses who believed there were intact minds and personalities behind bodies locked in “suspended animation,” he boldly administered the new drug levodopa. Super-8 footage reveals the thrilling result: an incredible awakening as the patients

burst into life, dancing, joking, and singing. Tragically, most developed side effects so debilitating that they discontinued the medicine, sinking back into frozen states.

The medical establishment, skeptical of his results, refused to publish his reports; Sacks’s frustration at this refusal, 45 years later, is still palpable. He shared the story of these patients in his book *Awakenings* (1973). The appearance of Penny Marshall’s 1990 movie version cemented Sacks’s celebrity, to both his delight and discomfort.

In his work, Sacks adopted the case study or medical narrative approach, combining biography and biology in detailed discussions of individual patients. Other neurologists considered these studies unscientific and merely anecdotal. But not all science is statistical; observational science is science, too.

Sacks considered himself a fieldworker providing facts to neuroscientists developing new theories of consciousness. Sacks’s observations, Christof Koch tells Burns, were integral to Koch’s understanding of the relation between different parts of the brain and specific aspects of vision, including how we perceive the flow of time.

Sacks’s case studies also undermined stereotypes of people with neurological differences. Autism activist Temple Grandin recounts that “[t]hey used to say that people on the autism spectrum had no inner world.” But by taking the time to get to know Grandin and others with autism, Sacks disproved this: “He got inside my emotions in a way no one else did.”

The film ends with Sacks and friends gathered in his apartment, raising glasses of wine with the Yiddish toast “l’chaim,” to life. This riveting and poignant documentary, which launches virtually on the Kino Marquee platform on 23 September, is Sacks’s final case study—and a celebration of the life of a remarkable man. ■

## Oliver Sacks: His Own Life

Ric Burns, director  
Vulcan Productions,  
2020. 114 minutes.

The reviewer is the author of *Eye of the Beholder: Johannes Vermeer, Antoni van Leeuwenhoek, and the Reinvention of Seeing* (Norton, 2015). She is currently writing a biography of Oliver Sacks. Email: mailbox@laurajsnyder.com



Sacks's verve and curiosity remained strong, even as his time on Earth drew short.

10.1126/science.abb2944





Thousands of Black-tailed godwits (*Limosa limosa*) passing through Portugal's Tagus estuary would be disrupted by flight paths to Lisbon's new airport.

Edited by Jennifer Sills

## Portugal's airport plans threaten wetlands

In December 2019, the European Commission announced The European Green Deal, a plan to facilitate a transition to sustainability with the goal of making Europe climate neutral by 2050 (1). Green Deal objectives include preserving and restoring biodiversity and reducing net emissions of greenhouse gases (1). The EU Parliament adopted a resolution supporting these environmental goals in January (2). Lisbon, Portugal's capital, has been designated the European Green Capital 2020 for spearheading sustainability efforts (3). However, Lisbon's airport has reached capacity, and plans to build an additional airport are at odds with Green Deal objectives.

The proposed location for the new airport is a peninsula at the heart of the Tagus estuary (4), a vast coastal wetland of key importance for breeding, wintering, and passing migratory birds in the East Atlantic Flyway (5, 6). This wetland is a major hub linking Palearctic and Nearctic breeding areas with Afro-tropical wintering areas for an estimated 300,000 waterbirds and many other migratory bird species. The region is protected under national legislation, EU directives, and international conventions (5–7). However, the privately funded proposed airport received an environmental license in early 2020 (8), and, despite the aviation sector facing unprecedented reductions in activity due to the coronavirus disease 2019 (COVID-19)

pandemic (9), the Portuguese government reiterated in July its intentions to go forward with this new infrastructure (10).

By expanding its airport capacity, this EU member state will deliver a negative contribution toward climate targets by neither retiring nor halting new infrastructure (11), as well as threaten biodiversity through negative, permanent, and irreversible effects on bird species in an EU-designated protected area. These species already face massive declines globally [(e.g., (12)]. We urge the Portuguese government and the European Union to put the Green Deal into action by abandoning this project.

José A. Alves<sup>1,2\*</sup> and Maria P. Dias<sup>3,4</sup>

<sup>1</sup>Department of Biology and Centre for Environmental and Marine Studies, University of Aveiro, Campus de Santiago, 3810-193 Aveiro, Portugal. <sup>2</sup>University of Iceland, South Iceland Research Centre, Lindarbraut 4, IS-840 Laugarvatn, Iceland. <sup>3</sup>Birdlife International, Cambridge CB2 3QZ, UK. <sup>4</sup>Marine and Environmental Sciences Center, Instituto Universitário, Lisboa, Portugal.

\*Corresponding author. Email: jose.alves@ua.pt

### REFERENCES AND NOTES

1. "The European Green Deal" [COM(2019) 640, European Commission, 2019]; [https://ec.europa.eu/info/sites/info/files/european-green-deal-communication\\_en.pdf](https://ec.europa.eu/info/sites/info/files/european-green-deal-communication_en.pdf).
2. "European Parliament resolution of 15 January 2020 on the European Green Deal" [2019/2956(RSP), European Parliament, 2020]; [www.europarl.europa.eu/doceo/document/TA-9-2020-0005\\_EN.html](http://www.europarl.europa.eu/doceo/document/TA-9-2020-0005_EN.html).
3. "European Green Capital" [European Commission, 2018]; <https://ec.europa.eu/environment/europeangreencapital/winning-cities/2020-lisbon/>.
4. "Estudo de Impacte Ambiental 2019: Aeroporto do Montijo e respetivas acessibilidades" (Resumo Não Técnico, Profico Ambiente, 2019); [https://siaia.apambiente.pt/AIADOC/AIA3280/vol%20i\\_rnt\\_eia\\_am2019726195328.pdf](https://siaia.apambiente.pt/AIADOC/AIA3280/vol%20i_rnt_eia_am2019726195328.pdf) [in Portuguese].
5. J. A. Alves et al., *Anuário Ornitológico* 9, 66 (2012).
6. D. Leitão, P. Catry, H. Costa, G. L. Elias, L. M. Reino, As Aves do Estuário do Tejo (ICN, 1998) [in Portuguese].
7. M. F. Heath, M. I. Evans, D. G. Hoccorn, A. J. Payne, N. B. Peet, Eds., *Important Bird Areas in Europe: Priority Sites for Conservation Volume 2* (Birdlife International, 2000).
8. "TUA" (TUA20200121000037, Agência Portuguesa do Ambiente, 2020); [https://siaia.apambiente.pt/AIADOC/AIA3280/aia3280\\_dia\\_tua202012217290.pdf](https://siaia.apambiente.pt/AIADOC/AIA3280/aia3280_dia_tua202012217290.pdf) [in Portuguese].
9. C. Le Quéré et al., *Nat. Clim. Change* 10, 647 (2020).
10. "Governo espera 'convencer' Moita e Seixal a darem parecer positivo ao aeroporto," *Público* (2020); [www.publico.pt/2020/07/21/economia/noticia/governo-espera-convencer-moita-seixal-darem-parecer-positivo-aeroporto-1925354](http://www.publico.pt/2020/07/21/economia/noticia/governo-espera-convencer-moita-seixal-darem-parecer-positivo-aeroporto-1925354) [in Portuguese].
11. D. Tong et al., *Nature* 572, 373 (2019).
12. K. V. Rosenberg et al., *Science* 366, 120 (2019).

10.1126/science.abe4325

## Systemic racism in higher education

The nexus of Black Lives Matter protests and a pandemic that disproportionately kills Black and Latinx people (1) highlights the need to end systemic racism, including in science, technology, engineering, and mathematics (STEM), where diversity has not meaningfully changed for decades (2). If we decry structural racism but return to the behaviors and processes that led us to this moment, this inexcusable stagnation will continue. We urge the Academy to combat systemic racism in STEM and catalyze transformational change.

Everyone in academia must acknowledge the role that universities—faculty, staff, and students—play in perpetuating structural racism by subjecting students of color to unwelcoming academic cultures (3). Universities are not level playing fields where all students have an equal opportunity to participate and succeed. The misuse of standardized tests such as the GRE excludes students who could have otherwise

succeeded (4). Once admitted, Black, Indigenous, and people of color (BIPOC) face challenges when transitioning to college life (5) and are more likely to be nontraditional students. Innovative pedagogies (6) and programs (7) can overcome these challenges but are not widely applied in higher education. Evidence-based, institution-wide approaches focused on equity in student learning are foundational to eliminating structural racism in higher education. Once we abandon the view of “fixed” student ability, more BIPOC students will succeed (8).

Academic culture also fails BIPOC faculty, who receive fewer federal grants due to systemic bias (9) and topic area (10). BIPOC faculty are most likely to invest substantial time in activities that promote diversity, which are devalued in the tenure and promotion process (11). BIPOC faculty are further disadvantaged in tenure decisions through cultural taxation of unequal service and mentoring demands. Given these burdens, BIPOC faculty cannot be expected to be the primary agents of institutional change. Instead, those most empowered to make change—non-BIPOC faculty—must join BIPOC faculty in their efforts to prioritize recruiting, supporting, and championing diversity.

Finally, the false dichotomy of “excellence or diversity” must end. Diversity results in better, more impactful, and more innovative science (12), and it is essential to building novel solutions to challenges faced by marginalized and nonmarginalized communities. Catalyzing these culture shifts in the Academy, however, will require making tenure dependent on excellence in research, teaching, and service that centers on equity and inclusion.

Making STEM equitable and inclusive requires actively combating racism and bias. All faculty, staff, and students should commit to learning about racism, engaging in courageous conversations with non-BIPOC colleagues, and calling out unfair practices to prevent the normalization of discriminatory behavior. Faculty should examine courses for ethnicity and gender performance disparities, ask whether departmental and lab demographics reflect society at large, and actively remedy any disparities.

Breaking down the barriers of systemic racism in STEM and achieving the promise of diversity, equity, and inclusion in STEM require unwavering dedication and real work. It is time to make the commitment to be an agent of change.

Paul H. Barber<sup>1\*</sup>, Tyrone B. Hayes<sup>2</sup>, Tracy L. Johnson<sup>3</sup>, Leticia Márquez-Magaña<sup>4</sup>, and 10,234 signatories

<sup>1</sup>Department of Ecology and Evolutionary Biology, University of California, Los Angeles, CA 90095,

USA. <sup>2</sup>Department of Integrative Biology, Museum of Vertebrate Zoology, Group in Endocrinology, Molecular Toxicology, and Energy and Resources Group, University of California, Berkeley, CA 94720, USA. <sup>3</sup>Department of Molecular, Cell, and Developmental Biology, University of California, Los Angeles, CA 90095, USA. <sup>4</sup>Department of Biology, Health and Equity Research Laboratory, San Francisco State University, San Francisco, CA 94132, USA.

\*Corresponding author.  
Email: paulbarber@ucla.edu

## REFERENCES AND NOTES

1. K. Bibbins-Domingo, *Ann. Int. Med.* **173**, 233 (2020).
2. R. E. Bernard, E. H. G. Cooperdock, *Nat. Geosci.* **11**, 292 (2018).
3. M. Ong et al., *Harvard Educ. Rev.* **81**, 172 (2011).
4. C. Miller, K. Stassun, *Nature* **510**, 303 (2014).
5. S. D. Museus, S. J. Quaye, *Rev. High. Educ.* **33**, 67 (2009).
6. E. J. Theobald et al., *Proc. Natl. Acad. Sci. U.S.A.* **117**, 6476 (2020).
7. B. Toven-Lindsey, M. Levis-Fitzgerald, P. H. Barber, T. Hasson, *CBE—Life Sci. Educ.* **14**, 1 (2015).
8. E. A. Canning et al., *Sci. Adv.* **5**, eaau4734 (2019).
9. E. A. Erosheva et al., *Sci. Adv.* **6**, eaaz4868 (2020).
10. T. A. Hoppe et al., *Sci. Adv.* **5**, eaaw7238 (2019).
11. W. R. Brown-Glaude, *J. Soc. Work Educ.* **45**, 336 (2009).
12. B. Hofstra et al., *Proc. Natl. Acad. Sci. U.S.A.* **117**, 9284 (2020).

## SUPPLEMENTARY MATERIALS

www.sciencemag.org/content/369/6510/1440.2/suppl/DC1  
List of signatories

10.1126/science.abd7140

# University-pharmacy partnerships for COVID-19

The global coronavirus disease 2019 (COVID-19) pandemic has accelerated epidemiologic data collection and reporting to a scale that has never before been achieved (1). Both data volume and segmentation have grown enormously, with granularity of data to track infection now available at the county level or below (2). Years of disinvestment in U.S. public health infrastructure (3) have resulted in the immediate need for new mechanisms to support micro-epidemiologic efforts. Universities and community pharmacies, both trusted institutions with established infrastructure, are uniquely positioned to facilitate micro-epidemiologic efforts by creating partnerships (4).

Micro-epidemiology has been used to track the spatial and temporal prevalence of infection in distinct communities (5). Coupled with longitudinal testing, micro-epidemiology serves as a sentinel for viral emergence and evolution (6), which can be applied to the COVID-19 pandemic. Harnessing the established infrastructure of community pharmacies enables coordination of appropriate testing, tracing, and isolation in these communities.

Ninety percent of U.S. residents live within 5 miles of a pharmacy, and in some underserved communities, pharmacists are the only health care provider (7).

Community pharmacists are pillars of their communities with trusted connections with patients (4). Pharmacists are trained and authorized to order and administer COVID-19 testing (8) and have widespread authority to administer vaccinations (9). In addition, increasing numbers of pharmacists are participating in practice-based research networks (PBRNs) (10), which are designed to improve community-based health care by providing higher-quality chronic disease management.

University-community pharmacy partnerships follow the PBRN paradigm and harness the strengths of both institutions. Community pharmacies provide a geographically distributed network of accessible health care professionals and can serve as nodes for patient recruitment, whereas the university serves as a logistical and research hub to provide testing, reporting, contact tracing, educational resources, and the research infrastructure required to facilitate such studies. The University can also provide research personnel capable of managing these efforts, allowing the pharmacists to prioritize patient care.

The U.S. Centers for Disease Control and Prevention has recommended that health departments leverage community pharmacy partnerships to improve public health emergency response (11, 12). We call on schools of pharmacy and public health to forge new relationships and leverage existing partnerships with community pharmacies to meet the current critical need to understand and mitigate COVID-19 and prepare for future pandemic response.

Vincent J. Venditto<sup>1\*</sup>, Brooke Hudspeth<sup>1</sup>, Patricia R. Freeman<sup>2</sup>, Clark Kebodeaux<sup>1</sup>, R. Kiplin Guy<sup>1</sup>

<sup>1</sup>College of Pharmacy, University of Kentucky, Lexington, KY 40536, USA. <sup>2</sup>Center for the Advancement of Pharmacy Practice, College of Pharmacy, University of Kentucky, Lexington, KY 40536, USA.

\*Corresponding author.  
Email: vincent.venditto@uky.edu

## REFERENCES AND NOTES

1. D. A. Drew et al., *Science* **368**, 1362 (2020).
2. A. Mollalo, B. Vahedi, K. M. Rivera, *Sci. Tot. Environ.* **728**, 138884 (2020).
3. D. U. Himmelstein, S. Woolhandler, *Am. J. Public Health* **106**, 56 (2016).
4. J. V. Goode, D. A. Mott, R. Chater, *J. Am. Pharm. Assoc.* **48**, 153 (2008).
5. C. S. Nelson et al., *Nat. Commun.* **10**, 5615 (2019).
6. P. Mogeni et al., *BMC Med.* **15**, 121 (2017).
7. National Association of Chain Drug Stores, “Pharmacies: A vital partner in reopening America” (2020).
8. U.S. Department of Health and Human Services, “Guidance for licensed pharmacists, COVID-19 testing, and immunity under the PREP Act” (2020).
9. S. M. Bartsch et al., *Vaccine* **36**, 7054 (2018).
10. J.-V. R. Goode et al., *J. Am. Pharm. Assoc.* **48**, 153 (2008).
11. S. E. Rubin et al., *Biosecur. Bioterror.* **12**, 76 (2014).
12. L. M. Koonin et al., *Disaster Med. Public Health Prep.* **5**, 253 (2011).

10.1126/science.abe3339



# RESEARCH

## IN SCIENCE JOURNALS

Edited by Michael Funk

### ARCHAEOLOGY

## Horses were not domesticated in Anatolia

**T**he domestication of the horse was one of the most consequential innovations in human history and led to profound changes in the economic, political, and social structures of prehistoric Eurasia. However, when, where, and how many times horses were domesticated remains an open question. Anatolia has been proposed as an early center of domestication because of the long history of exploitation of equids there. Using advanced paleogenomic methods, Guimaraes *et al.* tested this hypothesis on archaeological samples of equids from 14 sites from central Anatolia across a temporal span from about 8000 to 1000 BCE. They determined that the ancient wild horses of the region were never domesticated and identified the introduction of nonlocal and already domesticated horse lineages around 2000 BCE. —MSA *Sci. Adv.* 10.1126/sciadv.abb0030 (2020).



Modern horses in Anatolia, such as this wild herd, are descended from ancestors introduced from outside the region.

### MICROBIOME

## Inosine modulates antitumor immunity

Checkpoint blockade immunotherapy harnesses the immune system to kill cancer cells and has been used with great success to treat certain tumors, but not all cancer patients respond. The efficacy of checkpoint blockade immunotherapy has been shown to depend on the presence of distinct, beneficial bacteria residing in the gut of patients, but how the microbiome mediates such beneficial

effects is unclear. Mager *et al.* found that specific bacteria produce a metabolite called inosine that enhances the effect of checkpoint blockade immunotherapy (see the Perspective by Shaikh and Sears). In mouse models, inosine, together with proinflammatory stimuli and immunotherapy, strongly enhanced the antitumor capacities of T cells in multiple tumor types, including colorectal cancer, bladder cancer, and melanoma. —PNK

*Science*, this issue p. 1481;  
see also p. 1427

### STRUCTURAL BIOLOGY

## How ribosomes are made

The formation of eukaryotic ribosomes is a complex process that starts with transcription of a large precursor RNA that assembles into a large 90S preribosome, which matures to finally give the 40S small subunit of the ribosome. Cheng *et al.* and Du *et al.* give insight into this process, using cryo-electron microscopy to look at intermediates along the pathway. Together, these studies reveal how a cast of molecular

players act to coordinate the compositional and structural changes that transform the 90S preribosome into a pre-40S subunit. —VV

*Science*, this issue p. 1470, p. 1477

### PLASTIC POLLUTION

## A mess of plastic

It is not clear what strategies will be most effective in mitigating harm from the global problem of plastic pollution. Borrelle *et al.* and Lau *et al.* discuss possible solutions and their impacts. Both groups

found that substantial reductions in plastic-waste generation can be made in the coming decades with immediate, concerted, and vigorous action, but even in the best case scenario, huge quantities of plastic will still accumulate in the environment. —HJS

*Science*, this issue p. 1515, p. 1455

## SURFACE CHEMISTRY

### Nature of the molecule-surface encounter

Adsorption is an important initial step in all heterogeneous chemical processes. However, detailed adsorption dynamics are complex and challenging to follow experimentally. Using the fact that vibrationally excited carbon monoxide molecules can be trapped on the Au(111) surface with all degrees of freedom being equilibrated except the vibrational ones, Borodin *et al.* show that the vibrational relaxation time can serve as an internal clock to follow the microscopic pathways of adsorption and equilibration on the surface. On the basis of molecular beam experiments and theoretical modeling of this prototypical system, the authors reveal the intricate interplay between physisorption and chemisorption states. These observed characteristics are relevant to many other heterogeneous systems. —YS

*Science*, this issue p. 1461

## WATER STRUCTURE

### Supercooled water structures

Water displays a number of anomalous properties that are further enhanced in its supercooled state, but experimental studies at ambient pressure must obtain data before the onset of rapid crystallization at temperatures below ~240 kelvin. Kringle *et al.* obtained infrared spectra of supercooled water films at temperatures between 135 and 235 kelvin that formed for a few nanoseconds by ultrafast heating and cooling.

Supercooled water thermally equilibrates before crystallization above 170 kelvin, and over the range of temperatures studied, the structure of water was shown to be a linear combination of a high-density and a low-density liquid. —PDS

*Science*, this issue p. 1490

## STELLAR EVOLUTION

### Complex stellar winds from evolved stars

Stars less than eight times the mass of the Sun end their lives as planetary nebulae, structures of ionized gas thrown off by the star and heated by the exposed stellar core. Planetary nebulae are often bipolar in shape or contain complex morphological features such as rings or spirals. Decin *et al.* observed the stellar winds of 14 stars during their asymptotic giant branch (AGB) phase of stellar evolution, which immediately precedes the planetary nebula phase. They found morphologies in the AGB winds similar to planetary nebulae and demonstrated that they are produced by the influence of a binary companion on the AGB wind. —KTS

*Science*, this issue p. 1497

## CANCER IMMUNOLOGY

### PD-1 keeps immune and tumor cells apart

When cytotoxic T cells enter tumors and become tumor-infiltrating lymphocytes (TILs), they lose their ability to kill target tumor cells. TILs in this state express inhibitory receptors, including programmed cell death protein-1 (PD-1), which are engaged in the tumor environment. Ambler *et al.* found that the suppressed cells had impaired cytoskeletal rearrangements and a decreased ability to form productive contacts with their targets. Blocking PD-1 signaling in vivo, but not in vitro, reversed these defects, stabilized the interactions between tumor cells and TILs, and improved cell killing. —JFF

*Sci. Signal.* **13**, eaau4518 (2020).

## IN OTHER JOURNALS

Edited by **Caroline Ash** and **Jesse Smith**

## IMMUNOLOGY

### NK cell nanotubes to the rescue?

**D**uring pregnancy, maternal decidual natural killer (dNK) cells maintain fetal tolerance while simultaneously fighting placental infection. How this happens is unresolved. Crespo *et al.* report that dNK cells could treat *Listeria monocytogenes*-infected fetal cells by selectively transferring granulysin (GLNY), but not granzymes or perforin, to fetal cells through cytoplasmic bridges called nanotubes. Transfer of GLNY inhibited the pathogen without harming placental trophoblasts. Moreover, transgenic mice overexpressing human GLNY were protected from *L. monocytogenes*-induced miscarriage. This work provides insight into how the maternal immune system protects the fetus from pathogens, which may help to improve pregnancy outcomes after mother-to-offspring transmission of infection. —STS *Cell* **182**, P1125 (2020).

The bacterial pathogen *Listeria monocytogenes*, shown here in a colored scanning electron micrograph, can be cleared from the placenta by specialized immune cells without risk to the fetus.

## MEDICINE

### Encouraging results for ALS

Amyotrophic lateral sclerosis (ALS) is a motor neuron degeneration disorder that leads to progressive muscle loss. There are limited therapies to treat ALS patients. Paganoni *et al.* report a phase 2 randomized, placebo-controlled trial involving 137 ALS patients, 89 of whom were treated with the combination of sodium phenylbutyrate plus taurursodiol. This combination has been shown to reduce neuron death and features of neurodegenerative diseases (including ALS) in preclinical models. This small trial, which treated patients for 3 weeks and monitored their progress for 24 weeks, found a modest reduction in functional decline in patients receiving the combination therapy. This is an

encouraging finding, and larger trials testing more patients over a longer period are expected. —GKA

*N. Engl. J. Med.* **383**, 919 (2020).

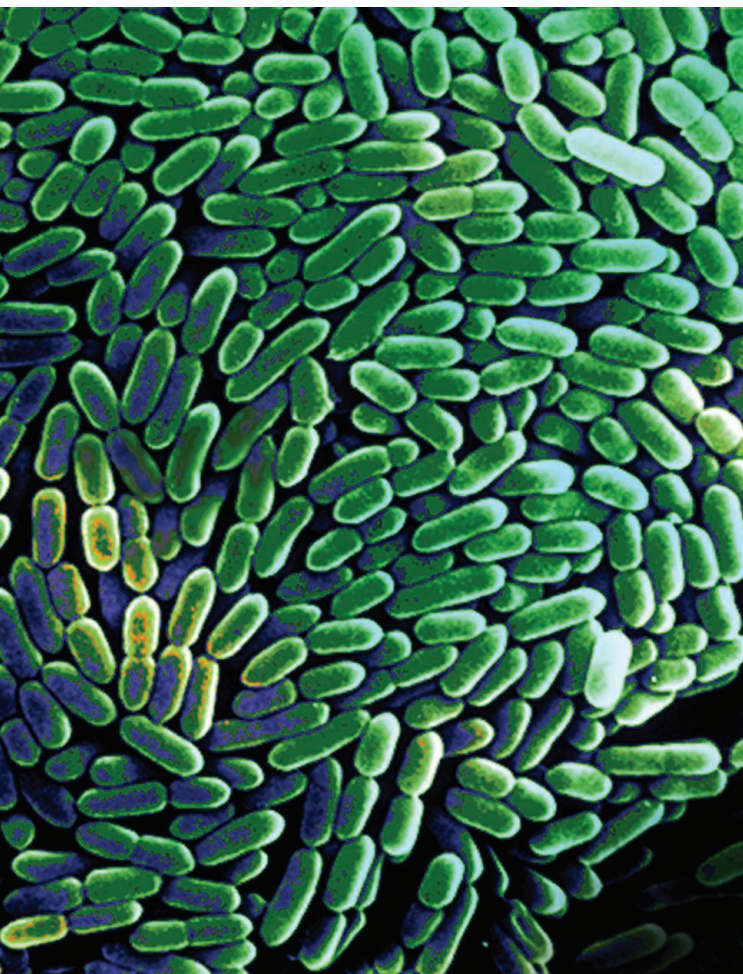
## CELL BIOLOGY

### Clonable EM labeling

Widespread use of the green fluorescent protein for protein localization at the light microscopy level has revolutionized cell biology. The search for a similar genetically encoded label for electron microscopy (EM) that could raise the resolution to the single-molecule level has not yet been successful. Jiang *et al.* developed a method for synthesizing 2- to 6-nm-diameter gold nanoparticles directly and specifically on individual cysteine-rich tags. This enables the unambiguous visualization of genetically tagged proteins in bacterial,

PHOTO: BSIP/SCIENCE SOURCE





as geomorphological changes. This work may hold lessons for promoting carbon sinks in peatlands more widely. —AMS  
*J. Ecol.* 10.1111/1365-2745.13453 (2020).

## ATMOSPHERIC MIXING

### Anti-aging scheme

The air of the lower stratosphere in the Southern Hemisphere has been getting younger since 1994. Strahan *et al.* report measurements of atmospheric  $\text{HNO}_3$  and  $\text{HCl}$  showing that changes in the transport circulation between the troposphere and stratosphere in the Southern Hemisphere are decreasing the age of its stratospheric air, whereas the age of its Northern Hemisphere counterpart is not declining. Understanding and quantifying the processes behind this differential aging is important for modeling how the protective stratospheric ozone layer will evolve in the future. —HJS  
*Geophys. Res. Lett.* **47**, e2020GL088567 (2020).

## MATERIALS SCIENCE

### Leather-based radiation shield

Shielding the human body from x-rays frequently requires heavy materials, which often have poor mechanical properties. Wang *et al.* developed a lightweight and flexible x-ray shielding material made of leather treated with a solution

of radiation-absorbing metals. This “retanning” process is inexpensive and produces a radiation-blocking, flexible material. One potential application is replacing the heavy and uncomfortable lead aprons used for x-ray shielding in the medical field. —BG  
*Adv. Mater. Technol.* 10.1002/admt.202000240 (2020).

## PHYSICS

### Magnons in 2D

Layered magnetic materials such as  $\text{CrI}_3$  can be thinned to the two-dimensional (2D) limit and still exhibit magnetic properties. These properties depend on the exact number of layers, with monolayer and bilayer materials having different symmetries. Cenker *et al.* studied the propagation of spin excitations, or magnons, in monolayers and bilayers of  $\text{CrI}_3$ . They used magneto-Raman spectroscopy to observe excitations consistent with magnons and tracked their dependence on the magnetic field and temperature. The optical selection rules extracted from these data agreed with theoretical predictions based on the threefold symmetry of the honeycomb crystal lattice of  $\text{CrI}_3$ . Because the material is insulating, the magnons are long-lived compared with those in metallic thin films, making this an attractive system for studying 2D magnon dynamics. —JS  
*Nat. Phys.* 10.1038/s41567-020-0999-1 (2020).

yeast, and mammalian cells with single-molecule resolution. This approach holds promise in circumventing the difficulties of conventional EM immunolabeling and enables biologists to probe the ultrastructure of cells with greater ease. —DJ  
*Nat. Methods* **17**, 937 (2020).

## ECOLOGY

### A tipping point to a carbon sink

The ability of soils to act as carbon sinks has tended to diminish under current climate change conditions and from other anthropogenic influences. More rarely, the reverse can be true. Milner *et al.* sampled cores from an upland peatbog site in Wales, revealing a tipping point in the late 19th century, when

peat loss through erosion switched to peat accumulation through revegetation. Since then, 5 to 10 kilograms of carbon per square meter has accumulated. The causes of this flip are uncertain and may reflect a combination of shifts in grazing and mining activity in the region, as well



Peat bogs, like these once severely eroded examples, can recover their carbon storage function if allowed to revegetate.

## ALSO IN SCIENCE JOURNALS

Edited by Michael Funk

## URBAN ECOLOGY

## Imprints of racism

Cities create challenging environments for many nonhuman species, and the presence of nonhumans in cities influences the health and well-being of the humans with which they share the environment. Distinct urban conditions are created by landscape modification, but the history of this transformation is not equal across urban environments. Schell *et al.* review how systematic racist practices such as residential segregation, enacted in part through redlining, have led to an unequal distribution of “nature” within cities. These inequities continue to play out in both the ecological processes of cities and the welfare of their residents. —SNV

*Science*, this issue p. 1446

## NEURODEVELOPMENT

## Insights from big data

The billions of neurons that make up the adult brain are organized into domains and circuits during development. High-resolution measurements such as those enabled by single-cell molecular profiling have revealed unexpected cellular diversity. Genomic tools are lending insight into mechanisms behind neurodevelopmental disorders. Briscoe and Marín review the insights gained as big data analyses are applied to neurodevelopmental questions. —PJH

*Science*, this issue p. 1447

## NEUROSCIENCE

## Magic for animals

Magical effects such as sleight-of-hand and distraction techniques can be informative about human cognition and blind spots in perception. Can this psychology of magic be applied to animals? In a Perspective, Garcia-Pelegrin *et al.* discuss how some animals, especially

corvid birds such as magpies and jays, already use some techniques common to magic effects. The authors propose that experiments using magic effects with animals could reveal information about their cognition and perception and may provide exciting insights about the animal mind. —GKA

*Science*, this issue p. 1424

## INFLAMMASOMES

## The MTOC is “speck”-tacular

Inflammasome complexes are formed in response to pathogen-associated molecules. They initiate both the maturation of inflammatory cytokines and pyroptosis, a type of programmed cell death. One notable feature for inflammasome activation is the formation of a single supramolecular punctum (or “speck”) in each affected cell. However, the location and mechanism of speck formation is poorly understood. Magupalli *et al.* report that for NLRP3- and pyrin-mediated inflammasomes, their assembly and downstream functions occur at the microtubule-organizing center (MTOC). This process requires the dynein adaptor HDAC6, which is also a central player in aggresome formation and autophagosomal degradation at the MTOC. This work links several important cellular processes and provides clues for how inflammasomes are efficiently regulated. —STS

*Science*, this issue p. 1448

## DEVELOPMENTAL BIOLOGY

## Setting the tempo for development

Many animals display similarities in their organization (body axis, organ systems, and so on). However, they can display vastly different life spans and thus must accommodate different developmental time scales. Two

studies now compare human and mouse development (see the Perspective by Iwata and Vanderhaeghen). Matsuda *et al.* studied the mechanism by which the human segmentation clock displays an oscillation period of 5 to 6 hours, whereas the mouse period is 2 to 3 hours. They found that biochemical reactions, including protein degradation and delays in gene expression processes, were slower in human cells compared with their mouse counterparts. Rayon *et al.* looked at the developmental tempo of mouse and human embryonic stem cells as they differentiate to motor neurons in vitro. Neither the sensitivity of cells to signals nor the sequence of gene-regulatory elements could explain the differing pace of differentiation. Instead, a twofold increase in protein stability and cell cycle duration in human cells compared with mouse cells was correlated with the twofold slower rate of human differentiation. These studies show that global biochemical rates play a major role in setting the pace of development. —BAP

*Science*, this issue p. 1450, p. 1449;

see also p. 1431

## CORONAVIRUS

## Better relaxing lockdown together

Even during a pandemic, all countries—even islands—are dependent in one way or another on their neighbors. Without coordinated relaxation of nonpharmaceutical interventions (NPIs) among the most closely connected countries, it is difficult to envisage maintaining control of infectious viruses such as severe acute respiratory syndrome coronavirus 2 (SARS-CoV-2). Ruktanonchai *et al.* used mobility data from smartphones to estimate movements between administrative units across Europe before and after the implementation of NPIs for coronavirus disease 2019

(COVID-19). Modeling disease dynamics under alternative scenarios of countries releasing NPIs, in particular stay-at-home orders, showed that if countries do not coordinate their NPIs when they relax lockdown, resurgence of disease occurs sooner. Coordination of on-off NPIs would significantly increase their effectiveness at reducing transmission across Europe. —CA

*Science*, this issue p. 1465

## QUANTUM SYSTEMS

## Dressed for coherence

Solid-state qubits based on the electron spin of defects in silicon carbide or diamond provide a robust and versatile architecture for developing quantum technologies. The longer the lifetime of a spin, the more manipulations and quantum calculations can be performed, making for a more powerful quantum computational platform. Miao *et al.* show that by dressing the spins associated with the divacancy in silicon carbide with microwave photons, the lifetime can be extended by several orders of magnitude into milliseconds (see the Perspective by Hemmer). The technique effectively creates a quiet space for the qubit, thereby protecting it from magnetic, electric, and temperature fluctuations. This approach could be applicable to other architectures and provide a universal route to protecting qubits. —ISO

*Science*, this issue p. 1493;

see also p. 1432

## CORONAVIRUS

## Stabilizing the prefusion SARS-CoV-2 spike

The development of therapeutic antibodies and vaccines against severe acute respiratory syndrome coronavirus 2 (SARS-CoV-2) is focused on the spike (S) protein that decorates the viral surface. A version of the spike ectodomain that includes



two proline substitutions (S-2P) and stabilizes the prefusion conformation has been used to determine high-resolution structures. However, even S-2P is unstable and difficult to produce in mammalian cells. Hsieh *et al.* characterized many individual and combined structure-guided substitutions and identified a variant, named HexaPro, that retains the prefusion conformation but shows higher expression than S-2P and can also withstand heating and freezing. This version of the protein is likely to be useful in the development of vaccines and diagnostics. —VV

*Science*, this issue p. 1501

## CORONAVIRUS

### A steric block to SARS-CoV-2

In response to infection by severe acute respiratory syndrome coronavirus 2 (SARS-CoV-2), the immune system makes antibodies, many of which target the spike protein, a key player in host cell entry. Antibodies that potentially neutralize the virus hold promise as therapeutics and could inform vaccine design. Lv *et al.* report a humanized monoclonal antibody that protected against SARS-CoV-2 in a mouse model. The cryo-electron microscopy structure, together with biochemical, cellular, and virological studies, showed that the antibody acts by binding to the receptor-binding domain of the spike and blocking its attachment to the host receptor. —VV

*Science*, this issue p. 1505

## OCEAN WARMING

### Hearing the heat

Most of the excess heat that causes global warming is absorbed by the oceans. Quantifying that heat increase is challenging because it requires many different temperature measurements over both the vertical and horizontal extent

of the oceans. Wu *et al.* report success in this effort through the use of a different method: They inferred temperature changes from sound waves generated by repeating earthquakes (see the Perspective by Wunsch). The travel time of these earthquakes from source to receiver reflects changes in the average water temperature that they encounter. This technique should substantially enhance our ability to monitor ocean warming. —HJS

*Science*, this issue p. 1510;  
see also p. 1433

## MICROBIOTA

### Microbiota protect the kidneys

Chronic kidney disease (CKD) afflicts millions of people globally. The first-line treatment for CKD is dietary intervention, so there may be a gut microbiota-associated component. Lobel *et al.* investigated the mechanistic links between the microbiota and protein intake, because the protein metabolites indole and indoxyl sulfate are known uremic toxins (see the Perspective by Pluznick). The authors used a mouse model of CKD precipitated by a paucity of the dietary sulfur-containing amino acids methionine and cysteine. Bacterial metabolism of sulfur-containing amino acids modulated indole production by sulfide inhibition of the enzyme tryptophanase, thus abrogating uremic toxicity by this metabolite in this model system. —CA

*Science*, this issue p. 1518;  
see also p. 1426

## MYELOID CELLS

### A sympathetic tumor response

The sympathetic nervous system (SNS) has been shown to regulate immune responses through various mechanisms. Nevin *et al.* now show that

ablation of SNS signaling can suppress tumor immunity, and this is caused by disruption in  $\alpha$ -adrenergic signaling that is needed for myeloid cell maturation. In tumor-bearing mice, this disruption promoted the accumulation of immature myeloid-derived suppressor cells, which allowed for tumor growth. In the absence of intact SNS signaling, these cells also promoted the expansion of regulatory T cells. These results provide insight into the contributions of SNS signaling in innate and adaptive immunity, particularly in the context of tumor immunity. —CNF

*Sci. Immunol.* **5**, eaay9368 (2020).

## METABOLISM

### How to mete out metformin

Metformin is the drug most commonly used to treat type 2 diabetes, though not all patients respond to it and others do not tolerate it at all. García-Calzón *et al.* analyzed genome-wide methylation in the blood of drug-naïve patients who were recently diagnosed with type 2 diabetes. They found that methylation at specific loci was associated with future metformin response or tolerance across multiple cohorts. These epigenetic markers may have theranostic potential regarding which patients should receive metformin. —CAC

*Sci. Transl. Med.* **12**, eaaz1803 (2020).

## REVIEW SUMMARY

## URBAN ECOLOGY

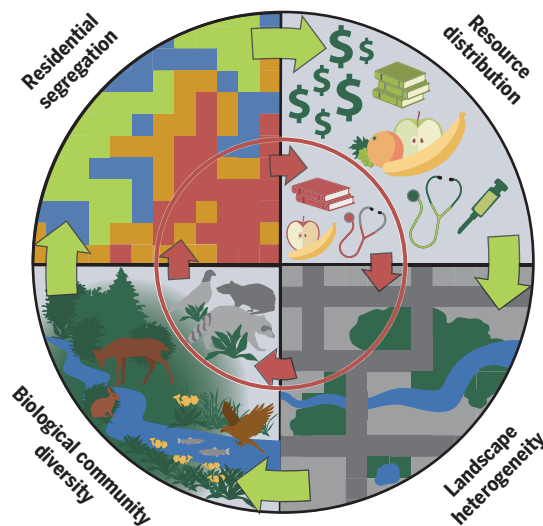
## The ecological and evolutionary consequences of systemic racism in urban environments

Christopher J. Schell\*, Karen Dyson, Tracy L. Fuentes, Simone Des Roches, Nyeema C. Harris, Danica Sterud Miller, Cleo A. Woelfle-Erskine, Max R. Lambert

**BACKGROUND:** Human activity and decisions drive all life in cities. Worldwide, cities are characterized by extensive anthropogenic transformation of the landscape, modification of biogeochemical processes, and alteration of biological communities. Underlying all of these characteristics of urban ecosystems is an extraordinary variability in human agency, culture, power, and identity. Though our understanding of cities as ecological systems with distinctive community assemblages and landscape features has broadened considerably, researchers still rarely consider the full range of social drivers that affect landscape heterogeneity. One of the most characteristic attributes of cities is social inequality—specifically the uneven distribution of resources and wealth primarily underpinned by structural racism and classism. Because structural inequalities form the foundation of city infrastructure, urban development, governance, management, and landscape heterogeneity, inequality among humans defines the ecological setting and evolutionary trajectories for all urban organisms. More broadly, systematic inequities have profound impacts on global biological change and biodiversity loss. Many emergent social inequity patterns are principally driven by systemic racism and white supremacy. Hence, centering racial and economic justice in urban biological research and conservation is imperative. Here, we show how social inequalities shape ecological and evolutionary processes in U.S. cities and highlight the need for research that integrates justice perspectives with ecological and evolutionary dynamics.

**ADVANCES:** Although a rich literature demonstrates how historical and contemporary inequities emerge and persist in human systems, a transdisciplinary perspective that integrates social and cultural processes into an urban eco-evolutionary framework remains unexplored. In today's world, humans often shape the ecological conditions that drive patterns of species distribution and evolution. Distinctive urban landscape features—including reduced habitat patch size, novel plant com-

munities, and increased distance among similar patches—affect key ecological processes such as population dynamics, species interactions, and food web structure. Recent research emphasizes that socioeconomic and demographic factors predict within-city variation in diverse environmental conditions. Humans directly control urban plant, animal, and microbe communities. Further, decisions



**Residential segregation and systemic racism have substantial impacts on ecological and evolutionary dynamics in cities.** Government-sponsored policies stratify neighborhoods on the basis of race and class (e.g., through “redlining” in the United States, represented here by the red circle), which results in restricted access to social services and environmental amenities for racial and/or ethnic minorities and low-income communities (red arrows). Habitat quantity and quality tend to be greater in wealthier and predominantly white neighborhoods (green arrows), which leads to variations in ecological and evolutionary processes, underscoring the influence of systemic racism and inequality in driving urban landscape characteristics.

about urban resource management are often dictated by a subset of individuals and institutions with social or economic capital. These decisions can bias the distribution of societal benefits derived from nature. Dominant social groups also enact and enforce policies and societal norms that exacerbate social and environmental inequities. Wealthier and predom-

inantly white neighborhoods generally have more green space, more trees, and greater plant diversity than less affluent neighborhoods. In addition, synergies among pollution (e.g., light, noise, chemical), resource distribution, subsidized predators, and non-native species present novel challenges to organisms, which must respond by moving elsewhere, acclimatizing, adapting, or facing local extirpation. These stressors are often stratified according to racial and/or ethnic backgrounds and wealth. Further, intraspecific variation in phenotypic and genotypic traits of urban species may reflect human-induced disturbances. These relationships highlight the potential for both adaptive and neutral evolutionary processes in urban subpopulations to vary across neighborhoods within cities.

**OUTLOOK:** Stratification of wealth and property ownership shapes the distribution and management of urban spaces, thus constructing the urban ecosystem. Systemic racism and classism drive urban wealth stratification, emphasizing the need to address inequality-driven environmental heterogeneity in urban ecological and evolutionary studies. Residential segregation and colonial annexation (as well as gentrification and displacement) generate predictable ecological patterns in vegetation, air and water quality, microclimate, soils, and the built environment through the rapid influx of resources to specific areas. Accounting for such processes will allow more accurate estimation of the effect of humans on urban organisms. Deconstructing the complex and nuanced attributes of social inequality in affecting biological phenomena can also inform more equitable and sustainable urban planning solutions that implement anti-racist and justice-centered actions. Racial oppression and economic injustice are jeopardizing urban and global ecosystem health and function. Structural racism and classism are further layered with other inequalities, thus necessitating an intersectional approach to urban ecology. Deeper integration across the natural and social sciences is therefore an urgent priority for advancing our understanding of urban ecosystems and developing applied solutions that promote environmental justice, equity, and sustainability. ■

The list of author affiliations is available in the full article online.  
\*Corresponding author. Email: cjschell@uw.edu  
Cite this article as C. J. Schell et al., *Science* 369, eaay4497 (2020). DOI: 10.1126/science.aay4497

**S READ THE FULL ARTICLE AT**  
<https://doi.org/10.1126/science.aay4497>



## REVIEW

## URBAN ECOLOGY

# The ecological and evolutionary consequences of systemic racism in urban environments

Christopher J. Schell<sup>1\*</sup>, Karen Dyson<sup>2,3</sup>, Tracy L. Fuentes<sup>2</sup>, Simone Des Roches<sup>2,4</sup>, Nyeema C. Harris<sup>5</sup>, Danica Sterud Miller<sup>1</sup>, Cleo A. Woelfle-Erskine<sup>6</sup>, Max R. Lambert<sup>7</sup>

Urban areas are dynamic ecological systems defined by interdependent biological, physical, and social components. The emergent structure and heterogeneity of urban landscapes drives biotic outcomes in these areas, and such spatial patterns are often attributed to the unequal stratification of wealth and power in human societies. Despite these patterns, few studies have effectively considered structural inequalities as drivers of ecological and evolutionary outcomes and have instead focused on indicator variables such as neighborhood wealth. In this analysis, we explicitly integrate ecology, evolution, and social processes to emphasize the relationships that bind social inequities—specifically racism—and biological change in urbanized landscapes. We draw on existing research to link racist practices, including residential segregation, to the heterogeneous patterns of flora and fauna observed by urban ecologists. In the future, urban ecology and evolution researchers must consider how systems of racial oppression affect the environmental factors that drive biological change in cities. Conceptual integration of the social and ecological sciences has amassed considerable scholarship in urban ecology over the past few decades, providing a solid foundation for incorporating environmental justice scholarship into urban ecological and evolutionary research. Such an undertaking is necessary to deconstruct urbanization's biophysical patterns and processes, inform equitable and anti-racist initiatives promoting justice in urban conservation, and strengthen community resilience to global environmental change.

Urban ecosystems encompass complex feedbacks between human activity, built and planted infrastructure, and natural landscapes that drive specific biological processes (1–3). Interactions between social and natural systems produce distinctive biogeochemical and biophysical signatures (4, 5) that alter the demography, life histories, diversity, behaviors, and distributions of non-human species (6, 7). Resultant environmental conditions (e.g., urban heat island effects, food subsidies, and pollution) can drive phenotypic shifts, emigration, or extinction within and across animal and plant populations (8, 9). Cities have, accordingly, become foci for research on biological responses to novel, rapidly changing environments (8–13). Recent urban ecosystems research can inform sustainable solutions that promote biodiversity, human well-being, and urban resilience in the face of global environmental change (3, 14–16). How-

ever, leveraging urban ecosystems as conduits of sustainability, conservation, and innovation, requires a comprehensive understanding of the underlying components, hierarchical structures, and key drivers of urban functions (Fig. 1) (3, 7, 16, 17).

Since its inception, the field of urban ecology has framed cities as quintessential socio-ecological systems (i.e., complex adaptive systems or coupled human and natural systems) where social processes alter ecological properties that reciprocally influence human societies (18–20). These formative urban ecology models placed human decisions and institutions at the core of urban ecosystems, emphasizing the need to quantify spatial and temporal feedbacks within cities (17, 21). For example, the National Science Foundation's urban Long-Term Ecological Research (LTER) programs in Phoenix, Arizona, and Baltimore, Maryland, United States (i.e., the Central Arizona–Phoenix LTER program and the Baltimore Ecosystem Study, respectively) have established links between social and ecological systems by overlaying habitat patch types with demographic information such as neighborhood wealth, housing density, and impervious surface cover (2, 3, 10, 16).

Socioeconomic status has been a standard metric for many socio-ecological studies, as it combines social factors such as culture, race, occupation, education, and societal power into a complex aggregated measure (22, 23). Many social variables that contribute to socioeconomic

status and related environmental variability are the result of historical government and societal actions (24, 25). Recent studies have begun to address the varied contributions of several social factors (e.g., race, sex, and age) to ecological heterogeneity in cities (25–28). However, social inequality remains insufficiently studied as a key driver of ecological and evolutionary change in cities (Fig. 1) (15, 21, 24). Social inequality is the unequal distribution or allocation of wealth and resources to specific socio-cultural groups. Such imbalances contribute to substantial injustices (i.e., social inequities; Fig. 1) that privilege certain individuals over others (29–31). Inequality and inequity disproportionately affect which individuals own and access land, functionally restricting the people who become the primary drivers of urban ecosystem structure and function (32, 33).

Urban social inequality stems from historical and contemporary power imbalances and produces deleterious effects that are often intersectional, involving race, economic class, gender, language, sexuality, nationality, ability, religion, and age (34). Various ecological attributes in cities are principally governed by the spatial and temporal scale of social inequities (23). For instance, the uneven distribution of urban heat islands (35–39), vegetation and tree canopy cover (27, 28, 40, 41), environmental hazards and pollutants (42–46), and access to healthy waterways (47, 48), as well as the relative proportion of native to introduced species (49, 50), are strongly dictated by structural racism and classism (Fig. 1) (21, 31, 32, 51). Concurrently, the environmental justice literature has long articulated the economic, health, and environmental implications of structural racism in cities (52–55). Integrating the contributions of social inequities to urban environmental structure is therefore crucial for informing our understanding of biological processes in cities (33, 55, 56).

Here we provide a transdisciplinary synthesis on how social inequities—and specifically systemic racism—serve as principal drivers of ecological and evolutionary processes by shaping landscape heterogeneity (Fig. 1). We draw on the social and political sciences to specifically stress how understanding systemic racism and racial oppression, rooted in settler colonialism and white supremacy, is essential for advancing research in urban ecology and evolutionary biology. First, we review the socio-ecological effects of wealth disparities in cities. We then describe how systemic racism drives inequitable patterns in wealth, health, and environmental heterogeneity, noting that intersectionality with other identities (e.g., gender, sexual orientation, and indigeneity) may have additive impacts on urban structure (29, 34, 57). We propose hypotheses linking systemic racism to urban ecological and evolutionary patterns and processes. We close by illustrating how centering

<sup>1</sup>School of Interdisciplinary Arts and Sciences, University of Washington, Tacoma, WA 98402, USA. <sup>2</sup>College of Built Environments, University of Washington, Seattle, WA 98195, USA. <sup>3</sup>Dendrolytics, Seattle, WA 98195, USA. <sup>4</sup>School of Aquatic and Fisheries Sciences, University of Washington, Seattle, WA 98195, USA. <sup>5</sup>Applied Wildlife Ecology Lab, Department of Ecology and Evolutionary Biology, University of Michigan, Ann Arbor, MI 48109, USA. <sup>6</sup>School of Marine and Environmental Affairs, College of the Environment, University of Washington, Seattle, WA 98195, USA. <sup>7</sup>Department of Environmental Science, Policy, and Management, University of California, Berkeley, CA 94720, USA.

\*Corresponding author. Email: cjschell@uw.edu

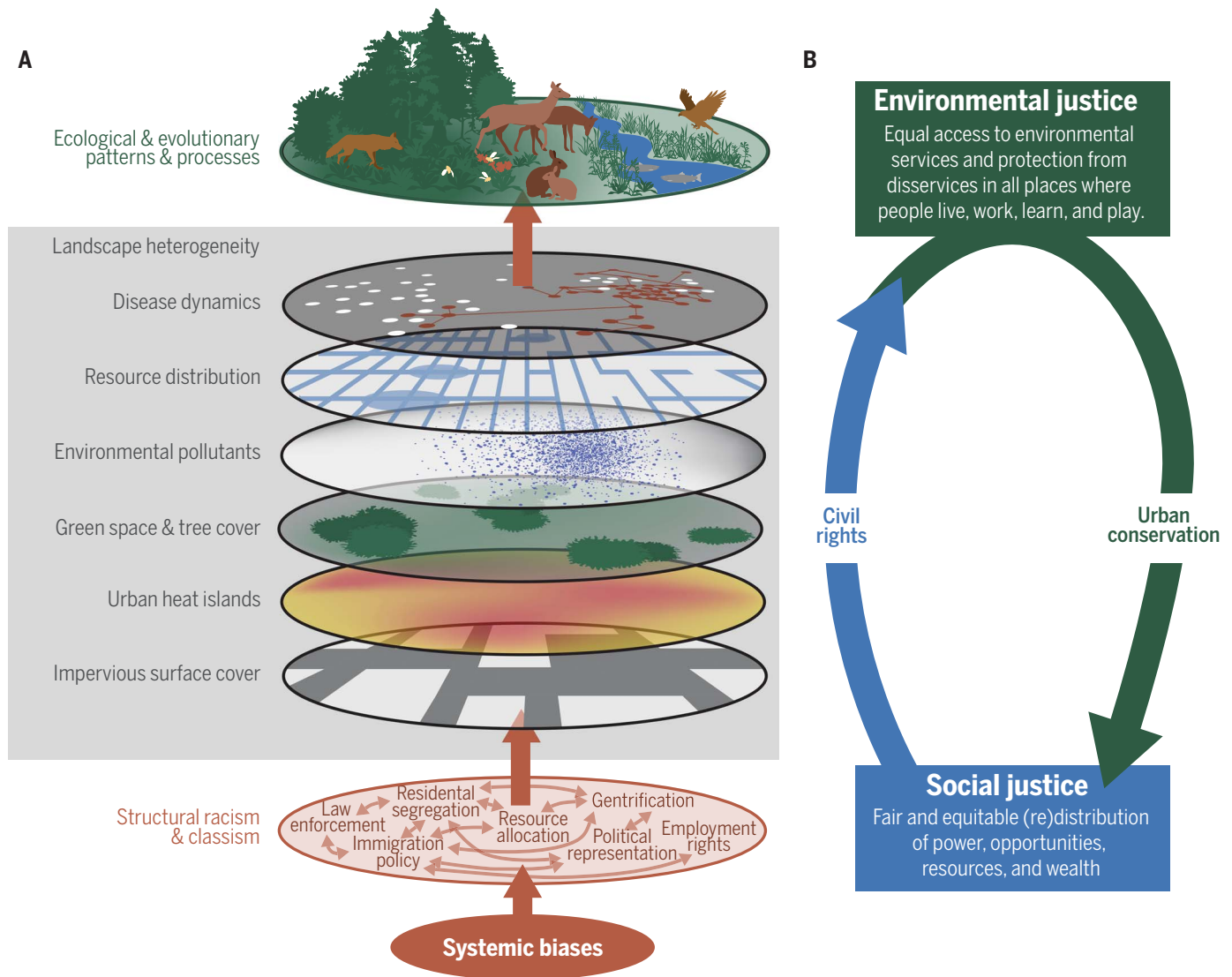


**Fig. 1. Structural racism and classism underpin landscape heterogeneity in cities.**

(A) Conscious and unconscious systemic biases and stereotypes contribute to shaping institutional policies that drive and exacerbate racist and classist structures in urban systems (e.g., law enforcement, residential segregation, and gentrification). The emergent properties of these structural inequalities have substantial impacts on multiple attributes across the urban landscape, including impervious surface cover, urban heat islands, green space and tree cover, environmental pollutants, resource

distribution, and disease dynamics. These physical and biological characteristics have known impacts on the ecological patterns and evolutionary processes of urban organisms. (B) Incorporating environmental justice principles and civil rights into ecological and evolutionary applications is an urgent priority for positively affecting the long-term success of urban conservation and sustainability. (C) Definitions of key terms for understanding the interconnectedness of racism, classism, and intersectionality as related to system inequality.



environmental justice and anti-racist activism in biological research is a priority for urban conservation (55, 56).

Although we predominantly focus on work from North America, the global ubiquity of social inequality and systemic racism across cities suggests that our synthesis is broadly applicable (58–60). Addressing systemic and structural racism in both cities and the scientific community is necessary to comprehensively understand urban ecological and evolutionary dynamics, conserve biodiversity, improve human health and well-being, and promote justice in nature and society.

### Socio-ecological effects of wealth

Household and neighborhood wealth are currently the most common social variables that ecologists use to describe within-city biodiversity patterns, especially in residential neighborhoods (26, 61–64). Wealth—specifically median household income—has repeatedly emerged as a key explanatory variable for predicting urban ecological patterns. One of the most well-known and robust hypotheses linking household income and ecology—the luxury effect—suggests that urban biodiversity, and plant diversity in particular, is positively correlated with neighborhood wealth (61, 63).

The wealth–biodiversity covariance is predicated on a fundamental tenet of urban ecosystems: Humans manage urban areas and, as the ultimate ecosystem engineers, can greatly augment or remove resource limitations that favor growth and abundance of some species over others (32, 61). As a result, households with greater discretionary income and capital, higher education levels, and reduced pressure for essential needs exert stronger influence on plant assemblages, establishing a residential ecological mosaic based on socioeconomic (32, 50, 62, 65).

The luxury effect is particularly pronounced in arid ecoregions and biomes and intensifies with increasing urbanization, vegetation loss, and wealth gaps (21, 35). Initial support for the luxury effect came from Phoenix, Arizona, with observed positive correlations between household income and woody perennial diversity (61). Studies investigating the luxury effect globally have implicated wealth as a strong correlate of faunal and floral diversity (26, 63), relative vegetation cover (27, 40), species abundances (49), and the distribution of abiotic attributes [such as urban heat islands (35, 66) and environmental hazards (44)] in cities. Recent meta-analyses have supported the wealth–biodiversity phenomenon yet emphasized that the causal social and political mechanisms behind these patterns are seldom explored (26, 64).

### Vegetation cover and biodiversity

Affluent urban residential neighborhoods generally have greater vegetation cover, canopy

cover, and plant diversity than their less wealthy counterparts (27, 63, 67). Public urban forests, recreational parks, and private green spaces also tend to be larger and more established with older trees and vegetation that provide greater niche space to support biodiversity at other trophic levels (49, 68, 69). For instance, strong positive correlations exist between urban tree cover and household income for seven major U.S. metropolitan regions (40). General vegetation cover in Los Angeles, California (27), and the distribution of urban forests throughout Cook County, Illinois (41), are also positively affected by increasing wealth, as well as several other socioeconomic factors (e.g., racial composition, education, and home ownership). In addition, recent work suggests that interactive effects between housing age and income predict tree biodiversity, with more established homes in high-income neighborhoods exhibiting greater diversity (27). Lawns are an unusual case: Wealthier residents intensively manage their lawns to be very green (70) and have few to no species other than turfgrasses (71). As a result, some studies have found neutral or negative wealth–plant biodiversity relationships in these areas (72, 73).

Luxury effects customarily scale from the household to the neighborhood level. A recent study found that yards in wealthier neighborhoods consistently had greater abundances and diversity of flowering plants, trees, and non-native species (65). Similarly, individual homeowners with landscaping priorities primarily driven by cost (i.e., the need for cheaper plants) have lawns with higher relative proportions of non-native plant species with lower functional diversity (50). These recent studies illustrate how socioeconomic drive variation among individuals and therefore influence choices at the household level, which can scale up to affect neighborhood biodiversity. These wealth-driven impacts on patterns of primary producers may have substantial effects on metacommunity composition and dynamics. Luxury effects often scale from the residential to the city-wide level, providing cross-city evidence that wealthier U.S. cities have better-resourced urban park systems (74). Whether such trends in vegetative structure are consistent across cities, or even across biomes, remains unexplored.

### Impacts on animal communities

Luxury effects extend beyond primary producers, with recent studies suggesting that colonization, species richness, and abundance of birds are related to neighborhood wealth (49, 75–77). Most prior studies have addressed these relationships in birds in multiple cities across the globe. For instance, bird community richness positively correlates with median household income across multiple urban centers in South Africa (49). However, negative

income–richness relationships in highly urbanized landscapes imply that highly built yet expensive downtown centers can deter or prevent successful colonization and persistence (49). Other studies in Phoenix, Arizona, similarly found that bird diversity was greatest in parks and residential yards in high-income neighborhoods, a pattern primarily explained by an increased relative abundance of native desert species and proximity to undeveloped desert landscapes (75, 76). Further, recent evidence from 45,000 observations of 160 passerine species found across U.S. cities shows that increasing household income predicts greater abundances of migratory species, as well as greater abundances of smaller, shorter-lived birds (77). These results are some of the first empirical examples linking the luxury effect to evolutionary ecology.

Few studies have addressed the luxury effect in other animal taxa, though evidence implies that these effects persist across multiple clades. Evidence for coyotes (*Canis latrans*) and raccoons (*Procyon lotor*) throughout Chicago, Illinois, United States, suggests that carnivores are more likely to colonize and persist in wealthier neighborhoods (68). Household income is also a strong predictor of lizard species richness in Phoenix, Arizona, with other factors such as traffic density and surface temperatures having weak effects (78). Evidence from arthropod research suggests that richness in high-income neighborhoods across North Carolina is greater regardless of vegetation cover at the property level (69).

Wealth–animal richness trends can also extend beyond city limits. Red bat (*Lasiurus borealis*) and evening bat (*Nycticeius humeralis*) activity is positively correlated to household income, regardless of land cover metrics (79). Activity patterns of hoary bats (*Lasiurus cinereus*), however, decrease with increasing neighborhood income, which suggests that luxury effects are more salient for some species than others (79).

### Urban heat islands and air pollution

Heat is unevenly distributed within cities: Temperatures are typically greater in lower-income neighborhoods than in higher-income areas (35, 36). Low-income neighborhoods have reduced tree and vegetation cover and increased impervious surface cover, which contribute to higher surface temperatures in Phoenix, Arizona (35, 66); Baltimore, Maryland (36); and other cities worldwide (38, 39, 80). Given the cooling capacity of trees, apparent luxury effects on tree and vegetation cover can substantially impede environmental cooling in low-income neighborhoods, making residents particularly vulnerable to heat-related illnesses (36, 81). Such wealth–tree–heat axes have emerged in other countries as well, including Canada (82), Brazil (83), and South Africa

(84, 85). Heterogeneity in the distribution of urban heat islands, and associated health outcomes, is thus a direct consequence of the luxury effect (24, 35).

Other environmental disamenities, especially pollutants, also reflect the luxury effect. Air pollution sources are often colocated near low-income neighborhoods; consequently, low-income residents frequently have higher risk of exposure to and vulnerabilities associated with air pollutants. For instance, low-income residents throughout North Carolina (44) and multiple cities in the Northeastern United States (86) experience greater exposure to atmospheric particulate matter. Low-income residents also experience greater ambient nitrogen dioxide concentrations in Montreal, Canada, though some high-income areas in the downtown region similarly experience increased ambient concentrations of this pollutant (87). Further, meta-analysis of data from the American Housing Survey suggests that low-income households have elevated indoor concentrations of nitrogen dioxide and particulate matter (42).

Research on heat islands and pollution supports the idea that inequality in neighborhood wealth leads to a diversity of environmental hazards and that these hazards compound to create distinctive, challenging environmental patches.

#### *Limitations of the luxury effect*

The luxury effect is far from universal across systems and taxa, and the underlying processes and causal mechanisms that contribute to emergent wealth–ecology relationships are seldom addressed (21, 40). In a meta-analysis of associations between wealth and biodiversity, the directional relationship (positive, negative, or no relationship) between biodiversity and wealth varies markedly according to differences in social conditions, which include cultural norms, individual and community preferences, and municipal policies (26). A pair of similar meta-analyses concluded that relationships between income inequality and urban forest cover are not always noteworthy, with neighborhood racial composition explaining divergent conditions in vegetation cover (64, 88).

The history of urban development, individual-level choices, and societal norms also distorts potential relationships between wealth and biodiversity. For instance, in some cities, wealthier neighborhoods may have a higher relative proportion of high-rise structures and built downtown areas that severely limit the amount of vegetated cover, reducing functional habitat space and biodiversity (26). Wealthier neighborhoods may also enact policies that reduce vegetation diversity and mandate the proliferation of monoculture lawns that yield considerable environmental homogeneity and serve

to similarly reduce biodiversity (26). Moreover, refined analytical approaches may help to disentangle the contributions of wealth, culture, and other socioeconomic factors to ecology. For example, evidence in New York City suggests that residential canopy cover is best explained as a signal of social status (the “ecology-of-prestige hypothesis”) (32). Hence, the convergence among policy, individual choices, and socioeconomic variables may be a better predictor of urban ecological variance than wealth alone (32). Indeed, recent work assessing the plant diversity of residential yards supports this conclusion, suggesting that individual homeowners’ landscaping priorities largely dictate private lawn community composition (50).

Luxury effects have been explored primarily in terrestrial systems, with less work in aquatic habitats. Lack of evidence for aquatic luxury effects in urban ponds, lakes, and rivers may be due to other abiotic factors regulating waterway health that do not necessarily correlate with wealth disparities (63). Small ponds or lakes are also seldom present in lower socioeconomic areas, functionally eliminating potential studies on aquatic luxury effects. Moreover, riverfront or coastal environments have increasingly become hotspots for the wealthy, excluding lower-income communities and thereby compounding ostensible luxury effects. Urban rivers and streams run through and interconnect high- and low-income areas, so downstream habitats may suffer consequences of upstream pollution and erosion.

Characteristically, the luxury effect has also resided at the community and ecosystem level, with few studies investigating how wealth heterogeneity affects organismal and population ecology (68, 79). Prior studies also predominantly address patterns but seldom articulate the underlying sociopolitical processes that contribute to wealth–ecology relationships. Integrating the study of systemic racism and that of environmental justice should emerge as the next development in socio-ecological scholarship.

#### **Beyond wealth: Structural racism, ecology, and evolution**

In multiple cases, neighborhood racial composition can be a stronger predictor of urban socio-ecological patterns than wealth (25, 37, 88). For example, exposure to particulate matter in cities such as Los Angeles (43), Phoenix (46), and other cities throughout North Carolina (44) is increased for racial and ethnic minority groups, especially Black, Latinx (i.e., a person of Latin American origin), and Native American populations (43, 45). The geographic distribution of urban heat islands and tree canopy cover in cities is also stratified by race: Multiple studies have repeatedly demonstrated that land surface temperatures are magnified for

racially minoritized groups in many U.S. cities (36, 37, 39), with certain racial groups more vulnerable than others (37, 38). Differential pollutant exposure extends to aquatic systems. For example, decades of neglected pollution in the Flint River led to an ecological disaster for the stream biota and a massive ongoing humanitarian crisis in the predominantly Black community of Flint, Michigan (47, 48). Pressures to save money motivated the local government to switch Flint’s source of drinking water from Lake Huron to the polluted river (89). The calamity of the polluted Flint drinking water is just one example of a larger pattern of minoritized communities bearing the brunt of ecosystem disamenities (48).

Recent studies have begun to reveal some of the underlying structural constructs—especially racism—that contribute to urban heterogeneity beyond household income (28, 37, 88). However, determining the true influence that systemic and structural racism exerts on ecological dynamics remains a novel area of investigation (28). Studies on the resultant evolutionary outcomes are also rare (90). Knowing the relative contribution of structural racism to wealth disparities informs our understanding of complex temporal dynamics in cities, which is not possible in approaches lacking historical context (21, 24). In addition, accounting for structural racism in biological models should improve their predictive value, thereby allowing us to more accurately estimate the effect of urbanization on evolutionary and ecological change. Frameworks that consider systemic and structural racism as principal drivers of urban form advance our ability to predict how and which species may acclimatize and evolve for life in cities (Figs. 2 and 3).

#### *Residential segregation and redlining*

Globally, residential segregation—characterized by a physical separation of groups within cities and further compounded by the concentration of government and ecosystem benefits (30)—is an especially potent form of social stratification. Residential segregation shapes ecological conditions along multiple environmental axes that cannot be neatly characterized by variables such as wealth or impervious surface cover (91). This is particularly important because social geographies vary for different racial, ethnic, and cultural groups depending on the historical forms of discrimination experienced by each minoritized group (31). The impact of structural racism on Black geographies in the United States has been particularly well documented, with substantial legacy effects on urban ecological patterns (21, 24, 27, 92).

Perhaps one of the most notorious examples of structural racism is the U.S.-sanctioned policy of “redlining” enacted between 1933 and 1968. This practice segregated urban



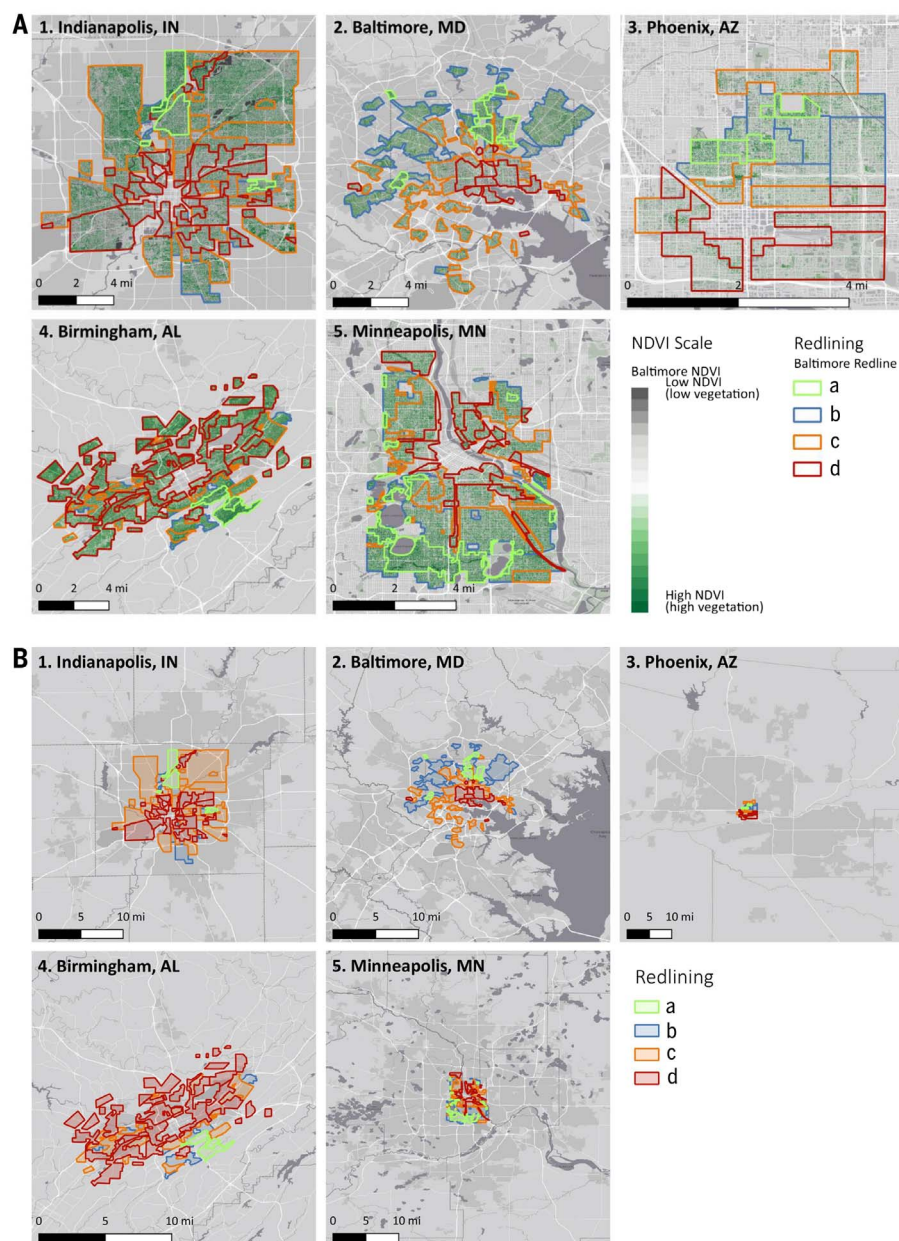


**Fig. 2. The practice of redlining in the United States functionally segregated neighborhoods by race and class.** The highest-rated neighborhoods (graded “a” and outlined in green) were wealthier and predominantly white. The lowest-rated neighborhoods (graded “d” and outlined in red) were poorer and predominantly Black. Demographics of intermediate-ranked neighborhoods (graded “b” and “c” and outlined in blue and orange, respectively) were between those of “a” and “d” areas. Segregation practices such as redlining leave lasting marks on urban landscapes. (A) Redlined neighborhoods still have substantially less green space (e.g., trees, parks, and lawns) than higher-graded neighborhoods. Although this pattern is consistent across cities, there is marked variation among neighborhoods and between cities, as seen in the comparison of Birmingham, Alabama, and Baltimore, Maryland. Other environmental amenities, such as urban water bodies in Minneapolis, Minnesota, are also segregated. (B) Historically greenlined or redlined neighborhoods are positioned differently relative to contemporary urban boundaries and access to natural areas outside the urban landscape. In Minneapolis, Minnesota, and Baltimore, Maryland, redlined neighborhoods are concentrated in the city center, far from the urban periphery. These cities have also grown over the past 50 years, meaning that human and nonhuman residents of redlined neighborhoods must travel farther to get out of the city. By contrast, the city extent of Birmingham, Alabama, has grown minimally, and redlined areas are near forested lands. Note that in the background maps, white represents roads, pale gray represents exurban land, gray represents urban land, and dark gray represents water. Redlining data are from the Mapping Inequality collaborative project (<https://dsl.richmond.edu/panorama/redlining/>). NDVI, normalized difference vegetation index.

residential neighborhoods principally by race and was used to formally suppress capital wealth gains of Black Americans (30). Redlining policy graded neighborhoods from most desirable (“a”; outlined in green in Fig. 2) to hazardous (“d”; outlined in red in Fig. 2) according to their perceived amenities and disamenities, including financial riskiness, environmental quality, proximity to industrial facilities, and racial composition (30). Black Americans were refused housing loans and walk-throughs in neighborhoods deemed “a” or “b” quality and were relegated to “c” and “d” areas, which received less governmental support.

Today, the ecological effects of redlining persist. Redlined “d” neighborhoods have, on average, 21% less tree canopy than “a” neighborhoods. Further, “a”-graded areas are frequently more uniformly green, have older tree canopy, and are closer to environmental amenities than redlined “d” neighborhoods (Fig. 2). Although redlining is no longer an active policy, studies have shown that its legacy remains a key driver of contemporary urban landscapes across at least 37 cities in the United States (24, 28, 92).

#### Ecological effects of structural racism

Redlining may greatly contribute to the asymmetric distribution of habitat that structures bottom-up processes influencing biodiversity (28, 35). Reductions in tree and vegetation cover necessarily diminish niche diversity and quality (63, 93), which frequently coincides with reduced species richness of birds, mammals, and arthropods (94–97). By concentrating Black Americans and other minoritized communities in urban centers, redlining often reduced the proximity of segregated areas to undeveloped landscape beyond the urban boundary (Fig. 2A), and patterns of segregation might have subsequently created variably permeable urban matrices (Fig. 2B). Therefore, we may hypothesize that emergent patterns of species colonization and extinction vary considerably within and among cities as a function of heterogeneous temporal and spatial legacies of racial segregation. A critical question is whether the severity and age of residential segregation affect the number of species co-occurring at a localized site (alpha diversity), a reduction in community composition across sites over space and time (beta diversity), or city-wide regional biodiversity (Fig. 3 and Table 1).

Archived redlined maps may prove valuable for predicting the spatial distribution of niches across cities (Fig. 2). Because redlining predicts the age, abundance, and distribution of urban tree canopy in many cities, it is likely that such maps may also provide substantial resolution to the geographic locations of potential sink habitats and ecological traps in

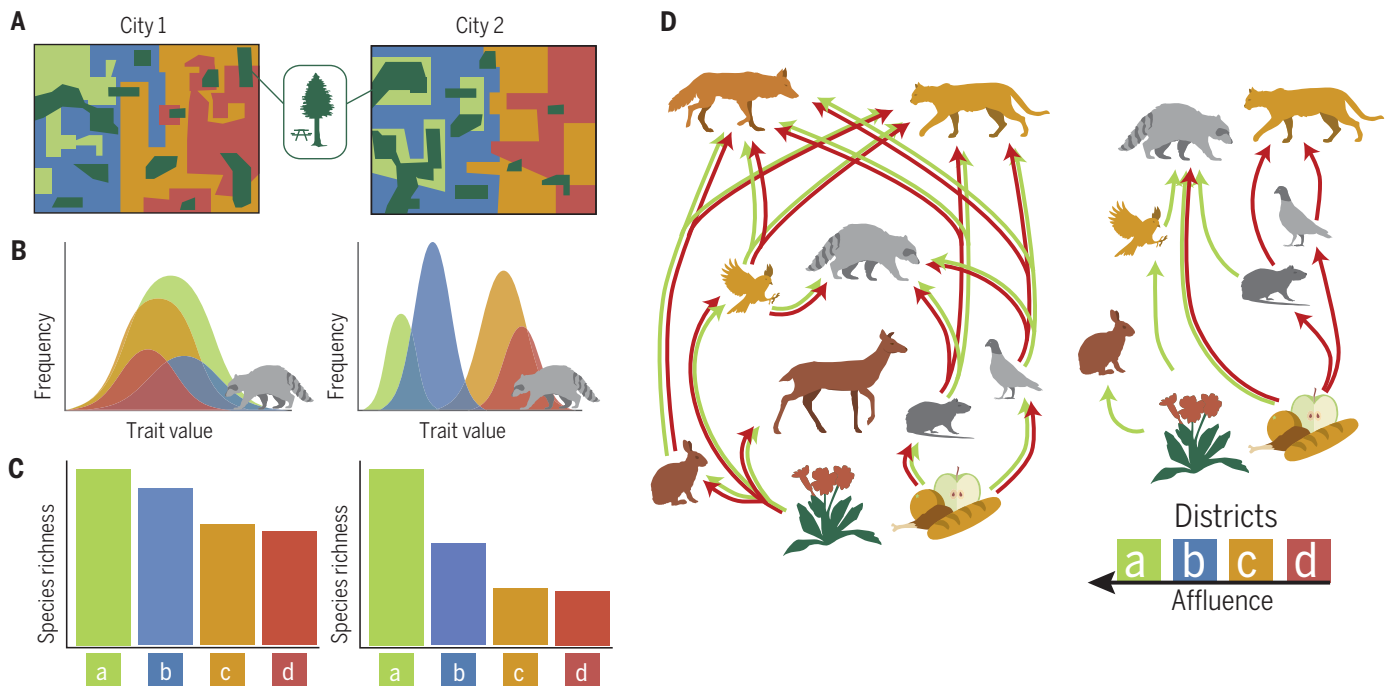


**Fig. 3. Conceptual diagram illustrating how between-city differences in segregation may produce disparate ecological and evolutionary outcomes.**

(A) In hypothetical city 1, green space is more evenly distributed and continuous from green- to redlined districts (Fig. 2) relative to city 2. (B) Between-city differences in connectivity may result in different selective gradients that contribute to varying distributions of genetic or phenotypic trait values of species found across districts ("a" through "d"). (C) Both cities have near-identical

species diversity and composition in "a" districts, and species diversity and composition decline from "a" to "d" neighborhoods. However, within each jurisdiction, city 2 has substantially less species diversity in "b," "c," and "d" districts relative to city 1, potentially as a result of differences in habitat distributions. (D) Food webs may be more diverse and interconnected across districts in city 1 (left) but are more simplified across districts in city 2 (right), owing to the relative differences in structural and functional habitat connectivity.

both terrestrial and aquatic environments (98). Though several studies have addressed the emergence of source and sink habitats (99–102), none have explicitly considered whether heterogeneity in pollutants, heat, and other disturbances shape their geographic distribution (Fig. 1A). The legacy effects of residential segregation could predict the locality and size of potential ecological sinks and traps, thereby helping to identify and predict geographic regions with compounding anthropogenic disturbances that require more sustained stewardship (Table 1).

Recent studies emphasize that the spatial arrangement of vegetation cover can drive evolutionary change (103), fundamentally linking segregation-driven patterns of vegetation cover to evolutionary trajectories of urban populations. Impervious surface is frequently associated with reduced movement of organisms across landscapes and therefore lower gene flow, more subdivided populations, and lower genetic diversity (104–106). Urban tree cover can ameliorate these effects; for example, tree cover facilitates gene flow in native white-footed mice in New York (107, 108). Increased land cover and habitat connectivity, however, may also boost transmission of zoonotic disease (e.g., Lyme disease), and adaptive management solutions to control disease

spread may produce additional evolutionary feedbacks (51, 109). Hypotheses that address the relative contributions of racial segregation and wealth disparities to tree cover can elucidate the socioeconomic attribute that most accurately predicts population genetic structure and connectivity (Table 1).

#### Evolutionary impacts of structural racism

The compounded impacts of heightened edge effects, smaller patch sizes, reduced niche diversity, and individual human behaviors may predict increased genetic drift in racially minoritized neighborhoods (Fig. 3). Urban development and habitat fragmentation are generally expected to increase drift and reduce genetic diversity (107, 110), and urban green spaces in minoritized communities are customarily fragmented (55). Habitat patches may also experience substantially reduced gene flow if adjacent habitats are not proximal (i.e., isolation by distance) or have barriers that prohibit successful immigration into a desired habitat (i.e., isolation by resistance) (107). Reduced tree canopy cover significantly reduces gene flow for some species (108), and canopy cover is significantly diminished in racially segregated neighborhoods (40). As a result, gene flow of native species may be detrimentally affected, whereas some pest species may

thrive in previously redlined neighborhoods (69, 90). Further, highways and impervious surfaces are formidable urban barriers for a variety of taxa (106, 111, 112), and these built structures tend to be more prevalent in racially minoritized neighborhoods (37). How other aspects of urban habitats (e.g., vacant lots, food availability from pets or waste, and homeless encampments) vary as a function of various forms of structural racism and, consequently, affect gene flow in different taxa remains an area worthy of exploration.

Redlining and similar discriminatory policies (e.g., Jim Crow laws) that increased Black Americans' proximity to polluting industries (45, 92, 113) and heightened exposure to intensified urban heat effects (36, 39) may have compounded to create strong selective pressures that drive adaptive and maladaptive evolution (Fig. 3B). Increased pollutant exposure can increase the rate of heritable mutations in mice (114) and selection for toxicity-mediating genes and connected signaling pathways in killifish (*Fundulus heteroclitus*) (115), respectively. Recent studies also provide evidence of rapidly evolved thermal tolerance in urban water fleas (*Daphnia magna*) (116, 117), ants (*Temnothorax curvispinosus*) (118), and damselflies (*Coenagrion puella*) (119). To our knowledge, no studies have explicitly explored



**Table 1. Key questions integrating systemic racism, ecology, and evolution.** A proposed list of potential research questions that integrate social heterogeneity, ecology, and evolution in urban systems. These questions could inform practitioners, planning professionals, and elected officials as to how such processes in cities can be leveraged for positive social change. Colored dots denote the primary research focus of each question (blue, ecological; gold, evolutionary).

Key questions	Research focus
1. How does biodiversity vary with the degree of residential segregation within a city?	
2. Do socioeconomic and racial stratification predict the locality of ecological traps and source-sink dynamics within cities?	
3. How does the severity of economic and racial segregation influence connectivity, dispersal, gene flow, and genetic isolation?	
4. Does equitable urban greening increase the probability of rescue effects of native species and ecological specialists?	
5. Do cities with increasing homelessness rates have reduced species occupancy rates?	
6. Is functional or structural connectivity reduced in cities with more pronounced economic or racial segregation?	
7. Are rates of local adaptation or maladaptation higher for urban organisms in redlined neighborhoods?	
8. How have urban renewal and associated displacement affected habitat fragmentation and ecological disturbances?	
9. Do carbon sequestration and soil microbial density differ as a function of neighborhood segregation?	
10. Does selection for non-dispersing seeds in plants vary with socioeconomic and demographic predictors?	
11. Do numerical responses in predator-prey or pollinator-plant dynamics vary across redlining categories?	
12. Is natural selection along multiple ecological conditions strongest in redlined or low-income neighborhoods?	
13. How do sublethal effects (e.g., life-history traits, physiology) vary as a function of pollution proximity and segregation in cities?	
14. Are rates of zoonotic disease transmission accelerated or dampened by residential segregation and/or urban renewal?	
15. Can improvements to public transportation infrastructure and greenways improve habitat connectivity?	
16. Do anti-displacement policies affect ecological stability and integrity over time?	
17. Are cities with smaller economic inequality indices (e.g., the Gini coefficient) more biodiverse relative to others?	
18. Does remediating pollution (air, soil, water) in marginalized neighborhoods enhance biodiversity and organismal abundances?	

how either neutral or adaptive evolutionary processes operate as a function of heterogeneity that stems from structural racism.

The lack of effective intervention, water sanitation, medical access and resources, and trash management programs due to structural racism may also shape mutation rates and emerging disease dynamics (90, 120).

Racially minoritized and low-income communities witness increased proximity to pest species known to harbor zoonotic diseases (90, 121, 122). For instance, brown rat (*Rattus norvegicus*) abundances negatively correlate with socioeconomic status, such that low-income neighborhoods report more frequent rat sightings across cities globally

(123–127). Racially diverse neighborhoods consistently receive inadequate sanitation services that are compounded with aging infrastructure and overgrown vegetation, all factors that attract brown rats and other non-native rodent pests (125, 128). Inconsistent administration of over-the-counter rodenticides may lead to various levels of immune resistance in local rat populations (129), further exacerbating health and disease risks for marginalized communities (130). Societal neglect underpinned by systemic racism may therefore promote the evolution of rodenticide immunity that heightens zoonotic disease risks in marginalized communities (57).

Infection and mortality rates from coronavirus disease 2019 (COVID-19), caused by severe acute respiratory syndrome coronavirus 2 (SARS-CoV-2), are disproportionately high for Latinx, Indigenous, and Black communities relative to other racial groups in the United States (91, 113, 131–135). Over decades of government policy and economic development, cities have disproportionately situated environmental hazards (e.g., petrochemical industries, waste facilities, and major roadways) near predominantly Black and Indigenous communities (43, 46). Such forms of environmental racism have substantially compromised neighborhood air quality and respiratory health of minoritized communities (43, 87). Recent evidence linking air pollution exposure with COVID-19 mortality risk (134, 136) thus indicates direct connections among environmental racism, air quality, and disproportionate death rates for Black and Indigenous communities. This epidemiological phenomenon is further compounded by reduced access to adequate health care, heightened risks of concomitant health comorbidities (e.g., cardiovascular disease, hypertension, and diabetes), and increased housing density (133). Communities with higher human densities can experience increased viral mutation rates, which subsequently increase the likelihood of viral host jumping (120). An alarming but plausible and insufficiently studied (137) hypothesis is that mutation rates in pathogens such as SARS-CoV-2 are greatest in racially minoritized and low-income communities, creating a pernicious socio-evolutionary loop between increasing virulence and the uneven distribution of social and health inequities in these communities.

*Intersecting forms of inequality*

Understanding the mechanisms that shape urban inequality and, thus, urban eco-evolutionary patterns and processes requires incorporating intersectional theories of inequality and evaluating accessibility to different spaces (34, 138, 139). The term “intersectionality” emphasizes that various marginalized identities of an individual or community more broadly intersect, compound, and interact, ultimately affecting the magnitude and severity of experienced social

inequities (Fig. 1) (57). For example, discrimination experienced by a queer Black woman in the United States may be intensified relative to that faced by individuals with similar racial, gender, and sexual orientation identities alone. Translating the concept of intersectionality onto the urban landscape can provide a more holistic understanding of the patterns and processes that shape urban ecosystems. For instance, we may hypothesize that characteristic differences between Indigenous ecological practices and those of forestland managers may contribute to variance in native species richness and community complexity (140, 141). Similarly, we may predict that gender differences as related to land cultivation and homeownership shape plant species assemblages and species turnover rates. Further, vegetation removal and increased nighttime lighting to deter LGBTQIA+ (lesbian, gay, bisexual, transgender, queer, intersex, asexual, and other) communities (95) may have subsequent effects on disturbance regimes and local biodiversity that reduce habitat value for multiple species. Though such empirical links are currently speculative and not well established, integration of various inequities in cities may provide additional resolution to understanding how social drivers affect urban ecology and evolution. Although our focus has been on racism and classism, we recognize the need for and encourage intersectional approaches in urban ecology.

### Centering justice in urban ecology and conservation

The origins of environmentalism in the United States were heavily influenced by white men who expressed racist perspectives in their efforts to protect nature. Writings by early environmentalists such as Aldo Leopold, John Muir, Madison Grant, Gifford Pinchot, and Theodore Roosevelt argued that nature is most pristine without human influence but should be reserved for white men as a resource for personal improvement (142–144). These early arguments greatly contributed to the exclusion of Black, Indigenous, and non-white immigrant communities from outdoor spaces and environmental narratives (145), despite these communities shouldering the brunt of environmental and climate crises and leading effective movements for environmental and climate justice (53, 146, 147). White-led environmental and climate movements have long marginalized issues of racial justice when crafting policy and legislation (148). In addition, such movements have traditionally considered structural violence to be unrelated to environmental issues, yet state-sanctioned police brutality (149, 150), environmental degradation (113), and the climate crisis (53, 147) all reinforce patterns of racial segregation and criminalization of minoritized people in urban public spaces (151, 152).

Black, Indigenous, Latinx, and immigrant communities possess cultural knowledge, ongoing land and water relations, and effective practices for community and ecological revitalization, honed through generations of struggle with and for the land (140, 141). Systemic racism in environmental policy excludes communities from ecocultural relations with urban ecosystems, urban planning processes, and urban ecological restoration (153, 154). As a result, these communities find that their longstanding and effective practices of managing and advocating for lands, waters, and species are limited. When judges, elected officials, planners, scientists, and others who hold power in environmental governance work in solidarity with frontline communities, urban organisms, ecosystems, and human communities move toward regeneration (155–157).

Racist research and conservation approaches must be challenged and redesigned to include justice, equity, and inclusion (24, 157–159). To do so, ecologists, biologists, and environmentalists must reimagine what is considered an ecological or conservation issue. Increasing economic opportunities, bolstering public transportation infrastructure, investing in affordable housing and health care, and strengthening voting rights and access are issues rarely considered by mainstream environmental organizations. Yet such societal initiatives reduce carbon emissions, dampen environmental hazards, enhance public health, and expand economic mobility of marginalized communities. Moreover, reallocating municipal funds to initiatives that aim to improve home ownership for minoritized communities reduces displacement and promotes local stewardship, which in turn affects overall public and environmental health. Such paradigm shifts will be essential, as accumulating evidence suggests that income inequality predicts biodiversity loss (63, 160). Centering racial and environmental justice that drives equitable policy changes is thus inextricably linked to urban conservation and ecological restoration initiatives (157, 159).

Improving green infrastructure and green-space access, paired with policies that shield against displacement, can greatly enhance community health and wealth (54, 161). Exposure and access to quality natural space in cities improve physical and mental health (162) and buffer against health comorbidities experienced by minoritized groups (31, 92, 161). Justice-centered applications of ecological and evolutionary tools can further spotlight convergences among social inequities and environmental disamenities (e.g., ecological modeling of habitat sinks and sources) to identify areas of high conservation and restoration need. Equitable restoration of urban habitat patches and infrastructure necessarily improves landscape connectivity and refugia to support successful

colonization of native species, guards against local extinctions, and increases urban biodiversity (159). Hence, equity-based ecological restoration will benefit both human and non-human communities (163, 164), but only if the foundation of such initiatives are rooted in anti-racist practices (156, 165). The maintenance of societal integrity should, in turn, lead to capital gains for minoritized communities that translate to ecological stability that positively affects species diversity in cities.

As urban ecologists and evolutionary biologists, we have a responsibility to implement anti-racist strategies that evaluate systems of oppression in how we perform our science. This necessarily means eradicating efforts that perpetuate inequities to knowledge access, neglect local community participation, or exploit community labor in the pursuit of academic knowledge (i.e., the practices of colonial and “parachute” science). Concurrently, increasing representation of individuals of diverse identities is inherently just and enhances our scholarship (166, 167). By directly including a diversity of scholars and incorporating an understanding of systemic racism and inequality, we can more holistically study urban ecosystems. We will not be able to successfully assess how racism and classism shape urban ecosystems, nor address their consequences, without a truly diverse and inclusive scientific community.

### Outlook

The decisions we make now will dictate our environmental reality for centuries to come, as illustrated by modern policies such as the Green New Deal proposal (168) and the Paris Agreement (169). Such endeavors are timely as we face a global pandemic that is both affected by and exacerbates the latent structural inequities underpinning modern cities, directly threatening environmental health and biodiversity conservation (170, 171). Concurrently, our contemporary fight for civil rights in the wake of unjust murders and continued racial oppression of Black and Indigenous communities stresses the need to question and abolish systemic racism. The insidious white supremacist structures that perpetuate racism throughout society compromise both public and environmental health, solidifying the need to radically dismantle systems of racial and economic oppression.

Consequently, our capacity to understand urban ecosystems and nonhuman organisms necessitates a more thorough integration of the natural and social parameters of our cities. We cannot generalize human behavior in urban ecosystems without dealing with systemic racism and other inequities. Further, incorporating environmental justice principles into how we perform and interpret urban ecology and evolution research will be essential, with restorative and environmental justice serving



as the foundation for effective ecological restoration and conservation (158, 159, 163). Doing so is both our civic responsibility and conservation imperative for advancing urban resiliency in the face of unrelenting global environmental change (172).

## REFERENCES AND NOTES

- M. Alberti, Eco-evolutionary dynamics in an urbanizing planet. *Trends Ecol. Evol.* **30**, 114–126 (2015). doi: [10.1016/j.tree.2014.11.007](#); pmid: 25498964
- S. Pickett *et al.*, A conceptual framework for the study of human ecosystems in urban areas. *Urban Ecosyst.* **1**, 185–199 (1997). doi: [10.1023/A:1018531712889](#)
- N. B. Grimm *et al.*, Global change and the ecology of cities. *Science* **319**, 756–760 (2008). doi: [10.1126/science.1150195](#); pmid: 18258902
- D. E. Pataki *et al.*, Coupling biogeochemical cycles in urban environments: Ecosystem services, green solutions, and misconceptions. *Front. Ecol. Environ.* **9**, 27–36 (2011). doi: [10.1890/090220](#)
- R. P. Kaye, P. M. Groffman, N. B. Grimm, L. A. Baker, R. V. Pouyat, A distinct urban biogeochemistry? *Trends Ecol. Evol.* **21**, 192–199 (2006). doi: [10.1016/j.tree.2005.12.006](#); pmid: 16701085
- S. H. Faeth, C. Bang, S. Saari, Urban biodiversity: Patterns and mechanisms. *Ann. N. Y. Acad. Sci.* **1223**, 69–81 (2011). doi: [10.1111/j.1749-6632.2010.05925.x](#); pmid: 21449966
- S. T. A. Pickett, M. L. Cadenasso, D. L. Childers, M. J. McDonnell, W. Zhou, Evolution and future of urban ecological science: Ecology in, of, and for the city. *Ecosyst. Health Sustain.* **2**, e01229 (2016). doi: [10.1002/ehs2.1229](#)
- C. M. Donihue, M. R. Lambert, Adaptive evolution in urban ecosystems. *Ambio* **44**, 194–203 (2015). doi: [10.1007/s13280-014-0547-2](#); pmid: 25056615
- J. Q. Ouyang *et al.*, A New Framework for Urban Ecology: An Integration of Proximate and Ultimate Responses to Anthropogenic Change. *Integr. Comp. Biol.* **58**, 915–928 (2018). doi: [10.1093/icb/icy110](#); pmid: 30376106
- D. E. Pataki, Grand challenges in urban ecology. *Front. Ecol. Evol.* **3**, 57 (2015). doi: [10.3389/fevo.2015.00057](#)
- L. R. Rivkin *et al.*, A roadmap for urban evolutionary ecology. *Evol. Appl.* **12**, 384–398 (2018). doi: [10.1111/eva.12734](#); pmid: 30828362
- M. T. J. Johnson, J. Munshi-South, Evolution of life in urban environments. *Science* **358**, eaam8327 (2017). doi: [10.1126/science.aam8327](#); pmid: 29097520
- E. C. Lahr, R. R. Dunn, S. D. Frank, Getting ahead of the curve: Cities as surrogates for global change. *Proc. R. Soc. B* **285**, 20180643 (2018). doi: [10.1098/rspb.2018.0643](#); pmid: 30051830
- D. L. Childers *et al.*, An ecology for cities: A transformational nexus of design and ecology to advance climate change resilience and urban sustainability. *Sustainability* **7**, 3774–3791 (2015). doi: [10.3390/su7043774](#)
- T. McPhearson *et al.*, Advancing Urban Ecology toward a Science of Cities. *Bioscience* **66**, 198–212 (2016). doi: [10.1093/biosci/biw002](#)
- C. L. Redman, J. M. Grove, L. H. Kubly, Integrating social science into the Long-Term Ecological Research (LTER) Network: Social dimensions of ecological change and ecological dimensions of social change. *Ecosystems* **7**, 161–171 (2004). doi: [10.1007/s10021-003-0215-z](#)
- C. J. Tanner *et al.*, Urban ecology: Advancing science and society. *Front. Ecol. Environ.* **12**, 574–581 (2014). doi: [10.1890/140019](#)
- J. Liu *et al.*, Complexity of coupled human and natural systems. *Science* **317**, 1513–1516 (2007). doi: [10.1126/science.1144004](#); pmid: 17872436
- W. F. Zipperer, W. F. Morse, C. J. Gaither, “Linking social and ecological systems” in *Urban Ecology*, J. Niemela, Ed. (Oxford Univ. Press, 2011), pp. 298–308; [www.fs.usda.gov/treesearch/pubs/39210](#)
- N. R. Dorey, M. A. R. Udell, C. D. L. Wynne, When do domestic dogs, *Canis familiaris*, start to understand human pointing? The role of ontogeny in the development of interspecies communication. *Anim. Behav.* **79**, 37–41 (2010). doi: [10.1016/j.anbehav.2009.09.032](#)
- L. A. Roman *et al.*, Human and biophysical legacies shape contemporary urban forests: A literature synthesis. *Urban For. Urban Green.* **31**, 157–168 (2018). doi: [10.1016/j.ufug.2018.03.004](#)
- K. E. Pickett, M. Pearl, Multilevel analyses of neighbourhood socioeconomic context and health outcomes: A critical review. *J. Epidemiol. Community Health* **55**, 111–122 (2001). doi: [10.1136/jech.55.2.111](#); pmid: 11154250
- S. T. A. Pickett *et al.*, Dynamic heterogeneity: A framework to promote ecological integration and hypothesis generation in urban systems. *Urban Ecosyst.* **20**, 1–14 (2017). doi: [10.1007/s11252-016-0574-9](#)
- J. M. Grove *et al.*, The Legacy Effect: Understanding How Segregation and Environmental Injustice Unfold over Time in Baltimore. *Ann. Am. Assoc. Geogr.* **108**, 524–537 (2018). doi: [10.1080/24694452.2017.1365585](#)
- D. H. Locke, G. Baine, The good, the bad, and the interested: How historical demographics explain present-day tree canopy, vacant lot and tree request spatial variability in New Haven, CT. *Urban Ecosyst.* **18**, 391–409 (2015). doi: [10.1007/s11252-014-0409-5](#)
- E. R. Kuras *et al.*, Urban socioeconomic inequality and biodiversity often converge, but not always: A global meta-analysis. *Landsc. Urban Plan.* **198**, 103799 (2020). doi: [10.1016/j.landurbplan.2020.103799](#)
- L. W. Clarke, G. D. Jenerette, A. Davila, The luxury of vegetation and the legacy of tree biodiversity in Los Angeles, CA. *Landsc. Urban Plan.* **116**, 48–59 (2013). doi: [10.1016/j.landurbplan.2013.04.006](#)
- D. Locke, B. Hall, J. M. Grove, S. T. Pickett, L. A. Ogden, C. Aoki, C. G. Boone, J. P. M. O’Neil-Dunne, Residential housing segregation and urban tree canopy in 37 US Cities. *SocArXiv* (6 January 2020); [https://doi.org/10.31235/osf.io/97zcs](#)
- P. Spencer, P. E. Perkins, J. D. Erickson, Re-establishing Justice as a Pillar of Ecological Economics Through Feminist Perspectives. *Ecol. Econ.* **152**, 191–198 (2018). doi: [10.1016/j.ecolecon.2018.05.022](#)
- A. Mills, The Color of Law: A Forgotten History of How Our Government Segregated America. *Berkeley Plan. J.* **29**, 159–163 (2018). doi: [10.5070/BP329138440](#)
- Z. D. Bailey *et al.*, Structural racism and health inequities in the USA: Evidence and interventions. *Lancet* **389**, 1453–1463 (2017). doi: [10.1016/S0140-6736\(17\)30569-X](#); pmid: 28402827
- J. M. Grove, D. H. Locke, J. P. M. O’Neil-Dunne, An ecology of prestige in New York City: Examining the relationships among population density, socio-economic status, group identity, and residential canopy cover. *Environ. Manage.* **54**, 402–419 (2014). doi: [10.1007/s00267-014-0310-2](#); pmid: 25034751
- P. S. Warren, S. Harlan, C. Boone, S. B. Lerman, E. Shochat, A. P. Kinzig, “Urban ecology and human social organisation” in *Urban Ecology*, K. J. Gaston, Ed. (Cambridge Univ. Press, 2013), pp. 172–201.
- G. Winker, N. Degele, Intersectionality as multi-level analysis: Dealing with social inequality. *Eur. J. Womens Stud.* **18**, 51–66 (2011). doi: [10.1177/1350506810386084](#)
- G. D. Jenerette, S. L. Harlan, W. L. Stefanov, C. A. Martin, Ecosystem services and urban heat riskscape moderation: Water, green spaces, and social inequality in Phoenix, USA. *Ecol. Appl.* **21**, 2637–2651 (2011). doi: [10.1890/10-1493.1](#); pmid: 22073649
- G. Huang, M. L. Cadenasso, People, landscape, and urban heat island: Dynamics among neighborhood social conditions, land cover and surface temperatures. *Landsc. Ecol.* **31**, 2507–2515 (2016). doi: [10.1007/s10980-016-0437-z](#)
- B. M. Jesdale, R. Morello-Frosch, L. Cushing, The racial/ethnic distribution of heat risk-related land cover in relation to residential segregation. *Environ. Health Perspect.* **121**, 811–817 (2013). doi: [10.1289/ehp.1205919](#); pmid: 23694846
- B. C. Mitchell, J. Chakraborty, Exploring the relationship between residential segregation and thermal inequity in 20 U.S. cities. *Local Environ.* **23**, 796–813 (2018). doi: [10.1080/13549839.2018.1474861](#)
- B. C. Mitchell, J. Chakraborty, Landscapes of thermal inequity: Disproportionate exposure to urban heat in the three largest US cities. *Environ. Res. Lett.* **10**, 115005 (2015). doi: [10.1088/1748-9326/10/11/115005](#)
- K. Schwarz *et al.*, Trees grow on money: Urban tree canopy cover and environmental justice. *PLOS ONE* **10**, e0122051 (2015). doi: [10.1371/journal.pone.0122051](#); pmid: 25830303
- C. Fan, M. Johnston, L. Darling, L. Scott, F. H. Liao, Land use and socio-economic determinants of urban forest structure and diversity. *Landsc. Urban Plan.* **181**, 10–21 (2019). doi: [10.1016/j.landurbplan.2018.09.012](#)
- G. Adamkiewicz *et al.*, Moving environmental justice indoors: Understanding structural influences on residential exposure patterns in low-income communities. *Am. J. Public Health* **101**, S238–S245 (2011). doi: [10.2105/AJPH.2011.300119](#); pmid: 21836112
- C. W. Tessum *et al.*, Inequity in consumption of goods and services adds to racial-ethnic disparities in air pollution exposure. *Proc. Natl. Acad. Sci. U.S.A.* **116**, 6001–6006 (2019). doi: [10.1073/pnas.1818859116](#); pmid: 30858319
- S. C. Gray, S. E. Edwards, M. L. Miranda, Race, socioeconomic status, and air pollution exposure in North Carolina. *Environ. Res.* **126**, 152–158 (2013). doi: [10.1016/j.envres.2013.06.005](#); pmid: 23850144
- M. A. Bravo, R. Anthopoulos, M. L. Bell, M. L. Miranda, Racial isolation and exposure to airborne particulate matter and ozone in understudied US populations: Environmental justice applications of downscaled numerical model output. *Environ. Int.* **92**, 247–255 (2016). doi: [10.1016/j.envint.2016.04.008](#); pmid: 27115915
- R. Pope, J. Wu, C. Boone, Spatial patterns of air pollutants and social groups: A distributive environmental justice study in the phoenix metropolitan region of USA. *Environ. Manage.* **58**, 753–766 (2016). doi: [10.1007/s00267-016-0741-z](#); pmid: 27631674
- L. A. Schaidler, L. Swetschinski, C. Campbell, R. A. Rudel, Environmental justice and drinking water quality: Are there socioeconomic disparities in nitrate levels in U.S. drinking water? *Environ. Health* **18**, 3 (2019). doi: [10.1186/s12940-018-0442-6](#); pmid: 30651108
- M. A. S. Laidlaw *et al.*, Children’s blood lead seasonality in flint, Michigan (USA), and soil-sourced lead hazard risks. *Int. J. Environ. Res. Public Health* **13**, 358 (2016). doi: [10.3390/ijerph13040358](#); pmid: 27023578
- D. E. Chamberlain, D. A. W. Henry, C. Reynolds, E. Caprio, A. Amar, The relationship between wealth and biodiversity: A test of the Luxury Effect on bird species richness in the developing world. *Global Change Biol.* **25**, 3045–3055 (2019). doi: [10.1111/gcb.14682](#); pmid: 31077502
- J. Paduella Cubino *et al.*, Linking yard plant diversity to homeowners’ landscaping priorities across the U.S. *Landsc. Urban Plan.* **196**, 103730 (2020). doi: [10.1016/j.landurbplan.2019.103730](#)
- S. Des Roches *et al.*, Socio-Eco-Evolutionary Dynamics in Cities. *Evol. Appl.* **10**, 1111/eva.13065 (2020). doi: [10.1111/eva.13065](#)
- D. M. Konisky, C. Reenock, Regulatory Enforcement, Riskscape, and Environmental Justice. *Policy Stud. J.* **46**, 7–36 (2018). doi: [10.1111/psj.12203](#)
- D. Schlosberg, L. B. Collins, From environmental to climate justice: Climate change and the discourse of environmental justice. *WIREs Clim. Change* **5**, 359–374 (2014). doi: [10.1002/wcc.275](#)
- J. R. Wolch, J. Byrne, J. P. Newell, Urban green space, public health, and environmental justice: The challenge of making cities “just green enough”. *Landsc. Urban Plan.* **125**, 234–244 (2014). doi: [10.1016/j.landurbplan.2014.01.017](#)
- V. Jennings, M. F. Floyd, D. Shanahan, C. Coutts, A. Sinykin, Emerging issues in urban ecology: Implications for research, social justice, human health, and well-being. *Popul. Environ.* **39**, 69–86 (2017). doi: [10.1007/s11111-017-0276-0](#)
- S. T. A. Pickett, C. G. Boone, M. L. Cadenasso, “Ecology and environmental justice: Understanding disturbance using ecological theory” in *Urbanization and Sustainability: Linking Urban Ecology, Environmental Justice and Global Environmental Change*, C. G. Boone, M. Fragkias, Eds. (Springer, 2013), pp. 27–47; [https://doi.org/10.1007/978-94-007-5666-3\\_3](#)
- K. Crenshaw, Mapping the Margins: Intersectionality, Identity Politics, and Violence against Women of Color. *Stanford Law Rev.* **43**, 1241 (1991). doi: [10.2307/1229039](#)
- L. Michael, “Anti-Black racism: Aphobia, exclusion and global racisms” in *Critical Perspectives on Hate Crime*, A. Haynes, J. Schwegge, S. Taylor, Eds. (Palgrave Macmillan, 2017), pp. 275–299; [https://link.springer.com/10.1057/978-1-137-52667-0\\_15](#)
- G. Beckles-Raymond, Implicit Bias, (Global) White Ignorance, and Bad Faith: The Problem of Whiteness and Anti-black Racism. *J. Appl. Philos.* **37**, 169–189 (2020). doi: [10.1111/japp.12385](#)
- A. Bledsoe, W. J. Wright, The anti-Blackness of global capital. *Environ. Plann. D* **37**, 8–26 (2019). doi: [10.1177/0263775818805102](#)
- D. Hope *et al.*, Socioeconomics drive urban plant diversity. *Proc. Natl. Acad. Sci. U.S.A.* **100**, 8788–8792 (2003). doi: [10.1073/pnas.1537557100](#); pmid: 12847293

62. J. S. Walker, N. B. Grimm, J. M. Briggs, C. Gries, L. Dugan, Effects of urbanization on plant species diversity in central Arizona. *Front. Ecol. Environ.* **7**, 465–470 (2009). doi: [10.1890/0800084](#)
63. M. Leong, R. R. Dunn, M. D. Trautwein, Biodiversity and socioeconomics in the city: A review of the luxury effect. *Biol. Lett.* **14**, 20180082 (2018). doi: [10.1098/rsbl.2018.0082](#); pmid: [29743266](#)
64. E. Gerrish, S. L. Watkins, The relationship between urban forests and income: A meta-analysis. *Landsc. Urban Plan.* **170**, 293–308 (2018). doi: [10.1016/j.landurbplan.2017.09.005](#); pmid: [29249844](#)
65. M. Avolio, A. Blanchette, N. F. Sonti, D. H. Locke, Time Is Not Money: Income Is More Important Than Lifestage for Explaining Patterns of Residential Yard Plant Community Structure and Diversity in Baltimore. *Front. Ecol. Evol.* **8**, 85 (2020). doi: [10.3389/fevo.2020.00085](#)
66. A. Buyantuyev, J. Wu, Urban heat islands and landscape heterogeneity: Linking spatiotemporal variations in surface temperatures to land-cover and socioeconomic patterns. *Landsc. Ecol.* **25**, 17–33 (2010). doi: [10.1007/s10980-009-9402-4](#)
67. A. Rigolon, A complex landscape of inequity in access to urban parks: A literature review. *Landsc. Urban Plan.* **153**, 160–169 (2016). doi: [10.1016/j.landurbplan.2016.05.017](#)
68. S. B. Magle, E. W. Lehrer, M. Fidino, Urban mesopredator distribution: Examining the relative effects of landscape and socioeconomic factors. *Anim. Conserv.* **19**, 163–175 (2016). doi: [10.1111/acv.12231](#)
69. M. Leong, M. A. Bertone, K. M. Bayless, R. R. Dunn, M. D. Trautwein, Exoskeletons and economics: Indoor arthropod diversity increases in affluent neighbourhoods. *Biol. Lett.* **12**, 20160322 (2016). doi: [10.1098/rsbl.2016.0322](#); pmid: [27484644](#)
70. W. Zhou, A. Troy, J. Morgan Grove, J. C. Jenkins, Can money buy green? demographic and socioeconomic predictors of lawn-care expenditures and lawn greenness in urban residential areas. *Soc. Nat. Resour.* **22**, 744–760 (2009). doi: [10.1080/08941920802074330](#)
71. M. M. Wheeler *et al.*, Continental-scale homogenization of residential lawn plant communities. *Landsc. Urban Plan.* **165**, 54–63 (2017). doi: [10.1016/j.landurbplan.2017.05.004](#)
72. J. M. Grove *et al.*, Data and methods comparing social structure and vegetation structure of urban neighborhoods in Baltimore, Maryland. *Soc. Nat. Resour.* **19**, 117–136 (2006). doi: [10.1080/08941920500394501](#)
73. K. A. Endsley, D. G. Brown, E. Bruch, Housing Market Activity is Associated with Disparities in Urban and Metropolitan Vegetation. *Ecosystems* **21**, 1593–1607 (2018). doi: [10.1007/s10021-018-0242-4](#)
74. A. Rigolon, M. Browning, V. Jennings, Inequities in the quality of urban park systems: An environmental justice investigation of cities in the United States. *Landsc. Urban Plan.* **178**, 156–169 (2018). doi: [10.1016/j.landurbplan.2018.05.026](#)
75. A. P. Kinzig, P. Warren, C. Martin, D. Hope, M. Katti, The effects of human socioeconomic status and cultural characteristics on urban patterns of biodiversity. *Ecol. Soc.* **10**, 23 (2005). doi: [10.5751/ES-01264-10023](#)
76. S. B. Lerman, P. S. Warren, The conservation value of residential yards: Linking birds and people. *Ecol. Appl.* **21**, 1327–1339 (2011). doi: [10.1890/10-0423.1](#); pmid: [21774433](#)
77. R. P. Kinnunen, K. Fraser, C. Schmidt, C. J. Garroway, Socioeconomic variation across multiple cities predicts avian life-history strategies. *bioRxiv* 058537 [Preprint]. 25 April 2020. doi: [10.1101/2020.04.23.058537](#)
78. J. W. Ackley, J. Wu, M. J. Angilletta Jr., S. W. Myint, B. Sullivan, Rich lizards: How affluence and land cover influence the diversity and abundance of desert reptiles persisting in an urban landscape. *Biol. Conserv.* **182**, 87–92 (2015). doi: [10.1016/j.biocon.2014.11.009](#)
79. H. Li, K. A. Parker Jr., M. C. Kalcounis-Rueppell, The luxury effect beyond cities: Bats respond to socioeconomic variation across landscapes. *BMC Ecol.* **19**, 46 (2019). doi: [10.1186/s12898-019-0262-8](#); pmid: [31676008](#)
80. T. T. H. Pham, P. Apparicio, S. Landry, A. M. Séguin, M. Gagnon, Predictors of the distribution of street and backyard vegetation in Montreal, Canada. *Urban For. Urban Green.* **12**, 18–27 (2013). doi: [10.1016/j.ufug.2012.09.002](#)
81. C. Wang, Z. H. Wang, C. Wang, S. W. Myint, Environmental cooling provided by urban trees under extreme heat and cold waves in U.S. cities. *Remote Sens. Environ.* **227**, 28–43 (2019). doi: [10.1016/j.rse.2019.03.024](#)
82. P. J. Villeneuve *et al.*, A cohort study relating urban green space with mortality in Ontario, Canada. *Environ. Res.* **115**, 51–58 (2012). doi: [10.1016/j.envres.2012.03.003](#); pmid: [22483437](#)
83. S. Hetrick, R. R. Chowdhury, E. Brondizio, E. Moran, Spatiotemporal patterns and socioeconomic contexts of vegetative cover in Altamira City, Brazil. *Land* **2**, 774–796 (2013). doi: [10.3390/land2040774](#)
84. S. S. Cilliers, S. J. Siebert, Urban ecology in cape town: South African comparisons and reflections. *Ecol. Soc.* **17**, 33 (2012). doi: [10.5751/ES-05146-170333](#)
85. M. R. McHale, D. N. Bunn, S. T. A. Pickett, W. Twine, Urban ecology in a developing world: Why advanced socioecological theory needs Africa. *Front. Ecol. Environ.* **11**, 556–564 (2013). doi: [10.1890/120157](#); pmid: [24891843](#)
86. P. J. Brochu *et al.*, Particulate air pollution and socioeconomic position in rural and urban areas of the Northeastern United States. *Am. J. Public Health* **101**, S224–S230 (2011). doi: [10.2105/AJPH.2011.300232](#); pmid: [21836114](#)
87. D. L. Crouse, N. A. Ross, M. S. Goldberg, Double burden of deprivation and high concentrations of ambient air pollution at the neighbourhood scale in Montreal, Canada. *Soc. Sci. Med.* **69**, 971–981 (2009). doi: [10.1016/j.socscimed.2009.07.010](#); pmid: [19656603](#)
88. S. L. Watkins, E. Gerrish, The relationship between urban forests and race: A meta-analysis. *J. Environ. Manage.* **209**, 152–168 (2018). doi: [10.1016/j.jenvman.2017.12.021](#); pmid: [29289843](#)
89. D. C. Bellinger, Lead contamination in Flint - An abject failure to protect public health. *N. Engl. J. Med.* **374**, 1101–1103 (2016). doi: [10.1056/NEJMp1601013](#); pmid: [26863114](#)
90. G. Katz, P. T. Leishnam, S. L. LaDeau, Aedes albopictus Body Size Differs Across Neighborhoods With Varying Infrastructural Abandonment. *J. Med. Entomol.* **57**, 615–619 (2020). pmid: [31584098](#)
91. S. E. L. Wakefield, J. Baxter, Linking health inequality and environmental justice: Articulating a precautionary framework for research and action. *Environ. Justice* **3**, 95–102 (2010). doi: [10.1089/env.2009.0044](#)
92. A. Nardone *et al.*, Associations between historical residential redlining and current age-adjusted rates of emergency department visits due to asthma across eight cities in California: An ecological study. *Lancet Planet. Health* **4**, e24–e31 (2020). doi: [10.1016/S2542-5196\(19\)30241-4](#); pmid: [31999951](#)
93. P. G. Angold *et al.*, Biodiversity in urban habitat patches. *Sci. Total Environ.* **360**, 196–204 (2006). doi: [10.1016/j.scitotenv.2005.08.035](#); pmid: [16297440](#)
94. F. Morelli *et al.*, Evidence of evolutionary homogenization of bird communities in urban environments across Europe. *Glob. Ecol. Biogeogr.* **25**, 1284–1293 (2016). doi: [10.1111/geb.12486](#)
95. J. Beninde, M. Veith, A. Hochkirch, Biodiversity in cities needs space: A meta-analysis of factors determining intra-urban biodiversity variation. *Ecol. Lett.* **18**, 581–592 (2015). doi: [10.1111/ele.12427](#); pmid: [25865805](#)
96. D. L. Narango, D. W. Tallamy, P. P. Marra, Nonnative plants reduce population growth of an insectivorous bird. *Proc. Natl. Acad. Sci. U.S.A.* **115**, 11549–11554 (2018). doi: [10.1073/pnas.1809259115](#); pmid: [30348792](#)
97. T. Gallo, M. Fidino, E. W. Lehrer, S. B. Magle, Mammal diversity and metacommunity dynamics in urban green spaces: Implications for urban wildlife conservation. *Ecol. Appl.* **27**, 2330–2341 (2017). doi: [10.1002/eap.1611](#); pmid: [28833978](#)
98. R. Hale, R. Coleman, V. Pettigrove, S. E. Swearer, Identifying, preventing and mitigating ecological traps to improve the management of urban aquatic ecosystems. *J. Appl. Ecol.* **52**, 928–939 (2015). doi: [10.1111/1365-2664.12458](#)
99. C. A. Morrissey *et al.*, Eurasian dipper eggs indicate elevated organohalogenated contaminants in urban rivers. *Environ. Sci. Technol.* **47**, 8931–8939 (2013). doi: [10.1021/es402124z](#); pmid: [23819781](#)
100. R. Dip *et al.*, Comparison of heavy metal concentrations in tissues of red foxes from adjacent urban, suburban, and rural areas. *Arch. Environ. Contam. Toxicol.* **40**, 551–556 (2001). doi: [10.1007/s002440010209](#); pmid: [11525499](#)
101. C. Isaksson, Urbanization, oxidative stress and inflammation: A question of evolving, acclimatizing or coping with urban environmental stress. *Funct. Ecol.* **29**, 913–923 (2015). doi: [10.1111/1365-2435.12477](#)
102. A. Herrera-Dueñas, J. Pineda, M. T. Antonio, J. I. Aguirre, Oxidative stress of House Sparrow as bioindicator of urban pollution. *Ecol. Indic.* **42**, 6–9 (2014). doi: [10.1016/j.ecolind.2013.08.014](#)
103. M. Alberti *et al.*, Global urban signatures of phenotypic change in animal and plant populations. *Proc. Natl. Acad. Sci. U.S.A.* **114**, 8951–8956 (2017). doi: [10.1073/pnas.1606034114](#); pmid: [28049817](#)
104. C. P. Kozakiewicz *et al.*, Urbanization reduces genetic connectivity in bobcats (*Lynx rufus*) at both intra- and interpopulation spatial scales. *Mol. Ecol.* **28**, 5068–5085 (2019). doi: [10.1111/mec.15274](#); pmid: [31613411](#)
105. D. R. Trumbo *et al.*, Urbanization impacts apex predator gene flow but not genetic diversity across an urban-rural divide. *Mol. Ecol.* **28**, 4926–4940 (2019). doi: [10.1111/mec.15261](#); pmid: [31587398](#)
106. S. Jha, C. Kremen, Urban land use limits regional bumble bee gene flow. *Mol. Ecol.* **22**, 2483–2495 (2013). doi: [10.1111/mec.12275](#); pmid: [23495763](#)
107. J. Munshi-South, C. P. Zolnik, S. E. Harris, Population genomics of the Anthropocene: Urbanization is negatively associated with genome-wide variation in white-footed mouse populations. *Evol. Appl.* **9**, 546–564 (2016). doi: [10.1111/eva.12357](#); pmid: [27099621](#)
108. J. Munshi-South, Urban landscape genetics: Canopy cover predicts gene flow between white-footed mouse (*Peromyscus leucopus*) populations in New York City. *Mol. Ecol.* **21**, 1360–1378 (2012). doi: [10.1111/j.1365-294X.2012.05476.x](#); pmid: [22320856](#)
109. M. C. VanAcker, E. A. H. Little, G. Molaei, W. I. Bajwa, M. A. Diuk-Wasser, Enhancement of Risk for Lyme Disease by Landscape Connectivity, New York, New York, USA. *Emerg. Infect. Dis.* **25**, 1136–1143 (2019). doi: [10.3201/eid2506.181741](#); pmid: [31107213](#)
110. L. S. Miles, L. R. Rivkin, M. T. J. Johnson, J. Munshi-South, B. C. Verrelli, Gene flow and genetic drift in urban environments. *Mol. Ecol.* **28**, 4138–4151 (2019). doi: [10.1111/mec.15221](#); pmid: [31482608](#)
111. S. LaPoint, N. Balkenhol, J. Hale, J. Sadler, R. van der Ree, Ecological connectivity research in urban areas. *Funct. Ecol.* **29**, 868–878 (2015). doi: [10.1111/1365-2494.2006.02907.x](#); pmid: [16689893](#)
112. S. P. D. Riley *et al.*, A southern California freeway is a physical and social barrier to gene flow in carnivores. *Mol. Ecol.* **15**, 1733–1741 (2006). doi: [10.1111/j.1365-294X.2006.02907.x](#); pmid: [16689893](#)
113. D. E. Kramar, A. Anderson, H. Hilfer, K. Branden, J. J. Gutrich, A Spatially Informed Analysis of Environmental Justice: Analyzing the Effects of Gerrymandering and the Proximity of Minority Populations to U.S. Superfund Sites. *Environ. Justice* **11**, 29–39 (2018). doi: [10.1089/env.2017.0031](#)
114. C. M. Somers, B. E. McCarry, F. Malek, J. S. Quinn, Reduction of particulate air pollution lowers the risk of heritable mutations in mice. *Science* **304**, 1008–1010 (2004). doi: [10.1126/science.1095815](#); pmid: [15143280](#)
115. N. M. Reid *et al.*, The genomic landscape of rapid repeated evolutionary adaptation to toxic pollution in wild fish. *Science* **354**, 1305–1308 (2016). doi: [10.1126/science. aah4993](#); pmid: [27940876](#)
116. K. I. Brans *et al.*, The heat is on: Genetic adaptation to urbanization mediated by thermal tolerance and body size. *Global Change Biol.* **23**, 5218–5227 (2017). doi: [10.1111/gcb.13784](#); pmid: [28614592](#)
117. K. I. Brans, L. De Meester, City life on fast lanes: Urbanization induces an evolutionary shift towards a faster lifestyle in the water flea *Daphnia*. *Funct. Ecol.* **32**, 2225–2240 (2018). doi: [10.1111/1365-2435.13184](#)
118. S. E. Diamond, L. D. Chick, A. Perez, S. A. Strickler, R. A. Martin, Evolution of thermal tolerance and its fitness consequences: Parallel and non-parallel responses to urban heat islands across three cities. *Proc. R. Soc. B* **285**, 20180036 (2018). doi: [10.1098/rspb.2018.0036](#); pmid: [30051828](#)
119. N. Tüzün, L. Op de Beeck, K. I. Brans, L. Janssens, R. Stoks, Microgeographic differentiation in thermal performance curves between rural and urban populations of an aquatic insect. *Evol. Appl.* **10**, 1067–1075 (2017). doi: [10.1111/eva.12512](#); pmid: [29151861](#)
120. J. M. Hassell, M. Begon, M. J. Ward, E. M. Fèvre, Urbanization and Disease Emergence: Dynamics at the Wildlife-Livestock-Human Interface. *Trends Ecol. Evol.* **32**, 55–67 (2017). doi: [10.1016/j.tree.2016.09.012](#); pmid: [28029378](#)
121. R. K. Plowright *et al.*, Urban habituation, ecological connectivity and epidemic dampening: The emergence of Hendra virus from flying foxes (*Pteropus* spp.). *Proc. R. Soc. B* **278**, 3703–3712 (2011). doi: [10.1098/rspb.2011.0522](#); pmid: [21561971](#)



122. C. G. Himsworth, K. L. Parsons, C. Jardine, D. M. Patrick, Rats, cities, people, and pathogens: A systematic review and narrative synthesis of literature regarding the ecology of rat-associated zoonoses in urban centers. *Vector Borne Zoonotic Dis.* **13**, 349–359 (2013). doi: [10.1089/vbz.2012.1195](#); pmid: [23590323](#)
123. A. C. Peterson *et al.*, Rodent assemblage structure reflects socioecological mosaics of counter-urbanization across post-Hurricane Katrina New Orleans. *Landsc. Urban Plan.* **195**, 103710 (2020). doi: [10.1016/j.landurbplan.2019.103710](#)
124. K. A. Byers, M. J. Lee, D. M. Patrick, C. G. Himsworth, Rats about town: A systematic review of rat movement in urban ecosystems. *Front. Ecol. Evol.* **7**, 13 (2019). doi: [10.3389/fevo.2019.00013](#)
125. M. G. Walsh, Rat sightings in New York City are associated with neighborhood sociodemographics, housing characteristics, and proximity to open public space. *Peer J* **2**, e533 (2014). doi: [10.7717/peerj.533](#); pmid: [25237595](#)
126. M. H. Murray *et al.*, City sanitation and socioeconomic predict rat zoonotic infection across diverse neighbourhoods. *Zoonoses Public Health* **10.1111/zph.12748** (2020). doi: [10.1111/zph.12748](#); pmid: [32583624](#)
127. M. H. Murray *et al.*, Public complaints reflect rat relative abundance across diverse urban neighborhoods. *Front. Ecol. Evol.* **6**, 189 (2018). doi: [10.3389/fevo.2018.00189](#)
128. J. L. Richardson *et al.*, Using fine-scale spatial genetics of Norway rats to improve control efforts and reduce leptospirosis risk in urban slum environments. *Evol. Appl.* **10**, 323–337 (2017). doi: [10.1111/eva.12449](#); pmid: [28352293](#)
129. A. Desvars-Larrive *et al.*, Population genetics, community of parasites, and resistance to rodenticides in an urban brown rat (*Rattus norvegicus*) population. *PLOS ONE* **12**, e0184015 (2017). doi: [10.1371/journal.pone.0184015](#); pmid: [28886097](#)
130. K. A. Byers, S. M. Cox, R. Lam, C. G. Himsworth, “They’re always there”: Resident experiences of living with rats in a disadvantaged urban neighbourhood. *BMC Public Health* **19**, 853 (2019). doi: [10.1186/s12889-019-7202-6](#); pmid: [3162276](#)
131. A. van Dorn, R. E. Cooney, M. L. Sabin, COVID-19 exacerbating inequalities in the US. *Lancet* **395**, 1243–1244 (2020). doi: [10.1016/S0140-6736\(20\)30893-X](#); pmid: [32305087](#)
132. F. Ahmed, N. Ahmed, C. Pissarides, J. Stiglitz, Why inequality could spread COVID-19. *Lancet Public Health* **5**, e240 (2020). doi: [10.1016/S2468-2667\(20\)30085-2](#); pmid: [32247329](#)
133. C. W. Yancy, COVID-19 and African Americans. *JAMA* **323**, 1891–1892 (2020). doi: [10.1001/jama.2020.6548](#)
134. K. Terrell, W. James, Air Pollution and COVID-19: A Double Whammy for African American and Impoverished Communities in Cancer Alley. *Environ. Law Clin.*, 1–26 (2020); <https://law.tulane.edu/sites/law.tulane.edu/files/Files/Terrell%20-%20COVID-19%20-%20PM%202.5%20Louisiana%202020-5-14%20WEB%20VERSION.pdf>.
135. R. A. Opper Jr., R. Gebeloff, K. K. R. Lai, W. Wright, M. Smith, “The Fullest Look Yet at the Racial Inequity of Coronavirus,” *New York Times* (5 July 2020); [www.nytimes.com/interactive/2020/07/05/us/coronavirus-latino-african-americans-cdc-data.html](https://www.nytimes.com/interactive/2020/07/05/us/coronavirus-latino-african-americans-cdc-data.html).
136. X. Wu, R. C. Nethery, B. M. Sabath, D. Braun, F. Dominici, Exposure to air pollution and COVID-19 mortality in the United States: A nationwide cross-sectional study. *medRxiv* 20054502 [Preprint]. 27 April 2020. <http://doi.org/10.1101/2020.04.05.20054502>.
137. S. M. Volk *et al.*, Genome-scale phylogenetic analyses of chikungunya virus reveal independent emergences of recent epidemics and various evolutionary rates. *J. Virol.* **84**, 6497–6504 (2010). doi: [10.1128/JVI.01603-09](#); pmid: [20410280](#)
138. M. Gandy, Queer ecology: Nature, sexuality, and heterotopic alliances. *Environ. Plann. D* **30**, 727–747 (2012). doi: [10.1068/d10511](#)
139. D. J. Patrick, The matter of displacement: A queer urban ecology of New York City’s High Line. *Soc. Cult. Geogr.* **15**, 920–941 (2014). doi: [10.1080/14649365.2013.851263](#)
140. D. L. Hankins, The effects of indigenous prescribed fire on riparian vegetation in central California. *Ecol. Process.* **2**, 24 (2013). doi: [10.1186/2192-1709-2-24](#)
141. D. M. Waller, N. J. Reo, First stewards: Ecological outcomes of forest and wildlife stewardship by indigenous peoples of Wisconsin, USA. *Ecol. Soc.* **23**, 45 (2018). doi: [10.5751/ES-09865-230145](#)
142. D. E. Taylor, “Race, class, gender, and American environmentalism” (General Tech. Rep. PNW-GTR-534, U.S. Department of Agriculture, Forest Service, 2002); [www.fs.fed.us/pnw/pubs/gtr534.pdf](http://www.fs.fed.us/pnw/pubs/gtr534.pdf).
143. J. Purdy, “Environmentalism’s Racist History,” *New Yorker* (13 August 2015); [www.newyorker.com/news/news-desk/environmentalism-racist-history](http://www.newyorker.com/news/news-desk/environmentalism-racist-history).
144. J. B. Noisecat, “The Environmental Movement Needs to Reckon with Its Racist History,” *Vice News* (13 September 2019); [www.vice.com/en\\_us/article/bjwn8/the-environmental-movement-needs-to-reckon-with-its-racist-history](http://www.vice.com/en_us/article/bjwn8/the-environmental-movement-needs-to-reckon-with-its-racist-history).
145. A. Agrawal, K. Redford, Conservation and displacement: An overview. *Conserv. Soc.* **7**, 1–10 (2009). doi: [10.4103/0972-4923.54790](#)
146. S. M. Wilson, R. Richard, L. Joseph, E. Williams, Climate change, environmental justice, and vulnerability: An exploratory spatial analysis. *Environ. Justice* **3**, 13–19 (2010). doi: [10.1089/env.2009.0035](#)
147. L. Shi *et al.*, Roadmap towards justice in urban climate adaptation research. *Nat. Clim. Change* **6**, 131–137 (2016). doi: [10.1038/nclimate2841](#)
148. A. R. Pearson, J. P. Schultdt, Facing the diversity crisis in climate science. *Nat. Clim. Change* **4**, 1039–1042 (2014). doi: [10.1038/nclimate2415](#)
149. F. Edwards, H. Lee, M. Esposito, Risk of being killed by police use of force in the United States by age, race-ethnicity, and sex. *Proc. Natl. Acad. Sci. U.S.A.* **116**, 16793–16798 (2019). doi: [10.1073/pnas.1821204116](#); pmid: [31383756](#)
150. J. Bor, A. S. Venkataramani, D. R. Williams, A. C. Tsai, Police killings and their spillover effects on the mental health of black Americans: A population-based, quasi-experimental study. *Lancet* **392**, 302–310 (2018). doi: [10.1016/S0140-6736\(18\)31130-9](#); pmid: [29937193](#)
151. C. Finney, *Black Faces, White Spaces: Reimagining the Relationship of African Americans to the Great Outdoors* (Univ. of North Carolina Press, 2014).
152. W. J. Wright, As Above, So Below: Anti-Black Violence as Environmental Racism. *Antipode* **10.1111/anti.12425** (2018). doi: [10.1111/anti.12425](#)
153. R. D. Hardy, R. A. Milligan, N. Heynen, Racial coastal formation: The environmental injustice of colorblind adaptation planning for sea-level rise. *Geoforum* **87**, 62–72 (2017). doi: [10.1016/j.geoforum.2017.10.005](#)
154. S. Meerow, P. Pajouhesh, T. R. Miller, Social equity in urban resilience planning. *Local Environ.* **24**, 793–808 (2019). doi: [10.1080/13549839.2019.1645103](#)
155. Ö. Bodin, Collaborative environmental governance: Achieving collective action in social-ecological systems. *Science* **357**, eaan1114 (2017). doi: [10.1126/science.aan1114](#); pmid: [28818915](#)
156. D. Haase *et al.*, Greening cities – To be socially inclusive? About the alleged paradox of society and ecology in cities. *Habitat Int.* **64**, 41–48 (2017). doi: [10.1016/j.habitatint.2017.04.005](#)
157. J. R. Montambault *et al.*, Social equity and urban nature conservation. *Conserv. Lett.* **11**, e12423 (2018). doi: [10.1111/conl.12423](#)
158. A. Martin, S. McGuire, S. Sullivan, Global environmental justice and biodiversity conservation. *Geogr. J.* **179**, 122–131 (2013). doi: [10.1111/geoj.12018](#)
159. G. Graddy-Lovelace, Beyond Biodiversity Conservation: Why Policy Needs Social Theory, Social Theory Needs Justice, and Justice Needs Policy. *Glob. Environ. Polit.* **17**, 144–151 (2017). doi: [10.1162/GLEP\\_a\\_00405](#)
160. G. M. Mikkelsen, A. Gonzalez, G. D. Peterson, Economic inequality predicts biodiversity loss. *PLOS ONE* **2**, e444 (2007). doi: [10.1371/journal.pone.0000444](#); pmid: [17505535](#)
161. M. C. Kondo *et al.*, Health impact assessment of Philadelphia’s 2025 tree canopy cover goals. *Lancet Planet. Health* **4**, e149–e157 (2020). doi: [10.1016/S2542-5196\(20\)30058-9](#); pmid: [32353295](#)
162. G. N. Bratman *et al.*, Nature and mental health: An ecosystem service perspective. *Sci. Adv.* **5**, eaax0903 (2019). doi: [10.1126/sciadv.aax0903](#); pmid: [31355340](#)
163. T. Sikor, A. Martin, J. Fisher, J. He, Toward an Empirical Analysis of Justice in Ecosystem Governance. *Conserv. Lett.* **7**, 524–532 (2014). doi: [10.1111/conl.12142](#)
164. G. Reese, L. Jacob, Principles of environmental justice and pro-environmental action: A two-step process model of moral anger and responsibility to act. *Environ. Sci. Policy* **51**, 88–94 (2015). doi: [10.1016/j.envsci.2015.03.011](#)
165. I. Angelouovski, From Toxic Sites to Parks as (Green) LULUs? New Challenges of Inequity, Privilege, Gentrification, and Exclusion for Urban Environmental Justice. *J. Plann. Lit.* **31**, 23–36 (2016). doi: [10.1177/0885412215610491](#)
166. T. A. Hoppe *et al.*, Topic choice contributes to the lower rate of NIH awards to African-American/black scientists. *Sci. Adv.* **5**, eaaw7238 (2019). doi: [10.1126/sciadv.aaw7238](#); pmid: [31633016](#)
167. B. Hofstra *et al.*, The diversity–innovation paradox in science. *Proc. Natl. Acad. Sci. U.S.A.* **117**, 9284–9291 (2020). doi: [10.1073/pnas.1915378117](#); pmid: [32291335](#)
168. E. B. Barbier, How to make the next Green New Deal work. *Nature* **565**, 6 (2019). doi: [10.1038/d41586-018-07845-5](#); pmid: [30602752](#)
169. P. B. Holden *et al.*, Climate-carbon cycle uncertainties and the Paris Agreement. *Nat. Clim. Change* **8**, 609–613 (2018). doi: [10.1038/s41558-018-0197-7](#)
170. R. T. Corlett *et al.*, Impacts of the coronavirus pandemic on biodiversity conservation. *Biol. Conserv.* **246**, 108571 (2020). doi: [10.1016/j.biocon.2020.108571](#); pmid: [32292203](#)
171. D. Neupane, How conservation will be impacted in the COVID-19 pandemic. *Wildl. Biol.* **2020**, 19–21 (2020). doi: [10.2981/wlb.00727](#)
172. X. Liu *et al.*, High-spatiotemporal-resolution mapping of global urban change from 1985 to 2015. *Nat. Sustain.* **3**, 564–570 (2020). doi: [10.1038/s41893-020-0521-x](#)

## ACKNOWLEDGMENTS

We thank M. Alberti and other core members of the Urban Eco-Evo RCN for transdisciplinary insight. We also thank the four anonymous reviewers, who greatly improved the quality of this manuscript. Several concepts in this manuscript also emerged from the 2019 International Urban Wildlife Conference (IUWC) in Portland, Oregon, and we thank T. Gallo, M. Fidino, D. Ferris, S. Hall, N. Grimm, L. Bliss-Ketchum, M. Murray, S. Magle, L. Lehrer, C. Kay, and other associated members of the Central Arizona-Phoenix (CAP) LTER and Urban Wildlife Information Network (UWIN) for formative conversations in advancing our narrative. Special thanks to B. Sterud and the Puyallup Tribe of Indians. **Funding:** S.D.R., C.J.S., C.A.W.-E. and D.S.M. were funded by the University of Washington. M.R.L. was funded by the University of California, Berkeley, and the David H. Smith Fellows program. S.D.R. and M.R.L. were also supported by the NSF-funded Urban Eco-Evo RCN. **Competing interests:** The authors have no competing interests to declare.

10.1126/science.aay4497

## REVIEW SUMMARY

## NEURODEVELOPMENT

## Looking at neurodevelopment through a big data lens

James Briscoe\* and Oscar Marin\*

**BACKGROUND:** The formation of the nervous system represents an astonishing feat of self-organization that is compromised in neuropsychiatric conditions such as autism and schizophrenia. Despite impressive progress in neuroscience over the past decades, our understanding of how billions of neurons come together to form the nervous system and enable function and behavior is in its infancy, especially when it comes to the human brain. However, the field is at a turning point. The introduction of new technologies that produce large volumes of high-resolution measurements—big data—has the potential to revolutionize the study of brain development.

**ADVANCES:** A foundation of developmental neuroscience is the detailed and systematic description of the nervous system. New methods are documenting the cellular composition and organization of neural tissue with ever-increasing resolution. The development of high-throughput and automated microscopy methods is charting the connectivity of thousands of neurons, delin-

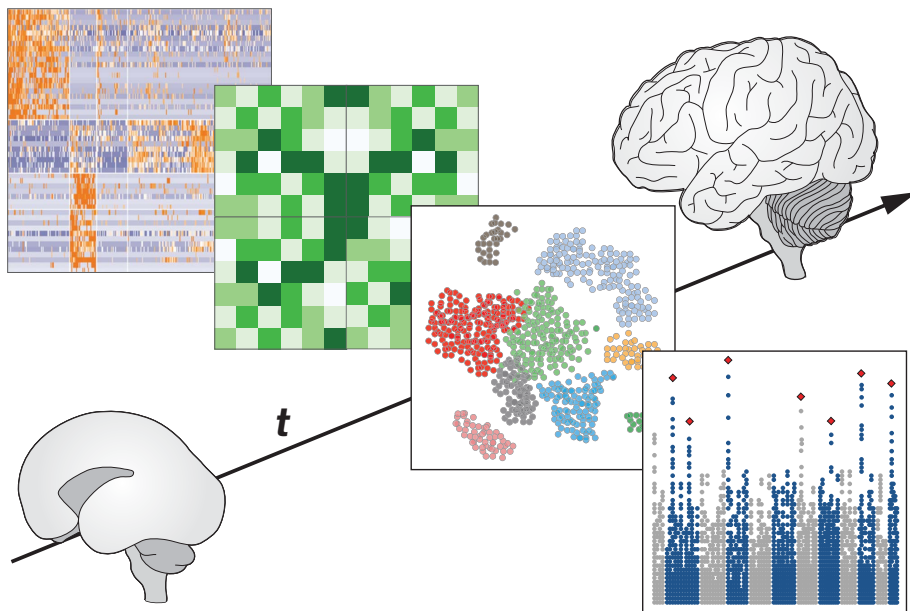
eating the structure of whole regions of the nervous system. Technology is also emerging for the large-scale analysis of the activity of entire brain regions. But probably the most obvious impact of high-throughput techniques is in the development of single-cell molecular profiling. A variety of approaches are being used to produce genome-wide molecular surveys with single-cell resolution from adult and embryonic tissue. In particular, transcriptomic analyses of thousands to millions of cells are providing an unprecedented molecular characterization of the brain, revealing previously unrecognized cell types, allowing interspecies comparisons, and suggesting mechanisms that account for the developmental origin of the diversity and function of neural cell types.

Most neuropsychiatric disorders have a prominent heritable component and arise from the altered developmental processes during the formation of the nervous system. Recent advances in human genetics are beginning to shed light on the genetic architecture of these disorders and suggest how genetic varia-

tion confers susceptibility to disease. Large-scale sequencing studies have revealed causes that range from large-effect heterozygous mutations to highly polygenic conditions. In addition, the contribution of de novo somatic mutations to neurodevelopmental diseases is being recognized. Nevertheless, progressing from genetic findings to underlying biological mechanisms has proved challenging, not least because in many cases identifying the cells relevant to a disease process has been difficult. In this context, a convergence between neurogenetics and developmental neurobiology, driven by the increased resolution of the molecular and genetic assays, is likely to improve our understanding of the origin of neurological disorders and provide insight into basic developmental mechanisms.

Whereas new molecular and genomic tools contribute to the identification of plausible neurobiological mechanisms, methods based on the directed development of pluripotent stem cells offer experimental access to developing human neural tissue to test hypotheses. Rapid progress is being made in the development of techniques that produce specific neural cell types or more complex mixtures of cell types that mimic the development of specific regions of the central nervous system. Questions remain about the accuracy of these in vitro models, and validation and refinement continue. Notwithstanding this uncertainty, the potential to study the etiology of neurological disorders in human neural tissue is already providing important insights.

**OUTLOOK:** New perspectives are emerging on long-standing questions about the ontogeny, composition, and function of the nervous system. They are addressing fundamental conceptual questions, such as what constitutes a cell type, and revealing biological mechanisms responsible for neurological disorders. The comparison of nervous system development between multiple individuals could conceivably identify individual variation in, for example, neural connectivity patterns that underpin behavioral individuality and may enable the investigation of the complex biological mechanisms underlying individuality. Certainly, integrating data from anatomical, developmental, genetic, and molecular studies has the potential to link cellular processes to functional and behavioral consequences. This strategy would provide fundamental insight and offer a new vision to the field. ■



**Big data approaches in developmental neurobiology.** New technologies that produce large volumes of high-resolution measurements are documenting gene expression, connectivity, and function in the developing brain with an unprecedented level of detail. In combination with large-scale genetic studies, big data approaches are transforming our ability to interrogate the developing brain and identify causal mechanisms for its associated disorders.

The list of author affiliations is available in the full article online.

\*Corresponding author. Email: james.briscoe@crick.ac.uk (J.B.); oscar.marin@kcl.ac.uk (O.M.)

Cite this article as J. Briscoe, O. Marin, *Science* 369, eaaz8627 (2020). DOI: 10.1126/science.aaz8627

**S READ THE FULL ARTICLE AT**  
<https://doi.org/10.1126/science.aaz8627>



## REVIEW

## NEURODEVELOPMENT

## Looking at neurodevelopment through a big data lens

James Briscoe<sup>1\*</sup> and Oscar Marín<sup>2,3\*</sup>

The formation of the human brain, which contains nearly 100 billion neurons making an average of 1000 connections each, represents an astonishing feat of self-organization. Despite impressive progress, our understanding of how neurons form the nervous system and enable function is very fragmentary, especially for the human brain. New technologies that produce large volumes of high-resolution measurements—big data—are now being brought to bear on this problem. Single-cell molecular profiling methods allow the exploration of neural diversity with increasing spatial and temporal resolution. Advances in human genetics are shedding light on the genetic architecture of neurodevelopmental disorders, and new approaches are revealing plausible neurobiological mechanisms underlying these conditions. Here, we review the opportunities and challenges of integrating large-scale genomics and genetics for the study of brain development.

A foundation of neuroscience is the description of the nervous system. In recent years, new methods are documenting gene expression in human and animal models with ever-increasing resolution in space and time, and technology is emerging that allows the structural and functional dissection of neural circuits. This is beginning to provide an unprecedented molecular characterization of the brain. At the same time, high-throughput genome sequencing and large-scale genetic studies are revealing how genetic variation confers susceptibility to neuropsychiatric disorders, and methods based on pluripotent stem cells hold the potential to offer insight into the neurobiological basis of these conditions by providing experimental access to the developing human nervous system. The use of big data approaches is therefore transforming our ability to document how cell diversity emerges in the nervous system, with implications for our understanding of neurodevelopmental disorders. A key challenge is to integrate molecular, cellular, and genomic data. For this, appropriate developmental models will be needed so that emerging genetic findings yield mechanistic insight into the neurobiological basis of neuropsychiatric disorders.

## Documenting the component parts

The morphological identification of neuronal types and their connectivity has a long tradition, dating back to Ramón y Cajal. The development of high-throughput light and electron microscopy methods and the increasing automation of image analysis indicate that this field has entered the big data era, and progress

continues apace. Three-dimensional electron microscopy reconstructions of neuronal connectivity in the *Drosophila melanogaster* brain and regions of the mouse brain comprehensively chart the location and connectivity of hundreds to thousands of neurons (Fig. 1) (1, 2). This is providing insight into the logic of nervous system wiring. For example, a reconstruction of the *D. melanogaster* larval nervous system revealed an architecture in which multiple sensory inputs converge to enable the rapid selection of escape responses (3). The speed and accuracy with which these massive datasets can be reconstructed are being improved by applying the latest machine learning methods (4). A challenge now is to link detailed maps of morphology and connectivity to molecular identity, function, and developmental origin.

To complement these structural plans of nervous systems, ways to scale physiological methods that assay the activity of neurons in situ are being developed. Advances in semiconductor technology and fabrication have enabled engineering of high-density silicon probes that allow the simultaneous recording from hundreds of neurons at fine spatial and temporal scales (5). Complementary to this are optical imaging approaches that take advantage of voltage or calcium indicators for in vivo imaging of the activity of hundreds and thousands of neurons (6–8). This has already allowed whole-brain imaging of optically accessible zebrafish larvae (9). Combining functional imaging with genetic markers for specific cell types in the zebrafish spinal cord tracked the assembly of motor circuits from the birth of the first neurons to the emergence of coordinated activity (10). The analysis revealed that motor neurons are the first to acquire physiological activity, and this guides the establishment of patterned activity in the rest of the local circuitry, suggesting

an explanation for why motor neurons differentiate earlier and at a higher rate in the developing spinal cord than the interneurons to which they connect (11). Advances in hardware, fluorophores, and computational methods will broaden the applicability of these approaches.

Perhaps the most obvious impact of high-throughput techniques is in the development of single-cell molecular profiling. New methods allow single-cell resolution genome-wide molecular surveys of cells captured from adult and embryonic tissue. A burgeoning number of studies describe the systematic profiling of the transcriptomes of thousands to millions of cells. Broad sampling of the nervous system (12–14) facilitates comparisons of gene expression in neuronal subtypes from different regions of the central nervous system (CNS). This has implicated common transcriptional programs in the maintenance and elaboration of axons and presynaptic terminals in different neuronal subtypes (14). Other studies focus on smaller regions to provide higher-resolution maps (15, 16), revealing that “phenotypic convergence,” in which distinct combinations of transcription factors are used in different cell types to control the expression of similar effector genes such as neurotransmitters, appears to be a widespread phenomenon (17). Detailed analyses of specific CNS regions also enable direct comparisons of cell identities across species (18) and the identification of more cell types than previously recognized, as shown, for instance in the rodent cerebral cortex (15).

There is increasing awareness of the importance of glia in the formation and function of neural circuits. Until recently, the diversity of these cell populations had been less well described, but single-cell RNA sequencing (scRNA-seq) studies are changing this. For instance, it has been shown that mature oligodendrocytes are transcriptionally heterogeneous, and distinct populations are present in different proportions in different brain regions (19). Similarly, multiple molecularly distinct astrocyte types, occupying regionally restricted territories, have been identified (20). Distinct types of astrocytes are associated with specific neural circuits, which suggests unique roles in modulating neuronal activity (21). Moreover, single-cell analyses have revealed specific time- and region-dependent subtypes of microglia (22), brain-resident macrophages, which are critically involved in wiring (23).

Together, these molecular profiling approaches raise the prospect of using the transcriptome to provide a comprehensive classification of cell types. This necessitates linking molecular identity to the location, morphology, connectivity, and function of neurons and glial cells. Conventional methods for

<sup>1</sup>The Francis Crick Institute, London NW1 1AT, UK. <sup>2</sup>Centre for Developmental Neurobiology, Institute of Psychiatry, Psychology and Neuroscience, King's College London, London SE1 1UL, UK. <sup>3</sup>MRC Centre for Neurodevelopmental Disorders, King's College London, London SE1 1UL, UK.

\*Corresponding author. Email: james.briscoe@crick.ac.uk (J.B.); oscar.marin@kcl.ac.uk (O.M.)

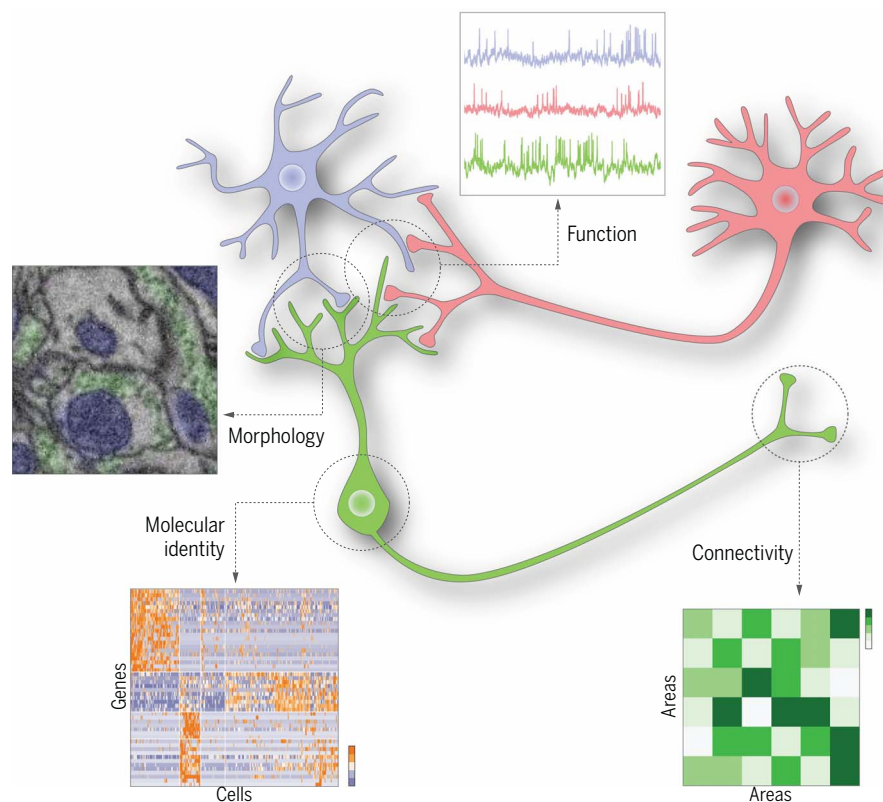


**Fig. 1. Big data methods characterizing neuronal identity.** Neurons can be classified by morphological, physiological, and molecular criteria and by their connectivity. Microfabricated silicon devices containing dense arrays of electrophysiology probes or genetically encoded voltage or calcium-activity indicators enable monitoring of the activity of hundreds of neurons simultaneously [traces adapted from (8)]. High-throughput electron microscopy and image processing allow the reconstruction of cellular morphology and synapses in regions of the central nervous system [image reproduced from (2)]. Combining the tagging of neurons with unique molecular barcodes and in situ methods to visualize them allows projections and connectivity of thousands of neurons to be mapped. Characterizing individual neurons by methods such as RNA-seq provides molecular catalogs of cell identity in the nervous system [image reproduced from (37), licensed under CC BY 4.0].

mapping gene expression in tissue have been low throughput. Newer approaches based on single-molecule fluorescent in situ hybridization (24), in situ sequencing (25), or spatially resolved capture of mRNA on slides (26) are scaling up efforts to connect the molecular identity of a neuron to its location within the nervous system. Methods that link a neuron's transcriptome to other features such as its connectivity, activity, or function are still in their infancy. For example, "Patch-seq" uses scRNA-seq to assay the transcriptome of cells following patch-clamp recording (27, 28), and "Connect-seq" combines retrograde viral tracing and single-cell transcriptomics to determine the molecular identity of neurons in a particular circuit (29). Moreover, DNA barcoding methods that link synaptic partners have the potential to reveal individual neuronal connectivity, although these do not yet have single-cell resolution (30). Hence, high-throughput analyses linking cell identity to connectivity

and function remain a challenge. Ultimately, however, these methods will be crucial in deciphering how neural circuits form and function in a coordinated manner.

### Defining cell types

Alongside the technical challenges, the new approaches prompt conceptual questions about the definition of cell type. The prevailing view is that each type of neuron utilizes a specific set of "functional modules" (e.g., morphology, neurotransmitter, channels, synaptic connectivity, etc.) that collectively define its identity and that are regulated by dedicated transcriptional programs. A cell type is therefore determined and maintained by regulatory programs, or core regulatory complexes (31), acting to govern a cell type-specific program of gene expression (32). This definition is consistent with the idea that recursively linked gene regulatory networks execute specific gene expression programs to define cell identity (33).

But is knowing the transcriptome of a neuron sufficient to define its identity and predict its morphology, connectivity, and function? A comparison of the morphological, connectivity, and functional classification of the 302 neurons of *Caenorhabditis elegans* with their gene expression profiles revealed a strong correlation between molecular and anatomical definitions (34). Most of the identified neuronal classes were distinguishable by the specific combination of transcription factors they expressed. However, there are complications. The analysis revealed a hierarchical structure to neuronal identity in which some neuronal classes could be further partitioned into subclasses based on differences in subsets of gene expression and synaptic partners. A hierarchical organization with subdivisions of increasingly fine-grained subtypes is also apparent in nervous systems that are more complex than that of *C. elegans*. Perhaps the best-characterized example is the muscle-innervating motor neurons of the vertebrate spinal cord (35). These are segregated into discrete columns, each of which projects to distinct locations in the periphery. Each column is then further divided into motor pools that target a single muscle; within a motor pool, alpha and gamma neurons, innervating muscle fibers or spindles, respectively, can be further distinguished. Molecular differences, notably in the combination of transcription factors expressed, correlate with these anatomical and functional distinctions and support a hierarchical Linnaean-like taxonomy for cell type classification (35). This is consistent with the view that cell types can be stratified to various levels of granularity: the extent of which then becomes a question of the purpose of the classification.

Nevertheless, functionally and morphologically distinct neurons located in different regions of the nervous system, or even within the same region of the adult brain, can appear transcriptionally similar (Fig. 2). This raises the question of what the limits of the molecular definition of cell type identity are. To address this, datasets systematically assessing the correspondence between neuronal morphology, function, and gene expression will provide insight. Developmental history is also likely to be an important feature. For example, although differentiating *Drosophila* olfactory projection neurons have gene expression differences that establish their different projection patterns, these transcriptomic differences disappear in mature neurons despite continued differences in innervation patterns and morphology (36). Hence an understanding and analysis of ontogeny is crucial for developing a principled and comprehensive means to define cell type identity.

An evolutionary explanation has been proposed to define cell types (37). In this view, a new cell type arises in evolution from an existing cell



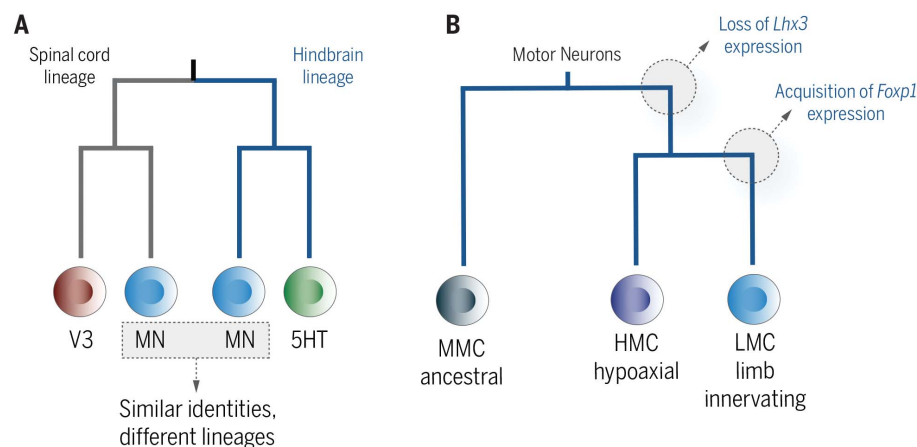


**Fig. 2. Developmental and evolutionary lineages of neuronal subtype identity.** (A) Example of a developmental lineage. Motor neurons (MN) are generated in both the spinal cord and hindbrain from progenitors with characteristic pedigrees that also include specific interneurons (V3) and serotonergic neurons (5HT), respectively. Despite the similarity of spinal cord and hindbrain MNs, they derive from distinct developmental lineages. (B) Example of the proposed evolutionary diversification of a neuronal subtype. Ancestral motor neurons are proposed to have had a medial motor column (MMC) identity; loss of expression of *LHX3* in a subset of these resulted in the acquisition of hypaxial motor column (HMC) identity, and then subsequent co-option of *FOXP1* gene expression produced lateral motor column (LMC) motor neurons that are responsible for innervating the limbs in tetrapods.

type by the gain, loss, or co-option of a new core regulatory complex—the set of transcriptional regulators that lead to the dedicated gene expression program that specifies the cell type (37) (Fig. 2). This implies a bifurcating hierarchy of cell types and emphasizes the importance of ontogeny in defining cell identity. Although this offers an elegant framework for cell type identity, it is possible that molecular demarcations between cell types are indistinct or that dynamic changes in gene expression, in response to activity or environmental cues, blur cell type definitions. Cross-species comparisons should provide insight into conserved identities and pinpoint the developmental and phylogenetic points at which changes in a core regulatory complex result in the emergence of a new neuronal subtype (37). Technical constraints will need to be overcome. Sequencing depth and sensitivity are currently limited, which may lead to the systematic loss of information, particularly of genes expressed at low levels. For example, downsampling data from the mouse cortex from 1,000,000 to 100,000 mapped reads per cell reduces the ability to separate neuronal classes (15). Interspecies comparisons could be confounded if sampling differences are conflated with ascertainment of identity. Conversely, current transcriptomic methods are destructive and result in static snapshots of gene expression that do not account for transient changes in gene expression. This could lead to the agglomeration of distinct cell types or the superfluous division of similar neurons

into distinct subtypes. It remains a possibility, however, that the absence of clear divisions between neuronal subtype identities is a reality and might reflect a fundamental property of nervous systems. Addressing this question will require further experimental and conceptual investigation, and this is of more than abstract interest because identifying neuronal subtypes is crucial for understanding the cellular basis of neuropsychiatric disorders.

### The ontogeny of neuronal diversity

Although much progress in defining cell type diversity had been made with conventional molecular, genetic, and developmental biology studies, single-cell transcriptomics is having an impact. For instance, analysis of the developing spinal cord revealed a previously overlooked temporal program diversifying neuronal identity that operates alongside the spatial program (38). Similarly, the transcriptional similarities of embryonic and adult cortical  $\gamma$ -aminobutyric acid (GABA)-releasing interneurons suggest that their fate is established early during development by transcriptional programs that then unfold over the course of several weeks (39).

There have been notable successes with the computational inference of differentiation trajectories from scRNA-seq datasets. At the heart of these methods is the idea that asynchrony within a population of cells means that some cells are further along a differentiation pathway than others and the trajectory of this pathway can be reconstructed by identifying and

ordering cells using the differences in gene expression (40). For example, data from the developing human cortex has been used to order the transition from radial glia cells through intermediate progenitors to maturing glutamatergic neurons. This has led to the suggestion that cell fate decisions occur prior to S phase of the cell cycle (41), although recent data indicate that cell fate can also be modulated shortly after mitosis (42). Moreover, widespread “multilineage priming,” in which a progenitor cell coexpresses genes that are specific to each of its molecularly distinct daughters, has been documented in *C. elegans* embryos (43).

However, inferring trajectories is not always possible, particularly when there are abrupt changes in the transcriptional program of differentiating cells. This can occur, for example, during the transition from a proliferating progenitor cell to a postmitotic neuron. Moreover, the multiplicity of cell types within any sample of neural tissue, which might have arisen from distinct lineages or a multiple-branching differentiation pathway (44), further confounds these methods.

Approaches that address some of these limitations are being developed. These include computational methods that predict gene expression changes from splicing information (45) and techniques that provide a temporal signature to facilitate the ordering of gene expression changes (46). In addition, high-throughput methods are being devised to allow lineage reconstruction. Conventional approaches to lineage reconstruction have relied on methods that indelibly mark a single cell and its progeny with a tracer that can later be visualized. The advent of single-cell profiling has facilitated the design of a new generation of techniques that rely on the introduction of molecular barcodes (47). Approaches include transposon-based libraries encoding a transcript harboring a random sequence that acts as a unique identifier, and systems based on the CRISPR-Cas9-mediated introduction of short insertions or deletions of variable length and position that act as heritable genetic changes. This latter strategy has revealed that although most individual embryonic progenitors generate multiple cell types in the zebrafish brain, these tend to remain in relatively restricted spatial domains (48).

In addition to experimentally introduced genetic barcodes, spontaneous somatic mutations provide information about lineage relationships between cells. Somatic mutations in mitochondrial DNA have been used as clonal markers to infer cellular relationships within the hematopoietic system (49, 50). Advances in single-cell genome sequencing have allowed the identification of naturally occurring somatic mutations in neurons, including new retrotransposition events, which occur at a rate of >1 mutation per cell division (51). These can also

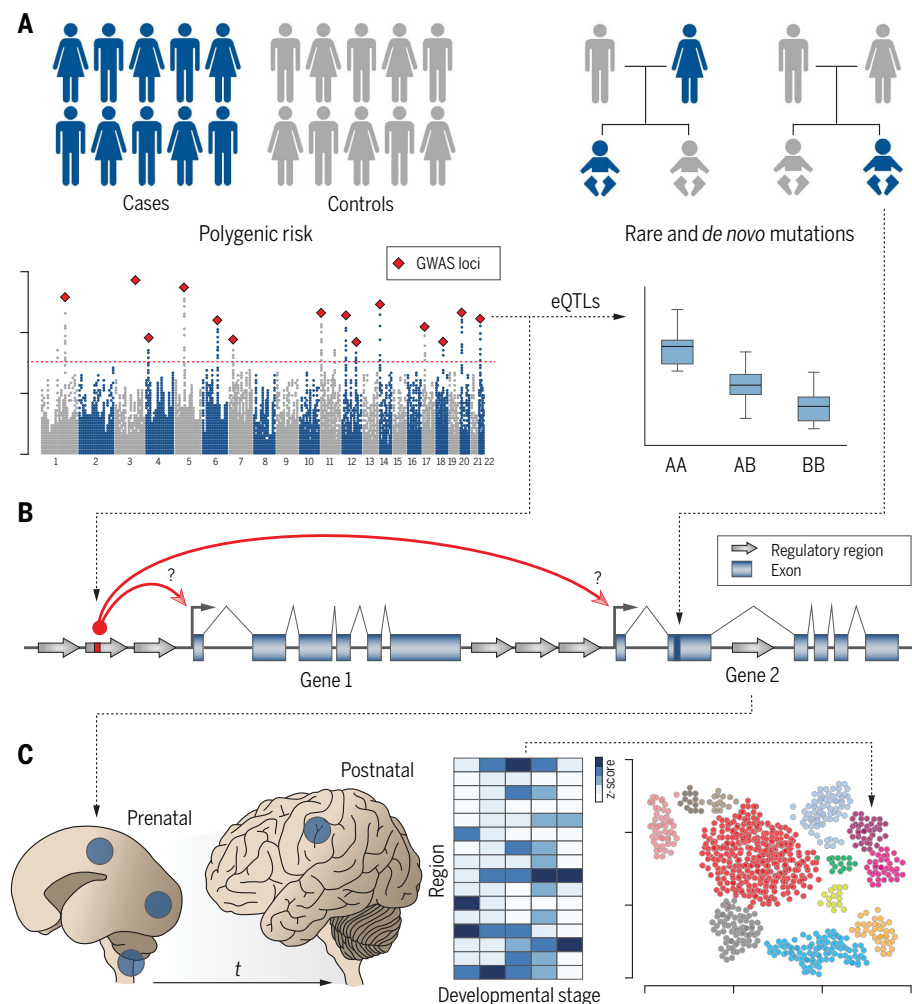


**Fig. 3. Neurobiological interpretation of disease-associated gene variants.** (A) Schematic representations of polygenic risk and rare and de novo coding mutations. The Manhattan plot indicates hypothetical loci (red rhomboids) reaching genome-wide significance (red dashed line). (B) Functional annotation of noncoding variants involves uncovering regulatory effects and identifying target gene(s) (question marks). Gene targets can also be inferred through computational methods such as eQTL. For coding variants, annotation is primarily based on impact to the amino acid sequence. (C) Single-cell genomic approaches have accelerated the identification of relevant cell types expressing disease-associated genes during brain development.

provide information about lineage relationships (52, 53). Exploiting endogenous mutations raises the possibility of inferring lineage relationships in the human brain, but this remains unproven, and the throughput, fidelity, and, most notably, cost of these methods will need to be improved if they are to become a practical reality.

It is apparent that in some cases, neurons of the same class can have distinct lineage histories. The transcriptomes of the six sets of IL-1 and IL-2 neurons in *C. elegans*, which arise from distinct lineages, gradually converge to the same molecular signature (43). In vertebrates, the somatic motor neurons that reside in the hindbrain have a distinct developmental history from those in the spinal cord but attain similar postmitotic identities (54). Likewise, oligodendrocytes through-

out the CNS transiently converge on a similar transcriptional identity despite spatially, temporally, and molecularly heterogeneous origins (55). Whether there are common features to the convergence of developmental trajectories in each of these cases needs to be investigated.

It is also unclear whether the genomic regulatory landscapes that produce the transcriptomes of equivalent neuronal classes originating from distinct lineages are similar. The application of techniques such as single-cell ATAC-seq (assay for transposase-accessible chromatin using sequencing) and CUT&Tag (cleavage under targets and tagmentation) that profile the regulatory genome of individual cells could address this question (56, 57). Identifying causal relationships between the regulatory genome and gene expression requires

overcoming the technical challenges of combining multiple assays on single cells (58, 59). Beyond insight into the mechanisms generating particular cell types, determining the developmental history of otherwise seemingly equivalent neuronal subtypes might explain why certain subsets of neurons are affected in particular disorders. Moreover, combining knowledge of cell lineage, developmental trajectory, and molecular mechanism has the potential to provide unprecedented insight into the central developmental neurobiology question of how neuronal diversity arises in the nervous system. The hope is that systematic analysis between different regions of the nervous system and different species might reveal rules that explain the underlying logic to the acquisition and maintenance of neuronal identity. This is of course only the first step in the assembly of functional neuronal circuits, and the role of stochastic and activity-dependent mechanisms will need to be investigated alongside the genetic programs specifying cell type identity.

### The genetics of neurodevelopmental disorders

In parallel to the explosion of data from molecular approaches, the field of neuropsychiatric genetics has seen spectacular advances over the past decade. Most neuropsychiatric disorders arise from the alteration of normal developmental trajectories and have a prominent heritable component, irrespective of the age at which they are clinically diagnosed (60). The genetic architecture of neurodevelopmental disorders is diverse, ranging from an abundance of large-effect heterozygous mutations in autism spectrum disorder (ASD) (61) to highly polygenic in schizophrenia, involving the simultaneous contribution of multiple alleles with small effects (62). Many specific genetic associations are shared between multiple disorders with the same genetic variant responsible for different disorders in different individuals (63). In addition, the contribution of de novo somatic mutations to neurodevelopmental diseases is increasingly recognized (64).

Understanding the etiology of neuropsychiatric disorders has been difficult because in most cases there is no obvious neuropathology, and so the underlying biological mechanisms and the cells involved in the disease process are largely unknown (Fig. 3). In this context, combining genomics and transcriptomics may get us closer to identifying the cellular substrates of neuropsychiatric conditions such as ASD, in which large-effect, likely gene-disrupting coding mutations are relatively common. Bulk transcriptomics of the developing human brain revealed that ASD risk genes are abundantly expressed in certain brain regions (prefrontal and primary motor cortices, striatum, cerebellum, and medial dorsal nucleus of the thalamus) particularly during early and mid-fetal periods (65, 66). Now, single-cell resolution



transcriptome atlases of these brain regions are allowing the identification of the specific cell types in which candidate genes are expressed (67–69). Thus, the combination of advanced genomics and transcriptomics may get us closer to defining the cellular points of convergence in neurodevelopmental disorders such as ASD (70).

Identifying the relevant cell types or specific brain development events in neuropsychiatric conditions characterized by highly polygenic risk will be much more challenging. Genome-wide association studies (GWASs) have identified hundreds of common genetic variants—often in the form of single-nucleotide polymorphisms—that are statistically associated with increased risk in schizophrenia (62). Most variants do not directly identify the cause of the biological effect (Fig. 3). The linkage disequilibrium structure of the human genome means that any GWAS variant usually has many hundreds of nearby variants, requiring fine mapping to define the causal polymorphism. Even once identified, there is often difficulty associating the causal variant with a gene and a function, as sequence differences most frequently occur in noncoding regions. Most common variants are far away from the nearest known gene or are located in non-protein-coding regions of the genome (71). Further hampering this effort is that much of the noncoding genome is evolutionarily divergent between humans and other species. Although initial attempts are encouraging (72), confidently associating specific risk genes to specific genes and cellular populations in the developing brain is an enormous challenge. The unequivocal association of common risk variants to specific genes will require precise mapping of the interactions between regulatory elements and genes.

Considering the complexity of transcriptional regulation in vertebrates and the three-dimensional structure of the genome, big data approaches are necessary to identify causal disease genes from GWASs. For example, many disease-associated variants seem to be enriched in predicted transcriptional regulatory regions, known as cis-regulatory elements (CREs). Computational methods are beginning to use epigenomic data to prioritize candidate causal variants. Encouragingly, cell and tissue-specific epigenomic analyses (chromatin accessibility, transcription factor binding, histone marks) suggest that common variants for a particular disease are particularly enriched in CREs active in disease-relevant cell types (73). Moreover, assays that identify chromatin loops and the interaction between gene-coding regions and putative regulatory elements further aid the interpretation of GWAS-identified alleles (74).

Extending these studies to single-cell resolution, to identify regulatory element usage in defined cell types, will enhance the interpretation of regions identified by GWASs (Fig. 3).

In recent years, expression quantitative trait loci (eQTL) analyses based on the integration of genetic information with bulk RNA-seq data have identified downstream expression changes caused by disease-associated genes (75). Because transcriptional alterations are often cell type-specific, the opportunity now arises to use scRNA-seq to map eQTL across different cell types and developmental stages relevant for the disease process. Although such approaches are still in their early stages, proof-of-concept studies have demonstrated the feasibility of using scRNA-seq data for eQTL and gene regulatory network analyses (76). Notwithstanding the difficulties, it has been proposed that risk variants for schizophrenia are particularly abundant among genes that regulate the development and function of the synapse. The functional analysis of complement component 4 (C4), a protein that is abnormally increased in the brain of schizophrenia patients (77), represents one of the best examples so far linking common genetic variation to a neurodevelopmental mechanism in schizophrenia. C4 is encoded in humans by multiple structurally diverse alleles, and common variation increases schizophrenia risk by increasing the amounts of a specific C4 form. In mice, C4 regulates synapse elimination during development (77), which implies that this important developmental process—known as synaptic pruning—is abnormally enhanced in the brain of schizophrenia patients. It should be emphasized, however, that the effect size of common variation in humans is very small (i.e., C4 which has the largest of the small effect sizes, is just one of hundreds of gene variants that collectively contribute a modest proportion of the overall disease risk), so it is difficult to infer the actual role of defective synaptic pruning in the disease process in the absence of independent functional validation of other risk variants or rare mutations associated with schizophrenia.

One area where our understanding remains poor is the role of somatic mutations in neurodevelopmental disorders. Neurodevelopmental disorders had been assumed to be caused by inherited or de novo germline mutations. However, next-generation sequencing and single-cell sequencing technologies have revealed that the rate of somatic mutations is particularly high during neurogenesis (53) and may contribute to neurodevelopmental diseases. Indeed, whole-exome sequencing has found that somatic mutations contribute to ~5% of ASD risk in families in which only a single individual has ASD (78). Further analyses that relate genomic alterations to transcriptomic changes and any abnormalities in cell function or brain development will be necessary to understand the contribution of somatic mutations to neurodevelopmental disorders.

Together, these observations highlight how a convergence between developmental neuro-

biology and neurogenetics, driven by the increased resolution of the molecular and genetic assays, is likely to improve our understanding of both basic developmental mechanisms and the origin of neurological disease.

### Modeling human brain development

The identification of genes and cells associated with neurodevelopmental disorders is only the beginning of a tortuous path to link gene variation with specific neurobiological functions. Experimental approaches are essential to identify the *in vivo* function of candidate genes. Unfortunately, whereas classical loss-of-function approaches might be useful to unravel the function of gene-disrupting coding mutations, knockouts are less likely to recapitulate the functionally subtle polymorphisms that are common in complex neurodevelopmental diseases, and animal models do not always recapitulate the social and cognitive deficits associated with human disorders. Nevertheless, large-scale phenotypic analyses of animal models carrying loss-of-function mutations in genes associated with common risk variants might be useful to identify functional convergence during brain development (79).

Cell culture-based assays represent a tractable and scalable approach for determining the function of particular genes and potential regulatory variants (Fig. 4). For example, human neurons derived from induced pluripotent stem cells (iPSCs) have been used to map gene regulatory element interactions *in vitro* (80). Protocols for generating specific neuronal subtypes (81) allow the landscape of epigenomic regulation to be explored in relatively well-characterized, specific types of neurons; the disadvantage is that it remains to be determined whether the right type of cells are being interrogated, leading to a circular problem. High-resolution molecular and genomic data from single-cell analyses provide a way to benchmark the similarity of *in vitro*-derived neurons to their *in vivo* counterparts (82, 83). More generally, neurons induced from patient-derived iPSCs or control iPSCs harboring engineered mutations can be used in cell biology and functional assays. For example, motor neurons derived from individuals with amyotrophic lateral sclerosis (ALS) caused by SOD1 mutations have been shown to display neurofilament aggregation and endoplasmic reticulum stress (84, 85), while glutamatergic cortical neurons differentiated from iPSCs derived from individuals with SHANK3 haploinsufficiency, associated with ASD, exhibited decreased glutamatergic neurotransmission that was corrected by reintroducing SHANK3 expression (86). Deriving neurons from iPSCs obtained from patients might currently be the only amenable way to investigate the functional consequences of highly polygenic risk traits (87). In addition, neurons derived from

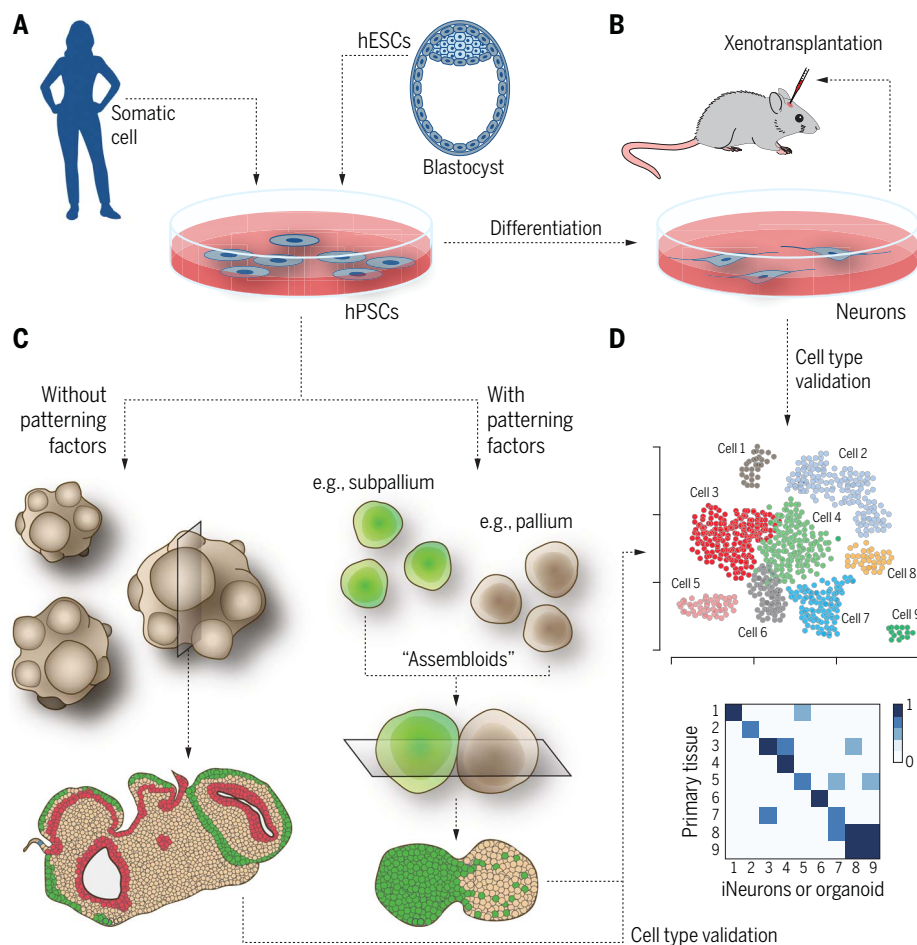


**Fig. 4. Modeling the impact of disease-associated gene variants in human brain development.**

(A) Human pluripotent stem cells (hPSCs) can be derived from somatic cells or embryonic stem cells (hESCs) and differentiated into distinct classes of neurons and glial cells. (B) The impact of disease-associated gene variants in neural development and function can be studied in vitro or through xenotransplantation in rodents. (C) hPSCs can also be used to derive brain organoids, with or without the use of patterning methods to direct the differentiation of specific classes of cells. Patterned brain organoids can be fused into “assembloids” to recreate regional features of brain development. (D) Single-cell genomic approaches can be used to benchmark the generation of relevant cell types in vitro by comparing transcriptional identities with those found in primary tissue.

human pluripotent stem cells integrate into functional circuits when transplanted into the mouse brain (88–90). Xenotransplantation is therefore a plausible methodology to study the formation and plasticity of neural circuits involving human neurons carrying specific mutations linked to neurodevelopmental disorders. For example, transplanted pyramidal projection neurons derived from individuals with Down syndrome exhibit substantial differences in synapse turnover in vivo compared with neurons derived from control iPSCs (91).

Brain organoids are also emerging as a powerful alternative to investigate human brain development in vitro (92). These three-dimensional neural tissues grown in culture from human stem cells have the potential to overcome some of the limitations of two-

dimensional culture systems, as they seem to recapitulate at least some of the anatomical and cytoarchitectural characteristics of specific brain regions in vitro (Fig. 4). The fusion of distinct brain region-specific organoids into more complex “assembloids” has been adopted as an approach that bypasses the difficulties of simultaneously patterning different brain regions in vitro. These allow the analysis of long-range neuronal migration across brain regions and the formation of major axonal tracts (93–97).

One issue that limits the use of brain organoids is that protocols for their generation have been prone to variable results. In this context, big data approaches are being used to validate organoids. Recent single-cell transcriptomic studies suggest that brain-region-specific organoids can consistently generate a diversity

of cell types (98, 99). Whether this is fully representative of primary tissue remains in contention, and it has been suggested that the activation of endoplasmic reticulum stress pathways might compromise cell type specification, at least in some types of organoids (100). In spite of these caveats, organoids allow the exploration of early events in human brain development. For instance, organoids derived from a patient with microcephaly, caused by a mutation in the cell cycle-related gene *CDK5RAP2*, have a premature depletion of the progenitor pool and are smaller than those derived from controls (101). Conversely, organoids engineered to carrying a mutation in the *PTEN* gene, which is found in patients with macrocephaly, exhibit a marked increase in proliferative cells, which results in abnormal overgrowth (102). These findings provide a foundation for the use of human brain organoids to investigate the mechanisms underlying polygenic and idiopathic developmental disorders. For example, transcriptional analysis of organoids derived from ASD patients with macrocephaly revealed consistent alterations in programs of gene expression associated with cell proliferation and differentiation of inhibitory neurons (103). These defects seem to be largely caused by the abnormal up-regulation in the expression of *FOXG1*, a gene crucial in forebrain patterning whose mutation causes an atypical form of Rett syndrome (104). Coordinated electrical activity has been observed in brain organoids (105–107), raising the prospect of modeling a range of neurological disorders and screening neuromodulatory drugs (107). Robust assays and rigorous controls will be crucial in experiments involving low-impact genes to overcome the inherent variability of organoids and differences between cell lines. The pleiotropy of many genetic variants implicated in neuropsychiatric disorders is an additional complication, but it might lead to unifying pathophysiological explanations by providing insight into the underlying cellular or molecular mechanisms.

Organoids have emerged as a powerful way to explore early brain development in humans, but their validation depends on our ability to systematically assess how similar they are to the primary tissue. Developing standardized protocols, quality controls, and analytical approaches will support this goal. At the moment, this comparison has been exclusively based on single-cell transcriptomic approaches, but we should ideally be able to integrate data across multiple levels of analysis (molecular, morphology, physiology) to better define the limitations of this approach for understanding how neural circuits are established in humans under normal circumstances and in disease.

## Outlook

New technology and ever-larger and higher-resolution datasets are providing new perspectives



on long-standing questions about the ontogeny, composition, and function of the nervous system. Progress will depend not only on the acquisition and analysis of data but on their successful application to address fundamental conceptual questions such as what constitutes a cell type. Similarly, it is unlikely that our understanding of the mechanisms underlying neuropsychiatric conditions will increase by simply identifying additional risk genes, especially if derived from GWAS associations. Consequently, methods to address the underlying biological mechanisms must be a priority.

The convergence of developmental neurobiology and neurogenetics is an exciting prospect. Integrating data from anatomical, developmental, genetic, and molecular studies has the potential to link cellular processes to functional and behavioral consequences. The analysis of developmental trajectories using big data approaches may enable the investigation of differences among multiple individuals and ultimately the complex biological mechanisms underlying individuality (9, 48, 108). This would provide fundamental insight and offer a new vision to the field.

#### REFERENCES AND NOTES

- Z. Zheng *et al.*, A complete electron microscopy volume of the brain of adult *Drosophila melanogaster*. *Cell* **174**, 730–743.e22 (2018). doi: [10.1016/j.cell.2018.06.019](#); pmid: [30033368](#)
- A. Motta *et al.*, Dense connectomic reconstruction in layer 4 of the somatosensory cortex. *Science* **366**, eaay3134 (2019). doi: [10.1126/science.aay3134](#); pmid: [31649140](#)
- T. Ohshima *et al.*, A multilevel multimodal circuit enhances action selection in *Drosophila*. *Nature* **520**, 633–639 (2015). doi: [10.1038/nature14297](#); pmid: [25896325](#)
- J. Kornfeld, W. Denk, Progress and remaining challenges in high-throughput volume electron microscopy. *Curr. Opin. Neurobiol.* **50**, 261–267 (2018). doi: [10.1016/j.conb.2018.04.030](#); pmid: [29758457](#)
- J. J. Jun *et al.*, Fully integrated silicon probes for high-density recording of neural activity. *Nature* **551**, 232–236 (2017). doi: [10.1038/nature24636](#); pmid: [29120427](#)
- T. Knöpfel, C. Song, Optical voltage imaging in neurons: Moving from technology development to practical tool. *Nat. Rev. Neurosci.* **20**, 719–727 (2019). doi: [10.1038/s41583-019-0231-4](#); pmid: [31705060](#)
- H. Dana *et al.*, High-performance calcium sensors for imaging activity in neuronal populations and microcompartments. *Nat. Methods* **16**, 649–657 (2019). doi: [10.1038/s41592-019-0435-6](#); pmid: [31209382](#)
- A. S. Abdelfattah *et al.*, Bright and photostable chemogenetic indicators for extended in vivo voltage imaging. *Science* **365**, 699–704 (2019). doi: [10.1126/science.aav6416](#); pmid: [31371562](#)
- E. A. Naumann *et al.*, From whole-brain data to functional circuit models: The zebrafish optomotor response. *Cell* **167**, 947–960.e20 (2016). doi: [10.1016/j.cell.2016.10.019](#); pmid: [27814522](#)
- Y. Wan *et al.*, Single-cell reconstruction of emerging population activity in an entire developing circuit. *Cell* **179**, 355–372.e23 (2019). doi: [10.1016/j.cell.2019.08.039](#); pmid: [31564455](#)
- A. Kicheva *et al.*, Coordination of progenitor specification and growth in mouse and chick spinal cord. *Science* **345**, 1254927 (2014). doi: [10.1126/science.1254927](#); pmid: [25258086](#)
- A. Zeisel *et al.*, Molecular architecture of the mouse nervous system. *Cell* **174**, 999–1014.e22 (2018). doi: [10.1016/j.cell.2018.06.021](#); pmid: [30096314](#)
- A. B. Rosenberg *et al.*, Single-cell profiling of the developing mouse brain and spinal cord with split-pool barcoding. *Science* **360**, 176–182 (2018). doi: [10.1126/science.aam8999](#); pmid: [29545511](#)
- A. Saunders *et al.*, Molecular diversity and specializations among the cells of the adult mouse brain. *Cell* **174**, 1015–1030.e16 (2018). doi: [10.1016/j.cell.2018.07.028](#); pmid: [30096299](#)
- B. Tasic *et al.*, Shared and distinct transcriptomic cell types across neocortical areas. *Nature* **563**, 72–78 (2018). doi: [10.1038/s41586-018-0654-5](#); pmid: [30382198](#)
- Y. R. Peng *et al.*, Molecular classification and comparative taxonomics of foveal and peripheral cells in primate retina. *Cell* **176**, 1222–1237.e22 (2019). doi: [10.1016/j.cell.2019.01.004](#); pmid: [30712875](#)
- N. Konstantinides *et al.*, Phenotypic convergence: Distinct transcription factors regulate common terminal features. *Cell* **174**, 622–635.e13 (2018). doi: [10.1016/j.cell.2018.05.021](#); pmid: [29909983](#)
- A. M. M. Sousa *et al.*, Molecular and cellular reorganization of neural circuits in the human lineage. *Science* **358**, 1027–1032 (2017). doi: [10.1126/science.aan3456](#); pmid: [29170230](#)
- S. Marques *et al.*, Oligodendrocyte heterogeneity in the mouse juvenile and adult central nervous system. *Science* **352**, 1326–1329 (2016). doi: [10.1126/science.aaf6463](#); pmid: [27284195](#)
- O. A. Bayraktar *et al.*, Astrocyte layers in the mammalian cerebral cortex revealed by a single-cell in situ transcriptomic map. *Nat. Neurosci.* **23**, 500–509 (2020). doi: [10.1038/s41593-020-0602-1](#); pmid: [32203496](#)
- H. Chai *et al.*, Neural circuit-specialized astrocytes: Transcriptomic, proteomic, morphological, and functional evidence. *Neuron* **95**, 531–549.e9 (2017). doi: [10.1016/j.neuron.2017.06.029](#); pmid: [28712653](#)
- T. Masuda *et al.*, Spatial and temporal heterogeneity of mouse and human microglia at single-cell resolution. *Nature* **566**, 388–392 (2019). doi: [10.1038/s41586-019-0924-x](#); pmid: [30760929](#)
- M. S. Thion, F. Ginhoux, S. Garel, Microglia and early brain development: An intimate journey. *Science* **362**, 185–189 (2018). doi: [10.1126/science.aaf0474](#); pmid: [30309946](#)
- E. Lubeck, A. F. Coskun, T. Zhiyentayev, M. Ahmad, L. Cai, Single-cell in situ RNA profiling by sequential hybridization. *Nat. Methods* **11**, 360–361 (2014). doi: [10.1038/nmeth.2892](#); pmid: [24681720](#)
- J. H. Lee *et al.*, Highly multiplexed subcellular RNA sequencing in situ. *Science* **343**, 1360–1363 (2014). doi: [10.1126/science.1250212](#); pmid: [24578530](#)
- S. G. Rodrigues *et al.*, Slide-seq: A scalable technology for measuring genome-wide expression at high spatial resolution. *Science* **363**, 1463–1467 (2019). doi: [10.1126/science.aaw1219](#); pmid: [30923225](#)
- C. R. Cadwell *et al.*, Electrophysiological, transcriptomic and morphological profiling of single neurons using Patch-seq. *Nat. Biotechnol.* **34**, 199–203 (2016). doi: [10.1038/nbt.3445](#); pmid: [26689543](#)
- J. Fuzik *et al.*, Integration of electrophysiological recordings with single-cell RNA-seq data identifies neuronal subtypes. *Nat. Biotechnol.* **34**, 175–183 (2016). doi: [10.1038/nbt.3443](#); pmid: [26689544](#)
- N. K. Hanchate *et al.*, Connect-seq to superimpose molecular on anatomical neural circuit maps. *Proc. Natl. Acad. Sci. U.S.A.* **117**, 4375–4384 (2020). doi: [10.1073/pnas.1912176117](#); pmid: [32034095](#)
- Y. Han *et al.*, The logic of single-cell projections from visual cortex. *Nature* **556**, 51–56 (2018). doi: [10.1038/nature26159](#); pmid: [29590093](#)
- D. Arendt *et al.*, The origin and evolution of cell types. *Nat. Rev. Genet.* **17**, 744–757 (2016). doi: [10.1038/nrg.2016.127](#); pmid: [27818507](#)
- E. A. Mukamel, J. Ngai, Perspectives on defining cell types in the brain. *Curr. Opin. Neurobiol.* **56**, 61–68 (2019). doi: [10.1016/j.conb.2018.11.007](#); pmid: [30530112](#)
- E. H. Davidson, D. H. Erwin, Gene regulatory networks and the evolution of animal body plans. *Science* **311**, 796–800 (2006). doi: [10.1126/science.1113832](#); pmid: [16469913](#)
- O. Hobert, L. Glenwinkel, J. White, Revisiting neuronal cell type classification in *Caenorhabditis elegans*. *Curr. Biol.* **26**, R1197–R1203 (2016). doi: [10.1016/j.cub.2016.10.027](#); pmid: [27875702](#)
- S. Arber, Motor circuits in action: Specification, connectivity, and function. *Neuron* **74**, 975–989 (2012). doi: [10.1016/j.neuron.2012.05.011](#); pmid: [22726829](#)
- H. Li *et al.*, Classifying *Drosophila* olfactory projection neuron subtypes by single-cell RNA sequencing. *Cell* **171**, 1206–1220.e22 (2017). doi: [10.1016/j.cell.2017.10.019](#); pmid: [29149607](#)
- J. M. Kebschull *et al.*, Cerebellar nuclei evolved by repeatedly duplicating a conserved cell type set. *bioRxiv* 20.06.25.170118 [Preprint]. 25 June 2020. doi: [10.1101/2020.06.25.170118](#)
- J. Delile *et al.*, Single cell transcriptomics reveals spatial and temporal dynamics of gene expression in the developing mouse spinal cord. *Development* **146**, dev173807 (2019). doi: [10.1242/dev.173807](#); pmid: [30846445](#)
- D. Mi *et al.*, Early emergence of cortical interneuron diversity in the mouse embryo. *Science* **360**, 81–85 (2018). doi: [10.1126/science.aar6821](#); pmid: [29472441](#)
- S. Tritschler *et al.*, Concepts and limitations for learning developmental trajectories from single cell genomics. *Development* **146**, dev170506 (2019). doi: [10.1242/dev.170506](#); pmid: [31249007](#)
- D. Polioudakis *et al.*, A single-cell transcriptomic atlas of human neocortical development during mid-gestation. *Neuron* **103**, 785–801.e8 (2019). doi: [10.1016/j.neuron.2019.06.011](#); pmid: [31303374](#)
- R. Iwata, P. Casimir, P. Vanderhaeghen, Mitochondrial dynamics in postmitotic cells regulate neurogenesis. *Science* **369**, 858–862 (2020). doi: [10.1126/science.aba9760](#); pmid: [32792401](#)
- J. S. Packer *et al.*, A lineage-resolved molecular atlas of *C. elegans* embryogenesis at single-cell resolution. *Science* **365**, eaax1971 (2019). doi: [10.1126/science.aax1971](#); pmid: [31488706](#)
- C. Mayer *et al.*, Developmental diversification of cortical inhibitory interneurons. *Nature* **555**, 457–462 (2018). doi: [10.1038/nature25999](#); pmid: [29513653](#)
- G. La Manno *et al.*, RNA velocity of single cells. *Nature* **560**, 494–498 (2018). doi: [10.1038/s41586-018-0414-6](#); pmid: [30089906](#)
- L. Telley *et al.*, Sequential transcriptional waves direct the differentiation of newborn neurons in the mouse neocortex. *Science* **351**, 1443–1446 (2016). doi: [10.1126/science.aad8361](#); pmid: [26940868](#)
- M. B. Woodworth, K. M. Girsakis, C. A. Walsh, Building a lineage from single cells: Genetic techniques for cell lineage tracking. *Nat. Rev. Genet.* **18**, 230–244 (2017). doi: [10.1038/nrg.2016.159](#); pmid: [28111472](#)
- B. Raj *et al.*, Simultaneous single-cell profiling of lineages and cell types in the vertebrate brain. *Nat. Biotechnol.* **36**, 442–450 (2018). doi: [10.1038/nbt.4103](#); pmid: [29608178](#)
- L. S. Ludwig *et al.*, Lineage tracing in humans enabled by mitochondrial mutations and single-cell genomics. *Cell* **176**, 1325–1339.e22 (2019). doi: [10.1016/j.cell.2019.01.022](#); pmid: [30827679](#)
- J. Xu *et al.*, Single-cell lineage tracing by endogenous mutations enriched in transposase accessible mitochondrial DNA. *eLife* **8**, e45105 (2019). doi: [10.7554/eLife.45105](#); pmid: [30958261](#)
- G. D. Evrony, E. Lee, P. J. Park, C. A. Walsh, Resolving rates of mutation in the brain using single-neuron genomics. *eLife* **5**, e12966 (2016). doi: [10.7554/eLife.12966](#); pmid: [26901440](#)
- M. A. Lodato *et al.*, Aging and neurodegeneration are associated with increased mutations in single human neurons. *Science* **359**, 555–559 (2018). doi: [10.1126/science.aao4426](#); pmid: [29217584](#)
- T. Bae *et al.*, Different mutational rates and mechanisms in human cells at pregastrulation and neurogenesis. *Science* **359**, 550–555 (2018). doi: [10.1126/science.aan8690](#); pmid: [29217587](#)
- V. Metzlis *et al.*, Nervous system regionalization entails axial allocation before neural differentiation. *Cell* **175**, 1105–1118.e17 (2018). doi: [10.1016/j.cell.2018.09.040](#); pmid: [30343898](#)
- S. Marques *et al.*, Transcriptional convergence of oligodendrocyte lineage progenitors during development. *Dev. Cell* **46**, 504–517.e7 (2018). doi: [10.1016/j.devcel.2018.07.005](#); pmid: [30078729](#)
- D. A. Cusanovich *et al.*, The cis-regulatory dynamics of embryonic development at single-cell resolution. *Nature* **555**, 538–542 (2018). doi: [10.1038/nature25981](#); pmid: [29539636](#)
- H. S. Kaya-Okur *et al.*, CUT&Tag for efficient epigenomic profiling of small samples and single cells. *Nat. Commun.* **10**, 1930 (2019). doi: [10.1038/s41467-019-0982-5](#); pmid: [31036827](#)
- J. Cao *et al.*, Joint profiling of chromatin accessibility and gene expression in thousands of single cells. *Science* **361**, 1380–1385 (2018). doi: [10.1126/science.aau0730](#); pmid: [30166440](#)
- S. J. Clark *et al.*, scNMT-seq enables joint profiling of chromatin accessibility DNA methylation and transcription in single cells. *Nat. Commun.* **9**, 781 (2018). doi: [10.1038/s41467-018-03149-4](#); pmid: [29472610](#)
- O. Marín, Developmental timing and critical windows for the treatment of psychiatric disorders. *Nat. Med.* **22**, 1229–1238 (2016). doi: [10.1038/nm.4225](#); pmid: [27783067](#)

61. L. M. Iakouchcheva, A. R. Muotri, J. Sebat, Getting to the cores of autism. *Cell* **178**, 1287–1298 (2019). doi: [10.1016/j.cell.2019.07.037](https://doi.org/10.1016/j.cell.2019.07.037); pmid: [31491383](https://pubmed.ncbi.nlm.nih.gov/31491383/)
62. I. Giegling et al., Genetics of schizophrenia: A consensus paper of the WFSBP Task Force on Genetics. *World J. Biol. Psychiatry* **18**, 492–505 (2017). doi: [10.1080/15622975.2016.1268715](https://doi.org/10.1080/15622975.2016.1268715); pmid: [28112043](https://pubmed.ncbi.nlm.nih.gov/28112043/)
63. M. C. O'Donovan, M. J. Owen, The implications of the shared genetics of psychiatric disorders. *Nat. Med.* **22**, 1214–1219 (2016). doi: [10.1038/nm.4196](https://doi.org/10.1038/nm.4196); pmid: [27783064](https://pubmed.ncbi.nlm.nih.gov/27783064/)
64. A. M. D'Gama, C. A. Walsh, Somatic mosaicism and neurodevelopmental disease. *Nat. Neurosci.* **21**, 1504–1514 (2018). doi: [10.1038/s41593-018-0257-3](https://doi.org/10.1038/s41593-018-0257-3); pmid: [30349109](https://pubmed.ncbi.nlm.nih.gov/30349109/)
65. N. N. Parikshak et al., Integrative functional genomic analyses implicate specific molecular pathways and circuits in autism. *Cell* **155**, 1008–1021 (2013). doi: [10.1016/j.cell.2013.10.031](https://doi.org/10.1016/j.cell.2013.10.031); pmid: [24267887](https://pubmed.ncbi.nlm.nih.gov/24267887/)
66. A. J. Willsey et al., Coexpression networks implicate human midfetal deep cortical projection neurons in the pathogenesis of autism. *Cell* **155**, 997–1007 (2013). doi: [10.1016/j.cell.2013.10.020](https://doi.org/10.1016/j.cell.2013.10.020); pmid: [24267886](https://pubmed.ncbi.nlm.nih.gov/24267886/)
67. M. Li et al., Integrative functional genomic analysis of human brain development and neuropsychiatric risks. *Science* **362**, eaat7615 (2018). doi: [10.1126/science.aat7615](https://doi.org/10.1126/science.aat7615); pmid: [30545854](https://pubmed.ncbi.nlm.nih.gov/30545854/)
68. S. Zhong et al., A single-cell RNA-seq survey of the developmental landscape of the human prefrontal cortex. *Nature* **555**, 524–528 (2018). doi: [10.1038/nature25980](https://doi.org/10.1038/nature25980); pmid: [29539641](https://pubmed.ncbi.nlm.nih.gov/29539641/)
69. D. S. Lee et al., Simultaneous profiling of 3D genome structure and DNA methylation in single human cells. *Nat. Methods* **16**, 999–1006 (2019). doi: [10.1038/s41592-019-0547-z](https://doi.org/10.1038/s41592-019-0547-z); pmid: [31501549](https://pubmed.ncbi.nlm.nih.gov/31501549/)
70. D. Velmeshev et al., Single-cell genomics identifies cell type-specific molecular changes in autism. *Science* **364**, 685–689 (2019). doi: [10.1126/science.aav8130](https://doi.org/10.1126/science.aav8130); pmid: [31097668](https://pubmed.ncbi.nlm.nih.gov/31097668/)
71. M. T. Maurano et al., Systematic localization of common disease-associated variation in regulatory DNA. *Science* **337**, 1190–1195 (2012). doi: [10.1126/science.1222794](https://doi.org/10.1126/science.1222794); pmid: [22955828](https://pubmed.ncbi.nlm.nih.gov/22955828/)
72. N. G. Skene et al., Genetic identification of brain cell types underlying schizophrenia. *Nat. Genet.* **50**, 825–833 (2018). doi: [10.1038/s41588-018-0129-5](https://doi.org/10.1038/s41588-018-0129-5); pmid: [29785013](https://pubmed.ncbi.nlm.nih.gov/29785013/)
73. L. de la Torre-Ubieta et al., The dynamic landscape of open chromatin during human cortical neurogenesis. *Cell* **172**, 289–304.e18 (2018). doi: [10.1016/j.cell.2017.12.014](https://doi.org/10.1016/j.cell.2017.12.014); pmid: [29307494](https://pubmed.ncbi.nlm.nih.gov/29307494/)
74. A. Nott et al., Brain cell type-specific enhancer-promoter interactome maps and disease-risk association. *Science* **366**, 1134–1139 (2019). doi: [10.1126/science.aay0793](https://doi.org/10.1126/science.aay0793); pmid: [31727856](https://pubmed.ncbi.nlm.nih.gov/31727856/)
75. D. Wang et al., Comprehensive functional genomic resource and integrative model for the human brain. *Science* **362**, eaat8464 (2018). doi: [10.1126/science.aat8464](https://doi.org/10.1126/science.aat8464); pmid: [30545857](https://pubmed.ncbi.nlm.nih.gov/30545857/)
76. M. G. P. van der Wijst et al., Single-cell RNA sequencing identifies celltype-specific cis-eQTLs and co-expression QTLs. *Nat. Genet.* **50**, 493–497 (2018). doi: [10.1038/s41588-018-0089-9](https://doi.org/10.1038/s41588-018-0089-9); pmid: [29610479](https://pubmed.ncbi.nlm.nih.gov/29610479/)
77. A. Sekar et al., Schizophrenia risk from complex variation of complement component 4. *Nature* **530**, 177–183 (2016). doi: [10.1038/nature16549](https://doi.org/10.1038/nature16549); pmid: [26814963](https://pubmed.ncbi.nlm.nih.gov/26814963/)
78. D. Freed, J. Pevsner, The contribution of mosaic variants to autism spectrum disorder. *PLOS Genet.* **12**, e1006245 (2016). doi: [10.1371/journal.pgen.1006245](https://doi.org/10.1371/journal.pgen.1006245); pmid: [27632392](https://pubmed.ncbi.nlm.nih.gov/27632392/)
79. S. B. Thyme et al., Phenotypic landscape of schizophrenia-associated genes defines candidates and their shared functions. *Cell* **177**, 478–491.e20 (2019). doi: [10.1016/j.cell.2019.01.048](https://doi.org/10.1016/j.cell.2019.01.048); pmid: [30929901](https://pubmed.ncbi.nlm.nih.gov/30929901/)
80. M. Song et al., Mapping cis-regulatory chromatin contacts in neural cells links neuropsychiatric disorder risk variants to target genes. *Nat. Genet.* **51**, 1252–1262 (2019). doi: [10.1038/s41588-019-0472-1](https://doi.org/10.1038/s41588-019-0472-1); pmid: [31367015](https://pubmed.ncbi.nlm.nih.gov/31367015/)
81. Y. Tao, S. C. Zhang, Neural subtype specification from human pluripotent stem cells. *Cell Stem Cell* **19**, 573–586 (2016). doi: [10.1016/j.stem.2016.10.015](https://doi.org/10.1016/j.stem.2016.10.015); pmid: [27814479](https://pubmed.ncbi.nlm.nih.gov/27814479/)
82. B. Treutlein et al., Dissecting direct reprogramming from fibroblast to neuron using single-cell RNA-seq. *Nature* **534**, 391–395 (2016). doi: [10.1038/nature18323](https://doi.org/10.1038/nature18323); pmid: [27281220](https://pubmed.ncbi.nlm.nih.gov/27281220/)
83. R. Tsunemoto et al., Diverse reprogramming codes for neuronal identity. *Nature* **557**, 375–380 (2018). doi: [10.1038/s41586-018-0103-5](https://doi.org/10.1038/s41586-018-0103-5); pmid: [29743677](https://pubmed.ncbi.nlm.nih.gov/29743677/)
84. E. Kiskinis et al., Pathways disrupted in human ALS motor neurons identified through genetic correction of mutant SOD1. *Cell Stem Cell* **14**, 781–795 (2014). doi: [10.1016/j.stem.2014.03.004](https://doi.org/10.1016/j.stem.2014.03.004); pmid: [24704492](https://pubmed.ncbi.nlm.nih.gov/24704492/)
85. H. Chen et al., Modeling ALS with iPSCs reveals that mutant SOD1 misregulates neurofilament balance in motor neurons. *Cell Stem Cell* **14**, 796–809 (2014). doi: [10.1016/j.stem.2014.02.004](https://doi.org/10.1016/j.stem.2014.02.004); pmid: [24704493](https://pubmed.ncbi.nlm.nih.gov/24704493/)
86. A. Shcheglovitov et al., SHANK3 and IGF1 restore synaptic deficits in neurons from 22q13 deletion syndrome patients. *Nature* **503**, 267–271 (2013). doi: [10.1038/nature12618](https://doi.org/10.1038/nature12618); pmid: [24132240](https://pubmed.ncbi.nlm.nih.gov/24132240/)
87. K. J. Brennand et al., Creating patient-specific neural cells for the in vitro study of brain disorders. *Stem Cell Reports* **5**, 933–945 (2015). doi: [10.1016/j.stemcr.2015.10.011](https://doi.org/10.1016/j.stemcr.2015.10.011); pmid: [26610635](https://pubmed.ncbi.nlm.nih.gov/26610635/)
88. I. Espuny-Camacho et al., Pyramidal neurons derived from human pluripotent stem cells integrate efficiently into mouse brain circuits in vivo. *Neuron* **77**, 440–456 (2013). doi: [10.1016/j.neuron.2012.12.011](https://doi.org/10.1016/j.neuron.2012.12.011); pmid: [23395372](https://pubmed.ncbi.nlm.nih.gov/23395372/)
89. A. M. Maroof et al., Directed differentiation and functional maturation of cortical interneurons from human embryonic stem cells. *Cell Stem Cell* **12**, 559–572 (2013). doi: [10.1016/j.stem.2013.04.008](https://doi.org/10.1016/j.stem.2013.04.008); pmid: [23642365](https://pubmed.ncbi.nlm.nih.gov/23642365/)
90. D. Linaro et al., Xenotransplanted human cortical neurons reveal species-specific development and functional integration into mouse visual circuits. *Neuron* **104**, 972–986.e6 (2019). doi: [10.1016/j.neuron.2019.10.002](https://doi.org/10.1016/j.neuron.2019.10.002); pmid: [31761708](https://pubmed.ncbi.nlm.nih.gov/31761708/)
91. R. Real et al., In vivo modeling of human neuron dynamics and Down syndrome. *Science* **362**, eaau1810 (2018). doi: [10.1126/science.aau1810](https://doi.org/10.1126/science.aau1810); pmid: [30309905](https://pubmed.ncbi.nlm.nih.gov/30309905/)
92. S. P. Pasca, The rise of three-dimensional human brain cultures. *Nature* **553**, 437–445 (2018). doi: [10.1038/nature25032](https://doi.org/10.1038/nature25032); pmid: [29364288](https://pubmed.ncbi.nlm.nih.gov/29364288/)
93. F. Birey et al., Assembly of functionally integrated human forebrain spheroids. *Nature* **545**, 54–59 (2017). doi: [10.1038/nature22330](https://doi.org/10.1038/nature22330); pmid: [28445465](https://pubmed.ncbi.nlm.nih.gov/28445465/)
94. J. A. Bagley, D. Reumann, S. Bian, J. Lévi-Strauss, J. A. Knoblich, Fused cerebral organoids model interactions between brain regions. *Nat. Methods* **14**, 743–751 (2017). doi: [10.1038/nmeth.4304](https://doi.org/10.1038/nmeth.4304); pmid: [28504681](https://pubmed.ncbi.nlm.nih.gov/28504681/)
95. Y. Xiang et al., hESC-derived thalamic organoids form reciprocal projections when fused with cortical organoids. *Cell Stem Cell* **24**, 487–497.e7 (2019). doi: [10.1016/j.stem.2018.12.015](https://doi.org/10.1016/j.stem.2018.12.015); pmid: [30799279](https://pubmed.ncbi.nlm.nih.gov/30799279/)
96. Y. Xiang et al., Fusion of regionally specified hPSC-derived organoids models human brain development and interneuron migration. *Cell Stem Cell* **21**, 383–398.e7 (2017). doi: [10.1016/j.stem.2017.07.007](https://doi.org/10.1016/j.stem.2017.07.007); pmid: [28757360](https://pubmed.ncbi.nlm.nih.gov/28757360/)
97. S. L. Giandomenico et al., Cerebral organoids at the air-liquid interface generate diverse nerve tracts with functional output. *Nat. Neurosci.* **22**, 669–679 (2019). doi: [10.1038/s41593-019-0350-2](https://doi.org/10.1038/s41593-019-0350-2); pmid: [30886407](https://pubmed.ncbi.nlm.nih.gov/30886407/)
98. S. J. Yoon et al., Reliability of human cortical organoid generation. *Nat. Methods* **16**, 75–78 (2019). doi: [10.1038/s41592-018-0255-0](https://doi.org/10.1038/s41592-018-0255-0); pmid: [30573846](https://pubmed.ncbi.nlm.nih.gov/30573846/)
99. S. Velasco et al., Individual brain organoids reproducibly form cell diversity of the human cerebral cortex. *Nature* **570**, 523–527 (2019). doi: [10.1038/s41586-019-1289-x](https://doi.org/10.1038/s41586-019-1289-x); pmid: [31168097](https://pubmed.ncbi.nlm.nih.gov/31168097/)
100. A. Bhaduri et al., Cell stress in cortical organoids impairs molecular subtype specification. *Nature* **578**, 142–148 (2020). doi: [10.1038/s41586-020-1962-0](https://doi.org/10.1038/s41586-020-1962-0); pmid: [31996853](https://pubmed.ncbi.nlm.nih.gov/31996853/)
101. M. A. Lancaster et al., Cerebral organoids model human brain development and microcephaly. *Nature* **501**, 373–379 (2013). doi: [10.1038/nature12517](https://doi.org/10.1038/nature12517); pmid: [23995685](https://pubmed.ncbi.nlm.nih.gov/23995685/)
102. Y. Li et al., Induction of expansion and folding in human cerebral organoids. *Cell Stem Cell* **20**, 385–396.e3 (2017). doi: [10.1016/j.stem.2016.11.017](https://doi.org/10.1016/j.stem.2016.11.017); pmid: [28041895](https://pubmed.ncbi.nlm.nih.gov/28041895/)
103. J. Mariani et al., FOXG1-dependent dysregulation of GABA/glutamate neuron differentiation in autism spectrum disorders. *Cell* **162**, 375–390 (2015). doi: [10.1016/j.cell.2015.06.034](https://doi.org/10.1016/j.cell.2015.06.034); pmid: [26186191](https://pubmed.ncbi.nlm.nih.gov/26186191/)
104. F. Ariani et al., FOXG1 is responsible for the congenital variant of Rett syndrome. *Am. J. Hum. Genet.* **83**, 89–93 (2008). doi: [10.1016/j.ajhg.2008.05.015](https://doi.org/10.1016/j.ajhg.2008.05.015); pmid: [18571142](https://pubmed.ncbi.nlm.nih.gov/18571142/)
105. G. Quadrato et al., Cell diversity and network dynamics in photosensitive human brain organoids. *Nature* **545**, 48–53 (2017). doi: [10.1038/nature22047](https://doi.org/10.1038/nature22047); pmid: [28445462](https://pubmed.ncbi.nlm.nih.gov/28445462/)
106. A. Trumpor, M. J. Depew, J. L. Rubenstein, J. M. Bishop, G. R. Martin, Cre-mediated gene inactivation demonstrates that FGF8 is required for cell survival and patterning of the first branchial arch. *Genes Dev.* **13**, 3136–3148 (1999). doi: [10.1101/gad.13.23.3136](https://doi.org/10.1101/gad.13.23.3136); pmid: [10601039](https://pubmed.ncbi.nlm.nih.gov/10601039/)
107. R. A. Samarasinghe et al., Identification of neural oscillations and epileptiform changes in human brain organoids. *bioRxiv* 820183 [Preprint]. 28 October 2019. doi: [10.1101/820183](https://doi.org/10.1101/820183)
108. G. A. Linneweber et al., A neurodevelopmental origin of behavioral individuality in the *Drosophila* visual system. *Science* **367**, 1112–1119 (2020). doi: [10.1126/science.aaw7182](https://doi.org/10.1126/science.aaw7182); pmid: [32139539](https://pubmed.ncbi.nlm.nih.gov/32139539/)

## ACKNOWLEDGMENTS

We thank B. Berninger, S.J. Butler, C. Houart, and A.F. Schier for feedback on an earlier version of this manuscript, and members of the Briscoe and Marin laboratories for stimulating discussions and ideas. We apologize to colleagues whose work is not cited in this review because of space limitations. **Funding:** Our research on this topic is supported by grants from the European Research Council (ERC-2017-AdG 787355) and Wellcome Trust (215556/Z/19/Z) to O.M.; by the Francis Crick Institute, which receives its core funding from Cancer Research UK, the UK Medical Research Council, and Wellcome Trust (all under FC001051); and by the European Research Council (ERC-2020-AdG 742138) to J.B. **Competing interests:** None declared.

10.1126/science.aaz8627



## RESEARCH ARTICLE SUMMARY

## INFLAMMASOMES

## HDAC6 mediates an aggresome-like mechanism for NLRP3 and pyrin inflammasome activation

Venkat Giri Magupalli<sup>\*†</sup>, Roberto Negro<sup>\*†</sup>, Yuzi Tian<sup>\*</sup>, Arthur V. Hauenstein<sup>\*</sup>, Giuseppe Di Caprio, Wesley Skillern, Qiufang Deng, Pontus Orning, Hasan B. Alam, Zoltan Maliga, Humayun Sharif, Jun Jacob Hu, Charles L. Evavold, Jonathan C. Kagan, Florian I. Schmidt, Katherine A. Fitzgerald, Tom Kirchhausen, Yongqing Li<sup>†</sup>, Hao Wu<sup>†</sup>

**INTRODUCTION:** Canonical inflammasomes are multicomponent protein complexes that play key roles in immune surveillance of infections and danger by activating caspase-1, which cleaves interleukin 1 $\beta$  (IL-1 $\beta$ ) and the pore-forming protein gasdermin D, leading to cytokine maturation and pyroptosis. The nucleotide-binding domain, leucine-rich repeat, and pyrin domain-containing protein 3 (NLRP3) can be activated by the bacterial toxin nigericin, extracellular ATP, and various particulates such as monosodium urate (MSU) crystals, alum, silica, and amyloids, whereas the pyrin inflammasome

can be stimulated by the Rho-glucosylation activity of *Clostridium difficile* toxin B. One important hallmark for inflammasome activation is the formation of a single supramolecular punctum (also known as a speck) per cell. However, the location and trafficking of such puncta remain unknown.

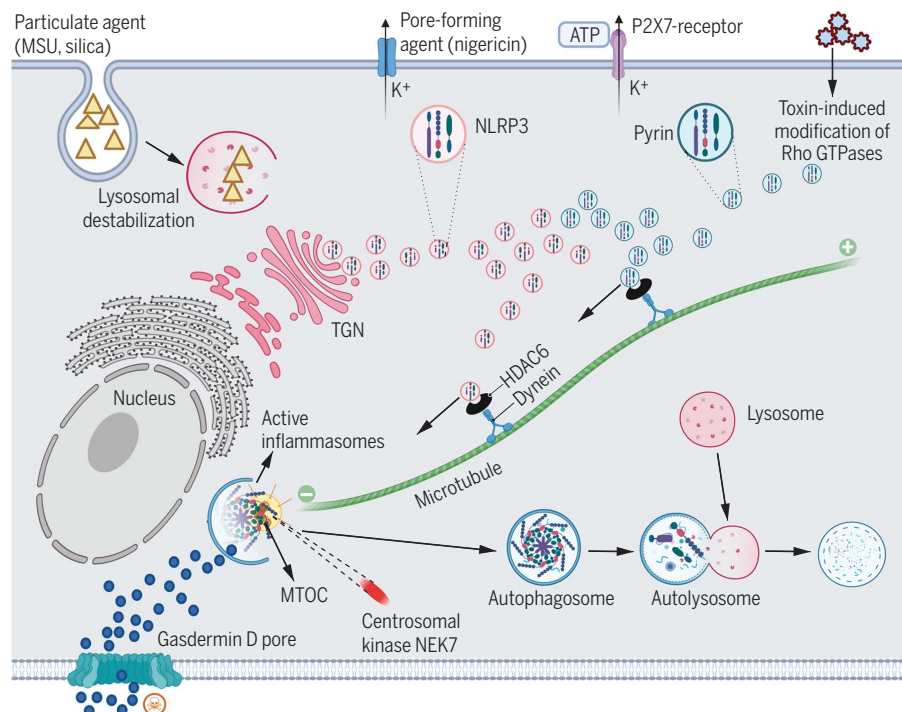
**RATIONALE:** To decode the site and the molecular machinery in inflammasome assembly and activation in macrophages, we aimed to visualize inflammasome assembly by cellular imaging complemented by pharmacological

inhibition and targeted deletion in cells and in mice.

**RESULTS:** We found that NLRP3 and pyrin inflammasomes are assembled at the centrosome, also known as the microtubule-organizing center (MTOC), of each cell, which serves as the major site for caspase-1 activation and IL-1 $\beta$  conversion. Pharmacological inhibitors of microtubule polymerization, dynein ATPase and the dynein adaptor histone deacetylase 6 (HDAC6), and targeted deletion or knockdown of *Hdac6* compromised the assembly and activation of these inflammasomes. Reconstitution of *Hdac6*<sup>-/-</sup> macrophages showed that the ubiquitin-binding ability of HDAC6, but not its deacetylase activity, is required for NLRP3 and pyrin inflammasome activation. In mice, *Hdac6* deficiency reduced lipopolysaccharide- and MSU-induced inflammation to a similar extent as direct NLRP3 inhibition, which demonstrates the requirement of HDAC6 and the microtubule retrograde transport machinery for NLRP3 activation. By contrast, AIM2 and NLRC4 inflammasome puncta do not localize at the MTOC, and these inflammasomes do not require microtubule retrograde transport for their activation. Thus, our studies revealed a specific mechanism of inflammasome activation for NLRP3 and pyrin.

For the NLRP3 inflammasome, MTOC localization may facilitate association with the centrosome-localized kinase NEK7 to enhance inflammasome assembly. We found that in *Hdac6*<sup>-/-</sup> macrophages, NLRP3 is trapped as small speckles at the trans-Golgi network (TGN), a previously recognized common site for NLRP3 association upon induction by multiple NLRP3 stimulators. These data suggested that HDAC6-mediated microtubule transport delivers NLRP3 from TGN to the MTOC. The NLRP3 inflammasome formed at the MTOC colocalizes with LC3b, an autophagy marker, and an autophagy inhibitor enhances NLRP3-induced IL-1 $\beta$  secretion.

**CONCLUSION:** Our study reveals an unexpected parallel between HDAC6-dependent assembly of NLRP3 and pyrin inflammasomes and the formation of aggresomes at the MTOC for autophagic degradation of ubiquitinated pathological aggregates. The dual activating and inhibiting roles played by the MTOC localization of NLRP3 and pyrin inflammasomes may be critical for achieving balanced inflammasome regulation. ■



#### HDAC6- and microtubule-dependent assembly and activation of NLRP3 and pyrin inflammasomes.

Multiple stimuli for NLRP3 (MSU, silica, nigericin, and ATP) and pyrin (Rho GTPase modification) are shown on the top part of the cell. NLRP3 and pyrin inflammasome components are represented in pink and light blue, respectively. NLRP3 inflammasome assembly may involve two steps: initial oligomerization at the TGN and further assembly into a single punctum with the centrosomal kinase NEK7, the adaptor ASC, and caspase-1 at the MTOC. The latter is achieved after being retrograde transported on the microtubule by the HDAC6-dynein machinery. Pyrin inflammasome activation also requires HDAC6, dynein, and microtubules. Assembled inflammasomes at the MTOC are subject to degradation by autophagy in a manner similar to aggresomes that degrade pathological aggregates. [Figure was created with BioRender (<https://BioRender.com>).]

The list of author affiliations is available in the full article online.  
\*These authors contributed equally to this work.

†Corresponding author: Email: [wu@crystal.harvard.edu](mailto:wu@crystal.harvard.edu) (H.W.); [venkat.magupalli@childrens.harvard.edu](mailto:venkat.magupalli@childrens.harvard.edu) (V.G.M.); [roberto.negro@childrens.harvard.edu](mailto:roberto.negro@childrens.harvard.edu) (R.N.); [yqli@med.umich.edu](mailto:yqli@med.umich.edu) (Y.L.)

Cite this article as V. G. Magupalli et al., *Science* **369**, eaas8995 (2020). DOI: [10.1126/science.aas8995](https://doi.org/10.1126/science.aas8995)

**S** READ THE FULL ARTICLE AT  
<https://doi.org/10.1126/science.aas8995>

## RESEARCH ARTICLE

## INFLAMMASOMES

## HDAC6 mediates an aggresome-like mechanism for NLRP3 and pyrin inflammasome activation

Venkat Giri Magupalli<sup>1,2,\*†</sup>, Roberto Negro<sup>1,2,\*†</sup>, Yuzi Tian<sup>3,4,\*</sup>, Arthur V. Hauenstein<sup>1,2,\*</sup>, Giuseppe Di Caprio<sup>2,5</sup>, Wesley Skillern<sup>2</sup>, Qiufang Deng<sup>3,4</sup>, Pontus Orning<sup>6,7</sup>, Hasan B. Alam<sup>3</sup>, Zoltan Maliga<sup>8</sup>, Humayun Sharif<sup>1,2</sup>, Jun Jacob Hu<sup>1,2</sup>, Charles L. Evavold<sup>9</sup>, Jonathan C. Kagan<sup>9</sup>, Florian I. Schmidt<sup>10</sup>, Katherine A. Fitzgerald<sup>6,7</sup>, Tom Kirchhausen<sup>2,5</sup>, Yongqing Li<sup>3,†</sup>, Hao Wu<sup>1,2,†</sup>

Inflammasomes are supramolecular complexes that play key roles in immune surveillance. This is accomplished by the activation of inflammatory caspases, which leads to the proteolytic maturation of interleukin 1 $\beta$  (IL-1 $\beta$ ) and pyroptosis. Here, we show that nucleotide-binding domain, leucine-rich repeat, and pyrin domain-containing protein 3 (NLRP3)- and pyrin-mediated inflammasome assembly, caspase activation, and IL-1 $\beta$  conversion occur at the microtubule-organizing center (MTOC). Furthermore, the dynein adapter histone deacetylase 6 (HDAC6) is indispensable for the microtubule transport and assembly of these inflammasomes both in vitro and in mice. Because HDAC6 can transport ubiquitinated pathological aggregates to the MTOC for aggresome formation and autophagosomal degradation, its role in NLRP3 and pyrin inflammasome activation also provides an inherent mechanism for the down-regulation of these inflammasomes by autophagy. This work suggests an unexpected parallel between the formation of physiological and pathological aggregates.

Inflammasomes play important roles in cytosolic host defense (1–5). Architecturally, canonical inflammasomes are composed of an upstream sensor, an adapter, and the downstream caspase-1 (6). By contrast, in noncanonical inflammasomes, when bacterial lipopolysaccharide (LPS) gains access to the cytosol, it directly engages and activates caspase-4 and -5 in humans and caspase-11 in mice (7). Nucleotide-binding domain, leucine-rich repeat, and pyrin domain-containing protein 3 (NLRP3) constitutes an extensively studied inflammasome sensor, which can be activated by diverse stimuli including the bacterial pore-forming toxin nigericin, extracellular ATP, and various particulates such as monosodium urate

(MSU) crystals, alum, and silica (2–4). Activated NLRP3 recruits the apoptosis-associated speck-like protein containing a CARD (ASC), which in turn recruits caspase-1 (Fig. 1A). Absent in melanoma 2 (AIM2) and pyrin are sensors for two other ASC-dependent inflammasomes. AIM2 is activated by cytosolic double-stranded DNA (dsDNA), and pyrin can be stimulated by Rho-glucosylation activity of *Clostridium difficile* toxin B (TcdB) (2, 7) (Fig. 1A). The NLR family CARD-containing protein 4 (NLRC4) can form an inflammasome with or without ASC upon complex formation with an NLR family apoptosis inhibitory protein (NAIP), which directly senses bacterial flagellin or type III secretion system proteins (1–5). The formation of inflammasomes leads to proximity-induced caspase dimerization, activation, and autoproteolysis. Caspase-1 cleaves pro-interleukin 1 $\beta$  (pro-IL-1 $\beta$ ) and pro-IL-18 to generate the mature cytokines, and caspase-1, -4, -5, and -11 can proteolytically activate gasdermin D to form membrane pores for cytokine release and pyroptosis (2–4, 8–10). Dysregulated inflammasome activity has been implicated in numerous human diseases, including hereditary autoinflammatory syndromes and common conditions such as gout, diabetes, atherosclerosis, Alzheimer's disease, and colorectal cancer (2–5).

#### NLRP3 and pyrin inflammasomes, but not the AIM2 inflammasome, localize at the MTOC

An intriguing observation has been that many inflammasomes assemble into a single major perinuclear punctum in each activated cell (11, 12). The singularity and perinuclear nature

of an inflammasome punctum led us to investigate its connection, if any, with the centrosome, which also acts as the microtubule-organizing center (MTOC) in eukaryotic cells and is perinuclear and punctate in appearance. We used both the human monocytic cell line THP-1 and immortalized mouse bone marrow-derived macrophages (iBMDMs), which endogenously express NLRP3 and other inflammasome components. NLRP3 and ASC colocalized with the centrosomal markers ninein and  $\gamma$ -tubulin (GTU) (13) upon priming by LPS and activation by MSU or nigericin (Fig. 1, B and C, and fig. S1, A to C). When THP-1 cells were stimulated with MSU, 88.5% (62/70 cells) showed colocalization between ASC and ninein. By contrast, only 1.4% (1/70 cells) lacked apparent colocalization. The location of the remaining ASC puncta could not be determined because of the lack of corresponding ninein staining. Similarly, 80% (40/50) of MSU-stimulated THP-1 cells exhibited ASC colocalization with GTU, 4% (2/50 cells) showed no colocalization, and the remaining 16% (8/50) showed no visible GTU staining. NEK7, a member of the NIMA-related kinase (NEK) family, which predominantly resides at the MTOC and is required for NLRP3 inflammasome activation (14–16), also colocalized with ASC and GTU (fig. S1D). The specificity of anti-NLRP3 and anti-ASC antibodies was thoroughly validated (figs. S1, E and F, and S2). Thirty minutes after nigericin stimulation, robust caspase-1 processing (fig. S3, A and B) and IL-1 $\beta$  secretion (fig. S3C) were observed.

In addition to NLRP3 and ASC, IL-1 $\beta$  also localized at the inflammasome puncta (fig. S3, D and E). Labeling of active caspase-1 by FAM-FLICA (17) showed that in 9% (2/22) and 18% (4/22) of cells, respectively, active caspase-1 completely and partially colocalized with the ASC puncta (fig. S3F, examples 1 and 2). In most cells (73%, 16/22), active caspase-1 surrounded the ASC punctum (fig. S3F, example 3), suggesting that caspase-1 is first activated at an inflammasome punctum by dimerization and then released into the cytosol upon autocleavage from the N-terminal CARD prodomain. Thus, NLRP3 inflammasome puncta at the MTOC may serve as a major site for both caspase-1 activation and IL-1 $\beta$  conversion.

We attempted to visualize NLRP3 inflammasome activation using live-cell imaging of fluorescent protein-fused ASC. However, unlike wild-type (WT) cells, nigericin stimulation induced an iBMDM cell line stably expressing ASC-mRuby3 and a THP-1 cell line expressing ASC-TagRFP-T to form puncta distinctly away from the MTOC marked by SiR-tubulin, a live-cell fluorogenic probe for microtubules (fig. S4, A to C, and movie S1). By contrast, an iBMDM cell line stably expressing Flag-ASC showed that the main puncta formed upon nigericin stimulation, which were visualized by anti-Flag

<sup>1</sup>Department of Biological Chemistry and Molecular Pharmacology, Harvard Medical School, Boston, MA 02115, USA. <sup>2</sup>Program in Cellular and Molecular Medicine, Boston Children's Hospital, Boston, MA 02115, USA. <sup>3</sup>Department of Surgery, North Campus Research Complex, University of Michigan, Ann Arbor, MI 48109, USA. <sup>4</sup>Department of Rheumatology and Immunology, Xiangya Hospital, Central South University, Changsha, Hunan, China. <sup>5</sup>Departments of Cell Biology and Pediatrics, Harvard Medical School, Boston, MA 02115, USA. <sup>6</sup>Program in Innate Immunity, Department of Medicine, Division of Infectious Diseases and Immunology, University of Massachusetts Medical School, Worcester, MA 01605, USA. <sup>7</sup>Centre of Molecular Inflammation Research, Department of Clinical and Molecular Medicine, Norwegian University of Science and Technology, 7491 Trondheim, Norway. <sup>8</sup>Laboratory of Systems Pharmacology, Harvard Medical School, Boston, MA 02115, USA. <sup>9</sup>Harvard Medical School and Division of Gastroenterology, Boston Children's Hospital, Boston, MA 02115, USA. <sup>10</sup>Institute of Innate Immunity, Biomedical Center, University Hospitals, University of Bonn, Venusberg-Campus 1, 53127 Bonn, Germany.

\*These authors contributed equally to this work.

†Corresponding author. Email: wu@crystal.harvard.edu (H.W.); venkat.magupalli@childrens.harvard.edu (V.G.M.); roberto.negro@childrens.harvard.edu (R.N.); yqli@med.umich.edu (Y.L.)



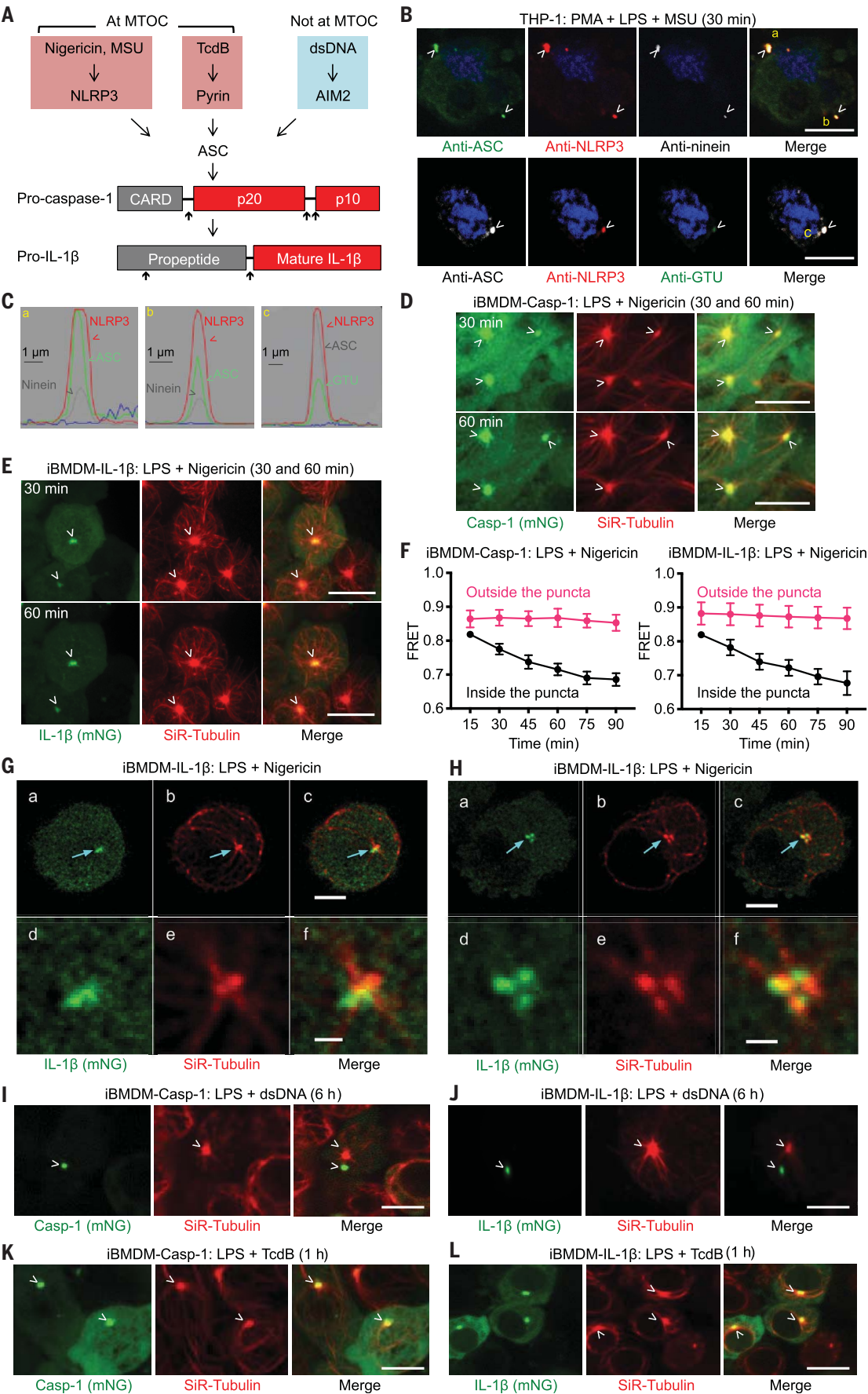


**Fig. 1. NLRP3 and pyrin inflammasomes, but not the AIM2 inflammasome, colocalize with the MTOC.** (A) The NLRP3, pyrin, and AIM2 inflammasome pathways triggered by nigericin or MSU, TcdB, and dsDNA, respectively. As shown below, NLRP3 and pyrin inflammasome puncta localize at the MTOC. Inflammasome activation culminates in pro-caspase-1 and pro-IL-1 $\beta$  processing. Upward arrows indicate processing sites. (B) Immunofluorescence images showing the colocalization of NLRP3 and ASC puncta with the centrosomal markers ninein and GTU in THP-1 cells. Blue represents nuclear staining by Hoechst 33342. (C) Line scan of intensity distribution profiles of puncta a, b, and c from (B). (D and E) Live-cell images of iBMDM-Casp-1 (D) and iBMDM-IL-1 $\beta$  (E) at 30 min (top panel) and 60 min (bottom panel) after nigericin stimulation showing colocalization of inflammasome puncta (depicted by mNeonGreen) with the MTOC (depicted by SiR-Tubulin staining that labels the microtubule network). (F) FRET analysis of caspase-1 cleavage and IL-1 $\beta$  processing at MTOC as a function of time for areas inside and outside the puncta in iBMDM-Casp-1 (left) and iBMDM-IL-1 $\beta$  (right) cells. FRET was calculated by dividing the FRET channel fluorescence intensity (donor

excitation with acceptor emission) with mTurquoise2 channel fluorescence intensity (donor excitation with donor emission). Data are shown as mean  $\pm$  SD for  $n = 10$  to 15 cells. (G and H) Recruitment of IL-1 $\beta$  to a region in proximity to the MTOC imaged using 3D LLSM. iBMDM-IL-1 $\beta$  cells stained with SiR-Tubulin were exposed to nigericin for 12 min (G) and 23 min (H). (a to c) Representative images deconvolved using the Richardson-Lucy algorithm corresponding to a single optical plane section. The arrows highlight the MTOC and the nearby locations where IL-1 $\beta$  was recruited. (d to f) Enlarged images of the regions indicated by the arrows. (I and J) Lack of colocalization of AIM2 inflammasome puncta with the MTOC in iBMDM-Casp-1 (I) and iBMDM-IL-1 $\beta$  (J) cells activated by dsDNA for 6 hours. (K and L) Colocalization of pyrin inflammasome puncta with the MTOC in iBMDM-Casp-1 (K) and iBMDM-IL-1 $\beta$  (L) cells activated by TcdB toxin for 1 hour. Images are representative of three or more independent experiments, and arrowheads indicate puncta or MTOC [(B), (D), (E), and (G) to (L)]. Scale bars: 10  $\mu$ m [(B), (D), (E)], 5  $\mu$ m [(G), (a) to (c); (H), (a) to (c); and (I) to (L)], and 1  $\mu$ m [(G), (d) to (f), and (H), (d) to (f)].

immunofluorescence, coincided with the MTOC (fig. S4D), suggesting that the green fluorescent protein (GFP) family of tags may have led to nonphysiological localization of ASC. Consequently, we did not use ASC for live-cell imaging of inflammasomes. Instead, we used iBMDM stable cell lines expressing fluorescent protein-fused pro-caspase-1 (iBMDM-Casp-1) or pro-IL-1 $\beta$  (iBMDM-IL-1 $\beta$ ).

To track both location and cleavage, a fluorescence resonance energy transfer (FRET) pair, mTurquoise2 (mTur) at the N terminus and mNeonGreen (mNG) at the C terminus, was fused together (fig. S5A). Both pro-caspase-1 and pro-IL-1 $\beta$  formed puncta at the MTOC upon nigericin stimulation (Fig. 1, D and E; fig. S5, B and C; and movies S2 and S3). For some cells, we also observed signal trails from the inflammasome puncta that matched the microtubule staining pattern (Fig. 1D, 60 min), suggesting trafficking of inflammasome complexes on the microtubule network. Three-dimensional (3D) lattice light-sheet microscopy (LLSM) (18) of nigericin-stimulated iBMDM-IL-1 $\beta$  cells at 12 and 23 min after treatment, respectively, further revealed that IL-1 $\beta$  was recruited to a region in close proximity to but not overlapping with the MTOC (Fig. 1, G and H, and movie S4). For both iBMDM-IL-1 $\beta$  and iBMDM-Casp-1 cells, FRET signals inside the puncta were high at the beginning, consistent with tethered FRET pairs, but decreased significantly with time, consistent with proteolytic processing (Fig. 1F). By contrast, the FRET signals outside the puncta stayed high (Fig. 1F). Thus, it is upon recruitment to the MTOC that pro-caspase-1 and pro-IL-1 $\beta$  are processed and activated.

To activate the AIM2 inflammasome, iBMDM-Casp-1 and iBMDM-IL-1 $\beta$  cells were transfected with dsDNA. Unlike NLRP3 stimulation, the puncta induced by AIM2 activation did not colocalize with the MTOC despite the dependence on ASC that was similar to that of NLRP3 (Fig. 1, I and J). By contrast, when iBMDM-Casp-1 and iBMDM-IL-1 $\beta$  cells were stimulated

with TcdB to activate the pyrin inflammasome, activation-induced puncta colocalized with the MTOC (Fig. 1, K and L, and movies S5 and S6). Similarly, immunofluorescent staining with anti-pyrin, anti-ASC, and anti-ninein antibodies confirmed the MTOC localization of the pyrin inflammasome (fig. S6).

#### Microtubule retrograde transport by HDAC6 is important for NLRP3 and pyrin inflammasome activation

A major cellular mechanism for the clearance of ubiquitinated protein aggregates, which are too large to be effectively degraded by the ubiquitin proteasome pathway, requires retrograde transport by the dynein adapter and the  $\alpha$ -tubulin deacetylase HDAC6 to form aggresomes at the MTOC for degradation by autophagy (19–23). The aggresome pathway is thought to play an important role in the regulation of protein aggregation diseases such as Alzheimer's disease and age-related macular degeneration (19, 21). Viruses including the influenza A virus are known to subvert the host aggresome pathway by forming viral inclusions at the MTOC in an HDAC6-dependent manner to facilitate replication and assembly (24, 25). The MTOC localization of NLRP3 and pyrin inflammasome puncta, their aggresome-like meshwork morphology (26), and ubiquitination of NLRP3 inflammasome components (27–30) suggest a possible link between inflammasomes and aggresomes.

To test the effects of HDAC6 and microtubule retrograde transport inhibition on NLRP3 function, we pretreated LPS-primed iBMDM-Casp-1 and iBMDM-IL-1 $\beta$  cells with microtubule, dynein, and HDAC6 inhibitors (31–33). Nigericin stimulation in iBMDM-Casp-1 and iBMDM-IL-1 $\beta$  cells pretreated with these inhibitors invariably failed to induce the generation of puncta. By contrast, untreated nigericin-stimulated cells readily formed puncta (fig. S7, A and B). Inhibitor pretreatment of WT iBMDMs markedly decreased nigericin-induced

caspase-1 processing (Fig. 2A), propidium iodide (PI) permeability (Fig. 2B), and IL-1 $\beta$  release (Fig. 2C and fig. S7C) without affecting nuclear factor  $\kappa$ B-dependent priming as measured by tumor necrosis factor  $\alpha$  (TNF $\alpha$ ) secretion (fig. S8A). Dynamin (also known as p50) is a subunit of the dynactin complex important in dynein function, the overexpression of which disrupts dynein-dependent transport (34). Stable expression of mRuby3-fused dynamin in iBMDM-Casp-1 and iBMDM-IL-1 $\beta$  cells severely compromised nigericin-induced punctum formation without affecting the MTOC localization of NEK7 (figs. S7, A and B, and S8B and movie S7) and caused defective caspase-1 processing, PI permeability, and IL-1 $\beta$  secretion (fig. S8, C to E). Thus, the microtubule-dynein machinery and the HDAC6 adapter both appear to be essential for NLRP3 inflammasome activation.

Our data contradict a previous report that increased  $\alpha$ -tubulin acetylation upon NLRP3 stimulation is responsible for dynein-dependent microtubule-mediated assembly of the NLRP3 inflammasome (35). Treatment with the HDAC6 inhibitors tubastatin A, roclitinostat, and tubacin markedly increased  $\alpha$ -tubulin acetylation. However, instead of increasing NLRP3 inflammasome activation, this treatment inhibited it (Fig. 2, A and D). MCC950, a control NLRP3 inhibitor that interferes with NLRP3 oligomerization (36), did not alter  $\alpha$ -tubulin acetylation but potentially impeded NLRP3 activation (Fig. 2D). Thus, retrograde transport by HDAC6 on the microtubule network aids NLRP3 and pyrin inflammasome activation independently of  $\alpha$ -tubulin acetylation.

We investigated the effects of pharmacological inhibition and dynamin overexpression in other inflammasomes. Consistent with the colocalization of the pyrin inflammasome with the MTOC, treatment with microtubule, dynein, and HDAC6 inhibitors or dynamin expression hindered TcdB-induced punctum formation (fig. S9, A to D) and compromised TcdB-induced caspase-1 processing, PI permeability, and



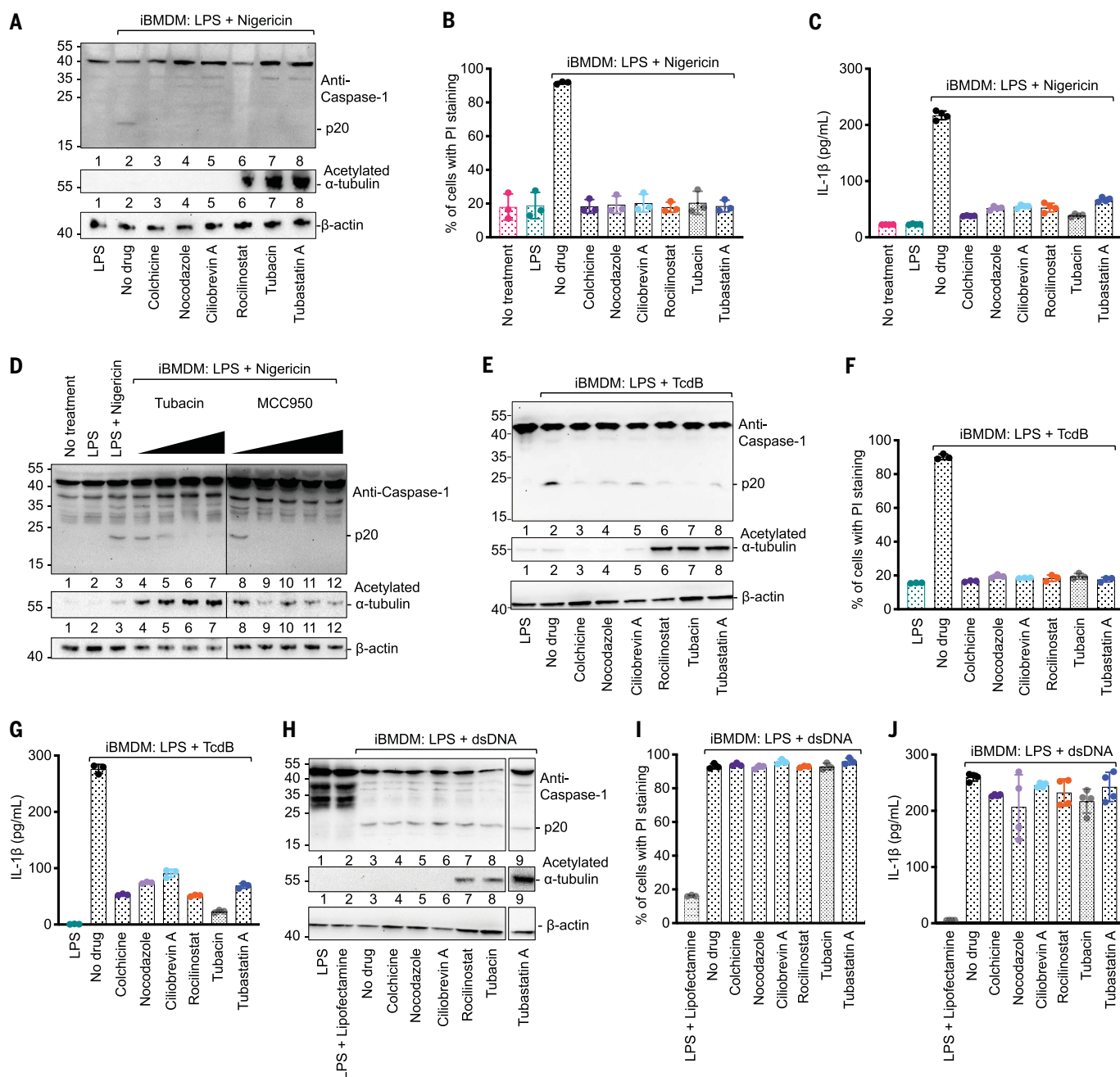


**Fig. 2. Microtubule retrograde transport is required for the activation of NLRP3 and pyrin inflammasomes but not the AIM2 inflammasome.** (A to C) NLRP3 inflammasome activation under various inhibition conditions analyzed by caspase-1 processing (p20) (A), quantification of PI permeability by flow cytometry (B), and secreted IL-1 $\beta$  quantified by ELISA (C). Colchicine and nocodazole are microtubule polymerization inhibitors; ciliobrevin A is a dynein ATPase inhibitor; and rocilinostat, tubacin, and tubastatin A are HDAC6 inhibitors. (D) Caspase-1 processing (p20) upon NLRP3 inflammasome activation with pretreatment of increasing concentrations of tubacin (left to right: 5, 10, 20,

and 40  $\mu$ M) or the NLRP3 inhibitor MCC950 (left to right: 0.1, 0.5, 1, 10, and 20  $\mu$ M). Anti-acetylated  $\alpha$ -tubulin and anti- $\beta$ -actin immunoblots are shown for tubulin acetylation and as the loading control, respectively. (E to G) Pyrin inflammasome activation under various pharmacological conditions analyzed by caspase-1 processing (p20) (E), PI permeability (F), and secreted IL-1 $\beta$  (G). (H to J) AIM2 inflammasome activation under various pharmacological conditions analyzed by caspase-1 processing (p20) (H), PI permeability (I), and secreted IL-1 $\beta$  (J). Data are shown as the mean  $\pm$  SD for three or four wells from three or more independent experiments.

IL-1 $\beta$  release (fig. S8, C to E, and Fig. 2, E to G). It is possible that the pyrin inflammasome is even more sensitive to microtubule transport inhibitors than the NLRP3 inflammasome. This is reflected in previous studies in which

lower concentrations of colchicine (1 to 4  $\mu$ M) inhibited the pyrin inflammasome alone (37, 38), whereas higher concentrations of colchicine (5 to 15  $\mu$ M), as in the present study (10  $\mu$ M), affected both the pyrin and

NLRP3 inflammasome (35). In contrast to the NLRP3 and pyrin inflammasomes, neither pharmacological treatment nor dynamin expression inhibited dsDNA-induced AIM2 inflammasome punctum formation (fig. S10, A

to D), caspase-1 processing, cell death, or IL-1 $\beta$  secretion (Fig. 2, H to J, and fig. S8, C to E), consistent with its failure to colocalize with the MTOC. Thus, HDAC6 is important for the activation NLRP3 and pyrin inflammasomes but not the AIM2 inflammasome.

### HDAC6 targeting compromises NLRP3 inflammasome activation

To further investigate the role of HDAC6 in inflammasome activation, we generated an HDAC6-deficient iBMDM cell line (*Hdac6*<sup>-/-</sup>) using the CRISPR/Cas9 system (39). Genomic polymerase chain reaction (PCR) confirmed that the targeting resulted in an internal deletion of the *Hdac6* gene (fig. S11A) and lack of HDAC6 protein expression (Fig. 3A). Normal physiology of *Hdac6*<sup>-/-</sup> iBMDMs was reflected in the unperturbed centrosome structure (fig. S11B), NEK7 distribution at the centrosome (fig. S11C), and transferrin uptake (fig. S11, D and E). HDAC6 deficiency also did not affect the expression of NLRP3, pyrin, ASC, pro-caspase-1, or pro-IL-1 $\beta$  upon LPS priming (fig. S11, F and G). However, the absence of HDAC6 resulted in markedly reduced caspase-1 cleavage (Fig. 3B), PI permeability (Fig. 3C), IL-1 $\beta$  secretion (Fig. 3D), and punctum formation (movies S8 and S9) upon nigericin stimulation.

To test the possibility that HDAC6 may have a role in ligand accessibility for NLRP3 stimuli that require endocytosis, we used several additional NLRP3 ligands. These included ATP, which directly engages its cell surface P2X7 receptor and should not depend on cellular uptake, as well as silica and alum, which are NLRP3-activating particulates and may require ligand accessibility. HDAC6 deficiency impaired caspase-1 cleavage, PI permeability, and IL-1 $\beta$  secretion after both ATP (fig. S12A) and silica and alum stimulation (fig. S12B). Additionally, puncta were formed upon treatment with all these ligands, whereas few puncta were observed in similarly treated *Hdac6*<sup>-/-</sup> iBMDMs (fig. S13, A to C). Thus, HDAC6 dependency exists for a broad range of NLRP3 activators regardless of their exact mechanism of action.

To corroborate the *Hdac6*<sup>-/-</sup> studies, we knocked down the expression of HDAC6 RNA and protein using small interfering RNA (siRNA) and the Trim-Away system (40), respectively. Seventy-two hours after iBMDMs were transfected with siRNA, HDAC6 was knocked down (fig. S14A) and iBMDMs exhibited markedly reduced nigericin-stimulated caspase-1 activation (fig. S14A), cell death (fig. S14B), and IL-1 $\beta$  secretion (fig. S14C). Similarly, electroporation of anti-HDAC6 antibody into TRIM21-iBMDMs resulted in substantial HDAC6 degradation after 24 hours (fig. S14D) and reduced caspase-1 processing (fig. S14D), PI permeability (fig. S14E), and IL-1 $\beta$  secretion (fig. S14F) after nigericin stimulation. By contrast, a previous study using small hairpin RNA (shRNA)

targeting HDAC6 showed modestly enhanced NLRP3 inflammasome activation in iBMDMs compared with a scrambled shRNA (41). However, no untreated iBMDMs were used as a control and it is unclear whether these shRNAs had off-target effects. Thus, these data further support the hypothesis that HDAC6 plays an important role in NLRP3 inflammasome activation.

### HDAC6 ubiquitin-binding domain, but not deacetylase activity, is required for NLRP3 activation

We reconstituted *Hdac6*<sup>-/-</sup> iBMDMs with human WT *HDAC6* and its deacetylase catalytic mutant H216A/H611A (DA) (42) (Fig. 3E and fig. S15A). WT *HDAC6* rescued caspase-1 activation upon nigericin stimulation (Fig. 3F). Unexpectedly, the deacetylase activity was not required to support NLRP3 inflammasome activation because the HDAC6 DA also restored NLRP3 inflammasome activation, as shown by caspase-1 processing (Fig. 3G), PI permeability (fig. S15B), and IL-1 $\beta$  secretion (fig. S15C). The effects of small-molecule HDAC6 inhibitors on inflammasome activation may be due to the inability of inhibitor-bound HDAC6 to interact with dynein (42, 43). Indeed, WT *HDAC6*-reconstituted *Hdac6*<sup>-/-</sup> iBMDMs were sensitive to the HDAC6 inhibitor rocilinostat. By contrast, *HDAC6* DA-reconstituted *Hdac6*<sup>-/-</sup> iBMDMs were insensitive to rocilinostat (Fig. 3H) because the inhibitor binding requires an intact active site. The  $\alpha$ -tubulin deacetylase activity of HDAC6 is also not required for HDAC6- and microtubule-mediated chemotaxis of T lymphocytes (44), whereas misfolded protein-induced aggresome formation appeared to require this catalytic activity (22). Thus, HDAC6 supports NLRP3 inflammasome activation by its scaffolding role in dynein-mediated transport without the need for its catalytic activity.

The C-terminal region of HDAC6 contains a zinc-finger domain for ubiquitin interaction (20). We reconstituted *Hdac6*<sup>-/-</sup> iBMDMs with the zinc-coordinating mutant H1160/H1164A (Ub1) and ubiquitin-binding site mutant W1182A (Ub2) (Fig. 3E and fig. S15A). Both mutants failed to rescue NLRP3 inflammasome activation shown by caspase-1 processing (Fig. 3G), PI permeability (fig. S15B), and IL-1 $\beta$  secretion (fig. S15C). Live-cell imaging of *Hdac6*<sup>-/-</sup> iBMDM-Casp-1 cells transiently transfected with mRuby3-fused WT human *HDAC6* showed a correlation between HDAC6 expression and punctum formation. Only cells with detectable HDAC6 expression formed puncta (Fig. 3I and movie S10). Furthermore, *Hdac6*<sup>-/-</sup> iBMDM-Casp-1 and iBMDM-IL-1 $\beta$  cells stably reconstituted with WT and DA mutant of mRuby3-HDAC6 rescued punctum formation, whereas those transfected with the zinc-finger mutants did not (Fig. 3J, fig. S15D, and movies S11 to S18).

Rocilinostat inhibited punctum formation in WT *HDAC6* reconstituted *Hdac6*<sup>-/-</sup> iBMDM-Casp-1 cells (Fig. 3J). Furthermore, NLRP3 activation by ATP, silica, and alum, as shown by PI permeability (fig. S16) and punctum formation (fig. S17), had the same dependence on the ubiquitin-interacting domain. Thus, HDAC6's ubiquitin-binding function is essential for its role in the NLRP3 inflammasome.

### Inflammasome puncta at the MTOC are subjected to autophagic regulation

Because HDAC6-mediated aggresome formation at the MTOC facilitates autophagosomal degradation, we hypothesized that inflammasome puncta are also subject to this regulation. Before nigericin stimulation, there was no colocalization of ASC with the microtubule-associated protein 1 light chain 3b (LC3b), a standard autophagosomal marker (Fig. 3K). By contrast, at 30 min after stimulation, ASC-containing inflammasome puncta were highly enriched in LC3b, suggesting induction of autophagy (Fig. 3L). We previously showed by anti-ASC immunogold electron microscopy (EM) that dense perinuclear structures represent inflammasome puncta (26). Here, we observed that the single perinuclear inflammasome punctum was surrounded by double-membrane bilayers, which are suggestive of autophagosome formation (fig. S18). LLSM analysis showed adjacency between an inflammasome punctum and the MTOC per se (Fig. 1, G and H). Thus, inflammasome puncta may be selectively engulfed without affecting the MTOC. Consistent with these findings, reduction or deficiency of the autophagic proteins LC3b, beclin-1, p62, and Atg16L1 can enhance inflammasome activation and maturation of IL-1 $\beta$  and IL-18 (30, 45, 46). Furthermore, IL-1 $\beta$  secretion was enhanced by the pharmacological blockade of autophagosome formation by 3-methyladenine (3-MA) (fig. S7C). As controls, a pan-caspase inhibitor (Z-VAD-FMK) and a caspase-1 inhibitor (YVAD-CHO) both reduced IL-1 $\beta$  secretion (fig. S7C). Thus, inflammasome puncta formed at the MTOC are regulated by autophagy.

### HDAC6 deficiency compromised activation of the pyrin inflammasome, but not the AIM2, NLRC4, and noncanonical inflammasomes

Consistent with the MTOC localization and the effects of HDAC6 inhibitors, pyrin inflammasome activation was compromised by knocking out *Hdac6*. This was evident in terms of caspase-1 cleavage, PI staining, IL-1 $\beta$  secretion, and puncta formation (Fig. 4, A to C, and movies S19 and S20). By contrast, dsDNA-induced AIM2 inflammasome activation in *Hdac6*<sup>-/-</sup> iBMDMs was similar to that in WT controls (Fig. 4, E to H). Reconstitution of WT and mutant human *HDAC6* into *Hdac6*<sup>-/-</sup> iBMDMs revealed that pyrin inflammasome



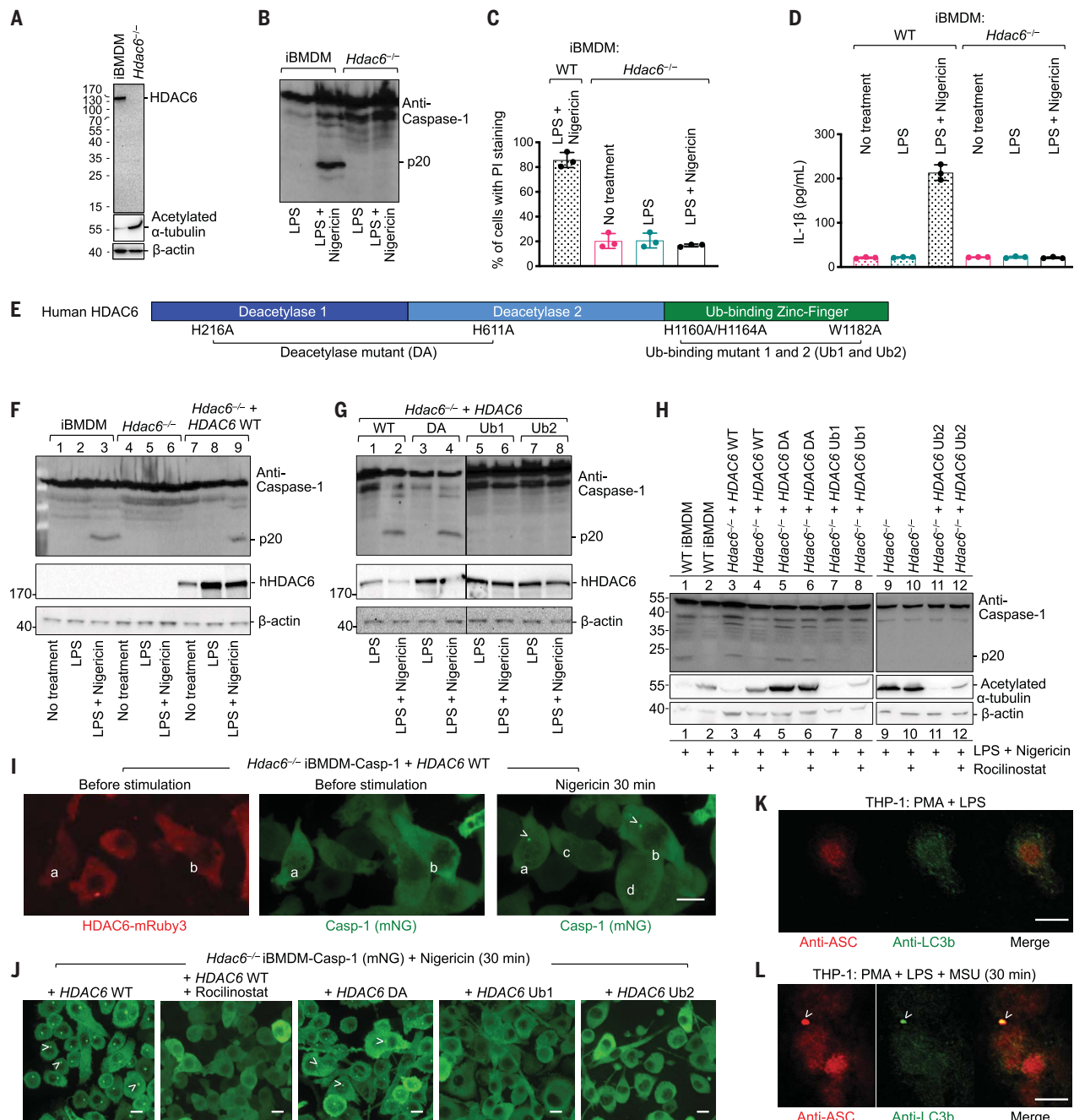


**Fig. 3. HDAC6 is required for NLRP3 inflammasome activation.** (A) Immunoblotting showing the absence of HDAC6 protein in CRISPR/Cas9 *Hdac6*<sup>-/-</sup> iBMDMs compared with WT iBMDMs. Loading control was provided by the anti- $\beta$ -actin antibody. The loss of HDAC6 leads to an increase in acetylated  $\alpha$ -tubulin depicted using anti-acetylated  $\alpha$ -tubulin antibody. (B to D) Compromised NLRP3 inflammasome activation in *Hdac6*<sup>-/-</sup> iBMDMs challenged with nigericin is shown for caspase-1 processing (B), PI permeability (C), and secreted IL-1 $\beta$  (D). Data are shown as the mean  $\pm$  SD for triplicate wells from three or more independent experiments in (C) and (D). (E) Domain architecture of human HDAC6 with important mutations (DA, Ub1, and Ub2) labeled. DA: H216A/H611A on catalytic residues, deacetylase mutant; Ub1: mutations H1160A/H1164A on zinc-coordinating residues; Ub2: mutation W1182A on the surface that binds ubiquitin. (F) Rescue of nigericin-mediated caspase-1 processing in *Hdac6*<sup>-/-</sup> iBMDMs by reconstituting with WT human HDAC6. (G) Analysis of nigericin-mediated caspase-1 processing in *Hdac6*<sup>-/-</sup> iBMDMs

reconstituted with WT HDAC6 and the DA, Ub1 and Ub2 mutants. (H) Sensitivity to rocilinoat in *Hdac6*<sup>-/-</sup> iBMDMs reconstituted with WT HDAC6, but not the DA mutant, as depicted by inhibition of p20 processing. (I) Rescue of nigericin-induced punctum formation in *Hdac6*<sup>-/-</sup> iBMDM-Casp-1 cells transfected with WT HDAC6-mRuby3. Arrowheads indicate puncta. Cells containing puncta had HDAC6 expression [(a) and (b)], whereas cells that do not contain puncta did not have HDAC6 expression [(c) and (d)]. (J) Rescue of nigericin-induced punctum formation in *Hdac6*<sup>-/-</sup> iBMDM-Casp-1 cells stably reconstituted with WT and DA mutant of HDAC6-mRuby3, but not with Ub1 and Ub2 mutants of HDAC6-mRuby3. Arrowheads indicate puncta. HDAC6 WT reconstituted cells failed to form puncta upon pretreatment by rocilinoat. (K and L) Inflammasome puncta formation and its link to autophagy analyzed by immunofluorescence of ASC and the autophagy marker LC3b before (K) and after (L) NLRP3 inflammasome stimulation. Arrowheads indicate puncta. Images are representative of three or more independent experiments. Scale bars, 10  $\mu$ m.

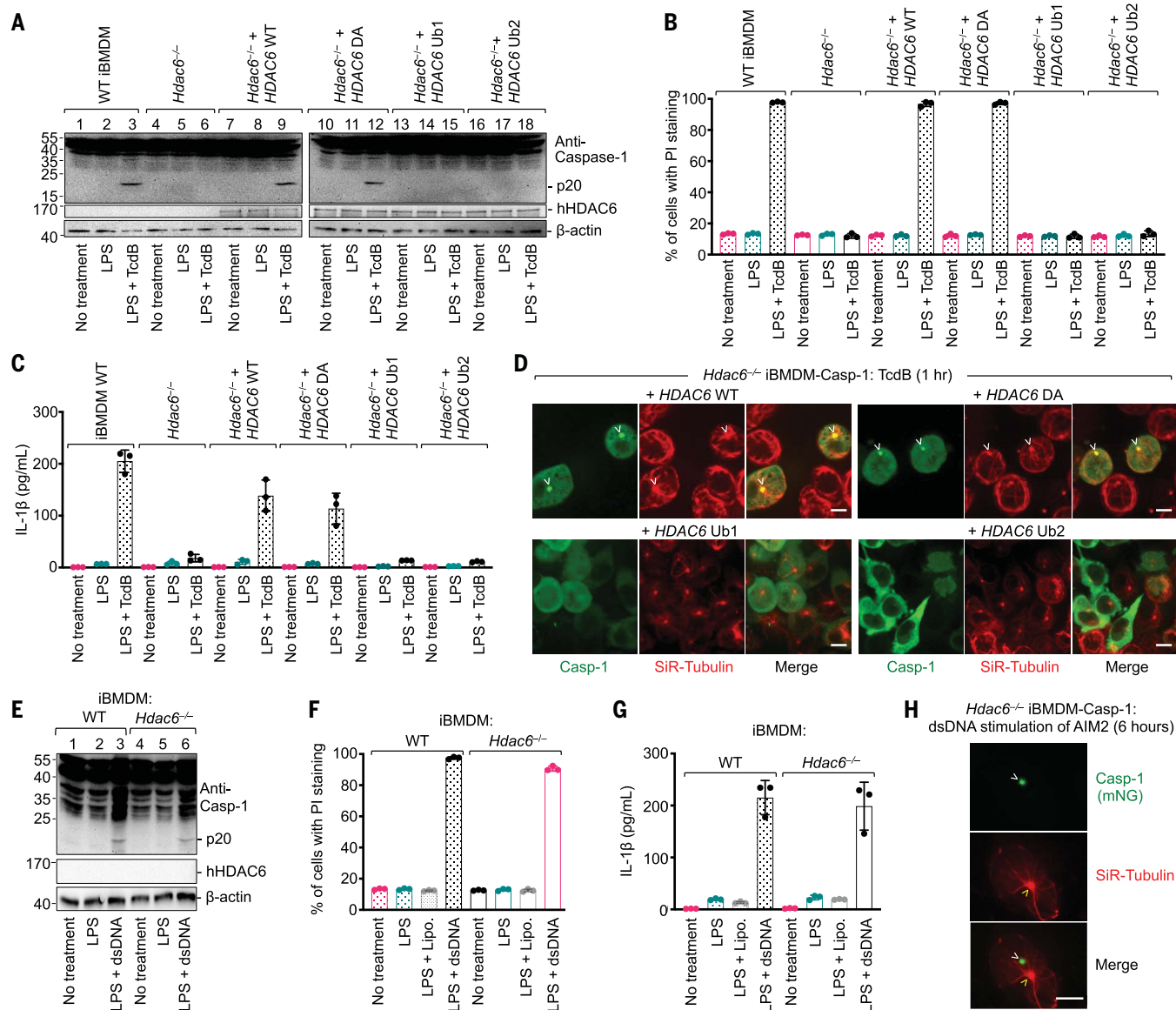


**Fig. 4. HDAC6 is required for pyrin inflammasome activation but not AIM2 inflammasome activation.** (A to D) Requirement of HDAC6 and its ubiquitin-binding ability in TcdB-induced pyrin inflammasome activation, as shown by caspase-1 processing (p20) (A), PI permeability (B), IL-1 $\beta$  secretion (C), and punctum formation (D). DA: H216A/H611A on catalytic residues, deacetylase mutant; Ub1: mutations H1160A/H1164A on zinc-coordinating residues; Ub2: mutation W1182A on the surface that binds ubiquitin.

(E to H) Lack of HDAC6 dependence in dsDNA-induced AIM2 inflammasome activation, as shown by caspase-1 processing (p20) (E), PI permeability (F), IL-1 $\beta$  secretion (G), and punctum formation (H). Arrowheads indicate puncta or MTOC. Data are shown as the mean  $\pm$  SD for triplicate wells from three or more independent experiments [(B), (C), (F), and (G)]. Images are representative of three or more independent experiments [(D) and (H)]. Scale bars, 5  $\mu$ m.

activation required its intact zinc-finger domain, but not its deacetylase activity, as shown by caspase-1 cleavage (Fig. 4A), PI staining (Fig. 4B), IL-1 $\beta$  secretion (Fig. 4C), and puncta formation (Fig. 4D).

Because the LPS-induced noncanonical inflammasome and the NLRC4 inflammasome are known to induce secondary NLRP3 activation (47–49), we generated CRISPR/Cas9 knockout of *Hdac6* in the *Nlrp3*<sup>-/-</sup> background. The noncanonical inflammasome engages mouse caspase-11 in iBMDMs but

does not engage caspase-1 for IL-1 $\beta$  processing (50, 51). PI staining indicated equivalent membrane disruption upon LPS transfection in *Nlrp3*<sup>-/-</sup> and *Nlrp3*<sup>-/-</sup>*Hdac6*<sup>-/-</sup> iBMDMs (Fig. 5A). The percentage of cells with caspase-11 activity was similar in *Nlrp3*<sup>-/-</sup> and *Nlrp3*<sup>-/-</sup>*Hdac6*<sup>-/-</sup> iBMDMs (Fig. 5B). For the NLRC4 inflammasome, we used *Legionella pneumophila* flagellin fused to the N-terminal domain of *Bacillus anthracis* lethal factor (FlaTox) (52). Inactive FlaTox that only engages TLR5 but not NAIP5 was used as a negative control.

FlaTox induced comparable caspase-1 processing and PI permeability in *Nlrp3*<sup>-/-</sup> and *Nlrp3*<sup>-/-</sup>*Hdac6*<sup>-/-</sup> iBMDMs (Fig. 5, C and D), supporting the notion that HDAC6 is dispensable for activation of the flagellin-NAIP5-NLRC4 inflammasome. NLRC4 inflammasome activation in *Nlrp3*<sup>-/-</sup> and *Nlrp3*<sup>-/-</sup>*Hdac6*<sup>-/-</sup> iBMDMs resulted in the formation of ASC puncta, but these puncta did not localize at the MTOC (Fig. 5E). These conclusions were confirmed in mouse primary BMDMs (fig. S19). Thus, HDAC6 only plays a role in inflammasomes



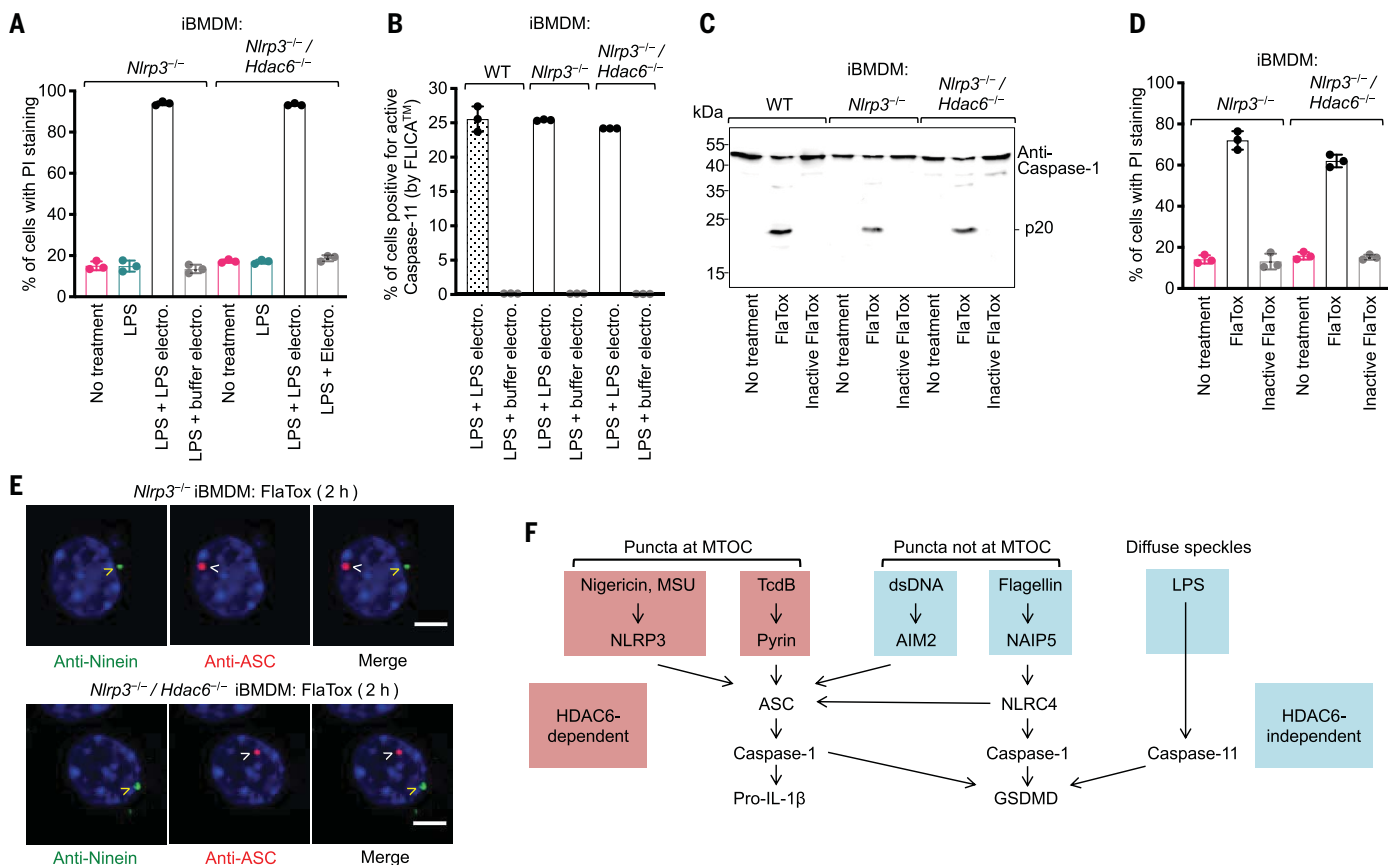


**Fig. 5. HDAC6 deficiency does not affect noncanonical and NLRC4 inflammasome activation in an *Nlrp3*<sup>-/-</sup> background.** (A and B) Non-canonical inflammasome activated by intracellular delivery of LPS (electroporation) quantified by PI permeability (A) and FAM-FLICA substrate cleavage by active caspase-11 (B). (C and D) NLRC4 inflammasome activation triggered by active FlaTox (inactive FlaTox served as a control) analyzed for caspase-1 processing (p20) (C) and PI permeability (D). Data are shown as the mean ± SD for triplicate wells from three or more independent

experiments. (E) Immunofluorescence analysis of NLRC4 punctum formation in *Nlrp3*<sup>-/-</sup> (top) and *Nlrp3*<sup>-/-</sup>/*Hdac6*<sup>-/-</sup> (bottom) iBMDMs upon treatment with FlaTox. Blue represents nuclear staining by Hoechst 33342. The NLRC4 inflammasome punctum represented by ASC staining is distinctly separated from the centrosomal marker ninein. Arrowheads depict puncta or MTOC. Images are representative of three or more independent experiments. Scale bars, 5 μm. (F) Summary of location of punctum formation and HDAC6 dependence in the different inflammasomes.

formed at the MTOC, as shown for NLRP3 and pyrin inflammasomes, but not for AIM2 and NLRC4 inflammasomes or the noncanonical inflammasome (Fig. 5F).

#### HDAC6 is required for transport of TGN-localized NLRP3

Diverse NLRP3 stimuli have been shown to disperse the trans-Golgi network (TGN), which recruits NLRP3 into multiple small speckles before ASC engagement (53). We observed partial colocalization between the TGN marker TGN38 and multiple NLRP3 speckles in *Asc*<sup>-/-</sup> iBMDMs after nigericin stimulation (Fig. 6A). Unexpectedly, in WT iBMDMs, TGN38 redistributed into a single punctum at the MTOC, which colocalized with the NLRP3 single punctum (Fig. 6B). This suggests that NLRP3 is transported by the dynein machinery while on TGN-derived vesicles. By contrast, in *Hdac6*<sup>-/-</sup> iBMDMs, NLRP3 showed multiple speckles similar to the TGN pattern observed in *Asc*<sup>-/-</sup> iBMDMs (Fig. 6C), confirming that HDAC6 is

required for the transport. NEK7 is required for NLRP3 activation (14–16), likely by bridging NLRP3 subunits in an inflammasome disk (54). However, NEK7 did not colocalize with NLRP3 at the TGN before HDAC6-mediated microtubule transport (Fig. 6D). This suggests that such transport may be required in NLRP3 activation to bring NLRP3 to the MTOC, where NEK7 resides. Subsequently, activated NLRP3 may nucleate ASC filament formation, which in turn recruits and activates caspase-1 to execute inflammasome effector functions.

#### HDAC6 is required for LPS- and MSU-induced inflammation in mice

To gain insights into the role of HDAC6 in vivo, we investigated an LPS-induced endotoxic shock model in mice using *Hdac6* deficiency and the HDAC6 inhibitor tubastatin A, as well as the NLRP3 inhibitor MCC950 (36). This model was chosen because it is known to engage secondary NLRP3 activation (55, 56) (Fig. 7, A to F, and fig. S20, A to H). Serum IL-1β levels were decreased

in mice challenged with LPS but treated with tubastatin A or MCC950 compared with mice challenged with LPS alone (Fig. 7, B and D). IL-18 and TNFα levels were also significantly reduced by tubastatin A or MCC950 treatment (fig. S20, A, C, and D). Harvested lung tissue showed less damage, such as septal mononuclear cell and lymphocyte infiltration, alveolar macrophage and neutrophil infiltration, and alveolar edema, in both the tubastatin A- and MCC950-treated groups, with a significantly reduced overall acute lung injury (ALI) score (Fig. 7, E and F, and fig. S20, G and H). Substantially decreased LPS-induced secretion of IL-1β and IL-18 and ALI were also recapitulated in *Hdac6*<sup>-/-</sup> mice compared with WT mice (Fig. 7C and fig. S20, B, E, and F). Collectively, these data support the requirement of HDAC6 in NLRP3 inflammasome activation in vivo.

To test a direct NLRP3 activation model, we used the bona fide NLRP3 stimulus MSU to induce peritonitis in mice (Fig. 7G). Consistent with the role of HDAC6 in the NLRP3

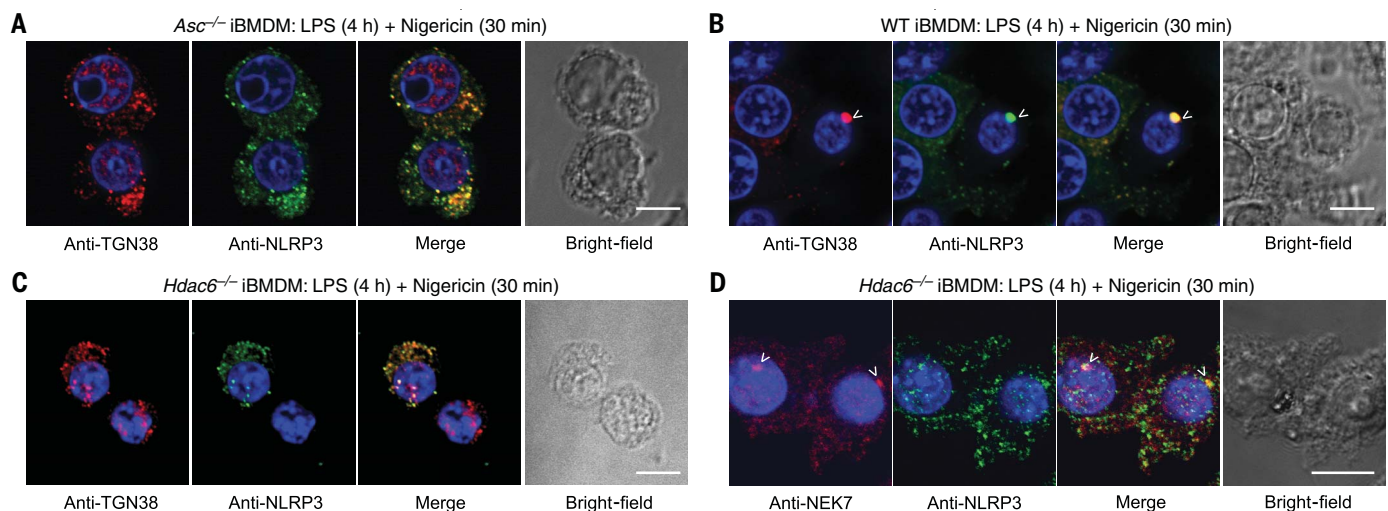


**Fig. 6. HDAC6 mediates microtubule transport of TGN-localized NLRP3.** (A to C) Immunofluorescence analysis of TGN38 and NLRP3 in *Asc*<sup>-/-</sup> iBMDMs (A), WT iBMDMs (B), and *Hdac6*<sup>-/-</sup> iBMDMs (C). (D) Immunofluorescence analysis of NEK7 and NLRP3 distribution in *Hdac6*<sup>-/-</sup> iBMDMs. Images are representative of three or more independent experiments containing ~100 cells. Arrowheads depict puncta. Scale bars, 10  $\mu$ m.

inflammasome, IL-1 $\beta$  and IL-18 secretion and neutrophil numbers in peritoneal lavage were decreased in *Hdac6*<sup>-/-</sup> mice compared with WT mice (Fig. 7, H and I, and fig. S20I). Treatment of WT mice with MCC950 exerted similar effects on IL-1 $\beta$  secretion and neutrophil recruitment as *Hdac6* deficiency (Fig. 7, J and K). Compared with LPS, MSU only induced minimal IL-18 activation, and MCC950 did not significantly reduce the level of IL-18 (fig. S20J). Additionally, MCC950 treatment in *Hdac6*<sup>-/-</sup> mice did not further suppress MSU-induced IL-1 $\beta$  and IL-18 secretion and neutrophil recruitment (Fig. 7, H and I, and fig. S20I). Thus, we have provided additional further evidence that NLRP3 inflammasome activation depends on HDAC6 in vivo.

## Discussion

Our studies support the marked mechanistic parallel between NLRP3 and pyrin inflammasome assembly and HDAC6-mediated transport of pathological aggregates to the MTOC for aggresome formation and degradation. Our results provide insights into the ever-evolving understanding of the complex process of inflammasome activation. They especially offer a framework to integrate the previously implicated role of the microtubule in inflammasome biology, including the importance of the centrosomal protein NEK7 and the microtubule-affinity regulating kinase 4 (MARK4) (14, 15, 57). The correlation between MTOC localization and sensitivity to microtubule transport disruption among inflammasomes further demonstrates the specificity of the mechanism and points to the importance of the physiological sites of assembly for their activation and regulation in cells (Fig. 5F). The microtubule polymerization inhibitor colchicine is an approved drug used

for both gout, an NLRP3 inflammasome disease, and familial Mediterranean fever, a pyrin inflammasome disease. Furthermore, the intermediate filament vimentin, an aggresome component, was shown to regulate NLRP3 inflammasome activation (22, 55). The additional role of the MTOC in inflammasome biology extends its previously established role in directional secretion by T cells at the immune synapse in adaptive immunity (58) to innate immunity.

Our data support a model of NLRP3 and pyrin inflammasome activation that depends on regulated ubiquitination (27–30) and engagement of the dynein adapter HDAC6 and possibly cargo adaptors such as p62. We do not yet know exactly which inflammasome components need to be ubiquitinated. Most likely, NLRP3 is not the inflammasome component recognized by the HDAC6-dynein machinery because the small NLRP3 clusters formed in the absence of ASC are not transported to assemble into one large punctum (53). ASC expression, however, leads to the formation of a single punctum per cell (59), and both NLRP3 and pyrin are ASC-dependent inflammasomes; critical ubiquitination sites on ASC and IL-1 $\beta$  have been mapped (27, 29). Because NLRP3 is already partially aggregated on the TGN, we hypothesize that small speckles of partially assembled inflammasomes are transported on TGN vesicles.

Why do some inflammasomes form at the MTOC? It is possible that the accumulated focal concentrations promote inflammasome assembly and caspase-1 activation. In the case of NLRP3, its MTOC targeting may ensure engagement of the upstream activator NEK7, a centrosomal kinase (14–16, 54). We further resolved that IL-1 $\beta$  conversion also occurs at

the MTOC, which although unexpected, is consistent with the recent finding that caspase-1 activity is most dominant at the puncta (60). Therefore, site-specific higher-order inflammasome complexes act as supramolecular organizing centers (61) to orchestrate inflammasome signaling. The flip side of MTOC localization may be the facilitation of autophagosome formation as a built-in checkpoint mechanism for inflammasome destruction to avoid unrestrained activation. The pericentriolar region is enriched in lysosomes (62), and the MTOC acts as a hub to promote the fusion of autophagosomes with lysosomes to accelerate inflammasome degradation. Thus, our data suggest that MTOC localization plays dual activating and inhibiting roles to achieve balanced inflammasome regulation. Although further mechanistic details of this model remain to be elucidated, our studies have clearly identified HDAC6 as a potential therapeutic target for inflammasome-associated diseases.

## Materials and methods

### Cloning and mutagenesis

The cDNA for human *IL-1B* was a generous gift from J. Yuan, Harvard Medical School. To construct the FRET reporters for IL-1 $\beta$  and caspase-1, the full-length inserts were amplified and ligated into the mTurquoise2-C1 plasmid (a gift from M. Davidson, Addgene no. 54842) between the XhoI and BamHI sites to yield mTurquoise2-IL-1 $\beta$  and mTurquoise2-Casp-1 with a SGLRSRG linker sequence. These constructs then were sub-cloned into the pLV-enhanced GFP (eGFP) lentiviral expression plasmid (a gift from P. Tsoulfas, Addgene no. 36083) between the XbaI and BamHI sites to yield mTurquoise2-IL-1 $\beta$ -eGFP and mTurquoise2-Casp-1-eGFP fusion proteins. Finally, eGFP was



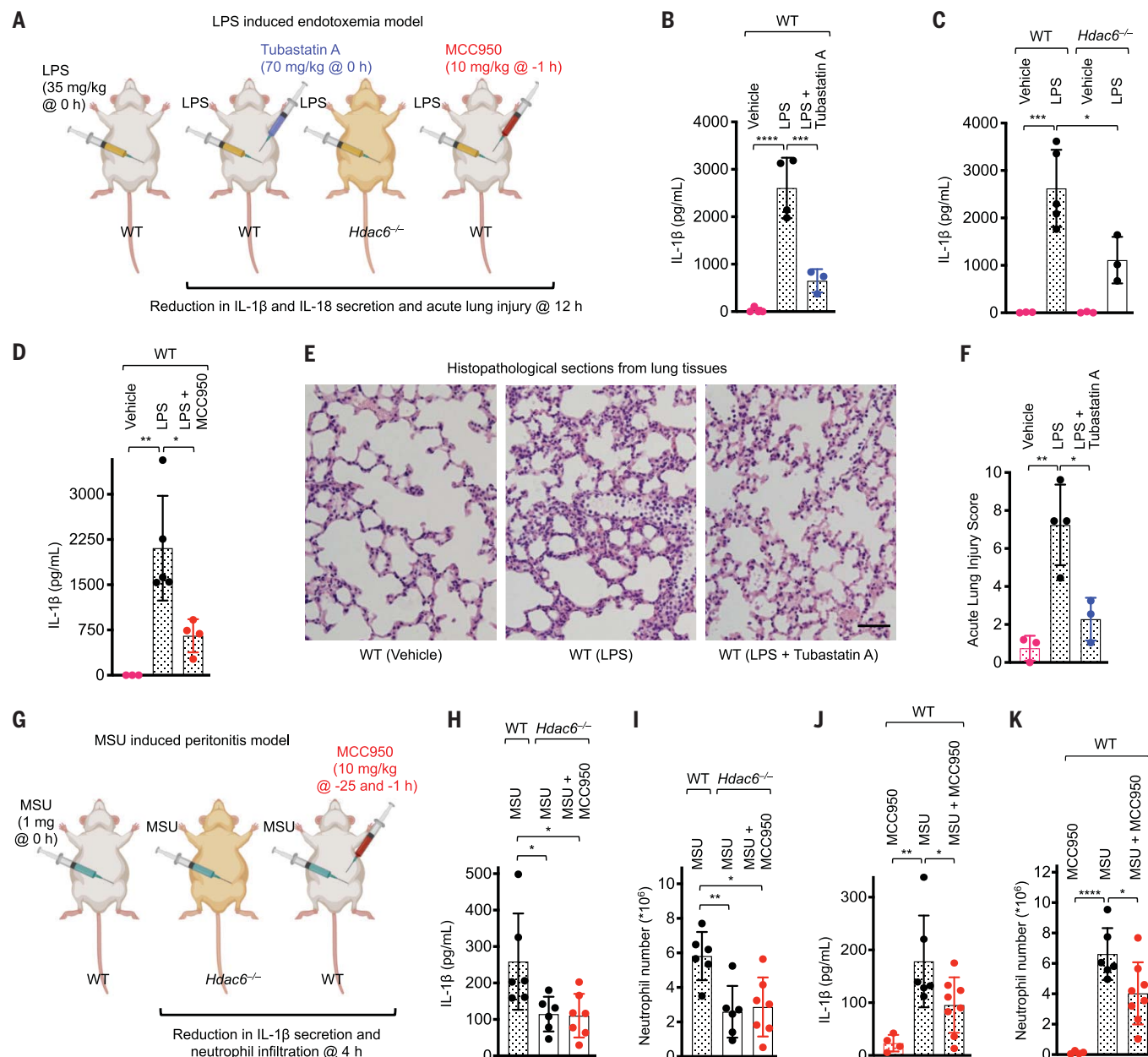


**Fig. 7. HDAC6 is required for NLRP3 inflammasome activation in mice.** (A to F) Mouse model of lethal LPS-induced endotoxemia. (A) Experimental layout with indicated timing and dose. (B to D) Effects of tubastatin A (HDAC6 inhibitor) (B), *Hdac6*<sup>-/-</sup> (C), or MCC950 (NLRP3 inhibitor) (D) on IL-1β secretion. Data are shown as mean ± SD (*n* = 3 to 5/group). (E) Effects of tubastatin A on ALI. Representative histopathological images from harvested lung tissues are shown. Scale bar, 50 μm. (F) Quantified lung injury depicted by defined clinical parameters in ALI score. ALI scores are shown as mean ± SD (*n* = 3 to 4/group). (G to K) Mouse model of MSU-induced peritonitis. (G) Experimental layout

with indicated timing and dose. (H and I) Effects of *Hdac6*<sup>-/-</sup> or *Hdac6*<sup>-/-</sup> + MCC950 on peritoneal IL-1β production (H) and neutrophil recruitment (I) upon MSU challenge. Data are shown as mean ± SD (*n* = 6 to 7/group). (J and K) Effects of MCC950 on peritoneal IL-1β production (J) and neutrophil recruitment (K) upon MSU challenge. Data are shown as mean ± SD (*n* = 5 to 8/group). For (B) to (D), (F), and (H) to (K), analysis of variance (ANOVA) followed by Bonferroni's multiple-comparisons test was performed for data analysis as used previously (66, 67). \**P* ≤ 0.05, \*\**P* ≤ 0.01, \*\*\**P* ≤ 0.001, and \*\*\*\**P* ≤ 0.0001.

replaced with mNeonGreen (mNG) with an engineered linker sequence of TGSGS between the AgeI and SalI sites using the following primers (Integrated DNA Technologies) to generate the mTurquoise2-IL-1β-mNG and mTurquoise2-Casp-1-mNG constructs: forward primer of 5'-GATGCAACCGGTAGCGG-

CTCAATGGTGAAGGGCGAG-3' and reverse primer of 5'-GATGCAGTCGACTTACTTGTA-CAGCTCGTC-3'.

The mRuby3-Dynamitin (p50) fusion construct was produced by first inserting mRuby3 into the pLV-eGFP plasmid between the XbaI and BamHI sites. Then, the full-length dynami-

tin insert was amplified and ligated between the AgeI and SalI sites from the cDNA (a gift from I. Cheeseman, Addgene no. 37388) using the following primers (Integrated DNA Technologies): forward primer of 5'-GATGCAACCGGTGGCGGCCGCTC-3' and reverse primer of 5'-GATGCAGTCGACTCACTTCCAGCTTC-3'.

The HDAC6-Flag-mRuby3 fusion construct was made by first subcloning mRuby3 into the pLV-eGFP plasmid between the AgeI and SalI sites to yield pLV-mRuby3, followed by amplifying HDAC6-Flag from the cDNA (P. Matthias) and ligating between XbaI and AgeI sites to yield HDAC6-Flag-mRuby3. The following primers were used (Integrated DNA Technologies): forward primer of 5'-GATGCA-TCTAGAAATGACCTCAACCGGCC-3' and reverse primer of 5'-GATGCAACCGGTCTTGTTCATCGT-CGTCC-3'.

The HDAC6 deacetylase mutant (DA, H216A/H611A) was produced similarly as above except with the plasmid pcDNA-HDAC6.DC-Flag (a gift from T.-P. Yao, Addgene no. 30483). The ubiquitin-binding mutants Ub1 (H1160A/H1164A) and Ub2 (W1182A) were produced by site-directed mutagenesis using the QuikChange Lightning Multi kit (Agilent Technologies) with the following primers (Integrated DNA Technologies): Ub1 forward primer: 5'-GTCGTT-ACATCAATGGCGCCATGCTCCAAGCCCATG-GAAATTCGGAC-3'; Ub1 reverse primer: 5'-GTCCAGAATTTCCATGGGCTTGGAGCATGG-CGCCATTGATGTAACGAC-3'; Ub2 forward primer: 5'-CATCGACCTGTGACCCCGTGT-TACTACTGTGACG-3'; and Ub2 reverse primer: 5'-CCTGACAGTAGTAACACGCGGCTGACAGT-CGATG-3'.

The GTU-eGFP construct was produced similarly as above except that it was cloned in the plasmid pLV-eGFP (a gift from P. Tsoufas, Addgene no. 36083). Before cloning, the existing XbaI site was mutated to NheI site in the plasmid. The human GTU insert was amplified using mRuby-Gamma-Tubulin-17 as a template (a gift from M. Davidson, Addgene no. 55864) using the following primers (Integrated DNA Technologies): forward primer of 5'-TTTTGCTAGCTGCCACCATGCCGAGGGAA-ATCATCA-3' and reverse primer of 5'-TT-TTACCGGTTTCTGCTCCTGGGTGCCC-3'.

pENTR221 mASC-tagRFP-T was generated by a BP gateway recombination reaction of pDONR221 with the PCR product attB1\_mASC-tagRFP-T\_attB2, catalyzed by BP clonase II (Thermo Fisher Scientific) according to the manufacturer's recommendations. Mouse ASC and tagRFP-T (63) coding sequences are connected by the linker SGGRSSGSGSTSGSG. pRRL mASC-tagRFP-T puro was generated by three-fragment gateway recombination of pRRL R4-R3 Puro with pENTR L4-R1 pMT (mouse metallothionein I promoter), pENTR221 mASC-EGFP, and pENTR R2-L3 STOP MCS using LR Clonase II Plus enzyme (Thermo Fisher Scientific). Vectors were kind gifts from S. Lindquist (Whitehead Institute for Biomedical Research, Cambridge, MA, USA).

Human ASC was subcloned into the pLV-mRuby3 plasmid (described previously) between the XbaI and AgeI sites using the following primers (Integrated DNA Technolo-

gies): forward primer of 5'-GATGCATCTA-GAATGGGGCGCGCGCGCG-3' and reverse primer of 5'-GATGCAACCGGTGGATCCGC-TTCCGCTCCGCTCCAGGTCC-3'. This resulted in pLV-ASC-mRuby3 with a short linker GSGSTGSAS between ASC and mRuby3. The full-length human Flag-ASC cDNA was generated by inserting the full-length human ASC-flag tagged at N terminus in the EcoRI and XhoI sites of plenti-CAG-IRES-GFP (a gift from W. Kaelin, Addgene no. 69047) using the following primers (Integrated DNA Technologies): forward primer of 5'-TGTGCTGTCTCATCAT-TTGGCAAAGAATTCGACTACAAAGACGAT-GACGACAAG-3' and reverse primer of 5'-CCAGTAACGTTAGGGGGGGGGCGGAATTG-ATCCCGCTCGAGTCAGCTCCGCTCCAGGTC-CTCCACC-3'.

pET15b LFn-Fla and LFn-Fla 3A fusion constructs were a gift from R. Vance (Addgene no. 84871 and 84872, respectively).

### Cell culture and transfection

iBMDMs from WT C57BL/6 mice were a gift from Prof. J. Kagan (Boston Children's Hospital, Boston, MA, USA). Immortalized *Asc*<sup>-/-</sup>, *Nlrp3*<sup>-/-</sup>, *Casp-1/11*<sup>-/-</sup> deficient macrophages were a gift from Prof. K. A. Fitzgerald (University of Massachusetts Medical School, Worcester, MA, USA). Immortalized *Nek7*<sup>-/-</sup> macrophages were a gift from Prof. G. Nuñez (University of Michigan, Ann Arbor, MI, USA).

HEK293T and iBMDMs were grown in Dulbecco's modified Eagle's medium (DMEM), with L-glutamine (Thermo Fisher Scientific, catalog no. 10569-004), supplemented with 10% fetal bovine serum (FBS) (Thermo Fisher Scientific, catalog no. 16000-044). Human monocytic THP-1 cells were maintained in Roswell Park Memorial Institute medium with L-glutamine (Thermo Fisher Scientific, catalog no. 11835-055) supplemented with 10% FBS and 0.05 mM 2-mercaptoethanol (Sigma-Aldrich, catalog no. D2650-100ML). Newly thawed HEK-Blue IL-1β cells were first grown in growth medium containing DMEM with L-glutamine, supplemented with heat-inactivated 10% FBS, 50 U/ml penicillin, 50 µg/ml streptomycin (Thermo Fisher Scientific, catalog no. 15140-163), and 100 µg/ml Normocin (Invivogen, catalog no. ant-nr-1). After two passages, the cells were grown in selective medium containing DMEM with L-glutamine, supplemented with heat inactivated 10% FBS, 100 µg/ml zeocin (Invivogen, catalog no. ant-zn-1), 200 µg/ml hygromycin B (Invivogen, catalog no. ant-hg-1), 50 U/ml penicillin, 50 µg/ml streptomycin, and 100 µg/ml Normocin. For preparation of L929-conditioned medium, 5×10<sup>5</sup> L929 cells were grown in a 75-cm<sup>2</sup> flask containing 50 ml of DMEM. Supernatant was collected on day 7 and passed through a 0.45-µm filter. The 25-ml aliquots of L929-conditioned medium were stored at -80°C.

All cells were maintained at 37°C with 5% CO<sub>2</sub>. For inflammasome activation studies, THP-1 cells were treated overnight with 300 ng/ml phorbol myristate acetate (Sigma-Aldrich, catalog no. P8139-5MG), followed by 4 hours of priming with 1 µg/ml LPS (Invivogen, catalog no. tlrl-b5lps). iBMDMs were primed for 4 hours with LPS. The following activators were used for inflammasome studies: 200 µg/ml MSU crystals (Santa Cruz Biotechnology, catalog no. sc-202711), 20 µM nigericin (Sigma-Aldrich, catalog no. N7143-5MG), 5 mM ATP (Sigma-Aldrich, catalog no. FLAAS-1VL), 100 µg/ml alum (Invivogen, catalog no. tlrl-alk), and 100 µg/ml Nano-SiO<sub>2</sub> (Invivogen, catalog no. tlrl-sio) for NLRP3 inflammasome activation; 0.5 µg/ml TcdB for pyrin inflammasome activation; 1 µg/ml dsDNA (Sigma-Aldrich, catalog no. P0883-25UN) for AIM2 inflammasome activation for the indicated time intervals; and active and inactive FlaTox (2 µg/ml) in combination with protective antigen (2 µg/ml) (List Biological Laboratories Inc., catalog no. 171E) for NLRC4 inflammasome activation.

For live-cell and-fixed cell confocal microscopy, cells were grown in microwell dishes (MatTek, catalog no. P35G-1.5-14-C). Transfection was performed at 60% confluency using linear PEI (MW 25,000; Polysciences Inc., catalog no. 23966-2) or FuGENE 6 (Promega, catalog no. E2691) according to the manufacturer's guidelines.

### Generation of stable cell lines

To generate stable cell lines, on day 0, lentivirus was produced using human embryonic kidney 293T (HEK293T) cells by cotransfecting 1 µg of pLV plasmid containing the gene, 750 ng of psPAX2 packaging plasmid, and 250 ng of pMD2.G envelope plasmid (both plasmids were a gift from D. Trono, Addgene no. 12260 and 12259, respectively). The transfected cells were incubated overnight. The following day (day 1), the medium was removed and the cells were replenished with 1 ml of fresh medium and incubated for another day. On day 2, the supernatant containing the virus was filtered using a 0.45-µm filter (Pall Corporation, catalog no. 4184) and used directly to infect iBMDMs with a spinfection protocol to increase the efficacy. Spinfection was performed at 2500g for 90 min at room temperature using 8 µg/ml polybrene (Santa Cruz Biotechnology, catalog no. sc-134220). After spinfection, cells were further incubated for the expression of marker genes to identify the positive clones. Positive clones were selected either by cell sorting or antibiotic selection, and colonies were expanded from single clones. Positive clones were extensively validated by PCR, immunoblotting, and immunofluorescence microscopy.

### FACS

Fluorescence-activated cell sorting (FACS) was performed using a FACSaria II cell sorter



from BD Biosciences equipped with FACS-Diva version 8.03. The instrument was set up with a 100- $\mu$ m nozzle at 20 psi, and the samples were introduced to the system at the lowest flow rate to minimize shear stress. The sorted populations were gated to exclude double, dead, and autofluorescent cells. The sort was performed with a purity precision mode.

#### Pharmacological inhibition

LPS-primed iBMDMs were pretreated for 1 hour with the HDAC6 inhibitors tubastatin A (10  $\mu$ M; Sigma-Aldrich, catalog no. SML0044), roclinator (30  $\mu$ M; Selleckchem, catalog no. S8001), or tubacin (20  $\mu$ M or 5 to 40  $\mu$ M; Enzo Life Sciences, catalog no. BML-GR362-0500), with the microtubule polymerization inhibitors colchicine (10  $\mu$ M; Sigma-Aldrich, catalog no. C9754-100MG) or nocodazole (10  $\mu$ M; Sigma-Aldrich, catalog no. M1404-2MG), or with the NLRP3 inhibitor MCC950 (0.1 to 20  $\mu$ M; CP-456773; Cayman Chemicals, catalog no. 210826-40-7, and Sigma-Aldrich, catalog no. PZ0280). Cytoplasmic dynein-dependent microtubule transport was inhibited using 25  $\mu$ M ciliobrevin A (TOCRIS Bioscience, catalog no. 4529). One hour after drug pretreatment, activation was performed either with nigericin (30 min), dsDNA (6 hours), or TcdB (1 hour). iBMDMs were pretreated with 5 mM 3-MA (Invivogen, catalog no. tlr1-3ma) for 6 hours to block autophagy.

#### Measurement of membrane disruption by PI-assisted flow cytometry

Membrane permeability was measured by PI exclusion assay. Untreated and treated cells were collected, including dead floating cells in the medium, and washed two times in PBS before resuspension in 2  $\mu$ g/ml PI (Immuno-Chemistry Technologies, catalog no. 638). The percentage of cells that took up PI was measured by flow cytometry (BD Biosciences, FACSaria II).

#### Detection of IL-1 $\beta$ by reporter HEK-Blue IL-1 $\beta$ cells

Procedures were performed according to manufacturer's instructions (Invivogen). Briefly, HEK-Blue IL-1 $\beta$  cells grown to 60% confluence were seeded on a flat-bottom, 96-well plate at ~50,000 cells per well. These cells were incubated overnight with 50  $\mu$ l of activated THP-1 or iBMDM supernatant along with the corresponding controls at 37°C in 5% CO<sub>2</sub>. The supernatants from the induced HEK-Blue IL-1 $\beta$  cells were collected for the soluble embryonic alkaline phosphatase assay (SEAP) using QUANTI-Blue (Invivogen, catalog no. rep-qb1). In this colorimetric assay, 150  $\mu$ l of resuspended QUANTI-Blue was incubated with 50  $\mu$ l of induced HEK-Blue<sup>TM</sup> IL-1 $\beta$  cell supernatant in a flat-bottom 96-well plate at 37°C from 30 min to 3 hours. SEAP levels were read

at 650 nm. The graphs were plotted using GraphPad Prism 7 software.

#### Detection of cytokines by ELISA

Detection kits for mouse IL-1 $\beta$  (Affymetrix eBioscience, catalog no. 88-7013; R&D Systems, catalog no. DY401), mouse TNF $\alpha$  (Invitrogen, catalog no. BMS607HS; R&D Systems, catalog no. DY410), mouse IL-18 (Thermo Fisher Scientific, catalog no. BMS618-3), and human IL-1 $\beta$  (BD Biosciences, catalog no. 557953) were used at the specified temperature and conditions according to the manufacturer's instructions. IL-18 concentration was also measured using sandwich enzyme linked immunosorbent assay (ELISA) with capture antibody: 500 ng/ml of mouse anti-IL-18 (MBL, catalog no. D047-3), standard (MBL, catalog no. B002-5), and biotinylated detecting antibody (MBL, catalog no. D048-6) at the Cancer Center Immunology Core at the University of Michigan.

#### Spinning-disk confocal live-cell microscopy

Sorted cells were grown in 35-mm petri dishes (10-mm microwell, no. 1.5 coverglass, MatTek, catalog no. P35G-1.5-14-C) and mounted in a 20/20 Technologies Bionomic microscope stage heated chamber warmed to 37°C. DMEM without phenol red (Thermo Fisher Scientific, catalog no. 21063-045) was used during image acquisition, with a layer of mineral oil on top of the medium to prevent evaporation. All images were collected with a Yokogawa spinning-disk confocal on a Nikon Ti inverted microscope equipped with Plan Apo phase 3 oil-immersion 40 $\times$  (1.3 numerical aperture) and oil-immersion 60 $\times$  (1.4 numerical aperture) lenses. The Perfect Focus System was in place for continuous maintenance of focus. IL-1 $\beta$  and caspase-1 mNG fluorescence was excited with a 491-nm line (selected with a 488/10 filter; Chroma, catalog no. 53044) from a 100mW cobalt diode laser and collected with a quadruple band pass dichroic mirror (Chroma, catalog no. 89100bs) and a 525/50 emission filter (Chroma, catalog no. 53051). Human HDAC6-mRuby3 and p50 dynamitin-mRuby3 fluorescence were excited with a 561-nm line 200-mW cobalt diode laser and collected with a quadruple band-pass dichroic mirror (Chroma, catalog no. 89100bs) and a 620/60 emission filter. SiR-Tubulin fluorescence was excited with a 642-nm line from a 101-mW cobalt diode laser and collected with a quadruple band-pass dichroic mirror (Chroma, catalog no. 89100bs) and a 700/75 emission filter (Chroma, catalog no. ET700/75m). Before acquisition, cells were primed with LPS for 4 hours, followed by activation using nigericin, MSU, and ATP for 30 min; alum and Nano-SiO<sub>2</sub> for 6 hours; TcdB for 1 hour; or dsDNA for 6 hours. SiR-Tubulin incubation was performed for 4 hours (Cytoskeleton, catalog no. CY-SC006 with 1  $\mu$ M SiR-Tubulin

and 10  $\mu$ M verapamil) to stain the microtubule network in live cells.

Images were acquired with a Hamamatsu ORCA ER cooled CCD camera controlled with MetaMorph version 7 software. Images were collected using an exposure time of 700 ms and 2  $\times$  2 binning, with illumination light shuttered between acquisitions. At each time point, z-series optical sections were collected with a step size of 1  $\mu$ m for the indicated time intervals using a Prior Proscan focus motor. Gamma, brightness, and contrast were adjusted on displayed images (identically for comparative image sets) using MetaMorph version 7 software.

#### Confocal laser-scanning microscopy

For imaging fixed cells, THP-1 cells or iBMDMs were seeded at a density of 2  $\times$  10<sup>5</sup>/ml. Eight to 12 hours after transfection, HEK293T cells were washed once with 1 $\times$  BRB80 buffer, fixed, and analyzed by immunofluorescence microscopy. After activation, THP-1 and iBMDMs were washed once with 1 $\times$  BRB buffer, fixed, and labeled with antibodies, as described in the immunolabeling and antibodies section. Confocal sections were obtained using an Olympus FV-1000 laser-scanning confocal microscope (Olympus America, Waltham, MA) with Olympus Fluoview version 3.0 software, using 405-nm excitation/425- to 475-nm emission, 488-nm excitation/500- to 545-nm emission, 559-nm excitation/575- to 620-nm emission, and 635-nm excitation/655- to 755-nm emission laser lines.

Images (512  $\times$  512 or 1024  $\times$  1024) were collected at 4  $\mu$ s/pixel using a 20 $\times$  [0.75 numerical aperture (NA), air objective], 40 $\times$  (0.95 NA, air objective), 40 $\times$  (1.15 NA, water-immersion objective), or 60 $\times$  (1.2 NA, water-immersion objective) lenses. The images were identically acquired and processed using Adobe Photoshop software. Distributions of fluorescence intensities and colocalization were analyzed by Velocity version 6.2.1 software.

#### LLSM

iBMDM-IL-1 $\beta$  cells stably expressing mTurquoise2-pro-IL-1 $\beta$ -mNG were plated on 5-mm round glass coverslips and stained with SiR-Tubulin. These coverslips were picked up with forceps and placed in the sample bath of the 3D LLSM (18). The sample was imaged in two ways. First, it was imaged in a time series in 3D using a dithered multi-Bessel lattice light-sheet by stepping the sample stage at 500-nm intervals in the s-axis equivalent to an ~261-nm translation in the z-axis. Thus, each 3D image took 450 ms to acquire for a total of 90 time points. Each 3D stack corresponded to a predesigned volume of ~30  $\mu$ m  $\times$  50  $\mu$ m  $\times$  4  $\mu$ m (300  $\times$  512  $\times$  15 pixels). The cell was excited with a 488-nm laser (~300-mW operating power with an illumination of ~400  $\mu$ W at the back aperture) and a 642-nm laser (~100-mW operating power

with an illumination of ~200  $\mu$ W at the back aperture) to acquire 15 imaging planes, each exposed for ~14.8 ms and recorded with two Andor iXon 897 EMCCD cameras. Second, the sample was imaged at a single time point in 3D using a dithered multi-Bessel lattice light-sheet by stepping the sample stage at 250 nm intervals in the *s*-axis equivalent to ~130-nm translation in the *z*-axis. The 3D image required 10 s to acquire. The stack corresponded to a predesigned volume of ~30  $\mu$ m  $\times$  50  $\mu$ m  $\times$  13  $\mu$ m (300  $\times$  512  $\times$  100 pixels). The cells were excited with a 488-nm laser (~300-mW operating power with an illumination of ~400  $\mu$ W at the back aperture) and a 642-nm laser (~15-mW operating power with an illumination of ~30  $\mu$ W at the back aperture) to acquire 100 imaging planes, each exposed for ~49.8 ms and recorded with two Andor iXon 897 EMCCD cameras. The inner and outer NAs of excitation were 0.35 and 0.4, respectively.

#### Immunolabeling and antibodies

THP-1 cells or iBMDMs were first primed for 4 hours with LPS and then activated with nigericin, TcdB, or dsDNA for various lengths of time. Fixative, permeabilization, and blocking buffers were prepared in Brinkley buffer 80 (BRB80) and kept at 37°C before use. BRB80 buffer was prepared freshly using 80 mM PIPES, 1 mM MgCl<sub>2</sub>, and 1 mM EGTA, titrated to pH 6.8 with a saturated solution of KOH.

Cells were fixed in 3.7% paraformaldehyde for 1 to 5 min at room temperature and then washed twice using BRB80 with 5-min intervals between washes. Permeabilization was performed for 5 min at room temperature using 0.15% Triton X-100 (in 1 $\times$  BRB80). Washing was performed to remove permeabilization buffer. Cells were then blocked for 1 hour at room temperature using blocking buffer (3% gelatin from cold-water fish skin prepared in 1 $\times$  BRB80). Cells were incubated with primary (3 hours to overnight) and secondary (1 hour) antibodies. Nuclei were stained using Hoechst 33342 (Invitrogen, catalog no. H3750). In between, extensive washing steps were performed to remove unbound antibodies and stains.

To stain for active caspase-1, the carboxy-fluorescein (FAM)-labeled inhibitor of caspase-1 (FAM-FLICA) kit (ImmunoChemistry Technologies, catalog no. 97) was used according to the manufacturer's instructions. After NLRP3 activation, the supernatant from macrophages was removed and was replaced with medium containing 1 $\times$  reconstituted fluorescently labeled inhibitor of active caspase-1 (FAM-FLICA), and incubated for 1 hour. Unbound fluorescent label was aspirated and replaced with regular medium. This washing step using regular medium was performed for 1 hour at 37°C at 5% CO<sub>2</sub>. After washing, live cells were fixed in 3.7% paraformaldehyde and stained as described above.

The following primary antibodies were used: anti-ASC (N-15), 1:1000 (rabbit polyclonal, Santa Cruz Biotechnology catalog no. sc-22514-R); anti-ASC (clone 2EI-7), 1:1,000 (mouse monoclonal, EMD Millipore, catalog no. 04-147); anti-ASC (D2W8U), 1:1,000 (rabbit monoclonal, Cell Signaling Technology, catalog no. 67824); anti-GTU, 1:500 (mouse monoclonal, Abcam catalog no. ab11316); anti-ninein (F-5), 1:2000 (goat polyclonal, Santa Cruz Biotechnology, catalog no. sc-376420); anti-pro-IL-1 $\beta$ , 1:1,000 (rabbit polyclonal, Abcam, catalog no. ab104279); anti-pro-IL-1 $\beta$ , 1:1000 (goat polyclonal, R&D Systems, catalog no. AF-401-NA); anti-TGN38, 1:1000 (rabbit polyclonal, Novus Biologicals, catalog no. NBP1-03495SS); anti-IL-1 $\beta$  (H-153), 1:1,000 (rabbit polyclonal, Santa Cruz Biotechnology, catalog no. sc-7884); anti-NLRP3, 1:100 (goat polyclonal, Abcam, catalog no. ab4207); mouse anti-caspase-1 (p20), 1:2000 (mouse monoclonal, Adipogen, catalog no. AG-20B-0042-C100); human anti-caspase-1 (p20), 1:2000 (mouse monoclonal, Adipogen, catalog no. AG-20B-0048-C100); human HDAC6 (D2E5), 1:1000 (rabbit monoclonal, Cell Signaling Technology, catalog no. 7558S); mouse HDAC6 (D2IB10), 1:1000 (rabbit monoclonal, Cell Signaling Technology, catalog no. 7612S); mouse anti-NEK7 (B-5), 1:1000 (mouse monoclonal, Santa Cruz Biotechnology, catalog no. sc-393539); anti-FLAG M2 1:500 (mouse monoclonal, Sigma-Aldrich, catalog no. A2220); rabbit immunoglobulin fraction (normal) (Agilent Dako, catalog no. X0903); goat IgG, polyclonal isotype control (Abcam, catalog no. ab37373); mouse IgG<sub>1</sub> isotype control (R&D Systems, catalog no. MAB002); anti- $\beta$ -actin 1:5000 (mouse monoclonal, Santa Cruz Biotechnology, catalog no. 47778); anti-acetylated  $\alpha$ -tubulin 1:5000 (mouse monoclonal, Sigma-Aldrich, catalog no. T7451); and anti-pyruvate kinase (PK) 1:1000 (rabbit monoclonal, Abcam, catalog no. ab214772).

The following secondary antibodies were used: Alexa Fluor 488-labeled goat anti-mouse IgG, IgM (H+L) (1:500, Thermo Fisher Scientific, catalog no. A10680); Alexa Fluor 647-labeled goat anti-rabbit IgG (H+L) (1:2000, Thermo Fisher Scientific, catalog no. A21244); Alexa Fluor 568-labeled donkey anti-goat IgG (H+L) (1:1000, Thermo Fisher Scientific, catalog no. A11057); Alexa Fluor 568-labeled goat anti-rabbit IgG (H+L) (1:1000, Thermo Fisher Scientific, catalog no. A11036); Alexa Fluor 647-labeled goat anti-mouse IgG (H+L) (1:1000, Thermo Fisher Scientific, catalog no. A21236); HRP-conjugated goat anti-rabbit IgG (1:10,000, Cell Signaling Technology, catalog no. 7074S); and HRP-conjugated horse anti-mouse IgG (1:10,000, Cell Signaling Technology, catalog no. 7076S).

The recruitment of neutrophils into the peritoneal cavity was analyzed by flow cytometry using Alexa Fluor 488-labeled rat anti-mouse Ly-6G/Ly-6C (Gr-1) IgG (1:200, BioLegend,

catalog no. 108417) and Alexa Fluor 700-labeled rat anti-mouse CD45 IgG (1:200, BioLegend, catalog no. 103128).

For the caspase-1 (p20) analysis, the whole cell lysate was prepared in 1 $\times$  sodium dodecyl sulfate (SDS) sample buffer as described previously (64). Lysates were resolved on 12.5% SDS-polyacrylamide gel electrophoresis (PAGE) gel and subjected to immunoblotting using the mouse caspase-1-specific antibodies listed above.

#### Affinity purification of NEK7 rabbit polyclonal antibodies

NEK7 antibody was a kind gift from K. Rhee of Seoul National University. The NEK7 antibody was affinity purified by incubation of the antiserum with a purified full-length NEK7 blotted on a nitrocellulose strip (SDS-PAGE separated and transferred on a nitrocellulose membrane). Elution was performed on a shaker at 50°C at 500 rpm (Mixer HC, USA Scientific) using 100 mM glycine, pH 2.5. The eluted antibody fraction was neutralized by 1.5 M Tris-HCl, pH 8.8.

#### Generation of Hdac6 CRISPR-knockout mouse iBMDMs

Two independent *Hdac6* CRISPR-knockout cell lines were generated. The first *Hdac6*<sup>-/-</sup> cell line was generated using two guide RNAs (gRNAs) targeting the first coding exon of mouse *Hdac6*. The sequences for mouse *Hdac6* gRNAs were as follows: gRNA#1, sense strand: 5'-AGTAGAAGAATCTTGGCCGG-3', antisense strand: 5'-CCGGCCAAGATTCTTCTACT-3'; gRNA#2, sense strand: 5'-GTGGGTGATTCTTCTGGGGAA-3', antisense strand: 5'-TTCCCCAGAAAATCACCCAC-3'. The second *Hdac6*<sup>-/-</sup> cell line was generated using two gRNAs targeting the fourth and eighteenth coding exon of mouse *Hdac6*. The sequences for mouse HDAC6 gRNAs were as follows: gRNA#3, sense strand: 5'-CCTGAGACAAGATGCCAGT-3', antisense strand: 5'-ACTGGCACTCTGTCTCAGGC-3'; gRNA#4, sense strand: 5'-CAGCGCATCTTACGCATCATC-3', antisense strand: 5'-ATGATGCGTAAGATGCGCTG-3'.

To clone the gRNA sequences into LentiCRISPR vector V2 (a gift from F. Zhang, Addgene no. 52961), the plasmid was cut and dephosphorylated with FastDigest BsmBI (Fermentas, catalog no. FD0454), and FastAP (Fermentas, catalog no. E0651) at 37°C for 2 hours. Oligonucleotides for the mouse HDAC6 gRNA sequences (Integrated DNA Technologies) were annealed by heating to 95°C for 5 min and cooling to 25°C at 1.5°C/min. The sequence of the oligonucleotides used for cloning into the LentiCRISPR vector V2 were as follows: forward primer for gRNA#1: 5'-CACCGAGTAGAAGAATCTTGGCCGG-3', reverse primer for gRNA#1: 5'-AAACCCGGCCAAGATTCTTCTACTC-3' and forward primer for gRNA#2:



5'-CACCGGTGGGTGATTTTCTGGGGAA-3', reverse primer for gRNA#2: 5'-AAACTTCCC-CAGAAAAATCACCCAC-3', forward primer for gRNA#3: 5'-CACCGCTGAGACAAGAGTGC-CAGT-3', reverse primer for gRNA#3: 5'-AAACACTGGCACTCTTGTCTCAGGC-3' and forward primer for gRNA#4: 5'-CACCGCA-GCGCATCTTACGCATCATC-3', reverse primer for gRNA#4: 5'-AAACATGATGCGTAAGAT-GCGCTGC-3'. Using T7 ligase (Enzymatics, catalog no. L602L), annealed oligos were ligated into gel-purified vectors at 25°C for 5 min. Cloned transfer plasmids were amplified using an endotoxin-free mini-prep kit (Qiagen, catalog no. 27104). LentiCRISPR vector V2 containing *Hdac6* gRNA was used to generate the virus in HEK293T cells followed by infection of WT mouse iBMDM cell line. Positive infected cells were isolated by puromycin selection (inserted into LentiCRISPR vector V2) at 10 µg/ml (Thermo Fisher Scientific, catalog no. A1113803). Colonies were expanded from single clones and selected for the puromycin resistance. *Hdac6*<sup>-/-</sup> iBMDMs were analyzed by PCR on genomic DNA and were further validated at the protein and functional levels.

#### Genomic PCR

Genomic DNA was extracted using the QiaAmp DNA mini kit (Qiagen, catalog no. 13323 according to the manufacturer's instructions, and the knockout phenotype was confirmed by PCR on the first coding exon using following primers (Integrated DNA Technologies): forward primer: 5'-GTGGGGTCTGAAGGATTCTGA-3'; reverse primer: 5'-TCTGTCTCAGGGTTCA-GATC-3'. For the second *Hdac6*<sup>-/-</sup> iBMDM cell line, the following primers were used to verify the positive clones: forward primer: 5'-TGATTGTAGTCCAGAGTGAA-3'; reverse primer: 5'-AGCAGGTAGGATGAGACA-3'.

#### Transferrin-647 uptake assay

For uptake assays, WT and *Hdac6*<sup>-/-</sup> cells were grown on 35-mm dishes, serum starved for 30 min in DMEM with 0.5% BSA-containing medium, and incubated with 25 µg/ml Alexa Fluor 647-conjugated transferrin (Invitrogen, catalog no. T23366) at 4°C for 10 min. Unbound Alexa Fluor 647-conjugated transferrin was removed by brief washing. Transferrin uptake was then analyzed by confocal laser-scanning microscopy.

#### Knockdown of HDAC6 using siRNA and TRIM21 ubiquitin ligase in iBMDMs

For *Hdac6*-knockdown experiments using siRNA, iBMDMs were electroporated with two *Hdac6* Silencer siRNAs (Thermo Fisher Scientific, catalog nos. 67164 and 158920 for siRNAs #1 and #2, respectively) or with Silencer siRNA Negative Control (Thermo Fisher Scientific, catalog no. AM4611). For HDAC6 protein knockdown using TRIM21 ubiquitin

ligase, iBMDMs (3.0×10<sup>6</sup>) stably overexpressing mouse pSMPP-mCherry-TRIM21 (a gift from L. James, Addgene no. 104971) were electroporated either with 2 µg of rabbit anti-human HDAC6 IgG that cross-reacts with mouse HDAC6 (Cell Signaling Technology, catalog no. 7612) or with 2 µg of isotype control IgG (Agilent Dako, catalog no. X0903), respectively. Nucleofection of siRNAs and HDAC6 antibody was performed with the Nucleofector 2b device (Lonza, catalog no. AAB-1001) using the Y-001 program according to the manufacturer's recommendations. siRNA- and HDAC6 antibody-electroporated cells were incubated for 72 and 24 hours, respectively, before being processed for further experiments.

#### Flow cytometry-assisted Caspase-11 FLICA assay

For the Caspase-11 FLICA assay (Immuno-Chemistry Technologies, catalog no. 97), after priming with LPS as described above, 1.0 × 10<sup>6</sup> buffer-electroporated and LPS-electroporated WT, *Nlrp3*<sup>-/-</sup>, or *Nlrp3*<sup>-/-</sup>/*Hdac6*<sup>-/-</sup> iBMDMs were incubated with medium containing 1× reconstituted fluorescently labeled inhibitor of active caspase (FAM-FLICA) and incubated for 1 hour. Cells were then washed three times with 1× apoptosis wash buffer and centrifuged at 218g for 10 min before being resuspended in regular DMEM and analyzed with a FACS Aria II flow cytometer.

#### Mice

Male and female C57BL/6J WT and *Hdac6*<sup>-/-</sup> mice (8 to 10 weeks old) were purchased from The Jackson Laboratory (Bar Harbor, ME). Animals were housed in an animal facility for 3 days before any procedures. All animal experiments were performed in compliance with guidelines approved by the institutional animal care and use committee at the University of Michigan (protocol no. PRO00008861).

#### In vivo mouse model of endotoxic shock

Three experiments were performed. First, WT mice were randomly divided into three groups to test the effect of the HDAC6 inhibitor tubastatin A: (i) WT + dimethyl sulfoxide (DMSO) vehicle (1 µl/g mouse body weight), (ii) WT + lipopolysaccharides (LPS, 35 mg/kg in PBS; L2630; SigmaAldrich) + vehicle, and (iii) WT + LPS + tubastatin A (HDAC6 inhibitor, 70 mg/kg) + vehicle. Tubastatin A and vehicle were administered immediately after the intraperitoneal LPS challenge. Second, WT and *Hdac6*<sup>-/-</sup> mice were randomly divided into four groups to test the effect of *Hdac6* deletion: (i) WT + vehicle, (ii) WT + LPS + vehicle, (iii) *Hdac6*<sup>-/-</sup> + vehicle, and (iv) *Hdac6*<sup>-/-</sup> + LPS + vehicle. LPS and vehicle were similarly administered intraperitoneally. Third, WT mice were randomly divided into three groups to test the effect of the NLRP3 inhibitor MCC950:

(i) WT + DMSO vehicle (1 µl/g mouse body weight), (ii) WT + LPS (35 mg/kg in PBS; L2630; SigmaAldrich) + vehicle, and (iii) WT + LPS + MCC950 (10 mg/kg) + vehicle. MCC950 and vehicle were administered 1 hour before the intraperitoneal LPS challenge. For all experiments, blood was collected at 12 hours after LPS injection. Serum was prepared by centrifugation of the blood at 500g at 4°C for 20 min and stored at -80°C for further use. Lung tissues were harvested for ALI scoring. Circulating levels of IL-1β and TNFα were measured using the mouse IL-1β/IL-1F2 DuoSet ELISA (DY401; R&D Systems) and mouse TNFα DuoSet ELISA (DY410-05; R&D Systems).

#### Histological analysis of ALI

Lung tissues were fixed in formalin and transferred to 70% ethanol before being embedded in paraffin and sliced into 5-µm sections. Hematoxylin & eosin staining was performed according to standard procedures. ALI scoring was performed by a pathologist blinded to the treatment assignment of the samples. In brief, ALI was classified into six categories based on the parameters of (i) septal mononuclear cell and/or lymphocyte infiltration, (ii) septal hemorrhage and congestion, (iii) neutrophils, (iv) alveolar macrophages, (v) alveolar hemorrhage, and (vi) alveolar edema. The severity of each category was graded from 0 (minimal) to 3 (maximal), and the total score was calculated by adding the scores in each of these categories.

#### In vivo mouse model of MSU-induced peritonitis

Peritonitis was induced by intraperitoneal injection of MSU crystals (1 mg; tlr-msu-25; Invivogen) in 200 µl of sterile PBS with or without intraperitoneal pretreatment with MCC950 (10 mg/kg) at 25 hours and 1 hour before the MSU challenge. After 4 hours, mice were euthanized by CO<sub>2</sub> exposure. Peritoneal cavities were flushed with 5 ml of cold PBS. Peritoneal lavage was centrifuged at 94g for 5 min. Cell pellets were collected, and the recruitment of CD45<sup>+</sup>/Ly6G<sup>+</sup> neutrophils into the peritoneal cavity was analyzed by flow cytometry. IL-1β levels were measured using ELISA (MLB00C; R&D Systems) after the peritoneal lavage supernatant was concentrated using an Amicon Ultra-0.5 Centrifugal Filter (UFC501096; Millipore).

#### Bone marrow isolation and BMDM differentiation

Bone marrow isolation and differentiation were performed in sterile and aseptic conditions in a laminar flow hood as described previously (65). The bones were flushed with 5 ml of PBS using a syringe fitted with a 25-G needle. The collected bone marrow was gently resuspended and passed through a 70-µm sterile cell strainer (Fisher Scientific, catalog no. 22363548). Cells were sedimented at 400g for 5 min at

room temperature. The cells were carefully collected in 100 × 20 mm sterile petri dishes containing 10 ml of conditioned media (DMEM + 10% FBS, penicillin/streptomycin, and 10% L929). On day 3, the dishes were supplemented with an additional 10 ml of conditioned medium (total 20 ml volume). Most cells were found to be adherent to the dish. Further growth was allowed until day 6, when the cells were split for the experiments performed on day 7.

### FRET analysis

For FRET channel images, a 447-nm laser was used in conjunction with a 535/30 emission filter. All images were collected with a Yokogawa spinning-disk confocal on a Nikon Ti inverted microscope equipped with Plan Apo phase 3 oil-immersion 60× lens (1.4 NA). The Perfect Focus System was in place for continuous maintenance of focus. Image processing was mainly performed using MATLAB 2014b. Images were imported from the original files and sorted into channels. All meta-data were extracted and saved. Dark current camera noise was corrected for using images acquired each session. Shading or “flat-field” correction based on empty fields from each sample was applied to correct for uneven illumination patterns. A background mask was generated by thresholding at a value three standard deviations above background, where the background intensity distribution is estimated by fitting the “left half” of a Gaussian function (the portion below its mean) to the left shoulder of the image intensity histogram. This mask was then used to find and subtract the average background intensity on a frame-by-frame basis. For all FRET calculations, the data were prefiltered with a 3 × 3 pixel Gaussian filter. Because the tension sensor module is a single-chain construct, FRET can be calculated by dividing the FRET channel fluorescence intensity (donor excitation with acceptor emission) with the mTurquoise2 channel fluorescence intensity (donor excitation with donor emission). To minimize artifacts from division of small integers, only pixels that had a value three times above the background standard deviation of the current frame were used. FRET data were visualized using an inverted heat map. The quantification of the loss of FRET inside and outside the puncta (as control) was performed using Fiji software on the inverted heat map.

### Embedding in resin (plastic sections) for TEM

For transmission electron microscopy (TEM), iBMDMs after nigericin activation were processed for plastic embedding as follows. Cells were incubated in fixative for 1 hour at room temperature. A 2× fixative mixture was added in a 1:1 ratio to the medium in the dish containing the cells to prevent shock and allow gentle fixation. Fresh fixative was prepared

using 1.25% paraformaldehyde, 2.5% glutaraldehyde, and 0.03% picric acid in a 0.1 M sodium cacodylate buffer, pH 7.4. After fixation, cells were washed three times in 0.1 M sodium cacodylate buffer, followed by incubation with 1% osmium tetroxide/1.5% potassium ferrocyanide for 1 hour at room temperature. Cells were then washed in water three times and incubated in aqueous 1% uranyl acetate for 30 min. This was followed by another three rounds of washing with water.

Dehydration steps were performed twice in grades of alcohol (70% ethanol for 15 min, 90% ethanol for 15 min, and 100% ethanol for 15 min. Samples were then placed in propyleneoxide for 1 hour and infiltration was performed with Epon mixed 1+1 with propyleneoxide for 2 to 3 hours at room temperature. Samples were moved to the embedding mold filled with freshly mixed Epon and allowed to polymerize for 24 to 48 hours at 60°C. Ultrathin sections (~60 nm) were cut on a Reichert Ultracut-S microtome, placed on copper grids, and stained with lead citrate. The grids from above-mentioned EM procedures were examined in a JEOL 1200EX 80 KeV TEM and images were recorded with an AMT 2k CCD camera (Harvard Medical School core facility).

### Protein expression and purification

pET15b LFn-Fla and LFn-Fla 3A fusion constructs were transfected into *Escherichia coli* BL21 (DE3) cells and grown in LB medium supplemented with ampicillin. Cells were grown at 37°C until the optical density (600 nm) reached 0.8. Protein expression was induced with 0.2 mM isopropyl-β-D-thiogalactopyranoside at 18°C overnight. Cells were then harvested and resuspended in lysis buffer (20 mM Tris-HCl, pH 7.4, 150 mM NaCl, 10 mM imidazole, and 5 mM β-mercaptoethanol). The proteins were purified by affinity chromatography using Ni-NTA beads (Qiagen). The proteins were further purified to homogeneity by size-exclusion chromatography in lysis buffer (20 mM HEPES, pH 7.4, 150 mM NaCl, 2 mM dithiothreitol) on a Superdex-200 column (GE Healthcare Life Sciences). Protein purified to homogeneity was analyzed by SDS-PAGE.

### REFERENCES AND NOTES

1. P. Broz, V. M. Dixit, Inflammasomes: Mechanism of assembly, regulation and signalling. *Nat. Rev. Immunol.* **16**, 407–420 (2016). doi: [10.1038/nri.2016.58](https://doi.org/10.1038/nri.2016.58); pmid: [27291964](https://pubmed.ncbi.nlm.nih.gov/27291964/)
2. V. A. Rathinam, S. K. Vanaja, K. A. Fitzgerald, Regulation of inflammasome signaling. *Nat. Immunol.* **13**, 333–342 (2012). doi: [10.1038/ni.2237](https://doi.org/10.1038/ni.2237); pmid: [22430786](https://pubmed.ncbi.nlm.nih.gov/22430786/)
3. M. Lamkanfi, V. M. Dixit, Mechanisms and functions of inflammasomes. *Cell* **157**, 1013–1022 (2014). doi: [10.1016/j.cell.2014.04.007](https://doi.org/10.1016/j.cell.2014.04.007); pmid: [24855941](https://pubmed.ncbi.nlm.nih.gov/24855941/)
4. T. Strowig, J. Henao-Mejia, E. Elinav, R. Flavell, Inflammasomes in health and disease. *Nature* **481**, 278–286 (2012). doi: [10.1038/nature10759](https://doi.org/10.1038/nature10759); pmid: [22258606](https://pubmed.ncbi.nlm.nih.gov/22258606/)
5. M. Bäck, G. K. Hansson, Anti-inflammatory therapies for atherosclerosis. *Nat. Rev. Cardiol.* **12**, 199–211 (2015). doi: [10.1038/nrcardio.2015.5](https://doi.org/10.1038/nrcardio.2015.5); pmid: [25666404](https://pubmed.ncbi.nlm.nih.gov/25666404/)

6. Q. Yin, T. M. Fu, J. Li, H. Wu, Structural biology of innate immunity. *Annu. Rev. Immunol.* **33**, 393–416 (2015). doi: [10.1146/annurev-immunol-032414-112258](https://doi.org/10.1146/annurev-immunol-032414-112258); pmid: [25622194](https://pubmed.ncbi.nlm.nih.gov/25622194/)
7. H. Xu et al., Innate immune sensing of bacterial modifications of Rho GTPases by the Pyrin inflammasome. *Nature* **513**, 237–241 (2014). doi: [10.1038/nature13449](https://doi.org/10.1038/nature13449); pmid: [24919149](https://pubmed.ncbi.nlm.nih.gov/24919149/)
8. F. Martinon, K. Burns, J. Tschopp, The inflammasome: A molecular platform triggering activation of inflammatory caspases and processing of proIL-β. *Mol. Cell* **10**, 417–426 (2002). doi: [10.1016/S1097-2765\(02\)00599-3](https://doi.org/10.1016/S1097-2765(02)00599-3); pmid: [12191486](https://pubmed.ncbi.nlm.nih.gov/12191486/)
9. X. Liu et al., Inflammasome-activated gasdermin D causes pyroptosis by forming membrane pores. *Nature* **535**, 153–158 (2016). doi: [10.1038/nature18629](https://doi.org/10.1038/nature18629); pmid: [27383986](https://pubmed.ncbi.nlm.nih.gov/27383986/)
10. J. Ding et al., Pore-forming activity and structural autoinhibition of the gasdermin family. *Nature* **535**, 111–116 (2016). doi: [10.1038/nature18590](https://doi.org/10.1038/nature18590); pmid: [27281216](https://pubmed.ncbi.nlm.nih.gov/27281216/)
11. V. Hornung et al., AIM2 recognizes cytosolic dsDNA and forms a caspase-1-activating inflammasome with ASC. *Nature* **458**, 514–518 (2009). doi: [10.1038/nature07725](https://doi.org/10.1038/nature07725); pmid: [19158675](https://pubmed.ncbi.nlm.nih.gov/19158675/)
12. J. Wu, T. Fernandes-Alnemri, E. S. Alnemri, Involvement of the AIM2, NLR4, and NLRP3 inflammasomes in caspase-1 activation by *Listeria monocytogenes*. *J. Clin. Immunol.* **30**, 693–702 (2010). doi: [10.1007/s10875-010-9425-2](https://doi.org/10.1007/s10875-010-9425-2); pmid: [20490635](https://pubmed.ncbi.nlm.nih.gov/20490635/)
13. G. A. Pihan, Centrosome dysfunction contributes to chromosome instability, chromoanagenesis, and genome reprogramming in cancer. *Front. Oncol.* **3**, 277 (2013). doi: [10.3389/fonc.2013.00277](https://doi.org/10.3389/fonc.2013.00277); pmid: [24282781](https://pubmed.ncbi.nlm.nih.gov/24282781/)
14. Y. He, M. Y. Zeng, D. Yang, B. Motro, G. Núñez, NEK7 is an essential mediator of NLRP3 activation downstream of potassium efflux. *Nature* **530**, 354–357 (2016). doi: [10.1038/nature16959](https://doi.org/10.1038/nature16959); pmid: [26814970](https://pubmed.ncbi.nlm.nih.gov/26814970/)
15. H. Shi et al., NLRP3 activation and mitosis are mutually exclusive events coordinated by NEK7, a new inflammasome component. *Nat. Immunol.* **17**, 250–258 (2016). doi: [10.1038/ni.3333](https://doi.org/10.1038/ni.3333); pmid: [26642356](https://pubmed.ncbi.nlm.nih.gov/26642356/)
16. J. L. Schmid-Burgk et al., A Genome-wide CRISPR (clustered regularly interspaced short palindromic repeats) screen identifies NEK7 as an essential component of NLRP3 inflammasome activation. *J. Biol. Chem.* **291**, 103–109 (2016). doi: [10.1074/jbc.C115.700492](https://doi.org/10.1074/jbc.C115.700492); pmid: [26553871](https://pubmed.ncbi.nlm.nih.gov/26553871/)
17. E. Bedner, P. Smolewski, P. Amstad, Z. Darzynkiewicz, Activation of caspases measured in situ by binding of fluorochrome-labeled inhibitors of caspases (FLICA): Correlation with DNA fragmentation. *Exp. Cell Res.* **259**, 308–313 (2000). doi: [10.1006/excr.2000.4955](https://doi.org/10.1006/excr.2000.4955); pmid: [10942603](https://pubmed.ncbi.nlm.nih.gov/10942603/)
18. F. Aguet et al., Membrane dynamics of dividing cells imaged by lattice light-sheet microscopy. *Mol. Biol. Cell* **27**, 3418–3435 (2016). doi: [10.1091/mbc.e16-03-0164](https://doi.org/10.1091/mbc.e16-03-0164); pmid: [27535432](https://pubmed.ncbi.nlm.nih.gov/27535432/)
19. J. M. Hyttinen et al., Clearance of misfolded and aggregated proteins by autophagy and implications for aggregation diseases. *Ageing Res. Rev.* **18**, 16–28 (2014). doi: [10.1016/j.arr.2014.07.002](https://doi.org/10.1016/j.arr.2014.07.002); pmid: [25062811](https://pubmed.ncbi.nlm.nih.gov/25062811/)
20. H. Ouyang et al., Protein aggregates are recruited to aggresomes by histone deacetylase 6 via unanchored ubiquitin C terminus. *J. Biol. Chem.* **287**, 2317–2327 (2012). doi: [10.1074/jbc.M111.273730](https://doi.org/10.1074/jbc.M111.273730); pmid: [22069321](https://pubmed.ncbi.nlm.nih.gov/22069321/)
21. U. B. Pandey et al., HDAC6 rescues neurodegeneration and provides an essential link between autophagy and the UPS. *Nature* **447**, 859–863 (2007). doi: [10.1038/nature05853](https://doi.org/10.1038/nature05853); pmid: [17568747](https://pubmed.ncbi.nlm.nih.gov/17568747/)
22. Y. Kawaguchi et al., The deacetylase HDAC6 regulates aggresome formation and cell viability in response to misfolded protein stress. *Cell* **115**, 727–738 (2003). doi: [10.1016/S0092-8674\(03\)00939-5](https://doi.org/10.1016/S0092-8674(03)00939-5); pmid: [14675537](https://pubmed.ncbi.nlm.nih.gov/14675537/)
23. R. R. Kopito, Aggresomes, inclusion bodies and protein aggregation. *Trends Cell Biol.* **10**, 524–530 (2000). doi: [10.1016/S0962-8924\(00\)01852-3](https://doi.org/10.1016/S0962-8924(00)01852-3); pmid: [11121744](https://pubmed.ncbi.nlm.nih.gov/11121744/)
24. T. Wileman, Aggresomes and pericentriolar sites of virus assembly: Cellular defense or viral design? *Annu. Rev. Microbiol.* **61**, 149–167 (2007). doi: [10.1146/annurev.micro.57.030502.090836](https://doi.org/10.1146/annurev.micro.57.030502.090836); pmid: [17896875](https://pubmed.ncbi.nlm.nih.gov/17896875/)
25. I. Banerjee et al., Influenza A virus uses the aggresome processing machinery for host cell entry. *Science* **346**, 473–477 (2014). doi: [10.1126/science.1257037](https://doi.org/10.1126/science.1257037); pmid: [25342804](https://pubmed.ncbi.nlm.nih.gov/25342804/)
26. A. Lu et al., Unified polymerization mechanism for the assembly of ASC-dependent inflammasomes. *Cell* **156**, 1193–1206 (2014). doi: [10.1016/j.cell.2014.02.008](https://doi.org/10.1016/j.cell.2014.02.008); pmid: [24630722](https://pubmed.ncbi.nlm.nih.gov/24630722/)
27. B. H. Duong et al., A20 restricts ubiquitination of pro-interleukin-1β protein complexes and suppresses NLRP3



- inflammasome activity. *Immunity* **42**, 55–67 (2015). doi: [10.1016/j.immuni.2014.12.031](https://doi.org/10.1016/j.immuni.2014.12.031); pmid: [25607459](https://pubmed.ncbi.nlm.nih.gov/25607459/)
28. M. A. Rodgers *et al.*, The linear ubiquitin assembly complex (LUBAC) is essential for NLRP3 inflammasome activation. *J. Exp. Med.* **211**, 1333–1347 (2014). doi: [10.1084/jem.20132486](https://doi.org/10.1084/jem.20132486); pmid: [24958845](https://pubmed.ncbi.nlm.nih.gov/24958845/)
  29. K. Guan *et al.*, MAVS promotes inflammasome activation by targeting ASC for K63-linked ubiquitination via the E3 ligase TRAF3. *J. Immunol.* **194**, 4880–4890 (2015). doi: [10.4049/jimmunol.1402851](https://doi.org/10.4049/jimmunol.1402851); pmid: [25847972](https://pubmed.ncbi.nlm.nih.gov/25847972/)
  30. C. S. Shi *et al.*, Activation of autophagy by inflammatory signals limits IL-1 $\beta$  production by targeting ubiquitinated inflammasomes for destruction. *Nat. Immunol.* **13**, 255–263 (2012). doi: [10.1038/ni.2215](https://doi.org/10.1038/ni.2215); pmid: [22286270](https://pubmed.ncbi.nlm.nih.gov/22286270/)
  31. X. X. Wang, R. Z. Wan, Z. P. Liu, Recent advances in the discovery of potent and selective HDAC6 inhibitors. *Eur. J. Med. Chem.* **143**, 1406–1418 (2018). doi: [10.1016/j.ejmech.2017.10.040](https://doi.org/10.1016/j.ejmech.2017.10.040); pmid: [29133060](https://pubmed.ncbi.nlm.nih.gov/29133060/)
  32. S. Florian, T. J. Mitchison, Anti-microtubule drugs. *Methods Mol. Biol.* **1413**, 403–421 (2016). doi: [10.1007/978-1-4939-3542-0\\_25](https://doi.org/10.1007/978-1-4939-3542-0_25); pmid: [27193863](https://pubmed.ncbi.nlm.nih.gov/27193863/)
  33. A. J. Firestone *et al.*, Small-molecule inhibitors of the AAA+ ATPase motor cytoplasmic dynein. *Nature* **484**, 125–129 (2012). doi: [10.1038/nature10936](https://doi.org/10.1038/nature10936); pmid: [22425997](https://pubmed.ncbi.nlm.nih.gov/22425997/)
  34. J. K. Burkhardt, C. J. Echeverri, T. Nilsson, R. B. Vallee, Overexpression of the dynamin (p50) subunit of the dynactin complex disrupts dynein-dependent maintenance of membrane organelle distribution. *J. Cell Biol.* **139**, 469–484 (1997). doi: [10.1083/jcb.139.2.469](https://doi.org/10.1083/jcb.139.2.469); pmid: [9334349](https://pubmed.ncbi.nlm.nih.gov/9334349/)
  35. T. Misawa *et al.*, Microtubule-driven spatial arrangement of mitochondria promotes activation of the NLRP3 inflammasome. *Nat. Immunol.* **14**, 454–460 (2013). doi: [10.1038/ni.2550](https://doi.org/10.1038/ni.2550); pmid: [23502856](https://pubmed.ncbi.nlm.nih.gov/23502856/)
  36. R. C. Coll *et al.*, A small-molecule inhibitor of the NLRP3 inflammasome for the treatment of inflammatory diseases. *Nat. Med.* **21**, 248–255 (2015). doi: [10.1038/nm.3806](https://doi.org/10.1038/nm.3806); pmid: [25686105](https://pubmed.ncbi.nlm.nih.gov/25686105/)
  37. Y. H. Park, G. Wood, D. L. Kastner, J. J. Chae, P. Pirin inflammasome activation and RhoA signaling in the autoinflammatory diseases FMF and HIDS. *Nat. Immunol.* **17**, 914–921 (2016). doi: [10.1038/ni.3457](https://doi.org/10.1038/ni.3457); pmid: [27270401](https://pubmed.ncbi.nlm.nih.gov/27270401/)
  38. H. Van Gorp *et al.*, Familial Mediterranean fever mutations lift the obligatory requirement for microtubules in P. Pirin inflammasome activation. *Proc. Natl. Acad. Sci. U.S.A.* **113**, 14384–14389 (2016). doi: [10.1073/pnas.1613156113](https://doi.org/10.1073/pnas.1613156113); pmid: [27911804](https://pubmed.ncbi.nlm.nih.gov/27911804/)
  39. P. D. Hsu, E. S. Lander, F. Zhang, Development and applications of CRISPR-Cas9 for genome engineering. *Cell* **157**, 1262–1278 (2014). doi: [10.1016/j.cell.2014.05.010](https://doi.org/10.1016/j.cell.2014.05.010); pmid: [24906146](https://pubmed.ncbi.nlm.nih.gov/24906146/)
  40. D. Clift *et al.*, A method for the acute and rapid degradation of endogenous proteins. *Cell* **171**, 1692–1706.e18 (2017). doi: [10.1016/j.cell.2017.10.033](https://doi.org/10.1016/j.cell.2017.10.033); pmid: [29153837](https://pubmed.ncbi.nlm.nih.gov/29153837/)
  41. I. Hwang, E. Lee, S. A. Jeon, J. W. Yu, Histone deacetylase 6 negatively regulates NLRP3 inflammasome activation. *Biochem. Biophys. Res. Commun.* **467**, 973–978 (2015). doi: [10.1016/j.bbrc.2015.10.033](https://doi.org/10.1016/j.bbrc.2015.10.033); pmid: [26471297](https://pubmed.ncbi.nlm.nih.gov/26471297/)
  42. Y. Miyake *et al.*, Structural insights into HDAC6 tubulin deacetylation and its selective inhibition. *Nat. Chem. Biol.* **12**, 748–754 (2016). doi: [10.1038/nchembio.2140](https://doi.org/10.1038/nchembio.2140); pmid: [27454931](https://pubmed.ncbi.nlm.nih.gov/27454931/)
  43. T. Hideshima *et al.*, Small-molecule inhibition of proteasome and aggresome function induces synergistic antitumor activity in multiple myeloma. *Proc. Natl. Acad. Sci. U.S.A.* **102**, 8567–8572 (2005). doi: [10.1073/pnas.0503221102](https://doi.org/10.1073/pnas.0503221102); pmid: [15937109](https://pubmed.ncbi.nlm.nih.gov/15937109/)
  44. J. R. Cabrero *et al.*, Lymphocyte chemotaxis is regulated by histone deacetylase 6, independently of its deacetylase activity. *Mol. Biol. Cell* **17**, 3435–3445 (2006). doi: [10.1091/mbc.e06-01-0008](https://doi.org/10.1091/mbc.e06-01-0008); pmid: [16738306](https://pubmed.ncbi.nlm.nih.gov/16738306/)
  45. K. Nakahira *et al.*, Autophagy proteins regulate innate immune responses by inhibiting the release of mitochondrial DNA mediated by the NALP3 inflammasome. *Nat. Immunol.* **12**, 222–230 (2011). doi: [10.1038/ni.1980](https://doi.org/10.1038/ni.1980); pmid: [21151103](https://pubmed.ncbi.nlm.nih.gov/21151103/)
  46. T. Saitoh *et al.*, Loss of the autophagy protein Atg16L1 enhances endotoxin-induced IL-1 $\beta$  production. *Nature* **456**, 264–268 (2008). doi: [10.1038/nature07383](https://doi.org/10.1038/nature07383); pmid: [18849965](https://pubmed.ncbi.nlm.nih.gov/18849965/)
  47. K. W. Chen *et al.*, Noncanonical inflammasome signaling elicits gasdermin D-dependent neutrophil extracellular traps. *Sci. Immunol.* **3**, eaar6676 (2018). doi: [10.1126/sciimmunol.aar6676](https://doi.org/10.1126/sciimmunol.aar6676); pmid: [30143554](https://pubmed.ncbi.nlm.nih.gov/30143554/)
  48. S. Rühl, P. Broz, Caspase-11 activates a canonical NLRP3 inflammasome by promoting K(+) efflux. *Eur. J. Immunol.* **45**, 2927–2936 (2015). doi: [10.1002/eji.201545772](https://doi.org/10.1002/eji.201545772); pmid: [26173909](https://pubmed.ncbi.nlm.nih.gov/26173909/)
  49. S. M. Man *et al.*, Inflammasome activation causes dual recruitment of NLR4 and NLRP3 to the same macromolecular complex. *Proc. Natl. Acad. Sci. U.S.A.* **111**, 7403–7408 (2014). doi: [10.1073/pnas.1402911111](https://doi.org/10.1073/pnas.1402911111); pmid: [24803432](https://pubmed.ncbi.nlm.nih.gov/24803432/)
  50. N. Kayagaki *et al.*, Non-canonical inflammasome activation targets caspase-11. *Nature* **479**, 117–121 (2011). doi: [10.1038/nature10558](https://doi.org/10.1038/nature10558); pmid: [22002608](https://pubmed.ncbi.nlm.nih.gov/22002608/)
  51. J. Shi *et al.*, Inflammatory caspases are innate immune receptors for intracellular LPS. *Nature* **514**, 187–192 (2014). doi: [10.1038/nature13683](https://doi.org/10.1038/nature13683); pmid: [25119034](https://pubmed.ncbi.nlm.nih.gov/25119034/)
  52. J. von Moltke *et al.*, Rapid induction of inflammatory lipid mediators by the inflammasome in vivo. *Nature* **490**, 107–111 (2012). doi: [10.1038/nature11351](https://doi.org/10.1038/nature11351); pmid: [22902502](https://pubmed.ncbi.nlm.nih.gov/22902502/)
  53. J. Chen, Z. J. Chen, PtdIns4P on dispersed trans-Golgi network mediates NLRP3 inflammasome activation. *Nature* **564**, 71–76 (2018). doi: [10.1038/s41586-018-0761-3](https://doi.org/10.1038/s41586-018-0761-3); pmid: [30487600](https://pubmed.ncbi.nlm.nih.gov/30487600/)
  54. H. Sharif *et al.*, Structural mechanism for NEK7-licensed activation of NLRP3 inflammasome. *Nature* **570**, 338–343 (2019). doi: [10.1038/s41586-019-1295-z](https://doi.org/10.1038/s41586-019-1295-z); pmid: [31189953](https://pubmed.ncbi.nlm.nih.gov/31189953/)
  55. G. dos Santos *et al.*, Vimentin regulates activation of the NLRP3 inflammasome. *Nat. Commun.* **6**, 6574 (2015). doi: [10.1038/ncomms7574](https://doi.org/10.1038/ncomms7574); pmid: [25762200](https://pubmed.ncbi.nlm.nih.gov/25762200/)
  56. Y. Liang *et al.*, Inhibition of peptidylarginine deiminase alleviates LPS-induced pulmonary dysfunction and improves survival in a mouse model of lethal endotoxemia. *Eur. J. Pharmacol.* **833**, 432–440 (2018). doi: [10.1016/j.ejphar.2018.07.005](https://doi.org/10.1016/j.ejphar.2018.07.005); pmid: [29981294](https://pubmed.ncbi.nlm.nih.gov/29981294/)
  57. X. Li *et al.*, MARK4 regulates NLRP3 positioning and inflammasome activation through a microtubule-dependent mechanism. *Nat. Commun.* **8**, 15986 (2017). doi: [10.1038/ncomms15986](https://doi.org/10.1038/ncomms15986); pmid: [28656979](https://pubmed.ncbi.nlm.nih.gov/28656979/)
  58. M. Huse, A. Le Floch, X. Liu, From lipid second messengers to molecular motors: Microtubule-organizing center reorientation in T cells. *Immunol. Rev.* **256**, 95–106 (2013). doi: [10.1111/immr.12116](https://doi.org/10.1111/immr.12116); pmid: [24117815](https://pubmed.ncbi.nlm.nih.gov/24117815/)
  59. M. Proell, M. Gerlic, P. D. Mace, J. C. Reed, S. J. Riedl, The CARD plays a critical role in ASC foci formation and inflammasome signalling. *Biochem. J.* **449**, 613–621 (2013). doi: [10.1042/BJ20121198](https://doi.org/10.1042/BJ20121198); pmid: [23110696](https://pubmed.ncbi.nlm.nih.gov/23110696/)
  60. D. Boucher *et al.*, Caspase-1 self-cleavage is an intrinsic mechanism to terminate inflammasome activity. *J. Exp. Med.* **215**, 827–840 (2018). doi: [10.1084/jem.20172222](https://doi.org/10.1084/jem.20172222); pmid: [29432122](https://pubmed.ncbi.nlm.nih.gov/29432122/)
  61. J. C. Kagan, V. G. Magupalli, H. Wu, SMOCs: Location-specific higher-order signalling complexes that control innate immunity. *Nat. Rev. Immunol.* **14**, 821–826 (2014). doi: [10.1038/nri3757](https://doi.org/10.1038/nri3757); pmid: [25359439](https://pubmed.ncbi.nlm.nih.gov/25359439/)
  62. P. H. Ren *et al.*, Cytoplasmic penetration and persistent infection of mammalian cells by polyglutamine aggregates. *Nat. Cell Biol.* **11**, 219–225 (2009). doi: [10.1038/ncb1830](https://doi.org/10.1038/ncb1830); pmid: [19151706](https://pubmed.ncbi.nlm.nih.gov/19151706/)
  63. N. C. Shaner *et al.*, Improving the photostability of bright monomeric orange and red fluorescent proteins. *Nat. Methods* **5**, 545–551 (2008). doi: [10.1038/nmeth.1209](https://doi.org/10.1038/nmeth.1209); pmid: [18454154](https://pubmed.ncbi.nlm.nih.gov/18454154/)
  64. C. Jakobs, E. Bartok, A. Kubarenko, F. Bauernfeind, V. Hornung, Immunoblotting for active caspase-1. *Methods Mol. Biol.* **1040**, 103–115 (2013). doi: [10.1007/978-1-62703-523-1\\_9](https://doi.org/10.1007/978-1-62703-523-1_9); pmid: [23852600](https://pubmed.ncbi.nlm.nih.gov/23852600/)
  65. J. Weischenfeldt, B. Porse, Bone marrow-derived macrophages (BMM): Isolation and applications. *CSH Protoc.* **2008**, prot5080 (2008). doi: [10.1101/pdb.prot5080](https://doi.org/10.1101/pdb.prot5080); pmid: [21356739](https://pubmed.ncbi.nlm.nih.gov/21356739/)
  66. V. Neudecker *et al.*, Neutrophil transfer of miR-223 to lung epithelial cells dampens acute lung injury in mice. *Sci. Transl. Med.* **9**, eaah5360 (2017). doi: [10.1126/scitranslmed.aah5360](https://doi.org/10.1126/scitranslmed.aah5360); pmid: [28931657](https://pubmed.ncbi.nlm.nih.gov/28931657/)
  67. K. A. Shirey *et al.*, The TLR4 antagonist Eritoran protects mice from lethal influenza infection. *Nature* **497**, 498–502 (2013). doi: [10.1038/nature12118](https://doi.org/10.1038/nature12118); pmid: [23636320](https://pubmed.ncbi.nlm.nih.gov/23636320/)

## ACKNOWLEDGMENTS

We thank J. Shah (Harvard Medical School), T. Mitchison (Harvard Medical School), and R. Vale (UCSF) for discussions; R. Mazitschek (Harvard Medical School) for discussions on HDAC inhibitors; G. Nuñez (University of Michigan) for Nek7<sup>-/-</sup> iBMDMs and for cDNA encoding human caspase-1; J. Yuan (Harvard Medical School) for cDNA encoding human IL-1 $\beta$ ; M. Dong (Boston Children's Hospital) for recombinant full-length TcdB toxin; P. Matthias (Friedrich Miescher Institute for Biomedical Research) for human HDAC6 and mouse Hdac6 plasmids; Y. Zhang and J. Lieberman (Boston Children's Hospital) for anesthetizing and dissecting out the bones from mice; K. Rhee (Seoul National University) for NEK7 antibody; HCIA/HHMI summer institute, Woods Hole, and H. Leung (Optical Microscopy Core Facility of Program in Cellular and Molecular Medicine, Boston Children's Hospital) for help with laser scanning confocal microscopy; J. Waters and T. Lambert (Nikon Imaging Center, Harvard Medical School) for help with live-cell microscopy; R. Mathieu (Flow Cytometry Research Facility, Boston Children's Hospital) for help with cell sorting and cell analysis; and M. Ericsson (Electron Microscopy Core Facility, Harvard Medical School) for help with transmission electron microscopy.

**Funding:** This work was supported by the National Institutes of Health (grant nos. HD087988 and AI124491 to H.W., MIRA award no. GM130386 to T.K., and a T32 training fellowship to A.V.H.), Biogen (SRA to T.K.), and the Joint Institute of University of Michigan and Peking University Health Science Center (grant no. U068874 to Y.L.). T.K. acknowledges support from the Janelia Visitor Program and E. Betzig, E. Marino, T. Liu, G. Upadhyayula, and W. Legant for help and advice in constructing and installing the LLSM. Construction of the LLSM was supported by grants from Biogen and Ionis Pharmaceuticals to T.K. **Author contributions:** H.W. and V.G.M. conceived the project. V.G.M. and R.N. performed bulk assays, immunofluorescence, and live-cell imaging. V.G.M., R.N., and A.V.H. conducted molecular cloning and reconstitution. Y.T. and Q.D. performed in vivo experiments under Y.L.'s and H.B.A.'s supervision. G.D.C. and W.S. performed LLSM under T.K.'s supervision. P.O. helped with NLR4 inflammasome assays and mouse primary cell experiments under K.A.F.'s supervision. F.I.S. provided the THP-1 cell line stably expressing ASC-tagRFP-T and certain NLR4 activators. H.S. purified FlaTox. J.J.H. conducted caspase-1 FLICA assay. C.L.E. and J.C.K. helped with LPS electroporation. Z.M. provided discussions early in the project. H.W. supervised the project. H.W., V.G.M., and R.N. wrote the manuscript with comments from all authors. **Competing interests:** The authors declare no competing interests.

**Data and materials availability:** All data needed to evaluate the conclusions in this study are available in the main text and the supplementary materials.

## SUPPLEMENTARY MATERIALS

[science.sciencemag.org/content/369/6510/eaas8995/suppl/DC1](https://science.sciencemag.org/content/369/6510/eaas8995/suppl/DC1)  
Figs. S1 to S20  
Captions for Movies S1 to S20

[View/request a protocol for this paper from Bio-protocol.](#)

2 January 2018; resubmitted 7 July 2019

Accepted 13 July 2020

10.1126/science.aas8995

## RESEARCH ARTICLE SUMMARY

## DEVELOPMENTAL BIOLOGY

## Species-specific pace of development is associated with differences in protein stability

Teresa Rayon<sup>\*</sup>, Despina Stamatakis<sup>†</sup>, Ruben Perez-Carrasco<sup>†</sup>, Lorena Garcia-Perez, Christopher Barrington, Manuela Melchionda, Katherine Exelby, Jorge Lazaro, Victor L. J. Tybulewicz, Elizabeth M. C. Fisher, James Briscoe<sup>\*</sup>

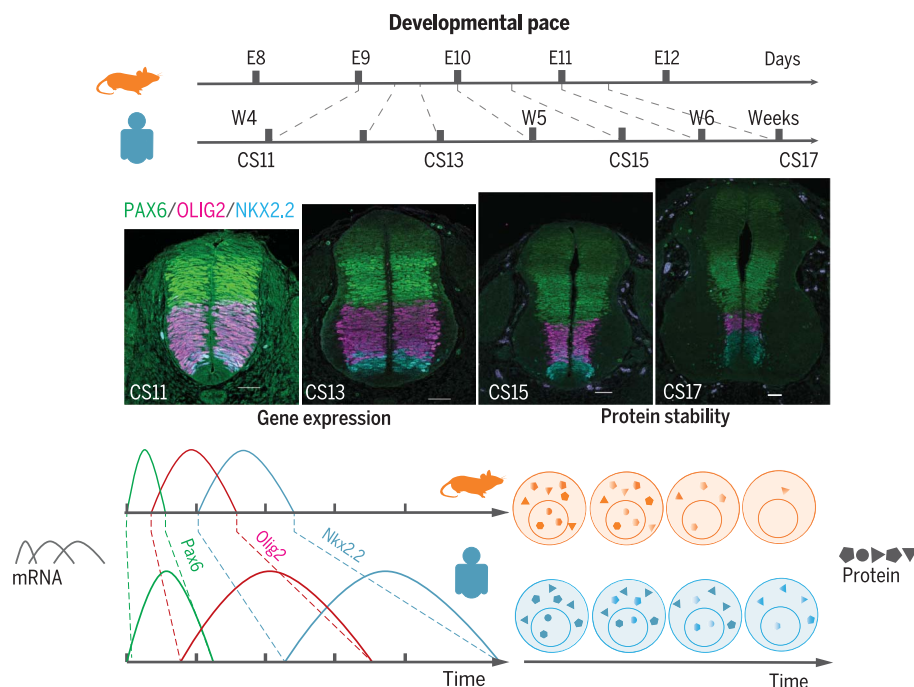
**INTRODUCTION:** What determines the pace of embryonic development? Although the molecular and cellular mechanisms of many developmental processes are evolutionarily conserved, the pace at which these operate varies considerably between species. The tempo of embryonic development controls the rate of individual differentiation processes and determines the overall duration of development. Despite its importance, however, the mechanisms that control developmental tempo remain elusive.

**RATIONALE:** Comparing highly conserved and well-characterized developmental processes in different species permits a search for mechanisms that explain differences in tempo. The specification of neuronal subtype identity in the vertebrate spinal cord is a prominent example, lasting less than a day in zebrafish, 3 to 4 days in mouse, and around 2 weeks in human. The development of the spinal cord involves a well-defined gene regulatory program comprising a series of stereotypic changes in gene expression, regulated by

extrinsic signaling as cells differentiate from neural progenitors to postmitotic neurons. The regulatory program and resulting neuronal cell types are highly similar in different vertebrates, despite the difference in tempo between species. We therefore set out to characterize the pace of differentiation of one specific neuronal subtype—motor neurons—in human and mouse and to identify molecular differences that explain differences in pace. To this end, we took advantage of the *in vitro* recapitulation of *in vivo* developmental programs using the directed differentiation of human and mouse embryonic stem cells.

**RESULTS:** We found that all stages of the developmental progression from neural progenitor to motor neuron were proportionally prolonged in human compared with mouse, resulting in human motor neuron differentiation taking about 2.5 times longer than mouse. Differences in tempo were not due to differences in the sensitivity of cells to signals, nor could they be attributed to differences in the sequence of the key genes or their regulatory elements. Instead, the data revealed that changes in protein stability correlated with developmental tempo, such that slower temporal progression in human corresponded to increased protein stability. An *in silico* model indicated that increased protein stability could account for the slower tempo of development in human compared with mouse.

**CONCLUSION:** The results suggest that differences in protein turnover play a role in interspecies differences in the pace of motor neuron differentiation. The identification of a molecular mechanism that can explain differences in the pace of embryonic development between species focuses attention on the role of protein stability in tempo control. This suggests a parsimonious explanation for the substantial variation in the tempo of development between species and indicates how the overall dynamics of developmental processes can be influenced by kinetic properties of gene regulation. What determines species-specific rates of protein turnover remains to be determined, but the availability of *in vitro* systems that mimic *in vivo* developmental tempo opens up the possibility of exploring this issue. ■



**Developmental tempo and protein stability.** Different animal species develop at different tempos, and equivalent developmental stages can be matched between mouse and human at different developmental time points. Neural progenitors in the spinal cord progress through the same succession of gene expression to generate motor neurons in mouse and human, and this serves as a model to study tempo differences. The *in vitro* directed differentiation of mouse embryonic stem cells to motor neurons advances at greater than twice the speed of human embryonic stem cell differentiation. The equivalent progression of development at different rates is shown for the transcription factors PAX6 (green), OLIG2 (red), and NKX2.2 (blue). E, embryonic day; W, embryonic week; CS, Carnegie stage. Scale bars are 50  $\mu$ m.

The list of author affiliations is available in the full article online.

<sup>\*</sup>Corresponding author. Email: james.briscoe@crick.ac.uk (J. B.); teresa.rayon@crick.ac.uk (T.R.)

<sup>†</sup>These authors contributed equally to this work.

Cite this article as T. Rayon *et al.*, *Science* 369, eaba7667 (2020). DOI: 10.1126/science.aba7667

**READ THE FULL ARTICLE AT**  
<https://doi.org/10.1126/science.aba7667>



## RESEARCH ARTICLE

## DEVELOPMENTAL BIOLOGY

## Species-specific pace of development is associated with differences in protein stability

Teresa Rayon<sup>1\*</sup>, Despina Stamatakis<sup>1†</sup>, Ruben Perez-Carrasco<sup>1,2,3†</sup>, Lorena Garcia-Perez<sup>1</sup>, Christopher Barrington<sup>1</sup>, Manuela Melchionda<sup>1</sup>, Katherine Exelby<sup>1</sup>, Jorge Lazaro<sup>1</sup>, Victor L. J. Tybulewicz<sup>1,4</sup>, Elizabeth M. C. Fisher<sup>5</sup>, James Briscoe<sup>1\*</sup>

Although many molecular mechanisms controlling developmental processes are evolutionarily conserved, the speed at which the embryo develops can vary substantially between species. For example, the same genetic program, comprising sequential changes in transcriptional states, governs the differentiation of motor neurons in mouse and human, but the tempo at which it operates differs between species. Using *in vitro* directed differentiation of embryonic stem cells to motor neurons, we show that the program runs more than twice as fast in mouse as in human. This is not due to differences in signaling, nor the genomic sequence of genes or their regulatory elements. Instead, there is an approximately two-fold increase in protein stability and cell cycle duration in human cells compared with mouse cells. This can account for the slower pace of human development and suggests that differences in protein turnover play a role in interspecies differences in developmental tempo.

The events of embryonic development take place in a stereotypic sequence and at a characteristic tempo (1, 2). Although the order and underlying molecular mechanisms are often indistinguishable between different species, the time scale and pace at which they progress can differ substantially. For example, compared with their rodent counterparts, neural progenitors in the primate cortex progress more slowly through a temporal sequence of neuronal subtype production (3, 4). Moreover, the duration of cortical progenitor expansion differs between species of primates, at least partly accounting for differences in brain size (5, 6). Even in more evolutionary conserved regions of the central nervous system (CNS), there are differences in tempo. The specification of neuronal subtype identity in the vertebrate spinal cord involves a well-defined gene regulatory program comprising a series of changes in transcriptional state as cells acquire specific identities as neural progenitors differentiate to postmitotic neurons (7). The pace of this process differs between species, despite the similarity in the regulatory program and the structural and functional correspondence of the resulting spinal cords. The differentiation of motor neurons (MNs), a prominent neuronal subtype

of the spinal cord, takes less than a day in zebrafish and 3 to 4 days in mouse but ~2 weeks in human (8, 9). Moreover, differences in developmental tempo are not confined to the CNS. The oscillatory gene expression that regulates the sequential formation of vertebrate body segments—the segmentation clock—has a period that ranges from ~30 min in zebrafish to 2 to 3 hours in mouse and 5 to 6 hours in human (10–12). It is unclear as to what causes the interspecies differences in developmental tempo, termed developmental allochry.

To address this question, we compared the generation of mouse and human MNs. Progenitors of the spinal cord initially express the transcription factors (TFs) Pax6 and Irx3 (13). Exposure to sonic hedgehog (Shh), emanating from the underlying notochord, results in ventrally located progenitors inducing Nkx6.1 and Olig2. This down-regulates Pax6 and Irx3 (14). Progenitors expressing Olig2 and Nkx6.1 are termed pMNs and these either differentiate into postmitotic MNs, which express a set of TFs including Hb9/Mnx1 and Isl1, or transition into p3 progenitors that express Nkx2.2 (15). This gene regulatory network (GRN), in which Olig2 represses Irx3 and Pax6 and promotes the differentiation of MNs, is conserved across vertebrates (16).

We used *in vitro* differentiation of MNs from mouse and human embryonic stem cells (ESCs) to investigate the pace of differentiation. We find that MN differentiation *in vitro* recapitulates species-specific global time scales observed in the embryos, lasting ~3 days in mouse and more than a week in human. We show that increased levels of signaling are unable to speed up the rate of differentiation of human cells. Moreover, by assaying the

expression of a human gene, with its regulatory landscape, in a mouse context, we rule out the possibility that species differences in genomic sequence play a major role in temporal scaling. Finally, we show that differences in protein degradation can explain the differences in developmental tempo.

## Results and discussion

The characteristic spatial-temporal changes in gene expression and the regulatory interactions between the genes responsible for neural tube development are well described (7). Despite the conservation of the GRN across vertebrates, only limited analysis has been performed on the relevant stages of human development (17, 18). We performed immunostainings on mouse and human embryonic spinal cords at brachial levels at equivalent stages (19) to more accurately correlate the major developmental events of neural differentiation processes *in vivo* between mouse and human (Fig. 1A). The dorsoventral (DV) length of the neural tube increases at the same rate in mouse and human (fig. S1A), and the shifts in gene expression are similar between mouse and human (fig. S1D). At their maximum extents, the OLIG2-expressing pMN domains comprise a large proportion of ventral progenitors, occupying about 30% of the DV length of the neural tube in mouse and a ~15% larger domain in human embryos (Fig. 1B and fig. S1E). Consistent with this, there were more pMNs in human but similar numbers of interneuron progenitors in mouse and human (fig. S1F). Over the next 2 days of mouse development, from embryonic day 9.5 (E9.5) to E11.5, many postmitotic MNs differentiate (Fig. 1C), resulting in a marked reduction in the size of the pMN domain (Fig. 1B), despite the continued proliferation of the progenitors (9). The proportion of neurons is higher in human compared with mouse (fig. S1B). By contrast, the pace of development is noticeably slower in human embryos. At Carnegie stage 11 (CS 11), the pMN domain occupies a large proportion of the human neural tube, similar to the pMN in E9.0 mouse embryos. During the next 1 to 2 weeks of development (CS13 to 19; Fig. 1B), the size of the pMN domain decreases as MNs accumulate (Fig. 1C), but the rate of this change is slower than that seen in mouse. MN production decreases at ~E11.5 in mouse, whereas MN production continues to at least CS17 in human (fig. S1C), and glial progenitors, coexpressing SOX9 and NFIA, begin to arise in both species at these stages (Fig. 1D). Together, the data indicate an equivalent progression in neural tube development of mouse and human that lasts around 3 days in mouse and more than a week in human (Fig. 1A).

We examined whether interspecies tempo differences were preserved *in vitro*. Methods for the differentiation of MNs from ESCs, which mimic *in vivo* developmental mechanisms, have

<sup>1</sup>The Francis Crick Institute, London NW1 1AT, UK.

<sup>2</sup>Department of Mathematics, University College London, London WC1E 6BT, UK. <sup>3</sup>Department of Life Sciences, Imperial College London, London SW7 2AZ, UK. <sup>4</sup>Department of Immunology and Inflammation, Imperial College, London W12 0NN, UK. <sup>5</sup>UCL Queen Square Institute of Neurology, University College London, London WC1N 3BG, UK.

\*Corresponding author. Email: james.briscoe@crick.ac.uk (J.B.); teresa.rayon@crick.ac.uk (T.R.)

†These authors contributed equally to this work.

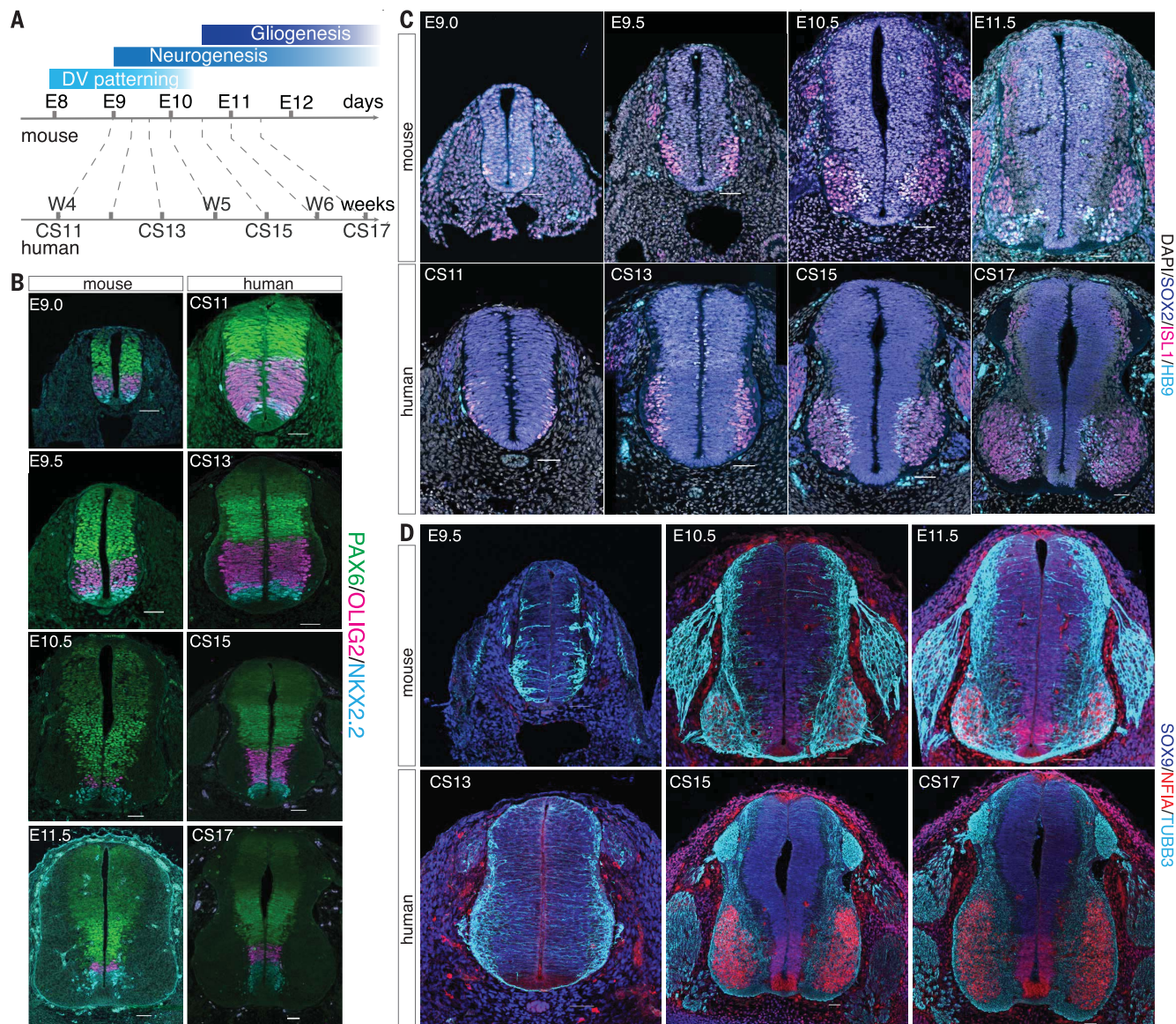


**Fig. 1. Comparison of neural tube development in mouse and human embryos.** (A) Schema of mouse and human neural tube development. W, embryonic week. (B to D) Immunofluorescence in transverse sections of mouse and human cervical neural tube from E9.0 to E11.5 in mouse embryos and CS11 to CS17 in human embryos. In (B), expression of progenitor markers PAX6 (green), OLIG2 (magenta), and NKX2.2 (cyan) is

shown. In (C), pan-neural progenitor marker SOX2 (blue) and motor neuron markers ISL1 (magenta) and HB9/MNX1 (cyan) at neurogenic stages are shown. As shown in (D), ventral expression of gliogenic markers NFIA (red) and SOX9 (blue) in the neural tube can be detected from E10.5 in mouse and CS15 in human. NFIA also labels neurons, as indicated by TUBB3 (cyan) staining. Scale bars are 50  $\mu$ m.

been established for both mouse and human (20–23). To ensure comparison of similar axial levels in both species, we initially exposed mouse ESCs to a 20-hour pulse of WNT signaling and human ESCs to a 72-hour pulse (20, 24). This generated cells with a posterior epiblast identity—so-called neuromesodermal progenitors—that express a suite of genes, including T/TBXT, SOX2, and CDX2 (20, 25) (fig. S2A). These were then exposed to 100 nM retinoic acid (RA), which acts as a neuralizing signal, and to 500 nM smoothened agonist (SAG) that ventralizes neural progenitors (26) (Fig. 2, A and B). For both mouse and human,

this resulted in the efficient generation of pMNs expressing OLIG2 (Fig. 2, C and D, and fig. S2, B and C) and MNs expressing ISLET1 (ISL1), HB9/MNX1, and neuronal class III  $\beta$  tubulin (TUBB3) (Fig. 2, E and F). Progenitors that had not differentiated into neurons switched from OLIG2 expressing pMNs to p3 progenitors expressing NKX2.2 (Fig. 2, C and D). Mouse and human MNs expressed HOXC6, characteristic of forelimb-level spinal cord MNs (27) (Fig. 2F), indicating that pMNs and MNs with similar axial levels were being produced in both cases.

Comparison of the two species revealed the same sequence of gene expression changes:

expression of Pax6 in newly induced neural progenitors, followed by the expression of the pMN marker Olig2, which precedes the induction of postmitotic MN markers, including Isl1 (Fig. 2, C to G, and fig. S2B). But the rate of progression differed. Immunofluorescence and reverse transcription–quantitative polymerase chain reaction (RT–qPCR) assays for specific components of the GRN indicated that, after the addition of RA and SAG, the onset of ISL1 expression took 2 to 3 days in mouse but ~6 days in human (Fig. 2, E to G and K), consistent with the slower developmental progression in the developing human embryonic spinal cord.



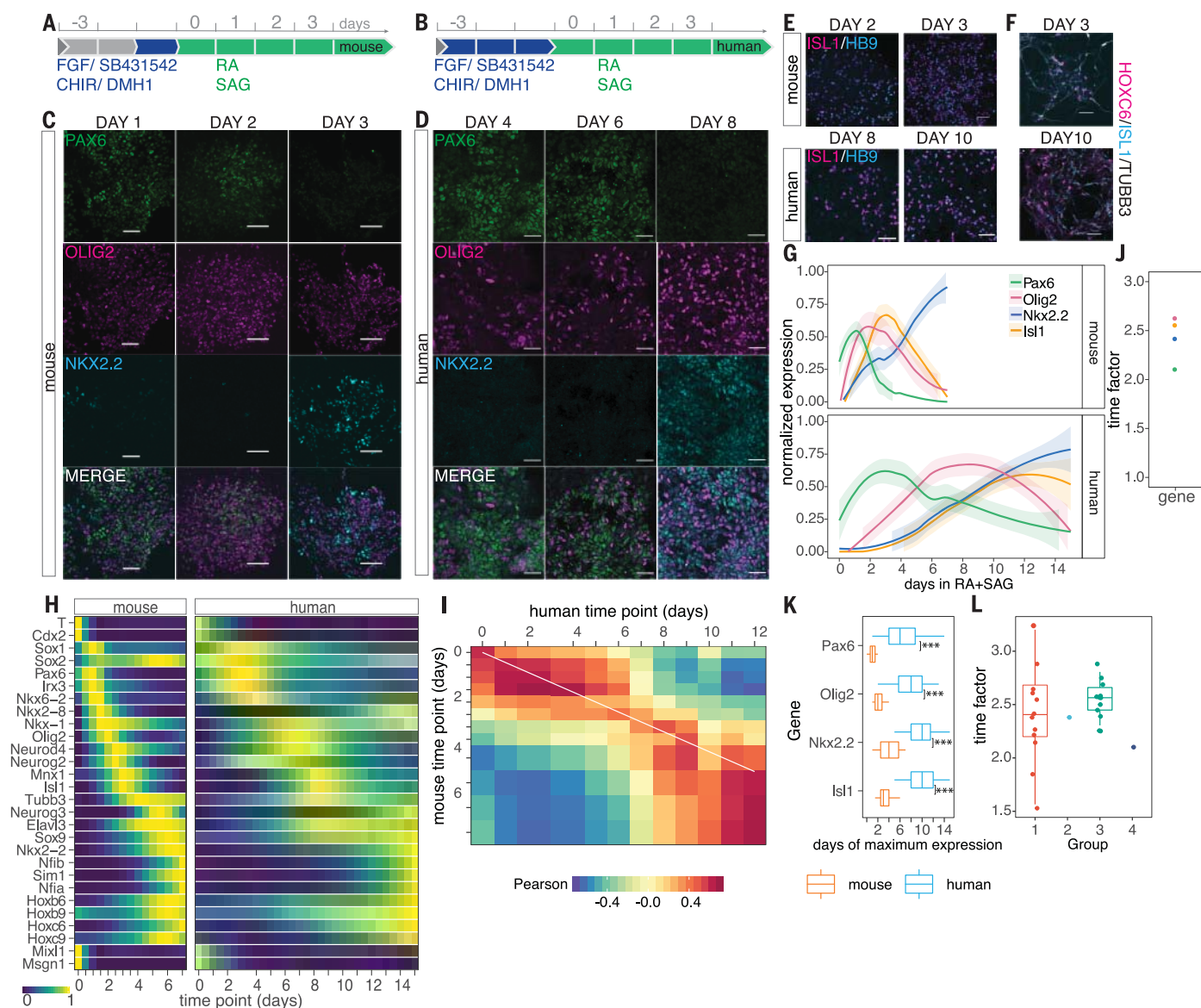


**Fig. 2. A global scaling factor for in vitro differentiation of mouse and human MNs.** (A) Schema of mouse ESCs differentiated to MNs. Spinal cord progenitors were generated via a neuromesodermal progenitor (NMP) state induced by the addition of FGF, WNT, and dual SMAD inhibition signals for 24 hours (blue rectangle) and subsequently exposed to the neuralizing signal RA and SAG to ventralize the cells (green). (B) Schema of the analogous strategy used for human ESCs to generate MNs, where the addition of FGF, WNT, and dual SMAD inhibition signals lasts 72 hours. (C) Expression of neural progenitor markers (PAX6, OLIG2, NKX2.2) between days 1 and 3 in mouse MN differentiation. (D) Expression of NP markers (PAX6, OLIG2, NKX2.2) at days 4, 6, and 8 in human MN differentiation. (E) Expression of MN markers (ISL1, HB9/MNX1) in mouse and human MNs. Mouse MNs can be detected by days 2 to 3, whereas human MNs are not detected until days 8 and 10. (F) HOXC6 expression in MNs characterized by ISL1 and TUBB3 expression at day 3 in mouse and at day 10 in human. In (C) to (F), scale bars are 50  $\mu$ m. (G) RT-qPCR analysis of Pax6, Olig2, Nkx2.2, and Isl1 expression in mouse and human differentiation reveals a conserved

progression in gene expression but a different tempo (human  $n = 3$  in triplicate, mouse  $n = 3$  in triplicate). Shaded areas indicate 95% CI. (H) Heatmap of RNA-seq data from mouse and human MN differentiation indicating the normalized expression of selected markers representative of neuromesodermal progenitors, neural progenitors, neurons, glia, and mesoderm cell types (mouse  $n = 3$ , human  $n = 3$ ). (I) Heatmap of the pairwise Pearson correlation coefficients of the transcriptomes of mouse (vertical) and human (horizontal) differentiation at the indicated time points. High positive correlation is indicated by values close to 1 (red). The white line shows a linear fit of the Pearson correlation with a temporal scaling factor of  $2.5 \pm 0.2$  (median  $\pm$  SD). (J) Scaling factor for transcriptome clusters that contain Pax6, Olig2, Nkx2.2, and Isl1. (K) Significant differences in the peak of gene expression in the RT-qPCR experiments between mouse (orange) and human (blue) (human  $n = 3$  in triplicate, mouse  $n = 3$  in triplicate). Two-way ANOVA with Tukey's multiple comparison post hoc test; \*\*\*adjusted  $p < 0.001$ . (L) Time-factor estimations for cluster pairs with a high proportion of orthologous genes.

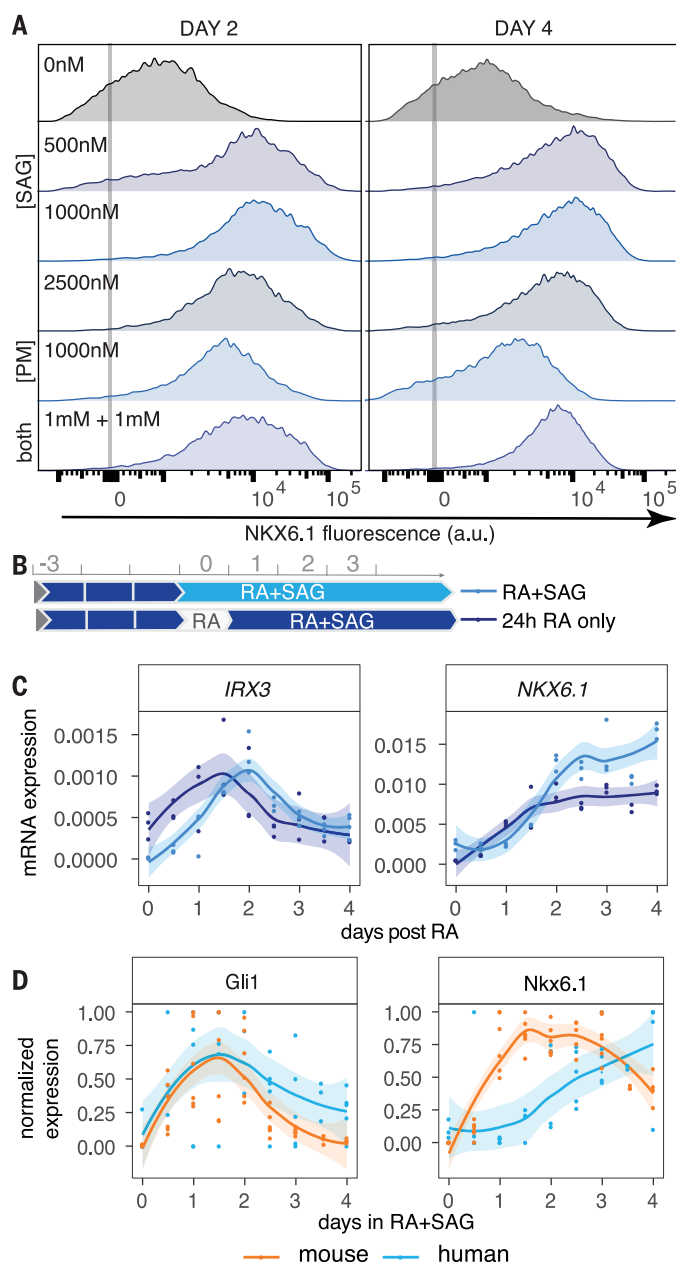


**Fig. 3. Dynamics of Shh signaling in mouse and human neural progenitors.** (A) Flow cytometry analysis of NKX6.1 expression in human neural progenitors treated with the smoothened agonists SAG, purmorphamine (PM), or the two combined (both) shows a similar distribution of NKX6.1 expression at days 2 and 4 ( $n = 3$ ). a.u., arbitrary units. (B) Scheme outlining the standard differentiation protocol, in which RA and SAG are added at the same time (light blue) versus a treatment where SAG addition is delayed for 24 hours (dark blue). (C) RT-qPCR data reveals higher expression of *IRX3* when cells are treated for 24 hours with only RA (dark blue), whereas there are no substantial differences in the induction dynamics for *NKX6.1*, measured from the time of SAG addition ( $n = 3$ ). (D) RT-qPCR data measured at 12-hour intervals reveal similar gene expression dynamics in mouse (orange) and human (blue) for *Gli1* but distinct dynamics for *Nkx6.1* (mouse  $n = 6$ , human  $n = 5$ ). In (C) and (D), shaded areas indicate 95% CI.

Moreover, *Olig2* induction peaked after 2 to 3 days in mouse and 6 to 8 days in human (Fig. 2G and fig. S2B). Differences in tempo have also been observed between the differentiation of mouse and human pluripotent stem cells (28). To test whether the difference in

tempo of mouse and human MN differentiation represented a global change in the rate of developmental progression, we performed bulk transcriptomics. This revealed a similar pattern of gene expression changes in mouse and human, but the changes occurred at a

faster rate in mouse cells than in human cells (Fig. 2H). Cross-species comparison of dynamic genes highly expressed across the differentiation showed a high degree of correlation, although altered in time between mouse and human (Fig. 2I and fig. S2D). Moreover, the relative difference in developmental tempo appears constant throughout the differentiation process, suggesting a global temporal scaling—developmental allochry—between mouse and human.

To relate the tempo of mouse and human MN differentiation, we estimated the global difference in the tempo of gene expression by comparing the Pearson correlation coefficients from the transcriptome analysis of both species. This identified a scaling factor of  $2.5 \pm 0.2$  (median  $\pm$  SD; Fig. 2I). Additionally, we clustered gene expression profiles into sets of genes with similar dynamics during the time course, and we measured the fold difference in the time of appearance of the clusters that contained *Pax6*, *Irx3*, *Olig2*, *Nkx2.2*, *Isl1*, and *Tubb3* genes. This confirmed that a scaling factor of  $\sim 2.5$  fit each of the gene expression clusters (Fig. 2J). Similarly, time-factor measurements for individual genes identified a scaling factor between 2 and 3 (fig. S2, F and G). To test if the identified time factor could be extended to the whole transcriptome, we selected four cluster pairs comprising a high proportion of orthologous genes (fig. S2E). A search for a scaling factor that accommodated the difference in the timing of expression in these groups indicated a factor of  $\sim 2.5$  for each of the clusters (Fig. 2L). Together, these results suggest that MN differentiation can be recapitulated in vitro from mouse and human ESCs and results in a global 2.5-fold decrease in the rate at which gene expression programs advance in human compared with mouse.

#### *Shh* signaling sensitivity does not regulate tempo

Having identified a global scaling factor for the GRN, we investigated the mechanism that sets the time scale. We reasoned that the mechanism was likely to be cell-autonomous because the temporal differences are observed between mouse and human cells grown in vitro, and it has been shown that in vitro differentiated cells transplanted to a host follow their own species-specific dynamics (29–31). Because the directed differentiation toward MNs occurs in response to *Shh* signaling, we hypothesized that the delay in the GRN in human compared with mouse could be a consequence of a reduced sensitivity to signaling. To test whether the human GRN could be sped up by higher levels of signaling, we differentiated human progenitors in the presence of increasing concentrations of SAG and in a combination of SAG and purmorphamine (Pur), another smoothened agonist (Fig. 3A). Single-cell measurements of NKX6.1, a GRN



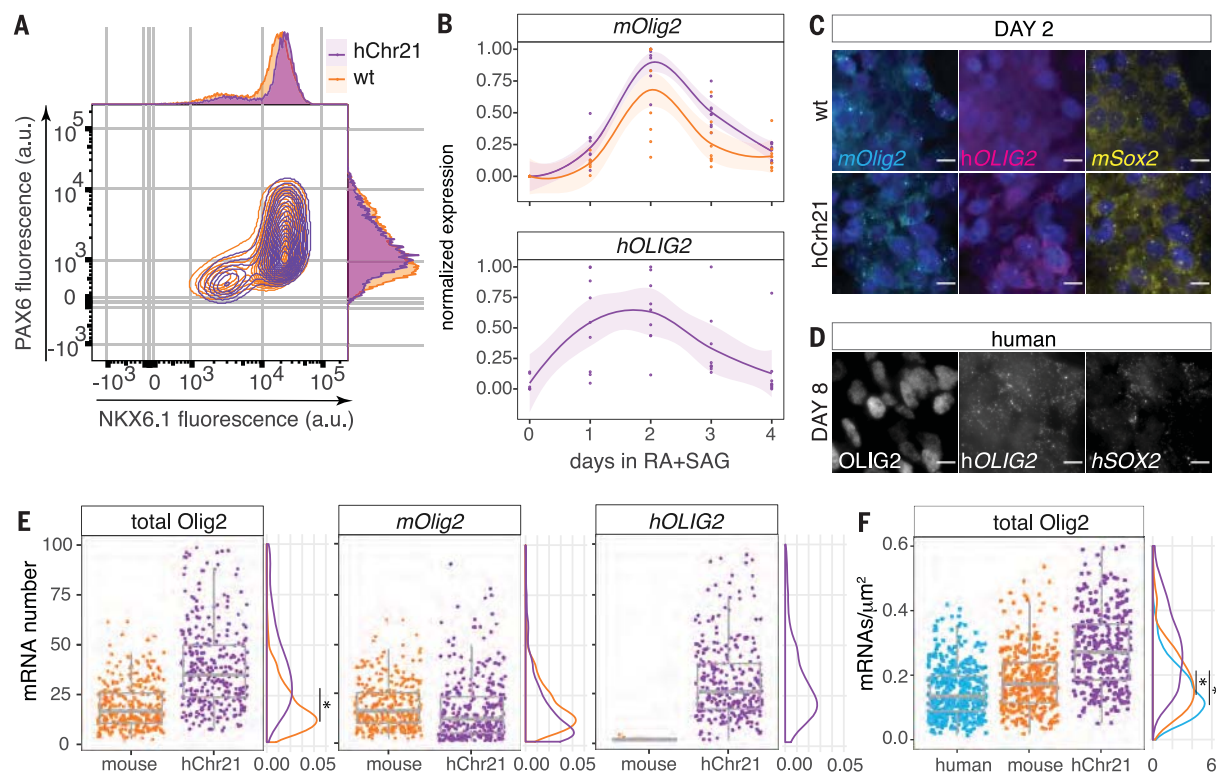


**Fig. 4. Temporal control of gene expression depends on the species' cellular environment.** (A) Scatter plot with histograms of PAX6 and NKX6.1 intensity measured by FACS in neural progenitors from wt (orange) and hChr21 (purple) mouse cells at day 2. (B) RT-qPCR expression of Olig2 from the mouse (*mOlig2*) and human (*hOLIG2*) alleles ( $n = 9$ ). Shaded areas indicate 95% CI. (C) smFISH at day 2 of differentiation in wt and hChr21 lines with probes for *mSox2*, and allele-specific detection of *mOlig2* or *hOLIG2*. Scale bars are 10  $\mu$ m. (D) smFISH in human neural progenitors at day 8 of differentiation for *hSOX2* and *hOLIG2*. Scale bars are 50  $\mu$ m. (E) Boxplots and density distributions in wt and hChr21 cells of the number of mRNA molecules per cell from Sox2, total Olig2, and human allele- and mouse allele-specific

probes. The estimated mean difference in molecule number between hChr21 cells and mouse is 25.7 [22.3; 29.7] (mouse  $n = 323$ , hChr21  $n = 337$ ). (F) Boxplots and density distributions of the concentration (number of mRNA molecules per area unit) of Olig2 per cell in human neural progenitors at day 8 and mouse wt and hChr21 cells at day 2. The estimated mean difference is 0.121 mRNAs/ $\mu$ m<sup>2</sup> [0.141; 0.101] between mouse and hChr21 cells, and the mean difference is 0.157 mRNAs/ $\mu$ m<sup>2</sup> [0.175; 0.139] for human and hChr21 cells. In (E) and (F), statistical significance (\*) corresponds with  $<0.05$  overlap between the distributions of mean estimations with a  $p < 0.001$  for a two-sided permutation  $t$  test (human  $n = 436$ , mouse  $n = 323$ , hChr21  $n = 337$ ).

TF induced by Shh in ventral progenitors, showed similar proportions and intensity of expression for all levels of signal at equivalent time points (fig. S3, A and B). To test whether the competence of neural progenitors to respond to Shh was delayed in human compared with mouse, we delayed addition of SAG for 24 hours. A 24-hour delay in Shh addition resulted in higher initial levels of *IRX3*, as expected, but did not change the time of *NKX6.1*, *GLI1*, or *PTCH1* induction relative to the time of SAG addition (Fig. 3, B and C; and fig. S3D), corroborating that the onset of Shh responsiveness is acquired at neural induction in human cells as in mouse cells.

We then compared the kinetics of Shh signaling in mouse and human cells by assaying the response of *Ptch1* and *Gli1*, two Shh pathway components that are Shh direct target genes (32, 33). Notably, the response dynamics of these two genes were similar in mouse and human. In both species, the expression levels

of *Ptch1* and *Gli1* were increased within 12 hours and peaked by 24 hours (Fig. 3D and fig. S3E). By contrast, the induction of *Nkx6.1* was delayed 48 hours in human compared with mouse (Fig. 3D). Additional components of the Shh signaling pathway—including *Gli2*, *Ptch2*, and *Hhip*—also showed increased expression within 24 hours (fig. S3F). The induction of Olig2, similarly to *Nkx6.1*, was delayed in human compared with mouse (fig. S3F). Together, these results suggest that differential sensitivity to extrinsic signals does not appear to have a major role in regulating the tempo of development.

#### No effect of interspecies sequence differences in gene regulation

Having ruled out a role for Shh signaling, we focused on possible interspecies sequence differences in gene regulation. Even though genes in the GRN are highly conserved compared with the average identity between human and

mouse (data S1), we hypothesized that sequence differences in the coding region and/or cis-regulatory elements might determine the pace of development. To study sequence differences between species, we focused on Olig2 because it is the major regulator of pMN identity and its cis-regulatory elements have been characterized (34, 35). We reasoned that if sequence differences were responsible for the different temporal dynamics in mouse and human cells, we would be able to detect species-specific changes in the timing of Olig2 expression from a human Olig2 locus introduced into mouse cells. The human Olig2 gene is located on chromosome 21, and we took advantage of the 47-1 mouse ESC line that contains the Hsa21q arm of human chromosome 21 (36). We differentiated the 47-1 line (hereafter referred to as hChr21) alongside its parental line, which lacked Hsa21q, from which it was generated (hereafter referred to as wt). The proportions of neural progenitors and the

dynamics of gene expression—measured by RNA expression, immunofluorescence, and flow cytometry—were similar between hChr21 and wt lines (Fig. 4, A and B, and fig. S4, A and B). We then assessed the timing of expression of the *hOLIG2* allele. We detected induction of *hOLIG2* at day 1 of differentiation (Fig. 4B), 24 hours after addition of RA and SAG. By contrast, in human cells, *hOLIG2* induction is not detected until days 2 to 3 (Fig. 2G). Thus, in mouse cells, *hOLIG2* follows the same dynamics of gene expression as mouse *Olig2* (*mOlig2*), indicating that the temporal control of gene expression depends on the cellular environment and not the species origin of the genomic sequence.

To compare *Olig2* expression levels between the mouse and human alleles, we performed single-molecule fluorescent in situ hybridization (smFISH) (Fig. 4, C and D, and fig. S5, A and B). We first assayed transcripts of *Sox2* (*mSox2*), a TF expressed in all neural progenitors. The mean and variance in *mSox2* transcripts were similar in both hChr21 and wt neural progenitors, supporting the comparability of the two cell lines (fig. S5C). We then measured *Olig2* transcripts using species-specific probes. The number of mouse *Olig2* (*mOlig2*) transcripts in hChr21 cells was lower than that in wt cells, but the mean total number of *Olig2* transcripts in hChr21 cells, combining mouse and human alleles, was higher than the mean number of transcripts in wt cells (Fig. 4E). This suggests that the number of transcripts that cells express depends on the number of the alleles.

We next asked whether the levels of specific mRNAs in human cells were similar to those in mouse. To this end, we performed smFISH in human neural progenitors for *SOX2* (*hSOX2*) and *OLIG2* (*hOLIG2*) (Fig. 4D and fig. S5B). The median number of *hOLIG2* molecules in human cells at days 4, 6, and 8 was similar, indicating that the number of transcripts is constant in cells (fig. S5E). The number of *Sox2* and *Olig2* transcripts in human neural progenitors were higher than in mouse wt (fig. S5C). However, human neural progenitors were larger than mouse progenitors (fig. S5D) and taking this into account allowed calculation of the concentration of RNAs (mRNAs/ $\mu\text{m}^2$ ) in human and mouse cells (Fig. 4F). The mean concentration of total *Olig2* in mouse hChr21 cells was more similar to the concentration of *mOlig2* in wt mouse cells than the concentration of *hOLIG2* in human cells (mean difference of 0.121 mRNAs/ $\mu\text{m}^2$  {95% confidence interval (CI): [0.101; 0.141]} between mouse and hChr21 cells; with a mean difference of 0.157 mRNAs/ $\mu\text{m}^2$  (95% CI: [0.139; 0.175]) between human and hChr21 cells) (Fig. 4F), indicating that mRNA concentration might be controlled by the cellular context. Overall, we conclude that gene regulation in mouse

cells follows mouse-specific characteristics, irrespective of the species origin of the allele, suggesting that species differences in gene expression dynamics are not encoded within the regulatory genome of individual genes.

#### Kinetics of the proteome correspond with the interspecies dynamics of differentiation

Given that the species difference in tempo did not appear to depend on species-specific differences in genomic elements, we reasoned that kinetic features of gene expression must explain the difference, similar to the findings in synthetic biology and modeling fields (37, 38). We therefore set out to measure the decay rate of transcripts and proteins in mouse and human neural progenitors, which encompasses both degradative mechanisms and dilution from cell division (39). To assay mRNA decay, we used the uridine analog, 5-ethynyluridine (EU), and assayed mouse neural progenitors from day 2 and human neural progenitors from days 4 and 8, representing equivalent developmental states in the two species (fig. S2C). We pulsed cells for 3 hours to label actively transcribing mRNAs, transferred them to media lacking EU, and assayed the EU remaining in cells at regular time points (fig. S6, A and B). Fluorescence-activated cell sorting (FACS) analysis suggested a similar global mRNA stability in mouse and human neural progenitors, with a median half-life ( $t_{1/2}$ ) of  $92 \pm 33.3$  min in mouse cells and a  $t_{1/2}$  of  $76 \pm 19.7$  min in human at day 4 and  $96 \pm 37.6$  min at day 8 (Fig. 5, A and B). This agrees with measurements of mRNA half-lives in other cell lines (40). Consistent with this, measuring the stability of selected individual mRNAs also suggested similar half-lives of mRNAs in mouse and human neural progenitors (fig. S6E). Nevertheless, extending and refining these measurements will provide insight into whether there are detectable differences in mRNA stability between species and how these contribute to the cellular concentrations of specific transcripts (12).

Next, we tested whether differences in protein decay rate could explain the allochry. To assay protein stability, we metabolically labeled nascent proteins by replacing methionine in the medium with the methionine analog 1-azidohomoalanine (AHA) and used FACS to measure the stability of newly synthesized proteins after removal of the amino acid analog over the course of 48 hours (fig. S6, C and D). We found that the half-life of the proteome in mouse neural progenitors was shorter than that in human progenitors ( $t_{1/2} = 7.8 \pm 1.6$  hours in mouse versus  $t_{1/2} = 19.3 \pm 5.2$  hours in human day 4 or  $t_{1/2} = 18.2 \pm 2.3$  hours in human day 8), corresponding to a 2- to 2.5-fold difference (Fig. 5, C and D). This identifies a general difference in the protein lifetime between mouse and human that corresponds to the difference in tempo, and further analysis

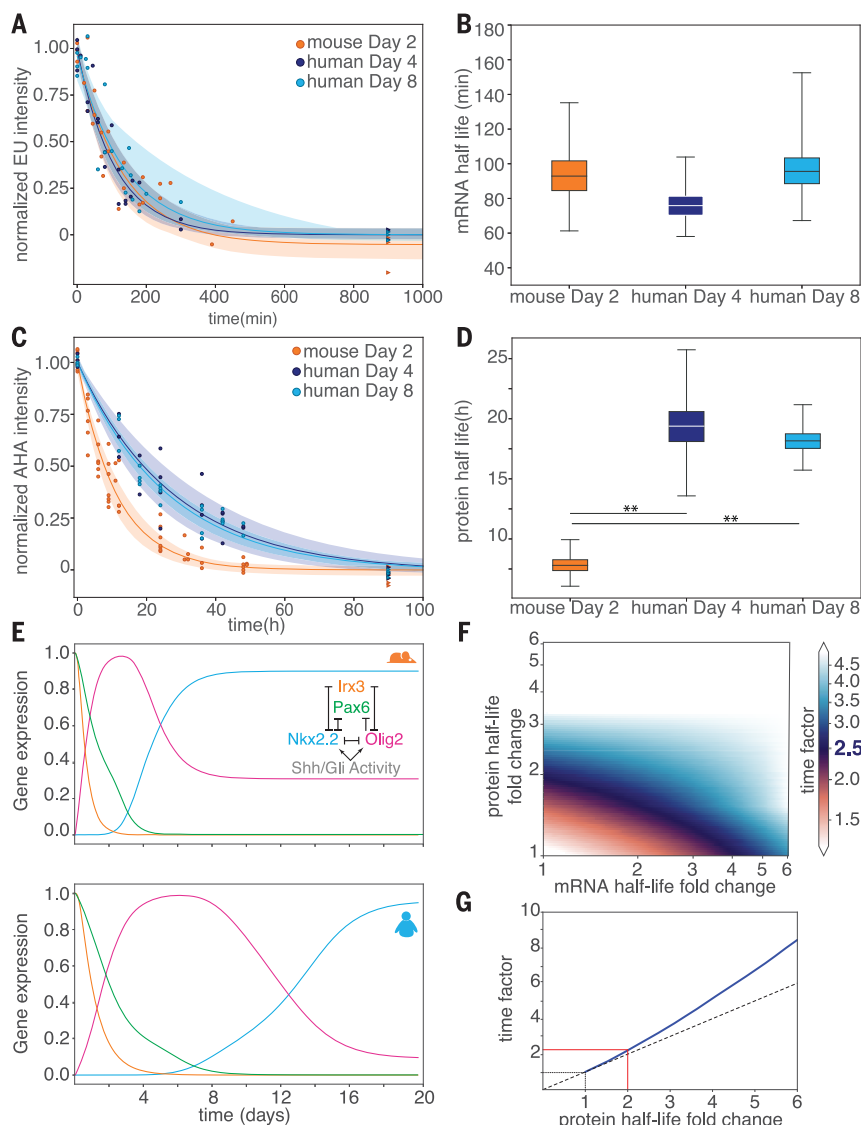
will be required to determine which specific proteins show a 2- to 2.5-fold difference.

To test whether changes in mRNA or protein stability could account for differences in developmental tempo, we developed a computational model of the GRN based on a previous model describing the dynamics of the mouse neural progenitor GRN (Fig. 5E) (41). The model incorporates separately the dynamics of mRNA and protein (see supplementary text). Simulations showed a good correspondence with the temporal dynamics measured in mouse cells (Figs. 2G and 5E). Halving the decay rate of the proteins (but not mRNA) to mimic the measured human kinetics resulted in the same sequence of gene expression but slower dynamics of the GRN (Fig. 5E). To explore further the connection between changes in protein stability and GRN dynamics, we measured the change in time of the onset of *Olig2* (we refer to this as the time factor) for different values of mRNA and protein stability. This revealed that increasing mRNA stability had less effect on the time factor than increasing protein stability. In particular, the model predicted that if protein decay was kept constant, a four-fold change in mRNA stability would be required to reproduce the observed temporal scaling of 2.5 in human versus mouse (Fig. 5F). Such a fold change in mRNA stability is not compatible with our global measurements (Fig. 5B), suggesting that differences in mRNA kinetics between species might be less influential given the time scales of MN differentiation. Moreover, the relationship between the tempo scaling observed in the simulations with the changes in protein decay rate revealed a superlinear relationship in which an increase in protein stability slowed GRN dynamics by slightly more than the fold increase in decay rate (Fig. 5G and fig. S7, C and D). These results indicated that the measured increase in protein stability can explain tempo changes in MN differentiation between mouse and human.

To explore whether other aspects of gene regulation might contribute to differences in tempo, we undertook a computational screen in which decay and production rates of mRNA and protein were allowed to change independently. In addition, the TF binding affinities of the model were also allowed to vary within previously defined constraints (41). We identified parameter sets that reproduced the ~2.5-fold difference in tempo (fig. S7, A and B). The resulting ensemble of parameters showed a wide range of transcription and translation rates for which the network reproduces the tempo differences between human and mouse (fig. S7, A and B). There were no apparent changes in the constraints on the parameters of the model, with the exception of the protein decay rate, which showed a narrow distribution centered around a 2.5-fold change (fig. S7A). These results indicate that control of protein



**Fig. 5. Protein stability in the GRN corresponds to tempo differences between species. (A)** Normalized EU incorporation measurements to estimate mRNA half-life in mouse (orange) and human (blue) neural progenitors. Line and shaded areas show best exponential fit and 70% HDI (mouse day 2  $n = 5$ , human day 4  $n = 3$ , human day 8  $n = 5$ ). **(B)** Half-life of the transcriptome in mouse neural progenitors at day 2 (orange) and in human neural progenitors at day 4 (dark blue) and day 8 (light blue). Boxplots indicate the 25th to the 75th percentile of the range, and whiskers show values within 1.5 times the interquartile range of the 25th and 75th percentiles. **(C)** Normalized AHA measurements of the proteome in mouse (orange) and human (blue) neural progenitors to estimate protein stability (mouse day 2  $n = 6$ , human day 4  $n = 4$ , human day 8  $n = 4$ ). **(D)** Global stability of the proteome in mouse neural progenitors at day 2 (orange) and in human neural progenitors at day 4 (dark blue) and day 8 (light blue). Boxplots indicate the 25th to the 75th percentile of the range, and whiskers show values within 1.5 times the interquartile range of the 25th and 75th percentiles. Statistical significance (\*\*) corresponds with  $<0.01$  overlap between the distributions of parameter estimations. **(E)** Temporal dynamics of the computational model of the neural tube GRN in mouse (top), and the predicted human behavior (bottom), simulated by halving the decay rates of the proteins in the network. The inset diagram shows the cross-repressive GRN comprising the transcription factors Pax6, Olig2, Nkx2.2, and *Irx3* used to model ventral patterning of the neural tube. **(F)** Predicted Olig2 time factor, indicating relative change in developmental pace, produced in response to fold changes in mRNA half-life and protein half-life. Relevant fold changes in mRNA and protein correspond to those that give a time factor of 2.5 (purple). **(G)** Predicted Olig2 time factor as a function of the fold change in the decay rate ratio (blue solid line). The change in time factor resulting from an increase in protein half-life grows faster than linearly (dashed line). This results in a time factor greater than 2 for a fold change of 2 in protein half-life (red line).



decay rate is an effective mechanism to regulate developmental tempo.

A prediction that arises from this analysis is that the TFs comprising the GRN that regulate MN differentiation should be more stable in human neural progenitors than in mouse neural progenitors, and that a two-fold decrease in protein decay would give a scaling factor of  $\sim 2.5$ . To test this, we performed pulse-chase experiments labeling nascent proteins with AHA, conjugated labeled proteins to biotin, and pulled them down with streptavidin beads to purify. This revealed that pan-neural proteins SOX1 and SOX2 had longer lifetimes than OLIG2 and NKX6.1 proteins in both species (Fig. 6A and fig. S6, F and G). Moreover, human NKX6.1 and OLIG2 were  $\sim 2$ -fold more stable than their mouse homologs (mNKX6.1  $\approx 2.5$  hours versus hNKX6.1  $\approx 6$  hours; mOLIG2  $\approx 3.5$  hours versus hOLIG2  $\approx 6.8$  hours) (Fig. 6A and fig. S6, F and G). These results are consistent with the predictions of the model

and the nonlinear relationship between decay rates and tempo scaling.

The identification of a global increase in the lifetime of proteins in human neural progenitors compared with mouse neural progenitors raised the possibility that exogenous proteins would show species-specific stability. To this end, we generated Patched1::mKate2 reporter lines in mouse and human stem cells. In these lines, the monomeric far-red fluorescent protein Katushka-2 (mKate2) was fused to the C terminus of endogenous Pth1 by means of a self-cleaving peptide (fig. S8A). In this way, we could modulate mKATE2 expression, driven by the Shh responsive Pth1, using small-molecule activators and inhibitors of Shh signaling. To measure mKATE2 stability in neural progenitors, we induced mKate2 expression by addition of SAG (fig. S8B). Then, we added the smoothened antagonist vismodegib (42) to block Shh signaling, thereby repressing new mKATE2 production. We assayed the decay of mKATE2

fluorescence in inhibited cells. FACS analysis showed a half-life of  $17.7 \pm 2.3$  hours for mKate2 in mouse cells. By contrast, the half-life of the same mKATE2 protein in human cells was  $32.9 \pm 7.3$  hours (Fig. 6, B and C). These results indicate that protein half-life is species-specific.

The long half-life of mKATE2 raised the possibility that dilution, after cell division, contributed to the measured decay rate (39). Differences in the cell cycle time between mouse and human cells have been measured (43–46) and could therefore contribute to the difference in mKATE2 lifetime in neural progenitors. To test this, we assayed total cell cycle length using cumulative 5-ethynyl-2'-deoxyuridine (EdU) labeling of mouse and human neural progenitors (Fig. 6, D and E, and fig. S9, A and B) (47). Cell cycle duration in equivalent staged neural progenitors from mouse and human was  $10.8 \pm 8.3$  hours compared with  $28.4 \pm 13.9$  hours, respectively, in accordance with cell cycle measurements in other human and

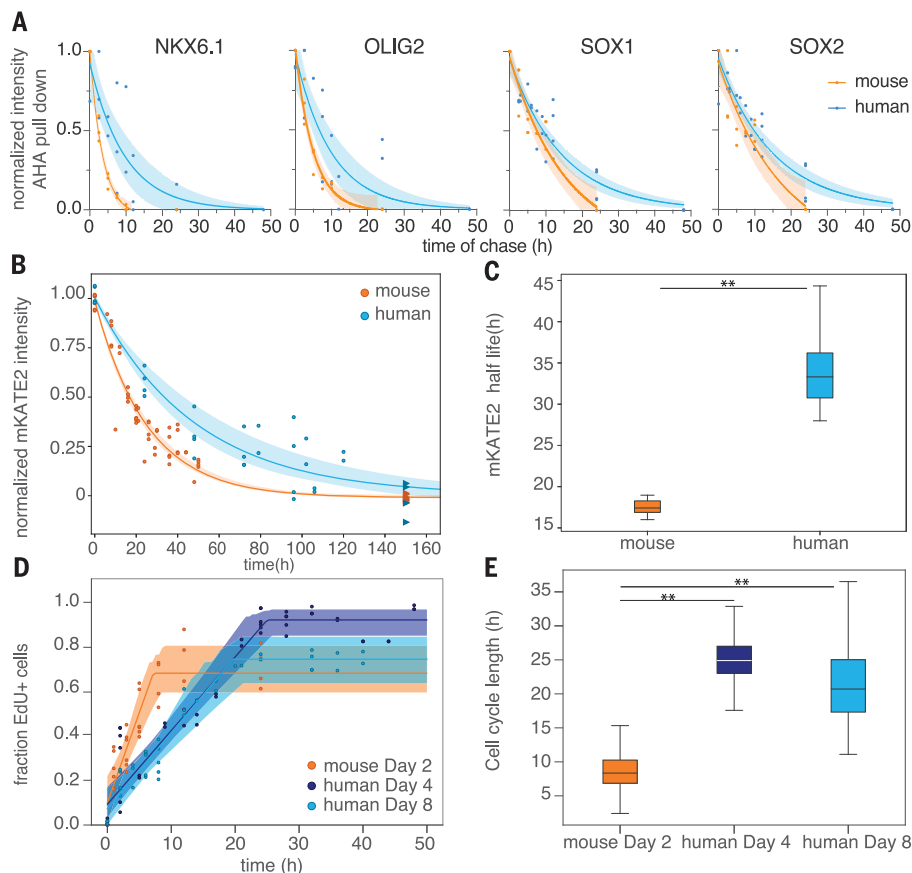


**Fig. 6. Protein decay and cell cycle account for the speed differences between species.** (A) Normalized measurements of mouse and human NKX6.1, OLIG2, SOX1, and SOX2 from AHA pulse-chase experiments using AHA-labeled and purified proteins. Line and shaded areas show best exponential fit and 95% CIs (mouse  $n = 3$ ; human  $n = 3$  for OLIG2 and NKX6.1,  $n = 4$  for SOX1 and SOX2). (B) Normalized intensity measurements of mKATE2 in mouse and human Ptch1::T2A-mKate2 cell lines. Line and shaded areas show best exponential fit and 70% HDI (mouse  $n = 7$ ; human  $n = 4$ ). (C) Estimated half-lives for mKATE2 in mouse (orange) and human (blue) cells. Boxplots indicate the 25th to the 75th percentile of the range, and whiskers show values within 1.5 times the interquartile range of the 25th and 75th percentiles. (D) Cell cycle measurements of mouse neural progenitors at day 2 and human neural progenitors at days 4 and 8. Line and shaded areas show best fit and 80% HDI (mouse  $n = 5$ , human day 4  $n = 4$ , human day 8  $n = 5$ ). (E) Cell cycle length estimations in mouse neural progenitors at day 2 and human neural progenitors at days 4 and 8. Boxplots indicate the 25th to the 75th interquartile range, and whiskers show values within 1.5 times the interquartile range of the 25th and 75th percentiles. For all plots, mouse data are colored orange and human data are blue. In (C) and (E), statistical significance (\*\*) corresponds with  $<0.01$  overlap between the distributions of parameter estimations.

mouse cell types (43–46). Thus, similar to the proteome, the cell cycle operates 2 to 2.5 times faster in mouse compared with human. Because progress through the cell cycle is controlled by protein degradation (48, 49), the difference in cell cycle rate between mouse and human cells may also be a consequence of a global change in protein stability.

Taken together, the data indicate that the dynamics of the GRN associated with the embryonic generation of MNs progresses two to three times faster in mouse cells than in human cells. A similar difference in the tempo of the segmentation clock between mouse and human has also been observed (10, 12). These differences do not appear to arise from a bottle-

neck caused by a specific rate-limiting event in MN generation. Moreover, neither changes in the dynamics of signaling nor variations in genomic regulatory sequences appear to account for the species-specific tempos. Instead, the correlated ~2.5-fold differences in cell cycle length and general protein stability suggest that the temporal scaling in developmental processes results from global differences in key kinetic parameters that broadly affect the tempo of molecular processes. What sets this global tempo remains to be determined but could involve the differences in the rates of pivotal molecular processes such as global changes in proteostasis or differences in the overall metabolic rate of cells. How these af-

fect the pace at which GRNs elaborate and how such variations are assimilated to ensure the development of robust and appropriately proportioned tissues need to be addressed. The availability of in vitro systems that mimic in vivo developmental allochroty open up the possibility of exploring these issues.

## Materials and methods

### Tissue preparation

Human embryonic material (4 to 6 weeks of gestation) was obtained from the MRC/Wellcome-Trust (grant no. 006237/1) funded Human Developmental Biology Resource (HDBR; [www.hdb.org](http://www.hdb.org)) with appropriate maternal written consent and approval from the London Fulham Research Ethics Committee (18/LO/0822) and the Newcastle and North Tyneside NHS Health Authority Joint Ethics Committee (08/H0906/21+5). HDBR is regulated by the UK Human Tissue Authority (HTA; [www.hta.gov.uk](http://www.hta.gov.uk)) and operates in accordance with the relevant HTA codes of practice. This work was part of project no. 200378 registered with the HDBR. Tissue was fixed in 4% paraformaldehyde (PFA) overnight at 4°C, washed in PBS, and transferred to 15% sucrose in phosphate buffer overnight at 4°C. Embryos were subsequently embedded in gelatin solution (7.5% gelatin, 15% sucrose in phosphate buffer) and snap-frozen in isopentane on dry ice. Transverse cryosections (thickness: 14  $\mu$ m) were cut using a Leica CM3050S cryostat (Leica Microsystems Limited, Milton Keynes, UK) and placed on Superfrost Plus slides (Thermo Scientific 10149870). Slides were stored at  $-80^{\circ}\text{C}$  until ready to be processed for immunohistochemistry. After immunohistochemistry, 22-mm-by-50-mm no. 1.5 thickness coverslips (VWR 631-0138) were mounted onto the sections using ProLong Gold antifade reagent (Invitrogen P36930).

Mouse spinal cord tissue was prepared in the same way as described (50). All animal procedures were carried out in accordance with the Animal (Scientific Procedures) Act 1986 under the Home Office project license PPL80/2528 and PD415DD17.

### Immunostaining and microscopy

Immunohistochemistry on human and mouse spinal cord tissues, and on mouse and human cells, was performed as described previously (50). Primary antibodies were diluted as follows: rabbit anti-PAX6 (Millipore AB2237, 1:500), goat anti-OLIG2 (R&D AF2418, 1:800), mouse anti-NKX2.2 (DSHB 74.5A5, 1:500), mouse anti-HB9/MNX1 (DSHB 81.5C10, 1:40), goat anti-ISL1 (R&D AF1837, 1:1,000), mouse anti-HOXC6 (Santa Cruz Biotechnology sc-376330, 1:200), mouse anti-TUBB3 (Covance MMS-435P, 1:500), chicken anti-TUBB3 (Abcam ab107216, 1:500), goat anti-SOX2 (R&D AF2018, 1:500), goat anti-SOX9 (R&D AF3075, 1:250), rabbit anti-NFIA (Atlas antibodies HPA008884, 1:500), mouse



anti-CDX2 (abcam ab157524, 1:500), and goat anti-BRACHYURY (R&D, AF2085, 1:500). The anti-NKX2.2 and anti-MNX1 monoclonal antibodies developed by T. M. Jessell were obtained from the Developmental Studies Hybridoma Bank. Alexa secondary antibodies (Life Technologies or Jackson ImmunoResearch) used throughout this study were diluted 1:1000, and nuclei were counterstained with 4',6-diamidino-2-phenylindole (DAPI).

Cryosections were imaged using a Leica SP8 confocal microscope equipped with a 20× NA 0.75 dry objective, or a Leica SP5 confocal microscope. Cells were imaged using a Zeiss Imager.Z2 microscope using the ApoTome.2 structured illumination platform or using a Leica SP5 confocal microscope. Z stacks were acquired and represented as maximum intensity projections using ImageJ software. Pixel intensities were adjusted across the entire image in Fiji. The same settings were applied to all images. Immunofluorescence was performed on a minimum of three biological replicates, from independent experiments.

#### Image analyses of mouse and human spinal cord sections

Image analysis was performed in Fiji (<http://fiji.sc/Fiji>) and data analysis in Python3.7 ([www.python.org](http://www.python.org)). Section length was first measured by tracing a straight line from roofplate to floorplate. The mean fluorescence intensity in immunostained sections was quantified across a 12-μm region adjacent to the apical lumen using a Fiji macro described in Zagorski and Kicheva (51). Hemisections of each tube were treated independently. The data was background-subtracted and smoothed with a 5-μm moving average. To unify the resolution across stages, profiles were rescaled to the same 100 relative spatial positions by linear interpolation. Domain boundaries were defined as the positions where the intensity increased or decreased above or below 20% of maximum. During this analysis, three human sections from different stages were discarded because of obvious irregularities in their background levels.

The number of progenitors in each TF domain was inferred from the TF expression domain area and the average density of colocalizing DAPI-stained nuclei. The number of total neurons per hemisection was inferred from the DAPI<sup>+</sup>, SOX2<sup>-</sup> area and the average density of ISL1<sup>+</sup> neurons. Finally, the number of motor neurons found in a ventral horn was inferred from the ISL1<sup>+</sup>, HB9<sup>+</sup> area and the average density of ISL1<sup>+</sup> neurons. In all cases, cellular density was manually determined from a subset of sections from each stage.

The following number of sections stained for DAPI, PAX6, OLIG2, and NKX2.2 were analyzed. For mouse: E8.5 *n* = 2, E9.0 *n* = 4, E9.5 *n* = 8, E10.0 *n* = 3, E10.5 *n* = 6, E11.5 *n* = 2;

and for human: CS11 *n* = 2 sections from one embryo, CS13 *n* = 5 from two embryos, CS14 *n* = 6 from three embryos, CS15 *n* = 7 from two embryos, CS17 *n* = 4 from one embryo, CS19 *n* = 2 from one embryo. For DAPI, ISL1, HB9, and SOX2 analyses, the following number of sections were analyzed. For mouse: E9.0 *n* = 2, E9.5 *n* = 4, E10.5 *n* = 9, E11.0 *n* = 4, E12.5 *n* = 3; and for human: CS11 *n* = 2 from one embryo, CS13 *n* = 2 from one embryo, CS15 *n* = 2 sections from one embryo, and CS17 *n* = 3 sections from one embryo.

#### Cell culture and neural progenitor differentiation

All mouse ESCs (HM1, D3, and Ptch1::T2A-mKate2 mouse ESC line) were propagated on mitotically inactivated mouse embryonic fibroblasts (feeders) in DMEM knockout medium (Thermo Fisher Scientific 10829018) supplemented with 2000 U/ml ESGRO-LIF (Sigma Aldrich ESG117), 10% cell-culture validated fetal bovine serum, penicillin and streptomycin, and 2 mM L-glutamine (Thermo Fisher Scientific 25030024). The 47-1 (hChr21) cell line (37) was maintained with 0.8 μl/ml of G418 (Thermo Fisher Scientific 10131027) to select for cells carrying the human chromosome 21.

H9 ESC line (WiCell), and Ptch1::T2A-mKate2 H9 ESC lines were routinely cultured in Essential 8 medium (Thermo Fisher Scientific A1517001) on 0.5-μg/cm<sup>2</sup> laminin-coated plates (Thermo Fisher Scientific A29249) and split using Versene (Gibco 15040066).

To obtain mouse neural progenitors of posterior identity, mouse ESCs were dissociated with 0.05% trypsin, feeders removed by differential binding to gelatin-coated plates, and 60,000 to 80,000 cells were plated per 35-mm CellBIND dish in N2B27 medium supplemented with 10 ng/ml of bFGF (Peprotech 100-18B), 5 μM CHIR99021 (Axon 1386), 10 μM SB431542 (LT S0400), and 2 μM DMH1 (Adooq Bioscience A12820). From day 0 onward, cells were cultured in N2B27 supplemented with 100 nM RA (Sigma Aldrich R2625) and 500 nM SAG (Calbiochem 566660) for neural induction. Medium was changed daily. N2B27 medium contained a 1:1 ratio of DMEM/F12:Neurobasal medium (Thermo Fisher Scientific 21331020 and 21103049) supplemented with 1X N2 (Thermo Fisher Scientific 17502001), 1X B27 (Thermo Fisher Scientific 17504001), 2 mM L-glutamine (Thermo Fisher Scientific 25030024), 40 mg/ml bovine serum albumin (BSA) (Sigma Aldrich A7979), penicillin and streptomycin (Thermo Fisher Scientific 15140122), and 0.1 mM 2-mercaptoethanol (Thermo Fisher Scientific 21985023).

For human MN differentiation, cells were split with Versene (Gibco 15040066) and plated as clusters of ~20 cells on 1-μg/cm<sup>2</sup> fibronectin-coated (Millipore FC010) wells in N2B27 me-

dium supplemented with 3 μM CHIR99021 (Axon 1386), 5 ng/ml bFGF (Peprotech 100-18B), 10 μM SB431542 (LT S0400), 2 μM DMH1 (Adooq Bioscience A12820), and 10 μM ROCK inhibitor (Tocris Y-27632) from days -3 to -1. Rock inhibitor was removed after 48 hours. On day 0, the cells were dissociated using accutase (Thermo Fisher Scientific A1110501), and 175,000 cells were plated per fibronectin-coated 35-mm dish on N2B27 medium containing 100 nM RA (Sigma Aldrich R2625) and 500 nM SAG (Calbiochem 566660) with 10 μM ROCK inhibitor (Tocris Y-27632). Rock inhibitor was removed 48 hours after plating, and medium was replaced every other day. All experiments involving hESCs have been approved by the UK Stem Cell Bank steering committee (ref SCSC14-18).

#### Generation of Ptch1::T2A-mKate2 mouse and human ESC lines by CRISPR

For CRISPR-Cas9-mediated homologous recombination, short guide RNA (sgRNA) sequences (mouse: GTGGGGGAGCAGCTCCAAGT, human: GTGAGTGCCACTGACAA) were cloned into pSpCas9(BB)-2A-Puro (Addgene pX459 plasmid no. 62988). As donor vector, the T2A-3xNLS-FLAG-mKate2 cassette (26) was inserted at the 3' end of the Patched1 open reading frame, using 2.1-Kb upstream and 2.8-Kb downstream arms for mouse and 1.88-Kb upstream and 0.98-Kb downstream homology arms for human.

For mouse ESC targeting, HM1 ESCs were electroporated as in Gouti *et al.* (52). For human ESC targeting, 2 × 10<sup>6</sup> cells were electroporated with 2 μg of each plasmid using program A23 of Nucleofector II (Amaxa) and human stem cell Nucleofector I kit (Lonza VPH-5012). Electroporated cells were plated on Matrigel (Corning 734-1101) coated six-well plates and maintained in mTeSR and 10 μM ROCK inhibitor (Tocris Y-27632). For selection, colonies were first treated with 0.5 μg/ml Puromycin (Sigma P9620) for 2 days followed by 50 μg/ml Geneticin (Thermo Fisher 10131027) selection. Then, the colonies were dissociated using accutase (Thermo Fisher Scientific A1110501) and plated at low density to allow for clonal growth. Individual colonies were picked using a 20-μl pipette tip, dissociated in accutase (Thermo Fisher Scientific A1110501), and replated to allow expansion and a second round of Geneticin selection. Correct integration of the T2A-3xNLS-FLAG-mKate2 transgene was verified using long-range PCRs and Sanger sequencing.

#### RNA extraction, cDNA synthesis, and qPCR analysis

RNA was extracted from cells using RNeasy mini kit (QIAGEN 74106), following the manufacturer's instructions. Extracts were digested with DNase I (QIAGEN 79254) to eliminate genomic DNA. First strand cDNA synthesis was performed using Superscript III (Thermo

Fisher 18080051) using random hexamers and was amplified using PowerUp SYBR green (Applied Biosystems A25918). qPCR was performed using the QuantStudio 5 Real-Time PCR system. For mouse samples, expression values for each gene were normalized against  $\beta$ -actin, using the delta-delta CT method. For human samples, expression values for each gene were normalized against  $\beta$ -ACTIN and glyceraldehyde phosphate dehydrogenase (*GAPDH*). All experiments were performed with at least two biological replicates. For human and mouse comparisons and to compare between the mouse wt line and hChr21, data was normalized to its maximum levels. Error bars represent standard deviation. Two-way analysis of variance (ANOVA) with multiple Tukey post hoc tests comparing the distribution of time points around the maximum expression between mouse and human for each gene were performed. Mouse and human qPCR primers used are listed in table S1. Data were processed, normalized, and plotted using `geom_smooth()` function with loess fitting in R.

#### RNA sequencing (RNA-seq) library preparation and data analysis

Total RNA was purified using the RNeasy mini kit (QIAGEN 74106) according to the manufacturer's instructions. Three separate RNA libraries were barcoded and prepared for each time point per species (biological triplicates). Indexed libraries were pooled and sequenced on an Illumina HiSeq 4000 flow cell configured to generate 101 cycles of single-ended data. Raw data was demultiplexed and FastQ files created using `bcl2fastq` (2.20.0). Technical replicates between lanes on the flow cells were merged by concatenation of the FastQ files prior to analysis into biological replicate datasets, each of which contained 30 million to 45 million reads.

Biological replicate datasets were analyzed using the BABS-RNASeq (<https://github.com/crickbabs/BABS-RNASeq>) Nextflow (53) pipeline developed at the Francis Crick Institute. The GRCh38 mouse and the GRCh38 human reference genomes were used with the Ensembl release-89 (54) gene annotations. Dataset quality was assessed by FastQC (0.11.7, Andrews, <https://www.bioinformatics.babraham.ac.uk/projects/fastqc/>), RSeQC (2.6.4 (55)), RNA-SeQC (56), and Picard (2.10.1, <http://broadinstitute.github.io/picard>), and expression was quantified by STAR [2.5.2a (57)] and RSEM (58) using the BABS-RNASeq pipeline.

DP\_GP\_cluster (59) was used to cluster the mean estimated transcripts per million (TPM) across time courses using default parameters and the `-fast`, `-true_times`, and `-check_convergence` options. Genes other than *Isl1*, *Nkx2-2*, *Olig2* and *Pax6*, whose range of TPM values was 50 or more, were considered for this analysis. Enrichment of homologous genes

between expression clusters was assessed using the `phyper()` function in R. After multiple testing correction by false discovery rate (FDR), a significance threshold of 0.001 was applied to identify homologous pairs. Groups of connected homologous pairs were identified using `cluster()` in `igraph` (1.2.2, 60) for R.

Expression profiles for specific genes during the time course were compared between human, mouse, and mouse-corrected using two-way ANOVA with multiple Tukey post hoc tests. The data were analyzed individually, without assuming a consistent standard deviation. Significant changes were considered below a FDR of 0.001.

#### Time factor estimations

The Pearson correlation time factor ( $f$ ) was obtained by minimizing the Euclidian distance between the linear relationship  $t$  and each interspecies time point pair weighted with the Pearson correlation coefficient of each pair. Error was calculated by bootstrapping.

Time-scaling factors  $f$  between RNA-seq profiles of genes and clusters were obtained from the normalized gene expression temporal profiles  $y(t)$ , by minimizing the distance  $d(y_{\text{human}}, y_{\text{mouse}})$  between the human expression profile and the scaled profile of mouse  $d = \int [y_{\text{human}}(t) - A y_{\text{mouse}}(t \cdot f + B)]^2 dt$ . Continuous profiles were obtained using Akima spline interpolation, whereas the minimization of the distance was performed using the Nelder-Mead method. The reported ensemble of time-scaling factors correspond with each possible interspecies pair of replicates.

#### Single-molecule RNA FISH

Mouse neural progenitors were seeded on Matrigel-coated (Corning 734-1101) coverslips, and human NPs were plated on fibronectin-coated coverslips. Samples were washed in 1 ml of 1X phosphate-buffered saline (PBS), and the coverslip was fixed in 1 ml of fixation buffer (4% paraformaldehyde in 1X PBS) at room temperature for 15 min. The fixed cells were washed with 1X PBS and then permeabilized at 4°C for at least 24 hours using 70% (vol/vol) ethanol. Cells were subsequently rehydrated with 1 ml of wash buffer (10% formamide, 2X SSC, and 0.25% Triton in water) for 15 min before incubating in 100  $\mu$ l of hybridization buffer (nuclease free water with 10% dextran sulfate, 10% formamide, and 2X SSC buffer) containing 125 nM probe and goat anti-OLIG2 (R&D AF2418, 1:800) at 37°C in the dark overnight. The next day, the coverslips were washed for 30 min at 37°C in wash buffer with Alexa Fluor 488 secondary antibody (Life Technologies A-11055, 1:2000). Nuclei were counterstained with DAPI for 5 min. Coverslips were washed once with GLOX solution (Tris pH 8.0 10mM, 2x SSC buffer, 0.4% glucose) and mounted on Antifade solution (GLOW

with 1  $\mu$ l of catalase (Sigma-Aldrich C3515) and 1  $\mu$ l of glucose oxidase (Sigma-Aldrich G2133; dissolved in 50 mM sodium acetate, pH 5.5, to a concentration of 3.7 mg/ml). Mouse-specific and human-specific Olig2 and Sox2 probes conjugated to Quasar 570, CAL Fluor Red 610, or Quasar 670 were designed using the Stellaris Probe Designer online tool and ordered from LGC Biosearch Technologies. A list of the individual probes in the probe sets used for this study is available in table S2.

Samples were imaged with an Olympus wide-field BX61 microscope equipped with a 60X oil UPlanFL N objective (with a 0.9 numerical aperture), an iXon Ultra EMCCD camera (Andor Technology), and a BX2 filter cube with the following filters specific for smFISH: 49304 (Gold FISH), 49310 (Red-2 FISH), and 49307 (Far Red FISH), all from Chroma Technology Corporation. Z-stacks of 8.1  $\mu$ m were acquired, with a 0.3- $\mu$ m distance between individual optical planes, for each wavelength, starting with DAPI, Alexa Fluor 488, Quasar 670, then CAL Fluor Red 610, and then Quasar 570. Typical illumination times are 1.5 s for Quasar 670, 1 s for CAL Fluor Red 610, 1 s for Quasar 570, 200 ms for Alexa Fluor 488, and 1 ms for DAPI. The acquired planes for each Z-stack were focused to ensure maximum coverage of cellular volume and minimum empty areas. The microscope, camera, and hardware were controlled through the Micro-Manager software (ImageJ).

A minimum of 10 Z-stacks were acquired per dataset. For quantifications, OLIG2<sup>+</sup> cells were manually segmented with Icy (61) on maximum-intensity projections of the images. The output of Icy plugin consisted of individual .xls files for each location and fluorescence channel imaged. Each file contained the spot XY coordinates, spot mean fluorescence intensity, and spot area for all the spots detected within the segmented cells in a given image. A custom-made Python script was used to gather all the information across multiple .xls files in just one file per experiment. The total number of spots detected per cell, which are presumed to be representative of the total number of mRNAs per cell, was obtained by counting the total number of detected spots within each cell, which were uniquely identified on the basis of their cell line, sample day, image, and cell identifier number. Data analysis and visualization were carried out in R. Estimation stats were performed using the R package `dabestr` (62).

#### Intracellular flow cytometry

Cells were dissociated with 0.5 ml of accutase (Thermo Fisher Scientific A1110501) and fixed in 4% paraformaldehyde in PBS for 5 min. For stainings,  $1 \times 10^6$  cells were used. Cells were incubated overnight with an antibody mix on PBST with 1% BSA at 4°C. The next day, and



when OLIG2 (R&D AF2418, 1:800) primary antibody was used, cells were pelleted and incubated with Alexa Fluor secondary antibodies (1:1000) at room temperature for 1 hour. Cells were resuspended in 0.5 ml of PBS and filtered for data acquisition on LSR Fortessa or LSRII cytometers. Ten thousand events gated on SOX2 were recorded. The following fluorophore-conjugated antibodies were used: SOX2-V450 (BD 561610, 1:100), PAX6-488 (BD 561664, 1:50), and NKX6.1-PE (BD 563338, 1:50). Analysis was performed using FlowJo software. Cells were gated on SOX2 before plotting. For comparisons between mouse and human, the time points with the maximum percentage of positive cells were compared using two-way ANOVA with multiple Tukey post hoc tests.

#### Global RNA and protein stability measurements

To measure RNA stability, cells were cultured for 3 hours in differentiation medium supplemented with 1 mM EU. After the pulse, cells were washed once with PBS, and cells were grown on fresh medium over the course of the experiment. For proteome stability measurements, cells were starved by replacing complete differentiation medium with methionine-free medium for 30 min. Next, 100  $\mu$ M AHA (L-azidohomoalanine, Sigma 900892) was added to the methionine-free medium for 1 hour. To measure protein stability, AHA pulse was removed by washing the cells once with PBS and growing the cells on complete differentiation medium for the course of the experiment. On the indicated days of differentiation and at specific time points after EU or AHA removal, cells were processed for intracellular flow cytometry. EU-incorporated RNAs were labeled using Click-iT RNA Alexa Fluor 488 HCS Assay (Thermo Fisher Scientific C10327), and AHA-incorporated proteins were labeled using Click-iT Cell Reaction Buffer Kit (Thermo Fisher Scientific C10269) on a volume of 150  $\mu$ l per sample reaction. A minimum of two biological replicates per species per time point from independent experiments were used. For EU quantifications, the mouse dataset consisted of three independent replicates and two measured in duplicates ( $n = 5$ ); human day 4 was measured with two biological replicates in duplicates ( $n = 4$ ); and human day 8 was performed in triplicate, two of them in duplicates ( $n = 5$ ). For AHA quantifications, the mouse dataset consists of three replicates, one of them including triplicates and one with duplicates ( $n = 6$ ); human day 4 and day 8 consists of two biological replicates with duplicates ( $n = 4$ ).

The geometric mean for each time point was obtained from the distributions of intensities and a time series  $F_i(t)$  was generated for each replicate. An initial exponential fit  $y_i(t) = B_i + (C_i - B_i)\exp(-k_i t)$  was used for

each individual replicate. These parameters were used to normalize each fluorescence time series as  $F_{i, \text{norm}} = \frac{F_i(t) - B_i}{C_i - B_i}$ , allowing the comparison of all replicates together. Bootstraps of the normalized replicate time series ensemble were fit to the exponential decay  $y(t) = \exp(-kt)$ . The intervals reported correspond with 99% high density interval (HDI) of the resulting distribution of decay rates.

#### Metabolic labeling, biotin conjugation, and streptavidin pull-down of nascent RNA

Mouse day 2 and human day 8 neural progenitors were pulsed with 1 mM of EU for 3 hours and chased with complete medium for 0, 50, 90, and 180 min postpulse. Cells were dissociated using accutase and rinsed in PBS, and pellets were resuspended in 600  $\mu$ l of RLT buffer (QIAGEN RNeasy kit) and stored at  $-80^\circ\text{C}$  until needed. RNA was extracted following the RNA extraction procedure indicated above. Next, the Click-iT Nascent RNA Capture Kit (Invitrogen C10365) was used to biotinylate and streptavidin purify nascent transcripts. Briefly, 2  $\mu$ g of RNA was clicked to biotin and cleaned up in a 50- $\mu$ l reaction according to the manufacturer's instructions. For biotinylated RNA binding to streptavidin T1 magnetic Dynabeads (Thermo Fisher Scientific 65601), 1  $\mu$ g of RNA was used and 24  $\mu$ l of Dynabeads were used per sample. RNA bound to the beads was immediately used for cDNA synthesis using the SuperScript VILO cDNA synthesis kit (cat. no. 11754-050) in a 50- $\mu$ l reaction, and cDNA was eluted from the beads by at  $85^\circ\text{C}$  for 5 min. Mouse cDNA samples were diluted 1/5, whereas human cDNA samples were diluted 1/4 for qPCR analysis. For RNA enrichment analysis, expression values for each gene were normalized against  $\beta$ -actin, using the delta-delta CT method. To compare between biological replicates and species, maximum levels were normalized to 1, and nonlinear one-phase decay with 95% CI curves were fitted using GraphPad Prism version 8. Three biological replicates from independent experiments were used.

#### Metabolic labeling, biotin conjugation, and streptavidin pull-down of nascent proteins

After 1-hour incubation in methionine free medium (Thermo Fisher Scientific 21013024), nascent proteins were labeled for 2 hours with 1 mM AHA (L-azidohomoalanine, Sigma 900892). AHA was washed away, and cells either collected for protein extracts or fed with complete differentiation medium then collected for protein extracts at the indicated time points. The cells were dissociated using accutase and rinsed in PBS, and the pellets were frozen on dry ice and stored at  $-80^\circ\text{C}$  until needed. To prepare protein extracts, cells were lysed in 50 mM Tris pH 8, 1% SDS, 250 U/ml benzonase (Pierce 88700), and one tablet per 3.5 ml of lysis buffer protease inhibitors (Roche 04693159001). Pro-

tein content of the cell lysates was measured using the BCA protein assay kit (Pierce 23225). One milligram of total protein per sample was labeled using biotin alkyne (Invitrogen B10185) and Click-it technology (Click it Protein Reaction Buffer kit, Invitrogen 10276). Labeled protein extracts were purified by desalting columns Zeba 7-kDa MWCO (Thermo Fisher Scientific 89892) and mixed with washed magnetic streptavidin beads (400  $\mu$ l of slurry per sample, Thermo Fisher Scientific 65602) for 16 hours at  $4^\circ\text{C}$ . The beads were washed four times with 0.1% SDS, 0.1% BSA PBS, once with 0.1% SDS, 0.1% BSA PBS, and biotinylated proteins were recovered by heating at  $92^\circ\text{C}$  for 10 min in 2X Laemmli buffer.

#### Western Blots and band intensity measurements

Samples were loaded on 12% precast gels (Biorad 10 or 15 wells, 4561043 or 4561046, respectively) and run at 110 V for 1 hour 45 min. Proteins were transferred on nitrocellulose membrane (Amersham 10600012) at 300 mA for 2 hours. Membranes were treated with tris-buffered saline (TBS) blocking buffer at room temperature for 30 min. Primary antibodies were applied in 0.1% Tween-20, TBS blocking buffer for 16 hours at  $4^\circ\text{C}$ . The primary antibodies used were rabbit anti-OLIG2 (Millipore AB9610, 1:2000), goat anti-OLIG2 (R&D AF2418, 1:1000), mouse anti-NKX6.1 (DSHB F55A10, 1:100), rabbit anti-NKX6.1 (Novus Biologicals NBPI-49672, 1:1000), goat anti-SOX1 (R&D AF3369, 1:500), and rabbit anti-SOX2 (Millipore AB5603, 1:500). Secondary antibodies were applied in 0.2% Tween-20, 0.01% SDS, TBS blocking buffer for 2 hours at room temperature. Secondary antibodies were sourced from LICOR: goat anti-rabbit 800CW (926-32211, 1:5000), donkey anti-mouse 680LT (925-68022, 1:10000), donkey anti-goat 800CW (925-32214, 1:5000), and donkey anti-rabbit 680LT (925-68023, 1:10000). When required, membranes were stripped using NewBlot IR stripping buffer (Licor 928-40028) for 30 min at room temperature. The membranes were scanned using an Odyssey CLx gel documentation set up. Band intensities were measured using Fiji and plotted using GraphPad Prism version 8 following the procedure described for nascent RNA pull-downs. A minimum of three biological replicates per species from independent experiments were used. The mouse dataset consists of three biological replicates; human detection of OLIG2 and NKX6.1 stability corresponds to three biological replicates, and detection for SOX1 and SOX2 was from four biological replicates.

#### mKATE2 stability measurements

To measure mKATE2 stability, cells were exposed to 100 nM RA and 1  $\mu$ M SAG from day 0 on the neural differentiation protocol to induce maximum levels of Ptch1::T2A-mKate2 expression driven from the Ptch1 locus. Next,

5  $\mu$ M Vismodegib (Cayman Chemical GDC-0449) was added when mKate2 intensity was maximal, and samples were collected at the indicated time points. Samples were stained with Live/Dead cell stain (Thermo Fisher Scientific L34976) as per the manufacturer's instructions and fixed. mKATE2 intensity was quantified by FACS using the 610/20 yellow red excitation laser on LSR Fortessa cytometers. Analysis was performed using FlowJo software. mKATE2 half-life estimations were performed following the same procedure as for the proteome stability. A minimum of two biological replicates in duplicates per species per time point from independent experiments were used. Mouse experiments comprised four biological replicates, with three performed in duplicates  $n = 7$ ; human quantifications correspond to two biological replicates in duplicates:  $n = 4$ )

### Cell cycle measurements

0.5  $\mu$ M EdU (Thermo Fisher Scientific C10633) was added to mouse and human neural progenitors at the indicated days of differentiation. Samples were then collected in duplicates at the indicated time points and processed for intracellular flow cytometry. For EdU detection, the Click-iT Plus EdU Alexa Fluor 488 Flow Cytometry Assay Kit (Thermo Fisher Scientific C10633) was used according to the manufacturer's instructions, at a volume of 200  $\mu$ l per sample reaction. For EdU incorporation measurements, cells were counterstained with DRAQ5 (Cell Signaling 4084S, 1:10,000) to measure DNA content. Cells were gated on SOX2 and EdU, and the percentage of positive cells per time point was recorded. Estimates of cell cycle parameters were obtained by assuming that independent cells in the population advance at the same speed along the cell cycle, so the fraction  $[r(t)]$  of Edu-positive cells increases linearly in time until a time equal to the cell cycle duration ( $T$ ) at which point all the responsive cells are stained (47)  $r(t) = r_M \min[1, r_0 + t(1 - r_0)/T]$ . The initial fraction of cells stained at the pulse ( $r_0$ ) and the maximum fraction of cells labeled in the population ( $r_M$ ) are parameters of the model. Flat prior distributions for the three parameters ( $T, r_0, r_M$ ), and a Gaussian distributed likelihood around the model prediction, were used to determine the posterior probability distribution of the parameters using PyDream Markov chain Monte Carlo implementation (63). The reported parameters in the manuscript correspond with the 99% HDI of the marginal posterior distribution for the cell cycle duration  $T$ . A minimum of two biological replicates in duplicates per species per time point from independent experiments was used. For mouse, three biological replicates with two in duplicates were performed ( $n = 5$ ); for human day 4, two biological replicates in duplicates  $n = 4$ ; and for human day 8, three biological

replicates, two of which were performed in duplicates ( $n = 5$ ).

### REFERENCES AND NOTES

- K. Toma, T.-C. Wang, C. Hanashima, Encoding and decoding time in neural development. *Dev. Growth Differ.* **58**, 59–72 (2016). doi: [10.1111/dgd.12257](#); pmid: [26748623](#)
- M. Ebisuya, J. Briscoe, What does time mean in development? *Development* **145**, dev164368 (2018). doi: [10.1242/dev.164368](#); pmid: [29945985](#)
- S. Herculano-Houzel, The remarkable, yet not extraordinary, human brain as a scaled-up primate brain and its associated cost. *Proc. Natl. Acad. Sci. U.S.A.* **109** (suppl. 1), 10661–10668 (2012). doi: [10.1073/pnas.1201895109](#); pmid: [22723358](#)
- J. van den Aamele, L. Tiberi, P. Vanderhaeghen, I. Espuny-Camacho, Thinking out of the dish: What to learn about cortical development using pluripotent stem cells. *Trends Neurosci.* **37**, 334–342 (2014). doi: [10.1016/j.trends.2014.03.005](#); pmid: [24745669](#)
- C. C. Gertz, J. H. Lui, B. E. LaMonica, X. Wang, A. R. Kriegstein, Diverse behaviors of outer radial glia in developing ferret and human cortex. *J. Neurosci.* **34**, 2559–2570 (2014). doi: [10.1523/JNEUROSCI.2645-13.2014](#); pmid: [24523546](#)
- D. V. Hansen, J. H. Lui, P. R. L. Parker, A. R. Kriegstein, Neurogenic radial glia in the outer subventricular zone of human neocortex. *Nature* **464**, 554–561 (2010). doi: [10.1038/nature08845](#); pmid: [20154730](#)
- J. Briscoe, S. Small, Morphogen rules: Design principles of gradient-mediated embryo patterning. *Development* **142**, 3996–4009 (2015). doi: [10.1242/dev.129452](#); pmid: [26628090](#)
- B. N. Davis-Dusenbery, L. A. Williams, J. R. Klim, K. Eggan, How to make spinal motor neurons. *Development* **141**, 491–501 (2014). doi: [10.1242/dev.097410](#); pmid: [24449832](#)
- A. Kicheva et al., Coordination of progenitor specification and growth in mouse and chick spinal cord. *Science* **345**, 1254927 (2014). doi: [10.1126/science.1254927](#); pmid: [25258086](#)
- C. Gomez et al., Control of segment number in vertebrate embryos. *Nature* **454**, 335–339 (2008). doi: [10.1038/nature07020](#); pmid: [18563087](#)
- A. Hubaud, O. Pourquie, Signalling dynamics in vertebrate segmentation. *Nat. Rev. Mol. Cell Biol.* **15**, 709–721 (2014). doi: [10.1038/nrm3891](#); pmid: [25335437](#)
- M. Matsuda, H. Hayashi, J. Garcia-Ojalvo, K. Yoshioka-Kobayashi, R. Kageyama, Y. Yamanaka, M. Ikeda, C. Alev, M. Ebisuya, Species-specific oscillation periods of human and mouse segmentation clocks are due to cell autonomous differences in biochemical reaction parameters. *bioRxiv* 650648 [Preprint]. 26 May 2019; doi: [10.1101/650648](#)
- J. Briscoe, A. Pierani, T. M. Jessell, J. Ericson, A homeodomain protein code specifies progenitor cell identity and neuronal fate in the ventral neural tube. *Cell* **101**, 435–445 (2000). doi: [10.1016/S0092-8674\(00\)80853-3](#); pmid: [10830170](#)
- E. Dessaud, A. P. McMahon, J. Briscoe, Pattern formation in the vertebrate neural tube: A sonic hedgehog morphogen-regulated transcriptional network. *Development* **135**, 2489–2503 (2008). doi: [10.1242/dev.009324](#); pmid: [18621990](#)
- E. Dessaud et al., Interpretation of the sonic hedgehog morphogen gradient by a temporal adaptation mechanism. *Nature* **450**, 717–720 (2007). doi: [10.1038/nature06347](#); pmid: [18046410](#)
- C. Catela, P. Kratsios, Transcriptional mechanisms of motor neuron development in vertebrates and invertebrates. *Dev. Biol.* S0012-1606(17)30472-4 (2019). doi: [10.1016/j.ydbio.2019.08.022](#); pmid: [31479648](#)
- U. Marklund et al., Domain-specific control of neurogenesis achieved through patterned regulation of Notch ligand expression. *Development* **137**, 437–445 (2010). doi: [10.1242/dev.036806](#); pmid: [20081190](#)
- M. W. Amoroso et al., Accelerated high-yield generation of limb-innervating motor neurons from human stem cells. *J. Neurosci.* **33**, 574–586 (2013). doi: [10.1523/JNEUROSCI.0906-12.2013](#); pmid: [23303937](#)
- J. Kerwin et al., The HUDSEN Atlas: A three-dimensional (3D) spatial framework for studying gene expression in the developing human brain. *J. Anat.* **217**, 289–299 (2010). doi: [10.1111/j.1469-7580.2010.01290.x](#); pmid: [20979583](#)
- M. Gouti et al., In vitro generation of neuromesodermal progenitors reveals distinct roles for wnt signalling in the specification of spinal cord and paraxial mesoderm identity. *PLOS Biol.* **12**, e1001937 (2014). doi: [10.1371/journal.pbio.1001937](#); pmid: [25157815](#)
- S. M. Chambers et al., Highly efficient neural conversion of human ES and iPS cells by dual inhibition of SMAD signaling. *Nat. Biotechnol.* **27**, 275–280 (2009). doi: [10.1038/nbt.1529](#); pmid: [19252484](#)
- H. Lee et al., Directed differentiation and transplantation of human embryonic stem cell-derived motoneurons. *Stem Cells* **25**, 1931–1939 (2007). doi: [10.1634/stemcells.2007-0097](#); pmid: [17478583](#)
- R. Patani et al., Retinoid-independent motor neurogenesis from human embryonic stem cells reveals a medial columnar ground state. *Nat. Commun.* **2**, 214 (2011). doi: [10.1038/ncomms1216](#); pmid: [21364553](#)
- E. S. Lippmann et al., Deterministic HOX patterning in human pluripotent stem cell-derived neuroectoderm. *Stem Cell Reports* **4**, 632–644 (2015). doi: [10.1016/j.stemcr.2015.02.018](#); pmid: [25843047](#)
- V. Metzlis et al., Nervous system regionalization entails axial allocation before neural differentiation. *Cell* **175**, 1105–1118.e17 (2018). doi: [10.1016/j.cell.2018.09.040](#); pmid: [30343898](#)
- A. Sagner et al., Olig2 and Hes regulatory dynamics during motor neuron differentiation revealed by single cell transcriptomics. *PLOS Biol.* **16**, e2003127 (2018). doi: [10.1371/journal.pbio.2003127](#); pmid: [29389974](#)
- J. S. Dassen, J.-P. Liu, T. M. Jessell, Motor neuron columnar fate imposed by sequential phases of Hox-c activity. *Nature* **425**, 926–933 (2003). doi: [10.1038/nature02051](#); pmid: [14586461](#)
- C. Barry et al., Automated minute scale RNA-seq of pluripotent stem cell differentiation reveals early divergence of human and mouse gene expression kinetics. *PLOS Comput. Biol.* **15**, e1007543 (2019). doi: [10.1371/journal.pcbi.1007543](#); pmid: [31815944](#)
- C. Barry et al., Species-specific developmental timing is maintained by pluripotent stem cells ex utero. *Dev. Biol.* **423**, 101–110 (2017). doi: [10.1016/j.ydbio.2017.02.002](#); pmid: [28179190](#)
- N. Gaspard et al., An intrinsic mechanism of corticogenesis from embryonic stem cells. *Nature* **455**, 351–357 (2008). doi: [10.1038/nature07287](#); pmid: [18716623](#)
- D. Linaro et al., Xenotransplanted human cortical neurons reveal species-specific development and functional integration into mouse visual circuits. *Neuron* **104**, 972–986.e6 (2019). doi: [10.1016/j.neuron.2019.10.002](#); pmid: [31761708](#)
- J. Lee, K. A. Platt, P. Censullo, A. Ruiz i Altaba, Gli1 is a target of sonic hedgehog that induces ventral neural tube development. *Development* **124**, 2537–2552 (1997). pmid: [9216996](#)
- V. Marigo, C. J. Tabin, Regulation of patched by sonic hedgehog in the developing neural tube. *Proc. Natl. Acad. Sci. U.S.A.* **93**, 9346–9351 (1996). doi: [10.1073/pnas.93.18.9346](#); pmid: [8790332](#)
- T. Oosterveen et al., Mechanistic differences in the transcriptional interpretation of local and long-range Shh morphogen signaling. *Dev. Cell* **23**, 1006–1019 (2012). doi: [10.1016/j.devcel.2012.09.015](#); pmid: [23153497](#)
- K. A. Peterson et al., Neural-specific Sox2 input and differential Gli-binding affinity provide context and positional information in Shh-directed neural patterning. *Genes Dev.* **26**, 2802–2816 (2012). doi: [10.1101/gad.207142.112](#); pmid: [23249739](#)
- D. Hernandez, P. J. Mee, J. E. Martin, V. L. J. Tybulewicz, E. M. C. Fisher, Transchromosomal mouse embryonic stem cell lines and chimeric mice that contain freely segregating segments of human chromosome 21. *Hum. Mol. Genet.* **8**, 923–933 (1999). doi: [10.1093/hmg/8.5.923](#); pmid: [10196383](#)
- F. Cacace, P. Paci, V. Cusimano, A. Germani, L. Farina, Stochastic modeling of expression kinetics identifies messenger half-lives and reveals sequential waves of co-ordinated transcription and decay. *PLOS Comput. Biol.* **8**, e1002772 (2012). doi: [10.1371/journal.pcbi.1002772](#); pmid: [23144606](#)
- N. Rosenfeld, U. Alon, Response delays and the structure of transcription networks. *J. Mol. Biol.* **329**, 645–654 (2003). doi: [10.1016/S0022-2836\(03\)00506-0](#); pmid: [12787666](#)
- E. Eden et al., Proteome half-life dynamics in living human cells. *Science* **331**, 764–768 (2011). doi: [10.1126/science.1199784](#); pmid: [21233346](#)
- C. C. Friedel, L. Dolken, Z. Ruzsics, U. H. Koszinowski, R. Zimmer, Conserved principles of mammalian transcriptional regulation revealed by RNA half-life. *Nucleic Acids Res.* **37**, e115 (2009). doi: [10.1093/nar/gkp542](#); pmid: [19561020](#)
- M. Cohen, K. M. Page, R. Perez-Carrasco, C. P. Barnes, J. Briscoe, A theoretical framework for the regulation of Shh morphogen-controlled gene expression. *Development* **141**, 3868–3878 (2014). doi: [10.1242/dev.112573](#); pmid: [25294939](#)
- C. M. Rudin et al., Treatment of medulloblastoma with hedgehog pathway inhibitor GDC-0449. *N. Engl. J. Med.* **361**, 1173–1178 (2009). doi: [10.1056/NEJMoa0902903](#); pmid: [19726761](#)
- D. R. Kornack, P. Rakic, Changes in cell-cycle kinetics during the development and evolution of primate neocortex. *Proc. Natl. Acad. Sci. U.S.A.* **95**, 1242–1246 (1998). doi: [10.1073/pnas.95.3.1242](#); pmid: [9448316](#)



44. N. A. J. Krentz *et al.*, Phosphorylation of NEUROG3 links endocrine differentiation to the cell cycle in pancreatic progenitors. *Dev. Cell* **41**, 129–142.e6 (2017). doi: [10.1016/j.devcel.2017.02.006](https://doi.org/10.1016/j.devcel.2017.02.006); pmid: [28441528](https://pubmed.ncbi.nlm.nih.gov/28441528/)
45. F. Mora-Bermúdez *et al.*, Differences and similarities between human and chimpanzee neural progenitors during cerebral cortex development. *eLife* **5**, e18683 (2016). doi: [10.7554/eLife.18683](https://doi.org/10.7554/eLife.18683); pmid: [27669147](https://pubmed.ncbi.nlm.nih.gov/27669147/)
46. T. Otani, M. C. C. Marchetto, F. H. H. Gage, B. D. D. Simons, F. J. J. Livesey, 2D and 3D stem cell models of primate cortical development identify species-specific differences in progenitor behavior contributing to brain size. *Cell Stem Cell* **18**, 467–480 (2016). doi: [10.1016/j.stem.2016.03.003](https://doi.org/10.1016/j.stem.2016.03.003); pmid: [27049876](https://pubmed.ncbi.nlm.nih.gov/27049876/)
47. R. S. Nowakowski, S. B. Lewin, M. W. Miller, Bromodeoxyuridine immunohistochemical determination of the lengths of the cell cycle and the DNA-synthetic phase for an anatomically defined population. *J. Neurocytol.* **18**, 311–318 (1989). doi: [10.1007/BF01190834](https://doi.org/10.1007/BF01190834); pmid: [2746304](https://pubmed.ncbi.nlm.nih.gov/2746304/)
48. R. W. King, R. J. Deshaies, J.-M. Peters, M. W. Kirschner, How proteolysis drives the cell cycle. *Science* **274**, 1652–1659 (1996). doi: [10.1126/science.274.5293.1652](https://doi.org/10.1126/science.274.5293.1652); pmid: [8939846](https://pubmed.ncbi.nlm.nih.gov/8939846/)
49. D. M. Koepp, “Cell cycle regulation by protein degradation” in *Cell Cycle Control*, vol. 1170 of *Methods in Molecular Biology*, E. Noguchi, M. Gadaleta, Eds. (Humana Press, 2014), pp. 61–73.
50. N. Balaskas *et al.*, Gene regulatory logic for reading the sonic hedgehog signaling gradient in the vertebrate neural tube. *Cell* **148**, 273–284 (2012). doi: [10.1016/j.cell.2011.10.047](https://doi.org/10.1016/j.cell.2011.10.047); pmid: [22265416](https://pubmed.ncbi.nlm.nih.gov/22265416/)
51. M. Zagorski, A. Kicheva, “Measuring dorsoventral pattern and morphogen signaling profiles in the growing neural tube” in *Morphogen Gradients*, vol. 1863 of *Methods in Molecular Biology*, J. Dubrulle, Ed. (Humana Press, 2018), pp. 47–63.
52. M. Gouti *et al.*, A gene regulatory network balances neural and mesoderm specification during vertebrate trunk development. *Dev. Cell* **41**, 243–261.e7 (2017). doi: [10.1016/j.devcel.2017.04.002](https://doi.org/10.1016/j.devcel.2017.04.002); pmid: [28457792](https://pubmed.ncbi.nlm.nih.gov/28457792/)
53. P. Di Tommaso *et al.*, Nextflow enables reproducible computational workflows. *Nat. Biotechnol.* **35**, 316–319 (2017). doi: [10.1038/nbt.3820](https://doi.org/10.1038/nbt.3820); pmid: [28398311](https://pubmed.ncbi.nlm.nih.gov/28398311/)
54. B. L. Aken *et al.*, Ensembl 2017. *Nucleic Acids Res.* **45**, D635–D642 (2017). doi: [10.1093/nar/gkw1104](https://doi.org/10.1093/nar/gkw1104); pmid: [27899575](https://pubmed.ncbi.nlm.nih.gov/27899575/)
55. L. Wang, S. Wang, W. Li, RSeQC: Quality control of RNA-seq experiments. *Bioinformatics* **28**, 2184–2185 (2012). doi: [10.1093/bioinformatics/bts356](https://doi.org/10.1093/bioinformatics/bts356); pmid: [22743226](https://pubmed.ncbi.nlm.nih.gov/22743226/)
56. D. S. DeLuca *et al.*, RNA-SeQC: RNA-seq metrics for quality control and process optimization. *Bioinformatics* **28**, 1530–1532 (2012). doi: [10.1093/bioinformatics/bts196](https://doi.org/10.1093/bioinformatics/bts196); pmid: [22539670](https://pubmed.ncbi.nlm.nih.gov/22539670/)
57. A. Dobin *et al.*, STAR: Ultrafast universal RNA-seq aligner. *Bioinformatics* **29**, 15–21 (2013). doi: [10.1093/bioinformatics/bts635](https://doi.org/10.1093/bioinformatics/bts635); pmid: [23104886](https://pubmed.ncbi.nlm.nih.gov/23104886/)
58. B. Li, C. N. Dewey, RSEM: Accurate transcript quantification from RNA-seq data with or without a reference genome. *BMC Bioinformatics* **12**, 323 (2011). doi: [10.1186/1471-2105-12-323](https://doi.org/10.1186/1471-2105-12-323); pmid: [21816040](https://pubmed.ncbi.nlm.nih.gov/21816040/)
59. I. C. McDowell *et al.*, Clustering gene expression time series data using an infinite Gaussian process mixture model. *PLOS Comput. Biol.* **14**, e1005896 (2018). doi: [10.1371/journal.pcbi.1005896](https://doi.org/10.1371/journal.pcbi.1005896); pmid: [29337990](https://pubmed.ncbi.nlm.nih.gov/29337990/)
60. G. Csardi, T. Nepusz, The igraph software package for complex network research. *InterJournal* **2006**, 1695 (2006).
61. F. de Chaumont *et al.*, Icy: An open bioimage informatics platform for extended reproducible research. *Nat. Methods* **9**, 690–696 (2012). doi: [10.1038/nmeth.2075](https://doi.org/10.1038/nmeth.2075); pmid: [22743774](https://pubmed.ncbi.nlm.nih.gov/22743774/)
62. J. Ho, T. Tumkaya, S. Aryal, H. Choi, A. Claridge-Chang, Moving beyond *P* values: Data analysis with estimation graphics. *Nat. Methods* **16**, 565–566 (2019). doi: [10.1038/s41592-019-0470-3](https://doi.org/10.1038/s41592-019-0470-3); pmid: [31217592](https://pubmed.ncbi.nlm.nih.gov/31217592/)
63. E. M. Shockley, J. A. Vrugt, C. F. Lopez, PyDREAM: High-dimensional parameter inference for biological models in python. *Bioinformatics* **34**, 695–697 (2018). doi: [10.1093/bioinformatics/btx626](https://doi.org/10.1093/bioinformatics/btx626); pmid: [29028896](https://pubmed.ncbi.nlm.nih.gov/29028896/)

# ACKNOWLEDGMENTS

We are grateful for the human embryonic material provided by MRC/Wellcome Trust (MR/R006237/1) Human Developmental Biology Resource and the generous donors whose contributions have enabled part of this research. We thank A. de la Peña, A. Tsakiridis, V. Metzis, A. Sagner, M. J. Delás, T. Watson, A. Pezzotta, R. Blassberg, J. Delile, T. A. Rodríguez, P. East, and R. Goldstone, as well as other members of the lab, for advice, reagents, and critical feedback. We thank the Crick Science

Technology Platforms, in particular the Advanced Sequencing Facility, the Equipment Park, the Flow Cytometry Facility, and the Bioinformatics and Biostatistics group. **Funding:** This work was supported by the Francis Crick Institute, which receives its core funding from Cancer Research UK, the UK Medical Research Council, and the Wellcome Trust (all under FC001051). T.R. received funding from an EMBO long-term fellowship (ALTF 328-2015). R.P.-C. is funded by the Clifford Fellowship of the Mathematics Department at UCL, and J.B. is also funded by the European Research Council under European Union (EU) Horizon 2020 research and innovation program grant 742138. V.L.J.T. was supported by the Francis Crick Institute, which receives its core funding from Cancer Research UK (FC001194), the UK Medical Research Council (FC001194), and the Wellcome Trust (FC001194). **Author contributions:** T.R. and J.B. conceived the project, interpreted the data, and wrote the manuscript with input from all authors. T.R. designed and performed experiments and data analysis. D.S. designed and performed experiments and data analysis. R.P.-C. performed theoretical modeling and data analysis. L.G.-P. designed experiments and performed data analysis for smFISH. C.B. performed bioinformatic analysis. M.M. performed embryo work and generated and characterized the Pth1::T2A-mKate2 mouse embryonic stem cell line. K.E. performed embryo work. J.L. analyzed embryo data. E.M.C.F. and V.L.J.T. provided reagents and feedback. **Competing interests:** The authors declare no competing or financial interests. **Data and materials availability:** The accession number for the bulk RNA-seq data reported in this paper is GSE140749.

# SUPPLEMENTARY MATERIALS

[science.sciencemag.org/content/369/6510/eaba7667/suppl/DC1](https://science.sciencemag.org/content/369/6510/eaba7667/suppl/DC1)  
 Supplementary Text  
 Figs. S1 to S8  
 Tables S1 and S2  
 Data S1  
 Reference (64)  
 MDAR Reproducibility Checklist

[View/request a protocol for this paper from Bio-protocol.](#)

3 January 2020; accepted 29 July 2020  
[10.1126/science.aba7667](https://doi.org/10.1126/science.aba7667)

## RESEARCH ARTICLE

## DEVELOPMENTAL BIOLOGY

## Species-specific segmentation clock periods are due to differential biochemical reaction speeds

Mitsuhiro Matsuda<sup>1,2</sup>, Hanako Hayashi<sup>1\*</sup>, Jordi Garcia-Ojalvo<sup>3</sup>, Kumiko Yoshioka-Kobayashi<sup>4†</sup>, Ryoichiro Kageyama<sup>4,5</sup>, Yoshihiro Yamanaka<sup>6,7</sup>, Makoto Ikeya<sup>6</sup>, Junya Toguchida<sup>4,6</sup>, Cantas Alev<sup>6,7</sup>, Miki Ebisuya<sup>1,2‡</sup>

Although mechanisms of embryonic development are similar between mice and humans, the time scale is generally slower in humans. To investigate these interspecies differences in development, we recapitulate murine and human segmentation clocks that display 2- to 3-hour and 5- to 6-hour oscillation periods, respectively. Our interspecies genome-swapping analyses indicate that the period difference is not due to sequence differences in the *HES7* locus, the core gene of the segmentation clock. Instead, we demonstrate that multiple biochemical reactions of *HES7*, including the degradation and expression delays, are slower in human cells than they are in mouse cells. With the measured biochemical parameters, our mathematical model accounts for the two- to threefold period difference between the species. We propose that cell-autonomous differences in biochemical reaction speeds underlie temporal differences in development between species.

Different animal species develop at different time scales (*1*). The mouse gestation period is ~20 days whereas that of a human is ~9 months. At each developmental stage, the order of developmental processes and the underlying mechanisms are largely conserved between the species, but the progression speed differs. For example, murine and human nervous systems generate multiple neuronal subtypes in the same order, but the sequential neurogenesis takes longer in humans (*1–3*). We propose to call such interspecies differences in developmental tempo—despite conservation of the mechanism—developmental allochry.

The causes of allochry remain a mystery. As embryos of different species differ in many aspects, including their sizes, geometries, and nutrients, direct interspecies comparison is challenging. Investigating developmental dynamics in human embryos is also ethically difficult. To overcome these difficulties, we

decided to use in vitro differentiation of pluripotent stem cells and compare the same types of cells under similar culture conditions between different species. As an example of well-defined developmental time, we focused on the segmentation clock—oscillatory gene expression that regulates the timing of the sequential formation of paired body segments out of presomitic mesoderm (PSM) cells (*4, 5*). The sequentially formed body segments are called somites, and they give rise to the vertebral column, ribs, skeletal muscles, and subcutaneous tissues in later stages of development. The oscillation period (i.e., the duration for one cycle) of the segmentation clock is species-specific: ~30 min in zebrafish, 90 min in chickens, 2 to 3 hours in mice, and 4 to 6 hours in humans (*5, 6*). In this study, we recapitulated murine and human segmentation clocks in vitro and showed that the allochry of oscillation periods is derived from cell-autonomous differences in the speeds of biochemical reactions between the species.

### Cell-autonomous period difference between species

To compare murine and human segmentation clocks in vitro, we induced PSM-like cells from mouse embryonic stem cells (ESCs) and human induced pluripotent stem cells (iPSCs) (fig. S1A and Fig. 1A). The detailed induction protocol and characterization of PSM-like cells have been described in our recent papers (*7, 8*), and several other groups have also reported similar PSM-induction protocols (*9–13*). The induced PSM-like cells are hereafter referred to as PSM. To visualize the segmentation clock, we introduced a *HES7* promoter-luciferase reporter (*8, 14*), which detected clear

synchronized oscillations of *HES7* expression in both murine and human PSM (Fig. 1A and movie S1). Consistent with previous in vivo and in vitro measurements (*6, 8, 12–15*), the mouse PSM oscillated with a period of  $122 \pm 2$  min (mean  $\pm$  SD), whereas the human PSM exhibited a period of  $322 \pm 6$  min (Fig. 1, B to D, and fig. S1B). Thus, our induced PSM serves as an ideal in vitro platform to investigate the cause of the two- to threefold period difference between murine and human segmentation clocks.

The gene regulatory network of the segmentation clock consists of two parts: the intracellular network that gives rise to a cell-autonomous oscillation and the intercellular network that synchronizes the oscillations among cells (fig. S2A) (*16, 17*). We attempted to clarify whether the interspecies period difference stems from the single-cell oscillator or the multicellular synchronized oscillations. Although intercellular communication through NOTCH-DELTA signaling synchronizes oscillations (*16, 18–20*), treatment of PSM cells with a NOTCH signaling inhibitor did not affect the oscillation period significantly (fig. S2, B and C). As WNT and FGF signaling pathways also modulate the segmentation clock (*21, 22*), we measured the oscillation period in a sparse cell culture, where cells were isolated from the neighboring cells (Fig. 1E, fig. S3, and movie S2). The isolated single PSM cells still displayed the two- to threefold period difference between the species (mouse,  $160 \pm 9$  min; human,  $376 \pm 51$  min) (Fig. 1F), even though the oscillations at the single-cell level were noisier and slower than the population-level oscillations (fig. S3, B and C). These results indicate that the period difference of *HES7* oscillation between mice and humans is cell autonomous and that the cause of the interspecies difference should lie in the oscillation mechanism at the single-cell level.

### Interspecies period difference is not due to *HES7* sequence differences

*HES7* oscillations arise from a delayed autoregulatory negative feedback loop: *HES7* is a transcription repressor that directly inhibits its own promoter with time delays (fig. S2A) (*16, 23*). We first hypothesized that differences in the sequences of *HES7* loci between murine and human genomes might lead to the observed oscillation-period difference. To test this hypothesis, we swapped murine and human *HES7* loci (Fig. 2A). The sequence of the human *HES7* locus, including the promoter, exons, introns, and untranslated regions (UTRs), was swapped into the mouse *Hes7* locus in mouse ESCs (fig. S4), and the resulting cells were induced into the PSM fate. The homozygous knock-in (homo swap) PSM and the heterozygous knock-in (hetero swap) PSM showed slightly longer oscillation periods of  $146 \pm 7$

<sup>1</sup>RIKEN Center for Biosystems Dynamics Research (RIKEN BDR), 2-2-3 Minatojima-minamimachi, Chuo-ku, 650-0047 Kobe, Japan. <sup>2</sup>European Molecular Biology Laboratory (EMBL) Barcelona, Dr. Aiguader 88, 08003 Barcelona, Spain. <sup>3</sup>Department of Experimental and Health Sciences, Universitat Pompeu Fabra, Dr. Aiguader 88, 08003 Barcelona, Spain. <sup>4</sup>Institute for Frontier Life and Medical Sciences, Kyoto University, Shogoin-Kawahara-cho, Sakyo-ku, 606-8507 Kyoto, Japan. <sup>5</sup>Institute for Integrated Cell-Material Sciences, Kyoto University, Yoshida Ushinomiya-cho, Sakyo-ku, 606-8501 Kyoto, Japan. <sup>6</sup>Center for iPS Cell Research and Application (CiRA), Kyoto University, 53 Shogoin-Kawahara-cho, Sakyo-ku, 606-8507 Kyoto, Japan. <sup>7</sup>Institute for the Advanced Study of Human Biology (ASHBI), Kyoto University, Yoshida-Konoe-cho, Sakyo-ku, 606-8501 Kyoto, Japan. \*Present address: Department of Biochemistry, University of Oxford, Oxford OX1 3QU, UK. †Present address: Institute for the Advanced Study of Human Biology (ASHBI), Kyoto University, Yoshida-Konoe-cho, Sakyo-ku, 606-8501 Kyoto, Japan. ‡Corresponding author. Email: miki.ebisuya@embl.es



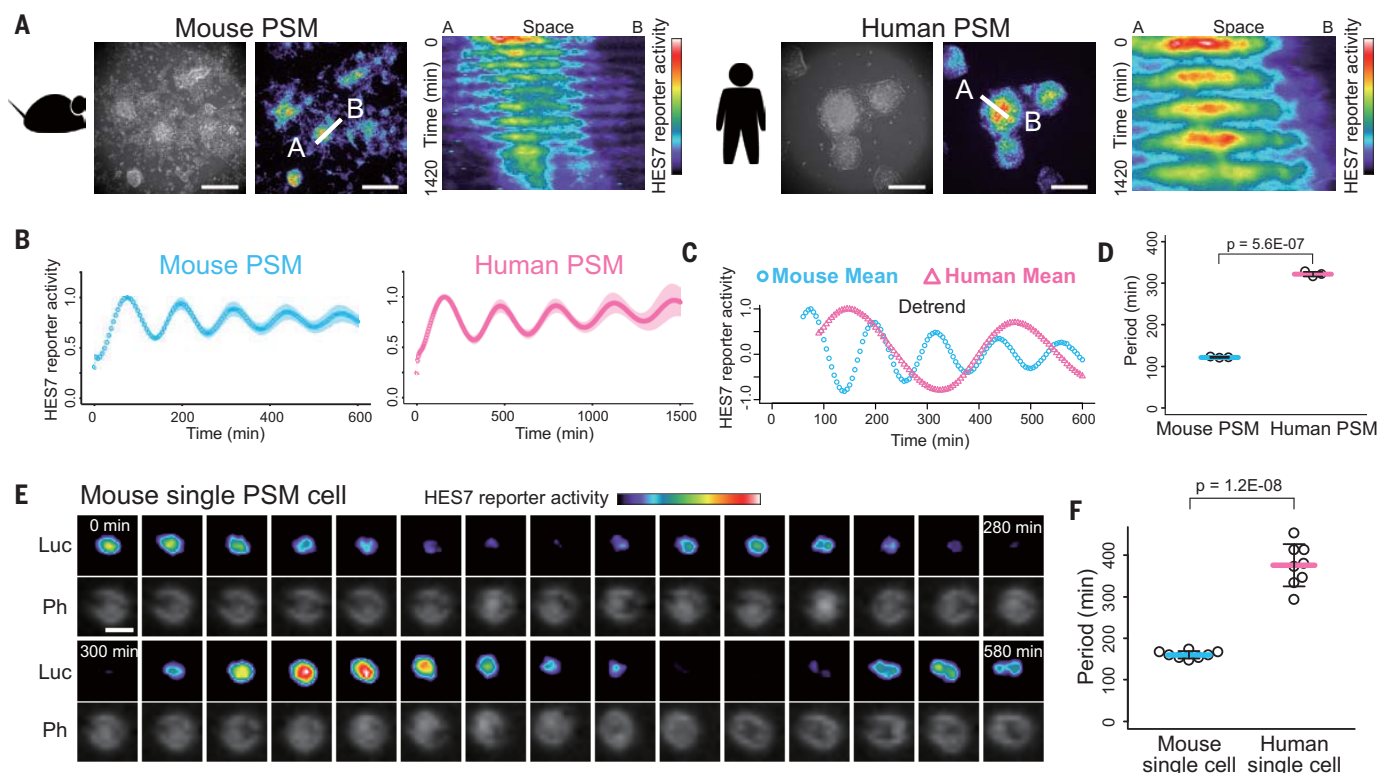


**Fig. 1. Period difference between murine and human segmentation clocks.**

(A) *HES7* reporter activities in murine and human PSM-like cells in time-lapse imaging with a luminescent microscope. Kymographs indicate spatiotemporal signals along the line between points A and B. Scale bars, 400  $\mu$ m. See also movie S1. (B) Oscillatory *HES7* reporter activity measured with a luminometer, using a collective signal from a 35-mm dish. Shaded regions indicate

means  $\pm$  SD ( $n = 3$  biological replicates). (C) Overlay of murine and human detrended signals. (D) Oscillation periods estimated from fig. S1B. (E) Time-lapse imaging of a sparsely seeded single PSM cell (movie S2). Luc, luciferase; Ph, phase. Scale bar, 20  $\mu$ m. (F) Periods of single cells estimated from fig. S3. Error bars in (D) and (F) indicate means  $\pm$  SD. *P* values are from a two-sided Student's *t* test.

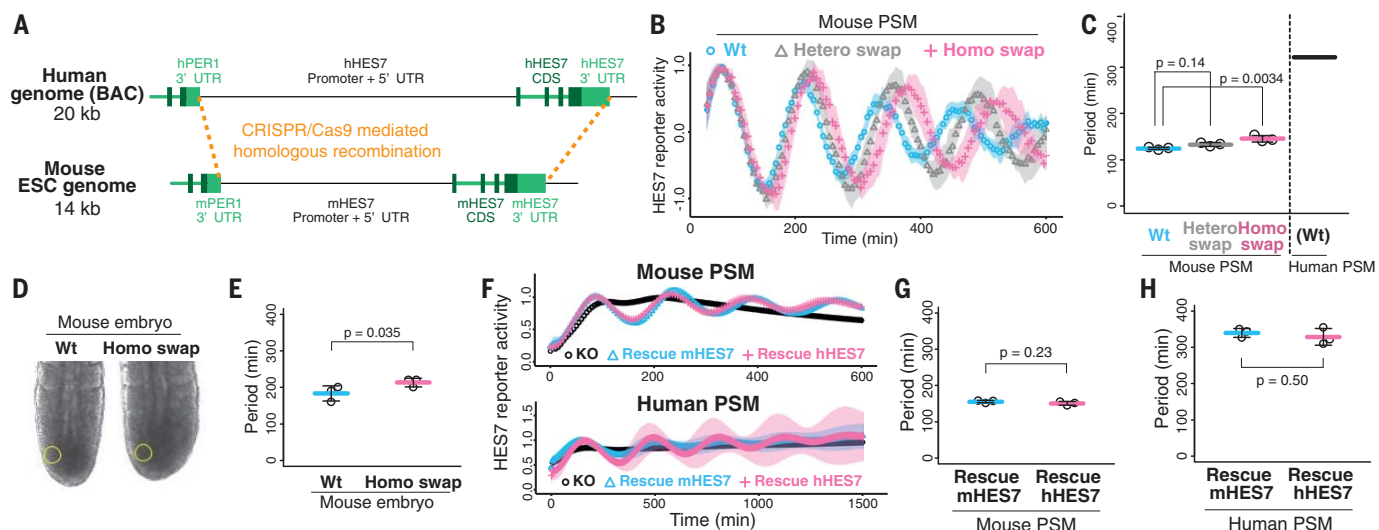


**Fig. 2. Swapping murine and human *HES7* loci.** (A) Homologous recombination between murine and human *HES7* loci. BAC, bacterial artificial chromosome. (B) *HES7* reporter activities in mouse PSM containing human *HES7* locus. WT indicates mouse *HES7*/mouse *HES7*; hetero swap indicates human *HES7*/mouse *HES7*; and homo swap indicates human *HES7*/human *HES7*. (C) Periods estimated from (B). WT human PSM period shown in Fig. 1D is displayed as a control. *P* values are from a two-sided Dunnett's test. (D) Time-lapse imaging of ex vivo tail bud cultures of E10.5 mouse

embryos containing human *HES7* locus. (E) Periods estimated from fig. S5B. *P* value is from a two-sided paired *t* test. (F) Knockout and rescue assay. Endogenous *HES7* genes were knocked out (KO), and the disrupted oscillations were rescued with an exogenous construct of either mouse *Hes7* (Rescue mHES7) or human *HES7* (Rescue hHES7). See also fig. S6A. (G and H) Periods estimated from fig. S6B. *P* values are from a two-sided Student's *t* test. Shading in (B) and (F) indicates means  $\pm$  SD ( $n = 3$ ). Error bars in (C), (E), (G), and (H) indicate means  $\pm$  SD.

and  $133 \pm 4$  min, respectively, compared with the  $124 \pm 3$  min period of wild-type (WT) mouse PSM (Fig. 2, B and C). Considering that the period of WT human PSM is 322 min, however, the period extension in homo swap mouse PSM is minor. We also created knock-in mice, and the homo swap mice appeared largely normal, though their vertebrae—which are derivatives of somites—displayed minor

defects (fig. S5A). The ex vivo measurements of the segmentation clock in homo swap embryos showed an ~30-min longer oscillation period compared with that of the WT embryos (Fig. 2, D and E, and fig. S5B), which is consistent with the ~20-min period extension in the homo swap samples of induced PSM (Fig. 2C). However, the 20- to 30-min period extension in homo swap PSM and embryos is

far from the ~200-min period difference between mice and humans, so the human *HES7* locus in mouse PSM gives rise to an essentially mouselike oscillation period.

One potential defect in our experimental design of interspecies genome swapping is that the swapped *HES7* region might not be long enough, and a crucial sequence for the oscillation period might exist upstream of the

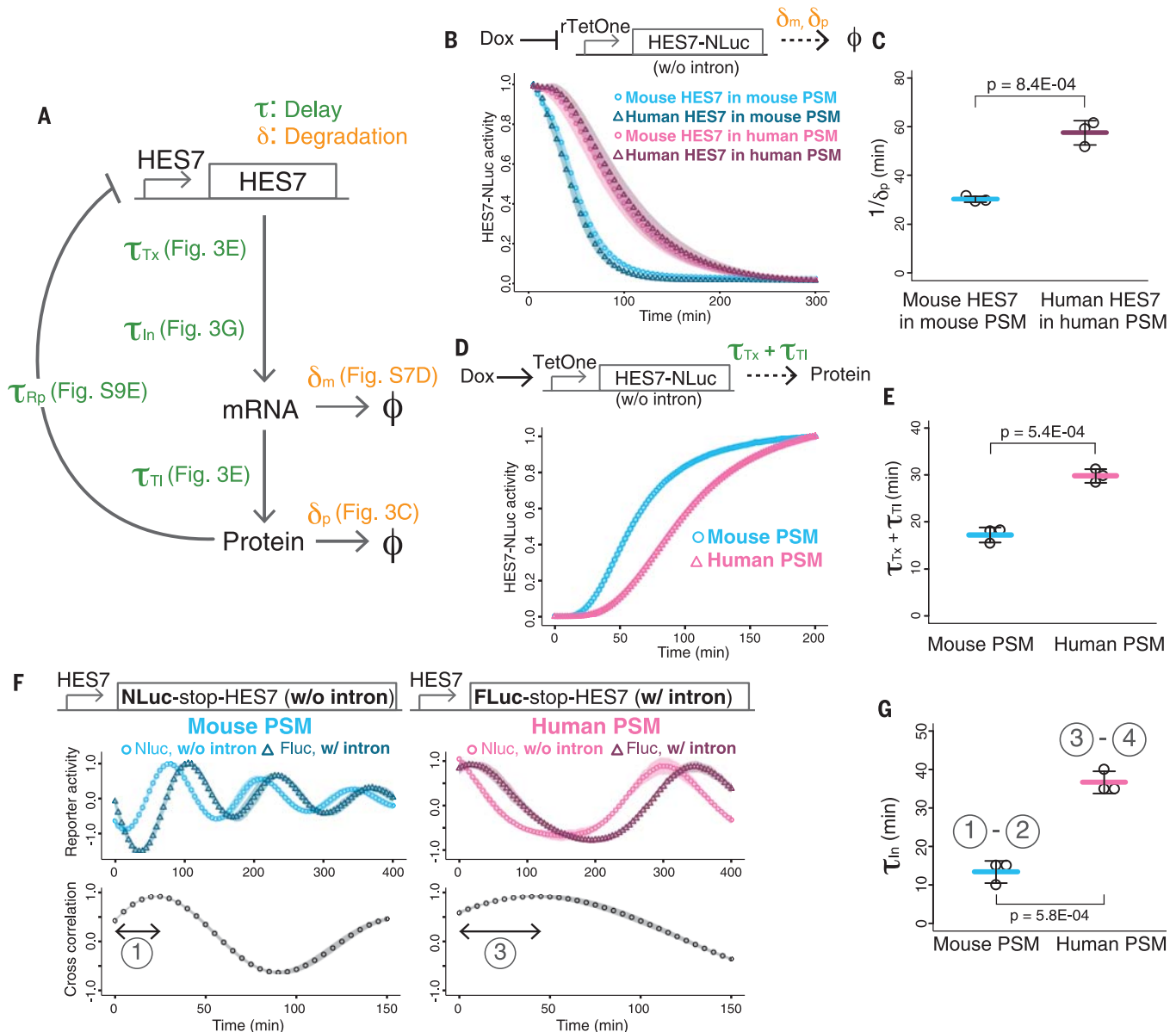


**Fig. 3. Measuring biochemical parameters of *HES7*.** (A) Negative feedback loop of *HES7*. Delays and degradation rates of the loop were measured in the indicated panels.  $\tau_{Tx}$ , transcription delay;  $\tau_{In}$ , intron delay;  $\tau_{Tl}$ , translation delay;  $\tau_{Rp}$ , repression delay;  $\delta_m$ , degradation rate of mRNA;  $\delta_p$ , degradation rate of protein. (B) Degradation assay of *HES7*. The transcription of *HES7* fused with NanoLuc (NLuc) was halted upon doxycycline (Dox) addition (top), and the decay of NLuc signal was monitored with a luminometer (bottom). (C) Inverse degradation rates of *HES7* protein estimated from fig. S7A. (D) Expression delay assay of *HES7*. The transcription of *HES7*-NLuc was induced

upon Dox addition (top), and the onset of NLuc signal was monitored (bottom). (E) Transcription and translation delays of *HES7* estimated from fig. S7, B and C. (F) Intron delay assay of *HES7*. Reporter constructs without (w/o) and with (w/) *HES7* intron sequence were introduced simultaneously (top and middle), and the cross-correlation of two reporters was calculated (bottom). See also fig. S8A. (G) Intron delays of *HES7* estimated from (F) and fig. S8B. Shading in (B), (D), and (F) indicates means  $\pm$  SD ( $n = 3$ ). Error bars in (C), (E), and (G) indicate means  $\pm$  SD. *P* values are from a two-sided Student's *t* test.



*HES7* promoter we defined. To rule out this possibility, we performed knockout and rescue assays (fig. S6A). The endogenous mouse *Hes7* gene was knocked out (KO) in mouse ESCs, which led to disruption of *Hes7* oscillation in the induced PSM (Fig. 2F, KO). Then, the disrupted oscillation was rescued by an exogenous construct containing a promoter, exons, introns, and UTRs of the murine or human *HES7* locus (Fig. 2F, Rescue mHES7 and Rescue hHES7). Note, these exogenous constructs were integrated into random locations of the genome by transposon vectors. Both murine and human *HES7* constructs at random genomic locations restored mouselike oscillation periods in the mouse PSM (Fig. 2G and fig. S6B). We further attempted a complementary experiment: The endogenous human *HES7* gene was knocked out, and the disrupted oscillation in human PSM was rescued with the murine or human *HES7* construct (Fig. 2F and fig. S6B). Again, murine and human *HES7* constructs were indistinguishable in terms of the restored oscillation periods (Fig. 2H). These results collectively indicate that the two- to threefold period difference is not caused by the sequence differences between murine and human *HES7* loci.

#### Interspecies period difference is due to different biochemical reaction speeds

We then hypothesized that differences in the biochemical reaction speeds of *HES7* between murine and human cells might lead to the observed oscillation-period difference. Biochemical parameters that strongly affect the *HES7* oscillation period are the degradation rates and delays in the regulatory feedback loop of *HES7* (Fig. 3A) (16, 24–27). In fact, genetic manipulations that modulate the degradation or delay of *Hes7* affect the oscillation period in mice (24, 26). Delays resulting from splicing and export of mRNAs are also reported to be different among mice, chickens, and zebrafish (27). Thus, we measured the degradation rates of *HES7* mRNA and protein (i.e.,  $\delta_m$  and  $\delta_p$ , respectively, in Fig. 3A) and the several delays in the *HES7* feedback loop ( $\tau_{Tx}$ ,  $\tau_{In}$ ,  $\tau_{Tr}$ , and  $\tau_{Rp}$  in Fig. 3A) in PSM cells, exploring which parameter(s) are different between mice and humans. To measure the degradation rate of the *HES7* protein ( $\delta_p$ ), we overexpressed either murine or human *HES7* sequence and then halted its expression (Fig. 3B). Both murine and human *HES7* proteins were degraded more slowly in human PSM compared with mouse PSM, which means that the changes in the degradation rate depend on the differences not in the *HES7* sequences but in the cellular environments (i.e., whether *HES7* is hosted in a murine or human cell). The half-life of the *Hes7* protein in mice is reported to be 22 min (24), which is consistent with our measurements where half-lives in murine and

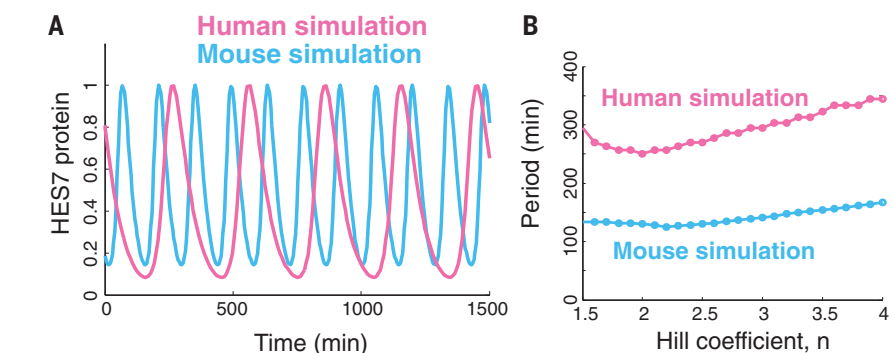


**Fig. 4. Simulating oscillations with measured biochemical parameters.** (A) *HES7* oscillations simulated with the parameters measured in murine or human PSM. Hill coefficient was set as  $n = 3$ . The other parameters are in table S1. (B) Periods estimated by computing the power spectra of simulated oscillations with different values of Hill coefficient.

human PSM were  $21 \pm 0.8$  and  $40 \pm 4$  min, respectively (Fig. 3C and fig. S7A).

To measure the delay caused by the transcription and translation of *HES7*, we induced the expression of *HES7* and estimated the onset time by fitting the results to a standard gene expression model where transcription and translation occur in a linear manner with corresponding delays (Fig. 3D and fig. S7, B and C). The transcription and translation delay ( $\tau_{TxTl}$ ) of *HES7* was longer in human PSM ( $30 \pm 1$  min) compared with mouse PSM ( $17 \pm 2$  min) (Fig. 3E). The fitting also allowed us to estimate the degradation rate of *HES7* mRNA ( $\delta_m$ ), which showed slower mRNA degradation in human PSM (half-life,  $16 \pm 0.3$  min) compared with mouse PSM (half-life,  $10 \pm 0.3$  min) (fig. S7D). Note, the *HES7* gene used in these measurements did not include the introns (Fig. 3, B and D). Because introns affect mRNA splicing and therefore serve as another source of delays (25–27), we measured the delay caused by *HES7* introns by creating *HES7* promoter-luciferase reporters with and without introns (fig. S8A) and estimating the phase difference between the oscillations of the two reporters (Fig. 3F and fig. S8B). Again, the *HES7* intron delay ( $\tau_{In}$ ) was longer in human PSM ( $37 \pm 3$  min) compared with mouse PSM ( $13 \pm 3$  min) (Fig. 3G). Roughly consistent with our measurements, the intron delay or splicing delay in mouse embryos has been reported to be 12 to 19 min (25, 27). Finally, to measure the delay for *HES7* to start repressing its own promoter, we induced the expression of *HES7* and estimated the onset of decline in the *HES7* promoter activity (fig. S9). Fitting the results to an open-loop repression model where the induced *HES7* protein represses the expression of *HES7* promoter-luciferase reporter suggested that the *HES7* repression delay ( $\tau_{Rp}$ ) is negligible in both murine and human PSM.

To confirm that the degradation rates and delays measured in murine and human PSM can explain the interspecies period difference,

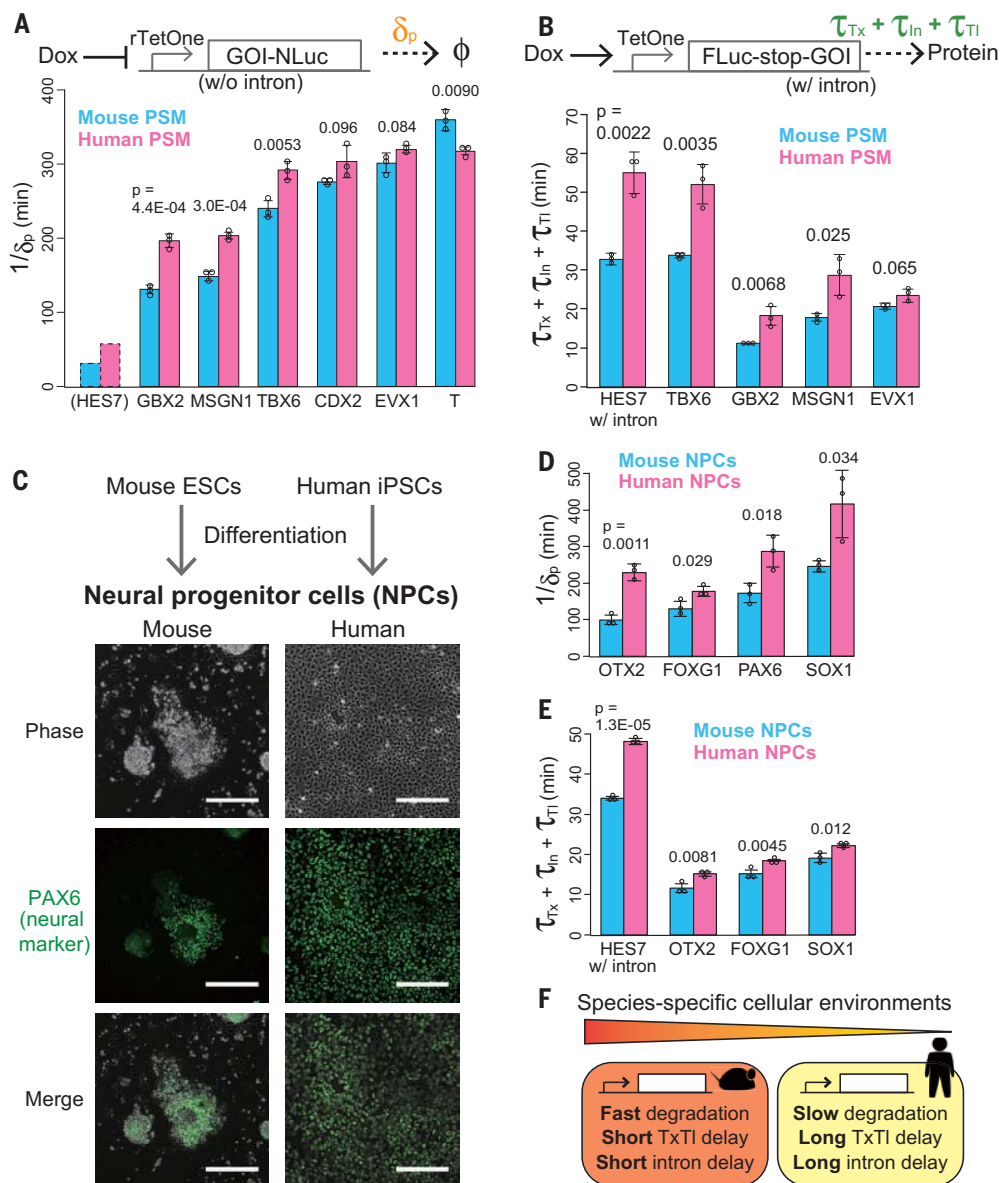
we built a simple mathematical model of *HES7* oscillation (16) based directly on the following parameters:  $\delta_p$ ,  $\delta_m$ ,  $\tau_{TxTl}$ ,  $\tau_{In}$ , and  $\tau_{Rp}$  (Fig. 4A). Mathematical analyses of the model showed that the oscillation period depends on these measured parameters (i.e., degradation rates and total delays) and that other parameters, such as the transcription and translation rates and the repression threshold, essentially do not affect the period (text S1) (16). Even though one unmeasured parameter, the repression Hill coefficient, potentially affects the oscillation period (text S1), varying this parameter within a realistic range did not substantially change the period (Fig. 4B). Our simulation of oscillations with the murine parameters showed periods of ~150 min, whereas that with human parameters showed ~300-min periods (Fig. 4B), reproducing the two- to threefold period difference between actual murine and human PSM (Fig. 1D). These results mean that the slower biochemical reactions of *HES7* (i.e., slower degradations and longer delays) in human PSM compared with mouse PSM are sufficient to quantitatively account for the longer oscillation period of the human segmentation clock.

#### Generality of slower biochemical reactions in human cells

Next, we explored how universal our finding of slower biochemical reactions in human cells is. To test whether it is specific to the *HES7* gene, we measured the degradation rates of six other genes, which are transcription factors expressed at the PSM stage (9) (Fig. 5A, fig. S10, and fig. S11). *GBX2*, *MSGN1*, and *TBX6* proteins showed slower degradation rates in human PSM compared with mouse PSM, whereas *CDX2*, *EVX1*, and *Brachyury T* did not show a significant interspecies difference (Fig. 5A). We also measured the transcription and intron delays ( $\tau_{Tx}$  and  $\tau_{In}$ ) (Fig. 5B, fig. S12, and fig. S13). *TBX6*, *GBX2*, and *MSGN1* showed longer delays in human PSM, whereas *EVX1*

**Fig. 5. Generality of slower biochemical reactions in human cells.** (A) Degradation assay of other genes expressed at the PSM stage. The transcription of a gene of interest (GOI) fused with NLuc was halted, and the decay of NLuc signal was monitored (top). Inverse protein degradation rates were estimated from fig. S11 (bottom). *HES7* degradation rate shown in Fig. 3C is displayed as a control. (B) Expression delay assay of other genes expressed at the PSM stage. The transcription of FLuc-GOI fusion construct flanked by a stop codon was induced, and the onset of FLuc signal was monitored (top). Sums of the transcription delay of fusion construct, intron delay of GOI, and translation delay of FLuc were estimated from fig. S13 (bottom).

(C) In vitro differentiation of NPCs from mouse ESCs and human iPSCs. Scale bars, 200  $\mu$ m. (D) Degradation assay in NPCs. Inverse protein degradation rates were estimated from fig. S15. (E) Expression delay assay in NPCs. Delays were estimated from fig. S17. (F) Proposed scheme. Murine and human cells have different cellular environments that affect the speeds of multiple biochemical reactions. TxTI, transcription and translation. Error bars in (A), (B), (D), and (E) indicate means  $\pm$  SD ( $n = 3$ ).  $P$  values are from a two-sided Student's  $t$  test.



did not (Fig. 5B). These results suggest that the slower biochemical reactions in human PSM compared with mouse PSM can extend at least to several other genes but not to all genes. Note, the same genetic construct (depicted in Fig. 5, A and B) was used for the measurements in murine and human cells, which means that the observed difference in reaction parameters is not due to genomic sequence differences of the target gene but rather is due to different cellular environments between the species.

Finally, to test whether the slower biochemical reactions in human cells are specific to the PSM cell type, we induced neural progenitor cells (NPCs) from mouse ESCs and human iPSCs (Fig. 5C) (28, 29). Most of the induced NPCs were PAX6 positive (Fig. 5C), even though they may constitute slightly different cell populations between the species. We mea-

sured the degradation rates of neural marker genes (29) in both murine and human NPCs (fig. S14 and fig. S15). All the four proteins tested, *Otx2*, *Foxg1*, *Pax6*, and *Sox1*, showed slower degradation rates in human NPCs compared with mouse NPCs (Fig. 5D). We also measured the transcription and intron delays of *Otx2*, *Foxg1*, and *Sox1* (fig. S16 and fig. S17), which demonstrated slightly longer delays in human NPCs for all three genes (Fig. 5E). Compared with PSM cells, NPCs tended to show larger interspecies differences in degradation rates and smaller differences in delays; however, the number of genes tested is too small to draw any conclusions. These results suggest that slower biochemical reactions in human cells can be generalizable not only to the PSM fate but also to other cell types. We propose that murine and human cells have

species-specific cellular environments that affect the speeds of several biochemical reactions, including degradations and delays (Fig. 5F), potentially causing other interspecies differences in developmental tempo. The identity of the cellular environments can be any gene set or any cellular characteristic, such as the metabolic rate and cell size.

## Discussion

We have shown that the human segmentation clock exhibits an oscillation period that is two to three times as long as that of the mouse segmentation clock because of slower biochemical reactions of *HES7* in the human PSM cell. It is noteworthy that multiple reaction parameters of *HES7*, including the degradation rates, transcription and translation delay, and intron delay, displayed interspecies differences



and collectively accounted for the two- to threefold period difference.

We have also revealed the existence of several genes other than *HES7* that show interspecies differences in reaction speeds in PSM cells or NPCs. A recent study has shown that human motor neuron generation takes two to three times as long as mouse motor neuron generation, and the key regulatory genes exhibit slower protein degradation rates in human motor NPCs (3). Oscillation dynamics and biochemical reaction speeds of the p53-Mdm2 network are also reported to be slower in a human cell line compared with a mouse line (30). These studies together with our results imply a general principle of allochry.

An obvious question that remains is the mechanism by which human cells display slower biochemical reactions. We attempted to find commonalities in sequences or functionalities among the genes that either showed or did not show differential reaction speeds between murine and human cells; however, the number of genes tested was not large enough to yield significant results. Thus, although this study has revealed cell-autonomous mechanisms of developmental allochry, their deep origin remains a mystery.

## REFERENCES AND NOTES

1. M. Ebisuya, J. Briscoe, *Development* **145**, dev164368 (2018).
2. J. van den Amele, L. Tiberi, P. Vanderhaeghen, I. Espuny-Camacho, *Trends Neurosci.* **37**, 334–342 (2014).
3. T. Rayon *et al.*, *Science*, **369** eaba7667 (2020).
4. A. C. Oates, L. G. Morelli, S. Ares, *Development* **139**, 625–639 (2012).

5. A. Hubaud, O. Pourquié, *Nat. Rev. Mol. Cell Biol.* **15**, 709–721 (2014).
6. P. D. Turnpenny *et al.*, *Dev. Dyn.* **236**, 1456–1474 (2007).
7. T. Nakajima *et al.*, *Development* **145**, dev165431 (2018).
8. M. Matsuda *et al.*, *Nature* **580**, 124–129 (2020).
9. J. Chal *et al.*, *Nat. Biotechnol.* **33**, 962–969 (2015).
10. K. M. Loh *et al.*, *Cell* **166**, 451–467 (2016).
11. M. Matsuura, T. Tomita, K. Yoshioka-Kobayashi, A. Isomura, R. Kageyama, *Development* **145**, dev156836 (2018).
12. L. F. Chu *et al.*, *Cell Rep.* **28**, 2247–2255.e5 (2019).
13. M. Diaz-Cuadros *et al.*, *Nature* **580**, 113–118 (2020).
14. Y. Masamizu *et al.*, *Proc. Natl. Acad. Sci. U.S.A.* **103**, 1313–1318 (2006).
15. C. D. Tsaiaris, A. Aulehla, *Cell* **164**, 656–667 (2016).
16. J. Lewis, *Curr. Biol.* **13**, 1398–1408 (2003).
17. A. Goldbeter, O. Pourquié, *J. Theor. Biol.* **252**, 574–585 (2008).
18. I. H. Riedel-Kruse, C. Müller, A. C. Oates, *Science* **317**, 1911–1915 (2007).
19. Z. Ferjentsik *et al.*, *PLOS Genet.* **5**, e1000662 (2009).
20. Y. Okubo *et al.*, *Nat. Commun.* **3**, 1141 (2012).
21. Y. Niwa *et al.*, *Dev. Cell* **13**, 298–304 (2007).
22. K. F. Sonnen *et al.*, *Cell* **172**, 1079–1090.e12 (2018).
23. Y. Bessho, H. Hirata, Y. Masamizu, R. Kageyama, *Genes Dev.* **17**, 1451–1456 (2003).
24. H. Hirata *et al.*, *Nat. Genet.* **36**, 750–754 (2004).
25. Y. Takashima, T. Ohtsuka, A. González, H. Miyachi, R. Kageyama, *Proc. Natl. Acad. Sci. U.S.A.* **108**, 3300–3305 (2011).
26. Y. Harima, Y. Takashima, Y. Ueda, T. Ohtsuka, R. Kageyama, *Cell Rep.* **3**, 1–7 (2013).
27. N. P. Hoyle, D. Ish-Horowitz, *Proc. Natl. Acad. Sci. U.S.A.* **110**, E4316–E4324 (2013).
28. Q. L. Ying, M. Stavridis, D. Griffiths, M. Li, A. Smith, *Nat. Biotechnol.* **21**, 183–186 (2003).
29. S. M. Chambers *et al.*, *Nat. Biotechnol.* **27**, 275–280 (2009).
30. J. Stewart-Ornstein, H. W. J. Cheng, G. Lahav, *Cell Syst.* **5**, 410–417.e4 (2017).

## ACKNOWLEDGMENTS

We thank J. Sharpe, V. Trivedi, J. Diego, and C. Villava for their comments; M. Ogawa and T. Tsuji for helping with the micro-computed tomography scans of knock-in mice; S. Sakurai and T. Yamamoto for helping with data analyses; and the Laboratory for Animal Resources and Genetic Engineering (LARGE), RIKEN

BDR, for generating knock-in mice and for animal housing.

**Funding:** This work was supported by internal grants from RIKEN and EMBL; the Takeda Science Foundation (to M.E.); project PGC2018-097872-A-I00 (MCIU/AEI/FEDER, UE) (to M.E.) funded by the Spanish Ministry of Science, Innovation and Universities (MCIU), and cofunded by the European Regional Development Fund (ERDF, EU); Grant-in-Aid for Scientific Research (KAKENHI) programs from the Japanese Ministry of Education, Culture, Sports, Science, and Technology (MEXT) (16KT0178 and 17H05777 to M.M., 16H06480 to R.K., and 16K15664 to C.A.); RIKEN Special Postdoctoral Researchers (SPDR) fellowship (to M.M.); CiRA Fellowship Program of Challenge (to C.A.); and a Naito Foundation Scientific Research Grant (to C.A.). ASHBI is supported by the World Premier International Research Center Initiative (WPI), MEXT, Japan. **Author contributions:** M.M., M.E., and C.A. conceived the usage of murine and human PSM. M.M. and M.E. conceived the swapping of *HES7* loci and comparison of biochemical parameters between mice and humans. M.M. and M.E. designed the work and wrote the manuscript. M.M. performed most of the experiments and analyzed the data. H.H. and C.A. developed the induction protocol of mouse PSM. Y.Y., M.I., J.T., and C.A. developed the induction protocol of human PSM. J.G.-O. constructed mathematical models and fitted them to the experimental data. K.Y.-K. and R.K. measured the oscillation period in mouse embryos. **Competing interests:** The authors declare no competing interests. **Data and materials availability:** All data are available in the manuscript or the supplementary materials. DNA constructs and mice are available from M.E. under a material transfer agreement with RIKEN.

## SUPPLEMENTARY MATERIALS

science.sciencemag.org/content/369/6510/1450/suppl/DC1  
Materials and Methods  
Figs. S1 to S17  
Tables S1 and S2  
References (31–41)  
MDAR Reproducibility Checklist  
Text S1  
Movies S1 and S2

[View/request a protocol for this paper from Bio-protocol.](#)

3 January 2020; accepted 17 July 2020  
10.1126/science.aba7668

## PLASTIC POLLUTION

## Evaluating scenarios toward zero plastic pollution

Winnie W. Y. Lau<sup>1\*†</sup>, Yonathan Shiran<sup>2\*†</sup>, Richard M. Bailey<sup>3\*†</sup>, Ed Cook<sup>4</sup>, Martin R. Stuchtey<sup>2,5</sup>, Julia Koskella<sup>2</sup>, Costas A. Velis<sup>4\*</sup>, Linda Godfrey<sup>6</sup>, Julien Boucher<sup>7,8</sup>, Margaret B. Murphy<sup>1</sup>, Richard C. Thompson<sup>9</sup>, Emilia Jankowska<sup>2</sup>, Arturo Castillo Castillo<sup>10</sup>, Toby D. Pilditch<sup>3</sup>, Ben Dixon<sup>2</sup>, Laura Koerselman<sup>2</sup>, Edward Kosior<sup>11</sup>, Enzo Favoino<sup>12</sup>, Jutta Gutberlet<sup>13</sup>, Sarah Baulch<sup>1</sup>, Meera E. Atreya<sup>2</sup>, David Fischer<sup>2</sup>, Kevin K. He<sup>1</sup>, Milan M. Petit<sup>2</sup>, U. Rashid Sumaila<sup>14</sup>, Emily Neil<sup>3</sup>, Mark V. Bernhofen<sup>4</sup>, Keith Lawrence<sup>1</sup>, James E. Palardy<sup>1\*†</sup>

Plastic pollution is a pervasive and growing problem. To estimate the effectiveness of interventions to reduce plastic pollution, we modeled stocks and flows of municipal solid waste and four sources of microplastics through the global plastic system for five scenarios between 2016 and 2040. Implementing all feasible interventions reduced plastic pollution by 40% from 2016 rates and 78% relative to “business as usual” in 2040. Even with immediate and concerted action, 710 million metric tons of plastic waste cumulatively entered aquatic and terrestrial ecosystems. To avoid a massive build-up of plastic in the environment, coordinated global action is urgently needed to reduce plastic consumption; increase rates of reuse, waste collection, and recycling; expand safe disposal systems; and accelerate innovation in the plastic value chain.

Plastic pollution is globally ubiquitous. It is found throughout the oceans, in lakes and rivers, in soils and sediments, in the atmosphere, and in animal biomass. This proliferation has been driven by rapid growth in plastic production and use combined with linear economic models that ignore the externalities of waste (1, 2). A sharp rise in single-use plastic consumption and an expanding “throw-away” culture (1) have exacerbated the problem. Waste management systems do not have sufficient capacity at the global level to safely dispose of or recycle waste plastic (3, 4), resulting in an inevitable increase in plastic pollution into the environment. Previous studies estimated that ~8 million metric tons (Mt) of macroplastic (5) and 1.5 Mt of primary microplastic (6) enter the ocean annually. Comparable estimates for terrestrial plastic pollution have yet to be quantified. If plastic production and waste generation continue to grow at current rates, the annual mass of mismanaged waste has been projected to more than double by 2050 (1, 2), and the cumulative mass of ocean plastic could increase by an order of magnitude from 2010 levels by 2025 (5). Despite the magnitude of these flows, the efficacy and economic costs of solutions proposed to solve the plastic waste problem—the uncontrolled release of plastic waste into the environment resulting from ineffective management—remain unknown.

A growing body of evidence points to a broad range of detrimental effects of plastic

pollution. Nearly 700 marine species and more than 50 freshwater species are known to have ingested or become entangled in macroplastic (7, 8), and there is growing evidence that plastic is ingested by a wide range of terrestrial organisms (9). Plastic pollution affects many aspects of human well-being: affecting the aesthetics of beaches (10), blocking drainage and wastewater engineering systems (11), and providing a breeding ground for disease vectors (10, 12). The lower-bound estimate of the economic impact on costs of plastic pollution to fishing, tourism, and shipping have been estimated at \$13 billion annually (13). Although harmful effects of microplastic (here defined as plastics <5 mm) have not been consistently demonstrated, ingestion has been documented across trophic levels and at all depths of the ocean, in individual organisms and species assemblages (8, 14) and in terrestrial organisms (15). Microplastics are also increasingly found in the human food system, although their impacts on human health are difficult to assert and require further research (16, 17). Plastic production, collection, and disposal are also major sources of greenhouse gas (GHG) emissions (18).

Cost-effective solutions to managing plastic waste vary considerably across geographies and social settings (3), and a variety of solutions to the plastic pollution problem have been proposed at local, national, and regional levels (19, 20). Some proposed interventions focus on postconsumption management, requiring

considerable growth in investment and capacity of waste management solutions (21, 22). Other interventions prioritize reducing plastic through replacement with alternative products, reuse, and the development of new delivery models (23). Individual countries have established bans or levies on select plastic products, with a particular focus on banning single-use carrier bags and microbeads in cosmetic products (24, 25). The European Union recently adopted a directive on single-use plastics (26), and the Basel Convention was amended to regulate the international trade of plastic waste (27). The scientific community and non-governmental organizations are also working to identify solutions (21, 28). Despite these efforts, a global evidence-based strategy that includes practical and measurable interventions aimed at reducing plastic pollution does not yet exist.

## Modeling approach

Designing an effective global strategy requires an understanding of the mitigation potential of different solutions and the magnitude of global effort needed to appreciably reduce plastic pollution. To estimate mitigation potential under different intervention scenarios, we developed the Plastics-to-Ocean (P<sub>2</sub>O) model. P<sub>2</sub>O is a data-driven coupled ordinary differential equation (ODE) model that calculates the flow of plastics through representative systems. We used the model to characterize key stocks and flows for land-based sources of plastic pollution across the entire value chain for municipal solid waste (MSW) macroplastics (figs. S1 and S2) and four sources of primary microplastics (those entering the environment as microplastics) [supplementary materials (SM) section 15 and figs. S3 to S6]. Crucially, it provides estimates of plastic waste input into the environment. Costs are calculated as a function of modeled plastic flows, and changes in costs due to production scale and technological advancement are accounted for through learning curves and returns to scale (SM section 16.1).

We calculated projected growth in demand for plastic using country-level population size (29), per capita macroplastic MSW (30, 31), and microplastic-generating product use and loss rates. Per capita waste generation and waste management processes (such as collection costs, collection and processing rates, and recycling recovery value) and rates of primary microplastic generation vary by geography and plastic

<sup>1</sup>The Pew Charitable Trusts, 901 E Street NW, Washington, DC 20004, USA. <sup>2</sup>SYSTEMIQ, 69 Carter Lane, London EC4V 5EQ, UK. <sup>3</sup>School of Geography and the Environment, University of Oxford, Oxford OX1 3QY, UK. <sup>4</sup>School of Civil Engineering, University of Leeds, Leeds LS2 9JT, UK. <sup>5</sup>Institute of Geography, University of Innsbruck, Innrain 52, 6020 Innsbruck, Austria. <sup>6</sup>Council for Scientific and Industrial Research, Pretoria 0001, South Africa. <sup>7</sup>EA—Shaping Environmental Action, Chemin des Vignes d'Argent 7, CH 1004 Lausanne, Switzerland. <sup>8</sup>University of Applied Sciences and Arts Western Switzerland—HES-SO, HEIG-VD, Yverdon-les-Bains, Switzerland. <sup>9</sup>School of Biological and Marine Sciences, University of Plymouth, Plymouth PL4 8AA, UK. <sup>10</sup>Faculty of Natural Sciences, Centre for Environmental Policy, Imperial College London, London SW7 2AX, UK. <sup>11</sup>Nextek, 1 Kensington Gore, London SW7 2AR, UK. <sup>12</sup>Scuola Agraria del Parco di Monza, Viale Cavriga 3 20900 Monza (MB), Italy. <sup>13</sup>Department of Geography, University of Victoria, Victoria, British Columbia V8W 2Y2, Canada. <sup>14</sup>Institute for the Oceans and Fisheries and School of Public Policy and Global Affairs, University of British Columbia, Vancouver, British Columbia V6T 1Z4, Canada.

\*Corresponding author. Email: wylau@pewtrusts.org (W.W.Y.L.); yonathan.shiran@systemiq.earth (Y.S.); richard.bailey@ouce.ox.ac.uk (R.M.B.); c.velis@leeds.ac.uk (C.A.V.); jpalardy@pewtrusts.org (J.E.P.)

†These authors contributed equally to this work.



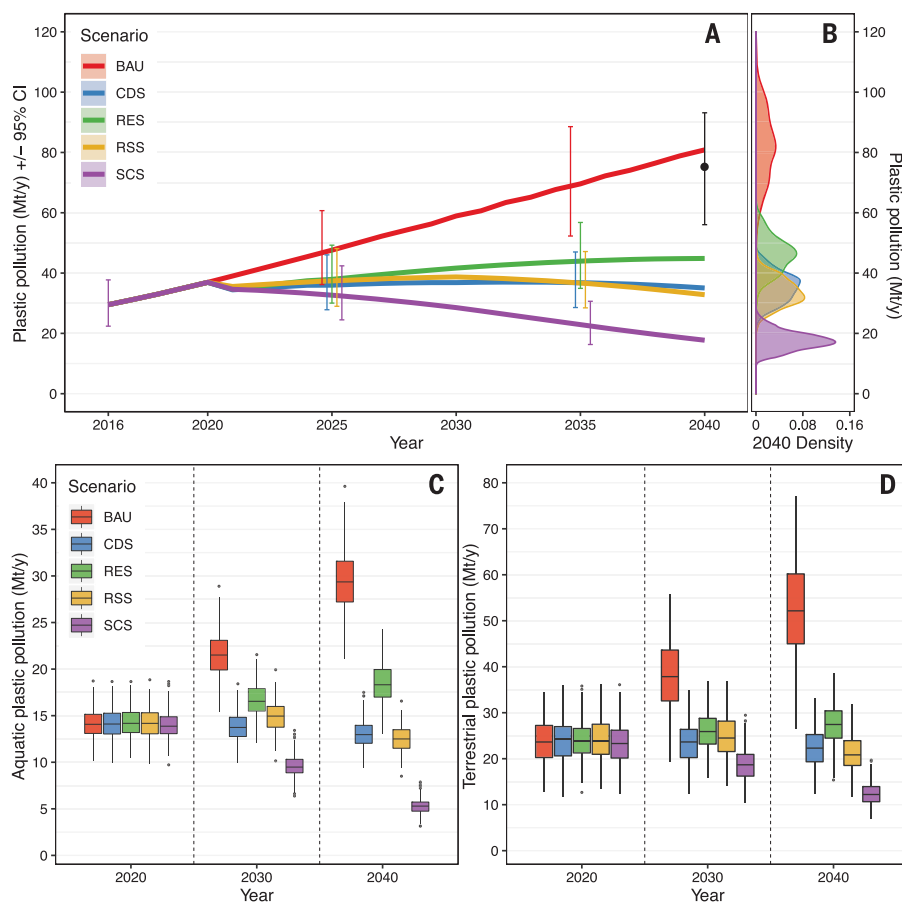


**Fig. 1. Annual rates of plastic pollution entering the environment estimated from 300 Monte Carlo simulations. (A)** Time series of plastic pollution entering aquatic and terrestrial ecosystems (million metric tons/year  $\pm$  95% CI) by scenario, 2016 to 2040. Scenarios are Business as Usual (BAU), Collect and Dispose scenario (CDS), Recycling scenario (RES), Reduce and Substitute scenario (RSS), and System Change scenario (SCS). Plastic pollution rates for all scenarios between 2016 and 2020 are identical. The black point estimate in 2040 represents the annual rate of plastic pollution assuming that global commitments to reduce plastic use and increase recycling announced before June 2019 are implemented before 2040. A time series for this scenario is not presented because timelines for implementation are unknown. **(B)** Kernel density estimates for plastic pollution (million metric tons) in 2040 by scenario. **(C and D)** Boxplots of plastic pollution entering (C) aquatic and (D) terrestrial ecosystems by scenario for beginning, middle, and end years of scenario implementation. Boxplots follow the Tukey convention: Hinges indicate first and third quartiles; whiskers indicate the most extreme value no further than 1.5 times the interquartile range from the hinge; and horizontal lines indicates the median.

**Table 1. Summary statistics and comparison of end-of-life fates for MSW plastic under BAU and SCS.** Shown from left to right are plastic mass, percent of total plastic demand under different end-of-life fates for year 2016 and for year 2040 under the Business as Usual (BAU) and System Change scenarios (SCS), and percent change in plastic mass, under different end-of-life fates for SCS in 2040 relative to 2016 and BAU in 2040. Values in square brackets represent the lower and upper bounds of the 95% CI for the values above them. Dashes indicate undefined values whose calculation involves division by zero.

End-of-life fate	Plastic mass (Mt/year)			Fate as % plastic demand			SCS 2040 % change	
	2016	BAU 2040	SCS 2040	2016	BAU 2040	SCS 2040	2016	BAU 2040
Reduction	0 [0, 0]	0 [0, 0]	130 [110, 150]	0 [0, 0]	0 [0, 0]	31 [28, 33]	—	—
Substitution	0 [0, 0]	0 [0, 0]	71 [62, 81]	0 [0, 0]	0 [0, 0]	17 [15, 18]	—	—
Recycling	31 [26, 32]	55 [46, 63]	84 [75, 93]	14 [12, 15]	13 [11, 15]	20 [18, 21]	170 [140, 200]	54 [46, 61]
Disposal	97 [83, 97]	140 [120, 150]	100 [89, 110]	44 [39, 45]	32 [28, 33]	24 [22, 26]	3.5 [3.3, 3.8]	-26 [-24, -28]
Mismanaged	91 [84, 100]	240 [220, 260]	44 [40, 49]	42 [41, 47]	56 [53, 59]	10 [9.4, 12]	-51 [-48, -54]	-81 [-76, -87]
Open burning*	49 [40, 60]	130 [110, 160]	23 [18, 29]	54 [42, 63]	56 [44, 65]	53 [41, 65]	-53 [-45, -61]	-82 [-70, -95]
Dumpsite*	12 [7.4, 21]	25 [14, 41]	3.2 [1.5, 5.0]	13 [8.2, 22]	11 [5.9, 17]	7.3 [3.3, 11]	-74 [-49, -99]	-87 [-54, -120]
Aquatic pollution*	11 [9.0, 14]	29 [23, 37]	5.3 [3.8, 7.0]	12 [9.8, 14]	12 [9.8, 15]	12 [9.0, 15]	-52 [-43, -60]	-82 [-68, -95]
Terrestrial pollution*	18 [13, 25]	52 [34, 70]	12 [7.8, 18]	20 [13, 27]	22 [14, 29]	28 [18, 39]	-33 [-23, -42]	-76 [-55, -97]

\*Components of the mismanaged end-of-life fate. These categories sum to the total for mismanaged waste.

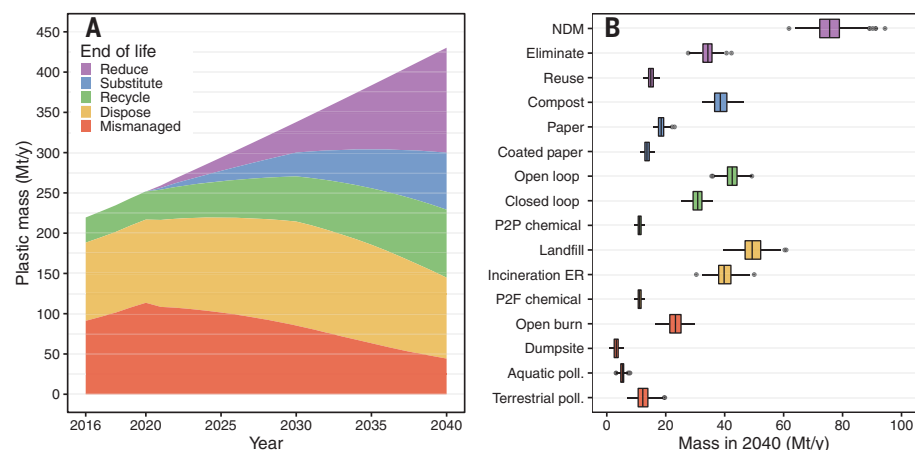


**Fig. 2. Fate for all MSW plastic, 2016 to 2040, under the System Change scenario (SCS).** (A) Annual mass of plastic (million metric tons/year) for each of five end-of-life fates. (B) Boxplots showing mass of plastic utility (million metric tons/year) addressed per modeled intervention in 2040, after 20 years of SCS implementation, organized by end-of-life fate. NDM, new delivery model; P2F chemical, plastic-to-fuel chemical conversion; P2P chemical, plastic-to-plastic chemical conversion; Incineration ER, incineration with energy recovery; Aquatic poll., plastic pollution into aquatic systems; Terrestrial poll., plastic pollution into terrestrial systems. Boxplots follow the Tukey convention: Hinges indicate first and third quartiles; whiskers indicate the most extreme value no further than 1.5 times the interquartile range from the hinge; and horizontal lines indicate the median.

category or source (6, 32–34). To account for these differences, the global population was split across eight geographic archetypes according to World Bank income categories (low income, lower- and upper- middle income, and high income) and United Nations urban-rural classifications (29). Populations were further differentiated by their distance to water (<1 km or >1 km) to estimate their relative flows of plastic pollution to terrestrial versus aquatic (lakes, rivers, and marine environments) systems. To account for different waste management pathways (35) and movement rates of waste in the environment (35), MSW plastics were differentiated into three material categories: rigid monomaterial, flexible monomaterial, and multimaterial or multilayer. Four microplastic sources were modeled: synthetic textiles, tires, plastic pellets, and personal care products.

Five scenarios were developed to estimate reductions in plastic pollution over the period 2016 to 2040. Scenarios were defined by four high-level classes of interventions (reduce, substitute, recycle, and dispose) and eight system interventions: (i) reducing plastic quantity in the system, (ii) substituting plastics with alternative materials and delivery systems, (iii) implementing design for recycling, (iv) increasing collection capacity, (v) scaling up sorting and mechanical recycling capacity, (vi) scaling up chemical conversion capacity, (vii) reducing postcollection environmental leakage, and (viii) reducing trade in plastic waste (table S7). Scenarios modeled include (i) “Business as Usual” (BAU), (ii) “Collect and Dispose,” (iii) “Recycling,” (iv) “Reduce and Substitute,” and (v) an integrated “System Change” scenario

that implemented the entire suite of interventions (tables S8 and S57).

At all relevant geographical scales, waste production and handling data are notoriously difficult to obtain. Many model inputs have a high degree of uncertainty, which was propagated with Monte Carlo sampling. Data inputs and assigned uncertainties are described in SM section 5.6. In the absence of datasets with

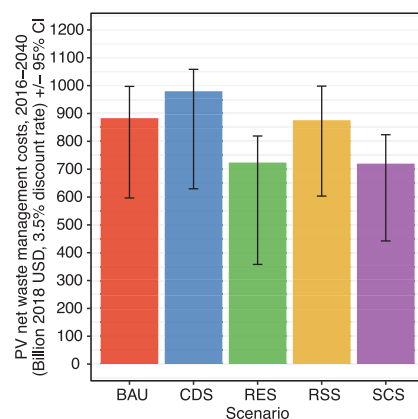


**Fig. 3. Present value costs for the management (collection, sorting, recycling, and disposal) of plastic MSW by scenario, 2016 to 2040.** Costs (billions 2018 U.S. dollars ± 95% CI) are calculated assuming 3.5% discount rate and are net of revenues associated with the sale of recycled plastic feedstock and electricity generated from plastic incineration with energy recovery. Scenarios are Business as Usual (BAU), Collect and Dispose scenario (CDS), Recycling scenario (RES), Reduce and Substitute scenario (RSS), and System Change scenario (SCS).

which to formally validate the model, we conducted sensitivity analyses to quantify the influence of individual model inputs and to identify key drivers of plastic pollution. Model outputs from the BAU scenario were also compared with results from other global studies (2, 5, 36).

### Business as usual

The BAU scenario highlights the scale of the plastic pollution problem and provides a baseline from which to compare alternative intervention strategies (Fig. 1). At a global scale from 2016 to 2040, the annual rate of macro- and microplastic entering aquatic systems from land increased 2.6-fold (Fig. 1C and Table 1). Over the same period, the rate of plastic pollution retained in terrestrial systems increased 2.8-fold (Fig. 1D and Table 1).

When we modeled current commitments to reducing plastic pollution assuming full implementation (SM section 9.1), annual plastic pollution rates into aquatic and terrestrial environments decreased by only 6.6% [95% confidence interval (CI): 5.4, 7.9] and 7.7% [5.2, 10] by 2040, respectively (Fig. 1A) (37). This result confirms that current commitments coupled with appropriate policies can reduce plastic waste input into the environment but also shows that considerable additional effort will be needed to match the unprecedented scale of projected environmental plastic pollution.

Plastic pollution rates were found to be particularly sensitive to total plastic mass, collection rates, and the ratio of managed to mismanaged waste. For example, a 1-ton reduction in plastic MSW mass (through reduce and substitute interventions) decreased aquatic plastic pollution by an average of 0.088 tons in low- and middle-income archetypes and an average of 0.0050 tons in high-income archetypes. Across all archetypes, an equivalent increase in the collection of plastic waste (through formal and informal sectors) resulted in an average 0.18-ton decrease in aquatic plastic pollution, whereas a similar decrease in postcollection mismanaged waste produced an average 0.10-ton decrease in aquatic plastic pollution.

### Scenarios to reduce plastic pollution

The focus of plastic pollution reduction strategies can be broadly partitioned into upstream (preconsumption, such as reducing demand) and downstream (postconsumption, such as collection and recycling) measures. To parameterize the development of waste management and recycling solutions in the Collect and Dispose, Recycling, and System Change scenarios, we estimated maximum foreseen growth and implementation rates on the basis of historical trends and expert panel consensus assessment (SM section 1). Compared with BAU, the annual combined terrestrial and aquatic plastic pollution rates were reduced by 57% in



2040 [45, 69] under the Collect and Dispose scenario and by 45% [35, 54] under the Recycling scenario (Fig. 1, A and B).

Strategies focused on upstream (pre-consumption) solutions were represented by the Reduce and Substitute scenario. We developed a feasibility assessment framework to model the potential development of upstream solutions aimed at reducing the volume of plastics used and disposed of into the waste stream (SM section 9). We assessed 15 major plastic applications against four criteria for technology readiness and unintended consequences related to health and food safety, consumer acceptance (for example, convenience and climate change impacts), and affordability (tables S21 and S22). We assessed the feasibility of substitution with alternative material against the potential for scaling to meaningful levels within the modeling period. Paper, coated paper, and compostable materials met these criteria. Under the Reduce and Substitute scenario, annual combined terrestrial and aquatic plastic pollution in 2040 decreased 59% [47, 72] relative to BAU, whereas annual plastic production decreased by 47% [44, 49]. Consequently, plastic production in 2040 under the Reduce and Substitute scenario (220 Mt/year [200, 240]) was similar to production in 2016 (210 Mt/year [200, 230]).

Neither pre- nor postconsumption interventions alone are sufficient to address the plastic problem. Combining the maximum foreseen application of pre- and postconsumption solutions represents the most aggressive possible solution given current technology: the System Change scenario. In this scenario, annual combined terrestrial and aquatic plastic pollution decreased by 78% [62, 94] relative to BAU in 2040 but only by 40% [31, 48] relative to 2016 pollution rates (Fig. 1, A and B, and Table 1). In 2040, the annual rate of land-based sources of plastic entering aquatic and terrestrial systems decreased by 82% [68, 95] and 76% [55, 97] relative to BAU, respectively (Fig. 1, C and D, and Table 1).

Under the System Change scenario in 2040, a substantial reduction in mismanaged and disposed waste was achieved through increases in the proportion of plastic demand reduced, substituted by alternative materials, and recycled (Fig. 2A and Table 1). These changes to the plastic system resulted in 11% [10, 12] less virgin plastic being produced in 2040 under the System Change scenario than was produced in 2016, and 55% [51, 58] less than in 2040 under BAU. Moreover, this reduction was driven by increases in recycled plastic feedstock, which have lower life-cycle GHG emissions (18). Taken together, the System Change scenario moves toward achieving a circular economy in which resources are conserved, waste generation is minimized (38), and GHG emissions reduced.

The present value of cumulative, global waste management operations from 2016 to 2040 was approximated to assess the relative cost of each scenario (Fig. 3). Among scenarios, costs varied by less than 20% relative to BAU, were lowest under the System Change and Recycling scenarios, and were highest for the Collect and Dispose scenario. Costs under the System Change scenario were 18% [14, 23] lower than BAU, with increased waste management costs offset by costs savings from reduced plastic production and revenues from recycle sales, which increased because of product redesign and improved economics of recycling (SM section 16.8). These costs represent only waste management costs, which are generally borne by taxpayers. Corporate engagement, through improved product design, alternative material development, and new business models will be necessary to achieve

pollution levels observed in the System Change scenario. This engagement will likely require a substantial shift in private sector investment.

Our results underline the urgency with which extensive interventions are needed. Despite a considerable reduction in annual plastic production and an increase in the proportion of MSW that is effectively managed under the best-case System Change scenario, a substantial amount of plastic waste remained mismanaged (not collected and sorted, recycled, or safely disposed) between 2016 and 2040. When implementation of interventions begins in 2020, the cumulative mass of plastic pollution added between 2016 and 2040 amounts to 250 Mt [190, 310] in aquatic systems (Fig. 4A) and 460 Mt [300, 640] in terrestrial systems (Fig. 4B), which are approximately 1 and 2 times the total annual plastic production in 2016, respectively. If implementation of interventions is delayed

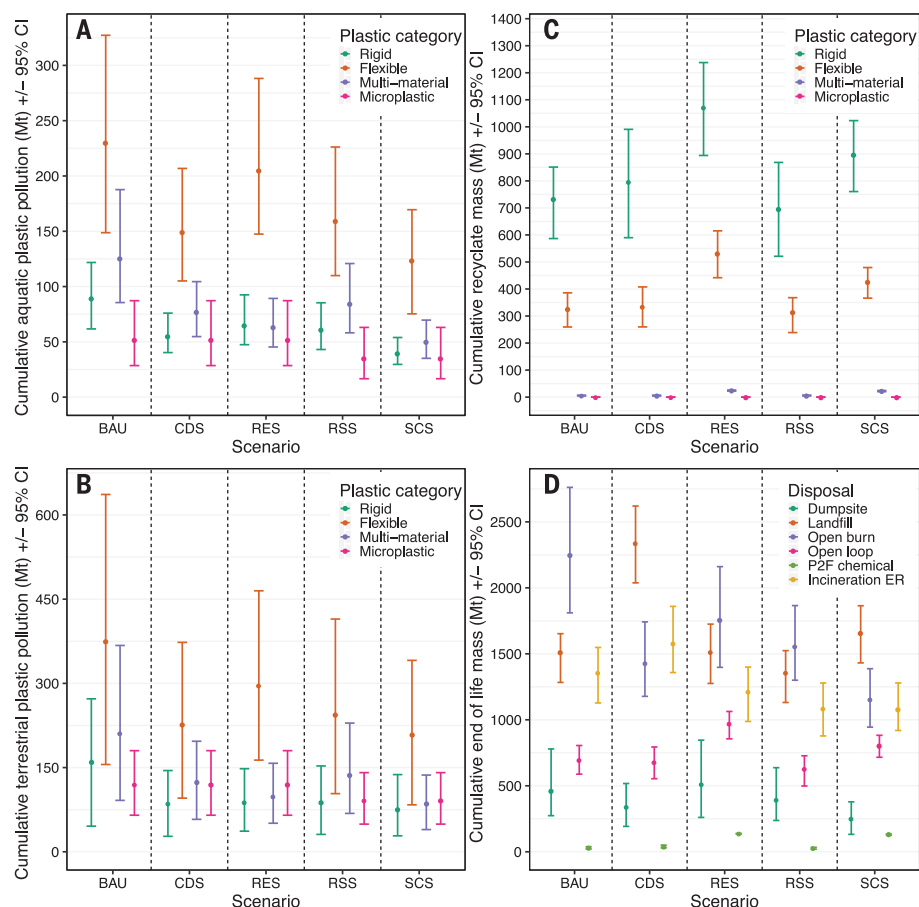


**Fig. 4. Cumulative mass of plastic MSW, 2016 to 2040.** (A and B) Cumulative mass of plastic MSW polluting (A) aquatic and (B) terrestrial systems by scenario and plastic type for years 2016 to 2040 (million metric tons  $\pm$  95% CI). (C) Cumulative mass of plastic MSW recycled for each of four plastic types modeled. (D) Cumulative mass of noncircular plastic MSW endpoints, including solutions in the mismanaged (dumpsite or open burning), effectively disposed [landfill, incineration with energy recovery, or plastic-to-fuel (P2F) chemical conversion], and recycling (open loop recycling) categories. Uncertainty bars for P2F chemical conversion are not visible because their endpoints do not exceed the radius of the plotted point estimate. Scenarios are Business as Usual (BAU), 'Collect and Dispose' scenario (CDS), 'Recycling' scenario (RES), 'Reduce and Substitute' scenario (RSS), and System Change scenario (SCS).

by only 5 years, an additional 300 Mt of mismanaged plastic waste is expected to accumulate in the environment.

### Outlook by plastic category

The complex composition of multimaterial plastics limits the technical feasibility of sorting and reprocessing (39), decreasing the economic attractiveness of recycling. Accordingly, the annual production of these plastics decreased by 19 Mt [18, 20] from 2016 to 2040 under the System Change scenario, with a shift of similar magnitude to flexible monomaterial plastic production (20 Mt/year [19, 21]).

Because of the relative ease of collection and sorting, recycling was dominated by rigid plastics in all archetypes and across all scenarios (Fig. 4C). Under the System Change scenario in 2040, rigid plastics represented 62% [58, 67] of the annual mass of recycling, with a sizeable component of flexible monomaterial plastic (33% [28, 37]) (Fig. 5A). In comparison, only 5.0% [4.2, 5.4] of recycled material was derived from multimaterial or multilayer waste plastic (Fig. 5A).

The diversity of polymer types, surface contamination, and low density of postconsumer flexible monomaterial limit their capacity for recycling, particularly in geographies where waste collection services are provided by the informal sector. At a global scale, the absolute and relative contribution of flexible monomaterial plastics to environmental pollution grew between 2016 and 2040, from 45% [35, 56] to 56% [40, 73] in aquatic environments and from 37% [18, 52] to 48% [22, 67] in terrestrial environments (Fig. 5, B and C). Accordingly, finding an economically viable solution to effectively manage flexible plastics will be essential for solving the plastic pollution problem.

Similarly, the proportion of total plastic pollution originating from microplastics in the System Change scenario grew from 11% [6.5, 18] to 23% [11, 42] in aquatic systems and from 16% [8.2, 27] to 31% [18, 51] in terrestrial systems over the modeled period (Fig. 5, B and C). Technologies to capture microplastics, which often rely on stormwater and wastewater management and treatment, are rarely economically feasible—even in wealthy regions—because of associated infrastructure costs. This technological challenge is particularly acute for tire particles, which contributed 93% [83, 96] of global microplastic pollution by mass in 2040.

### Difficulties to overcome

Scaling collection to all households at a global level is a monumental task that would require connecting over a million additional households to MSW collection services per week from 2020 to 2040; the majority of these unconnected households are in middle-income countries. The effort to increase household waste collection will therefore require a key role for “waste

pickers” [the informal collection and recycling sector (40)], who link the service chain (MSW collection) to the value chain (recycling) in low- and middle-income settings. Globally, this sector was responsible for 58% [55, 64] of postconsumer plastic waste collected for recycling in 2016. To incentivize the collection of

low-value plastics (flexible monomaterial and multimaterial or multilayer plastic) by the informal sector, the profitability of recycling these materials would need to rise to create demand for their collection. Accordingly, investments in collection infrastructure must be coordinated with improved governance around collection, sorting, and safe management of generated waste (41).

Mismanaged plastic waste (in dumpsites, openly burned, or released into aquatic or terrestrial environments) is associated with a range of risks to human and ecological health (42). Substantial quantities of such waste are likely to continue to be emitted into the environment or openly burned through time. Under the System Change scenario, in addition to aquatic and terrestrial pollution, ~250 Mt [130, 380] of waste plastic would accumulate in open dumpsites from 2016 to 2040 and remain a potential source of environmental pollution (Fig. 4D). Many communities in emerging economies with inadequate waste management services and infrastructure burn waste residentially or in open dumpsites without emissions controls. Open burning transfers the pollution burden to air, water, and land through the generation of GHGs, particulate matter (including microplastic particles), and harmful chemicals such as dioxins and other persistent organic pollutants (43, 44). Despite its human health and environmental consequences, open burning was the single largest component of mismanaged plastic waste under all scenarios, with 1200 Mt [940, 1400] of plastic burned in the System Change scenario between 2016 and 2040 (Fig. 4D). It therefore remains a stubborn pollution and social justice problem in need of an effective solution.

Although not strictly mismanaged, the net export of waste from high-income to upper- and lower-middle income countries grew from 2.7 Mt/year [2.4, 4.7] in 2016 to 3.8 Mt/year [0.7, 7.2] in 2040 under BAU. Although a comparatively small amount, these exports have the potential to increase the fraction of mismanaged plastic waste because receiving countries often have insufficient capacity to manage their own waste. Consequently, importing waste for recycling can have the unintended consequence of displacing these developing economies' capacity to recycle their domestic waste (45).

Although efforts to measure the amount of plastic pollution entering rivers and oceans have increased in recent years (46–48), key data gaps remain. To better estimate the effects of consumer, corporate, and policy actions on solving the plastic pollution problem, additional empirical data are needed throughout the plastics system—particularly in developing economies. Moreover, a more complete accounting of the benefits, costs, and externalities of plastic use is needed to design policies that align social and financial incentives and minimize

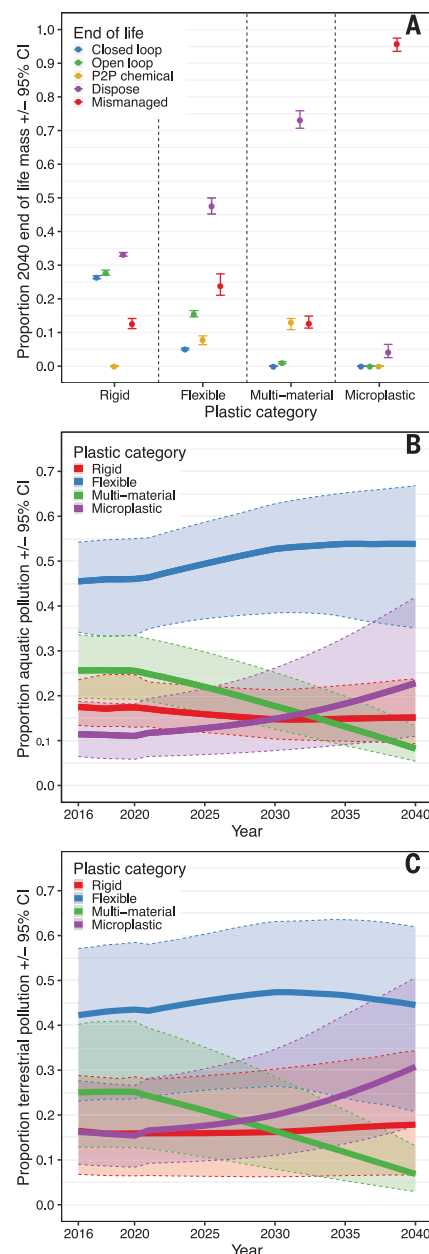


**Fig. 5. Fate of plastic MSW by plastic type under the System Change Scenario (SCS).** (A) Proportion of MSW ( $\pm$  95% CI) produced in 2040 absorbed by each of three recycling solutions and the dispose and mismanaged end-of-life categories. Even under SCS, few effective solutions are implemented to manage primary microplastics. (B and C) The proportion of plastic pollution ( $\pm$  95% CI) entering (B) global aquatic and (C) terrestrial systems by plastic type, 2016 to 2040.



plastic pollution. These data deficiencies currently prevent application of the model at finer geographical scales and limit the granularity of the system representation. In particular, data from the informal sector of the global waste management system are scarce, as are data that shed light on the importance of postcollection MSW mismanagement. Additional quantitative data are also needed to better understand key sources, rates, and pathways for microplastic pollution and for maritime sources of plastic pollution.

### Addressing the plastic pollution problem

Our analysis indicates that urgent and coordinated action combining pre- and postconsumption solutions could reverse the increasing trend of environmental plastic pollution. Although no silver bullet exists, 78% of the plastic pollution problem can be solved by 2040 through the use of current knowledge and technologies and at a lower net cost for waste management systems compared with that of BAU. However, with long degradation times, even a 78% reduction from BAU pollution rates results in a massive accumulation of plastic waste in the environment. Moreover, even if this system change is achieved, plastic production and un-sound waste management activities will continue to emit large quantities of GHGs. Further innovation in resource-efficient and low-emission business models, reuse and refill systems, sustainable substitute materials, waste management technologies, and effective government policies are needed. Such innovation could be financed by redirecting existing and future investments in virgin plastic infrastructure. Substantial commitments to improving the global plastic system are required from businesses, governments, and the international community to solve the ecological, social, and economic problems of plastic pollution and achieve near-zero input of plastics into the environment.

### REFERENCES AND NOTES

- R. Geyer, J. R. Jambeck, K. L. Law, *Sci. Adv.* **3**, e1700782 (2017).
- L. Lebreton, A. Andrad, *Palgrave Commun.* **5**, 6 (2019).
- C. A. Velis, D. Lerpinier, M. Tsakona, *Prevent Marine Plastic Litter—Now!* (International Solid Waste Association, 2017); <https://marinelitter.iswa.org/reports>.
- D. C. Wilson, C. A. Velis, *Waste Manag. Res.* **33**, 1049–1051 (2015).
- J. R. Jambeck *et al.*, *Science* **347**, 768–771 (2015).
- J. Boucher, D. Friot, *Primary Microplastics in the Oceans: A Global Evaluation of Sources* (IUCN, 2017).
- S. C. Gall, R. C. Thompson, *Mar. Pollut. Bull.* **92**, 170–179 (2015).
- C. M. Rochman *et al.*, *Ecology* **97**, 302–312 (2016).
- E. Huerta Lwanga *et al.*, *Sci. Rep.* **7**, 14071 (2017).
- K. J. Wyles, S. Pahl, K. Thomas, R. C. Thompson, *Environ. Behav.* **48**, 1095–1126 (2016).
- J. Fobell, J. Hogarth, *West Afr. J. Appl. Ecol.* **10**, 1 (2009).
- E. Boelee, G. Geerling, B. van der Zaan, A. Blauw, A. D. Vethaak, *Acta Trop.* **193**, 217–226 (2019).
- United Nations Environment Programme, “Valuing plastics: the business case for measuring, managing and disclosing plastic use in the consumer goods industry” (United Nations, 2014).
- D. S. Green, B. Boots, D. J. Blockley, C. Rocha, R. Thompson, *Environ. Sci. Technol.* **49**, 5380–5389 (2015).
- A. A. de Souza Machado, W. Kloas, C. Zarfl, S. Hempel, M. C. Rillig, *Glob. Change Biol.* **24**, 1405–1416 (2018).
- L. G. A. Barboza, A. Dick Vethaak, B. R. B. O. Lavorante, A. K. Lundebye, L. Guilhermino, *Mar. Pollut. Bull.* **133**, 336–348 (2018).
- D. Peixoto *et al.*, *Estuar. Coast. Shelf Sci.* **219**, 161–168 (2019).
- J. Zheng, S. Suh, *Nat. Clim. Chang.* **9**, 374–378 (2019).
- D. Xanthos, T. R. Walker, *Mar. Pollut. Bull.* **118**, 17–26 (2017).
- J. K. Abbott, U. R. Sumaila, *Rev. Environ. Econ. Policy* **13**, 327–336 (2019).
- M. Cordier, T. Uehara, *Sci. Total Environ.* **670**, 789–799 (2019).
- I. E. Napper, R. C. Thompson, *Environ. Sci. Technol.* **53**, 4775–4783 (2019).
- Ellen MacArthur Foundation, *The New Plastics Economy: Rethinking the Future of Plastics* (Ellen MacArthur Foundation, 2016).
- R. E. J. Schnurr *et al.*, *Mar. Pollut. Bull.* **137**, 157–171 (2018).
- P. Dauvergne, *Env. Polit.* **27**, 579–597 (2018).
- European Union, “Directive (EU) 2019/904 of the European Parliament and of the Council of 5 June 2019 on the reduction of the impact of certain plastic products on the environment,” 2019.
- United Nations Environment Programme Secretariat of the Basel Convention, “Decision BC-14/13: Further actions to address plastic waste under the Basel Convention” (United Nations, 2018).
- F. Oosterhuis, E. Papyrakis, B. Boteler, *Ocean Coast. Manage.* **102**, 47–54 (2014).
- United Nations Department of Economic and Social Affairs Population Division, “World Urbanization Prospects: The 2018 Revision (ST/ESA/SER.A/420)” (United Nations, 2019).
- S. Kaza, L. Yao, P. Bhada-Tata, F. Van Woerden, *What a Waste 2.0: A Global Snapshot of Solid Waste Management to 2050* (The World Bank, 2018).
- Material Economics, “The Circular Economy—A powerful force for climate mitigation” (Stockholm, 2018); <https://materialeconomics.com/publications/the-circular-economy-a-powerful-force-for-climate-mitigation-1>.
- OECD, *Environment at a Glance 2015: OECD Indicators* (OECD Publishing, 2015).
- WRAP, “Defining what’s recyclable and best in class polymer choices for packaging” (v1, 2019).
- E. G. Ashton, W. Kindlein Jr., R. Demori, L. H. A. Cândido, R. Mauler, *J. Clean. Prod.* **116**, 268–278 (2016).
- OECD, “Improving markets for recycled plastics” (OECD Publishing, 2018).
- Excluding microplastic pollution, the P<sub>2</sub>O model estimates that 9.8 Mt/year [7.7, 12] of plastic pollution enters aquatic systems in 2016 and 16 Mt/year [12, 20] in 2025. These outputs closely align with ranges reported by Jambeck *et al.* (5), who report a midpoint of 9.1 Mt/year (25% of mismanaged waste entering the ocean) [5.5 Mt/year for 15%; 14.6 Mt/year for 40%] in 2015 and 17.5 Mt/year [10.5, 28] in 2025. Estimated masses of mismanaged waste reported here (for 2016, 87 Mt [81, 93]; for 2020, 108 Mt [101, 126]) are higher than, but in the same order of magnitude, as those reported by Jambeck *et al.* (5) (2016, 36.5 Mt; 2020, 69.9 Mt). This is unsurprising because Jambeck *et al.* (5) do not estimate mismanaged waste generated >50 km from the coast. In early model time steps, estimated mismanaged MSW presented here (2016, 87 Mt [81, 93]; 2020, 108 Mt [101, 126]) align well with those presented by Lebreton and Andrad (2) (2015, 80 Mt [60, 99]; 2020, 96 Mt [75, 115]). Estimates of mismanaged MSW from the two models diverge into the future; we estimated 228 Mt [213, 252] in 2040, whereas Lebreton and Andrad (2) estimated 155 Mt [118, 188]. This divergence may be due to several differences among the models in urban/rural population splits and constraints on waste management and recycling capacities applied in P<sub>2</sub>O.
- Reported results represent model output when inputs are assumed to have no error. 95% CIs were calculated by using Monte Carlo sampling (SM section 5.6). Hereafter, values in square brackets represent the lower and upper bounds of the CI.
- M. Crippa *et al.*, *A Circular Economy for Plastics—Insights from Research and Innovation to Inform Policy and Funding Decisions* (European Commission, 2019).
- S. Slater, T. Crichton, *Recycling of Laminated Packaging* (Banbury, 2011).
- C. A. Velis *et al.*, *Waste Manag. Res.* **30** (Suppl), 43–66 (2012).
- D. C. Wilson *et al.*, *Waste Manag.* **35**, 329–342 (2015).
- K. L. Law, *Ann. Rev. Mar. Sci.* **9**, 205–229 (2017).
- C. Wiedinmyer, R. J. Yokelson, B. K. Gullett, *Environ. Sci. Technol.* **48**, 9523–9530 (2014).
- N. Reyna-Bensusan *et al.*, *Atmos. Environ.* **213**, 629–639 (2019).
- C. A. Velis, *Waste Manag. Res.* **33**, 389–391 (2015).
- R. Tramoy *et al.*, *Front. Mar. Sci.* **6**, 151 (2019).
- T. van Emmerik, M. Loozen, K. van Deventer, F. Buschman, G. Prinsen, *Environ. Res. Lett.* **14**, 084033 (2019).
- G. F. Schirrinzi *et al.*, *Sci. Total Environ.* **714**, 136807 (2020).
- R. M. Bailey, richardmbailey/P2O: P2O v1.0.0. Zenodo (2020); <https://dx.doi.org/10.5281/zenodo.3929470>.

### ACKNOWLEDGMENTS

We thank the anonymous peer reviewers for their suggestions, which improved this manuscript. M. Hestlin, L. Peake, G. Keoleian, J. Abbot, J. Muncke, and D. Mihaylova reviewed drafts of the supplementary materials and results. We are indebted to nonauthoring members of the expert panel—D. Russo, E. Moss, J. Boughton, C. Lao, D. Lerario, M. Gadgil, and M. Da—for contributing their knowledge and sharing data with this research. We are also indebted to A. Morlet, R. Opsomer, S. Defruyt, and S. Wingstrand from the Ellen MacArthur Foundation for substantial contribution on knowledge and data on the plastic system and circular economy. We are grateful to J. Calcagno, J. Mandirola, J. Sirko, M. Freeman, Z. Celik, H. Watson, G. Murphy, B. Towner Levine, M. Mahoney, E. Hogan, M. Wissner, L. Mudge, A. Valdivia, O. Tzadik, M. Ochocki, and B. Frinault for conducting accuracy checks of raw data inputs, the assembly of model input files, code review, and fact checks of the supplementary materials. We also thank I. Issifu and B. Frinault for reviewing manuscript drafts, C. Gonzales and A. Syed for help with data collection and curation, and P. Edwards for managing an informal review process. K. Gronsky assisted in the design of the research and provided project management support. R.-M. Paquin assisted in formatting figures and references. SYSTEMIQ provided generous in-kind support to this research. **Funding:** This project was funded by The Pew Charitable Trusts. **Author contributions:** W.W.Y.L., J.E.P., Y.S., and M.R.S. conceived the study and led the overall conceptual development of this work. This research represents the equal effort and intellectual contribution among research groups at four key institutions: The Pew Charitable Trusts, SYSTEMIQ, University of Oxford, and University of Leeds, led respectively by W.W.Y.L., Y.S., R.M.B., and C.A.V. The P<sub>2</sub>O model was developed by R.M.B., and R.M.B. ran all model simulations. J.E.P. and R.M.B. processed model outputs. C.A.V. and E.C. provided thought leadership and expertise on solid waste management systems and practices. E.K. was a key contributor to the recycling scenarios, especially their economics and sensitivities in future changes. J.K., A.C.C., E.F., and S.B. provided the expertise in reduce and substitute interventions to select material innovations and new delivery models as well as to assess their applicability across scenarios. J.E.P. prepared the figures. Y.S., J.K., E.C., E.J., L.K., M.E.A., M.M.P., T.D.P., and D.F. collected and curated the data. Working groups were led by J.K., E.C., M.E.A., D.F., and E.J. Manuscript drafting was led by W.W.Y.L., with substantial review and editing support from J.E.P., R.M.B., M.B.M., L.G., B.D., E.C., and C.A.V. with further input from all authors. Technical appendices were prepared by W.W.Y.L., Y.S., R.M.B., E.C., J.K., C.A.V., M.B.M., E.J., K.K.H., M.M.P., K.L., and J.E.P., coordinated by K.K.H. Data-checking of the model data inputs, including associated software development, was conducted by E.N. and managed by M.B.M. **Competing interests:** None declared. **Data and materials availability:** The Matlab code and input files used to run the P<sub>2</sub>O model and generate the results of this study and the resulting output files are available at (49).

### SUPPLEMENTARY MATERIALS

science.sciencemag.org/content/369/6510/1455/suppl/DC1  
Materials and Methods  
Figs. S1 to S6  
Tables S1 to S75  
References (50–217)

20 January 2020; accepted 2 July 2020  
Published online 23 July 2020  
10.1126/science.aba9475

## SURFACE CHEMISTRY

## Following the microscopic pathway to adsorption through chemisorption and physisorption wells

Dmitriy Borodin<sup>1,2</sup>, Igor Rahinov<sup>3</sup>, Pranav R. Shirhatti<sup>4</sup>, Meng Huang<sup>5</sup>, Alexander Kandratsenka<sup>2</sup>, Daniel J. Auerbach<sup>2</sup>, Tianli Zhong<sup>1,2</sup>, Hua Guo<sup>5</sup>, Dirk Schwarzer<sup>2</sup>, Theofanis N. Kitsopoulos<sup>1,2,6,7</sup>, Alec M. Wodtke<sup>1,2,8\*</sup>

Adsorption involves molecules colliding at the surface of a solid and losing their incidence energy by traversing a dynamical pathway to equilibrium. The interactions responsible for energy loss generally include both chemical bond formation (chemisorption) and nonbonding interactions (physisorption). In this work, we present experiments that revealed a quantitative energy landscape and the microscopic pathways underlying a molecule's equilibration with a surface in a prototypical system: CO adsorption on Au(111). Although the minimum energy state was physisorbed, initial capture of the gas-phase molecule, dosed with an energetic molecular beam, was into a metastable chemisorption state. Subsequent thermal decay of the chemisorbed state led molecules to the physisorption minimum. We found, through detailed balance, that thermal adsorption into both binding states was important at all temperatures.

Adsorption of molecules to metal surfaces initiates most heterogeneous chemistry; yet, the precise way it occurs is difficult to study. When hot molecules collide with a surface, they must lose translational and internal energy, ultimately reaching equilibrium with the solid. This process may involve forming transient chemical bonds to the surface, leading to chemisorption (1) or, alternatively, noncovalent (physisorption) interactions. Furthermore, which interactions prevail can strongly influence surface chemistry (2, 3); for example, chemisorbed O<sub>2</sub> on Pt(111) can dissociate producing highly reactive adsorbed atoms (4), whereas physisorbed O<sub>2</sub> desorbs, remaining unreactive (5).

Generally, molecules adsorb through both physisorption and chemisorption interactions (5). Hence, adsorption generally involves passage through multiple binding states before equilibrium is achieved. This process represents a complex and fundamental problem that is not well understood. For example, one might think that physisorption is more important for accommodation of impinging molecules. For the CO/Au(111) system, density functional theory (DFT) calculations suggest that when chemisorbed, CO binds with a fixed (OC-Au) orientation and at specific sites; but when

physisorbed, CO is nearly a free rotor and weakly bound at every surface site (6). When a molecule collides randomly at different surface sites and

with random orientation, physisorption is statistically favored. But this scenario ignores that rates of equilibration depend strongly on the nature of the interactions. For example, the vibrational relaxation time of chemisorbed CO to Cu is ~2 ps (7) but is 49 ps for CO physisorbed to Au (8).

The intricate interplay between physisorption and chemisorption states is believed to take place in precursor-mediated adsorption (9–11) and bear on a broad variety of surface science applications, ranging from catalytic steam reforming (10, 11) to designing molecular switches (12). Despite being central to a dynamical picture of surface chemistry, predicting and probing adsorption pathways exceeds our current understanding. Not only is electronic structure theory challenged to provide accurate, simultaneous descriptions of covalent and noncovalent interactions, but also no experiments so far have been reported that directly follow adsorption pathways through chemisorption and physisorption wells. Recently, we observed that vibrationally excited CO can trap to a gold surface, equilibrating

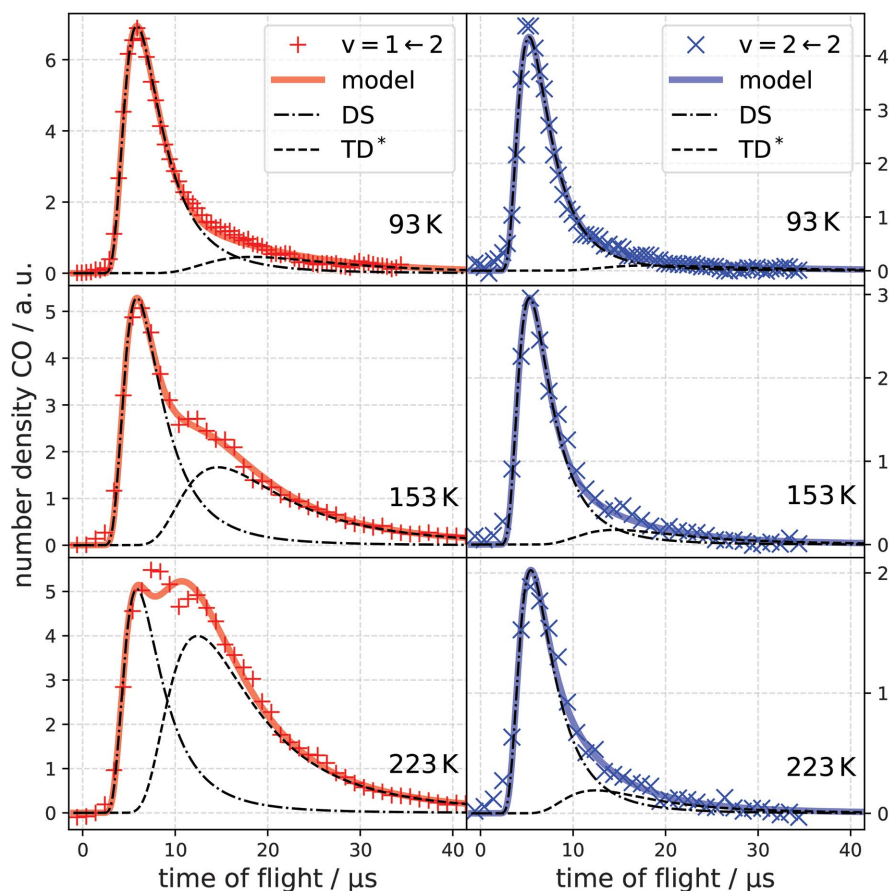


**Fig. 1. State-specific time of flight traces.** Measured TOF traces of CO( $v=1$ ) (+ symbols) and CO( $v=2$ ) (× symbols) at different surface temperatures along with their global fits (solid lines) revealing the DS (dash-dotted lines) and TD\* (dashed lines) components. The incidence energy is  $E_i = 0.32$  eV. The surface temperature is indicated in each panel. The method for decomposing the data into DS and TD\* components is explained in the supplementary materials, section 1.

<sup>1</sup>Institute for Physical Chemistry, Georg-August University of Göttingen, Tammannstraße 6, 37077 Göttingen, Germany.

<sup>2</sup>Department of Dynamics at Surfaces, Max Planck Institute for Biophysical Chemistry, Am Fassberg 11, 37077 Göttingen, Germany.

<sup>3</sup>Department of Natural Sciences, The Open University of Israel, 4353701 Raanana, Israel. <sup>4</sup>Tata Institute of Fundamental Research, 500046 Hyderabad, India.

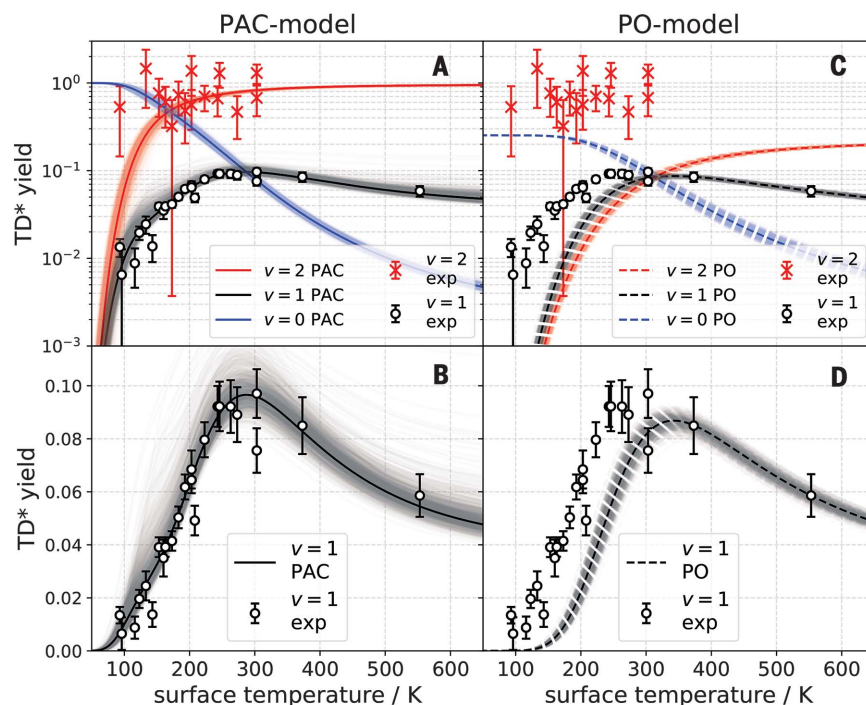
<sup>5</sup>Department of Chemistry and Chemical Biology, University of New Mexico, Albuquerque, NM 87131, USA. <sup>6</sup>Department of Chemistry, University of Crete, 71003 Heraklion, Greece.

<sup>7</sup>Institute of Electronic Structure and Laser, FORTH, 71110 Heraklion, Greece. <sup>8</sup>International Center for Advanced Studies of Energy Conversion, Georg-August University of Göttingen, Tammannstraße 6, 37077 Göttingen, Germany.

\*Corresponding author. Email: alec.wodtke@mpibpc.mpg.de



**Fig. 2. Vibrational state-specific yields of desorbing molecules.** (A to D) Experimentally observed CO( $v = 1$ ) (open circles) and CO( $v = 2$ ) ( $\times$  symbols) passing through the TD\* channel. The error bars indicate a 90% confidence interval. Black and red solid lines are results of fits to the PAC model. (A) Logarithmic scale. (B), Linear scale. Black and red dashed lines represent the PO model. (C) Logarithmic scale. (D) Linear scale. Blue solid line (PAC) and blue dashed line (PO) represent the desorbing yield of CO( $v = 0$ ) stemming from ultimate vibrational relaxation of CO( $v = 2$ ). The shading represents the uncertainty of the fit determined by random number sampling of the fit parameter distribution (supplementary materials, section 4).



both its rotational and translational motion but without vibrational equilibration (13). As we will show below, this feature provided a distinctive opportunity to follow the microscopic pathways of adsorption and equilibration on the surface, using the vibrational relaxation time as an internal clock.

Specifically, we have demonstrated that the adsorption of energetic CO to Au(111) involves pathways through a chemisorption state recently predicted by theory (6) as well as the known physisorption state (8, 14). We showed that although the overall free-energy minimum is the physisorbed state, when an energized molecule collides with the surface, it first becomes trapped in a metastable chemisorption state, in which it rapidly loses its vibrational and translational energy to the solid. We were able to derive the adsorption energies of the two states and the height of the energy barrier separating them. Application of the principle of detailed balance allowed us to use the information obtained in this molecular beam experiment to probe the pathway to thermal adsorption. This analysis showed that thermal adsorption involves substantial contributions from both chemisorption and physisorption at all temperatures.

The experiment involved scattering a molecular beam of optically prepared CO( $v = 2, J = 1$ ) from Au(111) (where  $v$  is a vibrational quantum number and  $J$  is a rotational quantum number) and state-selectively detecting, at controlled surface temperature ( $T_s$ ), the time of flight (TOF) of the thermally desorbing molecules in  $v = 1$  and  $v = 2$ , in addition to directly scattered ones (supplementary mate-

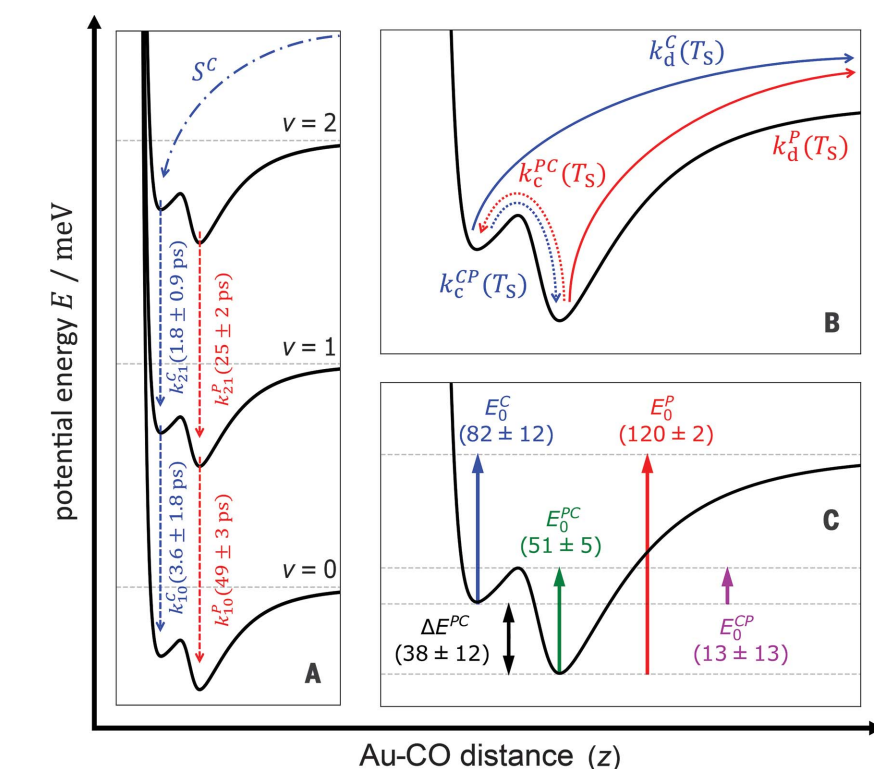


**Fig. 3. The PAC model.** (A and B) Rate processes describing the competition between (A) vibrational relaxation (dashed arrows) and (B) desorption (solid arrows) and interconversion between the chemisorbed and physisorbed states (dotted arrows). (C) Features of the Au(111)-CO interaction potential, derived from a fit of the PAC model to the experimental data.

rials, materials and methods) (13). We were inspired by recent theoretical predictions of a metastable chemisorption state with a short vibrational relaxation lifetime (6). We knew

that the physisorbed molecule undergoes slow vibrational relaxation (8, 15). So, it was clear that by varying  $T_s$  and thereby controlling the molecule's surface residence time, the

temperature-independent vibrational relaxation lifetime could act as an internal clock, sensitive to the type of interaction that the molecule had experienced at the surface. Our goal was to obtain quantitative insight into the pathways to adsorption from measured populations of thermally desorbing CO in  $v = 1$  and 2, which depend on the branching ratio between vibrational relaxation and desorption.

Examples of these TOF experiments are shown in Fig. 1. The traces comprise a high-speed direct scattering (DS) component and a slower component owing to thermal desorption ( $\text{TD}^*$ ) of CO( $v = 1$  or 2). We use the notation  $\text{TD}^*$  to indicate that the vibrational relaxation is not complete despite all other degrees of freedom (rotation and translation) being thermalized with the surface (13).

We fit data such as that of Fig. 1 to a simple model on the basis of the principle of detailed balance (supplementary materials, section 1). Hence, the fitting also yields the sticking probability versus incidence kinetic energy for CO on Au(111), which agrees well with a previous report (16). This procedure also yielded vibrational state-specific populations of desorbing molecules in the  $\text{TD}^*$  channel (Fig. 2). CO ( $v = 2$ ) (Fig. 2,  $\times$  symbols) dominated the  $\text{TD}^*$  channel, but some CO also desorbed in  $v = 1$  (Fig. 2, open circles). Desorption yield varied strongly with  $T_S$  and can be fit with a kinetic model involving physisorption and chemisorption states (PAC model).

The PAC model is shown schematically in Fig. 3, A and B, and is described further in the supplementary materials, section 2. The important rate processes are thermal desorption from the chemisorbed ( $k_d^C$ ) and physisorbed ( $k_d^P$ ) states; thermal conversion between the two states ( $k_c^{PC}$  and  $k_c^{CP}$ ); and vibrational relaxation of chemisorbed ( $k_{ij}^C$ ) and physisorbed ( $k_{ij}^P$ ) molecules. Here,  $i$  and  $j$  are vibrational quantum numbers.

We have fit the vibrational state-specific quantities of Fig. 2, the  $\times$  symbols and open circles, to the PAC model, optimizing only five parameters:  $k_{10}^C$ , the relaxation rate constant of chemisorbed CO( $v = 1$ );  $\Delta E^{PC}$ , the energy of the chemisorbed state relative to the physisorbed state;  $E_0^{PC}$ , the barrier to convert physisorbed molecules to the chemisorbed state;  $A_c^{PC}(T_S)$ , the Arrhenius prefactor to convert physisorbed molecules to the chemisorbed state; and  $S^C$ , the fraction of CO( $v = 2$ ) molecules that initially trap into the chemisorbed state. The values of parameters that result from the fits are provided in table S4.

Other constants in the model are known independently from temperature-programmed desorption (TPD) (17) or pump-probe measurements of vibrational lifetimes (8) or

can be derived with the help of first-principles electronic structure calculations (6) and transition state theory (supplementary materials, section 3) (18–20).

The best fit is shown in Fig. 2, A and B, as black and red lines; all of the relevant rate constants are tabulated in the supplementary materials, section 3. A host of useful information emerges from the fitting. The derived energy landscape for adsorption is shown in Fig. 3C; this includes an analysis of TPD data yielding  $E_0^P$ , the desorption barrier from the physisorbed state (supplementary materials, section 3). We emphasize that  $S^C = 0.98 \pm 0.02$ , indicating nearly exclusive initial population of the metastable chemisorption well

in the molecular beam experiment and that molecules initially trapped in the chemisorbed state need only pass over a small barrier (of  $E_0^{CP} = 13$  meV) to reach the physisorbed state, which is qualitatively consistent with predictions of first-principles electronic structure theory (6).

We also attempted to fit our results to models that neglect the chemisorption state (supplementary materials, section 5). In a physisorption-only (PO) model, adsorption occurs into a single physisorption well, and vibrational relaxation competes with thermal desorption. The PO model (Fig. 2, C and D, dashed black and red lines) failed to reproduce the experimental observations. Thermal desorption from the physisorbed

state was much slower than from the chemisorbed state ( $k_d^P \ll k_d^C$ ) (table S3); therefore, vibrationally excited molecules that were physisorbed relaxed more rapidly than they desorbed. This is mainly due to adsorbate entropy; the physisorbed state has the high entropy of a two-dimensional ideal gas, and the chemisorbed state has the low entropy of a hindered translator. By contrast, in the PAC model, rapid thermal desorption from the chemisorption well allowed CO ( $v = 2$ ) to survive, which is in agreement with experiment. We also tried a third model that was based on the hypothesis that vibrational relaxation from  $v = 2 \rightarrow 1$  occurred during the subpicosecond interaction time of a DS event and that a fraction of these nascent CO( $v = 1$ ) molecules became trapped in the physisorption well (supplementary materials, section 5). This model also fails to describe the experimental observations.

The PAC model was supported by first-principles predictions of the coexistence of chemisorbed and physisorbed states (6). The precise energies of these states, the height of the energy barrier separating them, and the predicted vibrational relaxation lifetimes all depend on the specific assumptions of the theory and the chosen functional. Nevertheless, they were consistent with the experimentally derived values (supplementary materials, section 6).

Calculated microscopic pathway fluxes obtained from the experimentally validated PAC model are shown in Fig. 4. This includes pathways leading to CO( $v = 1$ ) desorption (Fig. 4A) and adsorption to the lowest energy physisorption minimum (Fig. 4B). Details on how pathway fluxes were determined are provided in the supplementary materials, section 7. At all temperatures, the first step toward equilibrium involved trapping of CO( $v = 2$ ) into the chemisorption well. This state can then undergo vibrational relaxation, thermal

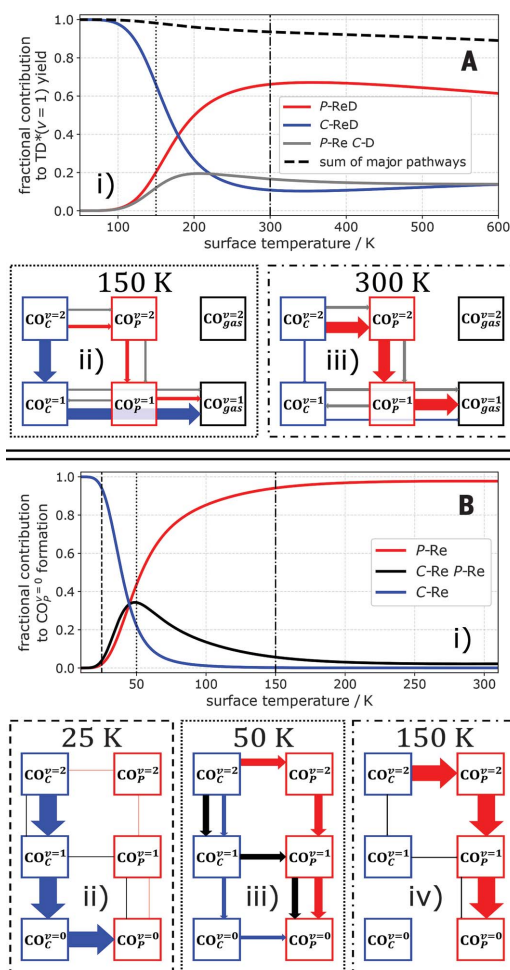


**Fig. 4. Pathway fluxes for adsorption and desorption.** (A) (Top) (i) Relative contribution of the most prominent pathways to CO( $v = 1$ ) desorption flux. (Bottom) Schematics illustrating the relative contributions of three most prominent pathways at (ii) low (150 K) and (iii) high (300 K) surface temperatures. (B) (Top) (i) Relative contribution of most prominent pathways of CO( $v = 2$ ) ultimate relaxation and formation of physisorbed CO( $v = 0$ ) on the surface. (Bottom) (ii to iv) Schematic representations of the most prominent pathways at different surface temperature regimes. The arrow thickness is proportional to the relative importance of the formation pathways.



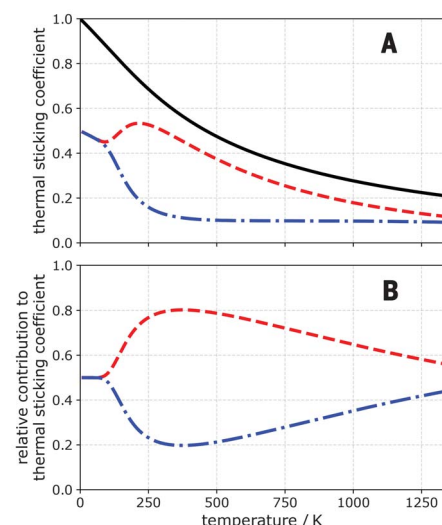


**Fig. 5. Thermal adsorption into chemisorbed and physisorbed states. (A)** Thermal sticking coefficients. **(B)** Relative contributions. Colored lines denote thermal adsorption into the physisorption (dashed, red) and chemisorption (dash-dotted, blue) wells. The black line is the total thermal adsorption coefficient.

desorption, and/or thermal conversion to the physisorbed state. At low temperatures (Fig. 4, blue lines and blue arrows), vibrational relaxation dominated because it required no thermal activation. At high temperature (Fig. 4, red lines and red arrows), conversion to the physisorbed species was rapid, followed by either desorption or vibrational relaxation. At intermediate temperatures, the physisorbed state could even transfer back to the chemisorption well.

Although the observations of these experiments are specific to vibrationally inelastic pathways to adsorption, the conclusions of this work are not. Vibrational motion has little influence on adsorption (21), and by applying the principle of detailed balance (supplementary materials, section 8) we can use the quantities derived from these molecular beam experiments to better understand thermal adsorption of CO to Au(111). Key results are shown in Fig. 5.

Thermal adsorption occurred initially into both the chemisorbed and physisorbed states, with similar probabilities at all temperatures. At low temperatures, adsorption into the two states was equally important. At intermediate temperatures, the higher-entropy physisorbed state increased in relative importance. But at the highest surface temperatures, the translational and rotational entropy of the chemisorbed CO approached that of the physisorbed CO and the chemisorbed CO again grew in importance. This increased entropy of the chemisorbed CO resulted from a greater sampling of higher-energy chemisorption states at different binding sites of the surface.

We also reconcile in Fig. 5 the seemingly contradictory observations that the molecular beam experiments exclusively probed the chemisorption state, but low-temperature thermal dosing experiments have never shown evidence of the chemisorption state (8, 14). In the molecular beam experiments that used high-energy CO, the chemisorption state could be initially and selectively populated; these states were the same ones that became increasingly important in the high temperature range shown in Fig. 5. The high-temperature thermal adsorption still populated both states because of the large width of the Maxwell-Boltzmann distribution, while the width of the energy distribution in the molecular beam was orders of magnitude narrower (supplementary materials, section 8). For low-temperature dosing, it is clear now that both binding states were initially populated. But when we consider the small barrier to interconversion, it turns out that experiments have never been done at low enough temperatures to suppress thermal interconversion of the chemisorption to the physisorption state (supplementary materials, section 9). This analysis suggests an interesting experiment that could be carried out in the future. If a molecular beam with 0.3 eV incidence energy is used to selectively populate the chemisorption state and the surface is cooled below 5 K, it may be possible to suppress interconversion to the physisorbed state long enough to observe directly the metastable chemisorbed state.

Last, we highlight the implications of our work within the context of an industrially important class of catalytic reactions. Catalytic oxidation is initiated on a variety of metals through the reaction  $\text{O}_{2(g)} \rightarrow \text{O}_{2^*}$ , where  $\text{O}_{2^*}$  can be either physisorbed or chemisorbed. Hence, catalytic activation of oxygen, similar to many other examples in heterogeneous catalysis, is a complex network of thermal rate processes that includes adsorption into, desorption from, and interconversion between physisorbed and chemisorbed molecular states (5). Although these qualitative statements are long established, it has never before been possible to construct a model that accurately describes such a kinetic adsorption network. As a result, there has also never been a way to test to what extent theory is capable of describing such an intricately balanced set of rate processes. With the results presented here, we successfully determined the rate constants of a thermal adsorption network, revealing the fundamental energetic and entropic characteristics of adsorption and desorption. We also showed that the results can be understood from first principles by comparison with a multidimensional potential energy surface constructed with DFT (6). This result strengthens the foundation on which a predictive theory of surface chemistry and heterogeneous catalysis may continue to be developed.

## REFERENCES AND NOTES

- H. Jiang *et al.*, *Science* **364**, 379–382 (2019).
- D. A. King, M. G. Wells, *Surf. Sci.* **29**, 454–482 (1972).
- D. A. King, M. G. Wells, *Proc. R. Soc. London Ser. A* **339**, 245–269 (1974).
- T. Zambelli, J. V. Barth, J. Wintterlin, G. Ertl, *Nature* **390**, 495–497 (1997).
- C. T. Rettner, C. B. Mullins, *J. Chem. Phys.* **94**, 1626–1635 (1991).
- M. Huang *et al.*, *Phys. Rev. B* **100**, 201407 (2019).
- M. Morin, N. J. Levins, A. L. Harris, *J. Chem. Phys.* **96**, 3950–3956 (1992).
- S. Kumar *et al.*, *Phys. Rev. Lett.* **123**, 156101 (2019).
- D. E. Brown, D. J. Moffatt, R. A. Wolkow, *Science* **279**, 542–544 (1998).
- E. Dombrowski, E. Peterson, D. Del Sesto, A. L. Utz, *Catal. Today* **244**, 10–18 (2015).
- R. Moiraghi *et al.*, *J. Phys. Chem. Lett.* **11**, 2211–2218 (2020).
- W. Liu, S. N. Filimonov, J. Carrasco, A. Tkatchenko, *Nat. Commun.* **4**, 2569 (2013).
- P. R. Shirhatti *et al.*, *Nat. Chem.* **10**, 592–598 (2018).
- J. Pischel, A. Pucci, *J. Phys. Chem. C* **119**, 18340–18351 (2015).
- I. Lončarić, M. Alducin, J. I. Juaristi, D. Novko, *J. Phys. Chem. Lett.* **10**, 1043–1047 (2019).
- C. T. Rettner, *J. Chem. Phys.* **99**, 5481–5489 (1993).
- D. P. Engelhart, R. J. V. Wagner, A. Meling, A. M. Wodtke, T. Schäfer, *Surf. Sci.* **650**, 11–16 (2016).
- J. C. Tully, *Surf. Sci.* **299–300**, 667–677 (1994).
- T. L. Hill, *Introduction to Statistical Thermodynamics* (Dover Publication, 1986).
- M. Jørgensen, H. Grönbeck, *J. Phys. Chem. C* **121**, 7199–7207 (2017).
- A. M. Wodtke, H. Yuhui, D. J. Auerbach, *Chem. Phys. Lett.* **413**, 326–330 (2005).
- D. Borodin, CO( $v=2$ ) scattering on Au(111) (TPD, TOF and TD( $v=1,2$ )). Zenodo (2020).

## ACKNOWLEDGMENTS

**Funding:** A.M.W. acknowledges support from the SFB1073 under project A04, from the Deutsche Forschungsgemeinschaft (DFG), and financial support from the Ministerium für Wissenschaft und Kultur (MWK) Niedersachsen and the Volkswagenstiftung under grant INST 186/901-1 to build parts of the experimental apparatus. A.M.W. and A.K. also acknowledge the Max Planck Society for the Advancement of Science. I.R. and A.M.W. acknowledge support from the Niedersächsisch-Israelische Gemeinschaftsvorhaben under project 574 7 022. T.N.K. acknowledges the European Research Council (ERC) under the European Union's Horizon 2020 research and innovation program (grant agreement 833404). D.B. thanks the BENCh graduate school, funded by the DFG (389479699/GRK2455). M.H. and H.G. acknowledge support from the National Science Foundation (grant CHE-1462109). H.G. also acknowledges the Alexander von Humboldt Foundation for a Humboldt Research Award. **Author contributions:** D.B., I.R., P.R.S., D.J.A., and A.K. developed the PAC kinetic model and carried out the analysis. I.R. and D.B. wrote the supplementary materials. I.R. and P.R.S. performed experiments that led to the data presented in this work. M.H. and H.G. performed the theoretical calculations and analyzed the results. T.Z. and D.S. carried out TPD measurements that were essential to the application of the PAC model. D.S. and T.N.K. participated in discussion of the results, analysis, data interpretation, and revisions. D.J.A. had major conceptual contributions to data interpretation and supplementary materials and manuscript revisions. A.M.W. wrote the manuscript and participated in revisions. All authors provided critical input to the writing of the paper. **Competing interests:** None declared. **Data and materials availability:** There are no restrictions on materials used in this work. All data needed to evaluate the conclusions in the paper are present in the paper or the supplementary materials and are publicly available in the repository (22).

## SUPPLEMENTARY MATERIALS

science.sciencemag.org/content/369/6510/1461/suppl/DC1  
Materials and Methods  
Supplementary Text  
Figs. S1 to S13  
Tables S1 to S4  
References (23–41)

24 May 2020; accepted 14 July 2020  
10.1126/science.abc9581

## CORONAVIRUS

# Assessing the impact of coordinated COVID-19 exit strategies across Europe

N. W. Ruktanonchai<sup>1,2\*</sup>†, J. R. Floyd<sup>1\*</sup>†, S. Lai<sup>1\*</sup>†, C. W. Ruktanonchai<sup>1</sup>†, A. Sadilek<sup>3</sup>, P. Rente-Loureiro<sup>4</sup>, X. Ben<sup>3</sup>, A. Carioli<sup>1</sup>, J. Gwinn<sup>5</sup>, J. E. Steele<sup>1</sup>, O. Prosper<sup>6</sup>, A. Schneider<sup>3</sup>, A. Oplinger<sup>3</sup>, P. Eastham<sup>3</sup>, A. J. Tatem<sup>1</sup>

As rates of new coronavirus disease 2019 (COVID-19) cases decline across Europe owing to nonpharmaceutical interventions such as social distancing policies and lockdown measures, countries require guidance on how to ease restrictions while minimizing the risk of resurgent outbreaks. We use mobility and case data to quantify how coordinated exit strategies could delay continental resurgence and limit community transmission of COVID-19. We find that a resurgent continental epidemic could occur as many as 5 weeks earlier when well-connected countries with stringent existing interventions end their interventions prematurely. Further, we find that appropriate coordination can greatly improve the likelihood of eliminating community transmission throughout Europe. In particular, synchronizing intermittent lockdowns across Europe means that half as many lockdown periods would be required to end continent-wide community transmission.

The ongoing coronavirus disease 2019 (COVID-19) pandemic rapidly spread across Europe in February and March 2020, making it the largest cluster of cases worldwide for much of March and April 2020 (1). In response, most of Europe implemented strict lockdown measures to control disease spread, which have been shown to be effective at reducing transmission (2–4). As rates of new cases decline, countries are now implementing various exit strategies to relax restrictions (5). Long-term success of any potential exit strategy hinges on what happens regionally, as international importation could overwhelm efforts to prevent resurgence through testing and contact tracing (6, 7). To account for potential international importation the European Commission recommended that governments provide advance warning of plans to relax nonpharmaceutical interventions (NPIs) (8) and has specifically focused on coordinated easing of travel restrictions (9). To better evaluate the importance and nature of an internationally coordinated exit strategy, governments require an evidence base for understanding importation and the consequences of easing interventions in an uncoordinated way.

Data from mobile phones can help address this need by informing connectivity patterns, contact rates, and the effect of various NPIs on mobility. In other settings, mobile phone data have been instrumental for understanding where infection occurs for various diseases

(10) such as malaria (11, 12), predicting disease spread (13), and quantifying population mobility during and after catastrophic events (14). More recently, for the COVID-19 pandemic, these data have been valuable in assessing NPI effectiveness (3, 4) and remain a leading way to understand whether populations are adhering to social distancing policies (15–18). These data also link well with theoretical models that provide a basis for understanding how heterogeneous mobility and exposure will affect disease invasion (19) in spatially structured populations (20).

Here, we provide an evidence base for coordinated exit strategies across Europe using mobile phone data and a metapopulation model of COVID-19 transmission (21). Specifically, we quantify the progression of a second continent-wide epidemic if countries act in a coordinated or uncoordinated manner. We also quantify how coordination could influence regionally interrupted transmission of COVID-19, testing the importance of synchronized NPIs if countries phase them to limit economic impact. We accomplished this by (i) estimating pre-COVID-19 mobility using a newly compiled anonymized and aggregated call data record dataset from Vodafone and an anonymized and aggregated continental NUTS3 (Nomenclature of Territorial Units for Statistics) mobility dataset from Google (table S1), (ii) measuring mobility reductions due to NPIs using a separate COVID-19 Google dataset, and (iii) propagating these reductions in an epidemiological model (see fig. S1 for data flow). All analyses were undertaken at the NUTS3 administrative unit level, which are administrative boundaries regulated by the European Union (EU) for use within EU member states (22), with spatial extents defined by population thresholds ranging from 150,000 to 800,000 residents.

## Baseline mobility and COVID-19–related reductions

First, we predicted the baseline probability of moving between NUTS3 regions across Europe using the Vodafone data in Spain and Italy and the continental Google NUTS3 dataset (Fig. 1). We then analyzed the Google COVID-19 dataset to quantify reductions in mobility and contact rates from January 2020 through the end of March 2020 in response to the COVID-19 pandemic (Fig. 2). In our simulations, we used observed reductions in mobility in each NUTS3 area to proportionally reduce outgoing flows, incoming flows, and local contact rates for that area.

Using these baseline mobility patterns and reductions in mobility, we simulated the spread of COVID-19 over 6 months, starting on 4 April 2020 while making various assumptions about where and when NPIs would be relaxed or reinstated. Across all simulations, we started transmission on 20 March 2020 because this predates large reductions in mobility (Fig. 2B), allowing the disease to spread initially in a data-driven way that can help account for spatial biases in reporting and testing. We parameterized the initial numbers of people infected using a repository maintained by the Johns Hopkins University Center for Systems Science and Engineering (CSSE) (23). Because the case data from this repository were at the country level, we distributed cases across NUTS3 area proportionally on the basis of population size (fig. S10).

To simulate different exit strategies and the overall impact of the different NPIs enacted, we reduced mobility the week after 28 March (29 March to 4 April) on the basis of the observed change between 15 to 21 March and 22 to 28 March to account for changes caused by further uptake of existing NPIs (Fig. 2). On average, we predicted an overall mean reduction in mobility of 65% compared with 28 January to 18 February through this process, agreeing with recent studies on contact rate reductions in the United Kingdom (24), which observed a 73% reduction in daily contacts. When simulating active lockdowns on dates after 4 April, we used the predicted mobility reduction for each NUTS3 area from 29 March to 4 April. When we simulated countries lifting their NPIs entirely, we used the relative mobility patterns observed from 1 to 7 March.

## Modeling the effect of lifting interventions early

First, we compared secondary epidemic timing when all countries coordinated their exit strategies with simulations where one country ended its interventions early. We iteratively tested the impact of each country in Europe easing lockdowns starting 15 April, while all other countries extended their NPIs for 4, 8, or 12 weeks, depending on the simulation run. For the country that lifted its NPIs early, we assumed that people in each NUTS3 area

<sup>1</sup>WorldPop, School of Geography and Environmental Science, University of Southampton, Southampton, UK. <sup>2</sup>Population Health Sciences, Virginia Tech, Blacksburg, VA, USA. <sup>3</sup>Google, Mountain View, CA, USA. <sup>4</sup>Vodafone Group, London, UK. <sup>5</sup>College of Public Health, University of Kentucky, Lexington, KY, USA. <sup>6</sup>Department of Mathematics, University of Tennessee, Knoxville, TN, USA.

\*Corresponding author. Email: nrukt00@gmail.com (N.W.R.); jrf15@soton.ac.uk (J.R.F.); shengjie.lai@soton.ac.uk (S.L.)

†These authors contributed equally to this work.



**Fig. 1. Predicted baseline mobility patterns for 28 January to 18 February 2020.** (A) Probability of moving from one NUTS3 administrative unit to another after 8 hours.

(B) Individual probability of moving between the top 20 European countries with the greatest outward mobility. For example, an individual in Germany (DE) is roughly twice as likely to travel internationally than an individual in Austria (AT). Colors shown in (B) correspond to the source country, and country codes are from Eurostat (34).

EL, Greece; ES, Spain; FI, Finland; FR, France; HR, Croatia; HU, Hungary; IT, Italy; NL, Netherlands; NO, Norway; PL, Poland; PT, Portugal; RO, Romania; SI, Slovenia; TR, Turkey; UK, United Kingdom; BE, Belgium; BG, Bulgaria; CH, Switzerland.

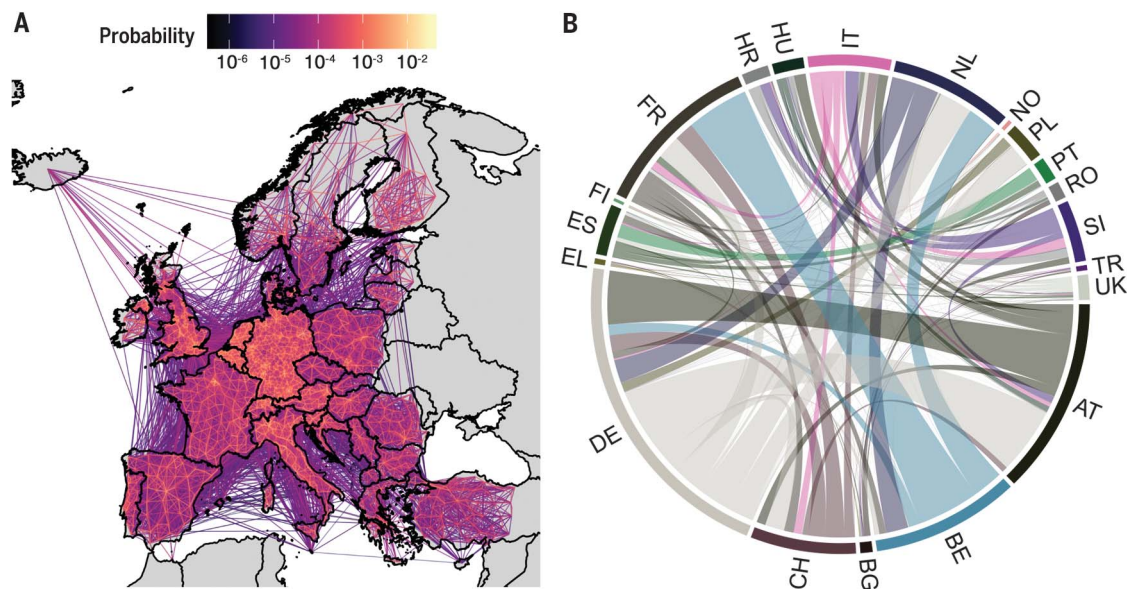
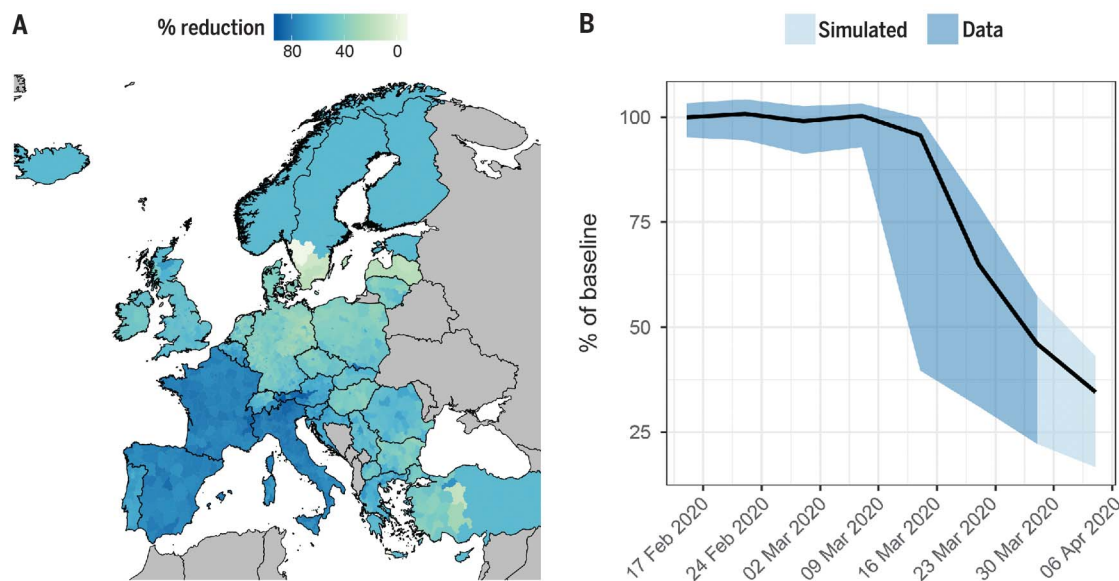


**Fig. 2. Reduction in mobility observed in NUTS3 areas from 11 February to 6 April 2020.** (A) Reduction in mobility observed in each NUTS3 administrative unit across Europe for the week of 21 to 28 March 2020 compared with average movement observed from January to February 2020. Movement data were not available for countries in gray.

(B) Weekly average change in mobility across all NUTS3 areas. Dark blue shows reductions observed in the Google COVID-19 dataset, and light blue shows extrapolation of reductions by 1 week. Black line shows mean change compared with baseline. When implementing NPIs in various NUTS3 areas, we used the movement reduction estimates for the end of this period, 6 April 2020.



would voluntarily reduce their average contact rate by 20% compared to the January and February baseline, or slightly less than the reduction in mobility observed on 23 March, because countries that have lifted NPIs have observed sustained limited mobility reductions beyond the relaxing of various restrictions (16).

If a country lifted its NPIs early, we found that a second epidemic could occur much earlier (Fig. 3B). Figure 3A illustrates the earlier timing

(in days) to reach 25% of people across Europe having had COVID-19 (infected + recovered + exposed; see fig. S13 for plot showing this explicitly). This measure captures when uncontrolled widespread transmission occurred, while accounting for multiple peaks and varying peak heights in Fig. 3B. The time to 25% infection was particularly sensitive to well-connected countries that implemented strong NPIs, such as France and Italy (Fig. 3A). France lifting its NPIs early led to the earliest second epidemic,

35 days earlier than if all countries lifted their NPIs simultaneously (interquartile range: 32.3 to 36.8 days). Despite having experienced relatively low reductions in mobility through 28 March, Germany remains important to continental resurgence, because of its high connectivity with neighboring countries (Fig. 1B). When exploring the epidemic curves over time for different countries lifting their NPIs early, we found that different types of mobility initiated continental epidemics. Whereas

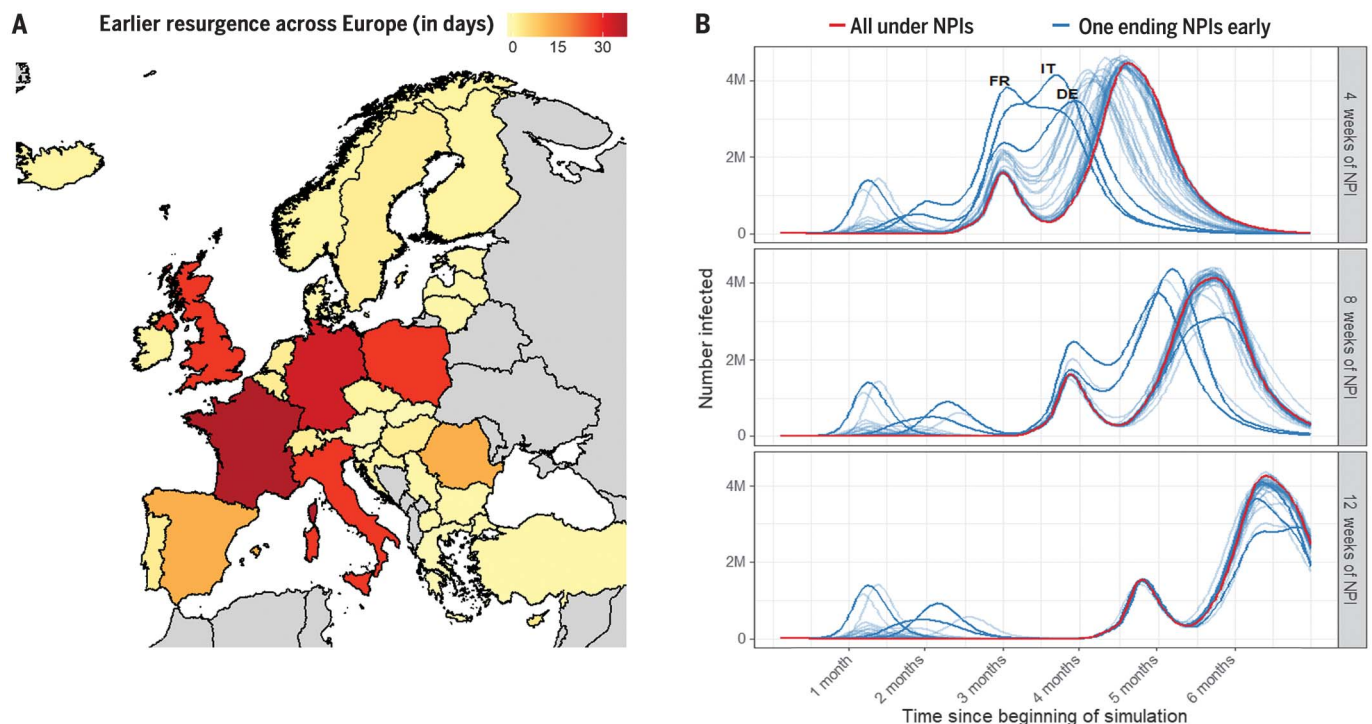


**Fig. 3. Epidemic spread if all countries but one maintain existing NPIs.**

(A and B) When lifting NPIs early, countries reverted to baseline mobility on 15 April. (B) Epidemic curves, with NPIs implemented for 4, 8, or 12 weeks. Curves indicate the number of active cases (M, million) at any given time rather than numbers of new cases per day. Red lines indicate epidemic curves where all countries maintain NPIs for the specified number of weeks. Blue lines indicate epidemic curves

if one country ends intervention policies early (each line represents one randomly chosen country that ends its policies early); France, Germany, and Italy are highlighted. (A) For the 4-week NPI scenario, the number of days earlier that an uncontrolled second epidemic occurs continent-wide if each country ends NPIs early, measured as the time to 25% of the population of Europe having had COVID-19. Movement data were not available for countries in gray.

France lifting its NPIs early led to resurgence in major population centers across the continent, Germany lifting its NPIs early led to resurgence in neighboring countries first (fig. S15). Further, certain areas keeping the reproductive number ( $R$ ) slightly above 1 under NPIs also led to an initial peak in some simulations and maintained the threat of resurgence even after 12 weeks of continent-wide NPIs (Fig. 3B) (for more detail, see the supplementary materials section “Exploring spatiotemporal dynamics of spread”). Along these lines, our simulations included consistent reproductive numbers above 1 in central Turkey, which drastically affected continental spread. In simulations where smaller or less-connected countries lifted their NPIs early, we found that resurgence was largely driven by importation from central Turkey and exhibited epidemic curves very similar to the scenario in which all countries maintained NPIs (Fig. 3B, red line).

#### Modeling the effect of synchronized intermittent NPIs

We also tested how cycling NPIs—alternating between being under interventions for several weeks and under no interventions for the same number of weeks for several cycles—in a

synchronized or unsynchronized manner affected the continent-wide epidemic. Synchronized NPIs meant all countries implemented lockdowns at the same time, while unsynchronized NPIs meant half of all countries (randomly chosen for each simulation run) were under lockdown at any time. Cycling NPIs reflect the intermittent lockdowns that could occur if countries reinstate interventions after surpassing threshold numbers of new cases (25, 26). Therefore, this test helps predict what may happen if countries do not coordinate the easing and reinstating of NPIs on the basis of regional rates of new cases. We ran various simulations where lockdown and nonlockdown periods were 3 or 4 weeks long over the course of two, three, or four cycles.

Across 1200 simulations, we found that synchronized NPIs were always more likely to end community transmission over 6 months and generally lowered transmission more than unsynchronized NPIs did (Fig. 4). In the most notable example, synchronizing four cycles of 3-week-long lockdowns led to local elimination of COVID-19 cases in 90% of simulations, whereas unsynchronized cycles only led to elimination 5% of the time (Fig. 4, bottom left). Two synchronized cycles of 4-week NPIs

were also sufficient to end community transmission, whereas four unsynchronized cycles of 4-week NPIs were necessary to end community transmission (Fig. 4, right). The only simulations in which unsynchronized NPIs resulted in fewer cases than synchronized NPIs at the end of simulation was with two cycles of 3-week-long NPIs (Fig. 4, top left), which occurred because enough people were infected under unsynchronized NPIs that herd immunity reduced transmission. Because these simulations do not include any importation from other regions of the globe, simulations reflecting zero local cases after a certain number of intermittent lockdowns are very unlikely to be realized. Instead, this result reflects the likelihood of reducing local cases to a low enough level that strong test-and-trace systems can catch importations before large outbreaks occur.

Intergovernmental organizations such as the World Health Organization have stressed the importance of international solidarity in terms of sharing resources and expertise in combating COVID-19 (1). Our results reiterate this, as one country ending NPIs before others could mean disease resurgence across Europe as many as 5 weeks earlier, reducing the time



available to expand test-and-treat and to develop new therapeutics or vaccines (Fig. 3). Heterogeneities in mobility reduction (Fig. 2), baseline mobility patterns (Fig. 1), and population sizes mean that certain countries—for example, France, Germany, Italy, and Poland—play a particularly important role in continental resurgence (Fig. 3).

These key countries varied in how local cases led to continental resurgence, implying the need for different key interventions for each. For example, while spread out of Germany led to epidemics in neighboring countries initially, spread out of France led to epidemics in population centers across the continent (fig. S12). Further, we found that small pockets of community transmission under NPIs could assure a second continent-wide epidemic wave. In our study, a small pocket of sustained community transmission occurred even under NPIs, because of central Turkey experiencing limited mobility reductions (Fig. 2) and exhibiting a high starting reproductive number (fig. S2) that kept local  $R$  slightly above 1 when under NPIs. Although the actual mobility reduction in central Turkey is uncertain and has likely changed since late March 2020, this highlights the importance of countries ensuring that  $R$  stays below 1 during lockdown periods and the importance of effective screening of international travelers from areas with sustained transmission well into the future.

We also found that the nature of coordination was key to reducing resurgence risk. When cycling NPIs, synchronized interventions across all countries meant that cases could be driven down more quickly (Fig. 4). Fewer cases at the end of the synchronized lockdowns led to much higher likelihoods of reaching zero cases locally, owing to a higher chance of stochastic recovery processes leading to interrupted transmission. In real terms, the synchronized scenario approximates what could happen if countries set case thresholds for lifting NPIs regionally, whereas the unsynchronized scenario simulates what could happen if countries only consider case numbers within their own boundaries.

Our study has several limitations that influence the direct applicability of the case number predictions across Europe. For example, we used observed mobility reductions as a proxy for reductions in contact rate, which may not reflect reality, although the contact rate reduction estimates from this process accord with those observed in other studies (24). Further, COVID-19 is known to exhibit age-dependent severity, and contact rates are strongly age-dependent (27, 28), which could introduce heterogeneities that we did not incorporate into our simulations. However, because we ran our simulations over different values of  $R$  and varying the serial interval, we believe that our results should be robust to these limitations. In these sensitivity analyses,

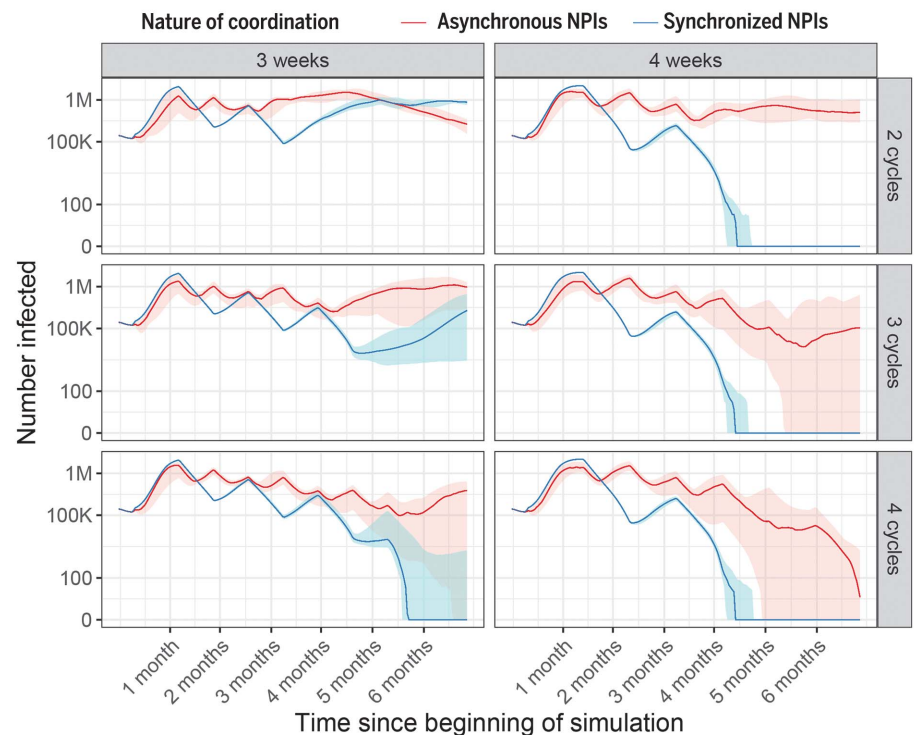


**Fig. 4. Cases over time, when NPIs are synchronized or unsynchronized across all European countries.** Rows vary the number of on-off cycles that occur, and columns indicate the number of on-off cycles implemented. For example, 4 weeks with two cycles (top right) indicates that we simulated two cycles of 4 weeks on lockdown, 4 weeks off lockdown for each country. Red: Cases when European countries do not synchronize NPI timing. Blue: Cases when European countries are all synchronized in NPI timing. Shaded areas indicate intervals within which 95% of the 200 simulations fell. K, thousand.

we found that the existence of key countries and the importance of coordinated NPIs were robust to these changes (see supplementary materials), although varying the serial interval could extend or shrink the second epidemic timings and epidemic peaks observed in Fig. 3. Additionally, we reduced mobility for each NUTS3 area uniformly, but long-distance movement reduced much more than short-distance movement owing to country-level travel restrictions and other NPIs (fig. S8). This likely provides a continental protective effect against early resurgence compared with our results, particularly if quarantining measures are put in place for long-distance travelers.

Our mobility estimates may also be biased owing to the populations included in the Google and Vodafone data. Google's consumer location history feature is only available for smartphone users, is turned off by default, and is viewed through the lens of differential privacy algorithms designed to protect user privacy and obscure fine detail. Vodafone's anonymized and aggregated data were based on network data from customers who had full control over their privacy settings, potentially introducing biases as well. This work takes a step toward using multiple datasets to capture population-level patterns that go beyond

any one service or system. Further, because both the Google and Vodafone data are aggregate datasets, we could not account for individual-level correlation in mobility patterns in our model (i.e., individuals who travel elsewhere but return home shortly thereafter). This likely means our model will overestimate spread and resurgence in general, as infectious people will end up less likely to return home.

Coordination will be key to an effective, equitable response to COVID-19. This means not just sharing resources but also ensuring that exit strategies account for neighboring countries and regions. Although coordinating exit strategies across an entire continent may prove politically difficult, the presence of key countries and community structure offer possible coordination groups that do not require engagement from all countries. We have explored some of these coordination groups in a community detection analysis in the supplementary materials (fig. S16). Further, coordinated exit strategies that account for real-time case data will likely improve outcomes compared with our predictions, as we simulated intermittent NPIs that were lifted regardless of actual transmission context. A multifaceted, reactive approach to lifting NPIs will be necessary to minimize resurgence risk. This means

that, beyond international cooperation, robust test-and-treat (29) and household quarantine (30) measures should be in place. Future work will further inform the role that mobility, NPIs, and international coordination can play in slowing COVID-19 resurgence, building on existing work (31) examining invasion, re-invasion, and disease extinction (32) in spatially structured populations. Critically, even if community transmission is reduced to very low levels within Europe (for example, through the intermittent NPIs shown in Fig. 4), importation from other regions of the globe mean coordination will be necessary to prevent continent-wide epidemics well into the future.

The implications of our study extend beyond Europe and COVID-19, broadly demonstrating the importance of communities coordinating the easing of various NPIs for any potential pandemic. In the United States, NPIs have been generally implemented at the state level, and because states will be strongly interconnected, our results emphasize national coordination of pandemic preparedness efforts moving forward. Elsewhere, relatively porous national borders between many lower and middle income countries mean that without coordination, these countries may have to deal with considerable international importation after controlling local transmission (33). COVID-19 transmission and the transmission of any infectious disease will ignore national and provincial borders; preventing resurgence and spread will mean ensuring that pockets of transmission do not persist in areas with limited interventions at the expense of later epidemics in others.

## REFERENCES AND NOTES

1. C. Sohrabi et al., *Int. J. Surg.* **76**, 71–76 (2020).
2. K. Prem et al., *Lancet Public Health* **5**, e261–e270 (2020).
3. S. Lai et al., *Nature* (2020).
4. M. U. G. Kraemer et al., *Science* **368**, 493–497 (2020).
5. T. Collbourn, *Lancet Public Health* **5**, e236–e237 (2020).
6. S. Lai et al., medRxiv 2020.02.04.20020479 [Preprint]. 9 March 2020. <https://doi.org/10.1101/2020.02.04.20020479>.
7. M. Chinazzi et al., *Science* **368**, 395–400 (2020).
8. M. McKee, *BMJ* **369**, m1556 (2020).
9. U. von der Leyen, C. Michel, "Joint European Roadmap towards lifting COVID-19 containment measures" (Communication, European Commission, Brussels, Belgium, 2020);

- [https://ec.europa.eu/info/sites/info/files/communication\\_-\\_a\\_european\\_roadmap\\_to\\_lifting\\_coronavirus\\_containment\\_measures\\_0.pdf](https://ec.europa.eu/info/sites/info/files/communication_-_a_european_roadmap_to_lifting_coronavirus_containment_measures_0.pdf).
10. A. Wesolowski, C. O. Buckee, K. Engø-Monsen, C. J. E. Metcalf, *J. Infect. Dis.* **214** (suppl. 4), S414–S420 (2016).
  11. N. W. Ruktanonchai et al., *PLOS Comput. Biol.* **12**, e1004846 (2016).
  12. D. K. Pindolia et al., *Malar. J.* **11**, 205 (2012).
  13. A. J. Tatem, D. L. Smith, *Proc. Natl. Acad. Sci. U.S.A.* **107**, 12222–12227 (2010).
  14. R. Wilson et al., *PLOS Curr.* **8**, 10.1371/currents.dis.d073fbce328e4c39087bc086d694b5c (2016).
  15. L. Queiroz et al., "Large-scale assessment of human mobility during COVID-19 outbreak," Open Science Framework Preprints (2020); <https://doi.org/10.31219/osf.io/nqxd>.
  16. Google LLC, "COVID-19 Community Mobility Reports"; [www.google.com/covid19/mobility](http://www.google.com/covid19/mobility).
  17. N. M. Kavanagh, R. R. Goel, A. S. Venkataramani, medRxiv 2020.04.06.20055632 [Preprint]. 11 April 2020. <https://doi.org/10.1101/2020.04.06.20055632>.
  18. A. L. Wright, K. Sonin, J. Driscoll, J. Wilson, "Poverty and Economic Dislocation Reduce Compliance with COVID-19 Shelter-in-Place Protocols" (University of Chicago, Becker Friedman Institute for Economics Working Paper No. 2020-40, 2020); <http://dx.doi.org/10.2139/ssrn.3573637>.
  19. P. C. Cross, J. O. Lloyd-Smith, P. L. F. Johnson, W. M. Getz, *Ecol. Lett.* **8**, 587–595 (2005).
  20. V. Colizza, A. Vespignani, *J. Theor. Biol.* **251**, 450–467 (2008).
  21. N. Ruktanonchai, wpgp/BEARmod: EU model code, Zenodo (2020); <https://doi.org/10.5281/zenodo.3932111>.
  22. R. Smith, in *Core EU Legislation* (Macmillan Education UK, 2015), pp. 183–186.
  23. Johns Hopkins University Center for Systems Science and Engineering, 2019 Novel Coronavirus COVID-19 (2019-nCoV) Data Repository by Johns Hopkins CSSE (2020); <https://github.com/CSSEGISandData/COVID-19>.
  24. C. I. Jarvis et al., "Impact of physical distance measures on transmission in the UK," Centre for Mathematical Modelling of Infectious Diseases Repository (2020); <https://cmimd.github.io/topics/covid19/comix-impact-of-physical-distance-measures-on-transmission-in-the-UK.html>.
  25. L. Tarrataca, C. M. Dias, D. B. Haddad, E. F. Arruda, arXiv:2004.06916 [q-bio.PE] (15 April 2020).
  26. M. Gollwitzer, C. Platzer, C. Zwarg, A. S. Göritz, PsyArXiv (14 April 2020); <https://doi.org/10.31234/osf.io/3a85z>.
  27. G. Onder, G. Rezza, S. Brusaferro, *JAMA* **323**, 1775–1776 (2020).
  28. F. Zhou et al., *Lancet* **395**, 1054–1062 (2020).
  29. Royal Society DELVE Initiative, "Test, Trace, Isolate" (27 May 2020); <https://rs-delve.github.io/reports/2020/05/27/test-trace-isolate.html>.
  30. A. Aleta et al., *Nat. Hum. Behav.* **10**, 1038/s41562-020-0931-9 (2020).
  31. C. Poletto, M. Tizzoni, V. Colizza, *J. Theor. Biol.* **338**, 41–58 (2013).
  32. G.-Q. Sun, Q.-X. Liu, Z. Jin, A. Chakraborty, B.-L. Li, *J. Theor. Biol.* **264**, 95–103 (2010).
  33. K. Wangdi, M. L. Gattton, G. C. Kelly, A. C. A. Clements, in *Advances in Parasitology*, Volume 89, D. Rollinson, J. R. Stothard, Eds. (Academic Press, 2015), pp. 79–107.
  34. European Commission, Eurostat, Statistics Explained, Glossary: Country codes; [https://ec.europa.eu/eurostat/statistics-explained/index.php/Glossary:Country\\_codes](https://ec.europa.eu/eurostat/statistics-explained/index.php/Glossary:Country_codes).

35. N. Ruktanonchai, Synthetic data based on IPUMS microcensus data for mobility between NUTS3 areas of Europe, Version 1, Zenodo (2020); <https://doi.org/10.5281/zenodo.3931987>.

## ACKNOWLEDGMENTS

We acknowledge E. Fawkes, J. Park, S. Woods, and the Data Gudes Group for insightful discussions on heterogeneously applied interventions. **Funding:** This study was supported by grants from the Vodafone Institute, the Bill & Melinda Gates Foundation (OPP1134076), and the European Union Horizon 2020 (MOOD 874850). A.J.T. is supported by funding from the Bill & Melinda Gates Foundation (INV-002697, OPP1106427, OPP1032350, OPP1134076, and OPP1094793), the Clinton Health Access Initiative, the U.K. Department for International Development (DFID), and the Wellcome Trust (106866/Z/15/Z and 204613/Z/16/Z). N.W.R. is supported by funding from the Bill & Melinda Gates Foundation (OPP1170969 and OPP1209812). O.P. is supported by the National Science Foundation (1816075). **Author contributions:** N.W.R., J.R.F., S.L., P.R.-L., and A.J.T. designed the research. N.W.R., J.R.F., S.L., C.W.R., P.R.-L., O.P., and A.C. built the model and ran simulations. N.W.R., J.R.F., S.L., C.W.R., A.Sa., P.R.-L., and A.C. carried out analyses. A.Sa., P.R.-L., X.B., A.C., J.E.S., A.Sc., A.O., and P.E. provided technical support. A.Sa., P.R.-L., X.B., A.Sc., A.O., and P.E. helped with data curation. A.Sa. and X.B. created the Google COVID-19 aggregated dataset. N.W.R., J.R.F., S.L., C.W.R., A.C., A.Sa., P.R.-L., J.G., O.P., and A.J.T. wrote and edited the manuscript. **Competing interests:** The authors declare no competing interests. **Data and materials availability:** Code for the model simulations is available at the following GitHub repository: <https://github.com/wpgp/BEARmod>. The specific version of the model used in this study, with simulation code, *R* estimates shown in fig. S2, and initial numbers infected shown in fig. S10 can be found in Zenodo (21). The population movement data obtained from Google and Vodafone for this study are not publicly available owing to stringent licensing agreements. The Google COVID-19 Aggregated Mobility Research Dataset used for this study is available with permission from Google LLC (contact: A.Sa., [sadilekadam@google.com](mailto:sadilekadam@google.com)). The Vodafone datasets can also be accessed with the permission of Vodafone through correspondence with the corresponding authors. A synthetic NUTS3-level dataset of mobility across Europe is also available in Zenodo (35). This work is licensed under a Creative Commons Attribution 4.0 International (CC BY 4.0) license, which permits unrestricted use, distribution, and reproduction in any medium, provided the original work is properly cited. To view a copy of this license, visit <https://creativecommons.org/licenses/by/4.0/>. This license does not apply to figures/photos/artwork or other content included in the article that is credited to a third party; obtain authorization from the rights holder before using such material.

## SUPPLEMENTARY MATERIALS

science.sciencemag.org/content/369/6510/1465/suppl/DC1  
Materials and Methods  
Supplementary Text  
Figs. S1 to S16  
Tables S1 and S2  
References (36–46)  
MDAR Reproducibility Checklist

[View/request a protocol for this paper from Bio-protocol.](#)

1 May 2020; accepted 13 July 2020  
Published online 17 July 2020  
10.1126/science.abc5096



## STRUCTURAL BIOLOGY

## 90S pre-ribosome transformation into the primordial 40S subunit

Jingdong Cheng<sup>1\*</sup>, Benjamin Lau<sup>2\*</sup>, Giuseppe La Venuta<sup>2</sup>, Michael Ameisemeier<sup>1</sup>, Otto Berninghausen<sup>1</sup>, Ed Hurt<sup>2†</sup>, Roland Beckmann<sup>1†</sup>

Production of small ribosomal subunits initially requires the formation of a 90S precursor followed by an enigmatic process of restructuring into the primordial pre-40S subunit. We elucidate this process by biochemical and cryo-electron microscopy analysis of intermediates along this pathway in yeast. First, the remodeling RNA helicase Dhr1 engages the 90S pre-ribosome, followed by Utp24 endonuclease-driven RNA cleavage at site A<sub>1</sub>, thereby separating the 5'-external transcribed spacer (ETS) from 18S ribosomal RNA. Next, the 5'-ETS and 90S assembly factors become dislodged, but this occurs sequentially, not en bloc. Eventually, the primordial pre-40S emerges, still retaining some 90S factors including Dhr1, now ready to unwind the final small nucleolar U3–18S RNA hybrid. Our data shed light on the elusive 90S to pre-40S transition and clarify the principles of assembly and remodeling of large ribonucleoproteins.

The formation of eukaryotic ribosomes requires transcription, processing, and modification of ribosomal RNA (rRNA) and the integration of ~80 ribosomal proteins. This highly complex process starts in the nucleolus with the transcription of a large rRNA precursor (35S in yeast, 47S in human), which contains the 18S rRNA of the 40S small subunit and the 5.8S and 25S rRNAs of the 60S large subunit, separated by the in-

ternal transcribed spacers ITS1 and ITS2 and flanked by the external transcribed spacers 5'-ETS and 3'-ETS. During transcription of the 35S pre-rRNA by RNA polymerase I, the earliest stable assembly intermediate, called the 90S pre-ribosome or small subunit processome, forms. This comprises more than 50 assembly factors, the U3 small nucleolar ribonucleoprotein (U3 snoRNP), the nascent pre-rRNA, and dozens of the small subunit

ribosomal proteins (1, 2). In the subsequent maturation steps, coordinated endonucleolytic cleavage at site A<sub>1</sub> within the 5'-ETS and at A<sub>2</sub> within the ITS1 is key to the separation of the 18S rRNA and 5.8S/25S rRNA (Fig. 1A), which then follow independent biogenesis pathways [reviewed in (3–5)]. The remaining 5'-ETS is degraded by RNA nucleases, including the nuclear exosome (6, 7).

Recently, several structures of the 90S pre-ribosome in stages prior to A<sub>1</sub> cleavage were solved by cryo-electron microscopy (cryo-EM) single-particle analysis from *Chaetomium thermophilum* and *Saccharomyces cerevisiae* (8–12). The four subdomains of the 18S rRNA (5', central, 3' major, and 3' minor) were found to fold independently and to associate with their set of early ribosomal proteins of the small subunit (S-proteins) cotranscriptionally, before integrating into the 90S pre-ribosome (13, 14). This integration happens in a reverse order, in which the 3' major and 3' minor domains incorporate first, followed by the central and 5' domain (15). Together with its

<sup>1</sup>Gene Center, Department of Biochemistry, University of Munich, 81377 Munich, Germany. <sup>2</sup>Biochemistry Center (BZH), University of Heidelberg, 69120 Heidelberg, Germany. \*These authors contributed equally to this work.

†Corresponding author. Email: beckmann@genezentrum.lmu.de (R.B.); ed.hurt@bzh.uni-heidelberg.de (E.H.)

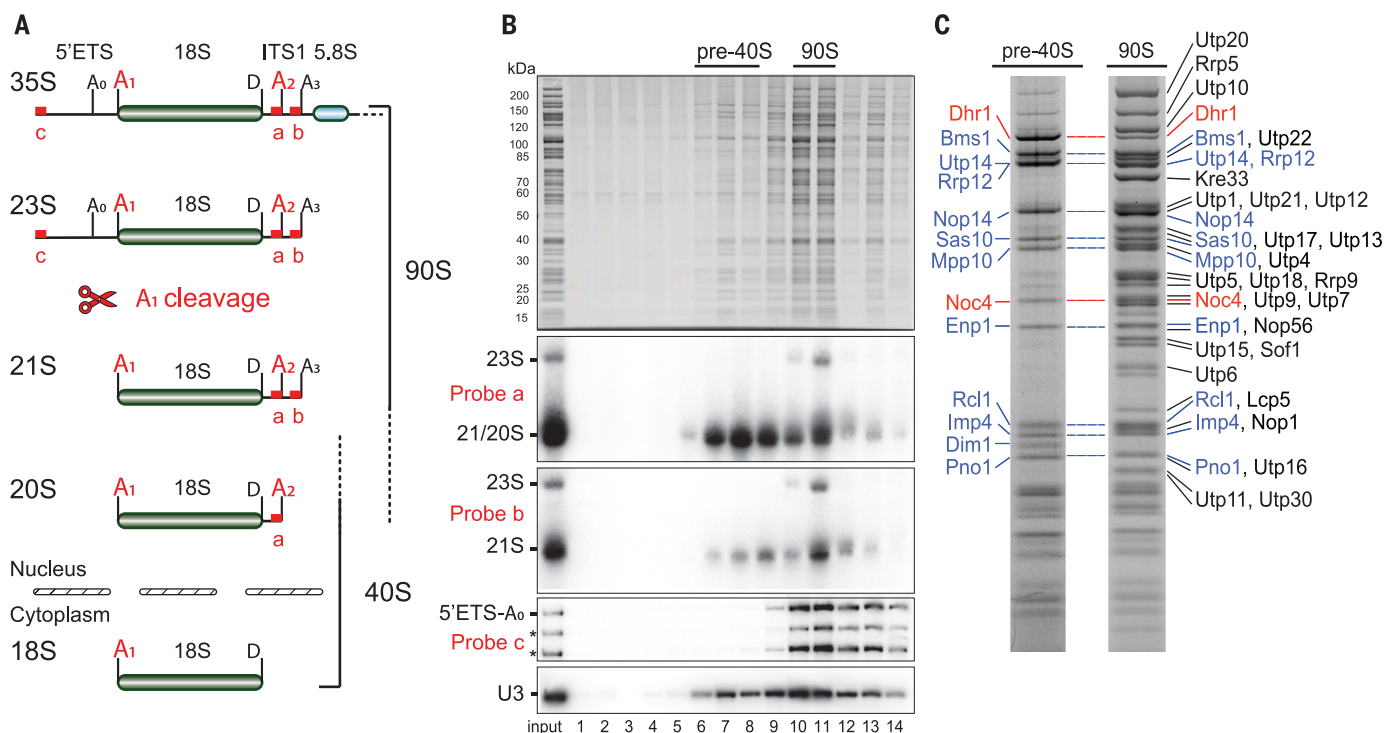


**Fig. 1. Pre-rRNA processing and purification of 90S to pre-40S transition intermediates.** (A) Sequence of rRNA processing events during 40S biogenesis in yeast with A<sub>0</sub>, A<sub>1</sub>, A<sub>2</sub>, A<sub>3</sub>, and D as cleavage sites on the pre-rRNA. (B) Analysis of split-tag (Noc4-TAP-Dhr1-Flag) affinity-purified assembly intermediates by sucrose gradient centrifugation, followed by SDS-polyacrylamide gel electrophoresis (PAGE) and

Coomassie staining or Northern blotting, using the RNA probes a, b, and c to detect the various indicated pre-rRNA forms (23S, 21S, 20S, 5'-ETS-A<sub>0</sub>). (C) SDS-PAGE of sucrose gradient fractions containing the pre-40S and 90S intermediates, with ribosome assembly factors identified by mass spectrometry indicated (bait proteins in red, factors shared by pre-40S and 90S in blue). See fig. S1B for the whole sucrose gradient.

numerous associated 90S assembly factors, which predominantly are organized in modules (e.g., UTP-A, UTP-B, UTP-C, U3 snoRNP, Mpp10 complex, Bms1-Rcl1 complex, Kre33 module, Noc4 module, Krr1-Faf1 complex), the 90S pre-ribosome is fully assembled and primed for subsequent A<sub>1</sub> cleavage (15–20).

After this cleavage, the 90S pre-ribosome is transformed into a primordial pre-40S intermediate (a process hereafter referred to as 90S transition) by a still-elusive mechanism; only later pre-40S intermediates have been described so far (21–30). The early 90S transition was initially uncovered by biochemical studies of Enp1, a ribosome assembly factor that is present in both early 90S and late pre-40S intermediates (21). However, many additional proteins have since been suggested to be intimately involved in this transition. Candidate factors include the methyltransferase Dim1 (31), the KH domain proteins Krr1 and Pno1 (previously called Dim2) (32), RNA helicase Dhr1 (33, 34), and the nuclear RNA exosome system (6). To decipher the mechanisms of this transition, we aimed at a structural analysis of 90S transition intermediates by cryo-EM.

### Isolation of ribosome assembly intermediates marking the 90S to pre-40S transition

Late 90S and early 40S pre-ribosomal intermediates were purified from *S. cerevisiae* using 90S assembly factors Noc4 and Dhr1 as baits in split-tag affinity purifications. Dhr1 was chosen because this RNA helicase regulates A<sub>1</sub> cleavage and eventually dissociates distinct heteroduplexes between U3 and pre-18S rRNA (35, 36). Subsequent separation of these preparations on a sucrose gradient yielded 90S and smaller unusual pre-40S intermediates, which contained not only classical pre-40S factors (e.g., Rrp12, Enp1, Dim1, Pno1) (21), but also Dhr1 and factors so far only assigned to 90S complexes (e.g., Bms1, Rcl1, Utp14, Sas10, Mpp10, and Imp4; Fig. 1, B and C, fig. S1, and data S1). After finding Dim1 enriched in this unusual pre-40S fraction (data S1; see also Fig. 1C), we used it together with Dhr1 in another split-tag affinity purification to enrich further intermediates of the 90S transition (fig. S1C).

Northern blotting of the Noc4-Dhr1 purification revealed that the 90S fraction contains the 5'-ETS-A<sub>0</sub> fragment, which is also typical for other 90S preparations [e.g., Enp1-FTpA,

Utp22-FTpA, or Pwp2-FTpA (8)]. It also contains 23S pre-rRNA (cleavage fragment 5' end-A<sub>3</sub>) and 21S pre-rRNA (A<sub>1</sub>-A<sub>3</sub> fragment), which together are indicative of both pre-A<sub>1</sub> and post-A<sub>1</sub> cleavage states. In contrast, the unusual pre-40S fraction exhibited the strong presence of 20S pre-rRNA (A<sub>1</sub>-A<sub>2</sub> fragment), which suggests that this intermediate completed both A<sub>1</sub> and A<sub>2</sub> processing. Both the 90S and 40S fractions contained the U3 snoRNA (Fig. 1, A and B).

### Cryo-EM structures revealing the 90S to pre-40S transition

After 3D classification, cryo-EM of the Noc4-Dhr1 and Dhr1-Dim1 samples revealed seven well-defined and distinct classes of pre-ribosomal particles, which were put in a temporal order covering the 90S transition (Fig. 2). Four of these states (called B2, Pre-A<sub>1</sub>, Post-A<sub>1</sub>, and Dis-C) were resolved at average resolution between 3.5 and 3.8 Å, allowing us to build and refine complete models. The other three states (A, Dis-A, and Dis-B) displayed average resolution between 4.4 and 7.1 Å, permitting rigid-body docking of molecular models (Fig. 2, figs. S2 to S6, and table S1).

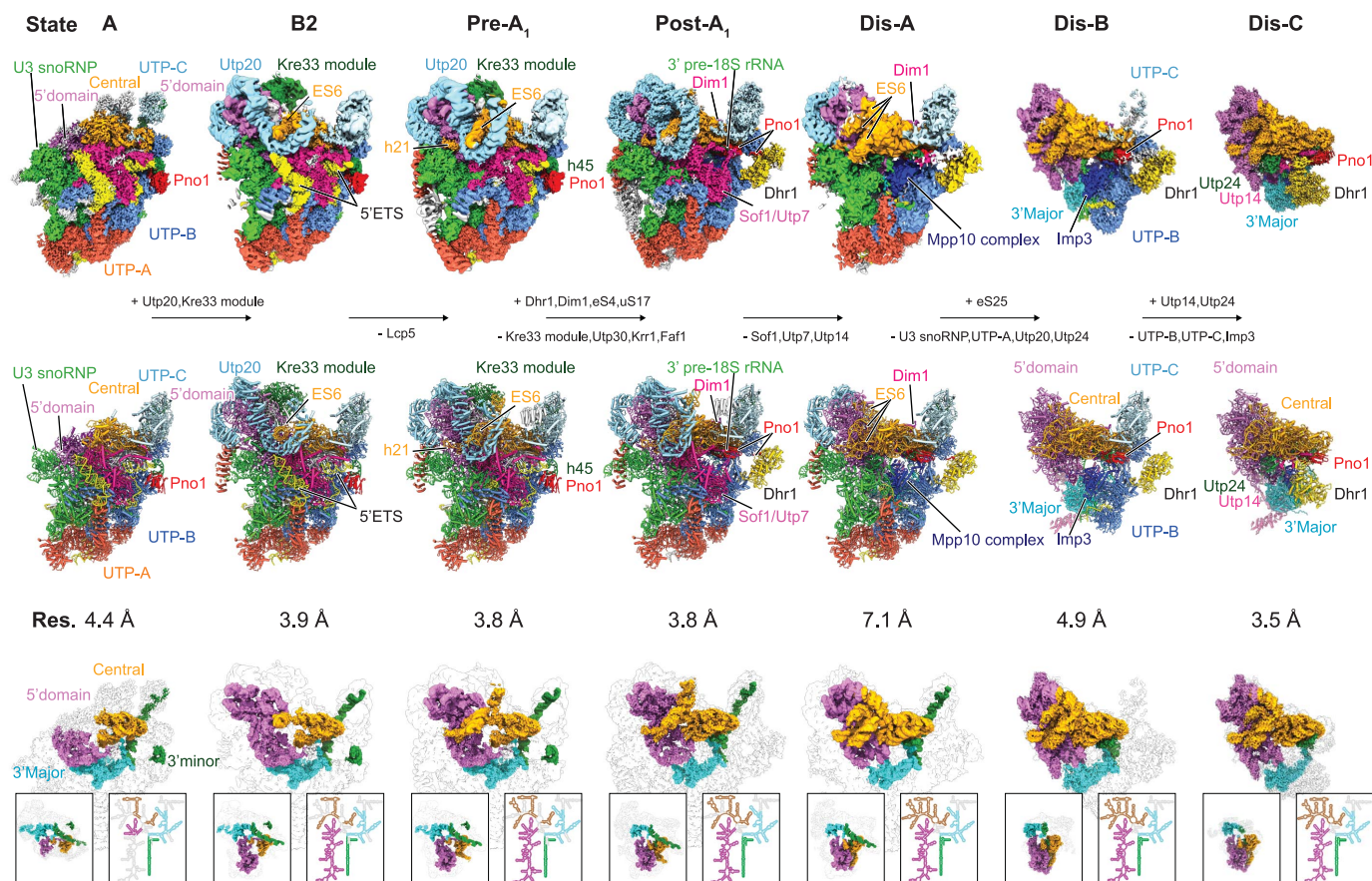


**Fig. 2. Cryo-EM analysis of 90S to pre-40S transition intermediates.** Cryo-EM maps (top) and molecular models (middle) of distinct states of yeast 90S to pre-40S transition observed after split-tag affinity purification using Noc4-Dhr1 (all states) and Dhr1-Dim1 (states B2, Post-A<sub>1</sub>, Dis-A, Dis-B, Dis-C) are shown. Assembly

factors and modules are labeled and compositional changes indicated. Bottom: Depiction of pre-18S rRNA density using 90S views with corresponding rRNA secondary structures; 40S views are shown in boxes (color code: magenta, 5' domain; orange, central domain; cyan, 3' major domain; green, 3' minor domain).



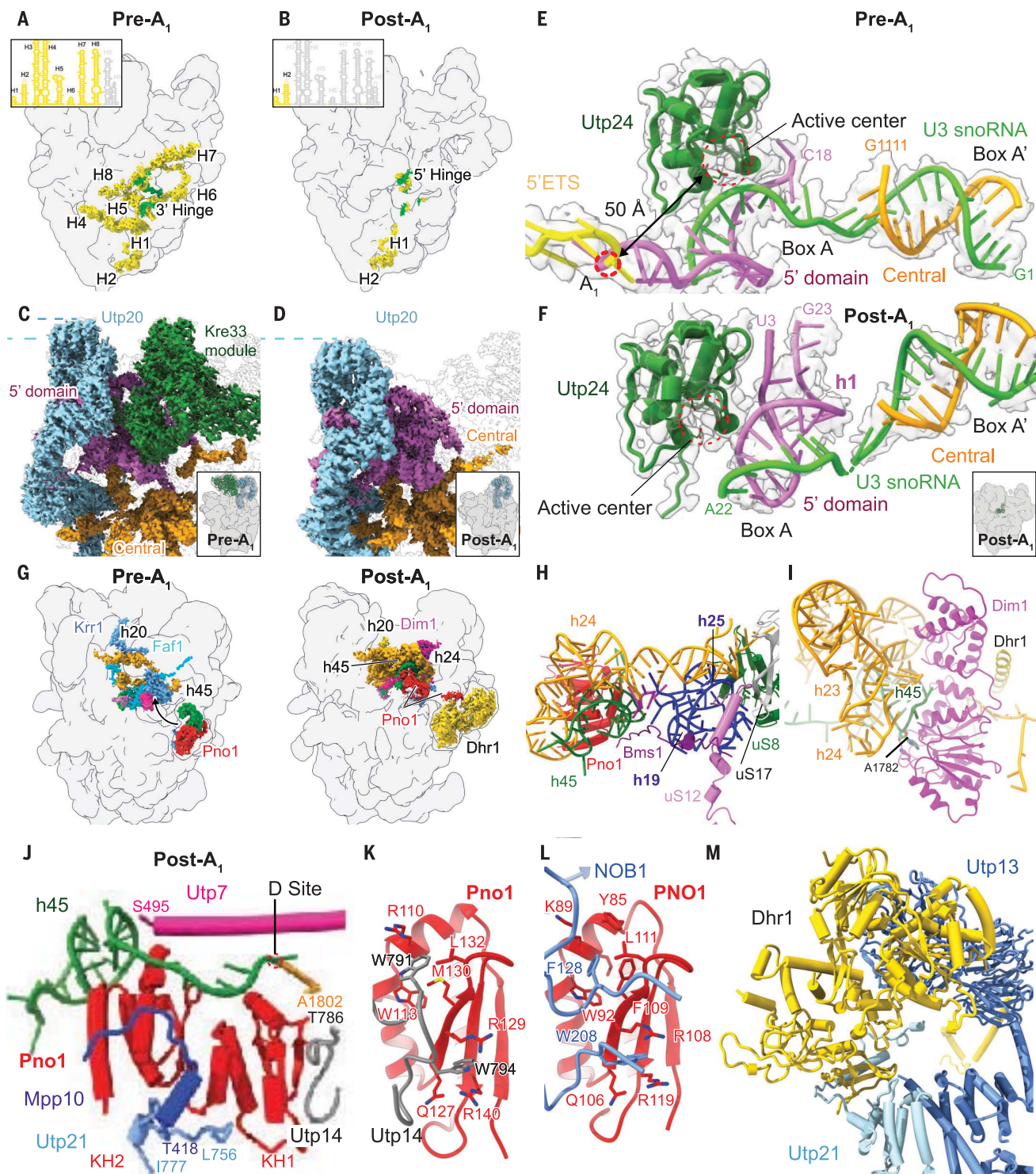


**Fig. 3. Conformational, positional, and compositional changes upon A1 cleavage.** (A and B) Dismantling of 5'-ETS RNA helices (yellow) from Pre-A<sub>1</sub> (A) and Post-A<sub>1</sub> (B) is shown with interacting U3 snoRNA (green) in transparent 90S density. The secondary structure of the 5'-ETS RNA is shown with observed helices in yellow and the dislodged helices in gray. (C and D) Volume representation of Utp20, the Kre33 module, and the 5' and central domains of the 18S pre-rRNA highlights the compaction from state Pre-A<sub>1</sub> (C) to Post-A<sub>1</sub> (D). Dashed lines indicate the movement of Utp20. (E and F) Model of the h1 region of the 18S pre-rRNA aligned at Utp24 shown before (E) and after (F) A<sub>1</sub> cleavage. The catalytic center of Utp24 and the A<sub>1</sub> cleavage site are indicated by dashed circles. (G) Differences in

the 18S central domain region are highlighted in states Pre-A<sub>1</sub> and Post-A<sub>1</sub>. (H) Ribbon representation of the platform region in state Post-A<sub>1</sub>. Nucleotides 1021 to 1025 of the 18S rRNA are shown in magenta. (I) Model of Dim1 bound to its substrate adenosine 1782 of the pre-18S in state Post-A<sub>1</sub>. (J) Model of Pno1 in state Post-A<sub>1</sub> with the 3' end of the 18S pre-rRNA and interacting segments of Mpp10, Utp7, Utp14, and Utp21. (K and L) Models of yeast and human Pno1 bound to Utp14 (K) and NOB1 (L, PDB ID 6G18), respectively, highlight overlapping interaction sites. Key residues are shown as sticks. (M) Ribbon representation showing the interaction of Dhr1 with Utp21 and Utp13 in state Post-A<sub>1</sub>. Amino acid abbreviations: F, Phe; I, Ile; K, Lys; L, Leu; M, Met; Q, Gln; R, Arg; S, Ser; T, Thr; W, Trp; Y, Tyr.

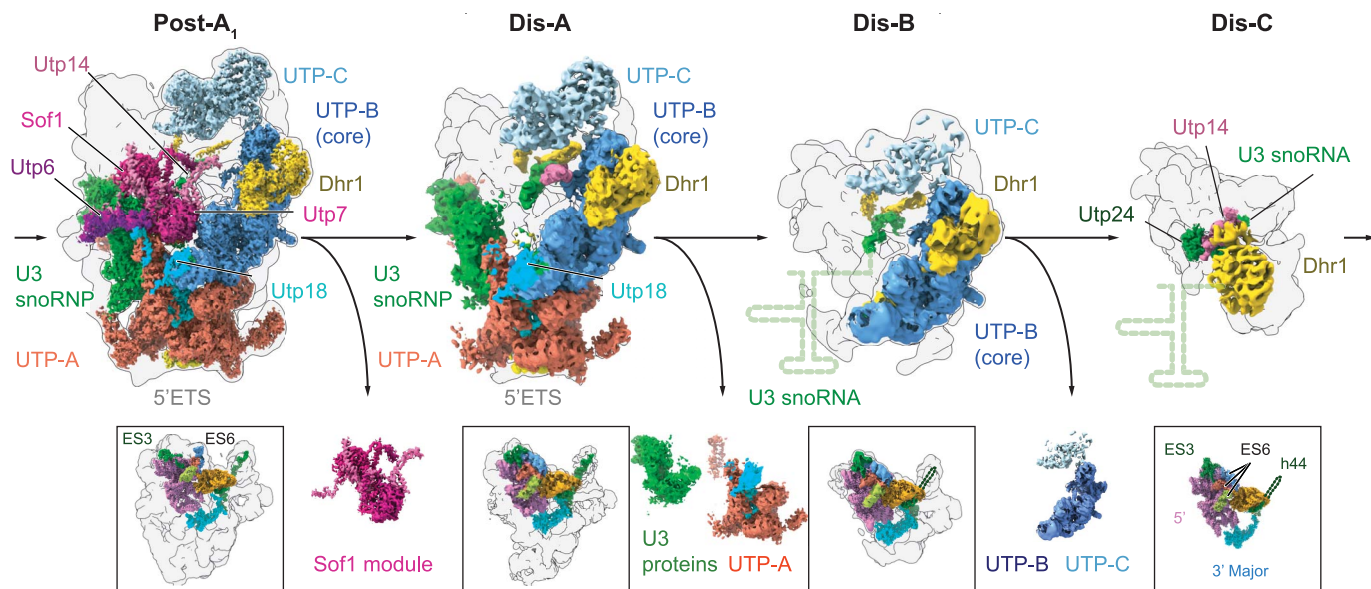


**Fig. 4. Successive shedding of factors during transition from 90S to primordial pre-40S.** EM densities reveal the shedding process of major 90S assembly factor modules during transition from state Post-A<sub>1</sub> to state Dis-C. Proteins, modules, and the U3 snoRNP are colored and labeled accordingly. The last remaining helices of the 5'-ETS (H1, H2) and Dhr1 are shown in yellow. A local resolution-filtered map of Dhr1 was used in state Dis-C. The color-coded 18S pre-rRNA and the dismantled modules are shown below.

The first two particles in this series, states A and B2, closely resemble previously described 90S assembly intermediates, with a noncleaved A<sub>1</sub> site as a characteristic feature (Fig. 2 and fig. S6) (8, 11, 12, 15). In the next state, Pre-A<sub>1</sub>, which is the last state preceding A<sub>1</sub> processing, we observed the integration of helix 21 (h21) of the pre-18S rRNA at its mature position (Fig. 2 and fig. S6). Subsequently and concomitant with cleavage at site A<sub>1</sub>, major structural changes lead to the Post-A<sub>1</sub> intermediate. Specifically, Pno1, together with h45 of the 18S rRNA, replaces the Krr1-Faf1 complex, bringing h45 from a peripheral to an integrated mature position. Furthermore, the remodeling helicase Dhr1 is observed for the first time in this post-A<sub>1</sub> state intermediate, positioned at the site vacated by Pno1 (Fig. 2 and fig. S6).

The succeeding group of intermediates comprises states Dis-A, Dis-B, and Dis-C (where Dis stands for dissociation), which represent the actual 90S to pre-40S transition intermediate states. Unexpectedly, the canonical pre-40S is not released as a whole entity after A<sub>1</sub> cleavage by leaving a presumed 5'-ETS particle behind. Instead, several prominent 90S assembly factor modules dissociate one after the other, leading to a progressive simplification of these complexes (Fig. 2 and fig. S6). The last state of this series, Dis-C, after ultimately losing the conspicuous UTP-B module, resembles a 40S shape for the first time, clearly displaying the 5', central (platform), and flexible and immature 3' major and 3' minor domains. Here, the characteristic h44 of the 3' minor domain, which in preceding states is held in a defined immature position by UTP-B and UTP-C, is mostly

delocalized. This is because the immature conformation is no longer stabilized by the 90S modules, and the mature position is still masked by the Bms1-Rcl1 complex (Fig. 2 and fig. S6).

#### Conformational changes and mechanism of A<sub>1</sub> cleavage

In contrast to the expected en bloc release of a 5'-ETS particle upon A<sub>1</sub> cleavage (5, 7, 8, 37), we observed that the 5'-ETS RNA becomes increasingly disordered during a stepwise 90S transition. Helix H9 at the 3' end of the 5'-ETS is the first to become detached from Utp20 (fig. S7, A to F). Next, after A<sub>1</sub> cleavage, other prominent 5'-ETS helices (H3 to H8) disappear, leaving behind empty cavities in this part of the 90S intermediate (Fig. 3A and fig. S7, A to C). Only the first two helices, H1 and H2, and two distinct internal 5'-ETS segments that form short heteroduplexes with the 3' hinge and 5' hinge of U3 snoRNA remain in position (Fig. 3B and figs. S4 and S7C). The cause for the increased structural freedom or partial degradation of the 5'-ETS is not clear. Notably, despite the dismantling of the 5'-ETS RNA, the overall shape and composition of this 90S intermediate remained largely unchanged at first.

Nonetheless, during this 90S transition, a clear structural compaction was observed. Initially, in state B2, the C terminus of Utp20 exhibits a superhelical HEAT repeat structure that wraps around the rRNA expansion segment ES6c (fig. S7D). Then, after transition to the Pre-A<sub>1</sub> state, the Utp20 superhelix adopts a more closed conformation (changing from a

"C" to an "O" shape), caused by the movement of the immature 5' domain toward the central domain. As a consequence, binding of Lcp5 and H9 to Utp20 is disrupted, allowing h21 (ES6d) to enter this previously occupied site (fig. S7, E and F). Similar to Utp20, the prominent Kre33 module also moves with the 5' domain during this transition; however, the Kre33 module finally dissociates when the intermediate reaches the Post-A<sub>1</sub> state (Fig. 3, C and D, and fig. S7, G to I). This brings the 5' domain even closer to the central domain (fig. S7H), and when state Post-A<sub>1</sub> is reached, the 5' and central domains eventually interact and adopt a mature-like conformation (Fig. 3D and fig. S7I).

This apparent domain compaction—together with the 5'-ETS RNA remodeling, which takes place during the first steps of 90S transition—results in a conformational state sufficiently dynamic to facilitate A<sub>1</sub> processing: The state Pre-A<sub>1</sub> shows the noncleaved A<sub>1</sub> site ~50 Å away from the catalytic center of the PIN domain endonuclease Utp24, which was suggested to carry out this cut (Fig. 3E) (38–41). The Post-A<sub>1</sub> state reveals the formation of a short RNA stem-loop (h1) at the 5' end of the mature 18S rRNA. The initial formation of this helix may have triggered endonucleolytic cleavage, because it results in repositioning the A<sub>1</sub> site close to the catalytic center of the Utp24 endonuclease (Fig. 3F). Consistent with this interpretation, at the base of the newly formed h1 we can retrace the RNA sequence until the third nucleotide (uridine 3) of the cleaved and mature 5' end of 18S rRNA. Such a sequence-independent but h1 stem-loop-dependent mechanism for



A<sub>1</sub> cleavage, requiring an arbitrary three-nucleotide spacer relative to the h1 base, has been predicted by genetic studies from the Tollervey lab (42). Unexpectedly, A<sub>1</sub> cleavage does not require unwinding of the Box A and Box A' heteroduplexes formed by pre-18S rRNA and U3 snoRNA, the latter two being retained in the Post-A<sub>1</sub> state (Fig. 3F). Together, the data show that A<sub>1</sub> cleavage is initiated by remodeling and relocation of the pre-18S rRNA substrate rather than by movement of the endonuclease Utp24 toward the A<sub>1</sub> cleavage site.

### A<sub>1</sub> cleavage coupled to Pno1 and 90S remodeling

A series of additional remodeling events can be observed when comparing the Pre-A<sub>1</sub> and Post-A<sub>1</sub> states, which includes the release of the Krr1-Faf1 complex and its replacement by the relocated Pno1 and h45 (Fig. 3, G and H, and fig. S8). With the translocation of Pno1 and the associated h45, the RNA platform region adopts a mature-like conformation, typically seen in both yeast and human later cytoplasmic pre-40S intermediates (26, 28, 29). This results in the formation of rRNA helices h19 and h25 (Fig. 3H), and, as a consequence,

a new interface is formed and stabilized by the newly recruited methyltransferase Dim1 (Fig. 3I, fig. S9, and supplementary text), thereby rendering these rearrangements irreversible.

The binding mode of Pno1 to h45 differs between the Pre-A<sub>1</sub> and Post-A<sub>1</sub> states (Fig. 3J and fig. S8B). Relocation of h45 relative to Pno1 is stabilized by the long C-terminal  $\alpha$  helix of Utp7, which previously was bound to H7 of the 5'-ETS before its dismantling (Fig. 3J and fig. S8C). The interaction of Utp14 with Pno1 prevents premature recruitment of the endonuclease Nob1, which later catalyzes the last processing step of the pre-18S rRNA at site D (Fig. 3, K and L) (28). Finally, by relocating to the central platform, Pno1 and its clamped h45 dissociate from Utp21 and Utp13 of the UTP-B module (fig. S8B), allowing for the first time the recruitment of the RNA helicase Dhr1 to the 90S via a two-site contact to Utp21 and Utp13 (see below and Fig. 3M).

### Successive factor shedding during 90S transition to primordial pre-40S

Following the formation of state Post-A<sub>1</sub>, the dismantled 5'-ETS allows for a cascade of structural and compositional changes that re-

sult in a stepwise reduction of the 90S complex (Fig. 4). First, the Sof1 module (Utp7, Utp14, and Sof1) is released together with Utp6 from its binding site close to the former helix H9 at the 3' region of the 5'-ETS, resulting in the state Dis-A. Then, in the second step, the UTP-A complex dissociates together with Utp18 and all protein components of the U3 snoRNP, leading to state Dis-B. In the last transition step from Dis-B to Dis-C, the core of the UTP-B complex and the remains of UTP-C are released. Also, the 5'-ETS, which served as RNA scaffold for all binding modules (UTP-A, UTP-B, UTP-C, and Imp3), is no longer detectable in this final intermediate. Of the U3 snoRNP, only a short segment of its RNA remains localized in states Dis-B and Dis-C, in particular the heteroduplexes with 18S rRNA; the rest becomes detached from these intermediates (Figs. 1B and 4). Interestingly, the domains of the pre-40S undergo rather limited maturation rearrangements during this shedding phase. Only rRNA expansion segments ES3a, ES3b, and ES6a to ES6d on the solvent side of the subunit adopt mature conformations, whereas the rest of the domains remain essentially unchanged (see boxes in Fig. 4 and fig. S10A).

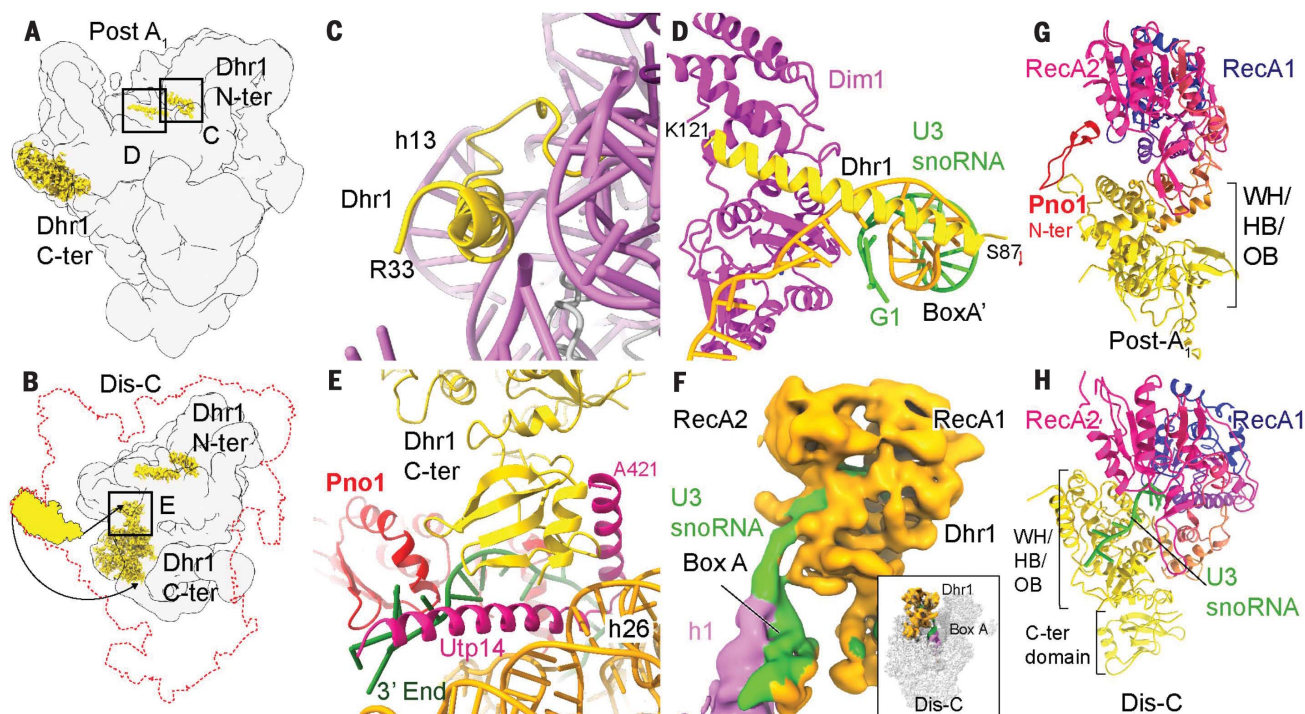


**Fig. 5. Differential interaction of Dhr1 during 90S transition.** (A and B) Locations of N and C termini (N-ter and C-ter) of Dhr1 in states Post-A<sub>1</sub> (A) and Dis-C (B). (C and D) Ribbon representation of the N-terminal helices of Dhr1. The first helix (yellow) binds to the h13 region of the 5' domain (C), and the second one interacts with Box A' duplex and Dim1 in all states after Pre-A<sub>1</sub> (D). (E) Model of the C-terminal domain of Dhr1 binding to the interface

formed by Utp14, Pno1, h26, and the 3' end of the 18S rRNA in state Dis-C.

(F) Density revealing that near the Box A duplex, U3 snoRNA directly connects to Dhr1. Dhr1 density is shown in orange; U3 snoRNA density is shown in green. (G and H) Model of Dhr1 in states Post-A<sub>1</sub> (G) and Dis-C (H), showing two different conformations. Dhr1 is colored from blue to red and yellow. Pno1 and the U3 snoRNA are highlighted in red and green, respectively.

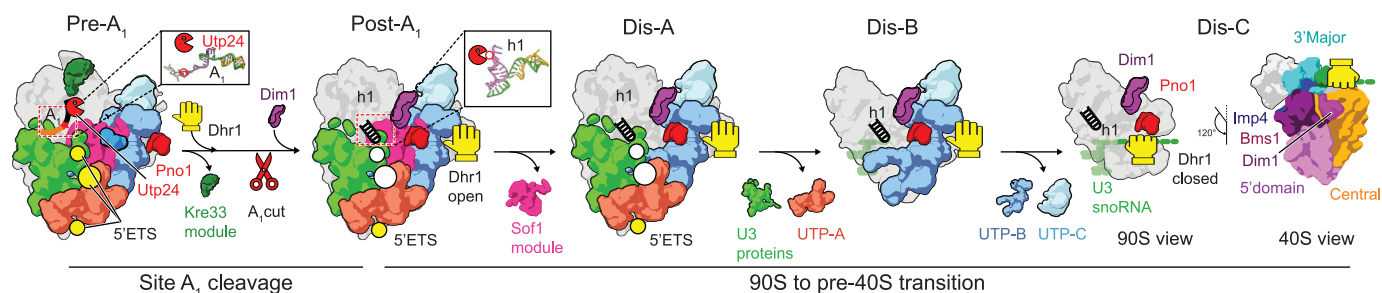


**Fig. 6. Scheme of the 90S to pre-40S transition upon A<sub>1</sub> cleavage.** Cartoons depict the shedding-like transition from a 90S to a primordial pre-40S ribosome. Assembly factor modules and selected proteins are colored and labeled accordingly. The helicase Dhr1 is shown as a grabbing hand, representing the open and closed conformations.

Although this successive shedding of large protein modules is the distinct hallmark of the 90S transition, several structural changes occur in addition. First, Dhr1 moves from its previous UTP-B binding site (Fig. 3M) toward Box A in state Dis-C, thereby bringing the helicase into an ideal position to dismantle the last remaining U3::18S rRNA hybrid on the intermediate (fig. S10, B and C). Concomitantly, the Utp24 endonuclease becomes detectable again in this state, where it occupies the binding site for the uS5 ribosomal protein. Moreover, Utp14, previously bound to Utp6 and helix H9 of the 5'ETS, relocates to a new position in state Dis-C, where it binds Pno1 and Dhr1 via four  $\alpha$  helices (fig. S10, D to F). Notably, two arginine residues of Utp14 inhibit the endonuclease activity of Utp24 by coordinating active-site residues, thus allowing Utp24 to serve as an endonuclease-inactive placeholder (fig. S10, G to I).

### Sequential Dhr1 helicase function during the 90S to pre-40S transition

Finally, the Dis-C intermediate sheds light on the diverse functioning of the Dhr1 helicase during the 90S transition by showing how it is primed to remove the U3 snoRNA from its last contact point to the 18S rRNA, Box A. From state Post-A<sub>1</sub> to state Dis-C, Dhr1 is tethered to the assembly intermediates via two invariant N-terminal helices: one that interacts with rRNA helix h13 at a site that is later occupied by Tsr1 (Fig. 5, A to C, and fig. S11, A and B) (26, 28, 29), and another that binds to the methyltransferase Dim1 (Fig. 5D and fig. S9B). The catalytic C-terminal domain, however, binds distantly from its N-terminal anchor region (Fig. 5, A and B, and fig. S11A). From state Post-A<sub>1</sub> to state Dis-B, this globular part is bound to Utp13 and Utp21, which is mediated by a  $\beta$  barrel-like domain of Dhr1 (fig. S11C). In state Dis-C, however, after dissociation of Utp21, Dhr1 relocates to the Box A and h1 region, close to its U3 snoRNA substrate. Here, its  $\beta$  barrel-like domain is bound to the interface formed by Utp14, Pno1, and the 3' region of the pre-18S rRNA (Fig. 5, E and F). The observed inter-

play between Utp14 and Dhr1 highlights the importance of Utp14 for the recruitment and relocation of Dhr1 during the 90S transition (36, 43–45).

In our ensemble of 90S transition structures, Dhr1 was observed in two distinct conformations. First, between states Post-A<sub>1</sub> and Dis-B, Dhr1 was in a conformation with an open RNA binding tunnel. Here, the N terminus of Pno1 prevents substrate binding and closing of the catalytic domain (Fig. 5G). This suggests that Dhr1 is bound to the 90S pre-ribosome in an adenosine diphosphate-bound, open conformation after A<sub>1</sub> cleavage (fig. S11D). After the transition to state Dis-C and relocation of Dhr1 toward the Box A duplex, however, the helicase domain engages a segment of the U3 snoRNA as substrate (Fig. 5F). Furthermore, Dhr1 appears now in a closed conformation, resembling the adenosine triphosphate (ATP)-free form of previously reported RNA-bound DHX37, the human homolog of Dhr1 (Fig. 5H and fig. S11E) (18). We conclude from these data that after the transition from state Dis-B to state Dis-C, Dhr1 is in a closed apo-state, awaiting ATP binding, and through successive cycles of ATP hydrolysis could exert its pulling force to completely expel the U3 snoRNA from this primordial pre-40S intermediate.

### Discussion

Our work shows how the huge 90S pre-ribosome transforms into its next major biogenesis intermediate, the primordial pre-40S, by large structural rearrangements, including the successive shedding of assembly factor modules. Several findings support the notion that the observed transition states Dis-A to Dis-C are of physiological relevance and are not merely the products of random disintegration. First, successive maturation of rRNA expansion segments occurs between the states: In the post-A<sub>1</sub> state, the expansion segments ES3a, ES3b, ES6a, ES6b, ES6c, and ES6d are still in an immature conformation (even with immature base pairing in ES6). In the Dis-A state, ES3b and ES6 adopt their mature conformation, even including the kissing loop formed between ES3b and ES6a.

When further progressing to Dis-B and Dis-C, ES3a was also observed to adopt the mature conformation. Second, from Dis-A to Dis-B, the 90S pre-ribosome incorporated ribosomal protein in its mature position. Third, in all the states until Dis-B, Dhr1 was present in an inactive conformation. Only after reaching the Dis-C state and UTP-B dissociation was Dhr1 captured in an active state, interacting with the U3 snoRNA. Fourth, Utp14 had already engaged in the pre-A<sub>1</sub> stage but was also present in the Dis-C state, yet adopted different and highly defined positions. Taken together, all these findings are difficult to reconcile with the notion of randomly disintegrating particles.

Our structures may also provide insight into the coordination of pre-rRNA processing at sites A<sub>1</sub> and A<sub>2</sub>, which is assumed to be performed by the same Utp24 endonuclease (38–40). After site A<sub>1</sub> cleavage, Utp24 is dislodged in state Dis-B while still tethered to the pre-ribosome. During this phase, Utp24 could access the second cleavage site A<sub>2</sub> in the flexible ITS1 to finally generate the 20S pre-rRNA, the predominant species in Dis-C.

Our findings do not support the current view of a sudden release of a 5'-ETS particle and its associated principal modules UTP-A, UTP-B, and U3 snoRNP during the 90S to pre-40S transition. It was previously shown that 5'-ETS particles can, in principle, exist on their own—for example, by inhibiting the exosome in combination with a Utp18 mutation (8) or during arrest of 90S assembly using 3'-truncated pre-rRNA (13, 14, 37). Here we show, however, that contrary to the implications of earlier research, the 5'-ETS and its associated principal modules are not released simultaneously upon A<sub>1</sub> cleavage, but rather in a sequential and stepwise shedding process. This mechanism for the 90S transition appears to be the more plausible, because it is difficult to imagine how segregation of an entire 5'-ETS particle can be induced by a single A<sub>1</sub> cut, in light of the highly interconnected nature of the 90S structure.

The initial trigger for the 90S to pre-40S transition is still unknown. We suggest that the decisive step in dismantling the 90S



intermediate depends on an advanced state of the pre-40S domain maturation as reflected by the degree of its compaction. Sufficient compaction may trigger the gradual deconstruction of the 5'-ETS scaffold, as previously observed in several states preceding A<sub>1</sub> cleavage (15). This assumption is in agreement with the earlier observation that A<sub>1</sub> cleavage is dependent on the presence of the helicase Mtr4 as a potential 5'-ETS remodeler (12). Successive dislocation of the RNA helices starting at the 3' region of the 5'-ETS then could allow for the relocation of Pno1 and h45 and, concomitantly, the recruitment and engagement of the helicase Dhr1. Dhr1 in turn may facilitate the partial formation of rRNA helix h1, which results in the cleavage at the A<sub>1</sub> site. This coincides with the dissociation of several factors and further destabilization of the 90S intermediate by 5'-ETS dismantling, eventually causing the sequential release of modules until the primordial pre-40S has emerged (Fig. 6).

Defects in ribosome biogenesis can have drastic consequences for human health as ribosomopathies (46). Therefore, gaining more mechanistic insights into this elaborate maturation process and its integration into cellular signaling pathways is desirable.

## REFERENCES AND NOTES

1. F. Dragon *et al.*, *Nature* **417**, 967–970 (2002).
2. P. Grandi *et al.*, *Mol. Cell* **10**, 105–115 (2002).
3. J. L. Woolford Jr., S. J. Baserga, *Genetics* **195**, 643–681 (2013).
4. J. Baßler, E. Hurt, *Annu. Rev. Biochem.* **88**, 281–306 (2019).
5. S. Klinge, J. L. Woolford Jr., *Nat. Rev. Mol. Cell Biol.* **20**, 116–131 (2019).
6. J. de la Cruz, D. Kressler, D. Tollervy, P. Linder, *EMBO J.* **17**, 1128–1140 (1998).
7. M. Thoms *et al.*, *Cell* **162**, 1029–1038 (2015).
8. M. Kornprobst *et al.*, *Cell* **166**, 380–393 (2016).
9. J. Barandun *et al.*, *Nat. Struct. Mol. Biol.* **24**, 944–953 (2017).
10. M. Chaker-Margot, J. Barandun, M. Hunziker, S. Klinge, *Science* **355**, eaal1880 (2017).
11. J. Cheng, N. Kellner, O. Berninghausen, E. Hurt, R. Beckmann, *Nat. Struct. Mol. Biol.* **24**, 954–964 (2017).
12. Q. Sun *et al.*, *eLife* **6**, e22086 (2017).
13. M. Chaker-Margot, M. Hunziker, J. Barandun, B. D. Dill, S. Klinge, *Nat. Struct. Mol. Biol.* **22**, 920–923 (2015).
14. L. Zhang, C. Wu, G. Cai, S. Chen, K. Ye, *Genes Dev.* **30**, 718–732 (2016).
15. J. Cheng *et al.*, *Mol. Cell* **75**, 1256–1269.e7 (2019).
16. T. Wegierski, E. Billy, F. Nasr, W. Filipowicz, *RNA* **7**, 1254–1267 (2001).
17. S. Granneman *et al.*, *Nucleic Acids Res.* **31**, 1877–1887 (2003).
18. N. J. Krogan *et al.*, *Mol. Cell* **13**, 225–239 (2004).
19. J. Pérez-Fernández, A. Román, J. De Las Rivas, X. R. Bustelo, M. Dosić, *Mol. Cell. Biol.* **27**, 5414–5429 (2007).
20. J. Pérez-Fernández, P. Martín-Marcos, M. Dosić, *Nucleic Acids Res.* **39**, 8105–8121 (2011).
21. T. Schäfer, D. Strauss, E. Petfalski, D. Tollervy, E. Hurt, *EMBO J.* **22**, 1370–1380 (2003).
22. T. Schäfer *et al.*, *Nature* **441**, 651–655 (2006).
23. B. S. Strunk *et al.*, *Science* **333**, 1449–1453 (2011).
24. E. Wyler *et al.*, *RNA* **17**, 189–200 (2011).
25. N. Larburu *et al.*, *Nucleic Acids Res.* **44**, 8465–8478 (2016).
26. A. Heuer *et al.*, *eLife* **6**, e30189 (2017).
27. M. C. Johnson, H. Ghalei, K. A. Dextader, K. Karbstein, M. E. Stroupe, *Structure* **25**, 329–340 (2017).
28. M. Ameisemeier, J. Cheng, O. Berninghausen, R. Beckmann, *Nature* **558**, 249–253 (2018).
29. A. Scaiola *et al.*, *EMBO J.* **37**, e98499 (2018).
30. V. Mitterer *et al.*, *Nat. Commun.* **10**, 2754 (2019).
31. D. Lafontaine, J. Vandenhaute, D. Tollervy, *Genes Dev.* **9**, 2470–2481 (1995).
32. M. Sturm, J. Cheng, J. Baßler, R. Beckmann, E. Hurt, *Nat. Commun.* **8**, 2213 (2017).
33. A. Colley, J. D. Beggs, D. Tollervy, D. L. Lafontaine, *Mol. Cell. Biol.* **20**, 7238–7246 (2000).
34. R. Sardana, J. Zhu, M. Gill, A. W. Johnson, *Mol. Cell. Biol.* **34**, 2208–2220 (2014).
35. R. Sardana *et al.*, *PLOS Biol.* **13**, e1002083 (2015).
36. J. Zhu, X. Liu, M. Anjos, C. C. Correll, A. W. Johnson, *Mol. Cell. Biol.* **36**, 965–978 (2016).
37. M. Hunziker *et al.*, *eLife* **8**, e45185 (2019).
38. F. Bleichert, S. Granneman, Y. N. Osheim, A. L. Beyer, S. J. Baserga, *Proc. Natl. Acad. Sci. U.S.A.* **103**, 9464–9469 (2006).
39. R. Tomecki, A. Labno, K. Drazkowska, D. Cysewski, A. Dziembowski, *RNA Biol.* **12**, 1010–1029 (2015).
40. G. R. Wells *et al.*, *Nucleic Acids Res.* **44**, 5399–5409 (2016).
41. W. An, Y. Du, K. Ye, *PLOS ONE* **13**, e0195723 (2018).
42. K. Sharma, D. Tollervy, *Mol. Cell. Biol.* **19**, 6012–6019 (1999).
43. J. J. Black, Z. Wang, L. M. Goering, A. W. Johnson, *RNA* **24**, 1214–1228 (2018).
44. F. M. Boneberg *et al.*, *RNA* **25**, 685–701 (2019).
45. A. Roychowdhury *et al.*, *Nucleic Acids Res.* **47**, 7548–7563 (2019).
46. A. Narla, B. L. Ebert, *Blood* **115**, 3196–3205 (2010).

## ACKNOWLEDGMENTS

We thank H. Sieber, C. Ungewickell, and S. Rieder for technical support. **Funding:** Supported by DFG grant HU363/12-1 and ERC grant ADG 741781 GLOWSOME (E.H.) and by DFG grant BE 1814/15-1 (R.B.). **Author contributions:** J.C., B.L., G.L.V., E.H., and R.B. designed the study; B.L. prepared and characterized the Noc4-Dhr1 and Dhr1-Dim1 samples for cryo-EM; G.L.V. performed the Northern blot analysis; O.B. performed the cryo-EM data collection; J.C. processed the cryo-EM data and built and refined the models; J.C. and R.B. analyzed and interpreted the structures; J.C., B.L., R.B., and E.H. wrote the manuscript; M.A. contributed to manuscript writing and figure making; and all authors commented on the manuscript. **Competing interests:** The authors declare no competing interests. **Data and materials availability:** All cryo-EM maps and molecular models have been deposited in the Electron Microscopy Data Bank with accession IDs EMD-11357 (state A), EMD-11358 (state B2), EMD-11359 (state pre-A<sub>1</sub>), EMD-11360 (state post-A<sub>1</sub>), EMD-11361 (state Dis-A), EMD-11362 (state Dis-B), and EMD-11363 (state Dis-C) and in the Protein Data Bank (PDB) with accession codes 6ZQA (state A), 6ZQB (state B2), 6ZQC (state pre-A<sub>1</sub>), 6ZQD (state post-A<sub>1</sub>), 6ZQE (state Dis-A), 6ZQF (state Dis-B), and 6ZQG (state Dis-C). All other data are in the main text or supplementary materials. Materials are available upon request.

## SUPPLEMENTARY MATERIALS

science.sciencemag.org/content/369/6510/1470/suppl/DC1  
Materials and Methods  
Supplementary Text  
Figs. S1 to S11  
Table S1  
References (47–66)  
Data S1  
Movie S1  
MDAR Reproducibility Checklist

[View/request a protocol for this paper from Bio-protocol.](#)

21 February 2020; accepted 10 July 2020  
10.1126/science.abb4119

## REPORT

## STRUCTURAL BIOLOGY

## Cryo-EM structure of 90S small ribosomal subunit precursors in transition states

Yifei Du<sup>1\*</sup>, Weidong An<sup>1\*</sup>, Xing Zhu<sup>1</sup>, Qi Sun<sup>1,2</sup>, Jia Qi<sup>1,2,3</sup>, Keqiong Ye<sup>1,4†</sup>

The 90S preribosome is a large, early assembly intermediate of small ribosomal subunits that undergoes structural changes to give a pre-40S ribosome. Here, we gained insight into this transition by determining cryo-electron microscopy structures of *Saccharomyces cerevisiae* intermediates in the path from the 90S to the pre-40S. The full transition is blocked by deletion of RNA helicase Dhr1. A series of structural snapshots revealed that the excised 5' external transcribed spacer (5' ETS) is degraded within 90S, driving stepwise disassembly of assembly factors and ribosome maturation. The nuclear exosome, an RNA degradation machine, docks on the 90S through helicase Mtr4 and is primed to digest the 3' end of the 5' ETS. The structures resolved between 3.2- and 8.6-angstrom resolution reveal key intermediates and the critical role of 5' ETS degradation in 90S progression.

**R**ibosomes, large RNA-protein complexes composed of a 40S small subunit (SSU) and a 60S large subunit, are responsible for protein synthesis. Assembly of eukaryotic ribosomes is a complicated and dynamic process that involves many preribosomal assembly intermediates (1–3). More than 200 trans-acting assembly factors (AFs) and many small nucleolar RNAs (snoRNAs) function in modification and processing of ribosomal RNA (rRNA) and assembly of ribosomal proteins (RPs).

The SSU is composed of an 18S rRNA and 33 RPs in the yeast *Saccharomyces cerevisiae*. The 90S preribosome (the SSU processome) is the earliest assembly intermediate of the SSU (4, 5) and forms cotranscriptionally on the 5' region of a nascent pre-rRNA transcript containing the 5' external transcribed spacer (5' ETS), the 18S rRNA sequence, and the internal transcribed spacer 1 (ITS1) (6–8). The 5' ETS initiates the assembly of 90S by recruiting a large number of AFs, including the large UTPA, UTPB, and U3 snoRNP complexes. After the assembly of 18S rRNA and release of labile factors, the 90S is compacted into a large structure comprising pre-rRNA, U3 snoRNA, ~50 AFs, and ~20 RPs. After the A0 and A1 sites of the 5' ETS and the A2 site of ITS1 are sequentially cleaved, the 90S is converted into a pre-40S particle that is rapidly exported to the cytoplasm for final maturation (Fig. 1A).

Several cryo-electron microscopy (cryo-EM) structures have been determined for the 90S of *S. cerevisiae* and *Chaetomium thermophilum* before A1 site cleavage (9–15). In the 90S structure, the 5', central, 3' major, and 3' minor domains of 18S rRNA are partially assembled and not yet packed. By contrast, the pre-40S that contains a 20S pre-rRNA without the 5' ETS, 31 RPs, and a few AFs has established the global architecture of mature SSUs (16–18). No intermediate states between 90S and pre-40S have been structurally analyzed, so how the transition occurs is not known. The cleaved 5' ETS fragment was proposed to be released together with associated factors during the transition (9). By cryo-EM analysis of 90S transition states, we show that the 5' ETS is degraded within the 90S, which further triggers AF release and maturation of the ribosome.

Several RNA helicases are required for ribosome assembly, potentially driving key structural reorganization of preribosomes (19). To stall the assembly of the SSU, we depleted the essential RNA helicase Dhr1, which acts after A0 cleavage (20, 21), and purified the SSU preribosomes from *S. cerevisiae* by Enp1, which is present in both 90S and pre-40S ribosomes (22) and should capture all transition states. Three states were previously determined at 8- to 9-Å resolution by cryo-EM. State 1, representing a fully assembled 90S, was described previously (13). To improve the structures, 18,028 images were collected in a Titan Krios 300-kV electron microscope with a K2 Summit camera (fig. S1, A and B, and table S1). Three-dimensional (3D) classification of 382,298 particles yielded seven distinct states, designated as A to E, A1, and C1 (Fig. 1B and fig. S1C). Local density was further improved with focused classification and refinement (fig. S1D). States A and D were reconstructed at 3.2- and 3.8-Å resolution, respectively, and the other

states were determined to 4- to 8.6-Å resolution (figs. S2 to S4 and data S1).

In all of these structures, the A1 site of pre-rRNA is intact and the A0 site is not visible. The A0 site should have been mostly processed in Dhr1-depleted 90S (13). States A to E can be ordered chronologically because structural changes occurring in one state are preserved in its following states, and the 5' ETS density is increasingly reduced in these states. State A1 is similar to state A but adopts an open conformation at the central domain, as shown in the 90S from starved yeast cells and state a/b of *C. thermophilum* 90S (10, 14). State C1 completely lacks the central domain and its surrounding structures and is likely a degradation product of state C.

State A resembles the previously described state 1 and represents a fully assembled 90S (13). The 5' ETS and its associated factors constitute the bulk of the structural core. The 5' and central domains of 18S rRNA with bound RPs and AFs form two bulky projections on the top, and the 3' major domain is bound at the center of the structural core (Fig. 1B and fig. S4).

The 5' ETS RNA folds into 10 helices (H1 to H10) and forms two intermolecular helices (Ha and Hb) with U3 snoRNA. The density of the 5' ETS is gradually and unevenly reduced in states B to E (Figs. 2, A to F, and 3A). The 5' ETS should be degraded, rather than adopting a relaxed conformation, because its level was greatly reduced in Dhr1-depleted 90S compared with wild-type 90S (13). The H2 to H4 and H6 and H7 regions show almost no density in state D, whereas the H1, Ha to H5, and Hb to H9 regions still retain 60 to 90% of their original densities and appear to be more resistant to degradation.

RNA helices H2, H3, H4, and H7 are located at an opening near the base of the 90S structure (Fig. 2C). Accompanying their degradation, the nearby regions also become disordered. Utp30, Rrt14, Rps18, an  $\alpha$ -helix of Sas10 that binds Utp30, and an  $\alpha$ -helix of Utp11 that binds H7 disappear altogether in state B (Fig. 2D). In state E, the base of 90S shows greatly reduced densities, suggesting that the UTPA complex and other nearby AFs begin to dissociate (Fig. 2F). Therefore, degradation of the 5' ETS destabilizes and promotes disassembly of the base of 90S.

The mature SSU structure can be divided into hallmark features of body, platform, and head, which are made up mainly by the 5', central, and 3' major domains of 18S rRNA, respectively (23, 24). The global architecture of SSU is further determined by quaternary interactions between individual domains (Fig. 1A and fig. S5A). For example, the 3' minor domain comprises helices h44 and h45 that interact with the platform and body, respectively. Extension segment 6 (ES6) in the central domain mediates two long-range interactions

<sup>1</sup>Key Laboratory of RNA Biology, CAS Center for Excellence in Biomacromolecules, Institute of Biophysics, Chinese Academy of Sciences, Beijing 100101, China. <sup>2</sup>National Institute of Biological Sciences, Beijing 102206, China.

<sup>3</sup>Department of Biochemistry and Molecular Biology, College of Life Sciences, Beijing Normal University, Beijing 100875, China. <sup>4</sup>University of Chinese Academy of Sciences, Beijing 100049, China.

\*These authors contributed equally to this work.

†Corresponding author. Email: yekeqiong@ibp.ac.cn



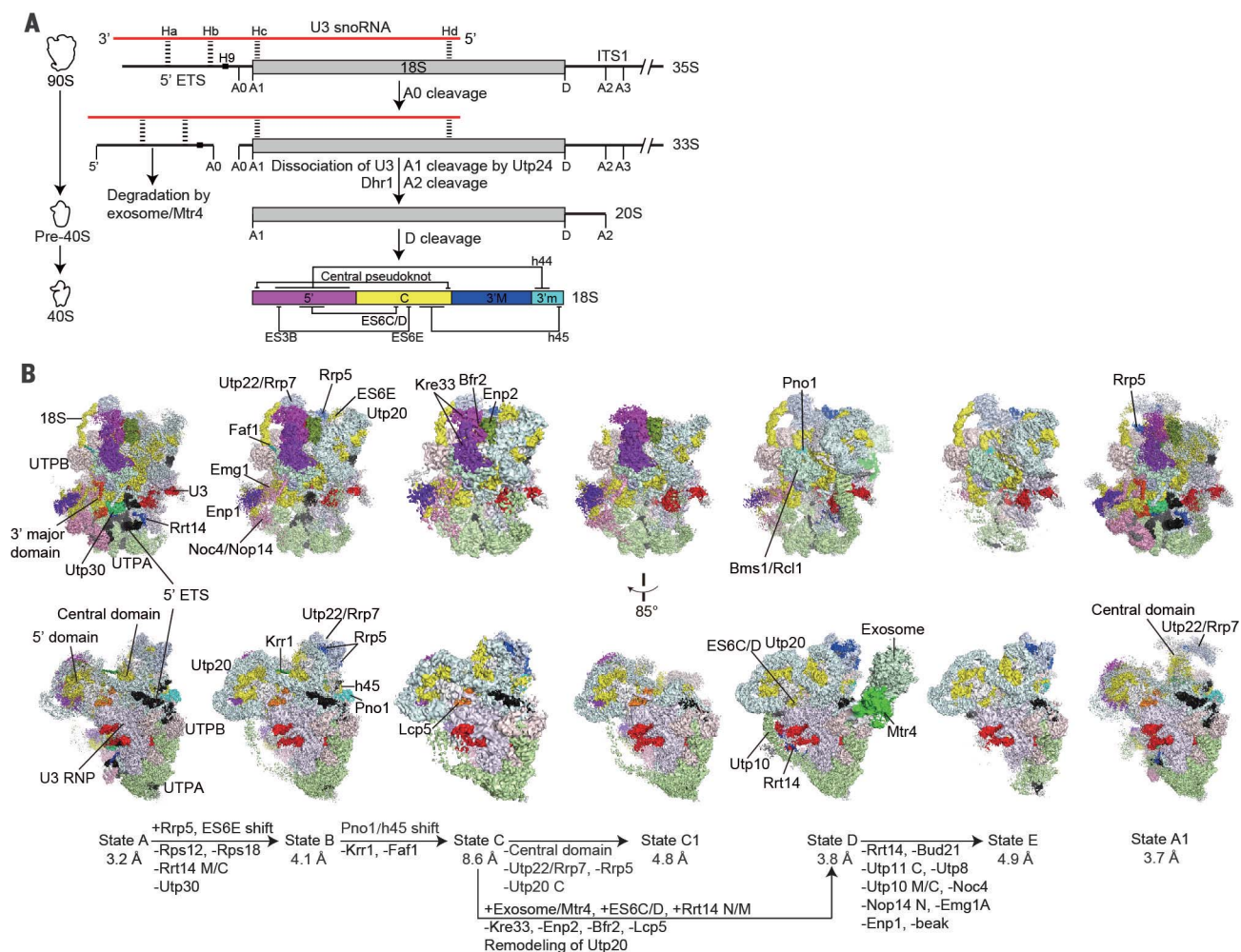


**Fig. 1. Cryo-EM structures of Dhr1-depleted 90S preribosomes.** (A) Schematic of pre-rRNA processing. Processing sites and interactions between the U3 snoRNA and the 5' ETS are marked. Long-range interactions among 5', central (C), 3' major (3'M), and 3' minor (3'm) domains of mature 18S rRNA are indicated. (B) Density maps of seven states are shown in two views. 18S, 5' ETS, and U3 RNAs are shown in yellow, black, and red, respectively. The large structural modules UTPA, UTPB, U3 snoRNP, Noc4/Nop14/Emg1, Mpp10/lmp3/

Imp4, Bms1/Rcl1, and Utp22/Rrp7 are shown in light colors. Proteins with major structural changes are shown in bright colors. Other AFs and RPs are shown in light cyan and white. Unmodeled densities are shown in white, and modeled but unassigned densities are shown in gray. The color theme is generally applied in the other figures. State D is a composite map with the exosome reconstructed from exosome-enriched particles. Compositional and conformational changes are indicated for the connected states.

with the 5' domain. These interdomain interactions are absent in state A but start to emerge in the subsequent states.

In states A and B, the ribosome assembly factor Krr1 binds to the central domain at the same position as h45 does in the mature SSU, preventing its assembly. Concomitant with removal of helix H6 of the 5' ETS, Krr1 and its binding protein Faf1, which bind to H6, are released in state C, allowing for integration of h45 (Fig. 3, A to C, and fig. S7A). In addition, Utp7, Mpp10, Utp12, Utp21, and Imp4, which are located near H6, become partially unstructured in state C, and Imp3, in complex with an  $\alpha$ -helix of Mpp10, rotates by  $\sim 15^\circ$  (Fig. 3B). Moreover, h45 and its binding protein Pno1, anchored on the UTPB complex, rotate as a whole unit by  $\sim 60^\circ$ , which brings h45 closer to its binding site in the central domain. The

movement of h45 also depends on prior removal of H6 because the new position of h45 was previously occupied by H6 and the H5 to H6 linker (Fig. 3A). Removal of H6 thus appears to drive maturation of the central domain.

Helix E of ES6 (ES6E) in the central domain of 18S rRNA makes a long-range interaction with helix B of ES3 (ES3B) in the 5' domain in mature SSU (Fig. 1A and fig. S5A). ES6E initially binds Utp22 in state A and is resituated to bind Utp20 in state B (Fig. 3C and fig. S6, A to C). The structural remodeling brings ES6E closer to, but not yet in contact with, the 5' domain (Fig. 3E). The original position of ES6E on Utp22 is occupied by the TPR domain of Rrp5, suggesting that Rrp5 drives the remodeling of ES6E. Rrp5 additionally contains 12 S1 RNA-binding domains, some

of which can be visualized (fig. S6, B to D). The TPR domain of Rrp5 was mistakenly modeled in previous state 1 because of insufficient classification.

In state D, Kre33, Enp2, Lcp5, and a short segment of Brf2, which are bound to the apical part of the 5' domain in earlier states, are missing (Figs. 2, D and E, and 3, C and D). Release of these AFs is probably facilitated by prior release of Krr1 in state C because the extended C-terminal tail of Krr1 binds Enp2 and Bfr2 (Fig. 3C). Utp20 is an extended superhelical structure that wraps the 5' and central domains of 18S rRNA with its N- and C-terminal half, respectively (Fig. 3D and fig. S7B). From state C to D, the N-half moves toward the central domain as a rigid body, whereas the C-half is greatly compressed (Fig. 3D and fig. S7, C to E). As a result of release of



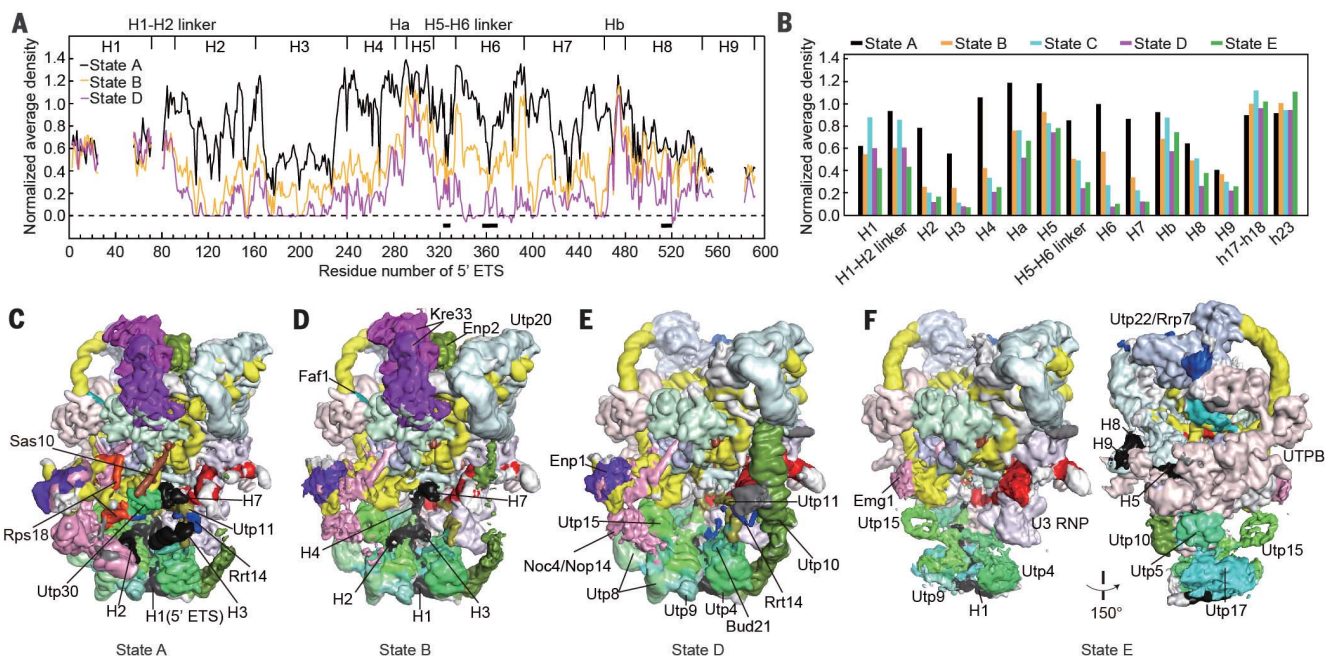


**Fig. 2. Degradation of 5' ETS in 90S.** (A) Normalized average density for the nucleotide of the 5' ETS. Density was normalized against a segment of 18S rRNA that is well ordered in all states. The secondary structures of the 5' ETS are shown on the top. Three short regions marked by lines are occupied by h45 and Utp20 in

state D and show an artificial increase of density. **(B)** Normalized average density for RNA secondary structures. Helices 17 to 18 and 23 are from the 18S rRNA. **(C to F)** Density maps of states A, B, D, and E illustrating structural changes at the base of 90S low-pass filtered to 10 Å. Two views are shown for state E.

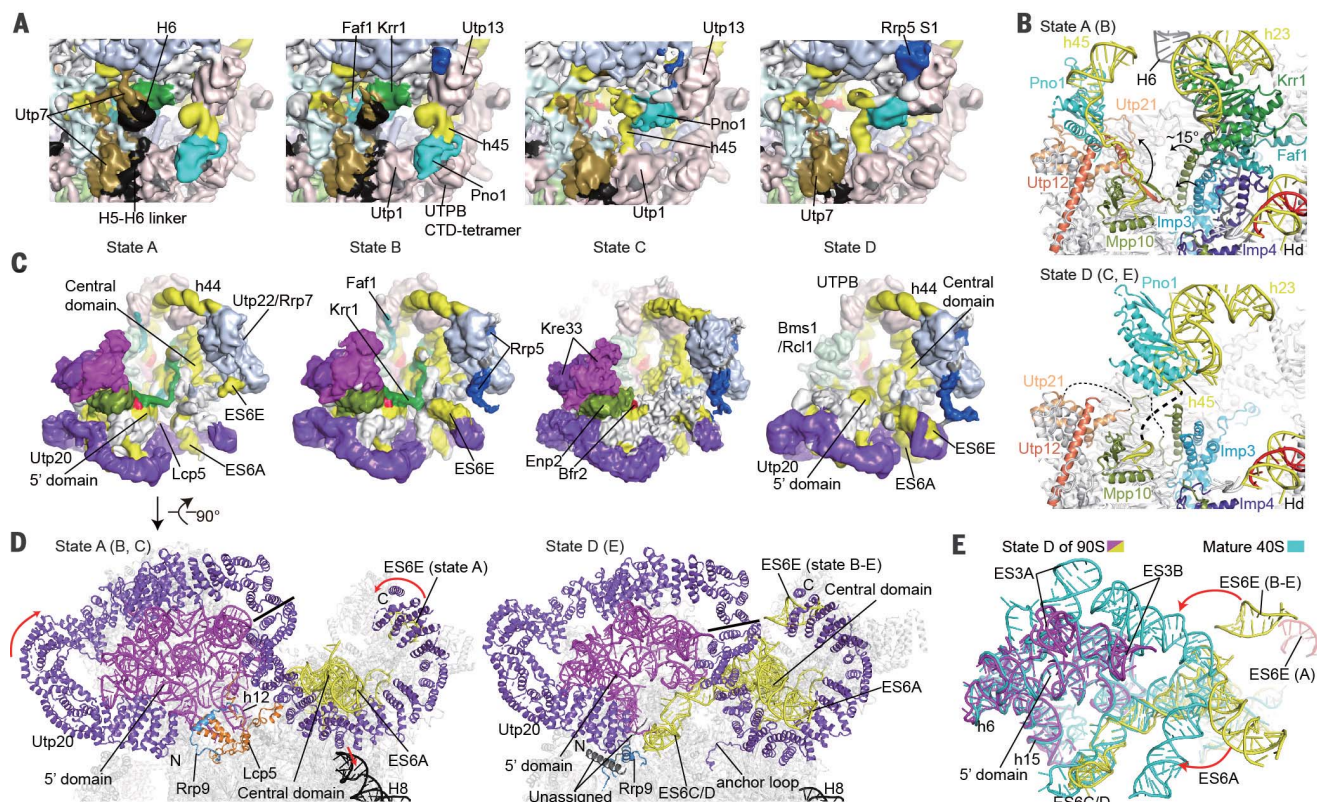


**Fig. 3. Maturation of the 5' and central domains.** (A) Density maps of states A to D illustrating structural changes around the central domain. (B) Models of state A and D around the central domain. Some obstructing structures are omitted for clarity. Other states with similar features are noted in parentheses. (C) Density maps of states A to D illustrating structural changes around the 5' and central domains. The

maps shown in (A) and (C) were low-pass filtered to 10 Å. **(D)** Models of state A and D at the 5' and central domains. This view is related to (C) by a 90° rotation. The N- and C-halves of Utp20 are divided by a line. **(E)** Structures of 18S rRNA in state D of 90S (5' domain, magenta; central domain, yellow) and a mature 40S ribosome (cyan) are aligned by the apical part of the 5' domain. E56E of state A (red) is also displayed.



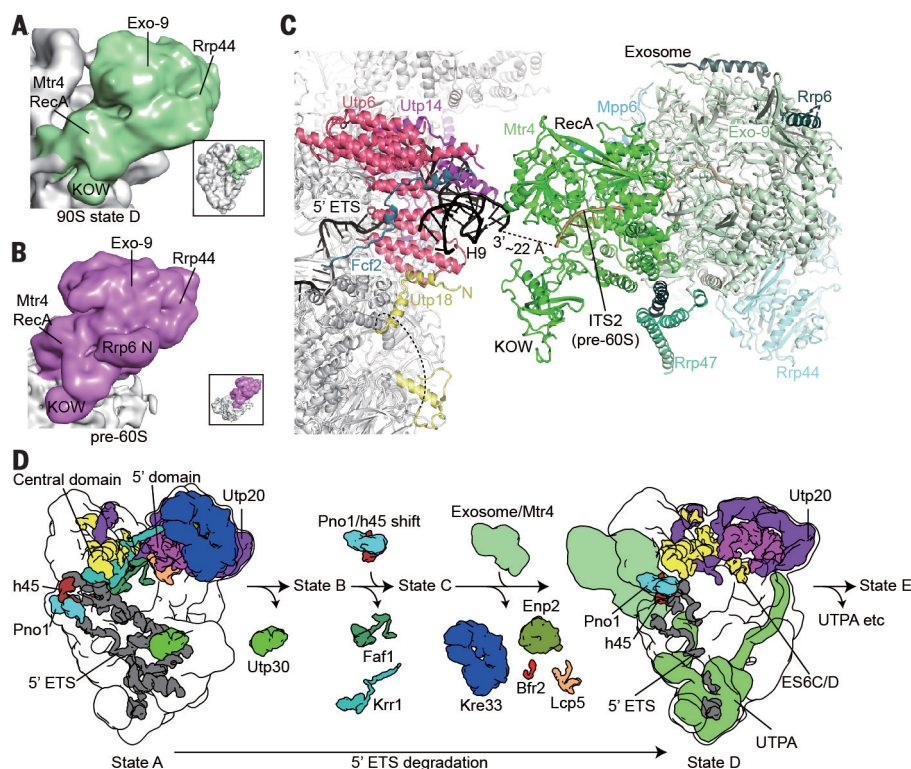


**Fig. 4. Binding of the exosome to 90S.** (A and B) Density maps of exosome-bound 90S (A) and pre-60S (B) ribosomes low-pass filtered to 20 Å. Exo-9 refers to the nine-subunit core of the exosome. Overall maps are shown in inserts. (C) Interaction between the exosome-Mtr4 and 90S. (D) Diagram of 90S progression showing major remodeling events.

the AFs bound to the 5' domain and remodeling of the Utp20 structure, the apical part of the 5' domain is pulled closer to the central domain by ~10 Å. By contrast, the basal part of the 5' domain, which is buried in the structural core of the 90S, and the central domain are static (fig. S7F). The apical part of the 5' domain maintains its core structure through the transition, but a few peripheral RNA elements (ES3B and h6) are shifted and helices 12 to 14 become disordered (fig. S7G). Helix C/D of ES6 (ES6C/D), which is invisible in states A to C, packs into the 5' domain in state D (Fig. 3D). ES6C/D mainly adopts a mature-like conformation (Fig. 3E) with only its tip, bound by an unassigned peptide, deviating (Fig. 3D). The binding site of ES6C/D on the 5' domain was originally occupied by Lcp5, Rrp9, and h12. Assembly of ES6C/D is only feasible after Lcp5 has been removed and the N-terminal residues of Rrp9 are remodeled to bind Utp20 (Fig. 3D).

The remodeling of Utp20 in state D also affects the core structure of 90S. The C-half of Utp20 moves closer to the structural core and projects an anchor loop to bind Rps22, Utp24, and Rps9 (Fig. 3D and fig. S7H). The N-half of Utp20 contacts Utp10 more extensively and straightens the C domain of this long superhelical protein (fig. S8C). This stabilizes several

structures around the C domain of Utp10 so that they are visualized for the first time, including a few N-terminal helices of Rrt14 that bind Utp10 and the P5 helix of U3 snoRNA, the P3 helix of U3 sandwiched between Utp10 and Rrp9, and an unassigned protein domain bound to Utp10 (Fig. 2E and fig. S8, A to G).

The exosome and RNA helicase Mtr4 are involved in degradation of the excised 5' ETS fragment and the 3' processing of the 5.8S rRNA (25–27). The nuclear exosome contains a nine-subunit ring structure (Exo-9), Rrp44 with 3' to 5' exoribonuclease and endoribonuclease domains, and cofactors Mpp6, Rrp6, and Rrp47. As shown by semiquantitative mass spectrometric analysis, Mtr4 and the exosome proteins are threefold more abundant in Dhr1-depleted 90S compared with wild-type 90S (fig. S9 and data S2), suggesting that the exosome-bound 90S is enriched in our sample. A block of very weak density was observed to project out from the H8 to H9 regions in states D and E. The density was improved when the particles of state D enriched with the extra density were selected for reconstruction (figs. S1D and S2B). The resulting density accommodates a structure of exosome-Mtr4 complex (Fig. 4A), which was determined in the context of a pre-60S ribosome (Fig. 4B) (28). The model shows that

Mtr4 mediates the binding of the exosome to 90S (Fig. 4C). Confirming the structural arrangement, the binding of the exosome was blocked upon depletion of Mtr4 (fig. S9). Two RecA domains of Mtr4 dock on a composite surface of Utp6, Utp14, Fcf2, and the base of H9. Utp14 at the interface is important for exosome binding (29). The N-terminal region of Utp18 that binds the KOW domain of Mtr4 is also close to the interface (26). The 3' end of H9 is ~22 Å away from the entry of the RNA channel in the exosome. This arrangement would allow the exosome to degrade the exposed 3' end of the 5' ETS after site A0 is cleaved. The exosome is visualized in states D and E, yet the 5' ETS is already degraded in state B. The exosome may be bound in earlier states but is too flexible to be visualized. Its conformation is somehow restricted after structural remodeling in state D.

On the basis of our structures, the excised 5' ETS is degraded in situ within the 90S structure, rather than being released together with associated 5' ETS AFs (9). We have captured the structure of 90S associated with the exosome that is primed to digest the 3' end of the excised 5' ETS fragment using the 3' to 5' exonuclease activity of Rrp44. However, the possibility that the exosome is recruited to degrade stalled precursors cannot be excluded at present. Three discontinuous regions (H1, Ha to H5, and Hb to H9) of the 5' ETS are persistently bound to 90S, suggesting that the digestion also occurs internally, likely involving the endonuclease activity of Rrp44 (30, 31).

States A to E show consecutive structural changes and features of maturing preribosomes, suggesting that they are evolvable physiological intermediates rather than dead-end products. Moreover, the RNA degradation is specific because only the 5' ETS, not the 18S region, is affected. States A1 and C1, which have an alternative or disrupted central domain structure and no detectable successive states, may have resulted from a quality control process.

These structural snapshots illustrate the order of molecular events during the early transition of the 90S to the pre-40S ribosome (Fig. 4D). With the release of Krr1, the central domain is ready to accommodate h45. Additional release of AFs bound to the 5' domain and remodeling of Utp20 bring the 5' and central domains closer, allowing helix ES6C/D to make the first interdomain interaction. The extended and flexible structure of Utp20 is well suited to scaffold the two domains during the dynamic packing process. At state E, the UTPA complex begins to dissociate. Further release of the U3 snoRNP probably requires the helicase activity of Dhr1 (20) and cannot proceed in the Dhr1-depleted 90S. From a structural point of view, digestion of 5' ETS is critical for starting the chain of remodeling events by destabilizing local structures of 90S

and making space for repositioned components. Supporting the driving role of 5' ETS digestion for 90S progression, the exosome components and Mtr4 are required for 18S rRNA processing (32). Our study reveals an unexpected strategy in remodeling of a large RNA-protein complex by digestion of its RNA and sets the stage for further investigation of the transition of the 90S to the pre-40S ribosome.

## REFERENCES AND NOTES

1. J. L. Woolford Jr., S. J. Baserga, *Genetics* **195**, 643–681 (2013).
2. J. Baßler, E. Hurt, *Annu. Rev. Biochem.* **88**, 281–306 (2019).
3. S. Klinge, J. L. Woolford Jr., *Nat. Rev. Mol. Cell Biol.* **20**, 116–131 (2019).
4. F. Dragon *et al.*, *Nature* **417**, 967–970 (2002).
5. P. Grandi *et al.*, *Mol. Cell* **10**, 105–115 (2002).
6. Y. N. Osheim *et al.*, *Mol. Cell* **16**, 943–954 (2004).
7. M. Chaker-Margot, M. Hunziker, J. Barandun, B. D. Dill, S. Klinge, *Nat. Struct. Mol. Biol.* **22**, 920–923 (2015).
8. L. Zhang, C. Wu, G. Cai, S. Chen, K. Ye, *Genes Dev.* **30**, 718–732 (2016).
9. M. Kornprobst *et al.*, *Cell* **166**, 380–393 (2016).
10. J. Barandun *et al.*, *Nat. Struct. Mol. Biol.* **24**, 944–953 (2017).
11. M. Chaker-Margot, J. Barandun, M. Hunziker, S. Klinge, *Science* **355**, eaal1880 (2017).
12. J. Cheng, N. Kellner, O. Berninghausen, E. Hurt, R. Beckmann, *Nat. Struct. Mol. Biol.* **24**, 954–964 (2017).
13. Q. Sun *et al.*, *eLife* **6**, e22086 (2017).
14. J. Cheng *et al.*, *Mol. Cell* **75**, 1256–1269.e7 (2019).
15. M. Hunziker *et al.*, *eLife* **8**, e45185 (2019).
16. A. Heuer *et al.*, *eLife* **6**, e30189 (2017).
17. M. Ameismeier, J. Cheng, O. Berninghausen, R. Beckmann, *Nature* **558**, 249–253 (2018).
18. A. Scaiola *et al.*, *EMBO J.* **37**, e98499 (2018).
19. O. Rodríguez-Galán, J. J. García-Gómez, J. de la Cruz, *Biochim. Biophys. Acta* **1829**, 775–790 (2013).
20. R. Sardana *et al.*, *PLOS Biol.* **13**, e1002083 (2015).
21. A. Colley, J. D. Beggs, D. Tollervey, D. L. Lafontaine, *Mol. Cell. Biol.* **20**, 7238–7246 (2000).
22. T. Schäfer, D. Strauss, E. Petfalski, D. Tollervey, E. Hurt, *EMBO J.* **22**, 1370–1380 (2003).
23. A. Ben-Shem *et al.*, *Science* **334**, 1524–1529 (2011).
24. J. Rabl, M. Leibundgut, S. F. Ataide, A. Haag, N. Ban, *Science* **331**, 730–736 (2011).
25. J. de la Cruz, D. Kressler, D. Tollervey, P. Linder, *EMBO J.* **17**, 1128–1140 (1998).
26. M. Thoms *et al.*, *Cell* **162**, 1029–1038 (2015).
27. C. Allmang *et al.*, *EMBO J.* **18**, 5399–5410 (1999).
28. J. M. Schuller, S. Falk, L. Fromm, E. Hurt, E. Conti, *Science* **360**, 219–222 (2018).
29. J. J. Black, Z. Wang, L. M. Goering, A. W. Johnson, *RNA* **24**, 1214–1228 (2018).
30. D. Schaeffer *et al.*, *Nat. Struct. Mol. Biol.* **16**, 56–62 (2009).
31. A. Lebreton, R. Tomecki, A. Dziembowski, B. Séraphin, *Nature* **456**, 993–996 (2008).
32. C. Allmang, P. Mitchell, E. Petfalski, D. Tollervey, *Nucleic Acids Res.* **28**, 1684–1691 (2000).

## ACKNOWLEDGMENTS

We thank the Center for Biological Imaging (CBI), Institute of Biophysics, Chinese Academy of Science (CAS), for cryo-EM study;

the HPC Service Station in the CBI for image processing; and F. Sun, X. Huang, G. Ji, B. Zhu, and D. Fan at the CBI for help in EM sample preparation and data collection. **Funding:** This work was supported by the National Key R&D Program of China (grant no. 2017YFA0504600), the Strategic Priority Research Program of the Chinese Academy of Sciences (grant no. XDB37010201), and the National Natural Science Foundation of China (grant nos. 91940302, 91540201, and 31430024). **Author contributions:** K.Y. initiated the project; Y.D. collected cryo-EM data and determined the structures; W.A. prepared samples; X.Z., Q.S., and J.Q. carried out the early-stage study; and Y.D. and K.Y. analyzed the structure and wrote the paper. **Competing interests:** The authors declare no competing interests. **Data and materials availability:** All data are available in the manuscript or the supplementary materials. The cryo-EM density maps and models have been deposited in EMDB and PDB with accession codes: EMD-0949, EMD-0950, EMD-0951, EMD-0952, EMD-0953, EMD-0954, EMD-0955, 6LQP, 6LQQ, 6LQR, 6LQS, 6LQT, 6LQU and 6LQV. Materials are available from K.Y. on request.

## SUPPLEMENTARY MATERIALS

science.sciencemag.org/content/369/6510/1477/suppl/DC1  
Materials and Methods  
Figs. S1 to S9  
Table S1  
References (33–49)  
Data S1 and S2  
MDAR Reproducibility Checklist

[View/request a protocol for this paper from Bio-protocol.](#)

10 February 2020; accepted 13 July 2020  
10.1126/science.aba9690



## MICROBIOME

# Microbiome-derived inosine modulates response to checkpoint inhibitor immunotherapy

Lukas F. Mager<sup>1\*</sup>, Regula Burkhard<sup>2</sup>, Nicola Pett<sup>1</sup>, Noah C. A. Cooke<sup>1</sup>, Kirsty Brown<sup>1</sup>, Hena Ramay<sup>3</sup>, Seungil Paik<sup>4</sup>, John Stagg<sup>5</sup>, Ryan A. Groves<sup>6</sup>, Marco Gallo<sup>4</sup>, Ian A. Lewis<sup>6</sup>, Markus B. Geuking<sup>2</sup>, Kathy D. McCoy<sup>1\*</sup>

Several species of intestinal bacteria have been associated with enhanced efficacy of checkpoint blockade immunotherapy, but the underlying mechanisms by which the microbiome enhances antitumor immunity are unclear. In this study, we isolated three bacterial species—*Bifidobacterium pseudolongum*, *Lactobacillus johnsonii*, and *Olsenella* species—that significantly enhanced efficacy of immune checkpoint inhibitors in four mouse models of cancer. We found that intestinal *B. pseudolongum* modulated enhanced immunotherapy response through production of the metabolite inosine. Decreased gut barrier function induced by immunotherapy increased systemic translocation of inosine and activated antitumor T cells. The effect of inosine was dependent on T cell expression of the adenosine A<sub>2A</sub> receptor and required costimulation. Collectively, our study identifies a previously unknown microbial metabolite immune pathway activated by immunotherapy that may be exploited to develop microbial-based adjuvant therapies.

Immune checkpoint blockade (ICB) therapy can be an effective therapy in some tumors and certain cancer patients by harnessing the therapeutic potential of the immune system. Targeting cytotoxic T lymphocyte-associated antigen 4 (CTLA-4) or programmed cell death protein 1 (PD-1) or its ligand (PD-L1) has revolutionized the treatment of some cancers, including melanoma, renal cell carcinoma, and non-small cell lung cancer (1, 2). Nevertheless, many other cancers show primary resistance to ICB therapy, and response rates remain low and differ between patients, even in those cancers where ICB therapy has provided benefit (3–5). There is therefore an urgent need to determine the underlying reasons for such nonresponsiveness. Recent studies have provided strong evidence that the gut microbiota can affect antitumor immunity, and composition of the intestinal microbiome may even predict the efficacy of ICB therapy. A series of seminal studies revealed that the efficacy of ICB therapies was dependent on specific gut bacteria (6–10) and that treatment with ICB-promoting bacteria

may help overcome primary resistance to ICB therapies (8). Despite the findings that specific bacterial species have been associated with increased antitumor immunity, the precise molecular mechanisms by which these microbes enhance ICB therapy remain elusive. In this study, we used an animal model of colorectal cancer (CRC) to identify specific ICB-promoting bacteria, elucidated the underlying molecular mechanism of how these microbes enhanced ICB therapy efficacy, and validated our findings in additional models of bladder cancer and melanoma.

Although the intestinal microbiota can affect CRC progression (11, 12) and may alter the efficacy of chemotherapeutics (13, 14), clinically, ICB therapies are notoriously ineffective in most CRC cases (15), and the role of the microbiome in nonresponsiveness has not yet been determined. We therefore investigated the efficacy of ICB therapy in a mouse model where colonic tumors are induced using azoxymethane (AOM) and dextran sulfate sodium (DSS) (Fig. 1A). Treatment with anti-CTLA-4 or anti-PD-L1 antibodies led to significantly fewer and smaller tumors (Fig. 1, B and C) and reduced the frequency of EpCam<sup>+</sup> Lgr5<sup>+</sup> cells in the tumor, which are markers for epithelial cell stemness (Fig. 1D). Anti-CTLA-4 treatment also resulted in increased immune cell infiltration into the tumors (Fig. 1E). Increased CD8<sup>+</sup> T cell frequencies in the tumor-draining lymph node (fig. S1A) was also observed together with increased IFN-γ<sup>+</sup>CD4<sup>+</sup> and IFN-γ<sup>+</sup>CD8<sup>+</sup> T cells in the spleen (IFN-γ, interferon-γ) (fig. S1, B and C). In this model, the effects of anti-CTLA-4 were greater than those induced by anti-PD-L1 treatment when using the same antibody dose. The difference in anti-CTLA-4 and anti-PD-L1 efficacy in this model may be dependent on the dose-

effect relationship, and higher doses have previously been described for anti-PD-1 therapy (8). Moreover, effector functions of anti-CTLA-4 and anti-PD-1 or anti-PD-L1 rely on distinct mechanisms, among them regulatory T cells (T<sub>regs</sub>) (16), and indeed T<sub>reg</sub> composition and function are different between cancer types (17). We next used this model system to screen for potentially beneficial bacteria that were associated with ICB responsiveness. Although no significant changes were observed in the overall fecal bacterial composition (β-diversity) between ICB-treated and control mice (fig. S1D), a few bacterial families were differentially abundant (fig. S1E). In contrast, sequencing of tumor-associated bacterial communities revealed differences in β-diversity (fig. S1F), and additional bacterial genera were differentially abundant in the ICB-treated tumors (Fig. 1F and fig. S1, G and H). We therefore performed anaerobic culture of homogenized tumors from both groups and were able to culture and identify 21 distinct bacterial isolates. Seven bacterial species were cultured only from ICB-treated tumors, whereas four were found only in the control group (Fig. 1G). *Bifidobacterium pseudolongum* was one of the isolates cultured only from ICB-treated tumors. *B. pseudolongum* belongs to the genus *Bifidobacterium*, which was identified as differentially abundant by sequencing (Fig. 1F and fig. S1, G and H). Interestingly, *Akkermansia muciniphila*, which was recently identified to enhance the efficacy of anti-PD-L1 and anti-PD-1 treatments in lung and kidney cancers (8), was also one of the seven bacteria cultured only from ICB-treated tumors (Fig. 1G). Isolation and identification of distinct bacterial species associated with ICB responsiveness provided us with the opportunity to identify the molecular mechanism involved.

Next, we determined whether the efficacy of ICB therapy in CRC was dependent on the microbiota, as has been shown with other tumor types (6). As the development of orthotopic adenocarcinomas is severely reduced in animals with a limited microbiota (18), we switched to a heterotopic in vivo model of CRC where MC38 colorectal cancer cells were implanted into the flank of germ-free (GF) or specific-pathogen-free (SPF) mice followed by ICB therapy once tumors were palpable (fig. S2A). Anti-CTLA-4 treatment led to smaller tumors (fig. S2B) and markedly increased intratumoral and splenic CD4<sup>+</sup> and CD8<sup>+</sup> T cell activation and proliferation in SPF mice compared with GF mice (fig. S2, C to F). To ensure that the lack of ICB efficacy was not merely a reflection of the immature immune system of GF mice, we also assessed the effect of ICB therapy in antibiotic-treated SPF mice (fig. S2G). Similar to what was observed in GF mice, broad-spectrum antibiotics reduced

<sup>1</sup>Department of Physiology and Pharmacology, Snyder Institute of Chronic Diseases, Cumming School of Medicine, University of Calgary, Calgary, Canada. <sup>2</sup>Department of Microbiology, Immunology and Infectious Diseases, Snyder Institute of Chronic Diseases, Cumming School of Medicine, University of Calgary, Calgary, Canada. <sup>3</sup>International Microbiome Centre, Cumming School of Medicine, University of Calgary, Calgary, Canada. <sup>4</sup>Department of Biochemistry and Molecular Biology and Department of Physiology and Pharmacology, Charbonneau Cancer Institute, Alberta Children's Hospital Research Institute, Cumming School of Medicine, University of Calgary, Calgary, Canada. <sup>5</sup>Centre de Recherche du Centre Hospitalier de l'Université de Montréal et Institut du Cancer de Montréal, Québec, Canada. <sup>6</sup>Department of Biological Sciences, University of Calgary, Calgary, Canada.

\*Corresponding author. Email: kathy.mccoy@ucalgary.ca (K.D.M.); lukas.mager@ucalgary.ca (L.F.M.)

ICB therapy efficacy in tumor-bearing SPF mice (fig. S2, H to J). To evaluate whether the isolated bacteria that were enriched in the tumors of ICB-treated mice (Fig. 1G) were able to boost the

efficacy of ICB therapy, GF mice were monocolonized with five different isolated bacterial species. MC38 tumor cells were injected heterotopically into monocolonized or GF mice and, upon palpable tumor development, all

mice were treated with anti-CTLA-4, after which tumor growth and antitumor immunity were assessed (Fig. 1H). Of the five bacterial species tested, monocolonization with *B. pseudolongum*, *Lactobacillus johnsonii*, and *Olsenella* species

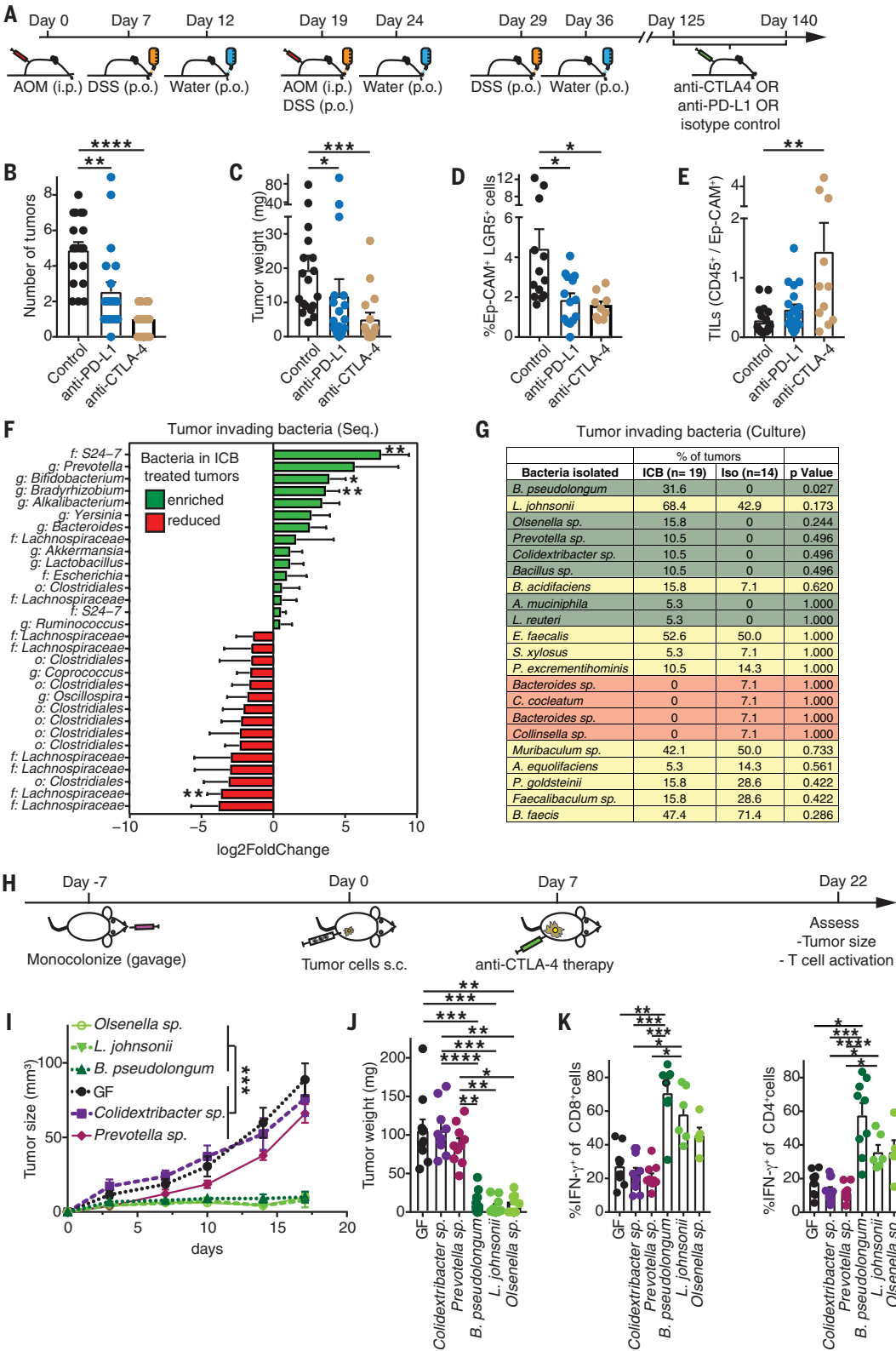
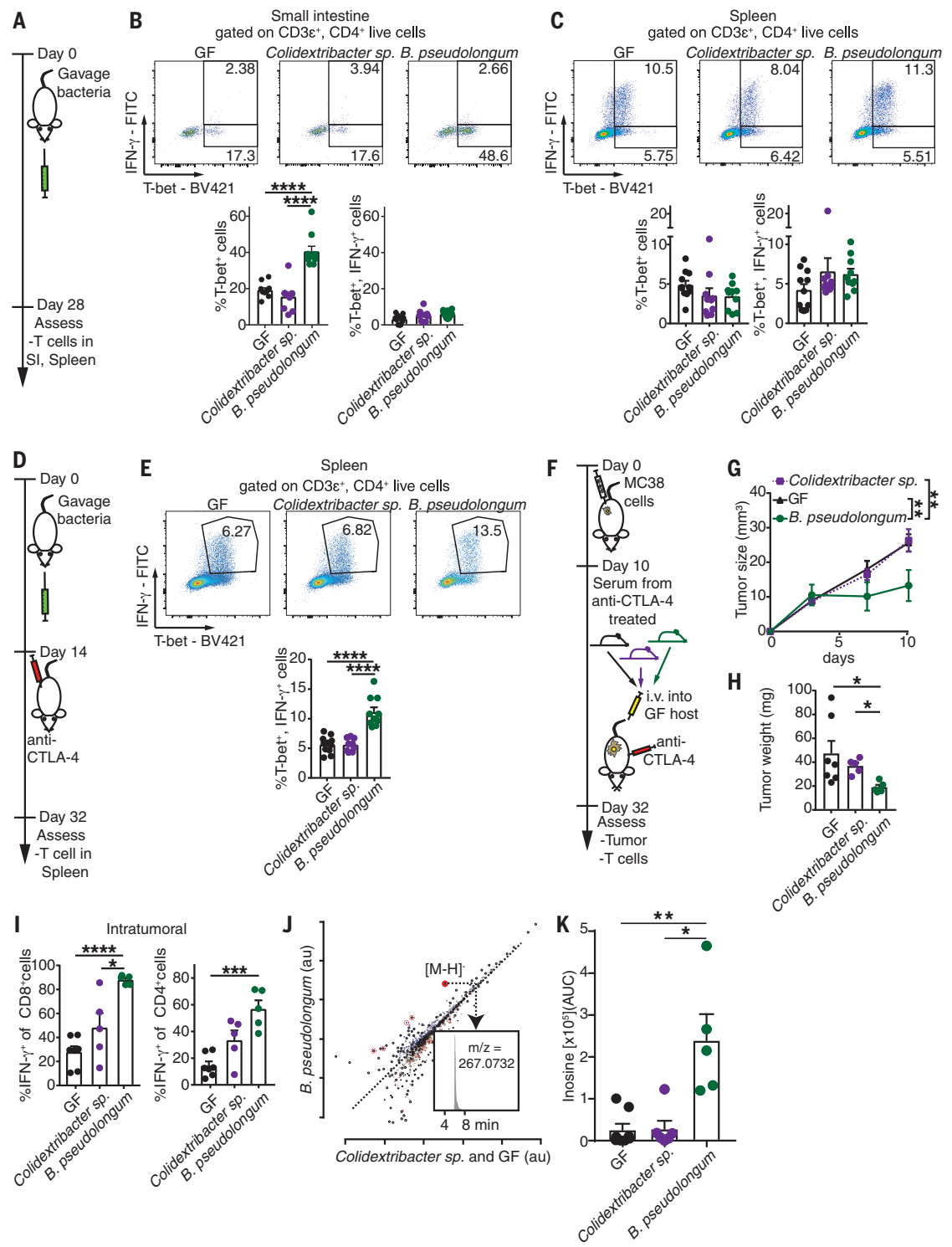


**Fig. 1. Identification of bacteria that promote response to ICB therapy.** (A) Schematic of the experimental setup. Animals were treated with either anti-CTLA-4, anti-PD-L1, or isotype control antibody. i.p., intraperitoneally; p.o., orally. (B) Number of tumors, (C) tumor weight, (D) EpCAM<sup>+</sup>LGR5<sup>+</sup> cancer stem cells, and (E) tumor-infiltrating leukocytes (TILs) of AOM/DSS intestinal tumors in SPF mice after treatment with isotype, anti-PD-L1, or anti-CTLA-4 antibodies. (F) 16S rRNA gene V4 region amplicon sequencing to identify bacteria in tumor tissue. Bacteria enriched or reduced in tumors of anti-PD-L1 or anti-CTLA-4 (ICB) compared with isotype-treated animals are shown in green and red, respectively. f, family; g, genus; o, order. (G) Bacteria cultured from homogenized tumors under anaerobic conditions from anti-PD-L1 or anti-CTLA-4 (ICB groups) or isotype (Iso group) treated animals. Bacteria isolated only from ICB-treated tumors shown in green, bacteria isolated only from isotype-treated tumors shown in orange, and bacteria isolated from both ICB- and isotype-treated tumors shown in yellow. (H) Schematic of the experimental setup. s.c., subcutaneously. (I) Tumor growth, (J) tumor weight, and (K) quantification of intratumoral IFN- $\gamma$ <sup>+</sup>CD8<sup>+</sup> and IFN- $\gamma$ <sup>+</sup>CD4<sup>+</sup> T cells are shown in GF or monocolonized (*B. pseudolongum*, *Colidextribacter* species, *L. johnsonii*, *Olsenella* species, or *Prevotella* species) MC38 tumor-bearing mice. Data indicate mean  $\pm$  SEM [(B) to (E), and (I) to (K)] or mean  $\pm$  log fold change standard error (F) and are pooled from three individual experiments. [(A) to (E)]  $n = 16$  to 20 mice per group. [(H) to (K)]  $n = 8$  to 15 mice per group. \* $P < 0.05$ ; \*\* $P < 0.01$ ; \*\*\* $P < 0.001$ ; \*\*\*\* $P < 0.0001$ .



**Fig. 2. Effect of *B. pseudolongum* and ICB on T<sub>H</sub>1 T cell phenotype and identification of the immunotherapy-promoting metabolite inosine. (A, D, and F) Schematic of the experimental setups. i.v., intravenously. (B) Representative plots and quantification of T-bet<sup>+</sup> and T-bet<sup>+</sup>IFN- $\gamma$ <sup>+</sup> events of CD3 $\epsilon$ <sup>+</sup>CD4<sup>+</sup> cells in the small intestine (SI) in the presence of indicated bacteria at day 28. (C) Same as (B), but in the spleen. (E) Representative plots and quantification of T-bet<sup>+</sup>IFN- $\gamma$ <sup>+</sup> events of CD3 $\epsilon$ <sup>+</sup>CD4<sup>+</sup> T cells in the spleen in the presence of indicated bacteria and anti-CTLA-4 treatment at day 32. (G) Tumor growth and (H) tumor weight are shown 32 days after MC38 tumor challenge and subsequent serum transfer and anti-CTLA-4 treatment. (I) Quantification of intratumoral IFN- $\gamma$ <sup>+</sup>CD8<sup>+</sup> and IFN- $\gamma$ <sup>+</sup>CD4<sup>+</sup> T cells. (J) Scatter plot of untargeted metabolomics data in the serum of anti-CTLA-4-treated tumor-bearing *B. pseudolongum*-monocolonized mice compared with *Colidextribacter* species-monocolonized and GF mice. Red circles or dotted red circles depict inosine or inosine fragments and adducts, respectively. Inset shows an extracted ion chromatogram of inosine. *m/z*, mass to charge ratio; au, arbitrary units. (K) Intensity of inosine (AUC, area under the curve) in sera shown in (J). Data indicate mean  $\pm$  SEM and are pooled from two individual experiments. [(A) to (E)] *n* = 10 or 11 mice per group. [(F) to (K)] *n* = 5 to 8 mice per group. \**P* < 0.05; \*\**P* < 0.01; \*\*\**P* < 0.001; \*\*\*\**P* < 0.0001.**



significantly enhanced the efficacy of anti-CTLA-4 treatment compared with GF mice or mice monocolonized with *Colidextribacter* species or *Prevotella* species (Fig. 1, I and J, and fig. S3, A and B). In addition, CD4<sup>+</sup> and CD8<sup>+</sup>

T cell activation was substantially increased (Fig. 1K), whereas proliferation of intratumoral CD8<sup>+</sup> T cells (fig. S3, C and D) was modestly increased in the tumors of *B. pseudolongum*, *L. johnsonii*, and *Olsenella* species-monocolonized animals.

The isolated ICB-promoting *B. pseudolongum* strain also improved the efficacy of anti-PD-L1 treatment in the MC38 heterotopic tumor model compared with the *Colidextribacter* species control bacteria (fig. S4), albeit to a lesser

extent than that observed for anti-CTLA-4 treatment (at the same dose), similar to our observations in the AOM/DSS model. Because *B. pseudolongum* provided the most robust ICB-promoting effect, it was selected for further mechanistic studies. Note that other *Bifidobacterium* species, such as *B. breve* and *B. longum*, have previously been found to promote antitumor immunity and enhance anti-PD-L1 efficacy in a murine model of melanoma (7). In humans, *B. longum* has been reported to be enriched in anti-PD-1 responders (9). Furthermore, *B. pseudolongum* species are widely distributed in the mammalian gut, with many different strains displaying genomic diversity and differential metabolic capacities (19), suggesting strain-dependent functions.

We found that antitumor immunity was dependent on ICB therapy, as monocolonization with *B. pseudolongum* in the absence of anti-CTLA-4 treatment was not able to reduce tumor growth (fig. S5, A to C) or induce antitumor immunity (fig. S5, D and E), which is similar to previous studies with other ICB-promoting bacteria (6, 8). And although previous studies have shown that some bacteria accumulate in the tumor environment, where they locally stimulate the immune system and kill tumor cells through toxic metabolites (20), we could not detect *B. pseudolongum* within the heterotopic tumors (fig. S6). Therefore, despite the fact that *B. pseudolongum* was initially isolated from intestinal tumors, the presence of bacteria within tumors was not required for the enhancement of ICB therapy in our model, suggesting the potential involvement of soluble factors.

Although *B. pseudolongum* did not induce antitumor immunity in the absence of ICB therapy (fig. S5), intestinal *B. pseudolongum* did induce a significant increase in expression of the T helper cell 1 ( $T_H1$ ) master transcription regulator T-bet in small intestinal lamina propria  $CD4^+$  T cells, which was not observed in GF or *Colidextribacter* species-monocolonized mice (Fig. 2, A and B). Induction of T-bet illustrated that *B. pseudolongum* has immunomodulatory capacity even in the absence of ICB. In its absence, the immunomodulatory effect was restricted to the gut-associated lymphoid tissue (GALT) and was also observed, albeit to a lesser extent, in the mesenteric lymph nodes (MLN) (fig. S7A), but it was not observed in the spleen (Fig. 2C). In the absence of ICB, *B. pseudolongum* did not increase the activation of effector function of  $T_H1$  cells, as  $IFN-\gamma^+$  T-bet $^+$  cells did not differ from controls in any of the tissues assessed (Fig. 2, B and C, and fig. S7A). Thus, in the absence of tumors and ICB therapy, *B. pseudolongum* promoted mucosal  $T_H1$  transcriptional differentiation in GALT without increasing effector function in the gut and draining lymph nodes. While

*B. pseudolongum* had no effect on other  $CD4^+$  T cell subsets in the small intestine (fig. S7B), it did increase  $CD8^+$  T-bet $^+$  T cells (fig. S7C). Moreover, *B. pseudolongum* had a minimal effect on  $T_H17$  cells and  $T_{reg}$ s in the MLN and spleen (fig. S7, D to G).

Because *B. pseudolongum* monocolonization in the absence of tumors and ICB therapy induced only local mucosal  $T_H1$  differentiation during homeostasis, we next asked whether the combination of *B. pseudolongum* and anti-CTLA-4 therapy (in the absence of a tumor) would lead to systemic  $T_H1$  activation. Indeed, colonization with *B. pseudolongum* combined with ICB treatment led to significantly enhanced splenic  $T_H1$  cell activation and effector function, as evidenced by  $IFN-\gamma$  production compared with *Colidextribacter* species-monocolonized or GF animals (Fig. 2, D and E, and fig. S7, H and I). We concluded that *B. pseudolongum* induces  $T_H1$  differentiation and, together with anti-CTLA-4, activation of  $T_H1$  effector T cells. Interestingly, a recently defined consortium of 11 bacteria (which did not include any *Bifidobacterium* spp.) induced  $IFN-\gamma$  production preferentially in  $CD8^+$  T cells and promoted antitumor immunity in the absence of immunotherapy (21). In contrast, *B. pseudolongum* induced  $IFN-\gamma$  production in both  $CD4^+$  and  $CD8^+$  T cells (fig. S7J), and ICB treatment was required for antitumor immunity.

We were intrigued by the ability of *B. pseudolongum* to induce  $T_H1$  transcriptional differentiation during homeostasis as opposed to activation of  $T_H1$  effector function after ICB treatment. Gastrointestinal inflammation is a common immune-related adverse effect of anti-CTLA-4 treatment (1), and we reasoned that this may be due to alterations in gut barrier integrity. Indeed, monocolonized animals treated with anti-CTLA-4 displayed increased systemic serum anticomensal antibody reactivity, particularly  $T_H1$ -associated immunoglobulin G2b, and reduced small intestinal transepithelial electrical resistance compared with controls (fig. S8, A and B). Despite this, anti-CTLA-4 treatment did not induce overt local or systemic inflammation (fig. S8, C and D). In this regard, it is notable that some *Bifidobacterium* species have been reported to provide protection from anti-CTLA-4-induced enterocolitis with no effect on tumor growth (22). The induction of systemic antibacterial antibodies after ICB therapy was not required for the ICB-promoting effect, as anti-CTLA-4 treatment was also effective in *B. pseudolongum*-monocolonized mice deficient in B cells and antibodies (fig. S9). Therefore, because bacteria did not accumulate in (heterotopic) tumors (fig. S6), anti-CTLA-4 reduced the integrity of the gut barrier (fig. S8), and B cells and anticomensal antibodies were not required for the ICB-promoting effect of *B. pseudolongum* (fig. S9), we hypothesized that increased systemic

translocation of metabolites may be responsible for the systemic effect of *B. pseudolongum* during ICB therapy. To address this hypothesis, serum collected from tumor-bearing GF, *B. pseudolongum*, or *Colidextribacter* species-monocolonized mice treated with anti-CTLA-4 was transferred concomitantly with anti-CTLA-4 into GF MC38 tumor-bearing mice (Fig. 2F). Unexpectedly, serum from anti-CTLA-4-treated *B. pseudolongum* monocolonized mice, but not serum from anti-CTLA-4-treated GF or *Colidextribacter* species-monocolonized mice, was sufficient to reduce tumor growth and elicit strong antitumor immunity in the tumor and spleen of GF mice (Fig. 2, G to I, and fig. S10). Together, these data show that soluble factors derived from, or induced by, *B. pseudolongum* were responsible for the observed ICB-promoting effects.

Untargeted metabolomics of the serum samples revealed increased levels of several metabolites in sera from *B. pseudolongum* compared with *Colidextribacter* species-monocolonized and GF mice (Fig. 2J and fig. S11, A and B). Notably, the purine metabolite inosine was the only metabolite that was significantly more abundant (eight to ninefold) in sera from *B. pseudolongum*-monocolonized mice compared with sera from *Colidextribacter* species-monocolonized or GF mice (Fig. 2K). Of note, xanthine and hypoxanthine, degradation products of inosine, were also elevated in the sera of *B. pseudolongum*-monocolonized mice (table S1). Analysis of bacterial culture supernatant revealed that both *B. pseudolongum* and *A. muciniphila* produced significantly higher amounts of inosine than did *Colidextribacter* species under the same culture conditions (fig. S11C), revealing that inosine is a bacterial metabolite produced by *B. pseudolongum* and *A. muciniphila*. In contrast, although *L. johnsonii* did not produce inosine, it did produce large amounts of hypoxanthine—a potent ligand binding to the same receptor as inosine—compared with *Colidextribacter* species (fig. S11D) (23). Inosine monophosphate and hypoxanthine were two of the most elevated metabolites in the cecum and serum of mice colonized with the consortium of 11 bacteria that Tanoue *et al.* recently identified to improve ICB therapies (21). The identity of inosine was confirmed by fragmentation analysis (fig. S11E).

To determine the physiological inosine levels in vivo, we measured inosine concentrations in duodenal, jejunal, and cecal contents of *B. pseudolongum*-monocolonized mice. Inosine concentrations were highest in the duodenum and gradually decreased along the gastrointestinal tract [duodenum ( $66.13 \pm 14.23 \mu\text{M}$ ) > jejunum ( $29.26 \pm 9.38 \mu\text{M}$ ) > cecum ( $0.5 \pm 0.05 \mu\text{M}$ )] (fig. S11F). We also quantified inosine concentrations in the serum of anti-CTLA-4- and anti-PD-L1-treated *B. pseudolongum*



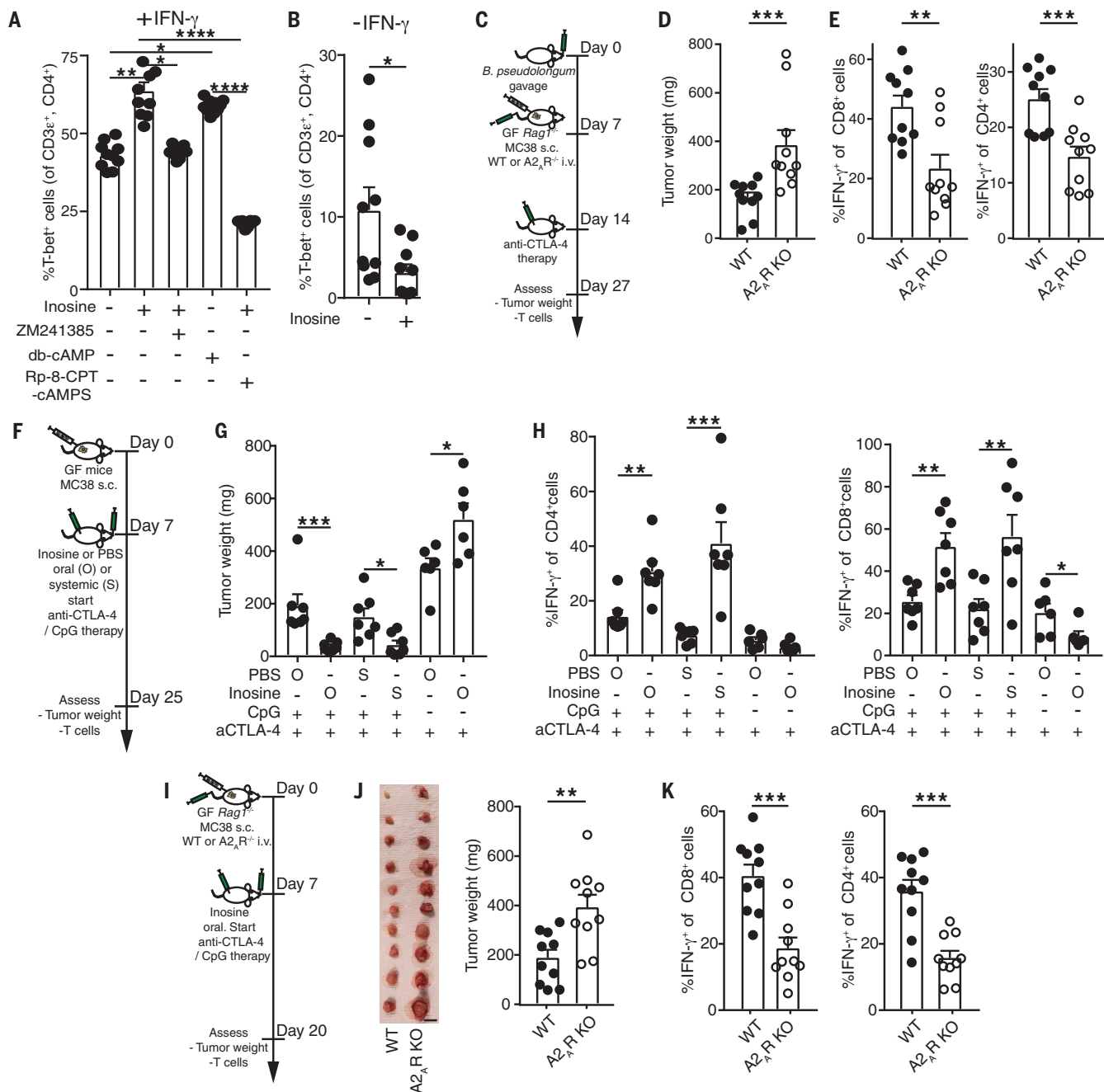


**Fig. 3. Inosine promotes T<sub>H</sub>1 activation and antitumor immunity.** (A) Naïve CD4<sup>+</sup> T cells were cocultured with BMDCs and IFN- $\gamma$ . Quantification of T-bet<sup>+</sup>CD3<sup>+</sup>CD4<sup>+</sup> T cells 48 hours after coculture in the presence or absence of inosine, A<sub>2A</sub> receptor inhibitor (ZM241385), cell-permeable cAMP (db-cAMP), and protein kinase A inhibitor (RP-8-CPT-cAMPS). (B) Same as (A), but without IFN- $\gamma$ . (C) Schematic overview to assess the requirement of A<sub>2A</sub>R signaling for *B. pseudolongum*-induced antitumor immunity. GF Rag1<sup>-/-</sup> mice were gavaged with *B. pseudolongum* and 7 days later 1 × 10<sup>6</sup> MC38 cells (s.c.) and wild-type (WT) or A<sub>2A</sub>R-deficient 1 × 10<sup>7</sup> T cells (i.v. 6 × 10<sup>6</sup> CD4<sup>+</sup> and 4 × 10<sup>6</sup> CD8<sup>+</sup> T cells) were injected. Upon development of palpable tumors, mice were treated with 100 μg anti-CTLA-4 i.p. (five times every 72 hours). (D) Tumor weight and (E) quantification of IFN- $\gamma$ <sup>+</sup> in CD8<sup>+</sup> or CD4<sup>+</sup> T cells in the tumor are shown. (F) Schematic overview of experimental setup to assess the effect of inosine on antitumor immunity. Upon development of palpable tumors, mice were treated with 100 μg anti-CTLA-4 i.p. (five times every 72 hours) and in

some groups 20 μg CpG i.p. (five times every 72 hours). In addition, inosine (300 mg per kilogram of body weight) or PBS was given daily orally (O) through gavage or systemically (S) through i.p. injection. (G) Tumor weight and quantification of intratumoral IFN- $\gamma$ <sup>+</sup> cells among (H) CD4<sup>+</sup> or CD8<sup>+</sup> T cells are shown. (I) Schematic overview to assess the requirement of A<sub>2A</sub>R signaling for inosine-induced antitumor immunity. GF Rag1<sup>-/-</sup> mice were injected with 1 × 10<sup>6</sup> MC38 cells (s.c.) and WT or A<sub>2A</sub>R-deficient 1 × 10<sup>7</sup> T cells (i.v. 6 × 10<sup>6</sup> CD4<sup>+</sup> and 4 × 10<sup>6</sup> CD8<sup>+</sup> T cells). Upon development of palpable tumors, mice were treated with 100 μg anti-CTLA-4, 20 μg CpG (four times every 72 hours, both i.p.) and inosine (daily, 300 mg per kilogram of body weight, through gavage). (J) Pictures of tumors and tumor weight are shown at day 20. KO, knockout. Scale bar, 1 cm. (K) Quantification of IFN- $\gamma$ <sup>+</sup> in CD8<sup>+</sup> or CD4<sup>+</sup> T cells in the tumor are shown. Data indicate mean ± SEM, pooled from two individual experiments. [(A) and (B)] *n* = 10 biological replicates per group. [(C) to (K)] *n* = 6 to 10 mice per group. \**P* < 0.05; \*\**P* < 0.01; \*\*\**P* < 0.001; \*\*\*\**P* < 0.0001.

(anti-CTLA-4:  $26.16 \pm 3.32 \mu\text{M}$ ; anti-PD-L1:  $37.5 \pm 10.2 \mu\text{M}$ ) and *Colidextribacter* species (anti-CTLA-4:  $3.26 \pm 1.01 \mu\text{M}$ ; anti-PD-L1:  $4.8 \pm 1.3 \mu\text{M}$ ) monoclonized mice (fig. S11F), in the serum of SPF mice before ( $4.08 \pm 1.12 \mu\text{M}$ ) and after anti-CTLA-4 treatment ( $11.65 \pm 2.09 \mu\text{M}$ ) and in the serum of antibiotic-treated SPF mice given anti-CTLA-4 ( $2.03 \pm 0.86 \mu\text{M}$ ) (fig. S11G). These data indicated that bacterial production of inosine in the upper gastrointestinal tract is likely to be the predominant source of elevated systemic inosine levels in *B. pseudolongum* monoclonized mice.

The identification of inosine was initially surprising because inosine binds to the adenosine 2A receptor ( $A_{2A}R$ ), which has been demonstrated to inhibit  $T_H1$  differentiation in vitro and antitumor immunity in vivo (24–27). Data supporting an immunosuppressive role for adenosine and  $A_{2A}R$  signaling have led to the development of novel immune checkpoint inhibitor targets, such as monoclonal antibody-targeting CD73, CD39, and CD38 and pharmacological antagonists of  $A_{2A}R$ , many of which are currently in clinical trials [reviewed in (28)]. However, a small body of literature has demonstrated that inosine analogs can be proinflammatory and that  $A_{2A}R$  signaling can sustain  $T_H1$  and antitumor immunity in mice (29–31). On the basis of these opposing findings, we investigated whether inosine could enhance  $T_H1$  cell differentiation in vitro. Activated ovalbumin 323–339 (OVA<sub>323–339</sub>) peptide-pulsed bone marrow-derived dendritic cells (BMDCs) were cocultured with naïve OVA<sub>323–339</sub>-specific OT-II  $CD4^+$  T cells in the presence or absence of inosine. The effect of inosine in terms of induction or inhibition of  $CD4^+$   $T_H1$  T cell differentiation turned out to be context dependent. Specifically, in the presence of exogenous IFN- $\gamma$ , inosine strongly boosted  $T_H1$  differentiation of naïve T cells (Fig. 3A), whereas in the absence of IFN- $\gamma$ , inosine inhibited  $T_H1$  differentiation (Fig. 3B and fig. S12A). We next dissected the molecular mechanism through which inosine enhanced  $T_H1$  differentiation. Whereas the pharmacological inhibition of  $A_{2A}R$  signaling (with the high affinity antagonist ligand ZM241385) completely abrogated the effect of inosine, the addition of cell-permeable dibutyl-adenosine monophosphate (db-cAMP), a signaling molecule downstream of  $A_{2A}R$ , restored  $T_H1$  differentiation and bypassed the need for inosine (Fig. 3A). Furthermore, inhibition of protein kinase A (PKA), a downstream effector molecule of cAMP, negated inosine-driven  $T_H1$  differentiation (Fig. 3A). In addition, the inosine- $A_{2A}R$ -cAMP-PKA signaling cascade led to phosphorylation of the transcription factor cAMP response element-binding protein (CREB) (fig. S12B), a known

transcriptional enhancer of key  $T_H1$  differentiation factors, such as interleukin-12 (IL-12) receptor and IFN- $\gamma$  (32–34). We also observed inosine-dependent up-regulation of the IL-12 receptor, beta 2 subunit (IL12R $\beta$ 2) (fig. S12C).

The effect of inosine was T cell-intrinsic, because the addition of inosine to naïve T cells that had been activated with anti-CD3- and anti-CD28-coated beads also enhanced  $T_H1$  differentiation, even in the absence of IFN- $\gamma$  (fig. S12D). Furthermore, induction of  $T_H1$  differentiation and phosphorylation of CREB was absent when  $A_{2A}R$ -deficient T cells were stimulated with inosine (fig. S12, E and F). In contrast, bypassing the need for  $A_{2A}R$  signaling by using db-cAMP increased  $T_H1$  differentiation and phosphorylation of CREB in  $A_{2A}R$ -deficient T cells, confirming that the  $T_H1$  promoting effect of inosine is dependent on  $A_{2A}R$  signaling (fig. S12, E and F). Additionally, given that phosphorylated CREB is known to bind to key  $T_H1$  target genes, we confirmed that inosine stimulation led to a sustained up-regulation of *Il12rb2* and *Ifng* gene expression in  $CD4^+$  T cells (fig. S12, G and H). Inosine dose response experiments revealed that the physiological concentrations of inosine observed in sera of *B. pseudolongum* but not *Colidextribacter* species-monoclonized mice were sufficient to induce  $T_H1$  activation (fig. S12I). In contrast, adenosine, which also binds to the  $A_{2A}R$ , was present only at extremely low levels in intestinal contents, and serum levels did not differ between *B. pseudolongum* and *Colidextribacter* species-monoclonized mice (fig. S12J), indicating that adenosine was unlikely to be mediating the ICB-promoting effects of *B. pseudolongum*. Furthermore, adenosine dose-response experiments revealed that the levels of adenosine in the serum were insufficient to promote  $T_H1$  activation and effector function (fig. S12K). To confirm whether the inosine-mediated  $T_H1$  promoting effect in vitro also applied to in vivo conditions, GF mice were immunized with ovalbumin in combination with CpG as a costimulus. Note that we used CpG as a costimulus because it is a widely used antitumor adjuvant in different settings [reviewed in (35)]. One day later, mice received inosine or vehicle by intraperitoneal administration. Inosine increased the proportions of T-bet $^+$ IFN- $\gamma^+$ CD8 $^+$  and T-bet $^+$ IFN- $\gamma^+$ CD4 $^+$  T cells in the MLN (fig. S12, L to N), validating our in vitro results.

We next determined whether the ICB-enhancing ability of *B. pseudolongum* required  $A_{2A}R$  expression specifically on T cells. Antitumor immunity was assessed in *B. pseudolongum* monoclonized *Rag1*-deficient mice bearing MC38 tumors that had been adoptively transferred with either  $A_{2A}R$ -deficient or wild-type T cells and treated with anti-CTLA-4 (Fig. 3C). We found that the absence of  $A_{2A}R$  expression

on T cells reduced the ICB-promoting effect of *B. pseudolongum* (Fig. 3, D and E).

We then determined whether inosine could promote antitumor immunity induced by anti-CTLA-4 in the absence of *B. pseudolongum*. GF mice were challenged with MC38 tumor cells and upon development of palpable tumors, inosine or phosphate-buffered saline (PBS) was given orally or systemically in combination with anti-CTLA-4 treatment and CpG as a costimulus (Fig. 3F). Compared with PBS, both oral and systemic administration of inosine led to reduced tumor weights and increased antitumor immunity when given together with anti-CTLA-4 and CpG (Fig. 3, G and H). But in the absence of CpG, inosine increased tumor weight and reduced antitumor immunity (Fig. 3, G and H), validating our previous in vitro findings demonstrating that the effect of inosine was context-dependent and based on the presence or absence of costimulation. Inosine-induced antitumor immunity was also dependent on  $A_{2A}R$  signaling in T cells, as oral supplementation with inosine failed to induce antitumor immunity in MC38 tumor-bearing GF *Rag1*-deficient animals adoptively transferred with  $A_{2A}R$ -deficient T cells (Fig. 3, I to K). These data indicated that the ICB-promoting effect of *B. pseudolongum* was mediated by inosine and was dependent on  $A_{2A}R$  signaling specifically in T cells.

Because we detected *A. muciniphila*—a species that was previously shown to increase ICB therapy efficacy (8) and to produce inosine in vitro (fig. S11C)—in ICB-treated tumors (Fig. 1G), we further investigated whether *A. muciniphila* also relies on  $A_{2A}R$  signaling to enhance ICB-therapy efficacy. We found that monoclonization with *A. muciniphila* in combination with anti-CTLA-4 led to smaller tumors and increased antitumor immunity, and this was dependent on T cell expression of  $A_{2A}R$  (fig. S13, A to D). Although monoclonization with *L. johnsonii* was able to promote the antitumor effects of anti-CTLA-4 (Fig. 1, I to K, and fig. S5), hypoxanthine (another ligand of the  $A_{2A}R$ ), not inosine, was elevated in in vitro cultures (fig. S11, C and D). Despite this, the ICB-promoting effect of *L. johnsonii*, although less potent than that of *B. pseudolongum* and *A. muciniphila*, was also partially dependent on T cell expression of  $A_{2A}R$  (fig. S13, E to H).

We next tested whether inosine could also promote the efficacy of anti-CTLA-4 therapy in the presence of a complex microbiota. We first used a gnotobiotic model where mice are stably colonized with a defined microbiota consisting of 12 bacterial species, referred to as Oligo-Mouse-Microbiota-12 (Oligo-MM<sup>12</sup>) (36), which lacks *B. pseudolongum*. We found that inosine was able to promote the antitumor effects of anti-CTLA-4, with reduced



**Fig. 4. The metabolite inosine promotes immunotherapy response in mouse models of intestinal cancer, bladder cancer, and melanoma. (A)** Schematic overview of experimental setup to assess the effect of inosine in SPF *Msh2<sup>LoxP/LoxP</sup> Villin-Cre* mice.

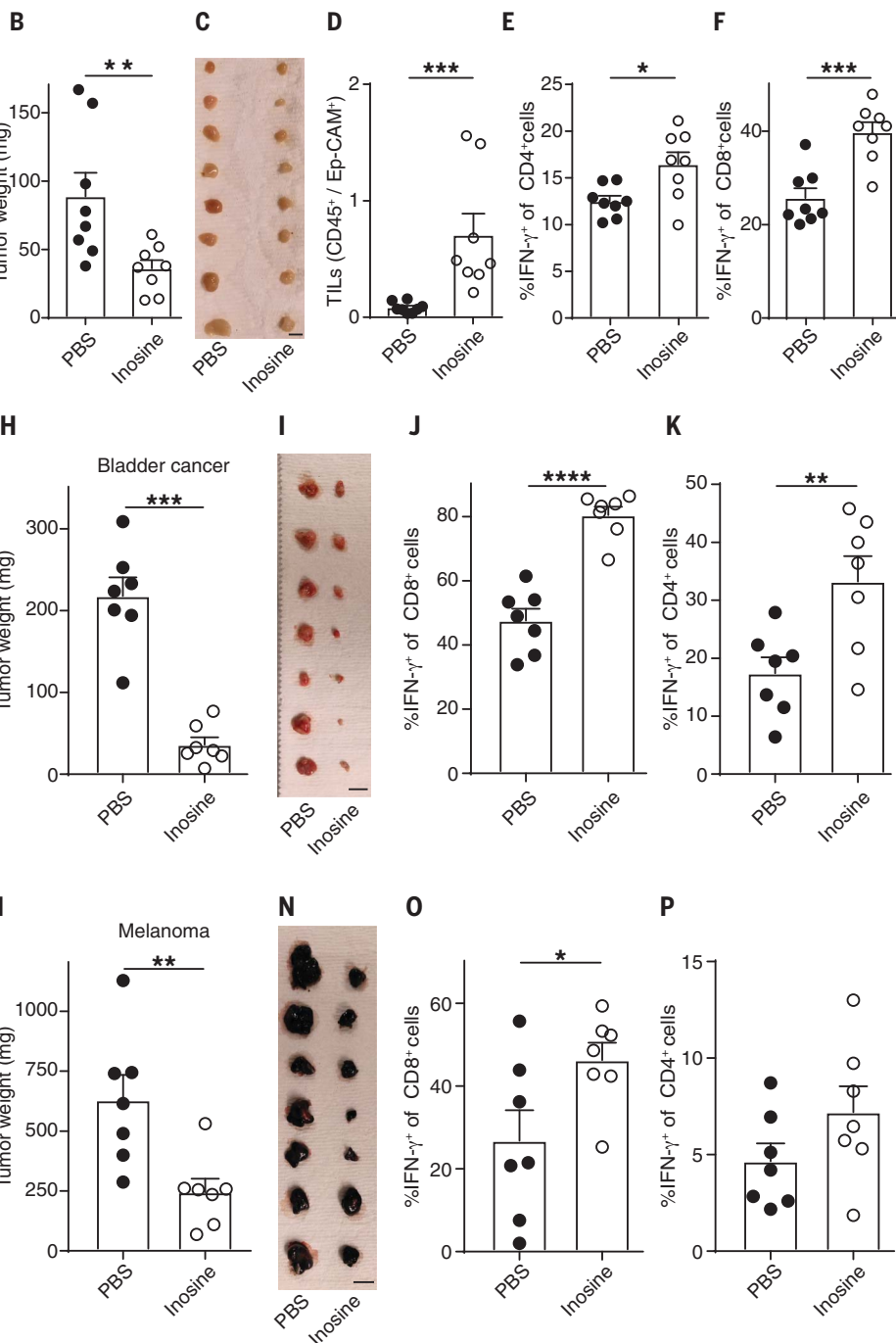
On day 312, mice received antibiotics orally (ampicillin, 1 mg/ml; colistin, 1 mg/ml; and streptomycin, 5 mg/ml) until the end of the experiment, and on day 319 mice received 100  $\mu$ g anti-CTLA-4 i.p. and 20  $\mu$ g CpG i.p. (both five times every 72 hours) and PBS or inosine (300 mg per kilogram of body weight) orally through gavage daily.

**(B)** Tumor weight, **(C)** representative pictures of dissected tumors, **(D)** quantification of TILs and splenic IFN- $\gamma$ <sup>+</sup> production of **(E)** CD4<sup>+</sup> and **(F)** CD8<sup>+</sup> T cells is shown. **(G)** Schematic overview of experimental setup to assess the effect of inosine on bladder cancer. GF animals were subcutaneously injected in the flank with  $2 \times 10^6$  MB49 bladder cancer cells. Upon development of palpable tumors, mice were treated with 100  $\mu$ g anti-CTLA-4 i.p. and 20  $\mu$ g CpG i.p. (three times every 72 hours) and PBS or inosine (300 mg per kilogram of body weight) orally through gavage daily.

**(H)** Tumor weight and **(I)** pictures of tumors are shown. Quantification of IFN- $\gamma$ <sup>+</sup> in **(J)** CD8<sup>+</sup> or **(K)** CD4<sup>+</sup> cells in the tumor are shown. **(L)** Schematic overview of experimental setup to assess the effect of inosine on melanoma. GF animals were subcutaneously injected in the flank with  $1 \times 10^6$  B16-F10 melanoma cells. Upon development of palpable tumors, mice were treated with 100  $\mu$ g anti-CTLA-4 i.p. and 20  $\mu$ g CpG i.p. (three times every 72 hours) and PBS or inosine (300 mg per kilogram of body weight) orally through gavage daily.

**(M)** Tumor weight and **(N)** pictures of tumors are shown. Quantification of IFN- $\gamma$ <sup>+</sup> in **(O)** CD8<sup>+</sup> or **(P)** CD4<sup>+</sup> cells in the tumor are shown. Data indicate mean  $\pm$  SEM. [(A) to (F)]  $n = 8$  mice per group. [(G) to (P)]  $n = 7$  mice per group. \* $P < 0.05$ ; \*\* $P < 0.01$ ; \*\*\* $P < 0.001$ ; \*\*\*\* $P < 0.0001$ . All scale bars, 1 cm.

tumor size and increased intra-tumoral IFN- $\gamma$ <sup>+</sup>CD8<sup>+</sup> and IFN- $\gamma$ <sup>+</sup>CD4<sup>+</sup> T cells even in gnotobiotic Oligo-MM<sup>12</sup> mice (fig. S14, A to D). We also found that inosine could promote the efficacy of anti-CTLA-4 in SPF mice, which contain a highly diverse microbiota (fig. S14, E to H). We then examined whether



daily. **(M)** Tumor weight and **(N)** pictures of tumors are shown. Quantification of IFN- $\gamma$ <sup>+</sup> in **(O)** CD8<sup>+</sup> or **(P)** CD4<sup>+</sup> cells in the tumor are shown. Data indicate mean  $\pm$  SEM. [(A) to (F)]  $n = 8$  mice per group. [(G) to (P)]  $n = 7$  mice per group. \* $P < 0.05$ ; \*\* $P < 0.01$ ; \*\*\* $P < 0.001$ ; \*\*\*\* $P < 0.0001$ . All scale bars, 1 cm.

*B. pseudolongum* needed to be viable to enhance anti-CTLA-4 efficacy. Whereas gavage of live *B. pseudolongum*, with or without antibiotic pretreatment, enhanced anti-CTLA-4 effects in SPF mice (fig. S14, E to H), heat-killed *B. pseudolongum* was unable to boost the effects of ICB therapy, likely because of

the inability to produce inosine (fig. S14, E to H).

In addition to direct stimulation of T cells, inosine could potentially affect tumor cells directly through altering tumor cell survival or susceptibility to T cell-mediated killing. However, direct in vitro exposure of MC38

tumor cells to inosine did not modulate tumor cell viability (fig. S15A), and pretreatment of MC38 tumor cells before coculture with activated tumor-specific T cells did not promote or inhibit T cell-mediated killing of tumor cells (fig. S15B), further supporting the conclusion that the antitumor effect of inosine was mediated primarily through T cells.

Together, these data indicate that the effect of inosine on T cells required sufficient costimulation (likely by DCs), IL-12 receptor engagement for  $T_H1$  differentiation, and IFN- $\gamma$  production for efficient antitumor immunity. Indeed, conventional dendritic cells (cDCs), not macrophages, were found to be the primary source of IL-12 (fig. S16, A and B). To further assess the role of cDCs in ICB-bacteria cotherapy, bone marrow (BM) cells from cDC-DTR mice (DTR, diphtheria toxin receptor) were transferred into lethally  $\gamma$ -irradiated recipient SPF mice to allow for inducible, conditional depletion of cDCs. After BM reconstitution, mice were treated with antibiotics and gavaged with a mixture of the three previously identified ICB-promoting bacteria: *B. pseudolongum*, *L. johnsonii*, and *Olsenella* species. Ten weeks later, mice were implanted with MC38 cells and when palpable tumors were established, cDCs were depleted by injection of diphtheria toxin followed by anti-CTLA-4 treatment (fig. S16C). Depletion of cDCs led to larger tumors (fig. S16D), a significant reduction in intratumoral CD8 $^{+}$  and CD4 $^{+}$  T cell frequencies and IFN- $\gamma$  production (fig. S16E), and markedly reduced IFN- $\gamma$  production and proliferation of splenic CD8 $^{+}$  and CD4 $^{+}$  T cells (fig. S16F). Therefore, depletion of cDCs strongly impeded the ability of the bacteria-elicited ICB response to reduce established tumors, which indicated the requirement for continuous antigen presentation, IL-12 production, and T cell costimulation by cDCs for efficient ICB therapy. The critical involvement of cDC and IL-12 has previously been reported for anti-PD-1 treatment (37).

Because enhanced  $T_H1$  immunity is generally considered to be beneficial for most antitumor responses [reviewed in (38)], we next determined whether intestinal colonization with the isolated ICB-promoting bacteria or treatment with inosine would be equally effective in other tumor models. First, we tested the ICB-promoting effect of *B. pseudolongum*, *L. johnsonii*, and *Olsenella* species in SPF *Msh2<sup>LoxP/LoxP</sup>Villin-Cre* (39) animals that have conditional inactivation of *Msh2* (a DNA mismatch repair gene) in intestinal epithelial cells and develop adenocarcinomas in the small intestine. Previous reports have shown greater efficacy of ICB in mismatch repair-deficient (MMRD) cancer in the clinical setting (15, 40). In the *Msh2<sup>LoxP/LoxP</sup>Villin-Cre* model, anti-

CTLA-4 treatment alone (without the addition of ICB-promoting bacteria) led to reduced tumor weights and EpCam $^{+}$ Lgr5 $^{+}$  cells in the tumor, markers for epithelial cell stemness, and increased T cell activation and immune cell infiltration in the tumor (fig. S17, A to F). Cotreatment with ICB-promoting bacteria markedly boosted the effect of anti-CTLA-4 (fig. S17G), leading to a further reduction of tumor weight and EpCam $^{+}$ Lgr5 $^{+}$  cells together with drastically enhanced T cell activation and immune cell infiltration in the tumor compared with control bacteria (fig. S17, H to L). These results suggested that bacterial cotherapy may optimize treatment regimens in MMRD tumors. Notably, anti-IL-12p75 treatment almost completely abrogated the effect of ICB-promoting, anti-CTLA-4 cotherapy in *Msh2<sup>LoxP/LoxP</sup>Villin-Cre* tumors (fig. S17, G to L), which supports a critical role for inosine-dependent up-regulation of IL12R $\beta$ 2 on T cells and cDC production of IL-12 and corroborates similar findings upon simultaneous depletion of IL-12 and IL-23, using anti-IL-12p40 treatment (6, 8). As oxaliplatin and anti-PD-L1 cotreatment is a more commonly used therapy in clinics, we also confirmed that ICB-promoting bacteria enhanced the efficacy of oxaliplatin and anti-PD-L1 cotreatment in SPF *Msh2<sup>LoxP/LoxP</sup>Villin-Cre* animals (fig. S18).

As *B. pseudolongum* was enriched in AOM/DSS tumors of ICB-treated animals (Fig. 1, F and G), and *Bifidobacteria* were previously associated with improved ICB-therapy efficacy in cancer patients (9), we wondered whether *Bifidobacteria* were also enriched in *Msh2<sup>LoxP/LoxP</sup>Villin-Cre* tumors of ICB-treated mice. While the total amount of tumor-associated bacteria did not change with anti-CTLA-4 or anti-PD-L1 treatment (fig. S19A), ICB treatment led to specific enrichment of tumor-associated *Bifidobacteria* (fig. S19B). A recent report revealed that, compared with other tissues, *Bifidobacteria* colonize tumors, likely owing to the hypoxic environment often found in tumors (41). At this point, it is unclear why *Bifidobacteria* seem to preferentially accumulate in ICB-treated conditions.

We next tested the ICB-promoting effect of *B. pseudolongum*, *L. johnsonii*, and *Olsenella* species in SPF *Apc<sup>2lox14/+</sup>;Kras<sup>LSL-G12D/+</sup>;Fabpl-Cre* (42) mice, which have conditional *Apc* deficiency and activation of *Kras* specifically in colonocytes. In this model of CRC, anti-CTLA-4 treatment did not improve survival compared with isotype-treated animals (fig. S20, A and B), and transfer of the ICB-promoting bacteria failed to enhance survival (fig. S20, C and D), revealing a limitation of bacterial cotherapy in this model.

Finally, we tested whether the bacterial metabolite inosine in combination with costimulation was sufficient to enhance the ef-

ficacy of ICB therapy in other cancer models. Oral administration of inosine together with anti-CTLA-4 and CpG treatment in SPF *Msh2<sup>LoxP/LoxP</sup>Villin-Cre* mice led to significant reduction in tumor weight and a corresponding increase in splenic IFN- $\gamma$ <sup>+</sup>CD4 $^{+}$  and IFN- $\gamma$ <sup>+</sup>CD8 $^{+}$  T cells (Fig. 4, A to F). Notably, inosine together with CpG was also found to be effective in promoting the efficacy of anti-CTLA-4 in two additional murine cancers—bladder cancer and melanoma. Specifically, inosine plus CpG administration to GF mice that had been injected with MB49 murine bladder cancer cells was able to significantly enhance the ability of anti-CTLA-4 to reduce tumor weight and increase the proportion of IFN- $\gamma$ <sup>+</sup>CD4 $^{+}$  and IFN- $\gamma$ <sup>+</sup>CD8 $^{+}$  T cells infiltrating the tumors (Fig. 4, G to K). Similarly, inosine plus CpG augmented the ability of anti-CTLA-4 to mediate antitumor immunity in a heterotopic mouse model of melanoma (Fig. 4, L to P).

Our results identify a *B. pseudolongum* strain isolated from ICB-treated CRC tumors as a key commensal intestinal bacterial species that is capable of boosting a cDC-dependent  $T_H1$  cell circuit to greatly enhance the effect of ICB therapies in mouse models of intestinal and epithelial tumors (fig. S21). These data support the premise that modification of the microbiota or targeted bacterial therapies with defined microbial consortia may provide a promising adjuvant therapy to ICB in CRC and other cancers. Although isolated from mice, all three ICB-promoting bacteria are also found in humans, indicating their potential for translation (43–45). Furthermore, we analyzed published human fecal microbiome metagenomic datasets (8, 9, 46) and found a trend, although not significant, where *B. pseudolongum* was enriched [up to 2.4-fold (8)] in responders compared with nonresponding cancer patients (fig. S22A). At the genus level, *Bifidobacteria* were also enriched (albeit nonsignificantly) in responders compared with nonresponders [5.9-fold (9)] (fig. S22B), with the species *B. longum* and *B. adolescentis* significantly enriched (47). Owing to the low abundance of *B. pseudolongum* in fecal samples of adults, higher-powered studies with larger sample sizes will be needed to confirm this trend. We also identified inosine as a key bacterial-derived metabolite acting through T cell-specific A $_2$ A $_R$  signaling to promote  $T_H1$  cell activation in a context-dependent manner. We further confirmed that *A. muciniphila*, which is known to be associated with responsiveness to ICB therapy in humans (8), uses inosine-A $_2$ A $_R$  signaling for its ICB-promoting effect. In light of our findings, one might caution against the blockade of inosine-A $_2$ A $_R$  signaling for cancer immunotherapy, as this may negate any positive effect provided by beneficial microbes. We suggest that A $_2$ A $_R$



signaling is likely an integral antitumor pathway for bacterial-ICB cotherapies. Further investigation of the effects of xanthine and hypoxanthine, degradation products of inosine, are warranted.

## REFERENCES AND NOTES

1. F. S. Hodi *et al.*, *N. Engl. J. Med.* **363**, 711–723 (2010).
2. J. R. Brahmer *et al.*, *N. Engl. J. Med.* **366**, 2455–2465 (2012).
3. R. J. Motzer *et al.*, *N. Engl. J. Med.* **373**, 1803–1813 (2015).
4. H. Borghaei *et al.*, *N. Engl. J. Med.* **373**, 1627–1639 (2015).
5. T. N. Gide, J. S. Wilmott, R. A. Scolyer, G. V. Long, *Clin. Cancer Res.* **24**, 1260–1270 (2018).
6. M. Vétizou *et al.*, *Science* **350**, 1079–1084 (2015).
7. A. Sivan *et al.*, *Science* **350**, 1084–1089 (2015).
8. B. Routy *et al.*, *Science* **359**, 91–97 (2018).
9. V. Matson *et al.*, *Science* **359**, 104–108 (2018).
10. V. Gopalakrishnan *et al.*, *Science* **359**, 97–103 (2018).
11. C. M. Dejea *et al.*, *Science* **359**, 592–597 (2018).
12. J. C. Arthur *et al.*, *Science* **338**, 120–123 (2012).
13. N. Iida *et al.*, *Science* **342**, 967–970 (2013).
14. S. Viaud *et al.*, *Science* **342**, 971–976 (2013).
15. D. T. Le *et al.*, *N. Engl. J. Med.* **372**, 2509–2520 (2015).
16. S. C. Wei *et al.*, *Cell* **170**, 1120–1133.e17 (2017).
17. K. A. Ward-Hartstonge, R. A. Kemp, *Clin. Transl. Immunology* **6**, e154 (2017).
18. R. F. Schwabe, C. Jobin, *Nat. Rev. Cancer* **13**, 800–812 (2013).
19. G. A. Lugli *et al.*, *Appl. Environ. Microbiol.* **85**, e03065-18 (2019).
20. D. W. Zheng *et al.*, *Nat. Commun.* **9**, 1680 (2018).
21. T. Tanoue *et al.*, *Nature* **565**, 600–605 (2019).
22. F. Wang, Q. Yin, L. Chen, M. M. Davis, *Proc. Natl. Acad. Sci. U.S.A.* **115**, 157–161 (2018).
23. A. A. Welihinda, M. Kaur, K. Greene, Y. Zhai, E. P. Amento, *Cell. Signal.* **28**, 552–560 (2016).
24. G. Haskó *et al.*, *J. Immunol.* **164**, 1013–1019 (2000).
25. B. He *et al.*, *J. Exp. Med.* **214**, 107–123 (2017).
26. B. Csóka *et al.*, *FASEB J.* **22**, 3491–3499 (2008).
27. A. Ohta *et al.*, *Proc. Natl. Acad. Sci. U.S.A.* **103**, 13132–13137 (2006).
28. S. Vigano *et al.*, *Front. Immunol.* **10**, 925 (2019).
29. C. Cekic, J. Linden, *Cancer Res.* **74**, 7239–7249 (2014).
30. W. Lasek *et al.*, *Acta Pharm.* **65**, 171–180 (2015).
31. T. Lioux *et al.*, *J. Med. Chem.* **59**, 10253–10267 (2016).
32. C. Yao *et al.*, *Nat. Commun.* **4**, 1685 (2013).
33. B. Samten *et al.*, *J. Immunol.* **181**, 2056–2064 (2008).
34. B. Samten *et al.*, *J. Immunol.* **174**, 6357–6363 (2005).
35. B. Jahrsdörfer, G. J. Weiner, *Update Cancer Ther.* **3**, 27–32 (2008).
36. S. Brugioux *et al.*, *Nat. Microbiol.* **2**, 16215 (2016).
37. C. S. Garis *et al.*, *Immunity* **49**, 1148–1161.e7 (2018).
38. D. Chraa, A. Naim, D. Olive, A. Badou, *J. Leukoc. Biol.* **105**, 243–255 (2019).
39. M. H. Kuchlerapati *et al.*, *Gastroenterology* **138**, 993–1002.e1 (2010).
40. D. T. Le *et al.*, *Science* **357**, 409–413 (2017).
41. Y. Shi *et al.*, *J. Exp. Med.* **217**, e20192282 (2020).
42. K. M. Haigis *et al.*, *Nat. Genet.* **40**, 600–608 (2008).
43. F. Turroni *et al.*, *Appl. Environ. Microbiol.* **75**, 1534–1545 (2009).
44. R. D. Pridmore, A. C. Pittet, F. Praplan, C. Cavadini, *FEMS Microbiol. Lett.* **283**, 210–215 (2008).
45. F. E. Dewhirst *et al.*, *Int. J. Syst. Evol. Microbiol.* **51**, 1797–1804 (2001).
46. A. E. Frankel *et al.*, *Neoplasia* **19**, 848–855 (2017).
47. B. A. Helmink, M. A. W. Khan, A. Hermann, V. Gopalakrishnan, J. A. Wargo, *Nat. Med.* **25**, 377–388 (2019).

## ACKNOWLEDGMENTS

We thank C. Thomson, A. Ignacio Silvestre da Silva, M. Wyss, M. Davoli-Ferreira, J. Yee, and M. Koegler for their help in tackling large-scale experiments, their technical knowledge, and critical feedback. We thank M. Dickey for performing the Ussing chamber experiments. **Funding:** L.F.M. was supported by the Early Postdoc Mobility Fellowship from the Swiss National Science Foundation. K.D.M. is supported by a Canadian Institutes of Health Research (CIHR) grant (PJT-165930), a Canadian Foundation for Innovation (CFI) John R. Evans Leaders Fund (JELF) grant, the Cumming School of Medicine, and the Carole May Yates Memorial Endowment for Cancer Research. M.B.G. is supported by CIHR (PJT-156073)

and CFI-JELF. R.A.G. is supported by a CFI-JELF (34986) and the International Microbiome Centre (IMC). K.B. is supported by a Canada Graduate Scholarship from the Natural Sciences and Engineering Research Council of Canada (NSERC). I.A.L. is supported by an Alberta Innovates Translational Health Chair. J.S. is supported by a CIHR grant and a Terry Fox Research Institute grant. The IMC is supported by the Cumming School of Medicine, University of Calgary, Western Economic Diversification (WED) and Alberta Economic Development and Trade (AEDT), Canada. **Author contributions:** L.F.M., R.B., N.P., N.C.A.C., K.B., H.R., S.P., R.A.G., I.A.L., and M.G. performed experiments and analyzed data. L.F.M., M.B.G., and K.D.M. wrote the manuscript, and all authors revised the manuscript and approved its final version. J.S. provided A<sub>2A</sub>R-deficient mice. L.F.M. and K.D.M. conceived of the project. K.D.M. and M.B.G. supervised the project. **Competing interests:** J.S. is a permanent member of the scientific advisory board of Surface Oncology and owns stocks of Surface Oncology. L.F.M. and K.D.M. are inventors on patent US 62/929,340 submitted by UTI Limited Partnership that covers the use of bacterial species and inosine as ICB adjuvants. All other authors declare no competing interests. **Data and materials availability:** Sequencing data from the V4 region of the 16S rRNA gene of tumor-associated and fecal bacteria is deposited in the BioProject database (BioProject ID: PRJNA528297; <https://www.ncbi.nlm.nih.gov/bioproject/528297>).

## SUPPLEMENTARY MATERIALS

[science.sciencemag.org/content/369/6510/1481/suppl/DC1](https://science.sciencemag.org/content/369/6510/1481/suppl/DC1)  
Materials and Methods  
Figs. S1 to S22  
Tables S1 and S2  
References (48–65)  
MDAR Reproducibility Checklist

[View/request a protocol for this paper from Bio-protocol.](#)

20 April 2020; resubmitted 8 July 2020  
Accepted 30 July 2020  
Published online 13 August 2020  
10.1126/science.abc3421

## WATER STRUCTURE

# Reversible structural transformations in supercooled liquid water from 135 to 245 K

Loni Kringle\*, Wyatt A. Thornley\*, Bruce D. Kay†, Greg A. Kimmel†

A fundamental understanding of the unusual properties of water remains elusive because of the limited data at the temperatures and pressures needed to decide among competing theories. We investigated the structural transformations of transiently heated supercooled water films, which evolved for several nanoseconds per pulse during fast laser heating before quenching to 70 kelvin (K). Water's structure relaxed from its initial configuration to a steady-state configuration before appreciable crystallization. Over the full temperature range investigated, all structural changes were reversible and reproducible by a linear combination of high- and low-temperature structural motifs. The fraction of the liquid with the high-temperature motif decreased rapidly as the temperature decreased from 245 to 190 K, consistent with the predictions of two-state "mixture" models for supercooled water in the supercritical regime.

Water has many anomalous properties compared with "simple" liquids (1–3). These anomalies, which are related to temperature-dependent changes in the hydrogen-bonding network [for example, (4)], are typically enhanced in supercooled water. However, no consensus has emerged on whether the changes arise from several structurally distinct components in the liquid or from a unimodal, continuous distribution of structures (2–7). Models that have been developed to explain water's properties include the liquid-liquid critical point (LLCP) scenario (8, 9) and the singularity-free scenario (10). The main difficulty in determining which of the models is correct is the limited data in the relevant temperature,  $T$ , and pressure,  $P$ , ranges. For water at ambient pressures, which is the focus of this work, data are largely missing from 160 to 235 K ("no man's land") because of rapid crystallization of the supercooled liquid (2, 3). Whether rapid crystallization is just an experimental obstacle or a fundamental problem signaling the inability of water to thermally equilibrate before crystallization is also a major unanswered question (9, 11, 12).

We used infrared (IR) spectroscopy to investigate the structural transformations of transiently heated, supercooled water with nanosecond time resolution. Because of the high cooling rates for the experiments and the low temperature at which all of the IR spectra were obtained, the results were related to the "inherent structure" of water as determined in molecular dynamics (MD) simulations (3, 6, 13). The results show that water relaxed from its initial configuration to a steady-state configuration before the onset of crystallization for the experimentally accessible temperature range (135 K <  $T$  < 245 K).

These structural changes were reversible over the full temperature range. Finally, water's inherent structure could be reproduced by a linear combination of two structural motifs corresponding to the liquid hyperquenched from high temperatures and water isothermally annealed at the glass transition temperature,  $T_g$  ( $\approx 136$  K). These results provided support for the hypothesis that supercooled water at low pressure can be described as a mixture of two, structurally distinct components from 135 to 245 K (6, 9, 14–23).

Water films with typical thicknesses of  $\sim 15$  nm were adsorbed on Pt(111) or graphene/Pt(111) in ultrahigh vacuum at 70 K and then heated at  $\sim 10^{10}$  K/s with nanosecond laser pulses (Fig. 1A) (24, 25). For each heat pulse,  $T(t)$ , the films spent  $\sim 3$  ns near the maximum

temperature,  $T_{\max}$ , before rapidly cooling to the base temperature (Fig. 1B). The changes in water's structure were monitored with IR spectroscopy. The results should be representative of bulk water and not strongly influenced by the nanoscale thickness of the films (supplementary text, section A).

Figure 1C shows the evolution of the IR spectra in the OH-stretch region for water films prepared with different initial configurations and then heated to  $T_{\max} = 215$  K. Isothermally annealing the water films at or near  $T_g$  for  $\sim 100$  s produced films with an IR spectrum characteristic of low-density amorphous ice (LDA) (2, 3) (plot a in Fig. 1C, blue line). Pulsed heating to high temperatures produced films with a different characteristic IR spectrum: plot a in Fig. 1C shows an example for a film heated to 297 K for three pulses (red line). The IR spectrum of crystalline ice (CI) is also shown for comparison (plot a in Fig. 1C, black line). Because the IR spectra were sensitive to the hydrogen-bonding configuration of the water molecules (23, 26, 27), these spectra indicated that there were substantial structural differences between the three films. We refer to water films prepared by pulsed heating to 297 K as "hyperquenched water" (HQW). For the experiments reported below, the initial configuration of the water was either LDA or HQW.

After heating the water to 215 K, the IR spectra evolved as the number of heat pulses,  $N_p$ , increased (plots b and c in Fig. 1C and fig. S1). For both LDA and HQW, the spectra observed just before the onset of measurable crystallization (e.g.,  $N_p = 670$ ) were the same

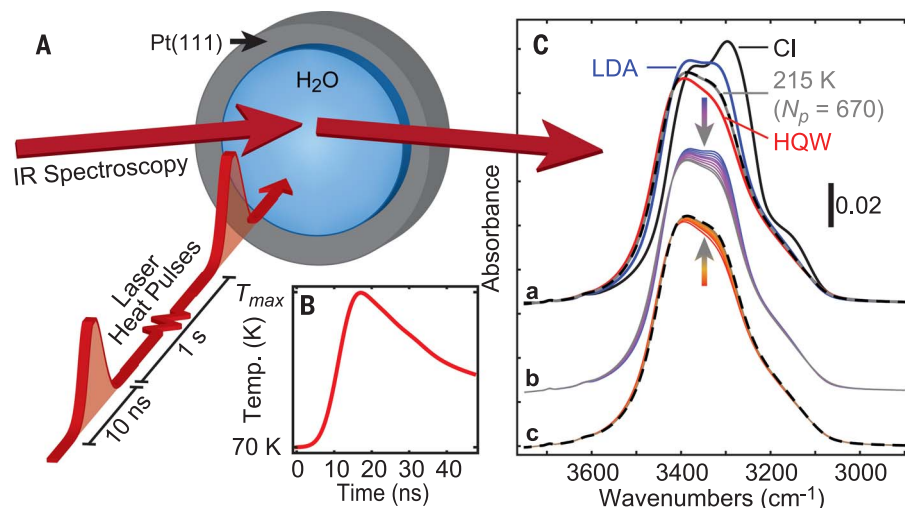


**Fig. 1. Experimental approach and IR spectra.** (A) Schematic of transiently heating nanoscale water films adsorbed on Pt(111) [or graphene/Pt(111)]. (B) Calculated temperature (Temp.) versus time,  $T(t)$ , during a typical heat pulse. (C) IR spectra of transiently heated, 50-monolayer water films on graphene/Pt(111) measured at 70 K. In plot a, spectra for HQW, LDA, and CI are all distinct. In plot b, LDA was heated to 215 K for  $N_p = 4, 10, 19, 31, 55, 100, 210$ , and 670. In plot c, HQW was heated to 215 K for  $N_p = 1, 2, 4, 7, 31, 100$ , and 670. For plots b and c, the arrows indicate the increasing  $N_p$ .

Physical Sciences Division, Pacific Northwest National Laboratory, P.O. Box 999, Richland, WA 99352, USA.

\*These authors contributed equally to this work.

†Corresponding author. Email: gregory.kimmel@pnnl.gov (G.A.K.); bruce.kay@pnnl.gov (B.D.K.)



(plot a in Fig. 1C, gray and dashed black lines). Further pulsed heating ultimately led to crystallization of the water films (fig. S2). Similar evolution of the IR spectra was observed for a wide range of pulsed-heating temperatures ( $170\text{ K} \leq T_{\max} \leq 260\text{ K}$ ). In all cases, the IR spectra of the transiently heated water could be reproduced by a linear combination of the LDA, HQW, and CI spectra, and the mole fraction of LDA, HQW, and CI ( $f_{\text{LDA}}$ ,  $f_{\text{HQW}}$ , and  $f_{\text{CI}}$ , respectively) in the water film could be determined (25).

Figure 2 shows  $f_{\text{LDA}}$ ,  $f_{\text{HQW}}$ , and  $f_{\text{CI}}$  versus  $N_p$  for  $T_{\max} = 215\text{ K}$ . For HQW and LDA,  $f_{\text{HQW}}$  asymptotically approached  $\sim 0.64$  before crystallization (solid and open circles). Similarly,  $f_{\text{LDA}}$  approached  $\sim 0.36$  (solid and open squares). Evolution of water's structure from LDA or HQW to a common intermediate structure was also observed for other temperatures (e.g., fig. S3). An assumption of the current approach is that transiently heating water multiple times near  $T_{\max}$  produced the same structural changes that would be observed versus time in an isothermal experiment (supplementary text, section B).

The pulsed-heating experiments allowed water films to be brought into the supercooled region multiple times. Thus, changing  $T_{\max}$  during an experiment allowed us to explore the reversibility of the structural changes in the transiently heated water films. Figure 3A shows  $f_{\text{HQW}}$  and  $f_{\text{LDA}}$  versus  $N_p$  where  $T_{\max}$  was repeatedly cycled between 215 K for 100 pulses and 252 K for 10 pulses (a subset of the corresponding IR spectra is shown in fig. S4). The key observation is that each time  $T_{\max}$  changed, the structure quickly evolved toward a new steady-state configuration characteristic of that temperature.

Reversible structural changes were also observed for water when the temperature was cycled between 135 K (isothermal heating for 130 s) and 215 K (pulsed heating for  $1 \leq N_p \leq 400$ ) (Fig. 3B and fig. S4B). Because of the slower relaxation kinetics for LDA compared with HQW, more heat pulses were required to approach the steady-state configuration in that case. As a result, the onset for crystallization occurred after only two temperature cycles in Fig. 3B (black triangles). However, for both experiments, the structural changes seen at 215 K could be reversed by simply changing the temperature. More examples of reversible structural transformations for supercooled water at other temperatures are shown in fig. S5. The results in Figs. 1 to 3 show that the observed changes in the water are not irreversible structural transformations associated with crystallization (11) or crossing a spinodal (1). The characteristic relaxation times for HQW and LDA compared with ice nucleation and growth rates at  $T_{\max} = 215\text{ K}$  are discussed in the supplementary text, section C.

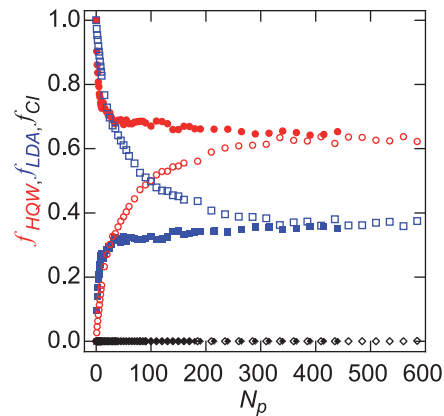


**Fig. 2. Structural relaxation for HQW and LDA.**

$f_{\text{HQW}}$  (circles),  $f_{\text{LDA}}$  (squares), and  $f_{\text{CI}}$  (diamonds) versus  $N_p$  for  $T_{\max} = 215\text{ K}$  and initial configuration of either LDA (open symbols) or HQW (solid symbols).

The results suggest that the (quenched) IR spectra observed just before crystallization reflected the steady-state structure of water at  $T_{\max}$ . The steady-state spectra,  $S(T_{\max}, \omega)$ , could all be fit as linear combinations of the HQW and LDA spectra [ $S_{\text{HQW}}(\omega)$  and  $S_{\text{LDA}}(\omega)$ , respectively] (fig. S6):

$$S(T_{\max}, \omega) = f_{\text{HQW}}^{\text{SS}}(T_{\max}) \cdot S_{\text{HQW}}(\omega) + f_{\text{LDA}}^{\text{SS}}(T_{\max}) \cdot S_{\text{LDA}}(\omega)$$

where  $\omega$  is the frequency and  $f_{\text{HQW}}^{\text{SS}}$  ( $f_{\text{LDA}}^{\text{SS}}$ ) is the fraction of the water corresponding to HQW (LDA) at steady state. Figure 4A shows  $f_{\text{HQW}}^{\text{SS}}(T_{\max})$  (circles) determined from the average of measurements of several individual experiments with LDA and HQW films on both Pt(111) and graphene/Pt(111) at each temperature (fig. S7). The red line shows a fit to the data using the logistic function (23)

$$f_{\text{HQW}}^{\text{SS}}(T) = \{1 + \exp[-(T - T_0)/\Delta T]\}^{-1}$$

with  $T_0 = 210 \pm 3\text{ K}$  and  $\Delta T = 8.5\text{ K}$ . For  $T_{\max} \leq 170\text{ K}$ , the steady-state IR spectra of the tran-

siently heated water films do not change (figs. S8 and S9), indicating that water over a wide temperature range has essentially the same structure as LDA.

Two-component models propose that water at ambient pressure is an inhomogeneous liquid with regions of higher density and entropy [a high-density liquid (HDL)] and lower density and entropy [a low-density liquid (LDL)] (6, 16, 19, 22). The ability to decompose the steady-state IR spectra of supercooled water into a linear combination of two components is consistent with these models, as were the differences between the HQW and LDA spectra, which indicated a higher proportion of local tetrahedral configurations in LDA (26, 27). IR spectra calculated from classical MD simulations at supercooled temperatures also agreed qualitatively with the IR spectra presented here (26).

The observation that  $f_{\text{HQW}}^{\text{SS}}$  was  $\sim 1$  for  $T_{\max} > 245\text{ K}$  was probably related to the rapid structural equilibration of mildly supercooled water and the experiment's finite cooling rate. At high temperatures, water maintained its equilibrium structure near  $T_{\max}$ . However, as the sample cooled, the relaxation rate slowed to the point where the structural changes could not keep up, quenching the film. Thus, the structural information from temperatures above  $\sim 245\text{ K}$  was lost as the samples cooled. Although HQW was probably a mixture of HDL and LDL (2, 3), the experiments did not allow us to unambiguously determine its composition. Furthermore, reported values for  $f_{\text{HDL}}(T)$  vary substantially, which made it difficult to decide which, if any, of these could be used to assign the composition of HQW (supplementary text, section D, and figs. S10 and S11). By contrast, we assume that LDA was essentially 100% LDL because it was prepared by annealing at  $T_g$ .

Previous experiments that used x-ray, Raman, and IR spectroscopy and the optical Kerr effect have shown bimodal characteristics for water above the homogeneous nucleation temperature

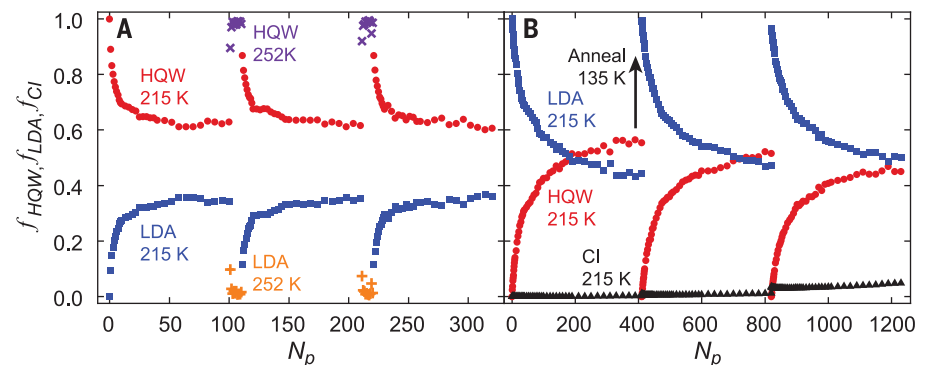


**Fig. 3. Reversible structural transformations.** (A and B)  $f_{\text{HQW}}(N_p)$  and  $f_{\text{LDA}}(N_p)$  for pulse-heating at (A)  $T_{\max} = 215$  and  $252\text{ K}$  or (B)  $T_{\max} = 215\text{ K}$  and isothermal annealing at  $135\text{ K}$ . The red circles and purple  $\times$ 's show  $f_{\text{HQW}}$  for  $T_{\max} = 215$  and  $252\text{ K}$ , respectively. The blue squares and orange crosses show  $f_{\text{LDA}}$  for  $T_{\max} = 215$  and  $252\text{ K}$ , respectively. In (B),  $f_{\text{CI}}$  (black triangles) is also shown.

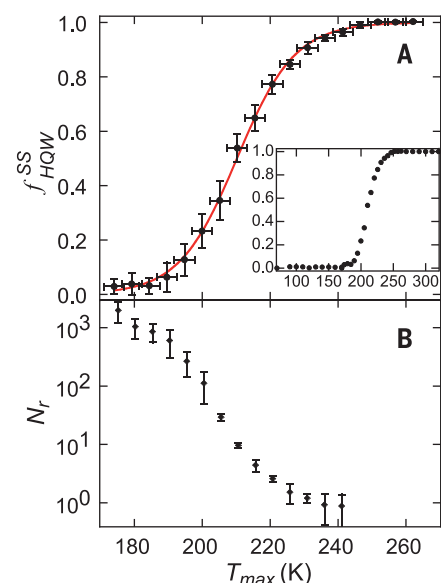


**Fig. 4. Steady-state structure and relaxation rates.** (A)  $f_{\text{HQW}}^{\text{SS}}$  versus  $T_{\text{max}}$  (black circles). The vertical error bars show 1 SD for the measured values, whereas the horizontal error bars arise from uncertainty in the laser power. A logistic function (red line) fits the data. The inset shows  $f_{\text{HQW}}^{\text{SS}}(T_{\text{max}})$  over a wider temperature range. (B) Characteristic number of pulses to relax HQW,  $N_r$ , versus  $T_{\text{max}}$ .

(~235 K) (17, 18, 28, 29). Our results were qualitatively consistent with these experiments. However, because all of the IR spectra reported here were measured at the same temperature,  $T_{\text{measure}} = 70$  K, the observed changes were not caused by thermal effects associated with measurements made at different temperatures (30). Instead, the quenched state reflected the structure of water at  $T_{\text{max}}$ , but with reduced thermal broadening because of the low temperature for the IR measurements. Thus, our results correspond to the “inherent structures” obtained from MD simulations where the systems were instantaneously quenched to 0 K (3, 6, 13) (supplementary text, section E).

The characteristic number of heat pulses,  $N_r$ , for water to relax was determined by fitting  $f_{\text{HQW}}$  with a stretched exponential function (eq. S2). Figure 4B shows  $N_r$  for experiments with HQW. For  $T_{\text{max}} > 240$  K,  $N_r$  could not be determined because there was little change in the structure. At lower temperatures,  $N_r$  rapidly increased from ~1 at  $T_{\text{max}} = 236$  K to ~2000 at  $T_{\text{max}} = 175$  K. The structural relaxation time,  $\tau_{\text{rel}}$ , was estimated by multiplying  $N_r$  by a characteristic duration for the heat pulses,  $\delta t_{\text{pulse}} \sim 3$  ns (25). This suggests that  $\tau_{\text{rel}}$  increased from ~3 ns to 6  $\mu$ s as  $T_{\text{max}}$  decreased from 236 to 175 K. The rapid increase in  $N_r$  (or  $\tau_{\text{rel}}$ ) is consistent with MD simulations (31, 32) and experiments on confined water (3).

The experiments reported here focused on water's relaxation before crystallization. To fully crystallize the films would have taken much longer (fig. S2), particularly for  $T_{\text{max}} < 215$  K, and was not explored in detail. An earlier report, which investigated the ice nucleation rate in transiently heated water films, followed the crystallization to completion for  $T_{\text{max}} \geq 212$  K (33). For 50-monolayer films, the number of pulses required to crystallize 50% of those films,  $N_{\text{xtal}}$ , were 4040, 2560, 1240, and 890 for  $T_{\text{max}} = 212$ , 216, 219, and 226 K, respectively. For the experiments shown in fig. S2,  $N_{\text{xtal}}$  was 2580 and 2050 for LDA and HQW, respectively, which was comparable to the earlier results.

Two-component models generally predict that water's structure changes rapidly only at intermediate temperatures, with comparatively slower changes at high and low temperatures, at which the structure is dominated by HDL-like and LDL-like species, respectively (fig. S10) (3, 16, 22, 31). Previous experiments, including x-ray scattering (34) and Raman spectroscopy (29), suggest that the high-temperature, HDL-dominated region extends down to ~245 K (fig. S11), whereas the structure of water changes more rapidly at lower temperatures (18, 20). The onset of rapid changes in water's structure indicated by x-ray scattering approximately corresponds to the temperature below which the transiently heated films became sensitive to the structure (Fig. 4A). Therefore, we expect that  $f_{\text{HQW}}^{\text{SS}}(T_{\text{max}})$  reflects the structural changes in water in the temperature range where it is changing rapidly, particularly at temperatures below 230 K, for which there are few existing data. However, because of the finite cooling rate in the experiments,  $f_{\text{HQW}}^{\text{SS}}(T_{\text{max}})$  does not directly correspond to the fraction of HDL-like species versus (isothermal) temperature,  $f_{\text{HDL}}(T)$ .

In the LLC scenario, the Widom line is the locus of maxima in the correlation length as a function of temperature and pressure in the one-phase region (14). At ambient pressure,  $f_{\text{HDL}}(T)$  is changing the most rapidly at the Widom line (3, 31). For micrometer-scale liquid drops, x-ray scattering data place the Widom line,  $T_{\text{WL}}$ , at 229 K (20). Although the midpoint for  $f_{\text{HQW}}^{\text{SS}}(T_{\text{max}})$  is at  $210 \pm 3$  K (Fig. 4A), we expect the results on transiently heated water films to be shifted to lower temperatures relative to  $f_{\text{HDL}}(T)$  because of the effects of the finite cooling rate (supplementary text, section D). Figure S12 shows an example in which  $f_{\text{HQW}}^{\text{SS}}(T_{\text{max}})$  is compared with the inherent structures obtained from MD simulations (13). We also note that the rapid heating and cooling in the current experiments could potentially favor different structures from those measured in the liquid drops where the cooling rate was low enough that the water maintained its equilibrium structure

as it cooled (supplementary text, section B). Nonetheless, the experiments on transiently heated nanoscale water films provide previously unreported data that are needed to test, validate, and refine various postulates advanced to explain water's anomalous properties.

## REFERENCES AND NOTES

1. R. J. Speedy, *J. Chem. Phys.* **86**, 982–991 (1982).
2. O. Mishima, H. E. Stanley, *Nature* **396**, 329–335 (1998).
3. P. Gallo et al., *Chem. Rev.* **116**, 7463–7500 (2016).
4. F. H. Stillinger, *Science* **209**, 451–457 (1980).
5. J. D. Smith et al., *Proc. Natl. Acad. Sci. U.S.A.* **102**, 14171–14174 (2005).
6. A. Nilsson, L. G. M. Pettersson, *Nat. Commun.* **6**, 8998 (2015).
7. A. K. Soper, *J. Chem. Phys.* **150**, 234503 (2019).
8. P. H. Poole, F. Sciortino, U. Essmann, H. E. Stanley, *Nature* **360**, 324–328 (1992).
9. J. C. Palmer et al., *Nature* **510**, 385–388 (2014).
10. S. Sastry, P. G. Debenedetti, F. Sciortino, H. E. Stanley, *Phys. Rev. E* **53**, 6144–6154 (1996).
11. D. T. Limmer, D. Chandler, *J. Chem. Phys.* **135**, 134503 (2011).
12. E. B. Moore, V. Molinero, *Nature* **479**, 506–508 (2011).
13. K. T. Wikfeldt, A. Nilsson, L. G. M. Pettersson, *Phys. Chem. Chem. Phys.* **13**, 19918–19924 (2011).
14. L. Xu et al., *Proc. Natl. Acad. Sci. U.S.A.* **102**, 16558–16562 (2005).
15. F. Mallamace et al., *Proc. Natl. Acad. Sci. U.S.A.* **104**, 424–428 (2007).
16. V. Holtzen, M. A. Anisimov, *Sci. Rep.* **2**, 713 (2012).
17. A. Taschin, P. Bartolini, R. Eramo, R. Righini, R. Torre, *Nat. Commun.* **4**, 2401 (2013).
18. J. A. Sellberg et al., *Nature* **510**, 381–384 (2014).
19. J. Russo, H. Tanaka, *Nat. Commun.* **5**, 3556 (2014).
20. K. H. Kim et al., *Science* **358**, 1589–1593 (2017).
21. L. P. Singh, B. Isenmann, F. Caupin, *Proc. Natl. Acad. Sci. U.S.A.* **114**, 4312–4317 (2017).
22. R. Shi, J. Russo, H. Tanaka, *Proc. Natl. Acad. Sci. U.S.A.* **115**, 9444–9449 (2018).
23. N. J. Hestand, J. L. Skinner, *J. Chem. Phys.* **149**, 140901 (2018).
24. Y. Xu, N. G. Petrik, R. S. Smith, B. D. Kay, G. A. Kimmel, *Proc. Natl. Acad. Sci. U.S.A.* **113**, 14921–14925 (2016).
25. Materials and methods are available as supplementary materials.
26. Y. Ni, J. L. Skinner, *J. Chem. Phys.* **145**, 124509 (2016).
27. B. M. Auer, J. L. Skinner, *J. Chem. Phys.* **128**, 224511 (2008).
28. Y. Maréchal, *J. Mol. Struct.* **1004**, 146–155 (2011).
29. Q. Sun, *Chem. Phys. Lett.* **568–569**, 90–94 (2013).
30. P. L. Geissler, *J. Am. Chem. Soc.* **127**, 14930–14935 (2005).
31. E. B. Moore, V. Molinero, *J. Chem. Phys.* **130**, 244505 (2009).
32. D. T. Limmer, D. Chandler, *Faraday Discuss.* **167**, 485–498 (2013).
33. G. A. Kimmel et al., *J. Chem. Phys.* **150**, 204509 (2019).
34. C. Benmore, L. C. Gallington, E. Soignard, *Mol. Phys.* **117**, 2470–2476 (2019).

## ACKNOWLEDGMENTS

**Funding:** This work was supported by the U.S. Department of Energy (DOE), Office of Science, Basic Energy Sciences, Chemical Sciences, Geosciences, and Biosciences Division. This research was performed by using EMSL, a national scientific user facility sponsored by DOE's Office of Biological and Environmental Research and located at the Pacific Northwest National Laboratory, which is operated by Battelle for the DOE. **Author contributions:** The research was designed and supervised by G.A.K. and B.D.K. L.K. and W.A.T. conducted the experiments. L.K., W.A.T., and G.A.K. analyzed the data. L.K. and G.A.K. wrote the manuscript, with input from all authors. **Competing interests:** None declared. **Data and materials availability:** All data are available in the main text or the supplementary materials.

## SUPPLEMENTARY MATERIALS

science.sciencemag.org/content/369/6510/1490/suppl/DC1  
Materials and Methods  
Supplementary Text  
Figs. S1 to S17  
References (35–53)

16 March 2020; accepted 28 July 2020  
10.1126/science.abb7542



## QUANTUM SYSTEMS

# Universal coherence protection in a solid-state spin qubit

Kevin C. Miao<sup>1</sup>, Joseph P. Blanton<sup>1,2</sup>, Christopher P. Anderson<sup>1,2</sup>, Alexandre Bourassa<sup>1</sup>, Alexander L. Crook<sup>1,2</sup>, Gary Wolfowicz<sup>1,4</sup>, Hiroshi Abe<sup>3</sup>, Takeshi Ohshima<sup>3</sup>, David D. Awschalom<sup>1,2,4\*</sup>

Decoherence limits the physical realization of qubits, and its mitigation is critical for the development of quantum science and technology. We construct a robust qubit embedded in a decoherence-protected subspace, obtained by applying microwave dressing to a clock transition of the ground-state electron spin of a silicon carbide divacancy defect. The qubit is universally protected from magnetic, electric, and temperature fluctuations, which account for nearly all relevant decoherence channels in the solid state. This culminates in an increase of the qubit's inhomogeneous dephasing time by more than four orders of magnitude (to >22 milliseconds), while its Hahn-echo coherence time approaches 64 milliseconds. Requiring few key platform-independent components, this result suggests that substantial coherence improvements can be achieved in a wide selection of quantum architectures.

**E**lectron spins embedded in a solid-state host, such as silicon carbide (SiC) and diamond, are attractive platforms for quantum information processing by virtue of their optical interface (1, 2) and engineered interactions with the host crystal (3–6).

These electron spins are highly controllable using external magnetic fields because of the electron's large magnetic moment. However, unwanted magnetic field noise will also couple intensely through this degree of freedom and quench spin coherences (7, 8). In particular, a naturally abundant host crystal typically has nonzero nuclear spin isotopes and paramagnetic impurities, whose fluctuations produce variations in the magnetic field at the electron spin with magnitudes as large as 0.45 mT (9).

These magnetic field fluctuations limit the electron spin's Hahn-echo coherence time ( $T_2$ ) to around a millisecond (6, 7, 10, 11) and suppress inhomogeneous spin dephasing times ( $T_2^*$ ) to a few microseconds (10, 11). These relatively short inhomogeneous dephasing times typically bound the time scales for quantum information storage and manipulation, requiring the development of nuclear spin quantum memories (12, 13) while also limiting the fidelity of quantum information transfer to coupled systems, such as superconducting resonators (14). These restrictions call for the extension of electron spin coherence, which is typically achieved by means of dynamical de-

coupling (15), isotopic purification (13, 16, 17), or Hamiltonian engineering (3, 4, 18, 19).

One particular solid-state electron spin system, the basally oriented  $kh$  divacancy in the 4H polytype of SiC, has recently been shown to have reduced sensitivity to magnetic noise when operated near zero external magnetic field (20). This robustness primarily arises from the transverse zero-field splitting (ZFS) intrinsic to the spin system's single mirror plane symmetry (Fig. 1A, lower left). When combined with the spin system's axial ZFS, clock transitions emerge near  $\mathbf{B} = 0$ . By operating at this point, the spin has lengthened inhomogeneous dephasing times, among other properties (21). We implement a protocol to further extend the ground-state spin inhomogeneous dephasing time, as well as the Hahn-echo coherence time, of a single  $kh$  divacancy in 4H-SiC by simply applying a continuous microwave dressing drive resonant with two of the three ground-state spin-1 sublevels at zero field. The combination of a clock transition and periodic driving allows for the advantages of both methods to manifest, whereas the individual weaknesses are diminished (21). Furthermore, there are many practical advantages of this protocol when compared to typical pulsed dynamical decoupling sequences, including uninterrupted coherence protection, lower peak drive powers, and fewer nonidealities in implementing the protocol. Notably, this dressed spin system retains its large magnetic and electric response to resonant microwave control fields, preserving the capability to rapidly perform quantum operations to coherently manipulate the long-lived quantum state and the ability to prepare arbitrary superpositions in this new basis.

We isolate the  $kh$  divacancy used in this study in naturally abundant, commercially available 4H-SiC at 5 K (21). The ground-state spin-1 system is initialized and read out through

optical pulses, whereas spin rotations are produced by microwave-frequency magnetic and electric fields from on-chip wires and capacitors, respectively (Fig. 1A). A three-axis electro-magnet provides vector control of the external magnetic field along the Cartesian axes of the spin system (Fig. 1A, lower left). At  $\mathbf{B} = 0$ , a spin transition can be driven between the upper two spin states,  $|+\rangle = \frac{1}{\sqrt{2}}(|+1_z\rangle + |-1_z\rangle)$  and  $|-\rangle = \frac{1}{\sqrt{2}}(|+1_z\rangle - |-1_z\rangle)$  (where  $|\pm 1_z\rangle$  denote the  $m_s = \pm 1$  sublevels in the  $S_z$  basis). Ramsey interferometry of the  $|+\rangle \leftrightarrow |-\rangle$  transition is used to determine the transverse ZFS magnitude  $E/(2\pi) = 18.353164(4)$  MHz to a high degree of precision and accuracy (21), allowing us to apply a continuous microwave-frequency magnetic drive at an angular frequency  $\omega = 2E$  resonant with the  $|+\rangle \leftrightarrow |-\rangle$  transition. At a sufficiently high drive Rabi frequency  $\Omega$ , the  $|\pm\rangle$  spin levels undergo Autler-Townes splitting (21) to form dressed spin states  $|\pm 1\rangle$  with energy levels offset from that of  $|+\rangle$  by  $\pm\Omega/2$ . These dressed states form the basis for the decoherence-protected subspace (DPS) and can be observed by applying a weaker microwave probe pulse and sweeping its frequency detuning  $\Delta$  from the  $|0\rangle \leftrightarrow |+\rangle$  transition frequency (Fig. 1C). For subsequent measurements, we operate at  $\Omega/(2\pi) = 350$  kHz to mitigate higher-order energy dispersion components (21). We realize coherent control within the dressed spin-1 system by driving  $\Delta m_s = \pm 1$  transitions  $|0\rangle \leftrightarrow |\pm 1\rangle$  with ac magnetic fields (Fig. 1D) and a  $\Delta m_s = \pm 2$  transition  $|+1\rangle \leftrightarrow |-1\rangle$  with ac electric fields (22) (Fig. 1E). Readout of the  $|\pm 1\rangle$  basis is accomplished by nonadiabatically disabling the dressing drive, rotating into the  $\{|0\rangle, |+\rangle\}$  basis, and optically probing the spin population in  $|0\rangle$  (21).

The energy inhomogeneity of the driven spin system can be quantified by preparing a superposition  $|\psi_0\rangle = \frac{1}{\sqrt{2}}(|+1\rangle + |-1\rangle)$  in the DPS and executing a Ramsey free precession sequence. With active feedback procedures in place, we measure a  $T_2^*$  inhomogeneous spin dephasing time in this basis to be 22.4(10) ms (Fig. 2A), which is more than four and two orders of magnitude longer than the  $T_2^*$  measured for the same  $kh$  divacancy at  $B_z = 1.2$  mT and  $\mathbf{B} = 0$ , respectively (Fig. 2B). Moreover, by adding a single refocusing pulse, we extend the lifetime of the superposition to a  $T_2$  Hahn-echo spin coherence time of 64(4) ms (Fig. 2C). The mechanism by which the coherence is protected in the DPS can be understood by examining the Hamiltonian with a dressing drive applied on resonance, in the frame rotating at the drive frequency,  $\omega = 2E$ ,

$$\tilde{H}/\hbar = \begin{bmatrix} 0 & \gamma_e B_x e^{-iEt} & \frac{\Omega}{2} + \gamma_e B_z e^{-2iEt} \\ \gamma_e B_x e^{iEt} & -D & -i\gamma_e B_y e^{iEt} \\ \frac{\Omega}{2} + \gamma_e B_z e^{2iEt} & i\gamma_e B_y e^{-iEt} & 0 \end{bmatrix}$$

<sup>1</sup>Pritzker School of Molecular Engineering, University of Chicago, Chicago, IL 60637, USA. <sup>2</sup>Department of Physics, University of Chicago, Chicago, IL 60637, USA. <sup>3</sup>National Institutes for Quantum and Radiological Science and Technology, 1233 Watanuki, Takasaki, Gunma 370-1292, Japan. <sup>4</sup>Center for Molecular Engineering and Materials Science Division, Argonne National Laboratory, Lemont, IL 60439, USA.

\*Corresponding author. Email: awschalom@uchicago.edu

where  $\gamma_e$  is the electron gyromagnetic ratio,  $D$  is the magnitude of the axial ZFS, and  $\Omega$  is the dressing drive Rabi frequency. As a first-order approximation, the magnetic noise contributions perturb the spin only when the matrix element becomes time independent. For  $B_x$  and  $B_y$  noise contributions, this is achieved for frequency components at  $\pm E$ . For  $B_z$  con-

tributions, this is achieved for frequency components at  $\pm 2E$ . Thus, within the DPS, an effective bandpass filter is applied on the magnetic noise, with passbands located at  $\pm E$  and  $\pm 2E$  each with bandwidths proportional to  $\Omega$ . Combined with the  $1/f$  dependence of noise power spectra, this results in a greatly reduced sensitivity to magnetic noise.

We then examine the energy dispersion relations between the dressed spin levels under magnetic, electric, and temperature fluctuations to reveal their contributions to inhomogeneity in the DPS. We first consider the effect of magnetic fields on the dressed spin levels, as magnetic noise typically limits the coherence of many electron spin systems.

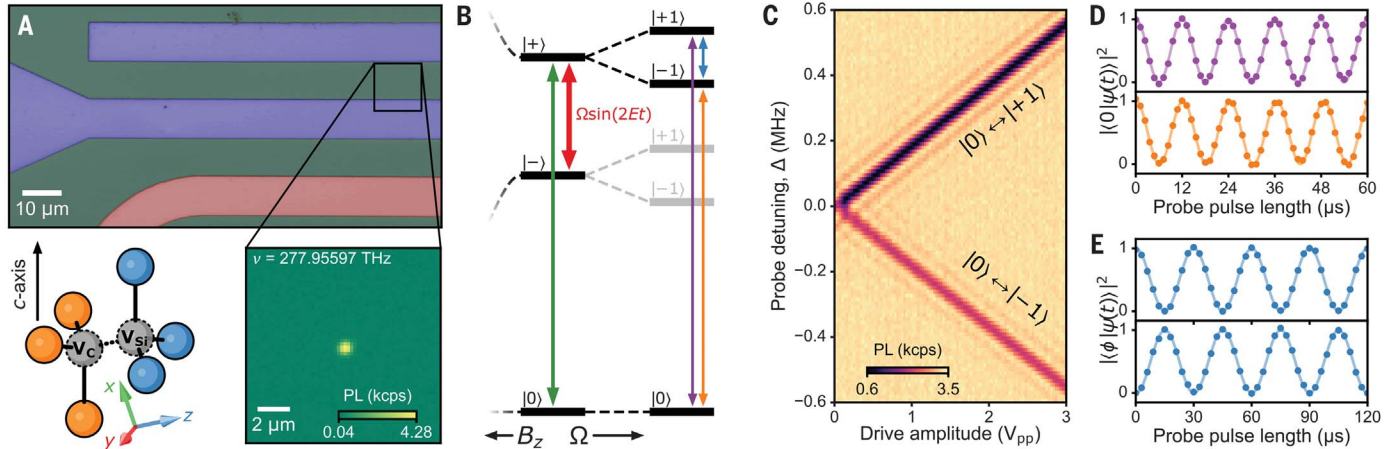


**Fig. 1. Driven  $kh$  divacancy spin system in 4H-SiC.** (A) False-color optical microscope image of the 4H-SiC sample showing an on-chip capacitor (blue) and wire (red) for microwave manipulation of the spin. Inset: Single  $kh$  divacancy under resonant optical excitation. Lower left: Lattice diagram of a  $kh$  divacancy and nearest-neighbor carbon atoms (blue) and silicon atoms (orange). Cartesian axes of the  $kh$  divacancy shown as colored vectors. (B) Energy diagram of the  $kh$  divacancy ground-state spin in the  $^3A_2$  orbital. At  $\mathbf{B} = 0$ , clock transitions form between the three spin-1 levels. Spin manipulation in this basis consists of driving  $|0\rangle \leftrightarrow |+ \rangle$  (green) and  $|+ \rangle \leftrightarrow | - \rangle$  (red). Sufficiently strong driving of  $|+ \rangle \leftrightarrow | - \rangle$  induces Autler-Townes splitting, forming a hybridized spin-photon

system, with an accessible upper branch and an inaccessible lower branch (gray). In this basis, spin manipulation consists of magnetically driving  $|0\rangle \leftrightarrow | \pm 1 \rangle$  (purple, orange), or electrically driving  $|+1\rangle \leftrightarrow | - 1 \rangle$  (blue). (C) Pulsed optically detected magnetic resonance resolving Autler-Townes splitting of the ground-state spin.  $\Delta$  is the probe frequency detuning from the  $|0\rangle \leftrightarrow |+ \rangle$  resonance frequency. (D) Magnetically driven Rabi oscillations using the  $|0\rangle \leftrightarrow |+1\rangle$  (upper) and  $|0\rangle \leftrightarrow | - 1 \rangle$  (lower) transitions corresponding to the purple and orange arrows in (B). (E) Electrically driven Rabi oscillations using the transition  $|+1\rangle \leftrightarrow | - 1 \rangle$  highlighted by the blue arrow in (B) after reading out the population of  $|+1\rangle$  ( $\varphi = +1$ ) (upper) and  $| - 1 \rangle$  ( $\varphi = -1$ ) (lower).

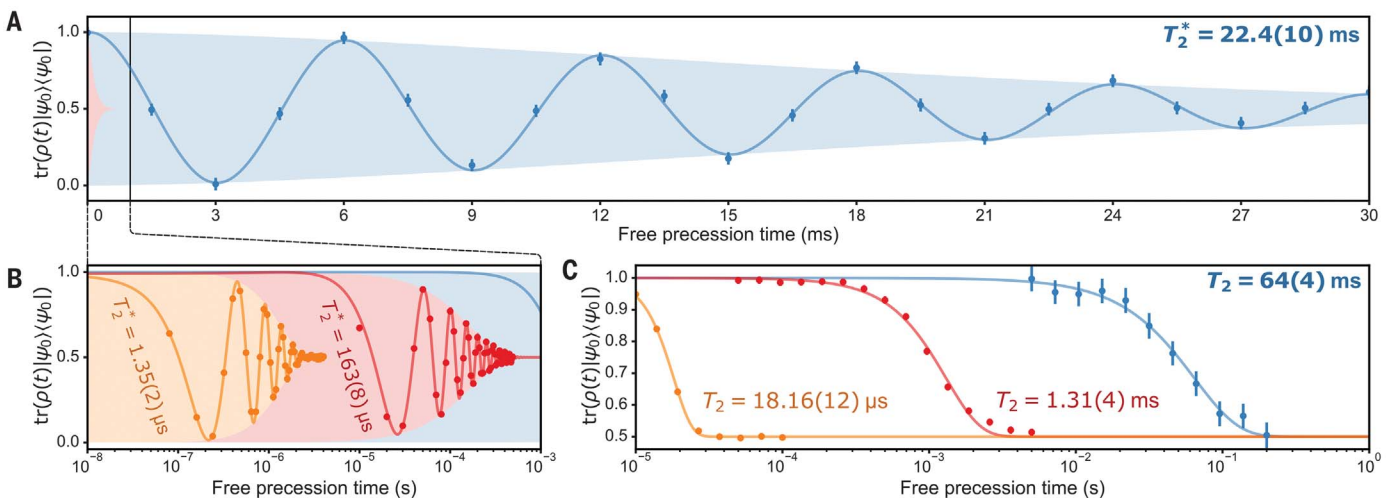


**Fig. 2. Spin coherence in the DPS.** (A) Ramsey free precession of  $|\psi_0\rangle = \frac{1}{\sqrt{2}}(|+1\rangle + | - 1 \rangle)$  in the DPS at  $\mathbf{B} = 0$  mT (blue). A microwave detuning of +166.6 Hz is added to increase visibility of the decay envelope. (B) Ramsey free precession of  $|\psi_0\rangle = \frac{1}{\sqrt{2}}(|0\rangle + |+1\rangle)$  (red) and  $|\psi_0\rangle = \frac{1}{\sqrt{2}}(|0\rangle + |+1z\rangle)$  (orange) prepared outside of the DPS at  $\mathbf{B} = 0$  mT and  $B_z = 1.2$  mT, respectively. (C) Hahn echo free precession of the spin when prepared in the DPS at  $\mathbf{B} = 0$  mT (blue,  $|\psi_0\rangle = \frac{1}{\sqrt{2}}(|+1\rangle + | - 1 \rangle)$ ), and outside of the DPS at  $\mathbf{B} = 0$  mT (red,  $|\psi_0\rangle = \frac{1}{\sqrt{2}}(|0\rangle + |+1\rangle)$ ) and at  $B_z = 1.2$  mT (orange,  $|\psi_0\rangle = \frac{1}{\sqrt{2}}(|0\rangle + |+1z\rangle)$ ). Error bars represent 1 SD.



Under a continuous drive resonant with the  $|+\rangle \leftrightarrow |-\rangle$  transition, the dispersion relation of the ground-state spin acquires both quadratic and quartic dependences on magnetic field (27). The dispersion relation is probed by applying magnetic fields along the  $x$  and  $z$  axes of the spin system while scanning the frequency detuning  $\Delta$  of a probe drive (Fig. 3, A and B). Rotational symmetry of the system about the  $z$  axis leads to indistinguishable effects from  $x$ - and  $y$ -axis fields (27). The resulting frequencies of the  $|0\rangle \leftrightarrow |\pm 1\rangle$  spin resonances provide us with the driven spin system's spectral response to magnetic fields. To confirm these observations, we develop an analytical model of the driven spin system using Floquet analysis alongside a numerical model through spin-1 master equation simulations (27). We find excellent agreement between the experimental data and these models (Fig. 3, C and D). We then consider the primary source of magnetic noise, the nuclear spin bath, as an isotropic magnetic fluctuator with an estimated fluctuation magnitude at this  $kh$  divacancy of 13  $\mu\text{T}$  (27). We perform fine scans of the  $|+1\rangle \leftrightarrow |-1\rangle$  transition using Ramsey interferometry (Fig. 3, E and F) and confirm the

high degree of insensitivity in this range, illustrating the primary mechanism for the largely increased spin coherence times. These results, once combined with a phenomenological model of the spin energy inhomogeneity (27), allow us to quantitatively confirm that residual inhomogeneity from magnetic fields still plays a role in limiting the spin coherence, even after substantial suppression in the DPS.

We can then apply the analytical energy dispersion relations to understand the effect of electric noise and temperature fluctuations on spin inhomogeneous dephasing in the DPS. Electric and temperature fluctuations affect the axial and transverse ZFS magnitudes, as well as a corresponding detuning of the dressing drive from the resonance frequency  $\omega = 2E$ . We use the undriven spin's first-order sensitivity to electric fields (23) at  $\mathbf{B} = 0$  to quantify the magnitude of electric field noise present in the system (27). In the DPS, we gain first-order protection against fluctuations in the ZFS magnitudes, resulting in increased robustness against electric field noise and temperature shifts. This leads to a reduction of electrically induced spin energy inhomogeneity by nearly two orders of magnitude (27) and diminishes electric field

contributions in limiting the spin coherence in the DPS. Further reduction of electric field contributions may emerge by applying a dc electric field to deplete fluctuating charges (6, 20), potentially leading to nearly complete elimination of electric field noise.

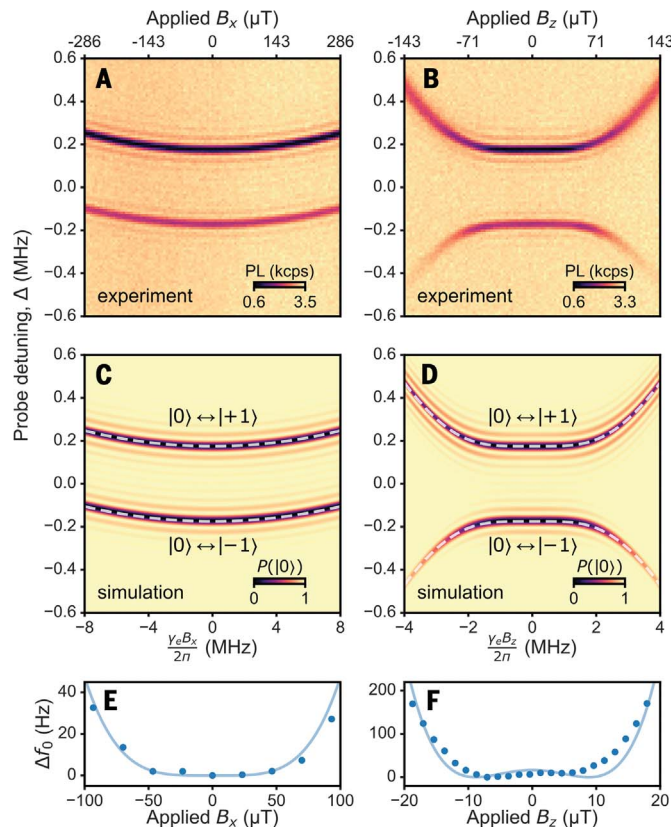
The energy dispersion relations in the driven basis confirm that the spin's energy levels depend linearly on the dressing drive Rabi frequency. Hence, amplitude drifts of the dressing drive and corresponding fluctuations in the Rabi frequency  $\delta\Omega$  introduce first-order inhomogeneity of the dressed spin levels and cause shortening of the measured  $T_2^*$ . To this end, we implement active feedback of the dressed spin resonance frequency to counteract these slow drifts and reduce inhomogeneity (Fig. 4A). By evaluating an error signal derived from Ramsey free precession of the dressed spin (Fig. 4B), we measure and correct drifts on the order of 30 Hz in the spin resonance frequency (27), consistent with the 100 parts per million/ $^\circ\text{C}$  stability of the dressing drive oscillator. To validate the effectiveness of our feedback protocol, we measure Ramsey free precession of  $|\psi_0\rangle = \frac{1}{\sqrt{2}}(|+1\rangle + |-1\rangle)$  with and without feedback enabled (Fig. 4C). With active feedback enabled, we measure our reported  $T_2^*$  of 22.4(10) ms; when disabled, this value shortens to 17.4(10) ms as the dressing drive inhomogeneity suppresses the spin's coherence on the time scale of hours (Fig. 4D). These results suggest that by incorporating this feedback protocol, we have largely mitigated the effects of dressing drive amplitude fluctuations and that noise sources intrinsic to the host crystal remain as the limiting factor for spin coherence in the DPS.

The few requirements for successful implementation of this protocol allow for immediate extension to other quantum systems. Specifically, a candidate system must have a coherently controllable clock transition, where upon being driven, the resulting dressed states are also coherently controllable (27). Other basally oriented defects in SiC (24–26) have transverse ZFS magnitudes larger than what has been observed here and are expected to experience even greater coherence protection. Strained diamond nitrogen-vacancy centers (14) may also stand to benefit from this protocol. Turning to other systems, donor spins in silicon with robust clock transitions (27, 28), superconducting qubits operated at a degeneracy point (29), and molecular spins with ZFS or hyperfine interactions (30, 31) may be driven to produce a DPS.

With an extended spin  $T_2^*$ , the prospects for unity-cooperativity systems between single solid-state spins and weakly interacting quantum systems are more promising. Hartmann-Hahn coupling between a pair of spins prepared in the DPS can mediate two-qubit interactions (18). By mitigating strain inhomogeneity through material improvements or dynamical

**Fig. 3. Energy dispersion in the DPS.** (A and B) Measured spectrum of the  $|0\rangle \leftrightarrow |\pm 1\rangle$  transitions over a range of applied  $x$ -axis (A) and  $z$ -axis (B) magnetic fields. The contrast recovery procedure (see supplementary materials)

produces unequal photoluminescence contrast between the two resonances. The probe detuning,  $\Delta$ , is referenced to the  $|0\rangle \leftrightarrow |+\rangle$  resonance frequency. In (B), high field induces inhomogeneous broadening, as the spin is no longer fully encoded in the DPS. (C and D) Simulated spin resonance spectrum of the driven  $|\pm 1\rangle$  states corresponding to (A) and (B), respectively. Dashed white lines indicate transition energy spectra derived from Floquet analysis. (E and F) Energy difference  $\Delta f_0$  between the  $|+1\rangle$  and  $|-1\rangle$  states as a function of applied  $B_x$  (E) and applied  $B_z$  (F), as measured using Ramsey interferometry of  $|\psi_0\rangle = \frac{1}{\sqrt{2}}(|+1\rangle + |-1\rangle)$ . Solid lines are the energy differences derived from Floquet analysis with no free parameters. Error bars are smaller than the symbol size.



decoupling, an ensemble of  $n$  driven spins can attain a  $\sqrt{n}$  enhancement in coupling strength, providing a near-term avenue toward a high-cooperativity coupled system. We have shown that the qubit in the DPS is still highly responsive to resonantly applied magnetic and electric

control fields, and thus magnetic, electric, and acoustic (3, 5) interactions can be used for coupling. Lastly, megahertz-scale tuning of the dressed spin energy levels allows for rapid adjustment of interaction strengths, enabling the spin to be an efficient quantum bus.

This protocol is compatible with additional forms of noise suppression, including isotopic purification, charge depletion, and pulsed dynamical decoupling. The residual electron spin energy shifts can be decreased substantially by reducing the volume density of fluctuating spins in the bath (13, 16, 17). Dynamic techniques such as spin bath driving (11) and hyperpolarization (32) may further reduce these contributions. Charge depletion, which has led to near-transform-limited optical linewidths in divacancies (6, 20), can further suppress electric field contributions. We have presently demonstrated compatibility with pulsed dynamical decoupling using a Hahn-echo sequence; higher-order dynamical decoupling sequences may allow for spin coherence to rapidly reach the spin-lattice relaxation limit with few control pulses. Considering these prospective avenues, this dressing protocol represents a major development for potentially improving coherence across a variety of quantum systems and is a crucial step toward integrating SiC divacancies into robust, real-world quantum technologies.

## REFERENCES AND NOTES

1. L. Robledo *et al.*, *Nature* **477**, 574–578 (2011).
2. D. J. Christle *et al.*, *Phys. Rev. X* **7**, 021046 (2017).
3. A. Barfuss, J. Teissier, E. Neu, A. Nunnenkamp, P. Maletinsky, *Nat. Phys.* **11**, 820–824 (2015).
4. E. R. MacQuarrie, T. A. Gosavi, S. A. Bhawe, G. D. Fuchs, *Phys. Rev. B Condens. Matter Mater. Phys.* **92**, 224419 (2015).
5. S. J. Whiteley *et al.*, *Nat. Phys.* **15**, 490–495 (2019).
6. C. P. Anderson *et al.*, Electrical and optical control of single spins integrated in scalable semiconductor devices. *Science* **1230**, 1225–1230 (2019).
7. H. Seo *et al.*, *Nat. Commun.* **7**, 12935 (2016).
8. P. L. Stanwix *et al.*, *Phys. Rev. B Condens. Matter Mater. Phys.* **82**, 201201 (2010).
9. P. V. Klimov, A. L. Falk, D. J. Christle, V. V. Dobrovitski, D. D. Awschalom, *Sci. Adv.* **1**, e1501015 (2015).
10. D. J. Christle *et al.*, *Nat. Mater.* **14**, 160–163 (2015).
11. E. Bauch *et al.*, *Phys. Rev. X* **8**, 031025 (2018).
12. G. D. Fuchs, G. Burkard, P. V. Klimov, D. D. Awschalom, *Nat. Phys.* **7**, 789–793 (2011).
13. P. C. Maurer *et al.*, *Science* **336**, 1283–1286 (2012).
14. Y. Kubo *et al.*, *Phys. Rev. Lett.* **105**, 140502 (2010).
15. M. H. Aboeleh *et al.*, *Nat. Commun.* **9**, 2552 (2018).
16. E. D. Herbschleb *et al.*, *Nat. Commun.* **10**, 3766 (2019).
17. A. Bourassa *et al.*, Entanglement and control of single quantum memories in isotopically engineered silicon carbide. *arXiv:2005.07602* [quant-ph] (2020).
18. A. Laucht *et al.*, *Nat. Nanotechnol.* **12**, 61–66 (2017).
19. J. Teissier, A. Barfuss, P. Maletinsky, *J. Opt.* **19**, 044003 (2017).
20. K. C. Miao *et al.*, *Sci. Adv.* **5**, eaay0527 (2019).
21. See supplementary materials.
22. P. V. Klimov, A. L. Falk, B. B. Buckley, D. D. Awschalom, *Phys. Rev. Lett.* **112**, 087601 (2014).
23. P. Jamonneau *et al.*, *Phys. Rev. B* **93**, 024305 (2016).
24. A. L. Falk *et al.*, *Nat. Commun.* **4**, 1819 (2013).
25. Z. Mu *et al.*, *Nano Lett.* **20**, 6142–6147 (2020).
26. K. Khazen *et al.*, *Phys. Rev. B* **100**, 205202 (2019).
27. G. Wolfowicz *et al.*, *Nat. Nanotechnol.* **8**, 561–564 (2013).
28. K. J. Morse *et al.*, *Phys. Rev. B* **97**, 115205 (2018).
29. M. H. Devoret, A. Wallraff, J. M. Martinis, Superconducting Qubits: A Short Review. *arXiv:cond-mat/0411174* [cond-mat.mes-hall] (2004).
30. S. L. Bayliss *et al.*, Optically addressable molecular spins for quantum information processing. *arXiv:2004.07998* [quant-ph] (2020).
31. M. Shiddiq *et al.*, *Nature* **531**, 348–351 (2016).
32. I. Schwartz *et al.*, *Sci. Adv.* **4**, eaat8978 (2018).

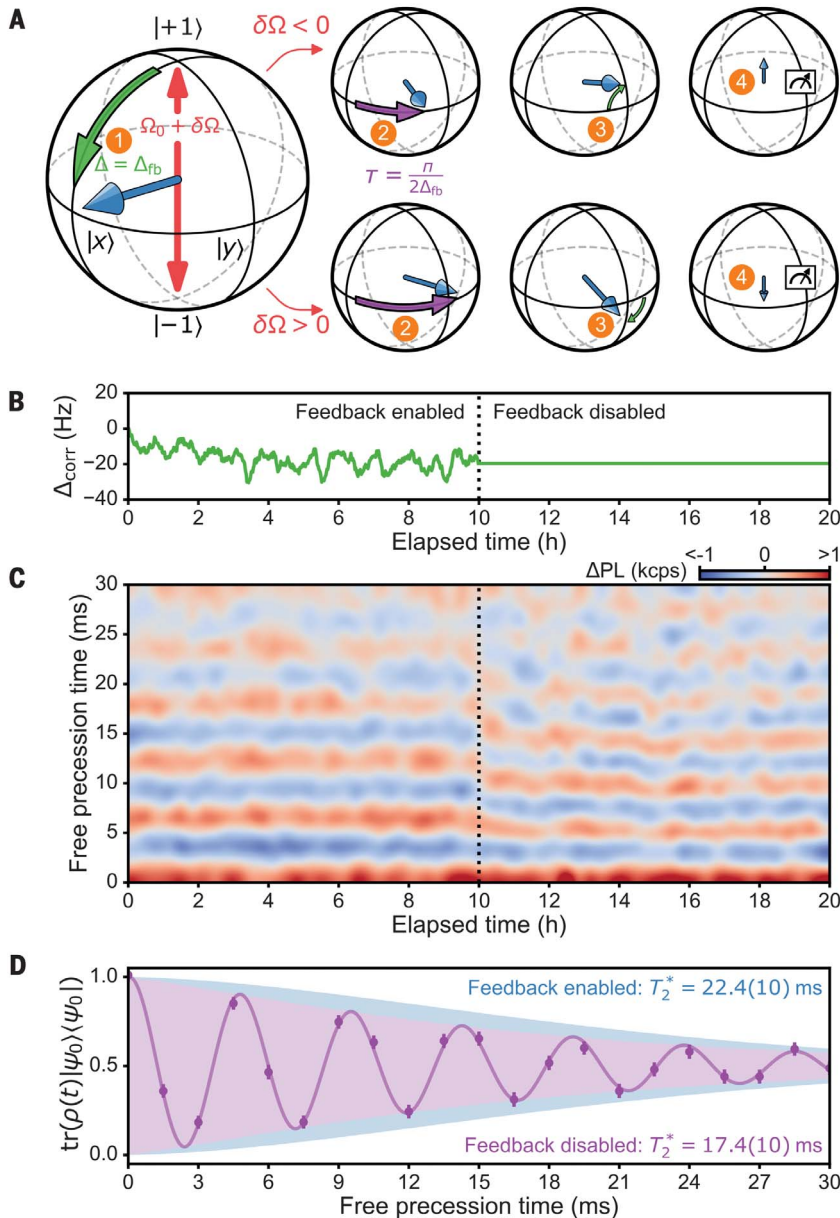


**Fig. 4. Active spin resonance feedback.** (A) Bloch spheres illustrating the spin resonance feedback protocol. See materials and methods for step-by-step details. (B) Applied corrective detuning to the frequency of the drive resonant with  $|+1\rangle \leftrightarrow |−1\rangle$ . During hours 0 to 10, active feedback is applied to the spin, and the corrective detuning is derived from a proportional factor of the measured error signal. (C) Stabilization of Ramsey free precession of  $|\psi_0\rangle = \frac{1}{\sqrt{2}}(|+1\rangle + |−1\rangle)$  with active spin resonance feedback. While active feedback is enabled, the observed Ramsey fringes are stable at the chosen detuning of +166.6 Hz. Once disabled, slow drifts in the dressing drive Rabi frequency shift the effective detuning of the microwave pulse used to prepare the superposition. Interpolation applied to emphasize fringe locations. (D) The Ramsey free precession decay envelope when integrating the individual Ramsey free precession iterations in (C), demonstrating the increased inhomogeneity without the feedback process. Error bars represent 1 SD.



33. K. C. Miao *et al.*, Datasets for “Universal coherence protection in a solid-state spin qubit”, Version 1.0, Zenodo (2020); <https://doi.org/10.5281/zenodo.3975269>.

#### ACKNOWLEDGMENTS

We thank M. Fukami, S. L. Bayliss, Y. Tsaturyan, P. C. Jerger, V. V. Dobrovitski, M. Onizhuk, and A. A. Clerk for fruitful discussions and comments, and for careful reading of the manuscript. **Funding:** K.C.M., J.P.B., C.P.A., A.B., A.L.C., G.W., and D.D.A. were supported by DARPA D18AC00015KK1932, AFOSR FA9550-19-1-0358, ONR N00014-17-1-3026, and the University of Chicago MRSEC NSF DMR-1420709. H.A. and T.O. were supported by JSPS KAKENHI 18H03770 and 20H00355. This work made use of the Pritzker Nanofabrication Facility part of the Pritzker School of Molecular

Engineering at the University of Chicago, which receives support from Soft and Hybrid Nanotechnology Experimental (SHyNE) Resource (NSF ECCS-1542205), a node of the National Science Foundation's National Nanotechnology Coordinated Infrastructure.

**Author contributions:** K.C.M. conceived and designed the experiment, and carried out theoretical calculations. K.C.M. and J.P.B. performed the experiments, with the assistance of G.W. C.P.A. annealed and fabricated the sample. K.C.M., J.P.B., A.B., and A.L.C. developed the confocal microscope setup. H.A. and T.O. performed electron irradiation of the SiC samples. D.D.A. advised on all fronts. All authors contributed to manuscript revision and preparation. **Competing interests:** K.C.M. and D.D.A. are inventors on a provisional patent application that has been filed relating to this work. All other authors declare that they have no competing

interests. **Data and materials availability:** The data within this study are available on Zenodo (33).

#### SUPPLEMENTARY MATERIALS

[science.sciencemag.org/content/369/6510/1493/suppl/DC1](https://science.sciencemag.org/content/369/6510/1493/suppl/DC1)

Materials and Methods

Figs. S1 to S3

Supplementary Text

References (34–41)

28 April 2020; accepted 31 July 2020

Published online 13 August 2020

10.1126/science.abc5186

## STELLAR EVOLUTION

# (Sub)stellar companions shape the winds of evolved stars

L. Decin<sup>1,2\*</sup>, M. Montargès<sup>1</sup>, A. M. S. Richards<sup>3</sup>, C. A. Gottlieb<sup>4</sup>, W. Homan<sup>1</sup>, I. McDonald<sup>3,5</sup>, I. El Mellah<sup>1,6</sup>, T. Danilovich<sup>1</sup>, S. H. J. Wallström<sup>1</sup>, A. Zijlstra<sup>3,7</sup>, A. Baudry<sup>8</sup>, J. Bolte<sup>1</sup>, E. Cannon<sup>1</sup>, E. De Beck<sup>9</sup>, F. De Ceuster<sup>1,10</sup>, A. de Koter<sup>1,11</sup>, J. De Ridder<sup>1</sup>, S. Etoka<sup>3</sup>, D. Gobrecht<sup>1</sup>, M. Gray<sup>3,12</sup>, F. Herpin<sup>8</sup>, M. Jesty<sup>13</sup>, E. Lagadec<sup>14</sup>, P. Kervella<sup>15</sup>, T. Khouri<sup>9</sup>, K. Menten<sup>13</sup>, T. J. Millar<sup>16</sup>, H. S. P. Müller<sup>17</sup>, J. M. C. Plane<sup>2</sup>, R. Sahai<sup>18</sup>, H. Sana<sup>1</sup>, M. Van de Sande<sup>1</sup>, L. B. F. M. Waters<sup>11,19</sup>, K. T. Wong<sup>20</sup>, J. Yates<sup>10</sup>

Binary interactions dominate the evolution of massive stars, but their role is less clear for low- and intermediate-mass stars. The evolution of a spherical wind from an asymptotic giant branch (AGB) star into a nonspherical planetary nebula (PN) could be due to binary interactions. We observed a sample of AGB stars with the Atacama Large Millimeter/submillimeter Array (ALMA) and found that their winds exhibit distinct nonspherical geometries with morphological similarities to planetary nebulae (PNe). We infer that the same physics shapes both AGB winds and PNe; additionally, the morphology and AGB mass-loss rate are correlated. These characteristics can be explained by binary interaction. We propose an evolutionary scenario for AGB morphologies that is consistent with observed phenomena in AGB stars and PNe.

At the end of their lives, stars with low and intermediate masses [ $0.8$  to  $8$  solar masses ( $M_{\odot}$ )] evolve into luminous cool red giant stars along the asymptotic giant branch (AGB). The Sun will reach that phase  $\sim 7.7$  billion years from now (1). During the AGB phase, a star's radius may become as large as 1 astronomical unit (au), and its luminosity may reach thousands of times the current solar luminosity. The AGB phase lasts between  $\sim 0.1$  and 20 million years, with the more massive stars being shorter-lived (2). At the start of the AGB phase, stars are oxygen rich with a carbon-to-oxygen (C/O) ratio  $< 1$  and have spectra classified as M-type. During the AGB phase, carbon fusion occurs in the stellar core, and the product elements are brought to the surface by convection. Eventually, the C/O ratio rises above 1, producing a carbon star. The AGB phase is characterized by a stellar wind with a mass-loss rate greater than  $\sim 10^{-8} M_{\odot} \text{ year}^{-1}$ . The increase in luminosity while a star evolves along the AGB induces an increase in the mass-loss rate of up to  $\sim 10^{-4} M_{\odot} \text{ year}^{-1}$  (3). For stars with mass-loss rates greater than  $10^{-7} M_{\odot} \text{ year}^{-1}$ , the mass-loss rate exceeds the hydrogen nuclear burning rate in the star's interior, so mass loss determines the further stellar evolution (4). The wind then strips away the star's outer envelope. When the remaining envelope constitutes less than  $\sim 1\%$

of the stellar mass, the star becomes a post-AGB star (5). During this short evolutionary phase, which takes a few thousand years, the temperature of the star increases at constant luminosity and it becomes a planetary nebula (PN), characterized by a hot central star that ionizes the gas ejected during the previous red giant phase. The lifetime of a PN is roughly 20,000 years. The PN then disperses quickly, leaving an inert white dwarf, which slowly cools (6).

Planetary nebulae (PNe) have a wide range of morphologies, including elliptical, bipolar, and butterfly-shaped geometries; the mechanism that produces these diverse shapes is unknown (7). Whereas  $\sim 80\%$  of the AGB stars have a wind with overall spherical symmetry (8),  $< 20\%$  of PNe are circularly symmetric (9, 10). Various hypotheses—including rapidly spinning or strongly magnetic single stars (11)—have been proposed to explain this morphological metamorphosis, but these ideas have been questioned because strong asymmetries are not formed efficiently (12). Short-period (orbital period  $P_{\text{orb}} \lesssim 10$  days) binary systems (orbital separation  $a \lesssim 0.2$  au) surrounded by a common gaseous envelope, referred to as the common-envelope phase, have become the favored hypothesis (13). The proposed PN-shaping mechanisms operate over a short time, either during the final few hundred years of the AGB phase or during the early post-

AGB phase (14). Identification of the shaping mechanism and its time of occurrence is observationally challenging, owing to the short lifetime of the post-AGB and PN stages; the strong observational bias toward detecting binary post-AGB stars and PNe with short orbital periods (15); and the high mass-loss rates at the end of the AGB phase, which surrounds the star with high-optical depth material that obscures the inner workings.

Observations at high spatial resolution have shown that AGB winds may exhibit small-scale structural complexity—including arcs, shells, bipolar structures, clumps, spirals, tori, and rotating disks (16, 17)—embedded in a smooth, radially outflowing wind. Only about a dozen AGB winds have been studied in detail (18). It has not been possible to determine any systematic morphological change during the AGB evolution, and the transition from the smaller-scale structures observed during the AGB to the PN morphologies is not understood.

In the ALMA ATOMIUM (ALMA Tracing the Origins of Molecules In dUst-forming oxygen-rich M-type stars) program (18), we observed a sample of oxygen-rich AGB stars spanning a range of (circum)stellar parameters and AGB evolutionary stages (table S1). We studied the wind morphology at spatial resolutions of  $\sim 0.24''$  and  $\sim 1''$  using the rotational lines of  $^{12}\text{CO } J = 2 \rightarrow 1$ ,  $^{28}\text{SiO } J = 5 \rightarrow 4$ , and  $^{28}\text{SiO } J = 6 \rightarrow 5$  in the ground vibrational state, where  $J$  is the rotational angular momentum quantum number. These two molecules (CO and SiO) have large fractional abundances with respect to that of molecular hydrogen and yield complementary information on the density (CO) and morphological and dynamical properties close to the stellar surface (SiO).

Figure 1 shows a gallery of the CO observations. None of the sources has a smooth, spherical geometry. The images exhibit various structures in common with post-AGB stars and PNe: bipolar morphologies with a central waist, equatorial density enhancements (EDEs) and disk-like geometries, eye-like shapes, spiral-like structures, and arcs at regularly spaced intervals (18). We infer from these images that the same physical mechanism shapes both AGB winds and PNe. These data constrain the wind-shaping mechanism, while it is in operation, in a sample of stars with a range of AGB properties—i.e., the data cover the moment in time when

<sup>1</sup>Institute of Astronomy, KU Leuven, 3001 Leuven, Belgium. <sup>2</sup>School of Chemistry, University of Leeds, Leeds LS2 9JT, UK. <sup>3</sup>Jodrell Bank Centre for Astrophysics, The University of Manchester, Manchester M13 9PL, UK. <sup>4</sup>Harvard-Smithsonian Center for Astrophysics, Cambridge, MA 02138, USA. <sup>5</sup>School of Physical Sciences, The Open University, Milton Keynes MK7 6AA, UK. <sup>6</sup>Centre for mathematical Plasma Astrophysics, KU Leuven, 3001 Leuven, Belgium. <sup>7</sup>Laboratory for Space Research, University of Hong Kong, Pokfulam, Hong Kong. <sup>8</sup>Laboratoire d'Astrophysique de Bordeaux, Université de Bordeaux, 33615 Pessac, France. <sup>9</sup>Onsala Space Observatory, Chalmers University of Technology, 43992 Onsala, Sweden. <sup>10</sup>Department of Physics and Astronomy, University College London, London WC1E 6BT, UK. <sup>11</sup>Anton Pannekoek Institute for Astronomy, University of Amsterdam, 1090 GE Amsterdam, Netherlands. <sup>12</sup>National Astronomical Research Institute of Thailand, Chiangmai 50180, Thailand. <sup>13</sup>Max-Planck-Institut für Radioastronomie, 53121 Bonn, Germany. <sup>14</sup>Laboratoire Lagrange, Observatoire de la Côte d'Azur, Université Côte d'Azur, F-06304 Nice Cedex 4, France. <sup>15</sup>Laboratoire d'Etudes Spatiales et d'Instrumentation en Astrophysique, Observatoire de Paris, Université Paris Sciences et Lettres, Centre National de la Recherche Scientifique, Sorbonne Université, Université de Paris, 92195 Meudon, France. <sup>16</sup>Astrophysics Research Centre, Queen's University Belfast, Belfast BT7 1NN, UK. <sup>17</sup>Physikalisches Institut, Universität zu Köln, 50937 Köln, Germany. <sup>18</sup>Jet Propulsion Laboratory, California Institute of Technology, Pasadena, CA 91109, USA. <sup>19</sup>SRON Netherlands Institute for Space Research, NL-3584 CA Utrecht, Netherlands. <sup>20</sup>Institut de Radioastronomie Millimétrique, 38406 Saint Martin d'Hères, France.

\*Corresponding author. Email: leen.decin@kuleuven.be



AGB morphologies are being transformed into aspherical geometries.

The combination of CO and SiO data provides an observational criterion (fig. S2) for classifying the prevailing wind morphologies (table S2). We find a correlation between the AGB mass-loss rate ( $\dot{M}$ ) and the prevailing geometry (Table 1), with a Kendall's rank correlation coefficient  $\tau_b$  of 0.79 (figs. S3 and S4)

(18). A dynamically complex EDE is often observed for oxygen-rich AGB stars with low mass-loss rates (which we refer to as “Class 1”), a bipolar structure tends to be dominant for stars with medium mass-loss rates (“Class 2”), and the winds of high mass-loss rate stars preferentially exhibit a spiral-like structure (“Class 3”). Other oxygen-rich AGB stars whose geometry was deduced from previous observations follow

this same schematic order (table S3). This correlation suggests that a common mechanism controls the wind morphology throughout the AGB phase and that it depends on the mass-loss rate.

Among the mechanisms proposed to explain asphericity, binary models, including long-period systems ( $P_{\text{orb}} \geq 1$  year,  $a \geq 2$  au) (19–21), can explain both the morphologies and the correlation with mass-loss rate (18). Stellar evolution models (22) show that most AGB stars with a mass-loss rate above  $10^{-7} M_{\odot} \text{ year}^{-1}$ —including all of those in the ATOMIUM sample—have masses above  $\sim 1.5 M_{\odot}$ . Stellar and substellar (including brown dwarfs and planets) binary population statistics (23, 24) indicate that stars with these masses have, on average,  $\geq 1$  companion(s) with masses above  $\sim 5$  Jupiter masses (18). Binary interaction is known to dominate the evolution of more massive stars (25). We conjecture that (sub)stellar binary interaction is the dominant wind-shaping agent for most AGB stars with a mass-loss rate that exceeds the nuclear burning rate. Our conjecture is supported by the growing number of detected aspherical PNe whose binary central stars have a long-period orbit ( $P_{\text{orb}} \geq 1$  year), not undergoing a common-envelope evolution (18).

On the assumption that binary interaction dominates, we derive (18) an analytical relation that estimates the probability of a binary system forming a (possibly rotating) EDE structure (large value of  $Q^1$ ) or being dominated by a spiral-like structure (low value of  $Q^1$ ) (18)

$$Q^1 = 8.32 \frac{1}{(1-e)^2} \frac{1}{f_w} \left( \frac{m_{\text{comp}}}{M_{\odot}} \right)^{1/3} \left( \frac{M_{\star}}{M_{\odot}} \right)^{7/6} \left( \frac{a}{1 \text{ au}} \right)^{-3/2} \left( \frac{\dot{M}}{10^{-6} M_{\odot} \text{ year}^{-1}} \right)^{-1}$$

where  $e$  is the eccentricity of the orbit,  $f_w$  is the fraction of the stellar wind mass present at a radial distance  $r = a$ , and  $M_{\star}$  and  $m_{\text{comp}}$  are the mass of the primary star and companion, respectively. This relation holds for a wind velocity at  $r = a$  that is lower than the orbital velocity, and it can be reformulated for the case of a high wind velocity (18). Our analytical relation supports the correlation observed in the ATOMIUM data. Higher mass-loss rate or orbital separation leads to lower injection of angular momentum into the initially spherical AGB wind by interactions with the orbiting companion and weaker shaping of the material along the orbital plane into an EDE, a circumbinary disk, or an accretion disk (18). Wide binaries, with a separation up to tens of astronomical units, produce a spiral-like structure (19).

The observed transition of the wind morphology during the AGB phase applies to oxygen-rich AGB stars, whereas carbon-rich winds most often display a (broken) spiral-like structure

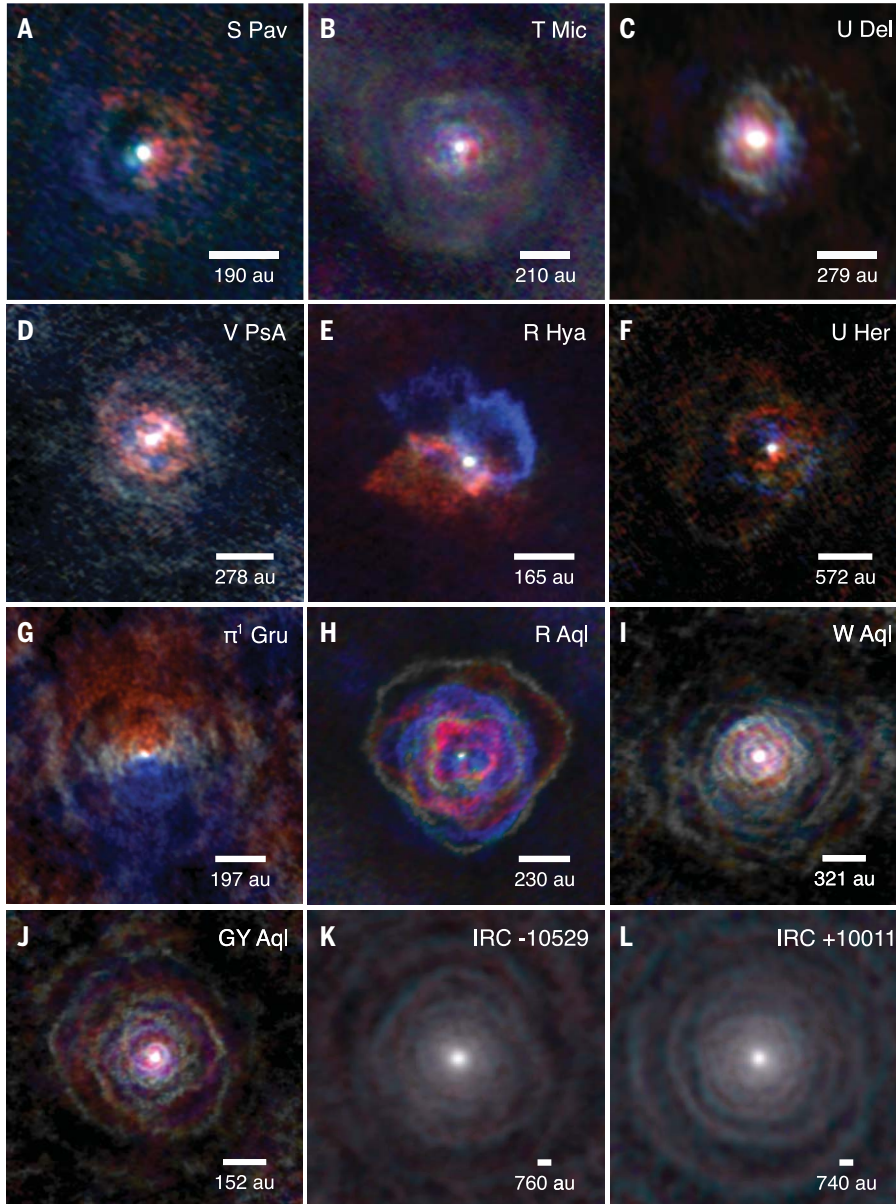


**Fig. 1. Gallery of AGB winds.** Emission maps of 12 AGB stars are shown, derived from the ATOMIUM  $^{12}\text{CO } J = 2 \rightarrow 1$  data. For each star, emission that is redshifted with respect to the local standard of rest velocity is shown in red, blueshifted emission is in blue, and rest velocity is in white. The scale bars have an angular extent of  $1''$ . Full channel maps and position-velocity diagrams for each source are shown in fig. S8 to S65. (A) S Pav, (B) T Mic, (C) U Del, (D) V PsA, (E) R Hya, (F) U Her, (G)  $\pi^1$  Gru, (H) R Aql, (I) W Aql, (J) GY Aql, (K) IRC -10529, and (L) IRC +10011. For the two other AGB stars that we observed (RW Sco and SV Aqr), the signal-to-noise ratio was too low to produce three-color maps, but the individual channels show asymmetry (figs. S20 and S28).

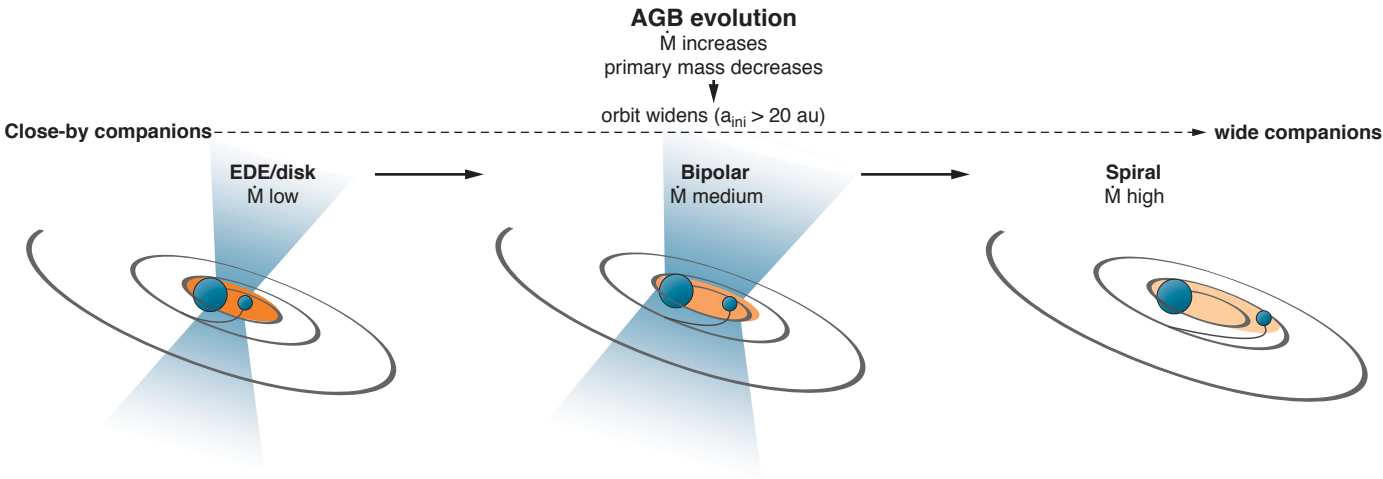


**Fig. 2. Schematic illustration of our inferred evolution of wind morphology during the AGB phase.** Most (sub)stellar companions have initial orbits ( $a_{\text{ini}}$ ) greater than 20 au (24). These orbits widen during AGB evolution because the stellar mass decreases. Binary systems with close-orbiting companions often have a high-density EDE and accretion disk (orange) and complex inner wind dynamics. For increasingly wider orbits and higher mass-loss rates, the prevailing outflow morphology initially transitions to a bipolar structure (blue shading) and then to a regularly spaced spiral structure. EDEs or accretion disks can be present at these later stages, but at lower density.

Table 1. Wind characteristics of the AGB stars in the ATOMIUM sample. The first six columns contain the source name, luminosity (in units of solar luminosity, $L_{\odot}$ ), mass-loss rate, wind velocity based on the $^{12}\text{CO } J = 2 \rightarrow 1$ line ( $v_{\text{wind}}$ ), the identification of arc morphologies in the CO $J = 2 \rightarrow 1$ channel map, and the SiO wind dynamics characterizing the velocity field ( $\mathbf{v}$ ) in the vicinity of the AGB star as derived from our ALMA data (figs. S8 to S65 and table S2) (18). The stars are ordered by increasing mass-loss rate. The last column indicates objects with similar wind characteristics. Class 1 designates sources with multiple density arcs and dynamically complex inner wind structures, with signs of a biconical outflow and/or rotation, shaping the wind in an EDE. Class 2 indicates a bipolar structure, sometimes with additional hourglass morphology in the CO channel maps. Class 3 denotes large density arc(s), often with a recognizable spiral-like structure.						
Name	Luminosity ( $L_{\odot}$ )	Mass-loss rate ( $M_{\odot} \text{ year}^{-1}$ )	$v_{\text{wind}}$ (km s $^{-1}$ )	CO morphology arcs*	SiO inner wind dynamics†	ATOMIUM classification
S Pav	4859	$8.0 \times 10^{-8}$	14	(x)	Skewed rotating $\mathbf{v}$ -field	Class 1
T Mic	4654	$8.0 \times 10^{-8}$	14	x	Skewed rotating $\mathbf{v}$ -field	Class 1
U Del	4092	$1.5 \times 10^{-7}$	17	c-xx	Bipolar/rotating flow	Class 2
RW Sco	7714	$2.1 \times 10^{-7}$	19	c-xx	– (low S/N)	Class 2
V PsA	4092	$3.0 \times 10^{-7}$	20	c-xx	Bipolar flow	Class 2
SV Aqr	4000	$3.0 \times 10^{-7}$	16	c-xx	– (low S/N)	Class 2
R Hya	7375	$4.0 \times 10^{-7}$	22	o-xx	Skewed rotating $\mathbf{v}$ -field	Class 2
U Her	8026	$5.9 \times 10^{-7}$	20	a-xx	Complex dynamics	Class 3
$\pi^{\circ}$ Gru	4683	$7.7 \times 10^{-7}$	65	o-xx	Bipolar/rotating flow	Class 2
R Aql	4937	$1.1 \times 10^{-6}$	16	xxx	–	Class 3
W Aql	9742	$3.0 \times 10^{-6}$	25	xxx	Complex dynamics	Class 3
GY Aql	9637	$4.1 \times 10^{-6}$	18	xxx	Complex dynamics	Class 3
IRC -10529	14421	$4.5 \times 10^{-6}$	20	xxx	Bipolar/rotating flow	Class 3
IRC +10011	13914	$1.9 \times 10^{-5}$	23	xxx	Complex dynamics	Class 3

\* (x): faint arc. x: several arcs with extent  $< 180^{\circ}$ . c-xx: circular or elliptical arc centered on the star. o-xx: arcs symmetrically offset from the central star. a-xx: pronounced asymmetric arcs. xxx: more than one arc with extent  $> 270^{\circ}$ , linked to a (complex) spiral structure. † Skewed rotating  $\mathbf{v}$ -field: systematic but complex signs of rotation; the  $\mathbf{v} = 0$  signature in the map of the intensity-weighted velocity field (moment1 map) is skewed. Bipolar/rotating flow: a directed bipolar flow or an EDE/disk-like structure, sometimes with Keplerian rotation. Dash: no conclusion could be drawn, sometimes because the signal-to-noise ratio of the SiO data was too low (low S/N). Complex dynamics: a clear blueshifted and redshifted velocity structure in the moment1 map, but no obvious systematic rotation can be deduced.



(18). We attribute this difference to stronger wind acceleration for carbon-rich stars than for oxygen-rich stars, owing to the different dust compositions (fig. S5). Stronger acceleration results in a smaller geometrical region in which the velocity field is nonradial, a lower probability of forming an EDE, and a smaller radius beyond which the wind shows a self-similar morphology (18). This implies that carbon-rich AGB stars are more commonly surrounded by an expanding and self-similar spiral structure, consistent with past observations (18). Although EDEs may form in carbon-rich winds, we expect EDEs to be more common around oxygen-rich AGB stars with low rates of mass loss and slowly accelerating winds (18).

Observations of binary companions around AGB progenitor stars indicate that the highest fraction of binary companions occurs at an orbital distance greater than  $\sim 20$  au (23). We calculate (18) that those orbits will widen during the AGB evolution as the mass-loss rate increases (figs. S6 and S7). This implies that early-type AGB stars with low rates of mass loss will often have an EDE, with complex flow patterns, and the wind of late-type AGB stars with high rates of mass loss is mainly shaped by spiral structures (Fig. 2). Our results also imply that the effects of planets around evolved stars are more easily detected in early-type oxygen-rich AGB stars (18).

Our proposed evolutionary scheme for AGB wind morphologies can explain multiple AGB, post-AGB, and PN phenomena (18), including why (i) circular detached shells are detected almost exclusively around carbon-rich AGB stars (26); (ii) disks are mainly found around oxygen-rich post-AGB and PN binaries (15); (iii) carbon-rich stars can be surrounded by silicate dust (27); (iv) PNe in the bulge of the Milky Way can have a mixed carbon-and-oxygen chemistry (28); (v) post-AGB envelopes can be classified according to two distinct morphological types (29); (vi) post-AGB binaries can have nonzero eccentricities with values as high as 0.3 (30); and (vii) there is a low fraction of round PNe (9, 10).

## REFERENCES AND NOTES

- K. P. Schröder, R. C. Smith, *Mon. Not. R. Astron. Soc.* **386**, 155–163 (2008).
- A. I. Karakas, *Mon. Not. R. Astron. Soc.* **445**, 347–358 (2014).
- H. J. Habing, H. Olofsson, Eds., *Asymptotic Giant Branch Stars* (Springer, 2004).
- I. McDonald, E. De Beck, A. A. Zijlstra, E. Lagadec, *Mon. Not. R. Astron. Soc.* **481**, 4984–4999 (2018).
- M. M. Miller Bertolami, *Astron. Astrophys.* **588**, A25 (2016).
- K. Gesicki, A. A. Zijlstra, M. M. Miller Bertolami, *New Astron.* **2**, 580–584 (2018).
- R. Sahai, J. T. Trauger, *Astron. J.* **116**, 1357–1366 (1998).
- R. Neri, C. Kahane, R. Lucas, V. Bujarrabal, C. Loup, *Astron. Astrophys. Suppl. Ser.* **130**, 1–64 (1998).
- R. Sahai, M. R. Morris, G. G. Villar, *Astron. J.* **141**, 134 (2011).
- Q. A. Parker et al., *Mon. Not. R. Astron. Soc.* **373**, 79–94 (2006).
- G. García-Segura, N. Langer, M. Różyczka, J. Franco, *Astrophys. J.* **517**, 767–781 (1999).
- J. Nordhaus, E. G. Blackman, A. Frank, *Mon. Not. R. Astron. Soc.* **376**, 599–608 (2007).
- B. Miszalski, A. Acker, A. F. J. Moffat, Q. A. Parker, A. Udalski, *Astron. Astrophys.* **496**, 813–825 (2009).
- B. Balick, A. Frank, *Annu. Rev. Astron. Astrophys.* **40**, 439–486 (2002).
- H. Van Winckel, *Annu. Rev. Astron. Astrophys.* **41**, 391–427 (2003).
- N. Maun, P. J. Huggins, *Astron. Astrophys.* **452**, 257–268 (2006).
- P. Kervella et al., *Astron. Astrophys.* **596**, A92 (2016).
- Materials and methods are available as supplementary materials.
- H. Kim, R. E. Taam, *Astrophys. J.* **759**, 59 (2012).
- Z. Chen, A. Frank, E. G. Blackman, J. Nordhaus, J. Carroll-Nellenback, *Mon. Not. R. Astron. Soc.* **468**, 4465–4477 (2017).
- M. I. Saladino, O. R. Pols, E. van der Helm, I. Pelupessy, S. Portegies Zwart, *Astron. Astrophys.* **618**, A50 (2018).
- P. Marigo, A. Bressan, A. Nanni, L. Girardi, M. L. Pumo, *Mon. Not. R. Astron. Soc.* **434**, 488–526 (2013).
- M. Moe, R. Di Stefano, *Astrophys. J. Suppl. Ser.* **230**, 15 (2017).
- B. J. Fulton, E. A. Petigura, *Astron. J.* **156**, 264 (2018).
- H. Sana et al., *Science* **337**, 444–446 (2012).
- H. Olofsson, U. Carlström, K. Eriksson, B. Gustafsson, L. A. Willson, *Astron. Astrophys.* **230**, L13–L16 (1990).
- F. J. Molster et al., *Astron. Astrophys.* **366**, 923–929 (2001).
- L. Guzman-Ramirez et al., *Mon. Not. R. Astron. Soc.* **414**, 1667–1678 (2011).
- T. Ueta, M. Meixner, M. Bobrowsky, *Astrophys. J.* **528**, 861–884 (2000).
- G.-M. Oomen et al., *Astron. Astrophys.* **620**, A85 (2018).

## ACKNOWLEDGMENTS

ALMA is a partnership of ESO (representing its member states), NSF (USA), and NINS (Japan), together with NRC (Canada) and NSC and ASIAA (Taiwan), in cooperation with the Republic of Chile. The Joint ALMA Observatory is operated by ESO, AUI/NRAO, and NAOJ. The CASA data reduction package was developed by an international consortium of scientists based at the National Radio Astronomical Observatory (NRAO), the European Southern Observatory (ESO), the National Astronomical Observatory of Japan (NAOJ), the CSIRO Australia Telescope National Facility (CSIRO/ATNF), and the Netherlands Institute for Radio Astronomy (ASTRON) under the guidance of NRAO. We thank the Data Reduction team at ESO for customizing the imaging pipeline. We thank the UK Science and Technology Facilities Council (STFC) IRIS for provision of high-performance computing facilities, allowing the UK ALMA Regional Centre to improve the data quality and enabling much more data to be processed. We thank the ALMA Archive scientist F. Stoehr for providing technical information. **Funding:** L.D., D.G., W.H., J.B., J.M.C.P., and S.H.J.W. acknowledge support from the ERC consolidator grant 646758 AEROSOL; L.D., H.S., and

E.C. acknowledge support from the KU Leuven under the C1 MAESTRO grant C16/17/007; H.S. acknowledges support from the European Research Council (ERC) under the European Union's DLV-77225-MULTIPLES Horizon 2020 research and innovation program; W.H. acknowledges support from the FWO Flemish Fund of Scientific Research under grant G086217N; F.H. acknowledges support from the "Programme National de Physique Stellaire" (PNPS) of CNRS/INSU cofunded by CEA and CNES; F.D.C. is supported by the EPSRC iCASE studentship program, Intel Corporation, and Cray Inc.; J.M.C.P. acknowledges support from the UK STFC grant ST/P00041X/1; J.Y. acknowledges support from the UK STFC grant ST/R001049/1; M.V.d.S. acknowledges support from the FWO through grant 12X6419N; T.D. acknowledges support from the FWO through grants 12N9917N and 12N9920N; M.M. acknowledges support from the European Union's Horizon 2020 research and innovation program under the Marie Skłodowska-Curie grant agreement 665501 with the FWO [PEGASUS]<sup>2</sup> Marie Curie fellowship 12U2717N; A.B. acknowledges support from the "Programme National de Physique Stellaire" (PNPS); I.M. acknowledges funding by the UK STFC grant ST/P000649/1; EDB acknowledges financial support from the Swedish National Space Agency; I.E.M. acknowledges support from the FWO and the European Union's Horizon 2020 research and innovation program under the Marie Skłodowska-Curie grant agreement 665501; S.E. acknowledges funding from the UK STFC as part of the consolidated grant ST/P000649/1 to the Jodrell Bank Centre for Astrophysics at the University of Manchester; P.K. acknowledges support from the French PNPS of CNRS/INSU; C.A.G. acknowledges support from NSF grant AST-1615847; T.J.M. is grateful to the STFC for support under grant ST/P000312/1; A.A.Z. was supported by the STFC under grants ST/T000414/1 and ST/P000649/1; and M.D.G. thanks the STFC for support under consolidated grant ST/P000649/1 to the JBCA. **Author contributions:** L.D. is principal investigator (PI) of the ALMA Large Program ATOMIUM, leads the ATOMIUM team, and supervises the ATOMIUM project and also developed the methodology for this work, analyzed the results, wrote the draft manuscript, contributed to Fig. 1, made Fig. 2 and figs. S1 and S2, and wrote the software for figs. S5 to S7 and figs. S8 to S65; M.M. developed the observational strategy and contributed to Fig. 1; A.M.S.R. led the ATOMIUM data reduction team and wrote software used in the data reduction; C.A.G. is co-PI of the ATOMIUM project; W.H., I.E.M., and J.B. performed hydrodynamical simulations of binary systems; I.McD. and H.S. investigated the (sub)stellar binary population statistics; M.M., T.D., W.H., S.H.J.W., A.B., S.E., F.H., and K.T.W. contributed to the data reduction; J.D.R. performed the statistical analysis and made figs. S3 and S4; J. Y. provided hardware for the ALMA data reduction; and P.K. and F.D.C. contributed to Fig. 1. All authors discussed the interpretation of the data, contributed scientific results, and helped prepare the paper. **Competing interests:** We declare no competing interests. **Data and materials availability:** The ALMA data are available from the ALMA data archive at <http://almascience.eso.org/> under project code 2018.1.00659.L. Scripts for producing figs. S5 to S7 are available at [https://github.com/LeenDecin/Supplementary\\_material\\_for\\_Science\\_paper\\_abbl229](https://github.com/LeenDecin/Supplementary_material_for_Science_paper_abbl229).

## SUPPLEMENTARY MATERIALS

[science.sciencemag.org/content/369/6510/1497/suppl/DC1](https://science.sciencemag.org/content/369/6510/1497/suppl/DC1)  
Materials and Methods  
Supplementary Text  
Figs. S1 to S65  
Tables S1 to S7  
References (31–168)  
Data S1 and S2

31 January 2020; accepted 28 July 2020  
10.1126/science.abbl229

## CORONAVIRUS

# Structure-based design of prefusion-stabilized SARS-CoV-2 spikes

Ching-Lin Hsieh<sup>1</sup>, Jory A. Goldsmith<sup>1</sup>, Jeffrey M. Schaub<sup>1</sup>, Andrea M. DiVenere<sup>2</sup>, Hung-Che Kuo<sup>1</sup>, Kamyab Javanmardi<sup>1</sup>, Kevin C. Le<sup>2</sup>, Daniel Wrapp<sup>1</sup>, Alison G. Lee<sup>1</sup>, Yutong Liu<sup>2</sup>, Chia-Wei Chou<sup>1</sup>, Patrick O. Byrne<sup>1</sup>, Christy K. Hjorth<sup>1</sup>, Nicole V. Johnson<sup>1</sup>, John Ludes-Meyers<sup>1</sup>, Annalee W. Nguyen<sup>2</sup>, Juyeon Park<sup>1</sup>, Nianshuang Wang<sup>1</sup>, Dzifa Amengor<sup>1</sup>, Jason J. Lavinder<sup>1,2</sup>, Gregory C. Ippolito<sup>1,3</sup>, Jennifer A. Maynard<sup>2\*</sup>, Ilya J. Finkelstein<sup>1,4\*</sup>, Jason S. McLellan<sup>1\*</sup>

The coronavirus disease 2019 (COVID-19) pandemic has led to accelerated efforts to develop therapeutics and vaccines. A key target of these efforts is the spike (S) protein, which is metastable and difficult to produce recombinantly. We characterized 100 structure-guided spike designs and identified 26 individual substitutions that increased protein yields and stability. Testing combinations of beneficial substitutions resulted in the identification of HexaPro, a variant with six beneficial proline substitutions exhibiting higher expression than its parental construct (by a factor of 10) as well as the ability to withstand heat stress, storage at room temperature, and three freeze-thaw cycles. A cryo-electron microscopy structure of HexaPro at a resolution of 3.2 angstroms confirmed that it retains the prefusion spike conformation. High-yield production of a stabilized prefusion spike protein will accelerate the development of vaccines and serological diagnostics for severe acute respiratory syndrome coronavirus 2 (SARS-CoV-2).

Severe acute respiratory syndrome coronavirus 2 (SARS-CoV-2) is a novel beta-coronavirus that emerged in Wuhan, China in December 2019 and is the causative agent of the coronavirus disease 2019 (COVID-19) pandemic (1, 2). Effective vaccines, therapeutic antibodies, and small-molecule inhibitors are urgently needed, and the development of these interventions is proceeding rapidly. Coronavirus virions are decorated with a spike (S) glycoprotein that binds to host cell receptors and mediates cell entry via fusion of the host and viral membranes (3). Binding of the SARS-CoV-2 spike to the angiotensin-converting enzyme 2 (ACE2) receptor (4–6) triggers a large conformational rearrangement of the spike from a metastable prefusion conformation to a highly stable postfusion conformation, facilitating membrane fusion (7, 8). Attachment and entry are essential for the viral life cycle, making the S protein a primary target of neutralizing antibodies and a critical vaccine antigen (9, 10).

Prefusion stabilization tends to increase the recombinant expression of viral fusion glycoproteins, possibly by preventing triggering or misfolding that results from a tendency to adopt the more stable postfusion structure. Prefusion-stabilized viral glycoproteins are also superior immunogens to their wild-type counterparts (11–13). Structure-based design of prefusion-stabilized MERS-CoV and SARS-CoV spike ectodomains resulted in homoge-

neous preparations of prefusion spikes and greatly increased yields (11). These variants (S-2P) contained two consecutive proline substitutions in the S2 subunit in a turn between the central helix and heptad repeat 1 (HR1) that must transition to a single, elongated  $\alpha$  helix in the postfusion conformation. These S-2P spikes have been used to determine high-resolution

structures by cryo-electron microscopy (cryo-EM) (14–17), including for SARS-CoV-2 (18, 19), and have accelerated the development of vaccine candidates. However, even with these substitutions, the SARS-CoV-2 S-2P ectodomain is unstable and difficult to produce reliably in mammalian cells, hampering biochemical research and development of subunit vaccines.

To generate a prefusion-stabilized SARS-CoV-2 spike protein that expresses at higher levels and is more stable than our original S-2P construct (18), we analyzed the SARS-CoV-2 S-2P cryo-EM structure (PDB ID 6VSB) and designed substitutions based on knowledge of class I viral fusion protein function and general protein stability principles. These strategies included the introduction of disulfide bonds to prevent conformational changes during the prefusion-postfusion transition, salt bridges to neutralize charge imbalances, hydrophobic residues to fill internal cavities, and prolines to cap helices or stabilize loops in the prefusion state. We cloned 100 single S-2P variants and characterized their relative expression levels (table S1), and for those that expressed well, we characterized their monodispersity, thermostability, and quaternary structure. Given that the S2 subunit undergoes large-scale refolding during the prefusion-postfusion transition, we exclusively focused our efforts on stabilizing S2. Substitutions of each category were identified that increased expression while

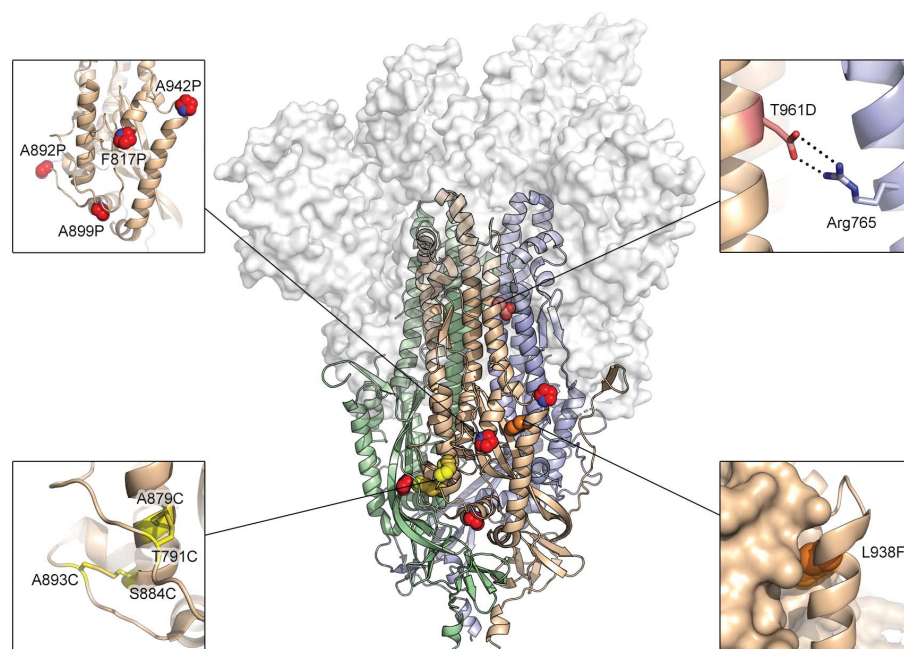


**Fig. 1. Exemplary substitutions for SARS-CoV-2 spike stabilization.** The main image is a side view of the trimeric SARS-CoV-2 spike ectodomain in a prefusion conformation (PDB ID 6VSB). The S1 domains are shown as a transparent molecular surface. The S2 domain for each protomer is shown as a ribbon diagram. Each inset corresponds to one of four types of spike modification: proline, salt bridge, disulfide, and cavity filling. Side chains in each inset are shown as red spheres (proline), yellow sticks (disulfide), red and blue sticks (salt bridge), and orange spheres (cavity filling).

<sup>1</sup>Department of Molecular Biosciences, University of Texas, Austin, TX 78712, USA. <sup>2</sup>Department of Chemical Engineering, University of Texas, Austin, TX 78712, USA. <sup>3</sup>Department of Oncology, Dell Medical School, University of Texas, Austin, TX 78712, USA. <sup>4</sup>Center for Systems and Synthetic Biology, University of Texas, Austin, TX 78712, USA.

\*Corresponding author. Email: maynard@che.utexas.edu (J.A.M.); ilya@finkelsteinlab.org (I.J.F.); jmcclellan@austin.utexas.edu (J.S.M.)



maintaining the prefusion conformation (Fig. 1 and Fig. 2A). Overall, 26 of the 100 single-substitution variants had higher expression than S-2P (table S1).

One common strategy to stabilize class I fusion proteins is to covalently link a region that undergoes a conformational change to a region that does not via a disulfide bond. For instance, the Q965C/S1003C (Gln<sup>965</sup> → Cys, Ser<sup>1003</sup> → Cys) substitution aims to link HR1 to the central helix, whereas G799C/A924C (Gly<sup>799</sup> → Cys, Ala<sup>924</sup> → Cys) aims to link HR1 to the upstream helix. Relative to S-2P, these two variants boosted protein expression by factors of 3.8 and 1.3, respectively (Fig. 2B). However, the

size-exclusion chromatography (SEC) traces of both variants showed a leftward shift relative to S-2P, indicating that the proteins were running larger than expected, which agreed well with negative-stain electron microscopy (nsEM) results that showed partially misfolded spike particles (fig. S1). Although introduction of disulfide bonds has been successful in the case of HIV-1 Env (SOSIP) and RSV F (DS-Cav1) (22, 20), it generally had detrimental effects for SARS-CoV-2 S, but there were a few exceptions. The S884C/A893C (Ser<sup>884</sup> → Cys, Ala<sup>893</sup> → Cys) and T791C/A879C (Thr<sup>791</sup> → Cys, Ala<sup>879</sup> → Cys) variants eluted on SEC at a volume similar to S-2P and were well-folded trimeric particles by

nsEM (Fig. 2E). These variants link the same  $\alpha$  helix to two different flexible loops that pack against a neighboring protomer (Fig. 1). Notably, the expression of S884C/A893C was double that of S-2P, with slightly increased thermostability (Fig. 2, F and G).

Introducing a salt bridge at the HIV-1 gp120-gp41 interface has been shown to boost expression and enhance the binding of trimer-specific antibodies (21). On the basis of a similar principle, the T961D (Thr<sup>961</sup> → Asp) and G769E (Gly<sup>769</sup> → Glu) substitutions were introduced to form interprotomeric electrostatic interactions with Arg<sup>765</sup> and Arg<sup>1014</sup>, respectively (Fig. 1). Both variants increased expression

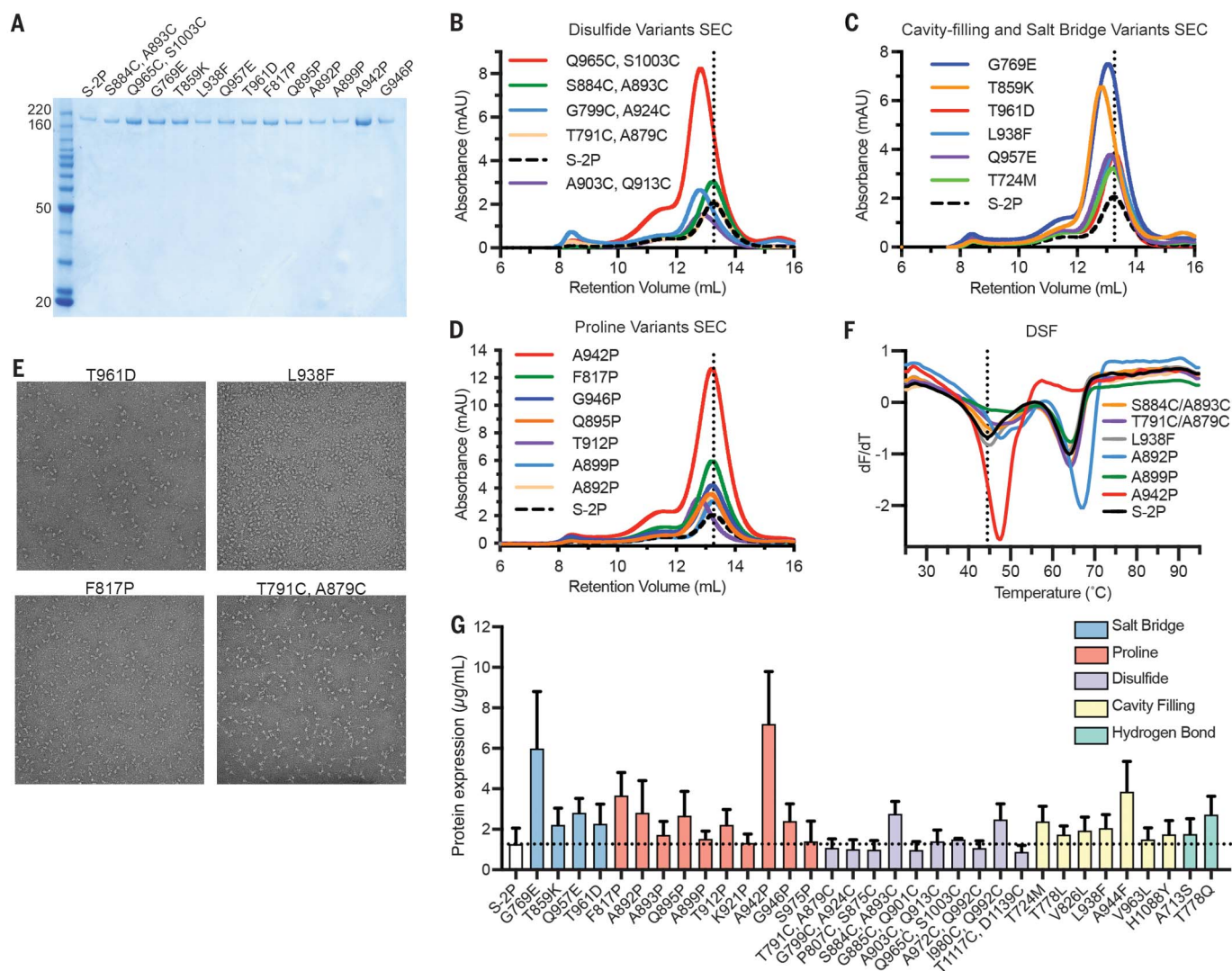


**Fig. 2. Characterization of single-substitution spike variants.** (A) SDS-polyacrylamide gel electrophoresis (PAGE) of SARS-CoV-2 S-2P and single-substitution spike variants. Molecular weight standards are indicated at the left in kDa. (B to D) Size-exclusion chromatography traces of purified spike variants, grouped by type: disulfide variants (B), cavity filling and salt bridge variants (C), and proline variants (D). A vertical dotted line indicates the characteristic peak retention volume for S-2P. (E) Representative negative-stain electron

micrographs for four variants. (F) Differential scanning fluorimetry analysis of spike variant thermostability. The vertical dotted line indicates the first apparent melting temperature for S-2P. (G) Expression levels of individual variants determined by quantitative biolayer interferometry. Variants are colored by type. The horizontal dotted line indicates the calculated concentration of S-2P, which was used as a control for comparison. Data are means  $\pm$  SD of three biological replicates.

and resembled well-folded trimeric spikes (Fig. 2, C and E, fig. S2, and table S1). In addition to salt bridges, filling loosely packed hydrophobic cores that allow the protein to refold can help to stabilize the prefusion state, as shown by previous cavity-filling substitutions in RSV F and HIV-1 Env (12, 20, 22). Here, the L938F (Leu<sup>938</sup> → Phe) substitution was de-

signed to fill a cavity formed in part by HR1, the fusion peptide, and a  $\beta$  hairpin (Fig. 1). This substitution resulted in a factor of 2 increase in expression (Fig. 2C) that was additive in combination with disulfide or proline substitutions (table S2).

Previous successes using proline substitutions inspired us to investigate 14 individual

variants wherein a proline was substituted into flexible loops or the N termini of helices in the fusion peptide, HR1, and the region connecting them (CR) (Fig. 2, D and G, and table S1). As expected, multiple proline variants boosted the protein expression and increased the thermostability (Fig. 2, D, F, and G). Two of the most successful substitutions, F817P

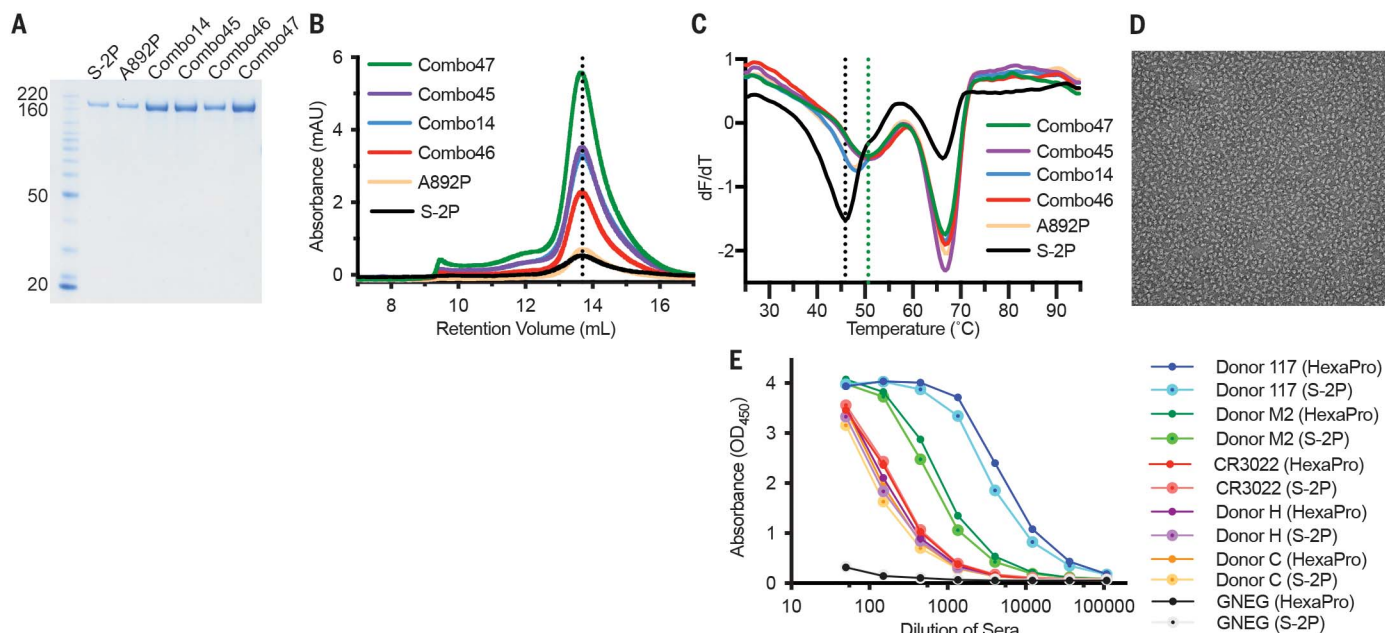


**Fig. 3. Characterization of multi-substitution spike variants.** (A) SDS-PAGE of SARS-CoV-2 Combo variants. Molecular weight standards are indicated at the left in kDa. (B) SEC traces for S-2P, A892P, and four Combo variants. The vertical dotted line indicates the peak retention volume for S-2P. (C) Differential scanning fluorimetry analysis of Combo variant thermostability. The black vertical dotted line indicates

the first apparent melting temperature for S-2P; the green vertical dotted line indicates the first apparent melting temperature for Combo47 (HexaPro).

(D) Negative-stain electron micrograph of purified Combo47 (HexaPro). (E) Binding of S-2P or HexaPro to convalescent human sera, mAb CR3022, and negative control serum (GNEG), measured by enzyme-linked immunosorbent assay.

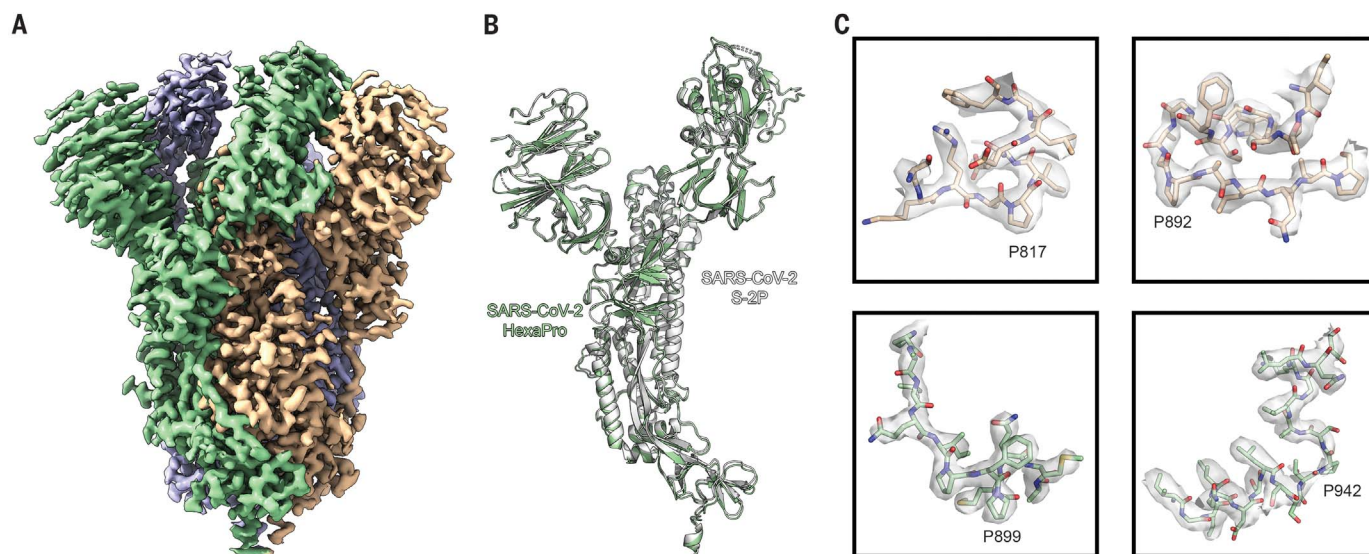


**Fig. 4. High-resolution cryo-EM structure of HexaPro.** (A) EM density map of trimeric HexaPro. Each protomer is shown in a different color; the protomer depicted in wheat adopts the RBD-up conformation. (B) Alignment of an RBD-down protomer from HexaPro (green ribbon) with an RBD-down protomer

from S-2P (white ribbon; PDB ID 6VSB). (C) Zoomed-in view of the four proline substitutions unique to HexaPro. The EM density map is shown as a transparent surface and individual atoms are shown as sticks. Blue, nitrogen atoms; red, oxygen atoms.



(Phe<sup>817</sup> → Pro) and A942P (Ala<sup>942</sup> → Pro), exhibited increases in protein yield relative to S-2P by factors of 2.8 and 6.0, respectively. The A942P substitution further increased the melting temperature ( $T_m$ ) by ~3°C, and both variants appeared as well-folded trimers by nsEM (Fig. 2E and fig. S2). This result is reminiscent of previous successful applications of proline substitutions to class I fusion proteins including HIV-1 Env, influenza HA, RSV F, hMPV F, MERS-CoV S, Lassa GPC, and Ebola GP (11, 12, 22–26).

We next generated combination (“Combo”) variants that combined the best-performing substitutions from our initial screen. The expression of the Combo variants containing two disulfide bonds was generally half that of the single-disulfide variants, which suggests that they interfered with each other (table S2). Adding one disulfide (S884C/A893C) to a single proline variant (F817P) also reduced the expression level, although the quaternary structure of the spikes was well maintained (table S2, Combo40). The beneficial effect of a disulfide bond was most prominent when combined with L938F, a cavity-filling variant. Combo23 (S884C/A893C, L938F) had higher protein yields than either of its parental variants, but the  $T_m$  of Combo23 did not increase relative to S884C/A893C (fig. S3). In addition, mixing one cavity-filling substitution with one proline substitution (Combo20) increased the expression relative to L938F alone (table S2).

Combining multiple proline substitutions resulted in the most substantial increases in expression and stability (Fig. 3A). Combo14, containing A892P (Ala<sup>892</sup> → Pro) and A942P, had a factor of 6.2 increase in protein yield relative to A892P alone (Fig. 3B). Adding a third proline, A899P (Ala<sup>899</sup> → Pro) (Combo45), increased thermostability ( $T_m$  = +1.2°C) but did not further increase expression (Fig. 3C). Combo46 (A892P, A899P, F817P) had a factor of 3.4 increase in protein yield and a 3.3°C rise in  $T_m$  as compared to A892P. The most promising variant, Combo47, renamed HexaPro, contains all four beneficial proline substitutions (F817P, A892P, A899P, A942P) as well as the two proline substitutions in S-2P. HexaPro displayed higher expression than S-2P by a factor of 9.8, had a ~5°C increase in  $T_m$ , and retained the trimeric prefusion conformation (Fig. 3D). We focused on this construct for additional characterization.

To assess the viability of HexaPro as a potential vaccine antigen or diagnostic reagent, we comprehensively examined large-scale production in FreeStyle 293-F cells, feasibility of protein expression in ExpiCHO cells, epitope integrity, and protein stability. We were able to generate ~21 mg of HexaPro from 2 liters of FreeStyle 293-F cells, or 10.5 mg/liter, which represents an improvement over S-2P by more than an order of magnitude (18). Large-scale

HexaPro preparations retained a monodisperse SEC peak corresponding to the molecular weight of a glycosylated trimer (fig. S4A) and were indistinguishable from S-2P by nsEM (fig. S4B). Industrial production of recombinant proteins typically relies on CHO cells rather than HEK293 cells. We thus investigated HexaPro expression in ExpiCHO cells via transient transfection. ExpiCHO cells produced 1.3 mg of well-folded protein per 40 ml of culture, or 32.5 mg/liter (fig. S4, C and D). In addition, the binding kinetics of HexaPro to the human ACE2 receptor were comparable to those of S-2P (fig. S4, E and F), with affinities of 13.3 nM and 11.3 nM, respectively. HexaPro remained folded in the prefusion conformation after three cycles of freeze-thaw, 2 days of incubation at room temperature, or 30 min at 55°C (fig. S4, G and H). In contrast, S-2P showed signs of aggregation after three cycles of freeze-thaw and began unfolding after 30 min at 50°C. HexaPro reacted to human convalescent sera and to receptor-binding domain (RBD)-specific monoclonal antibody (mAb) CR3022 (27) similarly to S-2P, which suggests that the antigenicity of HexaPro is well preserved (Fig. 3E). Collectively, these data indicate that HexaPro is a promising candidate for SARS-CoV-2 vaccine and diagnostic development.

To confirm that the stabilizing substitutions did not lead to any unintended conformational changes, we determined the cryo-EM structure of SARS-CoV-2 S HexaPro. From a single dataset, we were able to obtain high-resolution 3D reconstructions for two distinct conformations of S: one with a single RBD in the up conformation and the other with two RBDs in the up conformation. This two-RBD-up conformation was not observed during previous structural characterization of SARS-CoV-2 S-2P (18, 19). Although it is tempting to speculate that the enhanced stability of S2 in HexaPro allowed us to observe this less stable intermediate, validating this hypothesis will require further investigation. Roughly one-third (30.6%) of the particles were in the two-RBD-up conformation, leading to a 3.20 Å reconstruction. The remaining particles were captured in the one-RBD-up conformation, although some flexibility in the position of the receptor-accessible RBD prompted us to remove a subset of one-RBD-up particles that lacked clear density for this domain, resulting in a final set of 85,675 particles that led to a 3.21 Å reconstruction (Fig. 4A and figs. S5 and S6). Comparison of our one-RBD-up HexaPro structure with the previously determined 3.46 Å S-2P structure revealed a RMSD of 1.2 Å over 436 Cα atoms in S2 (Fig. 4B). The relatively high resolution of this reconstruction allowed us to confirm that the stabilizing proline substitutions did not distort the S2 subunit conformation (Fig. 4C).

The high yield and enhanced stability of HexaPro should enable industrial production

of subunit vaccines and could also improve DNA- or mRNA-based vaccines by producing more antigen per nucleic acid molecule, thus improving efficacy at the same dose or maintaining efficacy at lower doses. It is our hope that this work will accelerate the production of prefusion spikes to mitigate the public health emergency and has broad implications for next-generation coronavirus vaccine design.

## REFERENCES AND NOTES

1. J. F. W. Chan et al., *Lancet* **395**, 514–523 (2020).
2. C. Huang et al., *Lancet* **395**, 497–506 (2020).
3. F. Li, *Annu. Rev. Virol.* **3**, 237–261 (2016).
4. M. Hoffmann et al., *Cell* **181**, 271–280.e8 (2020).
5. Y. Wan, J. Shang, R. Graham, R. S. Baric, F. Li, *J. Virol.* **94**, e00127 (2020).
6. P. Zhou et al., *Nature* **579**, 270–273 (2020).
7. B. J. Bosch, R. van der Zee, C. A. de Haan, J. M. Rotteier, *J. Virol.* **77**, 8801–8811 (2003).
8. A. C. Walls et al., *Proc. Natl. Acad. Sci. U.S.A.* **114**, 11157–11162 (2017).
9. U. J. Buchholz et al., *Proc. Natl. Acad. Sci. U.S.A.* **101**, 9804–9809 (2004).
10. H. Hofmann et al., *J. Virol.* **78**, 6134–6142 (2004).
11. J. Pallesen et al., *Proc. Natl. Acad. Sci. U.S.A.* **114**, E7348–E7357 (2017).
12. R. W. Sanders et al., *PLOS Pathog.* **9**, e1003618 (2013).
13. M. C. Crank et al., *Science* **365**, 505–509 (2019).
14. Y. J. Park et al., *Nat. Struct. Mol. Biol.* **26**, 1151–1157 (2019).
15. Z. Li et al., *eLife* **8**, e51230 (2019).
16. N. Wang et al., *Cell Rep.* **28**, 3395–3405.e6 (2019).
17. A. C. Walls et al., *Cell* **176**, 1026–1039.e15 (2019).
18. D. Wrapp et al., *Science* **367**, 1260–1263 (2020).
19. A. C. Walls et al., *Cell* **181**, 281–292.e6 (2020).
20. J. S. McLellan et al., *Science* **342**, 592–598 (2013).
21. L. Rutten et al., *Cell Rep.* **23**, 584–595 (2018).
22. A. Krarup et al., *Nat. Commun.* **6**, 8143 (2015).
23. L. Rutten et al., *Cell Rep.* **30**, 4540–4550.e3 (2020).
24. M. B. Battles et al., *Nat. Commun.* **8**, 1528 (2017).
25. H. Qiao et al., *J. Cell Biol.* **141**, 1335–1347 (1998).
26. K. M. Hastie et al., *Science* **356**, 923–928 (2017).
27. M. Yuan et al., *Science* **368**, 630–633 (2020).

## ACKNOWLEDGMENTS

We thank members of the Maynard, Finkelstein, and McLellan Laboratories for providing helpful comments on the manuscript; T. Edwards and U. Baxa for cryo-EM data collection; and E. Fitch for providing helpful data analysis. **Funding:** Supported by NIH grants or contracts R01-A1127521 (J.S.M.), GM120554 and GM124141 (I.J.F.), A1122753 (J.A.M.), and 75N93019C00050 (J.J.L. and G.C.I.); the Bill & Melinda Gates Foundation (J.A.M., I.J.F., and J.S.M.); Welch Foundation grants F-1808 (I.J.F.) and F-1767 (J.A.M.); NSF grant 1453358 (I.J.F.); and the National Cancer Institute’s National Cryo-EM Facility at the Frederick National Laboratory for Cancer Research under contract HSSN261200800001E. I.J.F. is a Cancer Prevention and Research Institute of Texas (CPRIT) Scholar in Cancer Research. The Sauer Structural Biology Laboratory is supported by the University of Texas College of Natural Sciences and by award RR160023 from CPRIT. **Author contributions:** Conceptualization, C.-L.H. and J.S.M.; investigation and visualization, C.-L.H., J.A.G., C.-W.C., A.M.D., K.J., H.-C.K., K.C.L., A.G.L., Y.L., J.M.S., D.W., P.O.B., C.K.H., N.V.J., J.L.-M., A.W.N., J.P., G.I., J.J.L., and D.A.; writing—original draft, C.-L.H., J.A.G., D.W., P.O.B., C.K.H., N.V.J., and J.S.M.; writing—reviewing & editing, C.-L.H., J.A.G., D.W., P.O.B., N.W., C.K.H., N.V.J., J.A.M., I.J.F., and J.S.M.; supervision, J.A.M., I.J.F., and J.S.M. **Competing interests:** N.W. and J.S.M. are inventors on U.S. patent application no. 62/412,703 (“Prefusion Coronavirus Spike Proteins and Their Use”). D.W., N.W., and J.S.M. are inventors on U.S. patent application no. 62/972,886 (“2019-nCoV Vaccine”). C.-L.H., J.A.G., J.M.S., C.-W.C., A.M.D., K.J., H.-C.K., D.W., P.O.B., C.K.H., N.V.J., N.W., J.A.M., I.J.F., and J.S.M. are inventors on U.S. patent application no. 63/032,502 [“Engineered Coronavirus Spike (S) Protein and Methods of Use Thereof”]. **Data and materials availability:** Atomic coordinates and cryo-EM maps of the reported structures have been deposited

in the Protein Data Bank under accession code 6XKL and in the Electron Microscopy Data Bank under accession codes EMD-22221 and EMD-22222. HexaPro plasmid is available from Addgene (ID: 154754) or from J.S.M. under a material transfer agreement with the University of Texas at Austin. This work is licensed under a Creative Commons Attribution 4.0 International (CC BY 4.0) license, which permits unrestricted use, distribution, and reproduction in any medium, provided the original work is properly cited. To view a copy of this license, visit [https://](https://creativecommons.org/licenses/by/4.0/)

[creativecommons.org/licenses/by/4.0/](https://creativecommons.org/licenses/by/4.0/). This license does not apply to figures/photos/artwork or other content included in the article that is credited to a third party; obtain authorization from the rights holder before using such material.

#### SUPPLEMENTARY MATERIALS

[science.sciencemag.org/content/369/6510/1501/suppl/DC1](https://science.sciencemag.org/content/369/6510/1501/suppl/DC1)  
Materials and Methods

Figs. S1 to S6  
Tables S1 to S3  
References (28–33)

[View/request a protocol for this paper from Bio-protocol.](#)

30 May 2020; accepted 13 July 2020  
Published online 23 July 2020  
10.1126/science.abd0826



## CORONAVIRUS

# Structural basis for neutralization of SARS-CoV-2 and SARS-CoV by a potent therapeutic antibody

Zhe Lv<sup>1,2\*</sup>, Yong-Qiang Deng<sup>3\*</sup>, Qing Ye<sup>3\*</sup>, Lei Cao<sup>1\*</sup>, Chun-Yun Sun<sup>4\*</sup>, Changfa Fan<sup>5\*</sup>, Weijin Huang<sup>6</sup>, Shihui Sun<sup>3</sup>, Yao Sun<sup>1</sup>, Ling Zhu<sup>1</sup>, Qi Chen<sup>3</sup>, Nan Wang<sup>1,2</sup>, Jianhui Nie<sup>6</sup>, Zhen Cui<sup>1,2</sup>, Dandan Zhu<sup>1</sup>, Neil Shaw<sup>1</sup>, Xiao-Feng Li<sup>3</sup>, Qianqian Li<sup>6</sup>, Liangzhi Xie<sup>4,7,8†</sup>, Youchun Wang<sup>6†</sup>, Zihao Rao<sup>1†</sup>, Cheng-Feng Qin<sup>3†</sup>, Xiangxi Wang<sup>1,2†</sup>

The coronavirus disease 2019 (COVID-19) pandemic caused by severe acute respiratory syndrome coronavirus 2 (SARS-CoV-2) has resulted in an unprecedented public health crisis. There are no approved vaccines or therapeutics for treating COVID-19. Here we report a humanized monoclonal antibody, H014, that efficiently neutralizes SARS-CoV-2 and SARS-CoV pseudoviruses as well as authentic SARS-CoV-2 at nanomolar concentrations by engaging the spike (S) receptor binding domain (RBD). H014 administration reduced SARS-CoV-2 titers in infected lungs and prevented pulmonary pathology in a human angiotensin-converting enzyme 2 mouse model. Cryo-electron microscopy characterization of the SARS-CoV-2 S trimer in complex with the H014 Fab fragment unveiled a previously uncharacterized conformational epitope, which was only accessible when the RBD was in an open conformation. Biochemical, cellular, virological, and structural studies demonstrated that H014 prevents attachment of SARS-CoV-2 to its host cell receptors. Epitope analysis of available neutralizing antibodies against SARS-CoV and SARS-CoV-2 uncovered broad cross-protective epitopes. Our results highlight a key role for antibody-based therapeutic interventions in the treatment of COVID-19.

The coronavirus disease 2019 (COVID-19) pandemic has afflicted >7 million people in more than 200 countries and regions, resulting in 400,000 deaths as of 8 June, according to the World Health Organization. The etiological agent of this pandemic is the newly emerging coronavirus, severe acute respiratory syndrome coronavirus 2 (SARS-CoV-2), which, together with the closely related SARS-CoV, belongs to the lineage B of the genus *Betacoronavirus* in the *Coronaviridae* family (1). Sharing an amino acid sequence identity of ~80% in the envelope-located spike (S) glycoprotein, both SARS-CoV-2 and SARS-CoV use human angiotensin-converting enzyme 2 (hACE2) to enter host cells. Cellular entry is achieved by the homotrimeric S-mediated virus-receptor engagement through

the receptor-binding domain (RBD) followed by virus-host membrane fusion (1, 2). Abrogation of this crucial role played by the S protein in the establishment of an infection is the main goal of neutralizing antibodies and the focus of therapeutic interventions as well as vaccine design (3–6). Several previously characterized SARS-CoV neutralizing antibodies (NAbs) were demonstrated to exhibit very limited neutralization activities against SARS-CoV-2 (7–9). Among these, CR3022, a weakly neutralizing antibody against SARS-CoV, is tight binding, but non-neutralizing for SARS-CoV-2, indicative of possible conformational differences in the neutralizing epitopes (9). More recent studies have reported two SARS-CoV neutralizing antibodies, 47D11 and S309, that have been shown to neutralize SARS-CoV-2 as well (10, 11), suggesting that broad cross-neutralizing epitopes exist within lineage B. Convalescent plasma containing SARS-CoV-2 NAbs have been shown to confer clear protection in COVID-19 patients (12, 13), yet gaps in our knowledge concerning the immunogenic features and key epitopes of SARS-CoV-2 have hampered the development of effective immunotherapeutics against the virus.

The RBDs of SARS-CoV and SARS-CoV-2 have an amino acid sequence identity of around 75%, raising the possibility that RBD-targeting cross-neutralizing NAbs could possibly be identified. Using a phage display technique, we constructed an antibody library that was generated from RNAs extracted from peripheral lymphocytes of mice immunized with recombinant SARS-CoV RBD. SARS-CoV-2 RBD was used as the target for screening

the phage antibody library for potential hits. Antibodies that showed tight binding for SARS-CoV-2 RBD were further propagated as chimeric antibodies and tested for neutralizing activities with a vesicular stomatitis virus (VSV)-based pseudotyping system (fig. S1) (14). Among the antibodies tested, clone 014, which showed potent neutralizing activity against SARS-CoV-2 pseudovirus, was humanized and named H014. To evaluate the binding affinities, we monitored real-time association and dissociation of H014 binding to either SARS-CoV-2 RBD or SARS-CoV RBD using the OCTET system (Fortebio). Both H014 immunoglobulin G (IgG) and Fab fragments exhibited tight binding to both RBDs with comparable binding affinities at subnanomolar concentrations for SARS-CoV-2 RBD and SARS-CoV RBD, respectively (Fig. 1A and fig. S2). Pseudovirus neutralization assays revealed that H014 has potent neutralizing activities: a 50% neutralizing concentration value ( $IC_{50}$ ) of 3 nM and 1 nM against SARS-CoV-2 and SARS-CoV pseudoviruses, respectively (Fig. 1B). Plaque-reduction neutralization test (PRNT) conducted against an authentic SARS-CoV-2 strain (BetaCoV/Beijing/AMMS01/2020) verified the neutralizing activities with an  $IC_{50}$  of 38 nM, 10-fold lower than those observed in the pseudotyping system (Fig. 1C). We next sought to assess in vivo protection efficacy of H014 in our previously established hACE2 humanized mouse model that was sensitized to SARS-CoV-2 infection (15). In this model, as a result of hACE2 expression on lung cells, SARS-CoV-2 gains entry into the lungs and replicates as in a human disease, exhibiting lung pathology at 5 days post-infection (dpi). hACE2-humanized mice were treated by intraperitoneal injection of H014 at 50 mg per kilogram of body weight either 4 hours after (one dose, therapeutic) or 12 hours before and 4 hours after (two doses, prophylactic plus therapeutic) intranasal infection with  $5 \times 10^5$  plaque-forming units (PFU) of SARS-CoV-2 (BetaCoV/Beijing /AMMS01/2020). All challenged animals were sacrificed at day 5. Whereas the viral loads in the lungs of the phosphate-buffered saline (PBS) group (control) increased rapidly to  $\sim 10^7$  RNA copies/g at day 5 (Fig. 1D), in the prophylactic and prophylactic plus therapeutic groups, H014 treatment resulted in a ~10-fold and 100-fold reduction of viral titers in the lungs at day 5, respectively (Fig. 1D). Lung pathology analysis showed that SARS-CoV-2 caused mild interstitial pneumonia characterized by inflammatory cell infiltration, alveolar septal thickening, and distinctive vascular system injury upon PBS treatment. By contrast, no obvious lesions of alveolar epithelial cells or focal hemorrhage were observed in the lung sections from mice that received H014 treatment (Fig. 1E), indicative of a potential therapeutic role for H014 in treating COVID-19.

<sup>1</sup>CAS Key Laboratory of Infection and Immunity, National Laboratory of Macromolecules, Institute of Biophysics, Chinese Academy of Sciences, Beijing 100101, China.

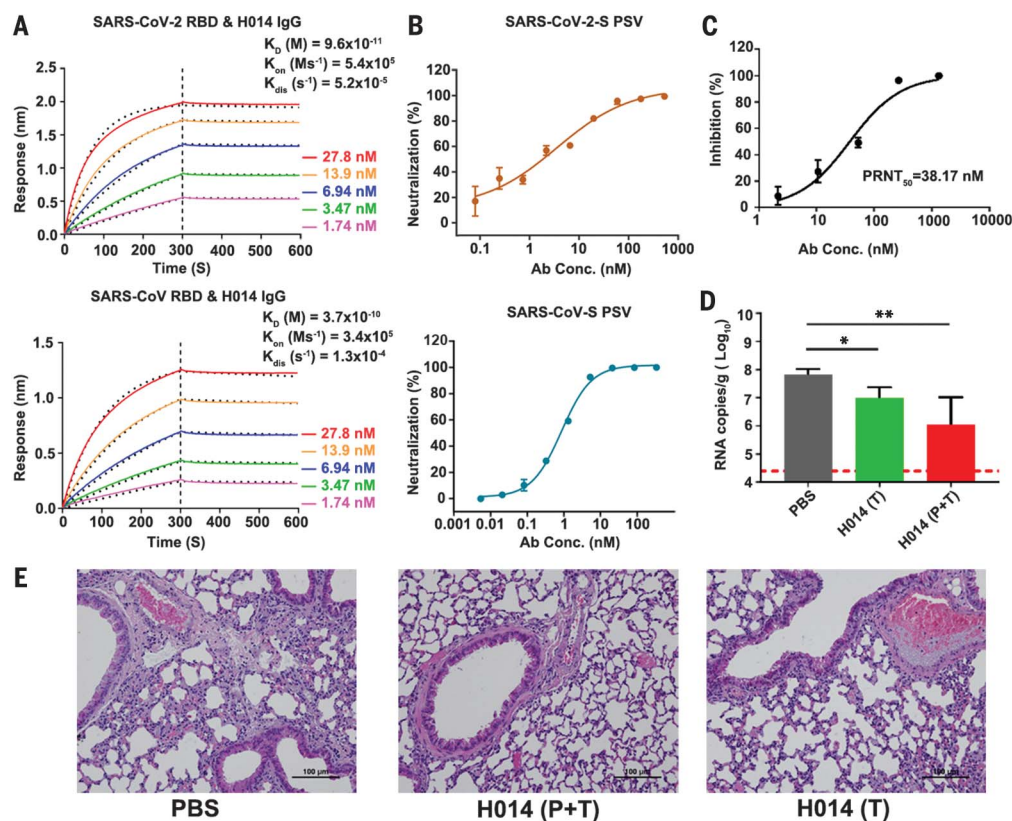
<sup>2</sup>University of Chinese Academy of Sciences, Beijing 100049, China.

<sup>3</sup>State Key Laboratory of Pathogen and Biosecurity, Institute of Microbiology and Epidemiology, Academy of Military Medical Sciences, Beijing, China. <sup>4</sup>Beijing Protein and Antibody R&D Engineering Center, Sinocelltech Ltd., Beijing 100176, China. <sup>5</sup>Division of Animal Model Research, Institute for Laboratory Animal Resources, National Institutes for Food and Drug Control (NIFDC), Beijing 102629, China. <sup>6</sup>Division of HIV/AIDS and Sex-Transmitted Virus Vaccines, Institute for Biological Product Control, National Institutes for Food and Drug Control (NIFDC), Beijing 102629, China. <sup>7</sup>Beijing Antibody Research Key Laboratory, Sino Biological Inc., Building 9, Jing Dong Bei Technology Park, No.18 Ke Chuang 10th St, BDA, Beijing, 100176, China. <sup>8</sup>Cell Culture Engineering Center, Chinese Academy of Medical Sciences & Peking Union Medical College, Beijing 100005, China.

\*These authors contributed equally to this work.

†Corresponding author. Email: xiangxi@ibp.ac.cn (X.W.); qincf@bmi.ac.cn (C.-F.Q.); wangyc@nifdc.org.cn (Y.W.); liangzhi@yahoo.com (L.X.); raozh@tsinghua.edu.cn (Z.R.)

**Fig. 1. H014 is a lineage B cross-neutralizing antibody of therapeutic value.** (A) Affinity analysis of the binding of H014 to RBD of SARS-CoV-2 and SARS-CoV. Biotinylated RBD proteins of (upper) SARS-CoV-2 or (lower) SARS-CoV were loaded on Octet SA sensor and tested for real-time association and dissociation of the H014 antibody. Global fit curves are shown as black dotted lines. The vertical dashed lines indicate the transition between association and dissociation phases. (B) Neutralizing activity of H014 against SARS-CoV-2 and SARS-CoV pseudoviruses (PSV). Serial dilutions of H014 were added to test its neutralizing activity against (upper) SARS-CoV-2 and (lower) SARS-CoV PSV. Neutralizing activities are represented as mean  $\pm$  SD. Experiments were performed in triplicate. (C) In vitro neutralization activity of H014 against SARS-CoV-2 by PRNT in Vero cells. Neutralizing activities are represented as mean  $\pm$  SD. Experiments were performed in duplicate. (D) Groups of hACE2 mice challenged with SARS-CoV-2 were treated intraperitoneally with H014 in two independent experimental settings: (i) a single dose at 4 hours after infection (therapeutic, T); and (ii) two doses at 12 hours before and 4 hours after challenge (prophylactic plus therapeutic, P+T). Virus titers in the lungs were measured 5 days post-infection (dpi) and are presented as RNA copies per gram of lung tissue.  $n = 7, 3$ , and  $3$ , respectively; ( $n$ : number of independent experiments of each group). \* $P < 0.05$ , \*\* $P < 0.01$ . Red dashed line represents limit of detection. (E) Histopathological analysis of lung samples at 5 dpi. Scale bars, 100  $\mu$ m.



The overall structure of SARS-CoV-2 S trimer resembles those of SARS-CoV and other coronaviruses. Each monomer of the S protein is composed of two functional subunits. The S1 subunit binds the host cell receptor, whereas the S2 subunit mediates fusion of the viral membrane with the host cell membrane (2, 16). The four domains within S1 include N-terminal domain (NTD), RBD, and two subdomains (SD1 and SD2), the latter of which are positioned adjacent to the S1 and S2 cleavage site. Hinge-like movements of the RBD give rise to two distinct conformational states referred to as “close” and “open,” where close corresponds to the receptor-inaccessible state and open corresponds to the receptor-accessible state, which is reported to be metastable (17–20). Cryo-electron microscopy (cryo-EM) characterization of the stabilized SARS-CoV-2 S ectodomain in complex with the H014 Fab fragment revealed that the complex adopts three distinct conformational states, corresponding to one RBD open + two RBDs closed (state 1), two RBDs open + one RBD closed (state 2), and all three open RBDs (state 3) (Fig. 2A). The structure of the completely closed (state 4) SARS-CoV-2 S trimer without any Fab bound was also observed during three-

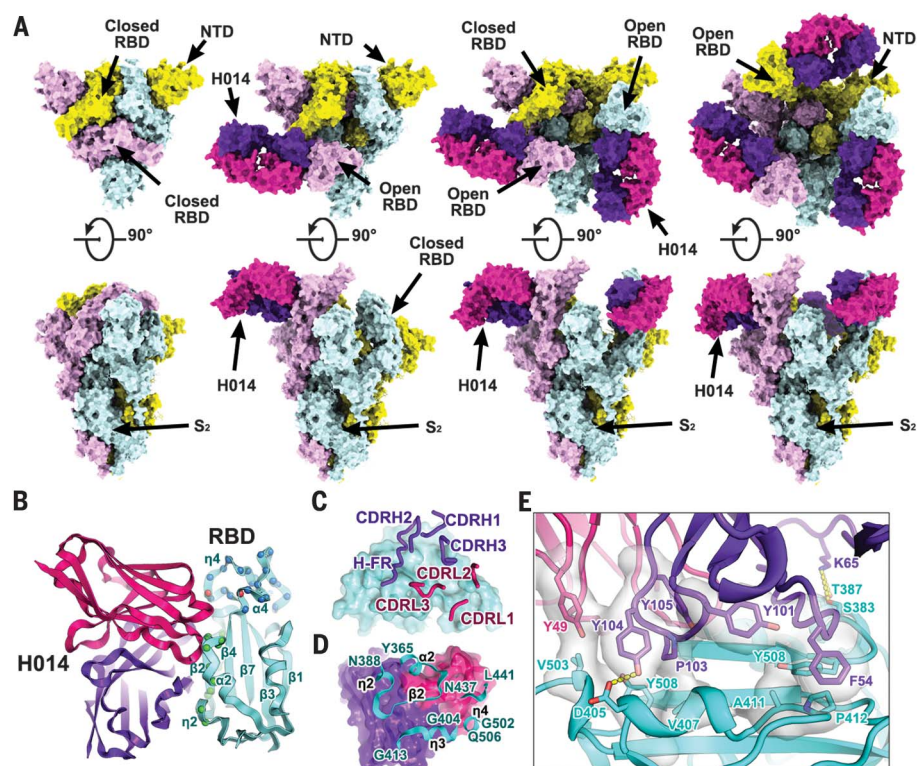
dimensional (3D) classification of the cryo-EM data, albeit in the presence of excessive Fab, suggesting that the binding sites of H014 are exposed through protein “breathing” followed by a stochastic RBD movement (Fig. 2A). We determined asymmetric cryo-EM reconstructions of the four states at 3.4 to 3.6 Å (figs. S3 to S6 and table S1). However, the electron potential maps for the binding interface between RBD and H014 are relatively weak, owing to conformational heterogeneity. To solve this problem, we performed focusing classification and refinement by using a “block-based” reconstruction approach to further improve the local resolution up to 3.9 Å, enabling reliable analysis of the interaction mode (figs. S5 and S6). Detailed analysis of the interactions between H014 and S was done using the binding interface structure.

H014 recognizes a conformational epitope on one side of the open RBD, only involving protein-protein contacts, distinct from the receptor-binding motif (RBM) (Fig. 2B). The H014 paratope constitutes all six complementary-determining region (CDR) loops (CDRL1 to -3 and CDRH1 to -3) and the unusual heavy-chain framework (HF-R, residues 58 to 65) that forges tight interactions with the RBD,

resulting in a buried area of  $\sim 1000$  Å<sup>2</sup> (Fig. 2C). Variable domains of the light chain and heavy chain contribute  $\sim 32$  and  $68\%$  of the buried surface area, respectively, through hydrophobic and hydrophilic contacts. The H014 epitope is composed of 21 residues, primarily located in the  $\alpha 2$ - $\beta 2$ - $\eta 2$  (residues 368 to 386),  $\eta 3$  (residues 405 to 408 and 411 to 413),  $\alpha 4$  (residue 439), and  $\eta 4$  (residues 503) regions, which construct a cavity on one side of the RBD (Fig. 2, B and D, and fig. S7). The 12-residue-long CDRH3 inserts into this cavity, and the hydrophobic residue (YDPYYVM)-enriched CDRH3 contacts the  $\eta 3$  and edge of the five-stranded  $\beta$ -sheet ( $\beta 2$ ) region of the RBD (Fig. 2D). Tight binding between the RBD and H014 is primarily due to extensive hydrophobic interactions contributed by two patches: one formed by F54 from CDRH2; Y101 from CDRH3; and A411, P412, and Y508 of the RBD and the other composed of Y49 from CDRL2; P103, Y104, and Y105 from CDRH3; and V407, V503, and Y508 of the RBD (Fig. 2E and table S2). Additionally, hydrophilic contacts from CDRH1 and HF-R further enhance the RBD-H014 interactions, leading to an extremely high binding affinity at subnanomolar concentration at temperatures of 25° or 37°C (Fig.



**Fig. 2. Cryo-EM structures of the SARS-CoV-2 S trimer in complex with H014.** (A) Orthogonal views of SARS-CoV-2 S trimer with three RBDs in the closed state (left), one RBD in the open state and complexed with one H014 Fab (middle), two RBDs in the open state and each complexed with one H014 Fab. NTD, N-terminal domain. All structures are presented as molecular surfaces with different colors for each S monomer (cyan, violet, and yellow), and the H014 Fab light (hot pink) and heavy (purple-blue) chains. (B) Cartoon representations of the structure of SARS-CoV-2 RBD in complex with H014 Fab with the same color scheme as in (A). Residues that constitute the H014 epitope and the RBM are shown as spheres and colored in green and blue, respectively. The overlapped residues between the H014 epitope and the RBM are shown in red. (C and D) Interactions between the H014 and SARS-CoV-2 RBD. The CDRs of the H014 that interact with SARS-CoV-2 RBD are displayed as thick tubes over the cyan surface of the RBD (C). The H014 epitope is shown as a cartoon representation over the surface of the RBD (D). (E) Details of the interactions between the H014 and SARS-CoV-2 RBD. Some residues involved in the formation of hydrophobic patches and hydrogen bonds are shown as sticks and labeled. Color scheme is the same as in (A). Abbreviations for the amino acid residues: A, Ala; D, Asp; F, Phe; G, Gly; K, Lys; L, Leu; N, Asn; P, Pro; Q, Gln; S, Ser; T, Thr; V, Val; and Y, Tyr.



2E and fig. S8). Residues that constitute the epitope are mostly conserved, with three single-site mutants (R408I, N439K, and V503F) in this region among currently circulating SARS-CoV-2 strains reported (fig. S9). In addition, a number of SARS-CoV-2 isolates bear a common mutation, V367F, in the RBD (27), which lies adjacent to the major epitope patch  $\alpha 2$ - $\beta 2$ - $\eta 2$ . Constructs of the recombinant RBD harboring point mutations of the above-mentioned residues and other reported substitutions exhibited an indistinguishable binding affinity for H014 (fig. S10), suggesting that H014 may exhibit broad neutralization activities against SARS-CoV-2 strains currently circulating worldwide. Of the 21 residues in the H014 epitope, 17 (81%) are identical between SARS-CoV-2 and SARS-CoV (fig. S9), which explains the cross-reactivity and comparable binding affinities.

To investigate whether H014 interferes with the binding of RBDs of SARS-CoV-2 or SARS-CoV to ACE2, we performed competitive binding assays at both protein and cellular levels. The enzyme-linked immunosorbent assay (ELISA) indicated that H014 competed with recombinant ACE2 for binding to RBDs of SARS-CoV-2 and SARS-CoV with  $EC_{50}$  values of 0.7 and 5 nM, respectively (Fig. 3A). Additionally, H014 efficiently blocked both the attachment of SARS-CoV-2 RBD to ACE2-expressing 293T cells and the binding of recombinant ACE2 to SARS-CoV-2 S expressing

293T cells (Fig. 3B). To verify its potential full occlusion on trimeric S, we conducted two sets of surface plasmon resonance (SPR) assays by exposing the trimeric S first to H014 and then to ACE2 or vice versa. As expected, binding of H014 completely blocked the attachment of ACE2 to trimeric S. Moreover, ACE2 could be displaced from trimeric S and replaced by H014 (Fig. 3C). To further verify these results in a cell-based viral infection model, we performed real time reverse transcription–quantitative polymerase chain reaction (RT-PCR) analysis to quantify the amount of virus remaining on the host cell surface, which was exposed to antibodies before or after attachment of virus to cells at 4°C. H014 efficiently prevented attachment of SARS-CoV-2 to the cell surface in a dose-dependent manner, and the viral particles that had already bound to the cell surface could be partially stripped by H014 (Fig. 3D). Superimposition of the structure of the H014-SARS-CoV-2 trimeric S complex over the ACE2-SARS-CoV-2 RBD complex structure revealed clashes between the ACE2 and H014, arising from an overlap of the regions belonging to the binding sites located at the apical helix ( $\eta 4$ ) of the RBD (Fig. 3E). This observation differs substantially from those of most known SARS RBD-targeted antibody complexes, where the antibodies directly recognize the RBM (22–25). Thus, the ability of H014 to prevent SARS-CoV-2

from attaching to host cells can be attributed to steric clashes with ACE2.

Similar to the RBM, the H014 epitope is only accessible in the open state, indicative of a role akin to that of the RBM—involving dynamic interferences in interactions with host cells. Our structures, together with previously reported coronavirus S structures, not including human coronavirus HKU1 (20), have observed the breathing of the S1 subunit, which mediates the transition between “closed” and “open” conformation (Fig. 4A) (2, 9, 20). In contrast to the hinge-like movement of the RBD observed in most structures, the conformational transition from “closed” to “open” observed in our structures mainly involves two steps of rotations: (i) counterclockwise movement of SD1 by  $\sim 25^\circ$  encircling the hinge point (at residue 320); (ii) counterclockwise rotation by  $\sim 60^\circ$  of the RBD itself (Fig. 4B). These conformational rotations of the SD1 and RBD at proximal points relay an amplified alteration at the distal end, leading to opening up of adequate space for the binding of H014 or ACE2 (Fig. 4B). Ambiguously, the special conformational transition observed in our complex structures results from the engagement of H014 or a synergistic movement of the SD1 and RBD.

Humoral immunity is essential for protection against coronavirus infections, and passive immunization of convalescent plasma has been



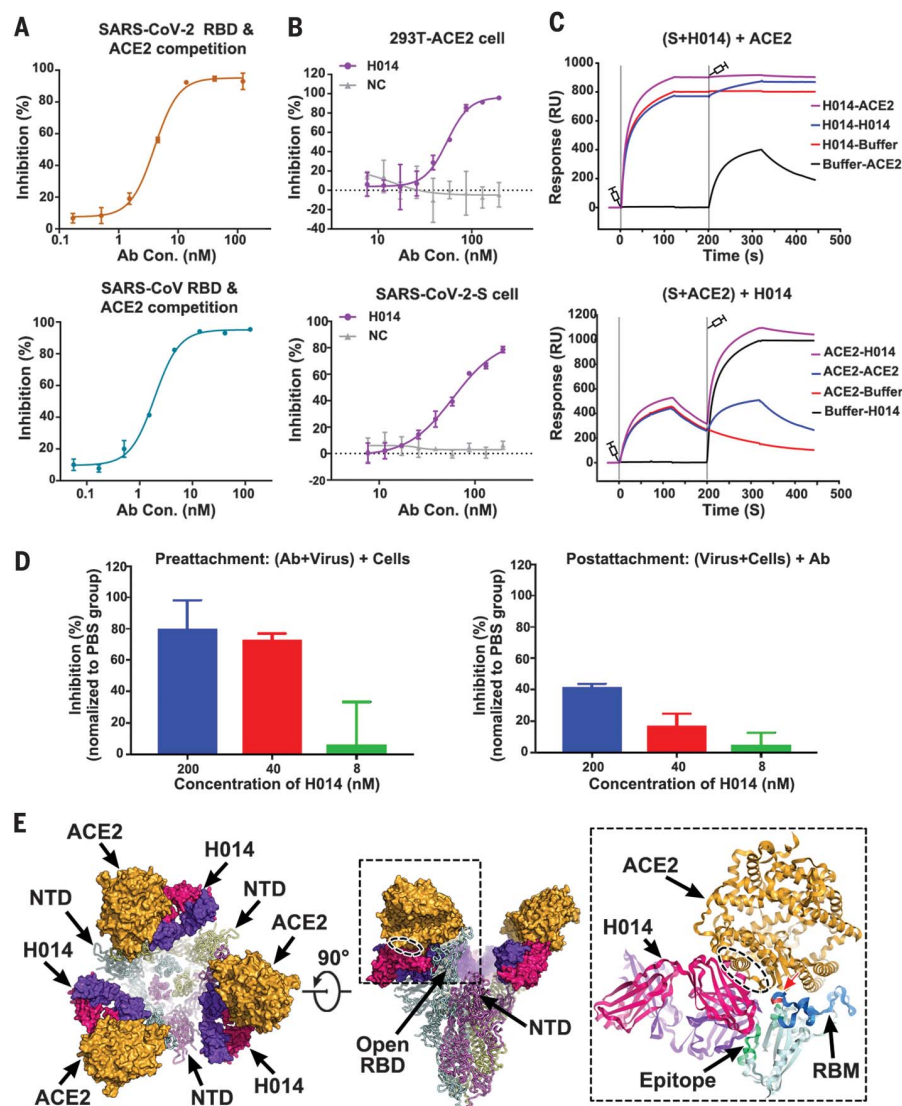


**Fig. 3. Mechanism of neutralization of H014.** (A) Competitive binding assays by ELISA. Recombinant SARS-CoV-2 (upper) or SARS-CoV (lower) RBD protein was coated on 96-well plates; recombinant ACE2 and serial dilutions of H014 were then added for competitive binding to SARS-CoV-2 or SARS-CoV RBD. Values are the mean  $\pm$  SD. Experiments were performed in triplicate. (B) Blocking of SARS-CoV-2 RBD binding to 293T-ACE2 cells by H014 (upper). Recombinant SARS-CoV-2 RBD protein and serially diluted H014 were incubated with ACE2-expressing 293T cells (293T-ACE2) and tested for binding of H014 to 293T-ACE2 cells. Competitive binding of H014 and ACE2 to SARS-CoV-2-S cells (lower). Recombinant ACE2 and serially diluted H014 were incubated with 293T cells expressing SARS-CoV-2 spike protein (SARS-CoV-2-S) and tested for binding of H014 to SARS-CoV-2-S cells. Bovine serum albumin was used as a negative control (NC). Values are mean  $\pm$  SD. Experiments were performed in triplicate. (C) Biacore SPR kinetics of competitive binding of H014 and ACE2 to SARS-CoV-2 S trimer. For both panels, SARS-CoV-2 S trimer was loaded onto the sensor. In the upper panel, H014 was first injected, followed by ACE2, whereas in the lower panel, ACE2 was injected first and then H014. The control groups are depicted by black curves. (D) Amount of virus on the cell surface, as detected by RT-PCR. Preattachment mode: Incubate SARS-CoV-2 and H014 first, then add the mixture into cells (left); postattachment mode: Uncubate SARS-CoV-2 and cells first, then add H014 into virus-cell mixtures (right). High concentrations of H014 prevented attachment of SARS-CoV-2 to the cell surface when SARS-CoV-2 was exposed to H014 before cell attachment. Values represent mean  $\pm$  SD. Experiments were performed in duplicates. (E) Clashes between H014 Fab and ACE2 upon binding to SARS-CoV-2 S. H014 and ACE2 are represented as the molecular surface; SARS-CoV-2 S trimer is shown in ribbon representation. Inset is a zoomed-in view of the interactions of the RBD, H014, and ACE2 and the clashed region (oval ellipse) between H014 and ACE2. The H014 Fab light and heavy chains, ACE2, and RBD, are presented as cartoons. The epitope, RBM, and the overlapped binding region of ACE2 and H014 on RBD are highlighted in green, blue, and red, respectively.

demonstrated to be effective in treating SARS and COVID-19 (12, 26). A number of SARS-CoV-specific neutralizing antibodies—including m396, 80R, and F26G19—have been previously reported to engage primarily the RBM core (residues 484 to 492 in SARS-CoV) provided that the RBD is in an open conformation (Fig. 4, C and D) (24, 27, 28). Unexpectedly, none of these antibodies has so far demonstrated impressive neutralizing activity against SARS-CoV-2 (7, 8). S230, a SARS-CoV neutralizing antibody that functionally mimics receptor attachment and promotes membrane fusion, despite requiring an open state of the RBD as well, recognizes a small patch at the top of the RBM (Fig. 4, C and D) (17). Recently, two other antibodies (CR3022 and S309) originating from the memory B cells of SARS survivors in 2003, demonstrated strong binding to SARS-CoV-2 (9, 10). However, CR3022 failed to neutralize SARS-CoV-2 in vitro, which could be attributed to the binding of CR3022 to a cryptic epitope, which is distal from the RBD and is only accessible when at least two RBDs are in the open state. Furthermore, CR3022 does not compete with ACE2 for binding to the RBD (Fig. 4, C and D) (9). By contrast, S309, a more recently reported neutralizing monoclonal antibody (mAb) against both SARS-CoV and SARS-CoV-2 recognizes a conserved glycan-containing epitope accessible in both the open and closed states of SARS-CoV and SARS-CoV-2 RBDs (10). The neutralization mechanism of S309 does not depend on direct blocking of receptor binding, but it induces antibody-dependent cell cytotoxicity (ADCC) and antibody-dependent cellular phagocytosis (ADCP). We reported a potent therapeutic antibody, H014, which can cross-neutralize SARS-CoV-2 and SARS-CoV infections by blocking attachment of the virus to the host cell (Fig. 3). Distinct from other antibodies, H014 binds one full side of the RBD, spanning from the proximal  $\eta$ 2 to the distal edge of the RBM, and possesses partially overlapping epitopes with SARS-CoV-specific antibodies such as m392, 80R, F26G19, CR3022, and S309 (Fig. 4, C and D). Although both SARS-CoV and SARS-CoV-2 use ACE2 to enter host cells, high sequence variations in the RBM and local conformational rearrangements at the distal end of the RBM from the two viruses have been observed (8). These probably lead to the failure of some antibodies, especially those targeting the RBM of SARS-CoV, in cross-binding and cross-neutralizing SARS-CoV-2. Three cross-reactive antibodies (CR3022, S309, and H014) recognize more conserved epitopes located beyond the RBM, among which the CR3022 epitope is most distant from the RBM (Fig. 4, C and D), suggesting a possible reason for its inability to neutralize SARS-CoV-2. H014 binds more conserved epitopes, some of which are in close proximity to the RBM, rendering it effective in cross-neutralizing

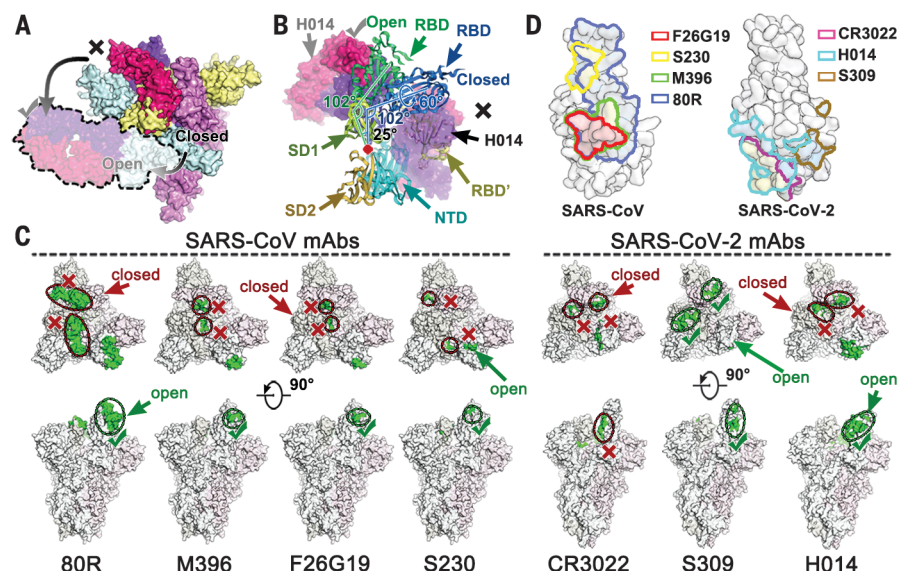


**Fig. 4. Breathing of the S1 subunit and epitopes of neutralizing antibodies.** (A) H014 can only interact with the “open” RBD, whereas the “closed” RBD is inaccessible to H014. The open RBD and RBD-bound H014 are depicted in lighter colors corresponding to the protein chain that they belong to. Color scheme is the same as in Fig. 2A. (B) Structural rearrangements of the S1 subunit of SARS-CoV-2 transition from the closed state to the open state. SD1, subdomain 1; SD2, subdomain 2; RBD’, RBD (closed state) from adjacent monomer. SD1, SD2, NTD, RBD, and RBD’ are colored in pale green, light orange, cyan, blue and yellow, respectively. The red dot indicates the hinge point. The angles between the RBD and SD1 are labeled. (C) Epitope location analysis of neutralizing antibodies on SARS-CoV and SARS-CoV-2 S trimers. The S trimer structures with one RBD open and two RBD closed from SARS-CoV and SARS-CoV-2 were used to show individual epitope information, which is highlighted in green. The accessible and inaccessible states are encircled and marked by green ticks and red crosses. (D) Footprints of the seven mAbs on RBDs of SARS-CoV (left) and SARS-CoV-2 (right). RBDs are rendered as molecular surfaces in light blue. Footprints of different mAbs are highlighted in different colors as labeled in the graph. Epitopes recognized by the indicated antibodies are labeled in blue (non-overlapped), yellow (overlapped once), and red (overlapped twice).

lineage B viruses. Additionally, antibodies recognizing more conserved patches beyond the RBM would function synergistically with antibodies targeting the RBM to enhance neutralization activities, which could mitigate the risk of viral escape. The molecular features of H014 epitopes unveiled in this study facilitate the discovery of broad cross-neutralizing epitopes within lineage B and pose interesting targets for structure-based rational vaccine design. Our studies also highlight the promise of antibody-based therapeutic interventions for the treatment of COVID-19.

## REFERENCES AND NOTES

1. P. Zhou et al., *Nature* **579**, 270–273 (2020).
2. A. C. Walls et al., *Cell* **181**, 281–292.e6 (2020).
3. Q. Gao et al., *Science* **369**, 77–81 (2020).
4. D. Corti et al., *Proc. Natl. Acad. Sci. U.S.A.* **112**, 10473–10478 (2015).
5. J. Pallesen et al., *Proc. Natl. Acad. Sci. U.S.A.* **114**, E7348–E7357 (2017).
6. A. C. Walls et al., *Nat. Struct. Mol. Biol.* **23**, 899–905 (2016).
7. X. Tian et al., *Emerg. Microbes Infect.* **9**, 382–385 (2020).
8. J. Lan et al., *Nature* **581**, 215–220 (2020).
9. M. Yuan et al., *Science* **368**, 630–633 (2020).
10. D. Pinto et al., *bioRxiv* 2020.04.07.023903 [Preprint]. 10 April 2020. <https://doi.org/10.1101/2020.04.07.023903>.
11. C. Wang et al., *Nat. Commun.* **11**, 2251 (2020).
12. A. Casadevall, L. A. Pirofski, *J. Clin. Invest.* **130**, 1545–1548 (2020).
13. C. Shen et al., *JAMA* **323**, 1582 (2020).
14. J. Nie et al., *Emerg. Microbes Infect.* **9**, 680–686 (2020).
15. S. H. Sun et al., *Cell Host Microbe* **28**, 124–133.e4 (2020).
16. D. Wrapp et al., *Science* **367**, 1260–1263 (2020).
17. A. C. Walls et al., *Cell* **176**, 1026–1039.e15 (2019).
18. M. Gui et al., *Cell Res.* **27**, 119–129 (2017).
19. Y. Yuan et al., *Nat. Commun.* **8**, 15092 (2017).
20. R. N. Kirchdoerfer et al., *Nature* **531**, 118–121 (2016).
21. Z. Z. Junxian Ou et al., *bioRxiv* 2020.03.15.991844 [Preprint]. 23 March 2020. <https://doi.org/10.1101/2020.03.15.991844>.
22. J. ter Meulen et al., *PLOS Med.* **3**, e237 (2006).
23. J. Sui et al., *Proc. Natl. Acad. Sci. U.S.A.* **101**, 2536–2541 (2004).
24. E. N. van den Brink et al., *J. Virol.* **79**, 1635–1644 (2005).
25. J. D. Berry et al., *J. Virol. Methods* **120**, 87–96 (2004).
26. A. C. Cunningham, H. P. Goh, D. Koh, *Crit. Care* **24**, 91 (2020).
27. P. Prabakaran et al., *J. Biol. Chem.* **281**, 15829–15836 (2006).
28. W. C. Hwang et al., *J. Biol. Chem.* **281**, 34610–34616 (2006).

## ACKNOWLEDGMENTS

We thank X. Huang, B. Zhu, and G. Ji for cryo-EM data collection and the Center for Biological imaging (CBI) at the Institute of Biophysics for EM work. This study was supported by the National Key Research and Development Program (2020YFA0707500, 2018YFA0900801), the Strategic Priority Research Program (XDB29010000), National Science and Technology Major Projects of Infectious Disease funds (grants 2017ZX103304402), Beijing Municipal Science and Technology Project (Z201100005420017), and Zhejiang Provincial Basic Public Welfare Research Project (LED20C010001). X.W. was supported by the Ten Thousand Talent Program and the NSFS Innovative Research Group (no. 81921005). C.-F.Q. was supported by the National Science Fund for Distinguished Young Scholar (no. 81925025) and the Innovative Research Group (no. 81621005) from the NSFC, and the Innovation Fund for Medical Sciences (no. 2019-I2M-5-049) from the Chinese Academy of Medical Sciences. L.X. and C.-Y.S. are inventors on patent application (202010219867.1) submitted by Sinocelltech Ltd. that covers the intellectual property of H014. **Author contributions:** Z.L., Y.-Q.D., C.-Y.S., Q.Y., L.C., C.F., W.H., Y.S., Q.C., S.S., N.W., D.Z., J.N., Z.C., N.S., and X.-F.L. performed experiments; X.W., C.-F.Q., Z.R., L.X., and Y.W. designed the study; all authors analyzed data; and X.W., L.Z., C.-F.Q., and Z.R. wrote the manuscript. **Competing interests:** All authors have no competing interests. **Data and materials availability:** Cryo-EM density maps of the apo SARS-CoV-2 S trimer, SARS-CoV-2 S trimer in complex with one Fab, SARS-CoV-2 S trimer in complex with two Fabs, SARS-CoV-2 S trimer in complex with three Fabs, and binding interface have been deposited at the Electron Microscopy Data Bank with accession codes EMD-30325, EMD-30326, EMD-30332, EMD-30333, and EMD-30331, and related atomic models have been deposited in Protein Data Bank under accession codes 7CAB, 7CAC, 7CAI, 7CAK, and 7CAH, respectively. H014 is available from Sinocelltech Group under a material transfer agreement with Sinocelltech. This work is licensed under a Creative Commons Attribution 4.0 International (CC BY 4.0) license, which permits unrestricted use, distribution, and reproduction in any medium, provided the original work is properly cited. To view a copy of this license, visit <https://creativecommons.org/licenses/by/4.0/>. This license does not apply to figures/photos/artwork or other content included in the article that is credited to a third party; obtain authorization from the rights holder before using such material.”

## SUPPLEMENTARY MATERIALS

[science.sciencemag.org/content/369/6510/1505/suppl/DC1](https://science.sciencemag.org/content/369/6510/1505/suppl/DC1)  
Materials and Methods  
Figs. S1 to S10  
Tables S1 and S2  
References (29–41)

[View/request a protocol for this paper from Bio-protocol.](#)

3 May 2020; accepted 16 July 2020  
Published online 23 July 2020  
10.1126/science.abc5881



## OCEAN WARMING

## Seismic ocean thermometry

Wenbo Wu<sup>1\*</sup>, Zhongwen Zhan<sup>1</sup>, Shirui Peng<sup>1</sup>, Sidao Ni<sup>2</sup>, Jörn Callies<sup>1</sup>

More than 90% of the energy trapped on Earth by increasingly abundant greenhouse gases is absorbed by the ocean. Monitoring the resulting ocean warming remains a challenging sampling problem. To complement existing point measurements, we introduce a method that infers basin-scale deep-ocean temperature changes from the travel times of sound waves that are generated by repeating earthquakes. A first implementation of this seismic ocean thermometry constrains temperature anomalies averaged across a 3000-kilometer-long section in the equatorial East Indian Ocean with a standard error of 0.0060 kelvin. Between 2005 and 2016, we find temperature fluctuations on time scales of 12 months, 6 months, and ~10 days, and we infer a decadal warming trend that substantially exceeds previous estimates.

Rising greenhouse gas concentrations in Earth's atmosphere cause an imbalance in the planet's energy budget that is, at present, on the order of 1 W per square meter of surface area (1). Almost all of this excess energy is absorbed by the ocean, which warms in response at an average rate of ~0.02 K per decade (2). How this warming is distributed between the surface and deep

ocean affects how rapidly the climate system approaches its new equilibrium (3–6). To predict the transient climate change of the coming decades and centuries, we must accurately observe and understand the rates and patterns of ocean warming (7).

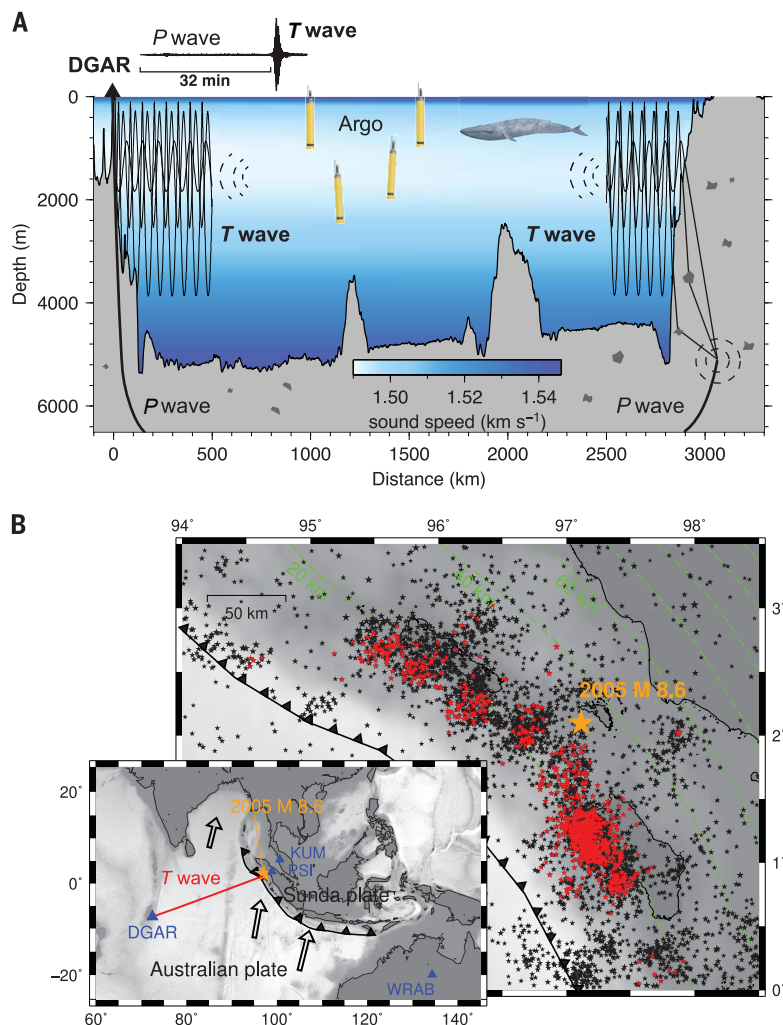
Observing secular trends on the order of a few hundredths of a kelvin per decade is a challenge because natural fluctuations on time

scales of weeks to decades often far exceed the magnitude of the expected trends (8, 9). Over the past 20 years, the Argo array of autonomous profiling floats has markedly improved the spatiotemporal coverage compared with that which had previously been possible with ship-based sampling (10). Currently, ~4000 floats each measure a profile of the upper 2000 m of the ocean every 10 days. Limitations remain, however, despite efforts to overcome them: Depths below 2000 m (11) and regions seasonally covered with sea ice (12) remain poorly sampled. Furthermore, the global coverage by Argo was sparse until about 2006 (13), and the even-sparser ship-based sampling in the pre-Argo period was exacerbated by additional complications that arose from the need to intercalibrate disparate instrumentation (14).

<sup>1</sup>Division of Geological and Planetary Sciences, California Institute of Technology, Pasadena, CA 91125, USA. <sup>2</sup>State Key Laboratory of Geodesy and Earth's Dynamics, Institute of Geodesy and Geophysics, Chinese Academy of Sciences, Wuhan 430077, China.

\*Corresponding author. Email: wenbow@caltech.edu

**Fig. 1. Principle of seismic ocean thermometry and study area. (A)** Section between Diego Garcia and Sumatra that is insonified by earthquakes off the coast of Sumatra (concentric dashed circles). The *P* wave propagates through the solid Earth, whereas the *T* wave propagates through the fluid ocean. Both are received at the seismic station DGAR on Diego Garcia. The example seismogram at the top shows a clear *T*-wave arrival at 32 min after the earthquake and a much weaker *P*-wave arrival earlier in the record. The sound speed in the ocean (calculated from ECCO) exhibits a familiar mid-depth minimum that provides a waveguide. **(B)** Study area showing the subduction of the Australian plate under the Sunda plate (inset), which causes the earthquakes we use for ocean thermometry. The large map shows all cataloged earthquakes around Nias Island (black stars) and the repeaters used for the inference of travel-time changes (red stars). The depth of the plate boundary is indicated by green contours, and the trench axis is depicted by the black line with triangles. The orange star indicates the 2005 M 8.6 Nias–Simeulue earthquake. The blue triangles in the inset show the seismic stations used in this study.



To complement the existing past and present observations, we build on an idea originally proposed by Munk and Wunsch in 1979: large-scale acoustic monitoring (15). The speed of sound in seawater depends on temperature, which allows one to infer temperature anomalies from changes in the travel time of sound waves between a source and a receiver. Thanks to the waveguide created by the mid-depth minimum in sound speed—the SOFAR (sound fixing and ranging) channel—sound waves in the ocean propagate over long distances with little attenuation, such that travel times can be used to measure temperature anomalies averaged across thousands of kilometers. These travel-time measurements intrinsically average out smaller-scale temperature fluctuations caused, for example, by mesoscale eddies and internal gravity waves. Although pilot programs were successful (16–19), a combination of concerns about the impact on marine mammals, the general unfamiliarity of the physical-oceanography community with acoustical methods, and the

expense of useful sources led to the abandonment of this scheme for global monitoring (20). Here, we demonstrate that acoustic ocean thermometry can be done passively, using natural submarine earthquakes as sources of low-frequency sound (1 to 10 Hz). We call the resulting procedure seismic ocean thermometry. [We use the term thermometry rather than tomography (15) because at present we do not have enough information to map out the temperature change.]

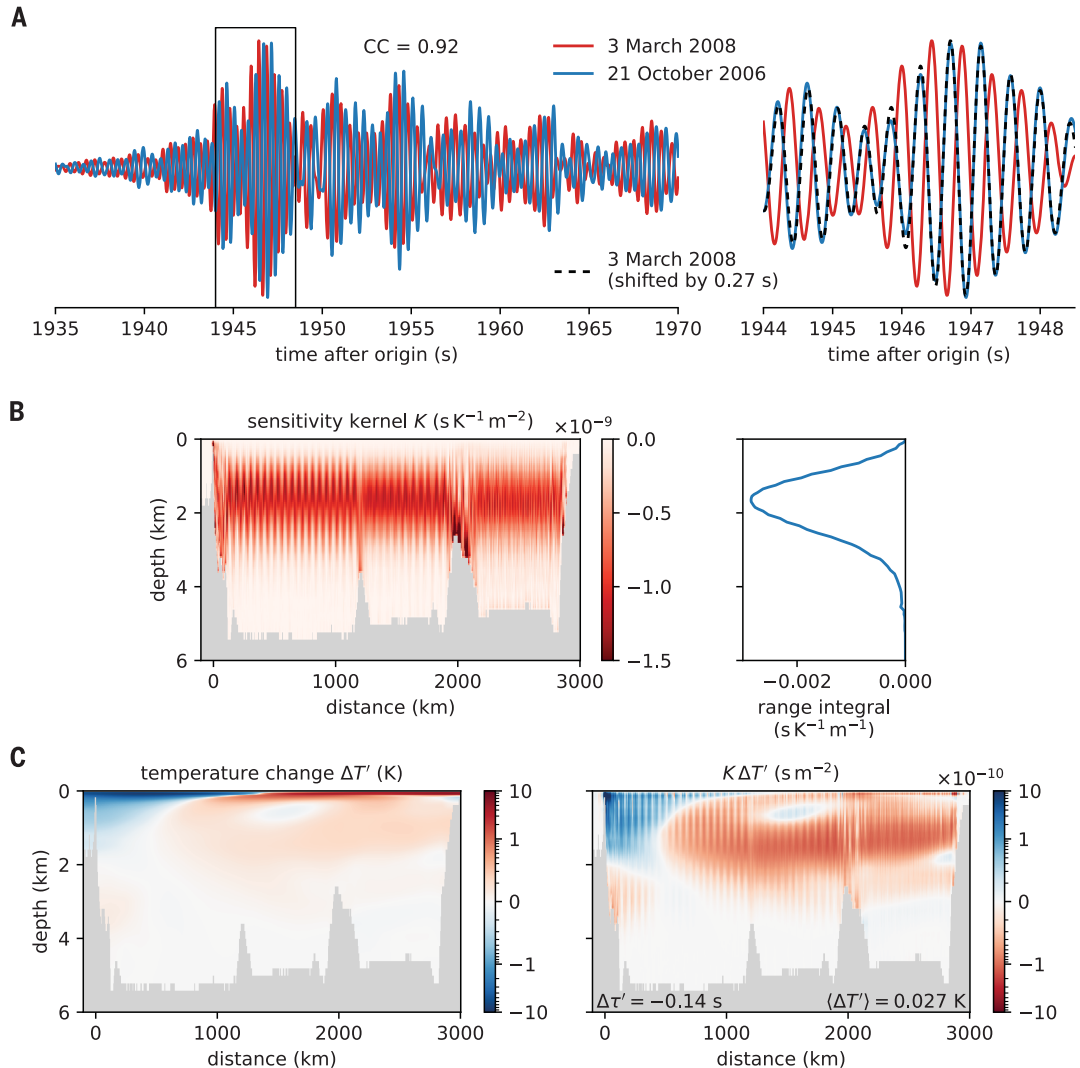
Cataloged natural earthquakes release much more energy than any anthropogenic marine sound sources. A portion of this energy vibrates the solid Earth and propagates out as seismic waves. Some of these waves encounter the seafloor and are partially converted from seismic waves in the solid Earth to sound waves in the fluid ocean. These sound waves propagate along the SOFAR channel and are typically the strongest seismic signals recorded by hydrophones (21, 22). They are also recorded at some near-shore seismic stations, where an efficient con-

version back to seismic waves causes ground motion (23, 24). Propagating at  $\sim 1.5 \text{ km s}^{-1}$ , these sound waves are much slower than seismic waves in the solid Earth and arrive minutes to hours after the direct *P* wave—the first arrival of a seismic wave traveling entirely within the solid Earth (23) (Fig. 1A). The sound waves produce a tertiary arrival in seismograms (after the *P* and *S* waves) and are therefore called *T* waves (25, 26).

As an example, *T* waves produced by earthquakes around Nias Island off the coast of Sumatra are received at the seismic station DGAR on the Central Indian Ocean atoll Diego Garcia,  $\sim 3000 \text{ km}$  from the origin (Fig. 1A). In the Nias Island region, the Australian plate is obliquely subducted below the Sunda plate, which produces one of the most seismically active regions on the planet (Fig. 1B). A few megathrust earthquakes have occurred in this region in the past 20 years, including the 2004 magnitude (M) 9.1 Sumatra and the 2005 M 8.6 Nias–Simeulue earthquakes.

**Fig. 2. Example of observed and predicted *T*-wave travel-time changes.** (A) Received

waveforms band-passed to 1.5 to 2.5 Hz for the events on 21 October 2006 (blue) and 3 March 2008 (red). The peak cross-correlation (CC) between these waveforms is 0.92, achieved by shifting the second waveform by  $\Delta\tau' = -0.27 \text{ s}$ . The right panel shows a magnification of the part of the waveform marked by the black rectangle in the left panel. (B) The sensitivity kernel *K* in the section between Diego Garcia and Sumatra (left) and its integral over the range (right). (C) Predicting the travel-time changes from the temperature anomalies estimated by ECCO. The temperature changes  $\Delta T'$  between the times of the events (left) and the contributions to the travel-time differences  $K\Delta T'$  (right) are shown. The predicted travel-time change  $\Delta\tau' = -0.14 \text{ s}$  is the range and depth integral of the right panel.





The DGAR station is an excellent receiver of  $T$  waves from the Sumatran earthquakes because there is no notable bathymetry to block the  $T$ -wave path, and the atoll's steeply sloping seafloor greatly facilitates the conversion

of sound waves back to seismic waves (27) (Fig. 1A).

The travel time of a  $T$  wave propagating from Nias Island to Diego Garcia is sensitive to the temperature anomalies it encounters

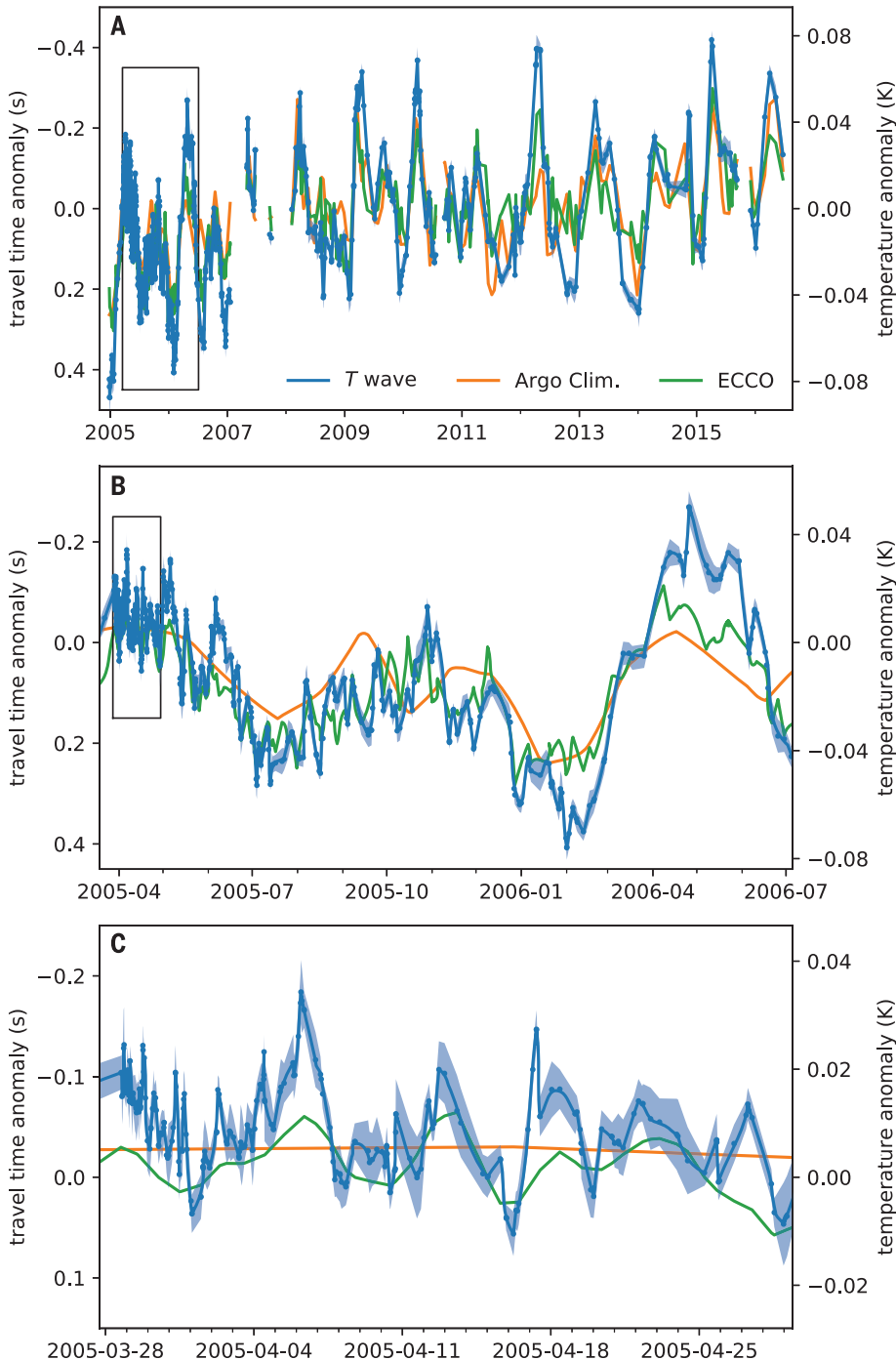


**Fig. 3. Travel-time anomalies and corresponding temperature changes. (A to C)** Travel-time anomalies  $\tau'$  (left axes) and corresponding temperature anomalies  $\langle T' \rangle$  (right axes) inferred from  $T$  waves (blue) compared with those predicted from the Argo Climatology data (orange) and ECCO data (green). Every blue dot corresponds to an earthquake that is part of at least one repeating pair. Gaps in the time series indicate gaps in the DGAR record. The Argo and ECCO estimates were interpolated to the same times as the  $T$ -wave events. The shading shows  $\pm 2$  SE. (B) and (C) show successive magnifications of the early part of the time series (indicated by the black rectangle in the preceding panel) when events were most abundant.

along its path. Typically, travel-time fluctuations from temperature anomalies strongly dominate over fluctuations arising from other factors, such as salinity anomalies or Doppler shifts by currents (28) (materials and methods). Measured  $T$ -wave travel-time anomalies can therefore be used to infer spatially averaged temperature anomalies. Expressing the travel-time anomaly  $\tau'$  at some instance  $t$  as a range ( $x$ ) and depth ( $z$ ) integral of temperature anomalies  $T'$

$$\tau'(t) = \iint K(x, z) T'(x, z, t) dx dz \quad (1)$$

and we can infer the weighted average of the temperature anomaly from the measured travel time

$$\begin{aligned} \langle T' \rangle(t) &\equiv \frac{\iint K(x, z) T'(x, z, t) dx dz}{\iint K(x, z) dx dz} \\ &= \frac{\tau'(t)}{\iint K(x, z) dx dz} \end{aligned} \quad (2)$$

The sensitivity kernel  $K(x, z)$  is crucial for the interpretation of the measured travel-time anomalies because it quantifies what part of the ocean is sampled by the  $T$  waves. We derive  $K(x, z)$  from numerical simulations of seismic- and sound-wave propagation (29) and the well-constrained dependence of the sound speed on ocean temperature (materials and methods).

The  $T$  waves' sampling of the water column—i.e., the vertical structure of  $K(x, z)$ —strongly depends on their frequency.  $T$  waves propagate largely in the form of the lowest available vertical mode, which has a frequency-dependent structure: High-frequency modes are more narrowly confined to the SOFAR channel axis, whereas low-frequency modes span a substantial portion of the water column (28).  $T$ -wave arrivals usually have a high signal-to-noise ratio in a frequency range of 1 to 10 Hz (23, 24, 30, 31). To maximize the sensitivity in the deep ocean, we filter the DGAR  $T$ -wave seismograms to the lowest-possible frequency band of 1.5 to 2.5 Hz (Fig. 2A). In this band, the sensitivity  $K(x, z)$  peaks at  $\sim 1700$ -m depth, decays to zero at the surface, and falls off relatively slowly with increasing depth—39% of the sensitivity is below 2000-m depth (Fig. 2B). The integrated sensitivity is  $\iint K(x, z) dx dz = -5.4 \text{ s K}^{-1}$ , so a uniform warming of  $T' = 0.02 \text{ K}$  would cause the travel time to reduce by  $\tau' = -0.1 \text{ s}$ . We show below that travel-time changes of this magnitude are detectable.

To infer changes in the ocean's temperature, we require pairs of  $T$  waves that originate from the same location. Repeating earthquakes (repeaters) are defined as having almost identical source properties—i.e., the location and geometry of the ruptured fault patches are nearly the same (32). Differences in the travel times

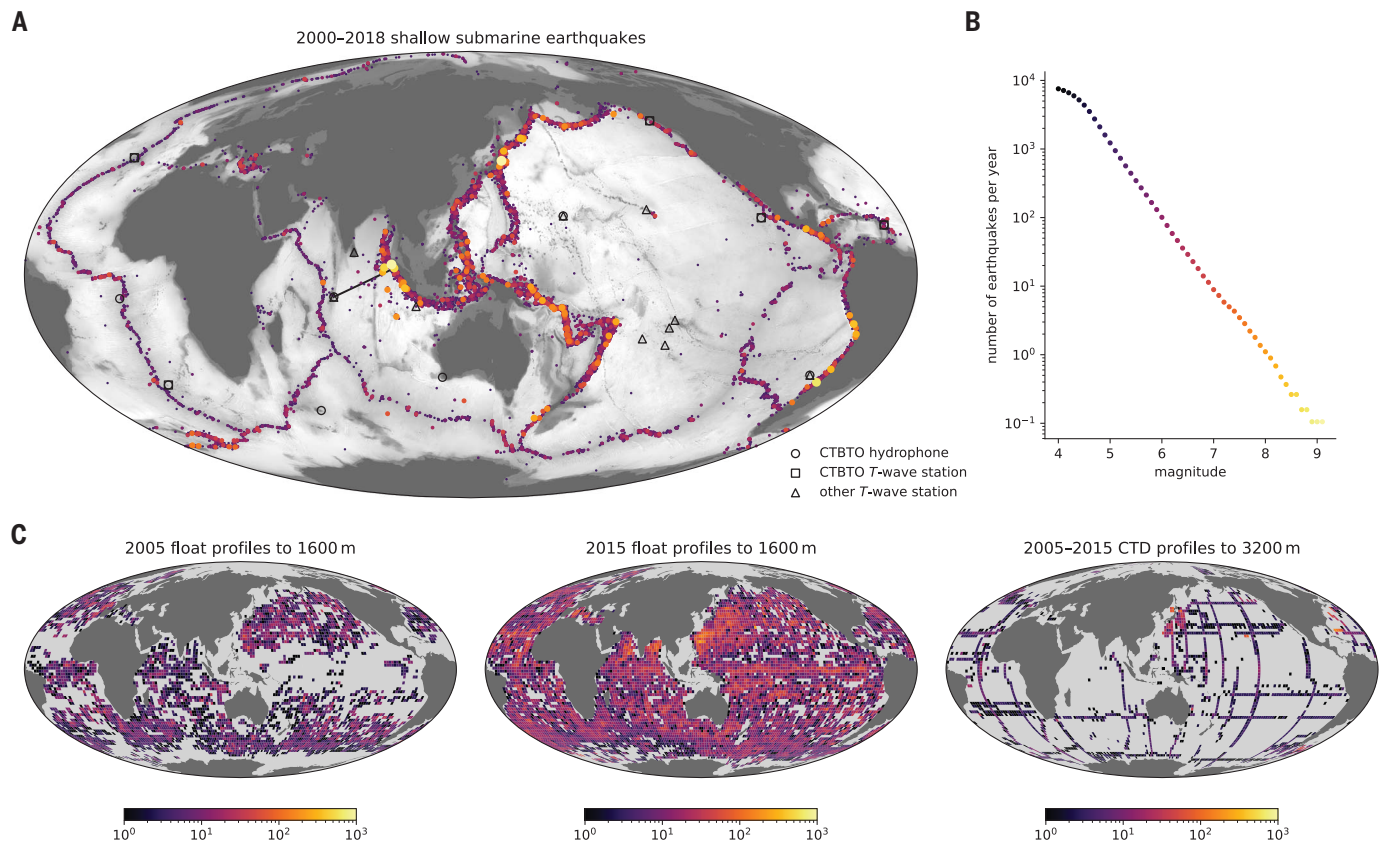


**Fig. 4. Global potential for seismic ocean thermometry and previous data coverage.** (A) Map of shallow  $M \geq 5.0$  submarine earthquakes in 2000 to 2018 (depth  $< 70$  km), with the magnitude of the earthquake indicated by the color of the dot. Also shown are the seismic and hydrophone stations that can be used to receive  $T$  waves and the  $T$ -wave path between Sumatra and Diego Garcia that we used in this study. (B) The number of

shallow submarine earthquakes per year exceeding a certain magnitude follows an exponential Gutenberg-Richter law (40). (C) Number of Argo float and conductivity-temperature-depth (CTD) profiles per  $2^\circ$  by  $2^\circ$  latitude-longitude box. The number of Argo float profiles is shown for the years 2005 and 2015, and the number of CTD profiles is shown for the full period between 2005 and 2015.

of  $P$  waves that are generated by repeaters have been used to detect weak temporal changes of Earth's crust (33) and inner core (34). Here, we use  $T$  waves from repeaters in a similar way to infer changes in the ocean.

Although the cataloged source locations of earthquakes are not typically accurate enough to identify repeaters, the waveforms of  $T$  waves can be used as fingerprints of the earthquakes' source properties. The complicated scattering history of seismic waves in the inhomogeneous crust before their arrival at the seafloor creates long and complicated waveforms that are sensitive to the earthquakes' source properties (Fig. 2A). We therefore identify repeaters by cross-correlating waveforms. Because the absolute origin times of  $T$  waves are also usually poorly constrained, we use direct  $P$  waves from at least one reference station (seismic station PSI, KUM, or WRAB, shown in Fig. 1B) to obtain the relative origin times of a pair of repeaters, assuming there are no substantial changes in the solid Earth between the two events (Fig. 1A, fig. S1, and fig. S6).

We collected data from the 4272 earthquakes that occurred in the Nias Island region between December 2004 and June 2016 and are included in the ISC (International Seismological Centre) catalog with  $M \geq 3.0$  (Fig. 1B and fig. S5). Many of these events can be considered aftershocks of the 2005  $M$  8.6 Nias-Simeulue earthquake, so the event density decays over time. We cross-correlated the waveforms of both  $T$ - and  $P$ -wave arrivals to search for repeaters. Each earthquake was paired with every other earthquake with a cataloged source location  $< 60$  km away, and we maximized the cross-correlation (CC), allowing for a time lag of up to 8 s. Using a CC threshold of 0.6 for  $T$  waves and 0.9 for  $P$  waves, we identified 2047 pairs of repeaters that arise from a total of 901 events (materials and methods). For these repeaters, we simultaneously determined the  $T$ -wave travel-time change  $\Delta\tau'$  as the time lag at which the CC is maximized (materials and methods). Given that we used three reference stations, each pair can produce up to three individual measurements of the travel-time change. We dismissed 13 outliers with

$|\Delta\tau'| > 0.65$  s, which correspond to unrealistically large temperature anomalies and may be a result of timing issues at the reference station, the skipping of multiple cycles, noise contamination, or large location discrepancy of the putative repeaters (materials and methods). We arrived at a total of 3380 measurements of  $\Delta\tau'$ .

As an example, consider the repeating earthquakes on 21 October 2006 and 3 March 2008 (Fig. 2). We measured a decrease in the  $T$ -wave travel time of  $\Delta\tau' = -0.27$  s between the two events, which amounts to an average warming of  $\langle\Delta T'\rangle = 0.051$  K. We compare this observation with the ECCO (Estimating the Circulation and Climate of the Ocean, version 4, release 4) state estimate (35, 36), which is based on Argo and most other previously available oceanographic data. In the weighted average defined by the  $T$ -wave sensitivity kernel  $K(x, z)$ , ECCO shows a warming of  $\langle\Delta T'\rangle = 0.027$  K between the two events, which corresponds to a decrease in the travel time of  $\Delta\tau' = -0.14$  s. The temperature change inferred from the  $T$  waves is thus qualitatively consistent with the deep-ocean warming that is indicated by ECCO, yet

the change inferred from the  $T$  waves is substantially larger. As discussed below, this degree of discrepancy is typical, and we speculate that it can be attributed to a lack of previous observations from the deep ocean and the smoothing that is inherent in state estimation.

The  $T$  waves from repeaters provide us with measurements of the travel-time changes  $\Delta\tau'$  between the paired events. We turn these measurements into a time series of travel-time anomalies  $\tau'$  relative to an arbitrary but common reference using a simple inversion (materials and methods). This inversion simultaneously minimizes the misfit with the measured travel-time changes and the curvature of the resulting time series, and it allows for a cycle-skipping correction. The root mean square error (RMSE) of this inversion is a travel-time change of 0.032 s, which corresponds to a temperature change of 0.0060 K. The error is likely dominated by source-location discrepancies and noise contamination (materials and methods).

The resulting time series exhibits a decadal trend toward shorter travel times and thus a warming ocean (Fig. 3A). This trend is superimposed by large fluctuations that include identifiable 12- and 6-month cycles (Fig. 3, A and B), likely induced by a seasonal cycle in the surface wind stress that causes up- or downwelling and thereby lifts or depresses temperature surfaces in the sampled region. We calculate the decadal trend by fitting a regression model to the time series that includes a linear trend and sinusoids with 12- and 6-month periods, which results in a trend of  $0.044 \pm 0.002$  K per decade. The stated error is the RMSE of the regression model and does not take the data error into account.

We compare the time series of temperature anomalies estimated from  $T$  waves with those of previous estimates: the Roemmich–Gilson Argo Climatology (37) and the ECCO state estimate (35, 36). Averaged with the same weighting  $K(x, z)$ , these two datasets show 12- and 6-month cycles that line up with those estimated with  $T$  waves (Fig. 3, A and B). The correlation coefficient between the  $T$ -wave and the Argo Climatology time series is 0.79, and that between the  $T$ -wave and the ECCO time series is 0.89; this indicates that the measured time delays are broadly consistent with previous measurements of temperature anomalies in the East Indian Ocean. The anomalies inferred from  $T$  waves tend to be larger, which may not be surprising given the smoothing that is inherent in the other two data products. The decadal trend derived from  $T$  waves is also larger: The Argo Climatology trend is  $0.026 \pm 0.001$  K per decade and the ECCO trend is  $0.039 \pm 0.001$  K per decade. These discrepancies demonstrate that the  $T$ -wave travel times add constraints on ocean warming that are complementary to the existing database.

The high density of events immediately after the 2005 Nias–Simeulue earthquake translates into a subdaily sampling of the ocean's temperature. This reveals substantial variability at a time scale on the order of 10 days (Fig. 3, B and C). The 10-day sampling cycle of Argo floats is prone to aliasing these high frequencies. ECCO does exhibit anomalies that are in phase with our estimate, likely because these anomalies are produced by the model physics and observations of other variables, for example the wind stress. Although, again, the amplitudes inferred from  $T$  waves are larger than those in ECCO, this qualitative consistency with ECCO increases our confidence that these high-frequency  $T$ -wave travel-time anomalies are the result of real ocean signals.

Although they already enhance the data coverage of temperature change in the East Indian Ocean (Fig. 4C), our  $T$ -wave estimates can also be extended in a number of ways. Unlike most other measurements (e.g., Argo profiles), the number of constraints on temperature change grows with the square of the number of  $T$ -wave observations. More events recorded in the future will keep refining the constraints on the past because new earthquakes will be identified as repeaters of past earthquakes that are not currently providing any constraints. One can also increase the number of usable events by increasing the sensitivity of the  $T$ -wave detection, for example by using hydrophones rather than seismic stations. Hydrophones are expected to have a higher signal-to-noise ratio, which may allow the use of even smaller earthquakes ( $M < 4.0$ ) and thus substantially increase the number of usable events, although such small earthquakes are typically not included in catalogs. A better signal-to-noise ratio might also allow frequency-dependent travel-time estimates, which would provide some vertical resolution of the warming.

Our first implementation of seismic ocean thermometry in the East Indian Ocean encourages an expansion of this scheme to the global ocean. Every year, ~10,000 shallow submarine earthquakes with  $M \geq 4.0$  occur across the globe (Fig. 4, A and B). Large-enough earthquakes are found in all ocean basins, both at subduction zones along the rims of basins and at mid-ocean ridges and transform faults in the basins' interiors (Fig. 4A). Records of the  $T$  waves generated by these events contain an immense amount of information on the ocean's temperature. These signals are captured by an existing network of hydrophones operated by the Comprehensive Nuclear-Test-Ban Treaty Organization (CTBTO) (Fig. 4A), and future expansions of the acoustic monitoring system (38)—possibly including hydrophones on Argo-like floats (39)—would further benefit seismic thermometry.  $T$ -wave data can provide a useful and low-cost complement to Argo data because

it constrains large-scale integrals and samples the ocean below 2000-m depth. It might also be possible to harvest data from the pre-Argo period and capture  $T$  waves propagating under sea ice. Global seismic ocean thermometry can thus substantially enhance our capability to monitor ocean warming.

## REFERENCES AND NOTES

- G. C. Johnson, J. M. Lyman, N. G. Loeb, *Nat. Clim. Chang.* **6**, 639–640 (2016).
- C. Wunsch, *Annu. Rev. Mar. Sci.* **8**, 1–33 (2016).
- J. Hansen, A. Lacis, D. Rind, G. Russell, P. Stone, I. Fung, R. Ruedy, J. Lerner, in *Climate Processes and Climate Sensitivity*, vol. 29, J. E. Hansen, T. Takahashi, Eds. (American Geophysical Union, 1984), pp. 130–163.
- J. M. Gregory, *Clim. Dyn.* **16**, 501–515 (2000).
- I. M. Held et al., *J. Clim.* **23**, 2418–2427 (2010).
- Y. Kostov, K. C. Armour, J. Marshall, *Geophys. Res. Lett.* **41**, 2108–2116 (2014).
- K. von Schuckmann et al., *Nat. Clim. Chang.* **6**, 138–144 (2016).
- C. Wunsch, *J. Phys. Oceanogr.* **40**, 2264–2281 (2010).
- B. D. Dushaw, *J. Atmos. Ocean. Technol.* **36**, 183–202 (2019).
- S. C. Riser et al., *Nat. Clim. Chang.* **6**, 145–153 (2016).
- G. C. Johnson, S. G. Purkey, N. V. Zilberman, D. Roemmich, *Geophys. Res. Lett.* **46**, 2662–2669 (2019).
- E. A. Wilson, S. C. Riser, E. C. Campbell, A. P. S. Wong, *J. Phys. Oceanogr.* **49**, 1099–1117 (2019).
- D. Roemmich et al., *Nat. Clim. Chang.* **5**, 240–245 (2015).
- J. P. Abraham et al., *Rev. Geophys.* **51**, 450–483 (2013).
- W. Munk, C. Wunsch, *Deep-Sea Res.* **26**, 123–161 (1979).
- W. H. Munk, A. M. G. Forbes, *J. Phys. Oceanogr.* **19**, 1765–1778 (1989).
- The ATOC Consortium, *Science* **281**, 1327–1332 (1998).
- P. F. Worcester et al., *J. Acoust. Soc. Am.* **105**, 3185–3201 (1999).
- B. D. Dushaw et al., *J. Geophys. Res.* **114**, C07021 (2009).
- N. Oreskes, in *Science and Technology in the Global Cold War*, N. Oreskes, J. Krige, Eds. (MIT Press, 2014), pp. 141–188.
- C. G. Fox, H. Matsumoto, T.-K. A. Lau, *J. Geophys. Res. Solid Earth* **106**, 4183–4206 (2001).
- R. P. Dziak, *Bull. Seismol. Soc. Am.* **94**, 665–677 (2004).
- E. A. Okal, in *Advances in Geophysics*, vol. 49, R. Dmowska, Ed. (Elsevier, 2008), pp. 1–65.
- J. S. Buehler, P. M. Shearer, *Geophys. Res. Lett.* **42**, 6607–6613 (2015).
- D. Linehan, *EOS Trans. Am. Geophys. Union* **21**, 229–232 (1940).
- I. Tolstoy, M. Ewing, *Bull. Seismol. Soc. Am.* **40**, 25–51 (1950).
- J. Talandier, E. A. Okal, *Bull. Seismol. Soc. Am.* **88**, 621–632 (1998).
- W. Munk, P. Worcester, C. Wunsch, *Ocean Acoustic Tomography* (Cambridge Univ. Press, 1995).
- D. Komatitsch, J. Tromp, *Geophys. J. Int.* **139**, 806–822 (1999).
- E. A. Okal, J. Talandier, *J. Geophys. Res.* **102**, 27421–27437 (1997).
- M. Sáez, S. Ruiz, *Geophys. Res. Lett.* **45**, 2610–2617 (2018).
- N. Uchida, R. Bürgmann, *Annu. Rev. Earth Planet. Sci.* **47**, 305–332 (2019).
- W. Yu, T.-R. A. Song, P. G. Silver, *Bull. Seismol. Soc. Am.* **103**, 2797–2809 (2013).
- X. Song, P. G. Richards, *Nature* **382**, 221–224 (1996).
- G. Forget et al., *Geosci. Model Dev.* **8**, 3071–3104 (2015).
- ECCO Consortium, I. Fukumori, O. Wang, I. Fenty, G. Forget, P. Heimbach, R. M. Ponte, ECCO Central Estimate (Version 4, Release 4) (2020); <https://ecco.jpl.nasa.gov/drive/files/Version4/Release4>.
- D. Roemmich, J. Gilson, *Prog. Oceanogr.* **82**, 81–100 (2009).
- B. M. Howe et al., *Front. Mar. Sci.* **6**, 426 (2019).
- A. Sukhovich et al., *Nat. Commun.* **6**, 8027 (2015).
- B. Gutenberg, C. F. Richter, *Bull. Seismol. Soc. Am.* **34**, 185–188 (1944).



41. Argo, Argo float data and metadata from Global Data Assembly Centre (Argo GDAC), SEANOE (2020); <https://doi.org/10.17882/42182>.

ACKNOWLEDGMENTS

**Funding:** This work was supported in part by the Caltech Seismological Laboratory Director’s Postdoctoral Scholar fellowship awarded to W.W. and by the Resnick Sustainability Institute. S.N. was supported by the National Natural Science Foundation of China (grant 41590854) and the Chinese Academy of Sciences (grant XDB18000000). **Author contributions:** W.W. conceived the original idea. Z.Z. and J.C. supervised the study. W.W. processed the seismic data and conducted the seismic

modeling. S.P. and J.C. processed the oceanographic data, and J.C. performed the data inversion. The paper was written by W.W. and J.C. with input from Z.Z. and S.N. All authors discussed the results and commented on the manuscript. **Competing interests:** The authors declare no competing interests. **Data and materials availability:** The seismic data are archived at the Incorporated Research Institutions for Seismology (IRIS) and are accessible through the IRIS Data Management Center (<http://ds.iris.edu/>). ECCO data are available from NASA’s Data Portal (<https://data.nas.nasa.gov/>). Argo data are collected and made freely available by the International Argo Program and the national programs that contribute to it. The float data are available from the Global Data Assembly Centre (41). The figures were prepared

using the Generic Mapping Tools ([www.soest.hawaii.edu/gmt/](http://www.soest.hawaii.edu/gmt/)), Obspy (<https://github.com/obspy/obspy>), Cartopy (<https://scitools.org.uk/cartopy/>), and Matplotlib (<https://matplotlib.org/>).

SUPPLEMENTARY MATERIALS

[science.sciencemag.org/content/369/6510/1510/suppl/DC1](https://science.sciencemag.org/content/369/6510/1510/suppl/DC1)  
Materials and Methods  
Figs. S1 to S16  
Table S1  
References (42–56)  
28 March 2020; accepted 31 July 2020  
10.1126/science.abb9519

## PLASTIC POLLUTION

# Predicted growth in plastic waste exceeds efforts to mitigate plastic pollution

Stephanie B. Borrelle<sup>1,2,3\*</sup>, Jeremy Ringma<sup>4,5,6</sup>, Kara Lavender Law<sup>7</sup>, Cole C. Monnahan<sup>8</sup>, Laurent Lebreton<sup>9,10</sup>, Alexis McGivern<sup>11</sup>, Erin Murphy<sup>12,13</sup>, Jenna Jambeck<sup>2</sup>, George H. Leonard<sup>14</sup>, Michelle A. Hilleary<sup>15</sup>, Marcus Eriksen<sup>16</sup>, Hugh P. Possingham<sup>17,18</sup>, Hannah De Frond<sup>1</sup>, Leah R. Gerber<sup>12,13</sup>, Beth Polidoro<sup>13,19</sup>, Akbar Tahir<sup>20,21</sup>, Miranda Bernard<sup>12,13</sup>, Nicholas Mallos<sup>14</sup>, Megan Barnes<sup>6,22</sup>, Chelsea M. Rochman<sup>1\*</sup>

Plastic pollution is a planetary threat, affecting nearly every marine and freshwater ecosystem globally. In response, multilevel mitigation strategies are being adopted but with a lack of quantitative assessment of how such strategies reduce plastic emissions. We assessed the impact of three broad management strategies, plastic waste reduction, waste management, and environmental recovery, at different levels of effort to estimate plastic emissions to 2030 for 173 countries. We estimate that 19 to 23 million metric tons, or 11%, of plastic waste generated globally in 2016 entered aquatic ecosystems. Considering the ambitious commitments currently set by governments, annual emissions may reach up to 53 million metric tons per year by 2030. To reduce emissions to a level well below this prediction, extraordinary efforts to transform the global plastics economy are needed.

Countries around the world are struggling to manage current volumes of plastic waste and ubiquitous plastic pollution (1, 2). From the poles to the deep ocean basins, marine and freshwater ecosystems are accumulating the world's plastic debris (3–5). Simultaneously, the petrochemical industry announced over \$204 billion U.S. in investment driven by the shale gas boom, leading to a projected acceleration in virgin plastic production (6).

As plastic production surges, multiscale commitments aim to reduce plastic emissions into the environment [e.g., Addressing Single-Use Plastic Products Pollution (Resolution EA.4/L9) (7), the United Nations Environment Assembly Resolutions Marine Litter and Microplastics (1), and Goal 14.1 of the United Nations Sustainable Development Goals (8)]. Communities, nongovernmental organizations (NGOs), and businesses are cleaning beaches and promoting zero-waste lifestyles (9). Governments are banning and placing levies on single-use consumer plastic products and, with the private sector, investing in plastic waste management including integration into a circular economy (10–12). A recent amendment to the Basel Convention targets marine plastic pollution by tracking the global trade of plastic

waste to address issues of oversupply to countries that lack the capacity to manage it (13). However, all commitments to date lack a quantitative model that connects these actions to a measurable reduction in plastic emissions.

Here, we present a mechanistic model to evaluate how different levels of effort would reduce plastic emissions into the world's freshwater and marine ecosystems, which includes major rivers, lakes, and oceans (hereafter referred to simply as “aquatic ecosystems”), by 2030. For 173 countries, representing ~97% of the world's population, we estimate the amount of inadequately managed plastic waste entering aquatic ecosystems annually from 2016 to 2030 for three scenarios: business as usual (BAU), in which plastic production and waste generation follow current trajectories; an ambitious scenario that draws upon existing global commitments to reduce plastic emissions (1, 9, 10, 14, 15); and a target scenario to reduce annual plastic emissions. Because an environmentally acceptable threshold has yet to be defined, we set the target scenario to 8 million metric tons (Mt), the estimated global emissions in 2010 to the oceans [(16); a subset of aquatic ecosystems considered here] that galvanized global action on plastic pollution by a variety of stakeholders (7). Scenarios

demonstrating the level of effort required to achieve lower targets can be found in the supplementary materials.

We can predict plastic emissions entering aquatic ecosystems to 2030 by integrating expected population growth (17), annual waste generation per capita (2), the proportion of plastic in waste [(2); incorporating an increase in plastic materials associated with predicted production increases], and the proportion of inadequately managed waste by country [(2, 16, 18); see the supplementary materials; fig. S1]. For 173 countries with available data, we calculated annual plastic emissions entering aquatic ecosystems using a distance-based probability function. This function estimates the proportion of inadequately managed waste to reach the nearest aquatic ecosystem based on spatially explicit waste generation and downhill flow accumulation [(18, 19); see the supplementary materials; figs. S1 and S2]. That is, the closer to an aquatic ecosystem that waste is generated and inadequately managed, the greater the probability it will enter that aquatic ecosystem.

To account for the differences in plastic waste generation rates and waste management infrastructure among economies [(2); Table 1; see the supplementary materials], we adjusted variables for each country based upon their socioeconomic status as defined by the World Bank (17): high income (HI), upper-middle income (UMI), lower-middle income (LMI), and low income (LI). Across the three scenarios, we modeled three types of mitigation strategies over time: reducing waste generation (e.g., bans on single-use plastics), improving waste management (capture and containment of plastic waste), and environmental recovery (e.g., clean-up). A list of example actions that could be taken to achieve each type of strategy can be found in the supplementary materials (table S2). We use a Monte Carlo simulation to propagate uncertainty of input parameters and scenarios (see the supplementary materials).

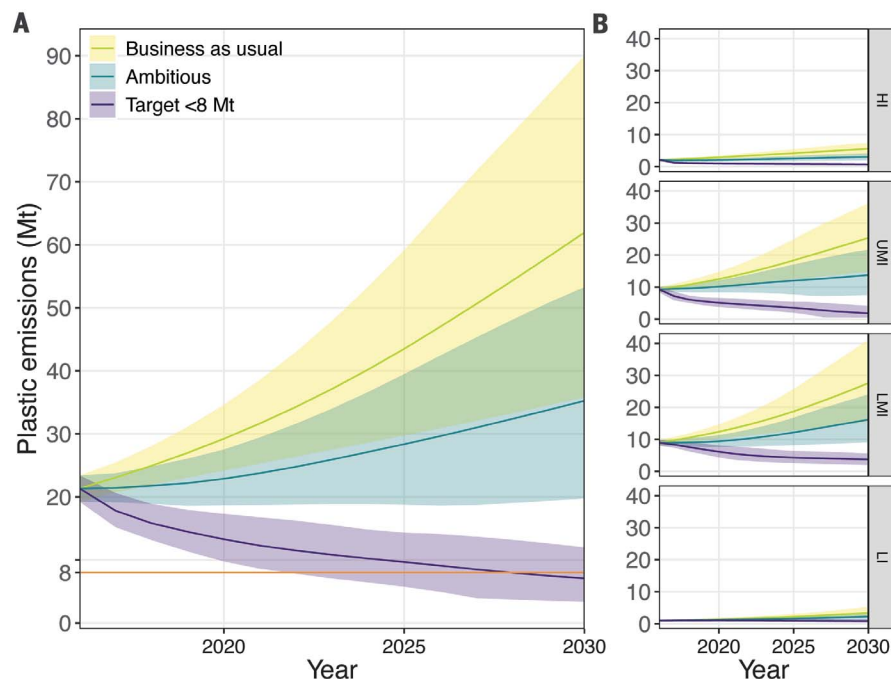
We estimate that ~19 to 23 Mt, or 11%, of plastic waste generated globally in 2016 entered aquatic ecosystems (Fig. 1 and table S4; see the supplementary materials). This is consistent with an estimate of annual river emissions to the global oceans [0.8 to 2.7 Mt (20)]

<sup>1</sup>Department of Ecology and Evolutionary Biology, University of Toronto, Toronto, Ontario, Canada. <sup>2</sup>College of Engineering, University of Georgia, Athens, GA, USA. <sup>3</sup>David H. Smith Conservation Research Program, Society for Conservation Biology, Washington, DC, USA. <sup>4</sup>School of Biological Sciences, The University of Western Australia, Crawley, Western Australia, Australia. <sup>5</sup>Centre for Biodiversity and Conservation Science, University of Queensland, St. Lucia, Queensland, Australia. <sup>6</sup>Department of Natural Resources and Environmental Management, University of Hawai'i at Mānoa, NREM, Honolulu, HI, USA. <sup>7</sup>Sea Education Association, Woods Hole, MA, USA. <sup>8</sup>Status of Stocks and Multispecies Assessments Program, Resource Ecology and Fisheries Management, Alaska Fisheries Science Center, National Oceanic and Atmospheric Administration, Seattle, WA, USA. <sup>9</sup>The Ocean Cleanup Foundation, Rotterdam, Netherlands. <sup>10</sup>The Modelling House, Raglan, New Zealand. <sup>11</sup>School of Geography and the Environment, University of Oxford, Oxford, UK. <sup>12</sup>Center for Biodiversity Outcomes, Arizona State University, Tempe, AZ, USA. <sup>13</sup>School of Life Sciences, Arizona State University, Tempe, AZ, USA. <sup>14</sup>Ocean Conservancy, Washington, DC, USA. <sup>15</sup>Center for Leadership in Global Sustainability, Virginia Polytechnic Institute and State University, Alexandria, VA, USA. <sup>16</sup>Gyres Institute, Los Angeles, CA, USA. <sup>17</sup>School of Biological Sciences, The University of Queensland, Brisbane, Queensland, Australia. <sup>18</sup>The Nature Conservancy, Arlington, VA, USA. <sup>19</sup>School Mathematics and Natural Sciences, Arizona State University, Glendale, AZ, USA. <sup>20</sup>Department of Marine Science, Faculty of Marine and Fisheries Sciences, Universitas Hasanuddin, Makassar, Indonesia. <sup>21</sup>Research Center for Natural Heritage, Biodiversity and Climate Change, Universitas Hasanuddin, Makassar, Indonesia. <sup>22</sup>Centre for Environmental Economics and Policy, The University of Western Australia, Crawley, Western Australia, Australia.

\*Corresponding author. Email: stephb@utoronto.ca (S.B.B.); chelsea.rochman@utoronto.ca (C.M.R.)

**Fig. 1. Annual global plastic emissions into aquatic ecosystems.**

Data include major rivers, lakes, and the oceans in million metric tons (Mt) from 2016 to 2030 (A) and for each income status (B) as defined by the World Bank (17) showing the BAU (yellow), ambitious (blue), and target <8 Mt (purple) scenarios. Shaded areas represent 80% credible intervals indicating the uncertainty in plastic waste generation and the scenario implementation into the future. Orange horizontal line represents the target of <8 Mt, which is a frequently cited statistic in global policy discussions as an unacceptable amount of plastic emissions to the marine ecosystem alone (a subset of the aquatic ecosystems considered here) (7).



that is calibrated with field observations. Our estimate is larger because it includes the amount that accumulates in lakes and rivers in addition to the plastic that escapes to the ocean. Under BAU, we predict that the amount of plastic waste entering the world's aquatic ecosystems could reach 90 Mt/year by 2030 if waste generation trends continue as expected with no improvements in waste management (Fig. 1A and table S4; see the supplementary materials).

Under the ambitious scenario, we predict between 20 and 53 Mt/year of plastic emissions to aquatic ecosystems by 2030, remaining at or exceeding 2016 levels despite tremendous reduction efforts by the global community (Fig. 1A, Table 1, and table S4; see the supplementary materials). The ambitious scenario to reduce plastic emissions is informed by global commitments from the G7 Plastics Charter, the European Union Strategy, the United Nations Environment Programme, Clean Seas, and the Our Oceans conferences. Because these commitments generally lack specific numerical targets and not all countries have made commitments, we apply reduction targets to all countries within an income status based upon existing commitments made by individual countries (see the supplementary materials). The ambitious scenario includes: (i) plastic waste generation reduced from predicted trends by 10% in HI, 5% in UMI, 5% in LMI, and no change from 2016 in LI countries; (ii) an increase in the proportion of managed waste, where HI countries reach a minimum of 90% managed waste (compared with a 2016 mean of 63%), UMI countries reach 70% (2016 mean of 40%), LMI countries reach 50% (2016 mean of

21%), and LI countries reach 30% (2016 mean of 6%); and (iii) recovery of annual global plastic emissions from aquatic environments of up to 10% by 2030 in all countries [Table 1; see the supplementary materials (21)].

For the third scenario, we used our model to estimate the effort necessary to achieve a specified plastic emissions target by 2030 (<8 Mt/year). We first focused on each intervention strategy (plastic reduction, waste management, and environmental recovery) independently while holding the others at the ambitious scenario levels. If additional actions were to solely focus on reduction, then plastic waste generation would need to be reduced by 85% across all income levels. If additional actions were to solely focus on waste management, then every country would have to make exceptional efforts to properly manage  $\geq 99\%$  of its plastic waste. If additional actions were to solely focus on recovery, then 85% of annual global emissions would have to be recovered from the environment by 2030 (table S3; see the supplementary materials). Although many stakeholders heavily promote only one of these strategies as the "best one," these results demonstrate that drastic reductions in future plastic emissions cannot be achieved with any one strategy independently (Table 1).

Next, we systematically increased the level of effort for all three strategies simultaneously until the target was reached in 2030 (mean global emissions of <8 Mt; Fig. 1A, fig. S3, and table S3; see the supplementary materials). This requires plastic waste generation to be reduced by 40% in HI, 35% in UMI and LMI, and 25% in LI countries compared with the BAU trajectory. Levels of managed waste must reach 99% in HI

and UMI countries, 80% in LMI countries, and 60% in LI countries. Recovery of 40% of annual global emissions by 2030 is needed (Fig. 1A and Table 1). Considering all three strategies combined, the effort required to meet a reduction target of even 8 Mt far exceeds the existing and highly ambitious commitments to date from governments, industries, NGOs, and communities combined (e.g., 1, 9, 10, 14, 15).

It is important to note that these values may be an underestimate of plastic emissions. Across all scenarios, UMI and LMI countries contribute the most plastic waste emissions compared with HI and LI countries (Fig. 1B and Table 1; see the supplementary materials, appendix 3). However, the trade of plastic waste was not accounted for in the current model (see the supplementary materials). Waste shipped predominantly from HI to UMI, LMI, and LI countries for processing may enter into a country with no formal waste management system or one that is less tractable, therefore misrepresenting HI countries' contributions to plastic emissions (22). Other factors may also lead to uncertainties in our results. Global scale data for plastic waste generation, collection, and disposal are often lacking or unreliable because of inconsistencies in reporting among countries, differences in methodologies and units used in reporting, and omitted values (2, 18). We do not include primary microplastics, microplastics produced from the wear of products still in use, or microplastics entering the environment through wastewater, although these are likely comparatively small in mass. We also do not include abandoned, lost, or discarded fishing gear, which is an important source of plastic waste, especially in marine



**Table 1. Mitigation strategy scenario values and projections of 2030 plastic emissions.** Shown are income status and global plastic emissions in 2030 and the levels of plastic waste reduction, waste management improvement, and recovery of plastic waste under BAU, ambitious, and target (<8 Mt) scenarios. Specific actions that can be taken to achieve reductions in plastic waste generation (e.g., product bans or taxes), waste management

improvement (e.g., increased collection and controlled landfill), and recovery (e.g., beach clean-ups) can be found in table S2. In the ambitious and target scenarios, changes in plastic waste generation are reductions implemented over time and fully achieved by 2030 and to the same level by countries in the same income status as defined by the World Bank (17). "No change" indicates that 2016 proportions of inadequately managed plastic remain at 2016 values.

Change in plastic waste generation from predicted growth to 2030, % per capita		Managed waste levels by 2030, %		Recovery by 2030, % of global annual emissions	2030 Income status emissions (Mt), 80% credible interval	2030 Global plastic emissions (Mt), 80% credible interval
Business as usual	Country-level projections based on predicted trends	HI:	No change	All: 0	HI:	3.6–7.4
		UMI:	No change		UMI:	14.8–36.1
		LMI:	No change		LMI:	15.6–41.1
		LI:	No change		LI:	1.9–5.3
Ambitious		HI:	90	All: 10	HI:	1.9–4.1
		UMI:	70		UMI:	7.5–21.6
		LMI:	50		LMI:	9.1–24.1
		LI:	30		LI:	1.2–3.5
Target (<8 Mt)		HI:	99	All: 40	HI:	0.5–0.9
		UMI:	99		UMI:	0.5–4.1
		LMI:	80		LMI:	2.0–5.6
		LI:	60		LI:	0.4–1.4

ecosystems (23), or the unregulated burning of inadequately managed plastic waste, which may decrease plastic emissions. Finally, there is a lack of data for most countries representing the efficacy of the informal waste management sector (2). One study in India estimated that 50 to 80% of generated plastic waste is recovered by the informal sectors (garbage collectors, waste pickers, and waste dealers) and is thus kept out of the environment [(24); see the supplementary materials]. The creation of a long-term standardized global monitoring program and open-access data for plastics placed on the market, waste generation and management, the international trade of waste, environmental emissions, and transport in the environment will improve our ability to quantify both plastic emission pathways and the efficacy of mitigation strategies.

Our results show that the efforts required to meaningfully reduce plastic emissions by 2030 are extraordinary (Fig. 1 and Table 1). Increased waste management capacity alone cannot keep pace with projected growth in plastic waste generation. Further, without major technological innovation, it is inconceivable that efforts to recover plastic waste from the environment could reach even 10% of annual emissions (~2.4 to 6 Mt in 2030), whereas our model shows that 40% recovery is required to reduce emissions to <8 Mt (Table 1). These findings emphasize that unless growth in plastic production and use is halted, a fundamental transformation of the plastic economy to a circular framework is essential, where end-of-life plastic products are valued rather than becoming waste.

Increasing global efforts to manage plastic waste must consider plastic pollution as a multidimensional issue. This includes evaluating the financial and social costs of implementing (or not implementing) mitigation strategies and also the impacts of different mitigation strategies on economies, social justice, and human and environmental health to achieve global sustainable development goals. For example, waste-to-energy processing (i.e., incineration) reduces plastic waste volumes but may cause human health impacts from hazardous byproducts, create social justice issues, and increase greenhouse gas emissions (25, 26). Without such considerations, we risk creating perverse outcomes from the transformational shifts needed to address plastic pollution.

Plastic pollution is a burgeoning threat to the sustainability of our planet (7, 8, 27). The world is responding at an already impressive scale, with grassroots action, national-level product bans, public-private partnerships for investment in waste management infrastructure, innovative alternatives to leakage-prone plastic products, and greater transparency in the trade of plastic waste (7, 10, 13). Still, our results show that achieving substantial reductions in global plastic emissions to the environment requires an urgent transformative change. Key policies to achieve such a transition include reducing or eliminating the use of unnecessary plastics, setting global limits for virgin plastic production, creating globally aligned standards for commodity plastics to be practically recoverable and recyclable by design, and developing and scaling plastic processing and recycling

technologies. Such harmonized policies can enable plastics to remain a valuable and useful commodity (10, 12). Further, some plastics will inevitably be emitted to the environment. Thus, recovery of plastic waste has to be a sustained priority to minimize adverse impacts on species and ecosystems (28) and to limit harmful waste management practices such as open burning (25). Without this transformation, we risk continuing to invest large amounts of human capital and financial resources with little to no hope of reducing plastic pollution in the world's rivers, lakes, and oceans.

## REFERENCES AND NOTES

- United Nations Environment Assembly, "UNEA resolutions: Marine litter and microplastics (1/6, 2/11, 3/7, 4/6)" (United Nations, 2019); [https://papersmart.unon.org/resolution/uploads/unep.ahneg\\_2019.3.inf\\_2\\_compilation\\_of\\_resolutions.pdf](https://papersmart.unon.org/resolution/uploads/unep.ahneg_2019.3.inf_2_compilation_of_resolutions.pdf).
- S. Kaza, L. C. Yao, P. Bhada-Tata, F. Van Woerden, "What a waste 2.0: A global snapshot of solid waste management to 2050" (World Bank, 2018); <https://openknowledge.worldbank.org/handle/10986/30317>.
- M. Wagner et al., *Environ. Sci. Eur.* **26**, 12 (2014).
- R. W. Obbard et al., *Earth's Future* **2**, 315–320 (2014).
- L. C. Woodall, L. F. Robinson, A. D. Rogers, B. E. Narayanaswamy, G. L. Paterson, *Front. Mar. Sci.* **2**, 2 (2015).
- America Chemistry Council, "Shale gas is driving new chemical investment in the U.S." (2020); <https://www.americanchemistry.com/Policy/Energy/Shale-Gas/Fact-Sheet-US-Chemical-Investment-Linked-to-Shale-Gas.pdf>.
- United Nations Environment Assembly, "Addressing single-use plastic products pollution" (UNEP/EA.4/L.10, 2019); <https://papersmart.unon.org/resolution/uploads/k1900861.pdf?overlay-context=node/271>.
- United Nations, "Sustainable development goal 14" (2018); <https://sustainabledevelopment.un.org/sdg14>.
- Ministry of Marine Affairs and Fisheries Republic of Indonesia, "Our ocean commitments" (2018); <https://ourocean2018.org/?l=our-ocean-commitments>.

10. European Commission, "Packaging and packaging waste" (2017); <https://ec.europa.eu/environment/waste/packaging/legis.htm>.
11. Y. Geng, J. Sarkis, R. Bleischwitz, *Nature* **565**, 153–155 (2019).
12. World Economic Forum, "The new plastics economy: rethinking the future of plastics" (2017); [http://www3.weforum.org/docs/WEF\\_The\\_New\\_Plastics\\_Economy.pdf](http://www3.weforum.org/docs/WEF_The_New_Plastics_Economy.pdf).
13. UN Environment Programme, "Basel convention on the control of transboundary movements of hazardous wastes and their disposal BC-14/12" (1995); <http://www.basel.int/Portals/4/download.aspx?d=UNEP-CHW-IMPL-CONVTEXT.English.pdf>.
14. Plastic Action Centre, "G7 ocean plastics charter" (2018); <https://plasticactioncentre.ca/directory/ocean-plastics-charter/>.
15. UN Environment Programme, "The Clean Seas global campaign on marine litter" (2017); <https://oceanconference.un.org/commitments/?id=13900>.
16. J. R. Jambeck *et al.*, *Science* **347**, 768–771 (2015).
17. The World Bank, "Data catalog: Population estimates and projections" (2019); <https://datacatalog.worldbank.org/dataset/population-estimates-and-projections>.
18. L. Lebreton, A. Andrady, *Palgrave Commun.* **5**, 6 (2019).
19. B. Lehner, K. Verdin, A. Jarvis, *Eos* **89**, 93–94 (2008).
20. L. J. J. Meijer, T. van Emmerik, L. Lebreton, C. Schmidt, R. van der Ent, Over 1000 rivers accountable for 80% of global riverine plastic emissions into the ocean. *EarthArXiv* [Preprint] 16 October 2019. <https://doi.org/10.31223/osf.io/zjgty>.
21. M. Cordier, T. Uehara, "Will innovation solve the global plastic contamination: how much innovation is needed for that?" (PeerJ Preprints, 2018); <https://peerj.com/preprints/27371/>.
22. A. L. Brooks, S. Wang, J. R. Jambeck, *Sci. Adv.* **4**, eaat0131 (2018).
23. G. Macfadyen, T. Huntington, R. Cappell, *Abandoned, Lost or Otherwise Discarded Fishing Gear* (FAO, 2009).
24. B. Nandy *et al.*, *Resour. Conserv. Recycling* **101**, 167–181 (2015).
25. Center for International Environmental Law, "Plastics and health: The hidden costs of a plastic planet" (2019); <https://www.ciel.org/wp-content/uploads/2019/02/Plastic-and-Health-The-Hidden-Costs-of-a-Plastic-Planet-February-2019.pdf>.
26. C. Wiedinmyer, R. J. Yokelson, B. K. Gullett, *Environ. Sci. Technol.* **48**, 9523–9530 (2014).
27. P. Villarrubia-Gómez, S. E. Cornell, J. Fabres, *Mar. Policy* **96**, 213–220 (2018).
28. K. Bucci, M. Tulio, C. Rochman, *Ecol. Appl.* (2019).

#### ACKNOWLEDGMENTS

We thank H. Savelli, K. Ingeman, and E. S. Darling for input and comments on earlier drafts and five anonymous reviewers for their suggestions on improving this manuscript. **Funding:** This work was supported by the National Socio-Environmental Synthesis Center (SESYNC) under funding received from the National Science Foundation (grant no. DBI-1639145). S.B.B. was supported by a

David H. Smith Postdoctoral Research Fellowship; **Author contributions:** Conceptualization: S.B.B., J.R., M.B., C.M.R.; Data curation: S.B.B., K.L.L.; Formal analysis: S.B.B., J.R., K.L.L., C.C.M., L.L., C.M.R.; Funding acquisition: S.B.B., M.B., C.M.R.; Investigation: S.B.B., J.R., C.C.M., L.L., A.M., E.M., J.L., G.L., M.A.H., M.E., H.P.P., L.R.G., B.P., A.T., H.D.F., M.Be., M.Ba., C.M.R.; Methodology: S.B.B., J.R., K.L.L., C.C.M., L.L., J.J., H.P.P., C.M.R.; Project administration: S.B.B., M.B., C.M.R.; Resources: S.B.B., C.M.R.; Software: S.B.B., J.R., C.C.M., L.L., M.B.; Validation: S.B.B., K.L.L., C.C.M., L.L.; Writing – original draft: S.B.B., C.C.M., L.L., C.M.R.; Writing – review & editing: S.B.B., J.R., K.L.L., L.L., A.M., E.M., J.J., G.L., H.P.P., L.R.G., H.D.F., N.M., M.Be., C.M.R. **Competing interests:** The authors declare no competing interests. **Data and materials availability:** All data are available in the main text or the supplementary materials and in the GitHub repository (<https://github.com/SBBorrelle/Borrelle-et-al-Science-Plastic-Emissions>).

#### SUPPLEMENTARY MATERIALS

[science.sciencemag.org/content/369/6510/1515/suppl/DC1](https://science.sciencemag.org/content/369/6510/1515/suppl/DC1)  
Materials and Methods  
Supplementary Text  
Figs S1 to S5  
Tables S1 to S4  
References (29–35)

7 January 2020; accepted 4 August 2020  
10.1126/science.aba3656

## MICROBIOTA

# Diet posttranslationally modifies the mouse gut microbial proteome to modulate renal function

Lior Lobel<sup>1</sup>, Y. Grace Cao<sup>1</sup>, Kathrin Fenn<sup>1</sup>, Jonathan N. Glickman<sup>2,3</sup>, Wendy S. Garrett<sup>1,4,5,6\*</sup>

Associations between chronic kidney disease (CKD) and the gut microbiota have been postulated, yet questions remain about the underlying mechanisms. In humans, dietary protein increases gut bacterial production of hydrogen sulfide (H<sub>2</sub>S), indole, and indoxyl sulfate. The latter are uremic toxins, and H<sub>2</sub>S has diverse physiological functions, some of which are mediated by posttranslational modification. In a mouse model of CKD, we found that a high sulfur amino acid-containing diet resulted in posttranslationally modified microbial tryptophanase activity. This reduced uremic toxin-producing activity and ameliorated progression to CKD in the mice. Thus, diet can tune microbiota function to support healthy host physiology through posttranslational modification without altering microbial community composition.

**C**hronic kidney disease (CKD) affects nearly 850 million people worldwide (1). Although dietary modification is a cornerstone of CKD treatment, the mechanistic roles of diet-microbiota interactions in CKD pathogenesis and treatment have been underexplored. Many diet-microbiome studies have focused on the effects of dietary fiber, fat, and carbohydrates (2). Less is known about the specific effects of dietary protein and amino acids, although 5 to 10% of dietary amino acids reach the colon, where most gut bacterial metabolism occurs (3). In humans, increasing dietary protein increases gut bacterial production of hydrogen sulfide (H<sub>2</sub>S), indole, and indoxyl sulfate (4, 5). Indole and indoxyl sulfate are uremic toxins, and H<sub>2</sub>S has diverse physiological functions, some of which are mediated by the posttranslational modification S-sulphydration (6, 7). Although a vast number of studies have been performed in mammalian systems, the physiological roles of H<sub>2</sub>S in regulating gut bacterial function within a host are understudied. Additionally, whether there are bona fide opportunities to improve CKD by manipulating diet-microbiota interactions remains unclear.

Modifying patient dietary protein intake has been a clinical strategy used in the management of CKD for many decades, and more specifically, dietary sulfur-containing amino acid (Saa) intake has been reported to affect CKD progression in patients and disease models (8, 9). Given the gaps in understanding the relationships between dietary protein, gut

microbial metabolism, and H<sub>2</sub>S and to address the role of gut microbial metabolism and diet in renal function, we used a mouse model of CKD that is driven by increased adenine (10) along with a Saa-based diet perturbation. We formulated isocaloric diets to represent extremes of mouse Saa consumption, relevant to human consumption, i.e., diets with low versus high amounts of methionine and cysteine (see table S1 for diet formulations and materials and methods) but with sufficient methionine to avoid methionine restriction (11). Conventionally reared, specific-pathogen-free (SPF) mice on a low-Saa plus adenine (Saa+Ade) diet had significantly increased serum creatinine levels compared with mice on a high-Saa+Ade (Fig. 1A), as well as more extensive and severe renal cortex histopathologic changes, including tubular dilatation and dropout, tubulitis with peritubular fibrosis, and cortical crystal deposition (Fig. 1, B to D). To determine the extent to which the Saa effects depend on the gut microbiota, we fed the Saa+Ade diets to gnotobiotically reared, germ-free (GF) mice. Serum creatinine and kidney damage were markedly reduced in the GF mice compared with SPF mice on the low-Saa+Ade diet, and there were similar phenotypes in the GF and SPF mice fed the high-Saa+Ade diet (Fig. 1, A to D). Given that the GF mice on the low-Saa + Ade diet still showed renal injury, although less than SPF mice, we examined the expression of a select panel of host genes implicated in CKD pathogenesis in both humans and the mouse adenine model (12). *Spp1* (*Osteopontin*), *Tgfb1*, and *Icam1* were increased in GF mice to greater levels than in SPF mice on the low-Saa+Ade diet (fig. S3D). By contrast, *Ccl2* and *Timp1* were increased to a greater extent in SPF mice on the low-Saa+Ade diet (fig. S3D). These data indicate that the microbiota may buffer expression of some host genes while stimulating expression of others. Overall, we found that a low-Saa diet exacerbated the CKD phenotypes observed

and that the presence of a gut microbiota further magnified these effects.

We tested whether there is a link between dietary Saa and gut bacteria through microbial metabolism of cysteine to H<sub>2</sub>S. We measured cecal sulfide levels from GF and SPF mice fed low- versus high-Saa diets by using both the lead acetate and methylene blue sulfide detection assays (13). SPF mice on the high-Saa diet had higher cecal sulfide levels than those on the low-Saa diet (Fig. 1, E and F). GF mouse ceca had significantly less sulfide than SPF mice, regardless of Saa diet (Fig. 1, E and F). We did not observe any significant differences in the taxonomic abundances of the gut microbiota members between SPF mice on the low- versus high-Saa diets using 16S ribosomal RNA (rRNA) gene amplicon surveys (fig. S1), supporting the idea that the differences in cecal sulfide in healthy mice may be mediated by altered microbial function rather than changes in microbiota community structure.

Given these findings and with the goal of more effectively modeling gut microbial activity shifts that could occur in CKD patients, we sought out publicly available CKD patient gut microbiota profiling studies to identify taxa enriched in CKD patients compared with healthy individuals. We re-analyzed fecal 16S rRNA gene amplicon datasets from Xu *et al.* (14) and from Southern Medical University (NCBI accession PRJEB5761), a fecal PhyloChip study by Vaziri *et al.* (15), and a fecal whole-genome shotgun sequencing dataset from Promogene Translational Research Institute (PTRI) (NCBI accession PRJNA449784). Enforcing stringent statistical cutoffs [linear discriminant analysis (LDA) score of >4 for LDA effect size and fold change of >2 for the PhyloChip analysis] revealed a clear and robust signal of *Enterobacteriaceae* enrichment in CKD patients (fig. S2, A to C). Although the 16S rRNA gene amplicon analyses did not afford strain-level *Escherichia coli* identification, the PhyloChip analysis showed a significant increase in the combined mean abundance of seven *E. coli* strains measured in fecal samples of CKD patients with end-stage renal disease compared with control subjects (fig. S2D). Further analysis of the PTRI whole-genome shotgun sequencing dataset strengthened this finding, as we found a higher normalized *E. coli* mean gene abundance in CKD patient samples than in non-CKD controls (Fig. 1G). Given these findings from reanalysis of human CKD gut microbiota and the genetic tractability and relatively well-characterized proteome of *E. coli*, we focused on the effects of *E. coli* in the adenine-driven CKD model. As the mice we obtain from Jackson Laboratory do not harbor any *Enterobacteriaceae* members (fig. S1) and to carry out a carefully controlled study of gut microbial activity in a reproducible model system, we used gnotobiotically reared mice colonized with the

<sup>1</sup>Departments of Immunology and Infectious Diseases and Molecular Metabolism, Harvard T.H. Chan School of Public Health, Boston, MA 02115, USA. <sup>2</sup>Beth Israel Deaconess Medical Center, Boston, MA 02215, USA. <sup>3</sup>Department of Pathology, Harvard Medical School, Boston, MA 02215, USA. <sup>4</sup>Department of Medicine, Harvard Medical School, Boston, MA 02215, USA. <sup>5</sup>Broad Institute of MIT and Harvard, Cambridge, MA 02142, USA. <sup>6</sup>Department of Medical Oncology, Dana-Farber Cancer Institute, Boston, MA 02215, USA.

\*Corresponding author. Email: wgarrett@hsph.harvard.edu



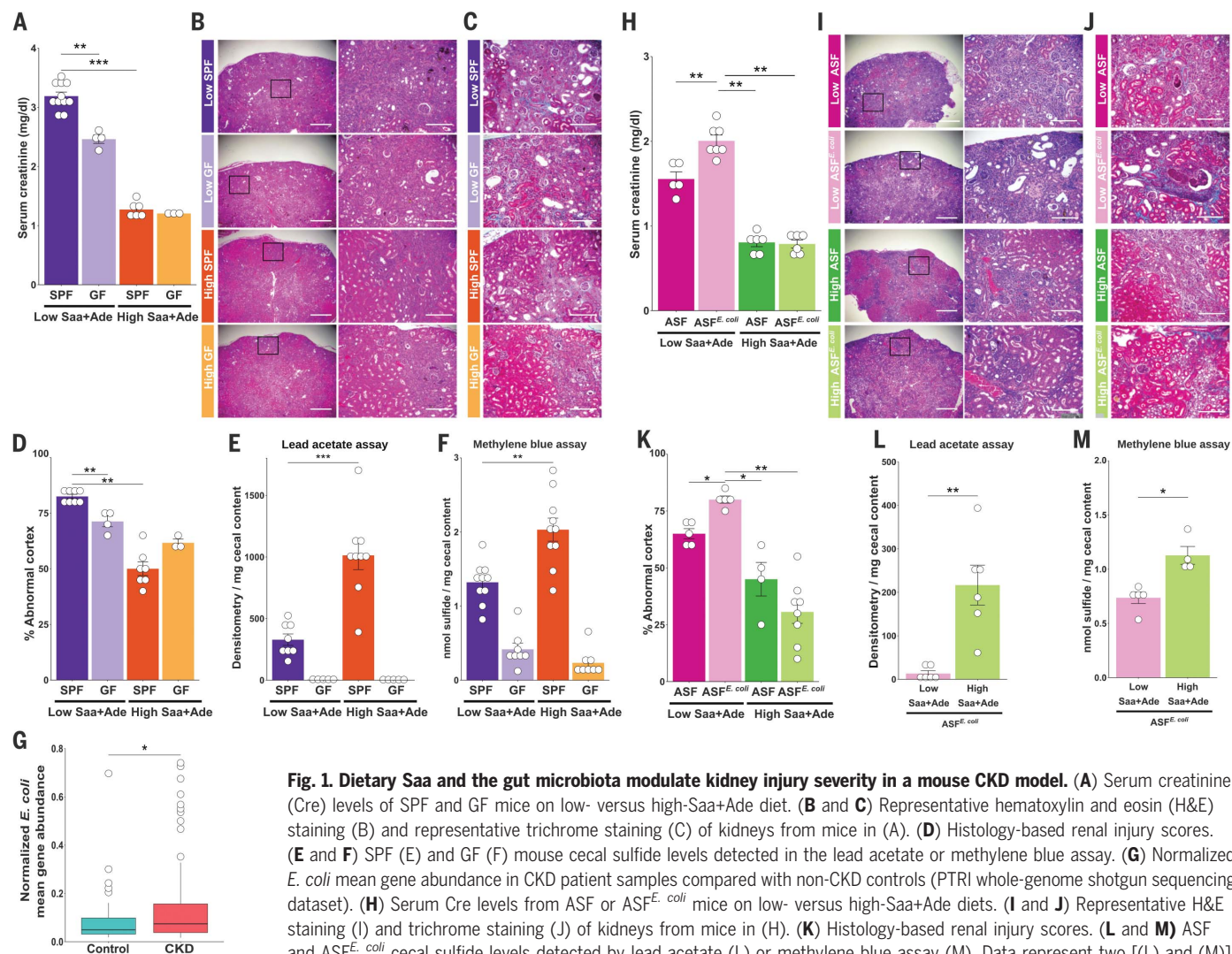


**Fig. 1. Dietary Saa and the gut microbiota modulate kidney injury severity in a mouse CKD model.** (A) Serum creatinine (Cre) levels of SPF and GF mice on low- versus high-Saa+Ade diet. (B and C) Representative hematoxylin and eosin (H&E) staining (B) and representative trichrome staining (C) of kidneys from mice in (A). (D) Histology-based renal injury scores. (E and F) SPF (E) and GF (F) mouse cecal sulfide levels detected in the lead acetate or methylene blue assay. (G) Normalized *E. coli* mean gene abundance in CKD patient samples compared with non-CKD controls (PTRI whole-genome shotgun sequencing dataset). (H) Serum Cre levels from ASF or ASF<sup>E. coli</sup> mice on low- versus high-Saa+Ade diets. (I and J) Representative H&E staining (I) and trichrome staining (J) of kidneys from mice in (H). (K) Histology-based renal injury scores. (L and M) ASF and ASF<sup>E. coli</sup> cecal sulfide levels detected by lead acetate (L) or methylene blue assay (M). Data represent two [(L) and (M)], three [(A), (D), (H), and (K)], or four [(E) and (F)] independent experiments. Symbols represent individual mice. Bars represent means ± SEM. \**P* < 0.05; \*\**P* < 0.01; \*\*\**P* < 0.001. Two-way analysis of variance (ANOVA) with Tukey's post hoc test was used for (A), (D), (E), (F), (H), and (K); the Mann-Whitney test for was used for (L) and (M). Scale bar, 1 mm for the 40× magnification in (B) and 200 μm for the 200× magnification in (B) and (C).

altered Schaedler flora (ASF) to which we added *E. coli* K-12. The ASF is a simplified microbial community consisting of eight bacterial species, none of which is related to *Enterobacteriaceae* (16). We used ASF mice, rather than mono-colonized mice, because ASF mice are more physiologically similar to SPF mice (16). *E. coli* colonization was similar on the low- and high-Saa diets with and without adenine (fig. S3, A and B), and we did not observe changes in the relative abundance of ASF members (fig. S3C). On the low-Saa+Ade diet, ASF mice colonized with *E. coli* (ASF<sup>E. coli</sup>) had higher serum creatinine and more extensive tubulitis, tubular atrophy and dropout, peritubular fibrosis, and cortical crystals than ASF mice (Fig. 1, H to K). By contrast, ASF<sup>E. coli</sup> and ASF mice on the high-Saa+Ade diet had similar serum creatinine levels and milder renal parenchymal pathology compared with their littermates on the low-

Saa+Ade diet (Fig. 1, H to K). As with SPF mice, we found higher cecal sulfide levels in ASF<sup>E. coli</sup> mice on the high- versus low-Saa+Ade diet (Fig. 1, L and M). To determine if changes in renal function would occur in these models in the absence of the adenine insult, we examined serum creatinine levels in SPF and ASF<sup>E. coli</sup> mice on the low- versus high-Saa diet. Notably, the low-Saa diet and *E. coli* were sufficient to increase serum creatinine levels in mice, and no overt histologic abnormalities were present (fig. S3E). Similar results were obtained with SPF mice on the Saa diets (fig. S3F). Overall, these results support that *E. coli* interacts with dietary Saa to modulate kidney function.

Given our observations regarding cecal H<sub>2</sub>S in SPF and ASF<sup>E. coli</sup> mice on the Saa diets and the literature on how H<sub>2</sub>S can posttranslationally modify mammalian proteins leading to a range of physiologic effects, we investigated

the effects of H<sub>2</sub>S on *E. coli*. In lead acetate sulfide detection assays, *E. coli*, grown either aerobically or anaerobically, produced sulfide from cysteine in a dose-dependent manner without any effects on growth (Fig. 2A and fig. S4, A to C). To serve as a control for the effects of endogenous H<sub>2</sub>S production on *E. coli* physiology, we generated an isogenic strain harboring a deletion of *decR*, which encodes a transcriptional activator of the cysteine desulfhydrase genes *yhaO* and *yhaM*, which drive cysteine-derived sulfide production in *E. coli* (17). Deletion of *decR* resulted in significant reduction of sulfide production, with no effect on growth kinetics (Fig. 2, A and B; fig. S4, A to D). Of note, SseA (3-mercaptopyruvate sulfurtransferase), which has been reported as a major source of cysteine-derived sulfide in *E. coli* (18), did not affect sulfide production in our system (fig. S4E). Sulfide exerts its effects

through generation of polysulfides that modify cysteine residues, resulting in S-sulfhydration (19). To identify *E. coli* proteins that are S-sulfhydrated (R-S-S), we adapted a pull-down method that specifically enriches for

S-sulfhydrated proteins (20). This technique leverages maleimide binding to free thiols and persulfides, resulting in thioether bonds, and the ability of dithiothreitol (DTT) to break disulfide bonds but not thioether bonds (Fig.

2C). We observed a robust enrichment of S-sulfhydrated proteins in DTT-eluted samples of wild-type (WT) *E. coli* lysates grown in medium supplemented with cysteine (Fig. 2D). We validated the pull-down assay's specificity

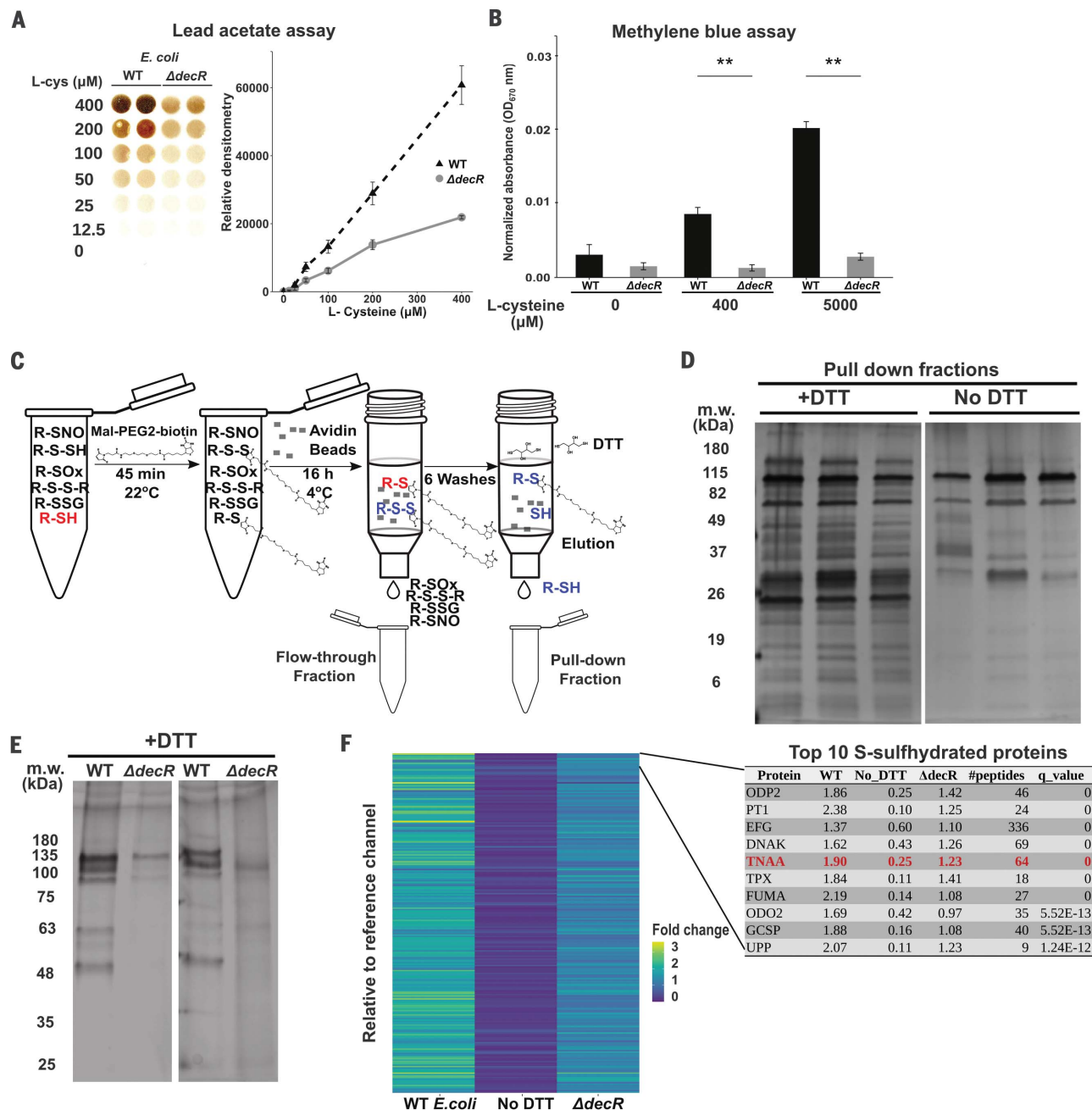


**Fig. 2. Characterization of *E. coli* S-sulfhydrome reveals that TnaA is a highly S-sulfhydrated protein.** (A) *E. coli* sulfide production, determined with lead acetate. (B) *E. coli* sulfide production, determined with methylene blue. OD<sub>670</sub>, optical density at 670 nm. (C) Schematic of S-sulfhydrated protein pull-down method. The S-sulfhydrated protein is highlighted in blue, to distinguish it from the native protein in red. (D) Silver staining of *E. coli* lysates subjected to S-sulfhydration pull-down and eluted either with or without DTT. m.w., molecular weight. (E) Silver staining of lysates from WT or ΔdecR *E. coli* lysates subjected to S-sulfhydration pull-down. (F) Heat map of

the relative quantity of the 212 S-sulfhydrated proteins by TMT LC-MS<sup>3</sup> analysis from S-sulfhydration pull-down fractions from WT *E. coli* samples eluted with or without DTT and ΔdecR mutant samples eluted with DTT. Proteins ordered based on q score for enrichment in the DTT-eluted versus non-DTT-eluted samples. Data represent two (E), three [(D) and (F)], four (A), or six (B) independent experiments. Bars represent means ± SEM. \*\*P < 0.01. Statistical significance was determined with a linear model test (A), two-way Kruskal-Wallis test with Dunn's post hoc test (B), or two-way ANOVA with Tukey's post hoc test (F).

and found that treating bacterial lysates with  $H_2O_2$ , and hence oxidizing free thiols, reduced the detection of S-sulfhydrated proteins (fig. S4D). By contrast, treatment with sodium hydrosulfide (NaHS), a fast-reacting sulfide donor, induced higher S-sulfhydration levels in bacterial lysates (fig. S4D). We detected a higher level of S-sulfhydration in *E. coli* lysates grown in medium supplemented with cysteine than in *E. coli* grown in Luria broth (LB) alone (fig. S4, E and F). By contrast, lysates of  $\Delta decR$  bacteria, which produce less  $H_2S$ , grown in cysteine-supplemented LB broth showed less S-sulfhydration than WT *E. coli* (Fig. 2E). Next, we sought to characterize the *E. coli* sulfhydrome using quantitative tandem mass tag (TMT) liquid chromatography–multistaged mass spectrometry (LC-MS<sup>3</sup>) analysis. This analysis revealed that most identified proteins enriched in *E. coli* lysates that were eluted with DTT were indeed S-sulfhydrated, compared with the same samples not treated with DTT (Fig. 2F). Furthermore, most detected S-sulfhydrated proteins were enriched in WT versus  $\Delta decR$  *E. coli*, as expected from the strains' different abilities to produce sulfide from cysteine. Ranking of the S-sulfhydrated proteins by their q values (DTT versus non-DTT) revealed the top 10 most abundant S-sulfhydrated proteins (Fig. 2F and fig. S4G). Although most of these proteins are highly expressed during logarithmic bacterial growth and are expected to be highly abundant, tryptophanase (TnaA) was overrepresented. Overall, our quantitative proteomics analysis identified 212 proteins as S-sulfhydrated with high confidence (table S2), and hypergeometric distribution analysis revealed 13 cellular pathways enriched with S-sulfhydrated proteins, several of which are related to protein translation (fig. S4H).

TnaA (Fig. 2F), a secreted enzyme that catalyzes the degradation of tryptophan to indole, pyruvate, and ammonia, offered a potential connection between our S-sulfhydrome analysis and the phenotypes we observed in the CKD mouse model. Indoles are a class of bacteria-produced molecules that not only regulate bacterial physiology (21) but also participate in bacteria–host interactions (22). Indoles can be transported through the portal vein to the liver, where they are oxidized, yielding the uremic toxin indoxyl sulfate (23). For these reasons, TnaA emerged as an attractive target for investigating host–microbe interactions in our CKD mouse model. We replaced the *E. coli* TnaA chromosomal copy with a cloned *tnaA-his* under its native promoter. We then validated our S-sulfhydrome results by analyzing TnaA S-sulfhydration in WT versus  $\Delta decR$  *E. coli* lysates using Western blot analysis and found reduced TnaA S-sulfhydration in  $\Delta decR$  lysates (Fig. 3A). *E. coli* lysates treated with  $H_2O_2$  and NaHS showed reduced and increased TnaA S-sulfhydration, respectively (Fig. 3B).

Since the S-sulfhydration pulldown method reduces the S-sulfhydrated cysteine residue (i.e., removes the S-sulfhydration), we could not pinpoint the exact cysteine residues being S-sulfhydrated, as TnaA has seven cysteines. Therefore, we purified natively expressed TnaA-His from *E. coli* grown in LB supplemented with cysteine and performed LC–tandem MS (LC-MS/MS) analysis to detect and map the

S-sulfhydration. We detected several TnaA-His peptides that had a +32-Da addition, matching the molecular weight of S-sulfhydration on a cysteine residue (fig. S5). As oxidation of a cysteine residue to sulfinic acid (R-S-O<sub>2</sub>) results in same mass shift and given the potential for oxidation during our analysis, we could not rule out that such oxidation occurs. However, an S-sulfhydrated cysteine can be oxidized to

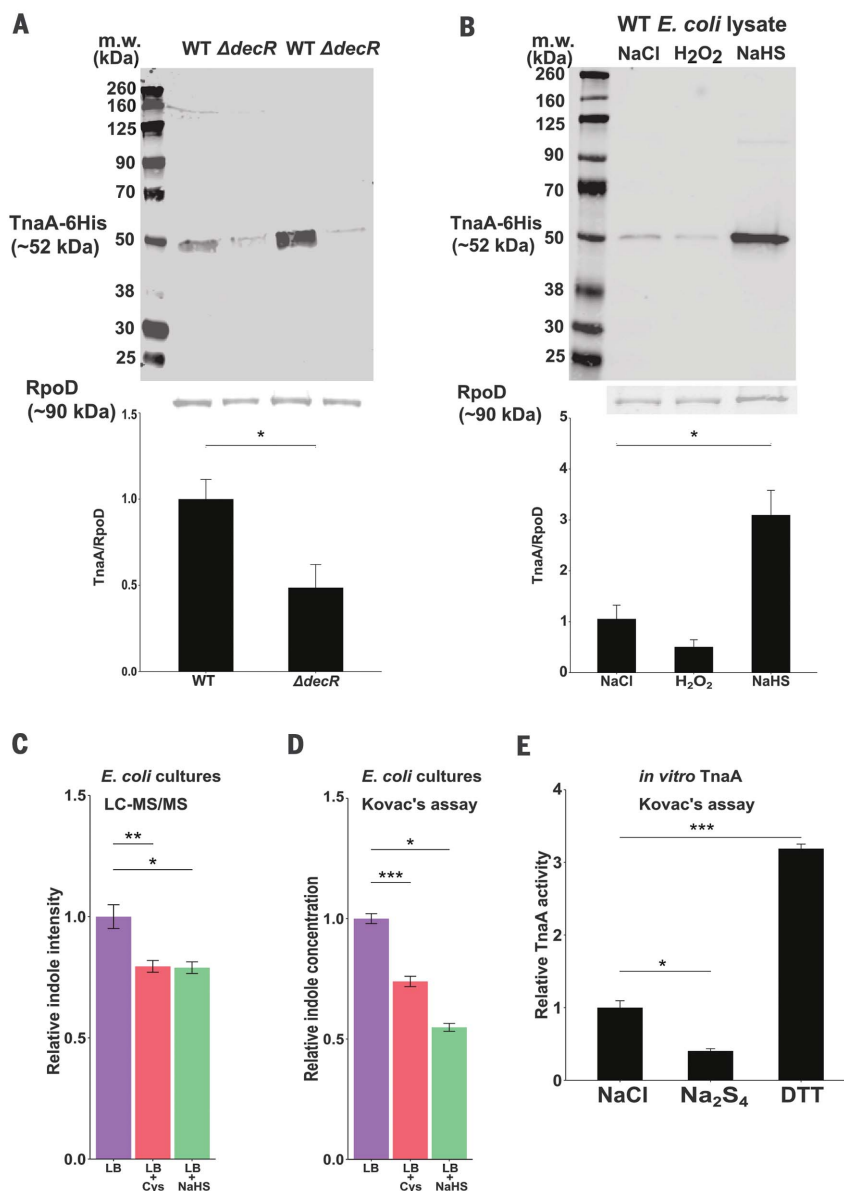


**Fig. 3. S-Sulfhydration inhibits the indole-producing enzymatic activity of *E. coli* TnaA.** (A) Representative Western blot analysis of TnaA-His from WT and  $\Delta decR$  *E. coli* lysates subjected to S-sulfhydration pulldown. Loading controls show RpoD in the flowthrough. (B) Same method as in (A) but with *E. coli* lysates treated with NaCl,  $H_2O_2$ , or NaHS. (C) LC-MS/MS analysis of indoles in WT *E. coli* cultures with cysteine or NaHS. (D and E) Kovac's assay for indole production in WT *E. coli* cultures with cysteine or NaHS (D) or with purified TnaA enzyme supplemented with NaCl,  $Na_2S_4$ , or DTT (E). Data represent three [(A) and (E)], four [(B) and (D)], or five (C) independent experiments. Bars represent means  $\pm$  SEM. \* $P < 0.05$ ; \*\* $P < 0.01$ ; \*\*\* $P < 0.001$ . Data were analyzed with the Mann-Whitney test (A), two-way ANOVA with Tukey's post hoc test [(B) and (E)], or two-way Kruskal-Wallis test with Dunn's post hoc test [(C) and (D)].



sulfinic acid (R-S-S-O<sub>2</sub>), resulting in a +64-Da increase, a shift that results from oxidation of an S-sulhydrylated cysteine or a second S-sulhydrylation (R-S-S-SH). We were able to detect a +64-Da shift in several cysteine residues of TnaA (fig. S5 and table S3). Although we

found evidence that six of the seven TnaA cysteine (C) residues were S-sulhydrylated (C148, C281, C294, C298, C352, and C383), we could not rule out that cysteine residue C413 is also S-sulhydrylated, as our coverage of TnaA (~78%) did not include peptides with high confidence

within this region. TnaA cysteine residues are involved in its enzymatic activity (24), as mutation of C298 results in altered TnaA activity (25). To study the effect of S-sulhydrylation on TnaA activity, we measured indole concentrations by both Kovac's reagent method and

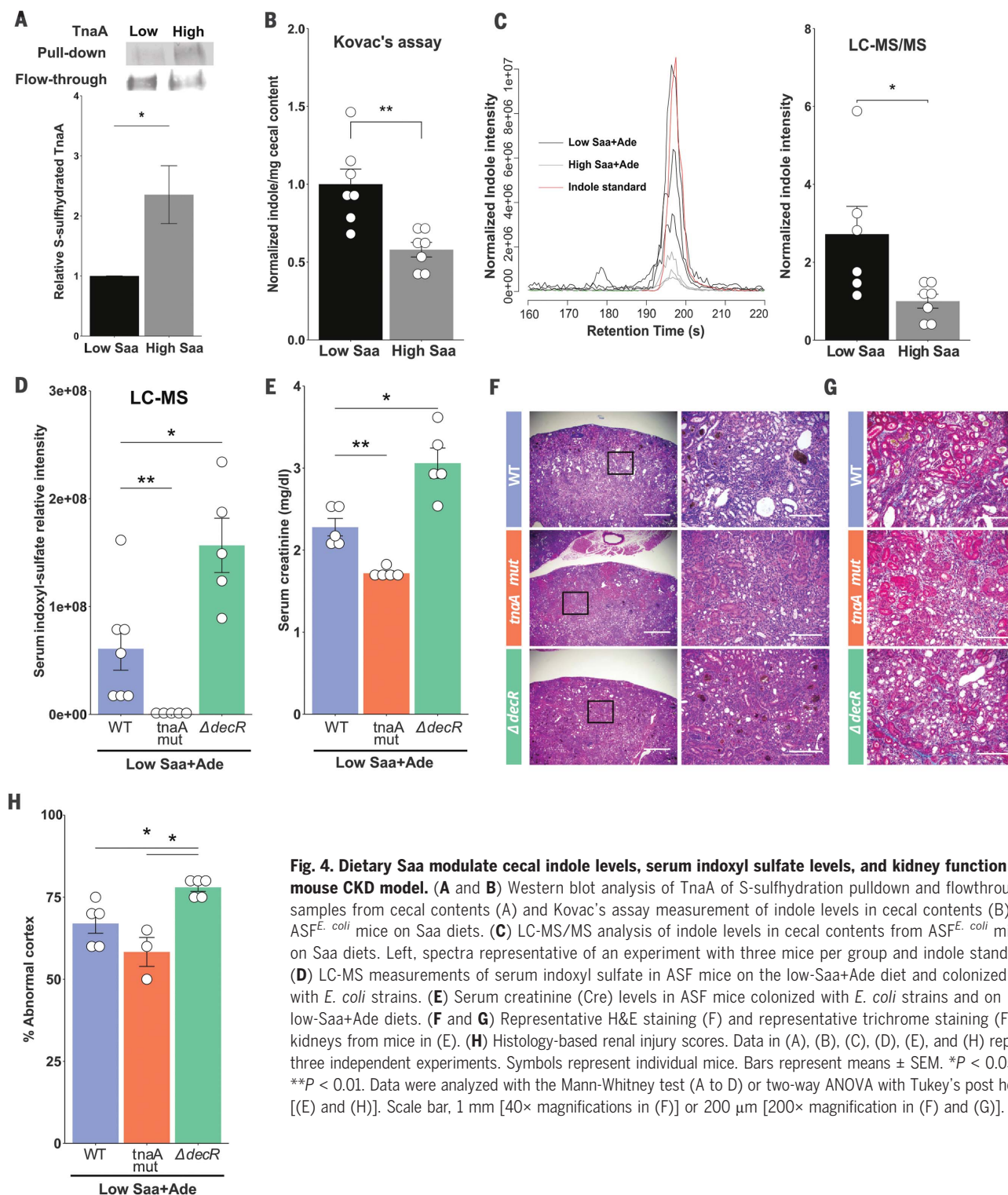


**Fig. 4. Dietary Saa modulate cecal indole levels, serum indoxyl sulfate levels, and kidney function in a mouse CKD model.** (A and B) Western blot analysis of TnaA of S-sulhydrylation pull-down and flow-through samples from cecal contents (A) and Kovac's assay measurement of indole levels in cecal contents (B) from ASF<sup>E. coli</sup> mice on Saa diets. (C) LC-MS/MS analysis of indole levels in cecal contents from ASF<sup>E. coli</sup> mice on Saa diets. Left, spectra representative of an experiment with three mice per group and indole standard. (D) LC-MS measurements of serum indoxyl sulfate in ASF mice on the low-Saa+Ade diet and colonized with *E. coli* strains. (E) Serum creatinine (Cre) levels in ASF mice colonized with *E. coli* strains and on low-Saa+Ade diets. (F and G) Representative H&E staining (F) and representative trichrome staining (F) of kidneys from mice in (E). (H) Histology-based renal injury scores. Data in (A), (B), (C), (D), (E), and (H) represent three independent experiments. Symbols represent individual mice. Bars represent means ± SEM. \**P* < 0.05; \*\**P* < 0.01. Data were analyzed with the Mann-Whitney test (A to D) or two-way ANOVA with Tukey's post hoc test [(E) and (H)]. Scale bar, 1 mm [40× magnifications in (F)] or 200 μm [200× magnification in (F) and (G)].

LC-MS/MS analysis of bacterial cultures. We found that supplementing LB broth with cysteine or NaHS reduced indole concentrations in the supernatants (Fig. 3, C and D). Also, supporting sulfide's role in TnaA inhibition,  $\Delta decR$  *E. coli* had higher indole levels than WT *E. coli* when grown in LB supplemented with cysteine (fig. S6A), and TnaA expression was similar under these conditions (fig. S6B). To show that indole production was dependent on TnaA, we ablated TnaA activity by using an isogenic *tnaA739::kan* mutant (*tnaA mut*) and did not detect indole in the culture supernatant (fig. S6C). To test that S-sulfhydration inhibits TnaA activity in a direct manner, we used a reductionist approach using purified *E. coli* TnaA. We observed that incubation with disodium tetrasulfide ( $\text{Na}_2\text{S}_4$ ), a polysulfide donor, led to TnaA S-sulfhydration (fig. S6D) and reduced enzymatic activity by 60% in vitro (Fig. 3E). As an assay control, we added DTT, which should reduce S-sulfhydrated TnaA to its functional native form, and we observed TnaA activity more than tripled (Fig. 3E). To provide a more physiological context for TnaA inhibition by cysteine-derived sulfide, we measured the activity of TnaA purified from WT and  $\Delta decR$  *E. coli* cultures grown with cysteine and found that TnaA $\Delta decR$  had higher activity (fig. S6E). Collectively, these results support that S-sulfhydration of *E. coli* TnaA reduces its activity as measured by indole production from tryptophan, both in vitro and in bacterial cultures.

Although we detected TnaA S-sulfhydration in vitro for both purified protein and TnaA from bacterial cell lysates and demonstrated that this modification inhibited its activity, we had yet to determine if this posttranslational modification occurred within the gut in response to dietary Saa and resulted in measurable physiological consequences for the host. To investigate this, we began by providing ASF<sup>*E. coli*</sup> mice with the high- and low-Saa diets. Although mice on the diets harbored similar levels of *E. coli* (fig. S7A), we detected higher TnaA S-sulfhydration in the cecal contents of mice on the high-Saa diet than in those on the low-Saa diet (Fig. 4A). None of the eight ASF bacterial genomes encode a *tnaA* gene, and we could not detect indoles in the ASF mouse cecal contents using LC-MS/MS, implying that *E. coli* is the sole producer of indoles in this model (fig. S7B). Taking advantage of that distinction, we measured indole in the cecal contents of ASF<sup>*E. coli*</sup> mice on the two diets. We found that mice on the high-Saa diet had significantly lower indole levels, demonstrating that high dietary Saa not only increased TnaA S-sulfhydration but also that this modification was sufficient to affect TnaA activity in vivo (Fig. 4, B and C). To strengthen the links between diet, microbial metabolism, and kidney damage, we leveraged the CKD mouse model by using the low-Saa+Ade diet, with

which we observed the most renal injury, and the gnotobiotic ASF mice we used previously (Fig. 1). We colonized these mice with either WT *E. coli* (ASF<sup>*E. coli*</sup>) or with one of two isogenic mutants, *tnaA mut* or  $\Delta decR$  (ASF<sup>*tnaA mut*</sup> or ASF <sup>$\Delta decR$</sup> , respectively). Unlike the ASF<sup>*E. coli*</sup> mice, no indoxyl sulfate was detected in the serum of ASF<sup>*tnaA mut*</sup> mice, as there was no tryptophanase present within the gut microbiota. As *E. coli*  $\Delta decR$  is deficient in producing sulfide from cysteine, TnaA remains less S-sulfhydrated and more highly active (fig. S6A). Consistent with that observation, ASF <sup>$\Delta decR$</sup>  mice showed reduced cecal sulfide (fig. S7C), increased cecal indole (fig. S7D), and increased serum indoxyl sulfate relative to ASF<sup>*E. coli*</sup> mice (Fig. 4D). Mice colonized with WT *E. coli* had higher serum creatinine levels than mice colonized with the *tnaA mut* strain (Fig. 4E). Concomitant with the serum indoxyl sulfate levels, mice colonized with the  $\Delta decR$  strain had the highest serum creatinine levels (Fig. 4E). Colonization of the three different *E. coli* strains was similar (fig. S7E). Histological findings of more severe tubulointerstitial damage, fibrosis, cortical crystal deposition, and more extensive parenchymal involvement mirrored the trends observed for indoxyl sulfate and creatinine for *E. coli*  $\Delta decR$  versus WT *E. coli* (Fig. 4, F and G). We also examined these mice on the high-Saa+Ade diet. Consistent with prior observations (Fig. 1), ASF<sup>*E. coli*</sup> mice on this diet showed milder phenotypes, although ASF <sup>$\Delta decR$</sup>  mice had slightly increased serum creatinine compared with the parental and *tnaA mut* strains (fig. S7, F to K). Collectively, these data support that a dietary component can generate a posttranslational modification of a gut microbial protein that affects extraintestinal host function, and our findings also furnish mechanistic insight into how host-diet-microbiota interactions can contribute to disease states such as CKD.

We found that sulfide derived from bacterial metabolism of dietary Saa regulates *E. coli* indole production through inhibition of tryptophanase by S-sulfhydration. Our work shows that a dietary component can be metabolized by the microbiota to generate a posttranslational modification of microbial proteins that affects host physiology and offers a framework for how host-diet-microbiota interactions can contribute to or stave off disease states such as CKD (fig. S8). Although metatranscriptomics have provided a window into functional changes within a community, our results show that a single modification on one specific protein can mediate such effects. Thus, in our mouse CKD model a subtle dietary change, which does not result in microbial composition changes, reveals that production of indoles by *E. coli* is differentially affected by levels of sulfide endogenously produced by gut bacteria. Our work indicates that bacterial metabolism not only

may have direct effects on host physiology but also may influence microbe-microbe interactions driven by bacterial posttranslational modifications mediated by host diet.

However, our findings need to be interpreted cautiously and their limitations noted. Our observations that GF mice exhibit a renal failure phenotype in the adenine model, though milder than in SPF mice, indicate that host factors, as well as redox status (e.g., altered glutathione levels) (8), also play a role in dietary Saa modulation of kidney function. Indole-independent dietary Saa effects on renal function are also indicated by the phenotype of ASF mice colonized with the *E. coli* *tnaA mut* strain; these mice lack indole and indoxyl sulfate yet still exhibit a CKD phenotype on the Saa+Ade diet. Thus, the contribution of dietary Saa and bacterial TnaA indole production to renal failure in human CKD warrants further investigation. The 2-fold increase in cecal indole culminating in a 10-fold serum indoxyl sulfate increase in the mouse CKD model is notable. The increase in indoxyl sulfate could be driven, in part, by indole-independent mechanisms in the adenine CKD mouse model that lead to a reduction in its excretion and accumulation in the serum. Alternatively, the kinetics of indole production in the cecum could be augmented by the rate of indole oxidation and accumulation in the liver and its release into the serum.

In summary, diet is a crucial aspect in managing CKD (26, 27), and we hypothesize that administration of TnaA inhibitors, such as sulfide donors, may help reduce gut indole levels and thus mitigate kidney damage. In support of this concept and its broad application, other gut bacteria, especially members of the *Bacteroidetes* phylum, also encode TnaA homologs (28), and a high degree of homology exists between bacterial TnaA alleles (fig. S9). Our study elucidates an interaction between diet, microbial metabolism, and kidney function that is mediated by posttranslational protein regulation. These findings might shed light on managing CKD and provide clinical approaches to improve human health that target the microbiota and the enzymatic activities of its proteome.

## REFERENCES AND NOTES

1. D. C. Crews, A. K. Bello, G. Saadi, World Kidney Day Steering Committee, *Saudi J. Kidney Dis. Transpl.* **30**, 281–290 (2019).
2. M. A. Conlon, A. R. Bird, *Nutrients* **7**, 17–44 (2014).
3. B. Ahlman, C. E. Leijonmarck, C. Lind, E. Vinnars, J. Wernerman, *J. Surg. Res.* **55**, 647–653 (1993).
4. E. A. Magee, C. J. Richardson, R. Hughes, J. H. Cummings, *Am. J. Clin. Nutr.* **72**, 1488–1494 (2000).
5. R. Poesen et al., *PLOS ONE* **10**, e0140820 (2015).
6. A. K. Mustafa et al., *Sci. Signal.* **2**, ra72 (2009).
7. B. D. Paul, S. H. Snyder, *Trends Biochem. Sci.* **40**, 687–700 (2015).
8. L. E. Thielemann, E. W. Oberhauser, G. Rosenblut, L. A. Videla, A. Valenzuela, *Cell Biochem. Funct.* **8**, 19–24 (1990).
9. H. Trachtman, J. A. Sturman, *Amino Acids* **11**, 1–13 (1996).

10. T. Jia *et al.*, *BMC Nephrol.* **14**, 116 (2013).
11. D. Cooke, A. Ouattara, G. P. Ables, *FASEB J.* **32**, 693–702 (2018).
12. W.-C. Liu, Y. Tomino, K.-C. Lu, *Toxins* **10**, 367 (2018).
13. C. Hine, J. R. Mitchell, *Bio Protoc.* **7**, e2382 (2017).
14. K.-Y. Xu *et al.*, *Sci. Rep.* **7**, 1445 (2017).
15. N. D. Vaziri *et al.*, *Kidney Int.* **83**, 308–315 (2013).
16. M. Wymore Brand *et al.*, *ILAR J.* **56**, 169–178 (2015).
17. T. Shimada, K. Tanaka, A. Ishihama, *Microbiology* **162**, 1698–1707 (2016).
18. K. Shatalin, E. Shatalina, A. Mironov, E. Nudler, *Science* **334**, 986–990 (2011).
19. T. V. Mishanina, P. K. Yadav, D. P. Ballou, R. Banerjee, *J. Biol. Chem.* **290**, 25072–25080 (2015).
20. X. H. Gao *et al.*, *eLife* **4**, e10067 (2015).
21. C. Darkoh, K. Plants-Paris, D. Bishoff, H. L. DuPont, *mSystems* **4**, e00346-18 (2019).
22. T. Zelante *et al.*, *Immunity* **39**, 372–385 (2013).
23. S. C. Leong, T. L. Sirich, *Toxins* **8**, 358 (2016).
24. M. Tokushige *et al.*, *Biochimie* **71**, 711–720 (1989).
25. R. S. Phillips, P. D. Gollnick, *J. Biol. Chem.* **264**, 10627–10632 (1989).
26. C.-Y. Yang, D.-C. Tarng, *Nephrology* **23** (Suppl 4), 16–20 (2018).
27. T. K. Chen, D. H. Knicely, M. E. Grams, *JAMA* **322**, 1294–1304 (2019).
28. A. S. Devlin *et al.*, *Cell Host Microbe* **20**, 709–715 (2016).

# ACKNOWLEDGMENTS

We thank J. X. Wang (Small Molecule Core Mass-Spectrometry, Harvard University), B. Budnik and R. Robinson (Harvard Center for Mass Spectrometry Proteomics), and R. Kuntz and S. Thakurta (Thermo Fisher Scientific Center for Multiplexed Proteomics, Harvard University). We also thank L. Ricci for graphic design (fig. S8), J. K. Lang and Kate Rosinski (Harvard T.H. Chan Gnotobiotic Center for Mechanistic Microbiome Studies) for technical support, and members of the Garrett lab for their discussion of this work. **Funding:** This work was supported by a CRI Irvington postdoctoral fellowship to L.L., NIH T32 AI118692 and F31 DK121375 to Y.G.C., and R01CA202704 and R24DK110499 to W.S.G. **Author contributions:** Conceptualization: L.L. and W.S.G. Formal analysis: L.L. Funding acquisition: W.S.G. Investigation: L.L., Y.G.C., and J.N.G. Software: L.L. Supervision: W.S.G. Visualization: L.L., Y.G.C., and W.S.G. Writing – original draft: L.L. and W.S.G. Writing – review and editing: L.L., Y.G.C., J.N.G., and W.S.G.

**Competing Interests:** The authors declare no competing financial

interests. W.S.G. is on the science advisory boards of Kintai Therapeutics, Leap Therapeutics, Evelo Biosciences, Tenza Inc., and SanaRx. On 21 February 2020, related to this work, a patent application was filed, U.S. Application no. 62/979,638. **Data and materials availability:** All data are available in the manuscript or the supplementary materials. Raw 16S rRNA gene amplicon sequences were deposited in NCBI SRA databank under the bioproject accession PRJNA603373. Bacterial strains generated for this study are available from the Garrett Laboratory under an MTA with Harvard University.

# SUPPLEMENTARY MATERIALS

science.sciencemag.org/content/369/6510/1518/suppl/DC1  
Materials and Methods  
Fig. S1 to S10  
Tables S1 to S5  
References (29–63)  
MDAR Reproducibility Checklist

[View/request a protocol for this paper from Bio-protocol.](#)

20 February 2020; accepted 5 August 2020  
10.1126/science.abb3763





COVID-19 presents financial, research, and project challenges that scientists need to overcome.

## Planning beyond the pandemic: Faculty career development in the age of COVID-19

*Navigating, sustaining, and advancing your career as a faculty member has been a difficult enterprise during the pandemic. While professors are learning many lessons about crisis management as it relates to career development, including strategic planning, resilience, and innovation in the face of adversity, many are using the time to refocus and clarify their dedication to science, students, and humanity.*

By **Alaina G. Levine**

When the pandemic closed down Rochester Institute of Technology (RIT), **Kaitlin Stack Whitney**, assistant professor of science, technology, and society, saw her research programs halted, her students scatter to the wind, and her own career in a tenuous situation, given that she is pre-tenure. But this insect ecologist snapped into action. With the money she had already lined up for her summer support, she “unfunded” herself and transferred the funds to pay two students who couldn’t do the work they were doing before quarantine. “It was so immediately clear this is what I should do,” she says. “I paid students to do a different project so they could still be doing science, even if it’s not the exact science they thought they’d be doing. I have a responsibility to check in with everyone on my team and prioritize their health and safety above any research goals.”

There are many factors that determine how faculty have continued to press on through the pandemic, including the nature of their research, their career level, and whether or not they have tenure, as well as their teaching load and even the type of university where they work. Timing is also a major element of response, as **Aníbal J. Valentín Acevedo**, assistant professor in the Department of Microbiology and Immunology at the Universidad Central del Caribe School of Medicine in Bayamón, Puerto Rico, attests. The government declared a total lockdown on March 15, but only announced it a few days before. His research relies on human cells that take time to grow and maintain, and with “no idea of where it was going,” he frantically assembled his students. “We started gathering all of our data that we could analyze from home and freezing all our samples,” he says. “We did this in one

day. Some experiments we were working on had to be thrown away because we had to stop in the middle.” As a result, he saw his timelines for research outputs upended. “We will not be able to reach any of our scientific goals for this year, and possibly not next year. So, this is a huge impact,” he says. Still, his university has been supportive. “In terms of academic activities, they were specific in saying we can identify academic activities so [that] the students’ training will not be halted,” he shares. And such activities will be considered during his progress evaluation and possible future promotion.

Other scientists have been able to shift quickly to pursue more remote work, but what happens if you’re between jobs? In February of this year, **Ulrike Endesfelder**, a biophysicist who was finishing up a stint as research group leader at the Max-Planck-Institute for Terrestrial Microbiology in Marburg, Germany, was excited. She was boarding up her laboratory and preparing to fly across the Atlantic for a new faculty role at Carnegie Mellon University (CMU) in Pittsburgh. With an initial start date of April 1, she packed everything into container ships, but two days after they left, the United States enacted a travel ban. “We couldn’t fly into the U.S., and all of my team was trapped in Germany and our equipment was on the ocean,” she says. Moreover, she could not be employed by CMU until she got there, and she had already resigned from Max Planck. Fortunately, Endesfelder was able to be re-employed by the Institute within a few hours, as were her postdoc and Ph.D. students.

When the Institute partially opened in June, she was able to do some basic experiments with equipment owned by former colleagues. And she got very creative about sourcing additional apparatus. “I approached microscope companies and asked them to put their demo microscopes in my lab so I could test them out for them,” she shares. The beta tests she offered were a strategic quid pro quo: “They got my feedback and I got their system for very affordable rental conditions.” But as the pandemic rages on, Endesfelder is still in limbo. “CMU is doing the best they can to help me, and the moment I can travel, I will join them. They gave me access to my startup funds and

cont.>

Upcoming features

■ Faculty—September 18 ■ Top Employers—October 30

**"I have a responsibility to check in with everyone on my team and prioritize their health and safety above any research goals."**

Kaitlin Stack  
Whitney



are continuing to renovate my lab space while I am not there," she says. In the meantime, she is trying to remain upbeat and serve her proteges and her field by planning future investigations.

### From bench to kitchen table (and back again)

As the pandemic spread and lockdowns were put into effect, scientists had to grapple with disturbances in their research, teaching, and mentorship plans. Experiments had to cease, sometimes permanently. Samples had to be destroyed, as they would not be viable for future data collection. Work transitioned from lab benches to kitchen counters, as professors contended with rapidly changing research and funding timelines, nonaccess to research infrastructure, full-time parenting duties, and other matters.

And yet, researchers have been able to take some steps while working from home. **Venugopalan Pallayil**, deputy head of the Acoustic Research Lab in the Tropical Marine Science Institute of the National University of Singapore, studies marine acoustics. "As a principal investigator, my role is to see that projects are progressing, support my staff, write proposals to get funding, and write up papers. All of these things I have been doing from home and I don't need to go to the lab," he says. He has also participated in virtual conferences. But his work depends on data from the ocean, often collected and analyzed by staff who are confined to small spaces on marine vessels. As COVID-19 hit, all studies were sidelined, and his laboratory- and field-based work has suffered as a result. "As long as social distancing is in place, it will be very difficult to organize those trips," he says.

**Daniel Abate-Daga**, a junior faculty member at Moffitt Cancer Center and the University of South Florida, works on cancer immunotherapy. Typically, his team's research involves 70% tissue culture with human cells and 30% animal modeling. As of June, his group was slowly returning to the laboratory after months of hiatus. "As mandated by the institution, my team is working in shifts, to maintain social distancing. All meetings are held via Zoom," he says. "We have adapted to these unfavorable circumstances by focusing on manuscript and grant writing. Also, we have outsourced as many experiments as we've been able to. One of the positive aspects of this crisis is that remote work and virtual meeting have been naturalized, and that is likely to stay."

Part of the overall response to the pandemic is tempering and changing expectations. "It is OK that we are not as productive at this

time," says Stack Whitney. "We need to prioritize our loved ones, and coming from this perspective of everyone's care, we will improve our science."

### Protocols revisited

For scientists whose work involves extensive field assignments, multiple challenges arose. **Isabelle M. Côté**, professor of marine ecology at Simon Fraser University in Burnaby, Canada, directs diverse studies that range from invasive species in the ocean to impacts from multiple stressors in shallow water ecosystems, with one commonality. "Almost all work we do is subtidal—sometimes we collect samples and do experiments in labs but almost everything is underwater," she says. As both department head and dive safety manager for her university (which involves training anyone who uses scuba for their research), she was especially keen on crafting a safe environment to continue with scientific activities during shutdowns. Her examination of exactly how to give guidance to her colleagues birthed a decision tree regarding whether fieldwork should be continued. She tweeted it and received praise for her creation: The Province of British Columbia, where her institution is based, adopted it as part of its own government process.

Indeed, systems engineering has become second nature to many researchers as they work to continue their scientific exploits. Much of Stack Whitney's research, which involves analyzing insect behavior along highways and in agricultural fields, is supported by federal government contracts, and thus she had to ensure that the contract obligations were being met. First, she turned to her networks and spoke with other ecologists about how they were safely pursuing fieldwork. She also utilized Côté's decision tree. And then she wrote protocol after protocol, creating written processes for every aspect of the research endeavor, from how to travel to the field site, to how to assess the safety of a data collection action, to who to call in an emergency. "It's not a bad thing to have a written document for the protocols," she says. "Some students really like it, and from an accessibility standpoint, it is always great to have multiple modalities for the protocols. It has also helped me to keep everything organized. I love binders and laminated things."

cont. >



**"As mandated by the institution, my team is working in shifts, to maintain social distancing."**  
Daniel Abate-Daga

PHOTOS: TOP, COURTESY OF ROCHESTER INSTITUTE OF TECHNOLOGY; BOTTOM, MOFFITT CANCER CENTER

## Featured participants

### Carnegie Mellon University

[www.cmu.edu](http://www.cmu.edu)

### Friends of Europe

[www.friendsofeurope.org](http://www.friendsofeurope.org)

### Imperial College London

[www.imperial.ac.uk](http://www.imperial.ac.uk)

### Moffitt Cancer Center

[moffitt.org](http://moffitt.org)

### National University of Singapore

[www.nus.edu.sg](http://www.nus.edu.sg)

### Next Einstein Initiative

[www.nexteinstein.org/about-us](http://www.nexteinstein.org/about-us)

### Purdue University

[www.purdue.edu](http://www.purdue.edu)

### Rochester Institute of Technology

[www.rit.edu](http://www.rit.edu)

### Simon Fraser University

[www.sfu.ca](http://www.sfu.ca)

### University of Cambridge

[www.cam.ac.uk](http://www.cam.ac.uk)

### Universidad Central del Caribe School of Medicine

[www.uccaribe.edu/medicine](http://www.uccaribe.edu/medicine)

## Opportunity from adversity

For faculty who have not secured tenure or are not on a tenure track, the pandemic is precarious. Some universities have offered to pause tenure clocks or add a year to the tenure and promotion process, as is the case at RIT. Stack Whitney is still deciding whether she will take advantage of this opportunity. Grants are another area of concern, but some agencies are offering lifelines: the Natural Sciences and Engineering Research Council of Canada is allowing grant extensions of up to 1 year.

"The life of a scientist is to carry on despite all the challenges that life throws at you," says **Stefano Sandrone**, a neuroscientist and Senior Teaching Fellow at Imperial College London. "I am very keen about taking challenges and turning them into opportunities." His work utilizes functional magnetic resonance imaging (fMRI) scans of the brain to conduct computational analysis of cognitive aspects in neurological and psychiatry conditions. Although the pandemic has blunted his chances of getting fresh information, "I am not running

out of data. I exploited the moment to write manuscripts on education and neuroscience," he says.

**Andrew J. Whelton**, associate professor of civil, environmental, and ecological engineering at Purdue University, is using this period to make his lab more efficient while reinforcing his protégés' critical leadership and crisis management skills. He has developed a plan requiring that every piece of equipment in the laboratory is assigned to two students who know how to operate and troubleshoot it. "If something happens to me, they need to be able to move forward and lessen the blow for themselves," he says.

"We are teaching how to be resilient in the face of failure," says Stack Whitney. "We want to show that so much of our work doesn't end in papers and prizes, and by living through this with them, that we don't stop, we just adapt. We are going to roll with the punches." Furthermore, she has been able to emphasize to her students the idea that people come before projects. "When we have a crisis, we show students they are not tools to get me data. They are my collaborators. I want to have that ethos even when we are not in a crisis."

Creativity has given rise to new solutions. "One thing we have done is try to identify parts of our experimental processes that could be outsourced to outside companies that do this automatically, such as generating reagents," says Abate-Daga. "We will use this resource in the future. I do think good things can come out of this."

## A Silver Linings Playbook

For many professors, the pandemic has reaffirmed their focus not only on serving society at large, but more immediately, on helping their local community of up-and-coming researchers. "Any available resource I can free up for my students is the right thing," says Stack Whitney. "This is not the time to compromise how I am going to run a lab. This is the time to say that we are going to live according to our values and that my students' health and safety is a priority. And it should always be."

Community building is something that **Youssef Travaly**, a senior fellow with Brussels-based think tank Friends of Europe and former vice president, Sciences, Innovation & Partnerships at the Next Einstein Initiative, sees as a global issue. The materials scientist views the pandemic as an opportunity to rally African scientists, especially in the diaspora (community of African scientists living abroad), toward the goal of public health solutions for the continent and beyond. "Our first reaction was how can we, African scientists, respond to this challenge and come up with solutions," he says.

**Tolullah Oni**, a public health physician, urban epidemiologist, and clinical senior research associate at the University of Cambridge, recognizes the invaluable opportunity her networks bring. "Through this experience, I've really come to understand the true value of the communities of like-minded scientists I belong to, such as the Global Young Academy and the Next Einstein Forum Community of Scientists," she says. "While these have always been an important nourishing space, in the context of the pandemic, they have now become a priceless source of advice on coping and research adaptation strategies from different parts of the world and a critical source of strength, support, ideas, and inspiration."

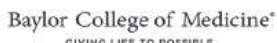
Adds Sandrone: "How lucky we are to be part of this powerful scientific community. We miss the daily contact, so the lesson is to treasure the time we spend with peers. Now is the time to be a mentor even more and to rebuild our scientific communities in the best possible way for the students, who represent the next generations of scientists."



PHOTO: COURTESY OF YOUSSEF TRAVALY

*Alaina G. Levine is a science writer, science careers consultant, professional speaker, and author of Networking for Nerds (Wiley, 2015).*





## DEPARTMENT OF MOLECULAR AND HUMAN GENETICS FACULTY POSITIONS

Among genetics departments at U.S. medical schools, the Department of Molecular and Human Genetics at Baylor College of Medicine (<https://www.bcm.edu/departments/molecular-and-human-genetics/>) ranks first in both number of grants and total funding from the National Institutes of Health (NIH). The Department of Molecular and Human Genetics provides a fully integrated environment for physicians and basic scientists, promoting a cross-species approach to functional genetics and a commitment to technology transfer. Activities within the Department include clinical genetics, basic and clinical research, a joint venture diagnostic laboratory, long-standing association with an NIH large scale human genome sequencing centers, medical student teaching, an MS Genetic Counseling program, a Ph.D. graduate program, and residency/fellowship training in medical genetics. The Department has over \$100 million in total research funding, 70 primary tenured and tenure-track research faculty members and a total of 140 primary faculty members, who are engaged in a variety of missions including basic and translational research, clinical diagnostic services, and prenatal, pediatric, and adult clinical care. Faculty will have an opportunity to interact with the vigorous ABMGG residency and clinical laboratory fellowship training programs that include over 40 clinical and diagnostic laboratory faculty and over 40 genetic counseling faculty and staff. The training programs attract four to six individuals per year for resident training in categorical Medical Genetics, Combined Pediatrics/Medical Genetics, Combined Internal Medicine/Medical Genetics, and Maternal Fetal Medicine/Medical Genetics, as well as three to four individuals for ABMGG-approved clinical laboratory fellowship training. The Department is seeking individuals for faculty appointments at rank appropriate for achievement and experience. We are currently recruiting for the following positions:

**Physician Scientist Geneticist** - The Department is seeking MD or MD/PhD trained individuals who have clearly demonstrated their ability to conduct high-impact basic, translational and/or clinical research and compete for scientific funding in the area of medical genetics and model organism genetics. Start-up package commensurate for experience will be provided.

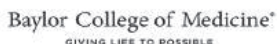
**Clinical Geneticist** - The Department is seeking MD or MD/PhD trained, ABMGG eligible and/or certified physicians in the area of clinical genetics and medical biochemical geneticist.

**Research Geneticist** - The Department is seeking PhD trained basic and translational research geneticists (studying any model system), statistical geneticists, and computational geneticists who are focused on elucidating the underlying genetic and genomic mechanisms of rare and common diseases.

Appointments will be at the **Assistant, Associate, or Full Professor** levels depending on experience. Qualified applicants should email a pdf version of their curriculum vitae and cover letter stating the position for which they are applying to the following email address: [mhgfacultyrecruits@bcm.edu](mailto:mhgfacultyrecruits@bcm.edu)

Department of Molecular and Human Genetics  
 Baylor College of Medicine  
 One Baylor College of Medicine, MS225  
 Houston, TX 77030

*Equal Opportunity, Affirmative Action and Equal Access Employer*



## DEPARTMENT OF MOLECULAR AND HUMAN GENETICS AND DAN L. DUNCAN COMPREHENSIVE CANCER CENTER TENURED/TENURE TRACK FACULTY POSITIONS IN GENETICS/GENOMICS

The Department of Molecular and Human Genetics and the Dan L. Duncan Comprehensive Cancer Center (DLCCCC) at Baylor College of Medicine are seeking the following positions:

**Genome Instability** - an individual for faculty appointment at rank appropriate for achievement and experience, working in any organism on problems in genomic instability, development of novel genetic/genomic tools or other fundamental genetic topics.

Successful candidates will have strong basic research programs related to genetic/genomic stability or instability, genome organization, genomics, genome engineering including, but not limited to DNA replication, repair, mutation, genome rearrangements, DNA damage response, mechanisms of heritability and evolution, studied in any organism from bacteria to human. This individual will join the Mechanisms in Cancer Evolution Program in the DLCCCC. However, outstanding individuals in any research area will be considered. Generous start-up support is available, and candidate will be put forward for a CPRIT award.

**Cancer Geneticist** - an individual for faculty appointment at rank appropriate for achievement and experience in cancer research. Applicants' research programs may focus on broad ranging topics in cancer genetic research including cancer genomics, mechanisms of cancer therapeutics, cancer model organisms, genome instability, epigenetics and gene expression, and others. Applicants with expertise in computational biology, in combination with basic and/or translational cancer research, are strongly encouraged to apply. Candidates will join a team of multidisciplinary research investigators studying cancer stem cell biology, genomics, epigenetics, and metabolic aberrations in cancer.

Both appointments will be at the **Assistant, Associate, or Full Professor** level depending on experience. Among genetics departments at U.S. medical schools, the Department of Molecular and Human Genetics at Baylor College of Medicine (<https://www.bcm.edu/departments/molecular-and-human-genetics/>) ranks first in both number of grants and total funding from the National Institutes of Health (NIH). The Dan L Duncan Comprehensive Cancer Center (DLCCCC) includes over 270 research members in seven different programs who bring in \$180M in total cancer relevant funding including nearly \$90M from NIH. Curriculum vitae, a brief summary of research plans, along with the names, addresses, and phone numbers of at least three references to the following email address: [mhgfacultyrecruits@bcm.edu](mailto:mhgfacultyrecruits@bcm.edu).

Department of Molecular and Human Genetics  
 Baylor College of Medicine  
 One Baylor Plaza, MS225  
 Houston, TX 77030

*Equal Opportunity, Affirmative Action and Equal Access Employer*

# Sloan Kettering Institute

Celebrating 75 years of breakthroughs

Join our faculty and help set the pace of biomedical science.

## JOIN US

Successful candidates will hold an appointment in one of SKI's research programs. Candidates may apply to up to two programs. MSK is an equal opportunity and affirmative action employer committed to diversity and inclusion in all aspects of recruiting and employment.

### Cancer Biology & Genetics

Chair: Scott Lowe, PhD

### Cell Biology

Chair: Kristian Helin, PhD

### Chemical Biology

Chair: Derek Tan, PhD

### Computational & Systems Biology

Chair: Dana Pe'er, PhD

### Developmental Biology

Chair: Anna-Katerina Hadjantonakis, PhD

### Immunology

Chair: Alexander Rudensky, PhD

### Molecular Biology

Chair: John Petrini, PhD

### Molecular Pharmacology

Chair: David Scheinberg, MD, PhD

### Structural Biology

Chair: Christopher Lima, PhD

## AREAS OF BASIC AND TRANSLATIONAL RESEARCH

- Stem Cell Biology
- Developmental Oncology
- Regenerative Medicine
- Machine Learning
- 3D Single-Cell Analytics
- Biophysics & Imaging
- Organelle Biology
- Chromatin & Gene Regulation
- Genome Integrity and Functional Genomics
- Chemistry & Chemical Biology
- Metastasis & Tumor Microenvironment
- Immunity, Host-Microbial Interactions and Microbiomes
- Tumor Immunobiology
- Experimental Therapeutics, Imaging and Bioengineering

## RESEARCH AND TRAINING

- 100 research laboratories housed in state-of-the-art buildings
- 26 Core facilities offering cutting-edge scientific services
- More than 900 pre- and postdoctoral trainees
- Appointments in the Gerstner Sloan Kettering Graduate School of Biomedical Sciences and the Weill Cornell Graduate School of Medical Sciences

Visit [www.ski.edu](http://www.ski.edu) to learn more.



MSK is an equal opportunity and affirmative action employer committed to diversity and inclusion in all aspects of recruiting and employment. All qualified individuals are encouraged to apply and will receive consideration without regard to race, color, gender, gender identity or expression, sexual orientation, national origin, age, religion, creed, disability, veteran status or any other factor which cannot lawfully be used as a basis for an employment decision.



Memorial Sloan Kettering  
Cancer Center

## UT Southwestern Medical Center

### FACULTY POSITION BACTERIAL PATHOGENESIS.

The Department of Microbiology at UT Southwestern Medical Center is seeking a new faculty member in bacterial pathogenesis at the **Assistant Professor** (tenure track) level. Appointment rank will be commensurate with academic accomplishments and experience. The appointee will be expected to develop a front-rank, competitive, independent research program on a medically relevant bacterial pathogen(s) and/or on concepts relevant to the human microbiome. An important academic responsibility also will be the instruction and mentoring of graduate students. An attractive start-up package, including a competitive salary and generous laboratory space in a modern building, is available to conduct research within a highly dynamic environment of a leading medical microbiology department (<https://www.utsouthwestern.edu/education/medical-school/departments/microbiology>).

Candidates will be considered for our \$2M Endowed Scholars (start-up) Program (<http://www.utsouthwestern.edu/education/programs/nondegree-programs/other-programs/endowed-scholars/index.html>).

Candidates should have a Ph.D. and/or M.D. degree with at least 3-4 years of postdoctoral experience and an exceptional publication record. Please send a cover letter, C.V., contact information for three letters of recommendation, and a brief summary of future research to: **Bacterial PathogenesisSearchCommittee@utsouthwestern.edu**.

*UT Southwestern Medical Center is an Affirmative Action/Equal Opportunity Employer. Women, minorities, veterans and individuals with disabilities are encouraged to apply.*

## UT Southwestern Medical Center

### TENURE-TRACK POSITION

The Department of Physiology invites outstanding scientists with Ph.D., M.D., or equivalent degrees to apply for tenure-track faculty positions at the level of **Assistant Professor**.

Candidates who bring innovative approaches to the study of any under-explored/unexplored questions broadly related to physiology are encouraged to apply. The scientific excellence of the candidates is more important than the specific area of research. These positions are part of the continuing growth of the Department at one of the country's leading academic medical centers. They will be supported by significant laboratory space, competitive salaries, state-of-the-art core facilities and exceptional start-up packages. The University of Texas Southwestern Medical Center is the scientific home to six Nobel Prize laureates and many members of the National Academy of Sciences and Institute of Medicine. UT Southwestern conducts more than 3,500 research projects annually totaling more than \$417 million. Additional information about the Department of Physiology can be found at <http://www.utsouthwestern.edu/education/medical-school/departments/physiology/index.html>.

Information regarding careers can be found at:  
<https://jobs.utsouthwestern.edu/>.

Applicants should submit a CV, a brief statement of current and proposed research, and a summary of your two most significant publications describing the importance of the work (100-150 words each). Please arrange to have three letters of recommendation sent on his/her behalf. All items should be submitted to: <http://academicjobsonline.org/ajo/jobs/16617>. Completed applications will be reviewed starting **November 1, 2020**. You may email questions to [ron.doris@utsouthwestern.edu](mailto:ron.doris@utsouthwestern.edu).

*UT Southwestern Medical Center is an Equal Opportunity/Affirmative Action Employer. Women, minorities, veterans and individuals with disabilities are encouraged to apply.*

## UT Southwestern Medical Center

### FACULTY POSITIONS IN DEPARTMENT OF MOLECULAR BIOLOGY

The Department of Molecular Biology and the Hamon Center for Regenerative Science and Medicine (CRSM) at the University of Texas Southwestern Medical Center invite applications or tenure track faculty positions at the level of **Assistant Professor**. We are seeking creative and interactive individuals with strong research programs focused on mechanistic aspects of gene regulation and cellular signaling, cell growth and differentiation, and stem cell biology, including the use of cellular and animal models to study development and disease. Attractive recruitment packages, state-of-the-art core facilities, and exceptional laboratory space are available. UT Southwestern has a vibrant graduate program and an atmosphere of collegiality and collaboration.

Candidates should apply online at <https://jobs.utsouthwestern.edu/> (search for **Job#482864**). Applicants should also submit a curriculum vitae containing a summary of past research accomplishments, a statement of future objectives, and names of three references via email to:

**MolBioSearch@UTSouthwestern.edu**  
Department of Molecular Biology  
Hamon Center for Regenerative Science and Medicine  
University of Texas Southwestern Medical Center

*UT Southwestern Medical Center is an Affirmative Action/Equal Opportunity Employer. Women, minorities, veterans and individuals with disabilities are encouraged to apply.*

SPECIAL JOB FOCUS:

## Faculty Careers

Issue date: Oct. 9

Reserve ad space by Sept. 24



Produced by the Science/AAAS  
Custom Publishing Office.

To book your ad, contact:  
[advertise@sciencecareers.org](mailto:advertise@sciencecareers.org)

**The Americas**  
+1 201 748 6702  
**Europe & ROW**  
+44 (0) 1273 810850  
**Japan**  
+81 3 6459 4174  
**Greater China, South Korea,  
Singapore, Thailand**  
+86 131 4114 0012

**Why choose this job focus  
for your advertisement?**

- Relevant ads lead off this career section with a special faculty careers banner.

**ScienceCareers**  
AAAS

SCIENCECAREERS.ORG



**FOR RECRUITMENT IN SCIENCE, THERE'S ONLY ONE SCIENCE.**



## Faculty Recruiting in Gene Regulation

The Cecil H. and Ida Green Center for Reproductive Biology Sciences, an endowed basic science research center focusing on gene regulation, is recruiting Tenure-track Assistant Professor Positions. We invite applications from outstanding candidates studying aspects of signaling, gene regulation, and genome function, especially in the areas of chromatin and transcription, epigenetics, nuclear endpoints of cellular signaling pathways, nuclear receptors, RNA biology, genome organization, and genome evolution. We are interested in a wide variety of model systems and experimental approaches, including biochemistry, molecular biology, structural biology, animal models, genetics, genomics, proteomics, bioinformatics, and computational biology. The Green Center's research programs cover diverse areas of biology, including reproduction, development, endocrinology, stem cells, cancer, metabolism, inflammation, immunity, and neurobiology.

• **Focus 1: Signaling, chromatin, and gene regulation** – Candidates using a wide array of experimental approaches to address fundamental questions in nuclear signaling, chromatin, transcription, epigenetics, and RNA biology.

• **Focus 2: Genomic, proteomic, bioinformatic, computational, and evolutionary approaches to understanding gene regulation** - Candidates using state-of-the-art methodologies that will connect to broader “omic” initiatives in the center.

The Green Center promotes and supports cutting-edge, integrative, and collaborative basic research, as well as strong connections between basic and clinical research. Successful candidates will be housed in a state-of-the-art research facility with a generous start-up package and are expected to establish scientifically rigorous and externally funded research programs and participate in center and university teaching and training programs. To learn more about the Green Center, visit: <https://www.utsouthwestern.edu/education/medical-school/departments/green-center/>.

Candidates must have a Ph.D. or M.D. or equivalent in a relevant field of study, postdoctoral or comparable experience, and a demonstrated record of research excellence. Applicants should apply online at <https://jobs.utsouthwestern.edu/> (search for Job ID 486395) and upload a letter of application, curriculum vitae, and a statement of planned research projects as pdf files. Applicants should also arrange for three letters of reference to be sent directly to [GreenCenter@UTSouthwestern.edu](mailto:GreenCenter@UTSouthwestern.edu). Collection and review of applications will commence October 1, 2020 and will continue during the 2020-2021 academic year until the position is filled, but applicants are encouraged to submit their materials as soon as possible.

*UT Southwestern Medical Center is committed to an educational and working environment that provides equal opportunity to all members of the University community. In accordance with federal and state law, the University prohibits unlawful discrimination, including harassment, on the basis of: race; color; religion; national origin; sex; including sexual harassment; age; disability; genetic information; citizenship status; and protected veteran status. In addition, it is UT Southwestern policy to prohibit discrimination on the basis of sexual orientation, gender identity, or gender expression.*



## DEPARTMENT OF CARDIOTHORACIC SURGERY

The **Stanford Department of Cardiothoracic Surgery** seeks to recruit a **scholar with an interest in studying cardiothoracic surgical diseases and their therapies**. Areas of investigation would include but not be limited to: atherosclerosis, genetics, molecular and cellular biology, metabolism/myocardial protection, transplant immunology, hematology/blood-prosthesis surface interface, neuroprotection, biomechanics, engineering, device development, thoracic cancer biology, cardiac development, regenerative medicine, translational therapies, and other areas.

The ideal candidate will possess PhD, MD/PhD, or other advanced academic degrees, have completed rigorous training, exemplify innovation, and demonstrate the potential for a successful track record of publishing. Appropriate resources will be made available to help the applicant develop their research program. The applicant will be expected to evolve a funded research effort focused in their area of expertise and to participate in mentorship and teaching activities in the Department of Cardiothoracic Surgery. Surgeon-scientists are also encouraged to apply and will have appropriate clinical responsibilities and resources provided.

Depending upon experience and focus, the applicant will be appointed in the University Tenure Line, the Non-Tenure Research Line, or the Medical Center Line at the Assistant, Associate, or Professor rank. The predominant criterion for appointment in the University Tenure Line is a major commitment to scholarship and teaching. The predominant criterion for appointment in the Non-Tenure Research Line is evidence of high-level performance as a researcher for whose special knowledge a programmatic need exists. The predominant criterion for appointment in the Medical Center Line is a major commitment to demonstrate excellence in the overall mix of scholarship, clinical care, and teaching.

Stanford is an equal employment opportunity and affirmative action employer. All qualified applicants will receive consideration for employment without regard to race, color, religion, sex, sexual orientation, gender identity, national origin, disability, veteran status, or any other characteristic protected by law. Stanford is committed to increasing the diversity of its faculty. It welcomes nominations of and applications from women and members of minority groups, veterans, and individuals with disabilities, as well as others who would bring additional dimensions to the university's research, teaching and clinical missions.

Applicants should send their curriculum vitae and a very brief letter outlining their interests electronically to Ms. Corrine Sanchez ([corrine.sanchez@stanford.edu](mailto:corrine.sanchez@stanford.edu)) or via regular mail to:

Philip Oyer, MD, PhD  
Search Committee Chair  
c/o Corrine Sanchez  
CVRB, Falk Bldg., Mail Code 5407  
300 Pasteur Drive  
Stanford, CA 94305-5407



Massachusetts  
Institute of  
Technology

## Koch Institute for Integrative Cancer Research and Department of Biology - Faculty Position

The Koch Institute for Integrative Cancer Research (<https://ki.mit.edu>), together with the Department of Biology (<https://biology.mit.edu/>) at the Massachusetts Institute of Technology (Cambridge, Massachusetts) invites applications for a junior faculty appointment. Appointments are expected to be in the MIT Department of Biology, but other MIT departments will be considered, if appropriate. Applicants are expected to develop and lead a vibrant, independent research program and to share our commitment to undergraduate and graduate education by teaching courses and supervising graduate and undergraduate research. We are particularly interested in candidates who will help promote and provide diversity.

The Koch Institute is an NCI-designated Cancer Center, featuring a broad spectrum of cancer relevant research ranging from basic mechanistic through to applied science. This is an open search with regard to field of study and specific research focus, but we particularly encourage applications related to basic biological mechanisms as well as computational and machine learning approaches to cancer research. The successful candidate will have laboratory space in the Koch Institute.

Applicants should include curriculum vitae, brief summaries of past accomplishments, a description of future research plans, and a statement on commitment to teaching, mentoring, diversity, and outreach that describes the candidate's experience in these areas and/or how they envision contributing to our ongoing efforts (<https://biology.mit.edu/about/diversity/>). Letters of recommendation should be sent separately from three individuals able to evaluate the candidate's accomplishments and future potential for both research and teaching.

To apply, submit application materials to <https://academicjobsonline.org/ajol/jobs/16771>. Completed applications will be reviewed starting October 1, 2020. Note that there are two other searches to fill faculty positions in the Biology Department (<http://biology.mit.edu>). Applicants may apply to any or all of the searches.

MIT is an Equal Opportunity/  
Affirmative Action employer

<http://web.mit.edu>



School of Medicine  
Columbia

## TENURE-TRACK ASSISTANT PROFESSOR

The NIH Center for Dietary Supplements and Inflammation (CDSI) at the University of South Carolina (UofSC) invites applications for two tenure-track **ASSISTANT PROFESSOR** positions with research expertise in Inflammation. The phase-2 Center of Biomedical Research Excellence (COBRE) will provide NIH research support and mentoring to junior faculty who have not received NIH R01 or similar grants as a PI, to become successful independent investigators. More information is available at: [https://sc.edu/study/colleges\\_schools/medicine/centers\\_and\\_institutes\\_new/center\\_for\\_dietary\\_supplements\\_and\\_inflammation/index.php](https://sc.edu/study/colleges_schools/medicine/centers_and_institutes_new/center_for_dietary_supplements_and_inflammation/index.php)

Candidates must have a PhD or equivalent, and at least 3 years of postdoctoral research experience. Competitive salary and startup funds are available. Please submit CV and a statement of research and teaching interests with names of 3 references to **Dr. Mitzi Nagarkatti, Chair, Department of Pathology, Microbiology, and Immunology, University of South Carolina School of Medicine, Columbia, SC 29208** by applying to: <http://uscjobs.sc.edu/postings/85684>. The search will start immediately and will continue until the position is filled.

*The University of South Carolina does not discriminate in educational or employment opportunities on the basis of race, sex, gender, gender identity, transgender status, age, color, religion, national origin, disability, sexual orientation, genetics, protected veteran status, pregnancy, childbirth or related medical conditions.*

SPECIAL JOB FOCUS:

## Neuroscience

Issue date: Oct. 2

Reserve ad space by Sept. 17

Ads accepted until Sept. 25 if space allows

To book your ad, contact:  
[advertise@sciencecareers.org](mailto:advertise@sciencecareers.org)

**The Americas**  
+1 201 748 6702

**Europe & ROW**  
+44 (0) 1273 810850

**Japan**  
+81 3 6459 4174

**Greater China, South Korea,  
Singapore, Thailand**  
+86 131 4114 0012

Produced by the Science/AAAS  
Custom Publishing Office.

### Why choose this job focus for your advertisement?

- Relevant ads lead off the career section with a special neuroscience banner.

### Expand your exposure by posting your print ad online:

- Additional marketing driving relevant job seekers to the job board
- Science online job postings are now being served to thousands of passive job seekers in the Wiley Online Library.

Science  
Careers  
AAAS

SCIENCECAREERS.ORG



FOR RECRUITMENT IN SCIENCE, THERE'S ONLY ONE SCIENCE.





**OPEN FACULTY POSITION  
INSTITUTE OF MOLECULAR BIOLOGY  
ACADEMIA SINICA, TAIWAN, ROC**

One tenure-track faculty position is open for a highly qualified individual to establish an independent research program in **all disciplines of molecular and cellular biology**. Applicants should hold a Ph.D. degree or its equivalent, with appropriate postdoctoral research experience. The successful recruit will be appointed at the levels of **Assistant, Associate, or Full Research Fellow** (equivalent to academic ranks of Assistant, Associate or Full Professor at university), and receive a generous multi-year start-up package, followed by annual intramural support.

The Institute of Molecular Biology at Academia Sinica (<http://www.imb.sinica.edu.tw/en>) provides an active and stimulating research environment. It is well supported by both extramural and long-term intramural funding, and features several core facilities (imaging, Next Generation Sequencing, RNAi, electrophysiology, FACS, biophysics, bioinformatics, transgenic core, and animal facility) that provide state-of-the-art resources and key technical expertise to the Institute's research community. Currently two Ph.D. programs, with one recruiting international students, are formally affiliated with the Institute. English is the official language for seminars and lectures at the Institute, and proficiency in Chinese language is not a prerequisite for application.

Applicants should send electronic files of their Curriculum Vitae and a description of past research accomplishments and future research plans, and should arrange for three letters of recommendation to be sent directly to **Director Hwai-Jong Cheng c/o Ms. Vivi Chiang** ([vivi@imb.sinica.edu.tw](mailto:vivi@imb.sinica.edu.tw)).

The selection process will start on **December 1, 2020** until the positions are filled. Further information can be obtained from **Ms. Vivi Chiang** at [vivi@imb.sinica.edu.tw](mailto:vivi@imb.sinica.edu.tw)

**Yale University  
School of Medicine**

**FACULTY POSITION AT THE ASSISTANT  
PROFESSOR LEVEL**

**DEPARTMENT OF CELLULAR AND  
MOLECULAR PHYSIOLOGY**

The Department of Cellular and Molecular Physiology is conducting a search for new faculty members at the assistant professor level.

The search seeks candidates whose research connects the properties of molecules to the properties of physiological systems.

Excellent opportunities are available for collaborative research, as well as for graduate and medical student teaching. Candidates must hold a Ph.D., M.D., or equivalent degree. Applicants should include a cover letter, curriculum vitae, a statement that describes past research accomplishments and future goals, and should arrange to have three letters of reference sent. Applicants should apply at the following website: <http://apply.interfolio.com/78493>

Application Deadline: **November 2, 2020**

*Yale University is an Affirmative Action/Equal Opportunity Employer and welcomes applications from women, persons with disabilities, protected veterans, and members of minority groups.*



**Tenure Track Assistant  
Professor in Chemistry or  
Chemical Engineering**

**at the Ecole polytechnique fédérale de Lausanne (EPFL)**

EPFL is a leading university with strong emphasis on basic sciences, engineering and life sciences. Research within its Institute of Chemistry & Chemical Engineering (ISIC) includes synthetic and biological chemistry, chemical engineering and physical, analytical and theoretical chemistry.

ISIC is in particular involved in a national multi-disciplinary effort to promote the development of more sustainable processes for energy and chemical production via a National Centre of Competence in Research, the NCCR catalysis, composed of about 30 research groups at EPFL, ETHZ and further Swiss Institutes and Universities: [www.nccr-catalysis.ch](http://www.nccr-catalysis.ch)

We invite applications for a tenure-track assistant professor position in all areas of chemistry and chemical engineering.

Areas of particular interest are digital chemistry, including but not limited to machine learning and automated laboratories, and biotechnology/synthetic biology related to chemical production.

We seek candidates with a strong commitment to excellence in teaching at the undergraduate and graduate levels and an outstanding research record. As professor of chemistry or chemical engineering, the successful candidate is expected to initiate and develop a creative research and teaching program at the forefront of the discipline. They will participate actively in the NCCR catalysis, as part of a multi-disciplinary effort to develop sustainable chemistry at the national and international level.

Significant start-up resources, research budget (including a fixed annual budget for salaries and consumables) and state-of-the-art research infrastructure are available. Salaries and benefits are internationally competitive. We offer a highly international environment that is multi-lingual and multi-cultural.

Applications including cover letter, curriculum vitae, publications list, concise statement of research and teaching interests as well as the names and addresses (including email) of at least three references should be submitted in PDF format exclusively via the website

<https://facultyrecruiting.epfl.ch/position/23691278>

by **November 1<sup>st</sup>, 2020**

Enquiries regarding the position may be addressed to

**Prof. Nicolai Cramer**

Director of the Institute of Chemistry & Chemical Engineering at EPFL

Email: [nicolai.cramer@epfl.ch](mailto:nicolai.cramer@epfl.ch)

Enquiries regarding the NCCR catalysis may be addressed to

**Prof. Jerome Waser**

co-Director at EPFL

Email: [jerome.waser@epfl.ch](mailto:jerome.waser@epfl.ch)

For additional information on EPFL and ISIC, please consult: [www.epfl.ch](http://www.epfl.ch) or [www.isic.epfl.ch](http://www.isic.epfl.ch)

EPFL is an equal opportunity employer and family friendly university. It is committed to increasing the diversity of its faculty. It strongly encourages women to apply.



By Dennis Macejak

## Delivering a difference

**“W**hat would you do if you were not in science?” the principal investigator asked me during a postdoc interview in Denver many years ago. I hadn’t really thought about it before. Construction? I had spent some summers in college as a frame carpenter and gotten pretty good at it. A musician? Appealing—I’m not too bad on blues harmonica—but I knew I wasn’t good enough to make a living at it. “A mailman,” I blurted out, “so I could walk around all day and think about things.” I’m not sure where the idea came from; I had just flown from New Orleans—where I completed my Ph.D.—to the Mile High City, so I was probably a bit lightheaded at the time. Little did I know then that, after a 30-year career in science, I would in fact end up as a letter carrier, making a difference in a way I never would have expected.

I first became inspired by the idea that my work could make a positive, practical impact in the world after I transitioned from academia to biotech. I had initially been attracted to scientific research by the fun of solving problems and discovering something new. During my Ph.D. and postdoctoral research, that meant uncovering the mechanisms certain viruses use to replicate in cells. But as I started in biotech and my work became more applied, I realized that my research could lead to potential treatments for human disease. I worked on developing gene therapy approaches to treat osteoarthritis and restenosis, antiviral drugs against hepatitis B and C, and—in a late-career return to academia—a less costly vaccine for human papillomavirus (HPV).

Still, none of my projects resulted in anything tangible to help people.

I also became accustomed to being bounced around by forces that felt outside of my control and to taking career opportunities as they came up. My first biotech job ended when the company restructured and my position was eliminated. I landed a job at another biotech company, but just 1 year in, it went bankrupt and I was laid off. Next, I secured a “senior postdoc” in academia—which lasted until Congress instigated sequestration in 2013, the grant that funded my project was cut, and I was out of a job again. Eventually, after some part-time consulting work with a few small startups, I decided I needed something more substantial and permanent.

I felt I still had some good years left, and that I had not yet made a difference in society, but I wasn’t able to find another full-time position in a science-related field. I started to ponder that question from my postdoc interview all those



**“I’m trained as a virologist [but] it is in my new role that I am considered an ‘essential worker.’”**

years ago. What else could I do besides science? How could I still make a meaningful contribution?

I decided to completely change gears and get a job as a letter carrier for the United States Postal Service. Even by my standards of adaptability, this last change was pretty dramatic—and a little hard to get used to. I have a Ph.D. and 30 years of experience conducting scientific research, yet here I am, delivering mail. But I try to keep an open mind. Although I miss research, I do enjoy getting to walk around and think about things. What would my life look like if, after my first biotech furlough, I had taken that interview for a director of biology position in San Francisco? Will that HPV vaccine patent I co-authored ever amount to anything? Why is my car making that noise?

Lately I’ve been thinking about the COVID-19 pandemic and my career. It’s ironic that although I’m trained as a virologist—surely an essential skill these days—it is in my new role that I am considered an “essential worker.” I certainly hope I’m helping in the fight against COVID-19 by delivering election ballots, medicines, and checks (among the bills, too, of course). Truth be told, I believe I am making a more direct and positive impact on people’s lives now than when I was in science. Finding out that viral protein X interacts with cellular protein Y was cool—but it doesn’t touch the average person on the street the way getting the mail does. ■

Dennis Macejak is a United States Postal Service letter carrier in Arvada, Colorado. Send your career story to [SciCareerEditor@aaas.org](mailto:SciCareerEditor@aaas.org).

ILLUSTRATION: ROBERT NEUBECKER